論文 / 著書情報
Article / Book Information

題目(和文)	
Title(English)	Equivalent static seismic loads for double-layered domes supported by multistorey substructures
著者(和文)	NairDeepshikha
Author(English)	Deepshikha Nair
出典(和文)	学位:博士（工学）, 学位授与機関:東京工業大学, 報告番号:甲第12217号, 授与年月日:2022年9月22日, 学位の種別:課程博士, 審査員:竹内 徹,坂田 弘安,五十嵐 規矩夫,田村 修次,石原 直
Citation(English)	Degree:Doctor (Engineering), Conferring organization: Tokyo Institute of Technology, Report number:甲第12217号, Conferred date:2022/9/22, Degree Type:Course doctor, Examiner:,,,,
学位種別(和文)	博士論文
Type(English)	Doctoral Thesis

Equivalent static seismic loads for double-layered domes supported by multistorey substructures

by

Deepshikha Nair

B. Tech., Indian Institute of Technology Bombay (2017)
M. Eng., Tokyo Institute of Technology (2019)

Submitted to the Department of Architecture and Building Engineering
in partial fulfillment of the requirements for the degree of

Doctor of Engineering

at the

Tokyo Institute of Technology

September 2022

Thesis Advisor: Prof. Toru Takeuchi

Equivalent static seismic loads for double-layered domes supported by multistorey substructures

by

Deepshikha Nair

Submitted to the Department of Architecture and Building Engineering
on June 29, 2022, in partial fulfillment of the
requirements for the degree of
Doctor of Engineering

Abstract

This thesis proposes horizontal and vertical equivalent static seismic loads for double-layered domes considering their coupled horizontal-vertical response, closely spaced modes and substructure-roof interaction. These are determined from the input horizontal acceleration at the substructure's roof level, an assumed acceleration distribution, nodal roof masses and amplification factors derived from the dynamic characteristics of the dome and substructure. Compared to the current AIJ/IASS methodology which only considers the substructure T1 mode, the greatest benefit was for substructures with dominant T2 modes (in the period range $0.2< R_{T2} <2$), with the percentage of roof members with underestimated forces dropping from 100% to just 1% when considering both T1 and T2 modes. The proposal is also extended to nonlinear multistorey structures with displacement-dependent damping devices by computing the peak horizontal acceleration of the structure using the inelastic response spectrum computed from ductility based reduction factors (as well as an alternative equivalent linearization approach). The proposed static approach is a simple and efficient alternative to the time-consuming nonlinear response history analyses for estimating the peak roof response at the preliminary design stage.

Thesis Advisor: Prof. Toru Takeuchi

Nomenclature

Acronyms

BRB	Buckling-restrained brace
BRBF	Buckling-restrained brace frame
CQC	Complete quadratic modal combination rule
DBE	Design basis earthquake intensity level
LRHA	Linear response history analysis
MCE	Maximum considered earthquake intensity level
MRF	Moment resisting frame
NLRHA	Nonlinear response history analysis
RSA	Response spectrum analysis
SLE	Serviceability earthquake intensity level
SRSS	Square-root-of-sum-of-squares combination rule

Greek symbols

α	Substructure stiffness variation factor
β	Modal participation factor
Γ	Modal mass participation factor
μ	Displacement ductility
ϕ_i	i^{th} mode shape vector
σ_y	Minimum yield stress
θ	Half-subtended angle of sphere/dome

Roman Symbols

A_c	Core area of BRB
A_e	Elastic area of BRB

L_p	Plastic length of BRB
Δ	Roof-level displacement of substructure
${}_rf$	Median response ratio of response parameter r
A_H	Horizontal acceleration
A_i	Elastic acceleration of substructure (roof level) in i^{th} mode
A_V	Vertical acceleration
C_d	Displacement amplification factor
D_{hi}	Response reduction ratio (Kasai) in i^{th} mode
D_i	Elastic displacement of substructure (roof level) in i^{th} mode
DR_i	Dominance ratio in i^{th} mode
E	Young's modulus
F'_H	Modified horizontal roof amplification factor
F_H	Horizontal roof amplification factor
F'_V	Modified vertical roof amplification factor
F_V	Vertical roof amplification factor
h_{eqi}	Equivalent damping ratio in i^{th} mode
K_{1i}	Initial substructure stiffness (pushover curve) in i^{th} mode
K_{2i}	Post-yield substructure stiffness (pushover curve) in i^{th} mode
K_{eff}	Effective axial stiffness of BRB
K_{eqi}	Secant stiffness of i^{th} substructure mode
L	Span of the dome
L_t	Total length of BRB
M	Major axis bending moment
M_{eqi}	Effective seismic mass in i^{th} mode
N	Axial force
p	Post-yield stiffness
R	Response reduction factor from ASCE-7
R_μ	Ductility reduction factor
R_{ai}	Reduction in substructure acceleration in i^{th} mode
R_{di}	Reduction in substructure displacement in i^{th} mode

R_{Mi} Mass ratio of ${}_sM_{eqi}$ and ${}_rM_R$

R_{Ti} Period ratio of T_i and T_R

S_{ai} Spectral acceleration of i^{th} mode

T_1 Fundamental (translational) period (T1) of substructure model

T_2 Second (translational) period (T2) of substructure model

T_R Fundamental (O1 mode) period of domed roof model

T_{eqi} Secant substructure period in i^{th} mode

V Base-shear force

Subscript symbols

${}_cb$ Parameter b obtained from combined model

${}_rb$ Parameter b obtained from roof model

${}_sb$ Parameter b obtained from substructure model

b_{T1+T2} Parameter b obtained considering substructure T1 and T2 modes

b_{T1} Parameter b obtained considering substructure T1 mode only

Contents

Contents

Contents

Chapter-1: List of Figures

Chapter-2: List of Figures

Chapter-3: List of Figures

Chapter-4: List of Figures

Chapter-5: List of Figures

Chapter-6: List of Figures

Chapter-2: List of Tables

Chapter-3: List of Tables

Chapter-4: List of Tables

Chapter-5: List of Tables

Chapter-6: List of Tables

Chapter 1

Introduction

Contents

1.1 Background

The interest in metal latticed domes can be traced back to the development of materials when domes made of concrete and requiring complicated framework started to become rather expensive. Because of the high cost of the alternative material- aluminium, majority of the structures were built with steel. After the second world war, the lattice dome, which is essentially a hollow hemisphere that has evolved from the basic arch form became popular. It is defined by the radius of the sphere and the half-subtended angle of the cutting plane. The famous designer, Richard Buckminster Fuller, played an instrumental role in reviving the attention of designers to this structural shape through his patented geodesic dome. The pattern of a geodesic dome is generated by subdividing the faces of a regular polyhedron, and projecting the subdivided polyhedron onto the surface of its circumscribed sphere. Being one of the most efficient lightweight structural forms, it can span vast distances in an economical way. This also provides an added advantage of reduced inertial forces transferred to the supports during earthquakes.

Structurally, domes can be divided into two main groups:

1. Single-layered Domes

   These domes consist of a single layer of sheet on which the nodes and members, which are either straight or curved, are placed. These domes are used to cover clear spans of up to 100m. Typical structural shapes for grid of dome members include triangle and square (Figure 1-1 (a) and (b)). Usually, single layer gridshells are very thin compared with span dimensions, and they provide practically no depth to install equipment, although recent applications have employed transparent covers made of glass or membrane that are designed as skylight to allow sunlight inwards or artificial light outwards at night. Structurally, single layer reticulated shells are quite flexible in the out-of-plane direction, making them prone to shell-like buckling, if no appropriate measures against instability are taken [1].

2. Double-layered Domes

   These domes (Figure 1-1 (c) and (d)) consist of two layers of parallel sheets where the members and nodes are placed. These members are connected by web members

that provides the depth to increase the out-of-plane stiffness to stabilise the structure. The larger bending stiffness enables the spanning of longer distances. These domes are also typically found in regions of high-seismic demand where out-of-plane roof displacements have been proved to be the primary cause of failure of gymnasium roofs in earthquakes [2], [3]. Researchers studying optimum designs of space structures also sometimes refer to such dome shaped gridshell structures as 'dome-shaped truss' [4] or 'dome-truss' [5].

Single layer

(a) Square grid (b) Triangle grid

Double layer

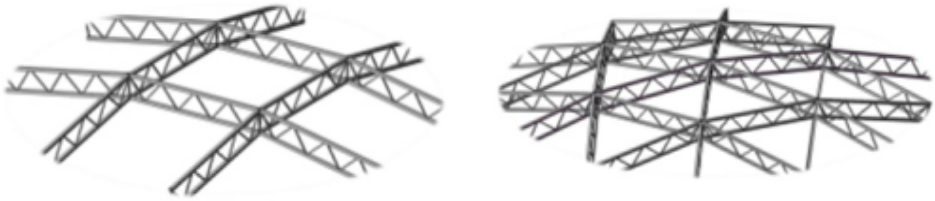

(a) Square grid (b) Triangle grid

Figure 1-1: Grid types in dome [6]

1.2 Realised large-scale domed roofs

This section reviews (selected) four selected long-span steel domed structures that have been realised in the past. Researchers have summarised the history of realised shell and

spatial structures in several reports [7]–[9].

Nagoya dome (Figure 1-2(a)) is a multi-purpose stadium located in Japan, with a seating capacity of 40,500 spectators for a baseball game. The roof is designed as a single-layer steel lattice dome to minimise the shadow effects from sunlight and to meet the required ceiling height demand of 60m for baseball. The roof has a span of 187.2m, which makes it one of the largest single-layer lattice dome structures in the world. To realise this large-scale single-layer dome, the effects of construction imposed geometrical imperfections have been analysed in detail by the design team as reported by Sahashi et al. [10].

Osaka Dome (Figure 1-2 (b)) is a multi-purpose entertainment complex with a seating capacity of up to 55,000 people located in the city of Osaka. The design of roof as a dome allows for a large indoor space that can be used for a variety of events. The central dome is a steel lamella which transitions into Y-shaped steel girders spaced equidistantly along the perimeter with a perimeter compression ring [11]. The ceiling consists of concentric 'super-rings' that move according to acoustic and weather needs.

Fukuoka Dome, (Figure 1-2(c)) is Japan's largest stadium with a retractable roof [12]. It is also a multi-purpose facility which can be used for baseball and other sports, exhibitions, concerts, and even trade shows, as the roof can be kept open or closed as required. It has a maximum seating capacity of 52,000. The roof has a maximum span of about 213m and the crown of the roof has a height of 84m above the ground. It consists of three spherical lamellar panels with a rise-to-span ratio of 0.2.

Civic Arena in Pittsburgh USA (Figure 1-2(d)) was the first sports venue with a heavy retractable roof [13]. The dome structure is made of tapered steel truss with a span of 126m (the largest at the time). It was constructed in 1961 and consisted of 6 movable 300-ton radial leaves that would rotate on perimeter rails and two additional leaves are fixed segments supported by a fixed 260-foot-long cantilevered central box beam [14], [15]. It is still considered an engineering marvel for being realised in an age without computer modelling.

(a) Nagoya Dome (184 m)

Photo by Yoshito Isono [16])

(b) Osaka Dome (167 m)

Photo by Kenpei [17]

(c) Fukuoka Dome (212 m)

Photo taken from [18]

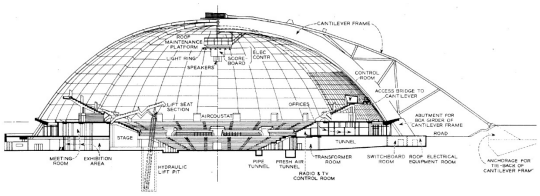

(d) Civic Arena Section view (126m)

Photo taken from [15]

Figure 1-2: (Selected) Realised Long-span Domes and spans

1.3 Damage to curved gridshell roofs

Structural and nonstructural damage to gridshell roofs in past earthquakes have been extensively documented in Japan and China. Compared to other regular buildings structures, spatial structures generally experienced less damage [7]. As a result, few of these structures in China which did not sustain severe damage during the earthquake were used as post-earthquake emergency shelters.

In the past earthquakes in Japan, steel gridshell domes typically suffered damage due to buckled (or fractured) substructure braces or the failure of bearings at the substructure-roof joints, and so the roof remained relatively undamaged [19]. The seismic retrofit, therefore, involved replacing the braces in the substructure with energy dissipating dampers with low yield strength, which reduced the substructure's peak response thereby reducing the roof's horizontal and vertical roof response [19]. Nevertheless, some prominent examples of damage to domes and gridshells from past earthquakes are shown below.

(a) Damage to the roof trusses in gymnasiums (as shown in Figure 1-3) was observed in the 2016 Kumamoto earthquake due to the asymmetric vertical roof response, and roof-substructure interaction as a result of the out-of-plane response of the concrete substructure [20].

(a) Curved space truss roof (b) Buckled roof chord members

Figure 1-3: Damage to a curved high-school gymnasium roof in Kumamoto [7], [20]

(b) One gridshell lattice shell roof in Mianyang city in China experienced partial damage to the roof as a result of the effect of substructure response to the Wenchuan earthquake in 2008. Cantilever columns supported the bolted grid shell. During the

earthquake, displacements on top of the columns exceeded the design limit, causing some members attached to the supports to collapse or buckle (Figure 1-4).

(a) Grid shell roof (b) Buckled roof members

Figure 1-4: Seismic damage to Mianyang gridshell roof due to substructure's out-of-plane response [7]

(c) The Lushan Gymnasium (which was reconstructed after the major Wenchuan earthquake in China) was a double-layer lattice dome with an inclined arch (Figure 1-5a). Due to the Ya'an (Lushan) earthquake in 2013, there was extensive damage to the Gymnasium, including permanent displacements in the lattice roof and bearing failures. Global buckling, fractures, and failures of bolted connections at spherical nodes were typical causes of damage to the members of the truss (Figure 1-5b). The overall damage was visually inspected and quantified in Figure 1-5c. The anchor bolts at two of the bearings at the top of the RC columns were seen to be loosening and displacing slightly, while the anchor bars at two of the nine ground supports showed inelastic elongation and fracture. According to a visual inspection, 131 of the shell's truss members were damaged, including 17 top chords, 36 bottom chords, 70 web members, and eight supporting struts. Most of the damage was attributed to higher mode vibration characteristics of irregular special shape, large vertical ground motions, and the mixed use of flexible and fixed supports that may have had a major impact on the global dynamic behaviour of these structures.

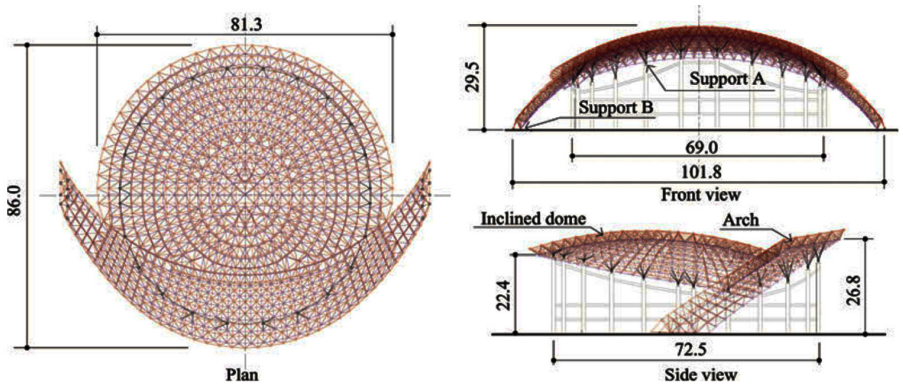

(a) Lushan gymnasium: domed roof with inclined arch

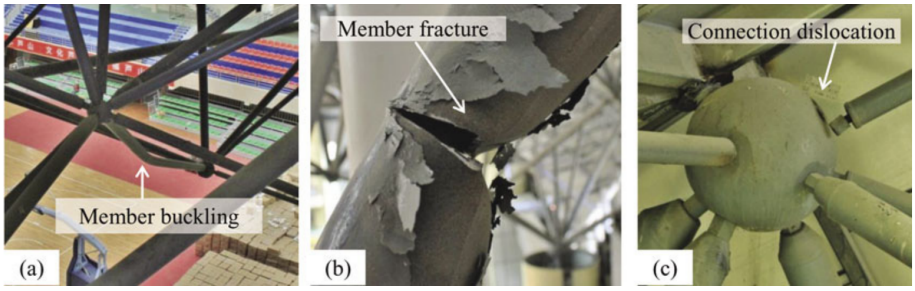

(b) Lushan gymnasium: Buckled/fractured roof members and bolted connection failure

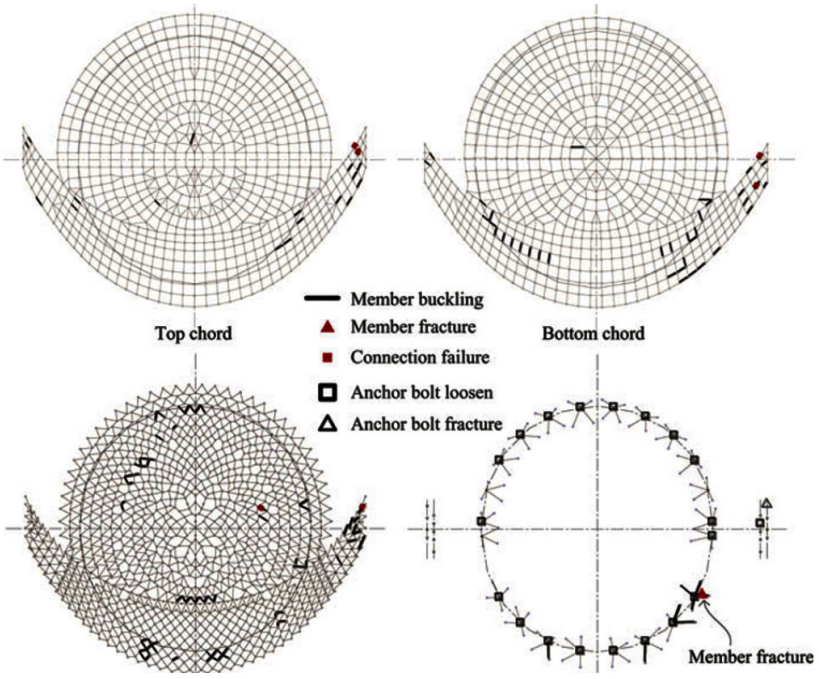

(c) Lushan gymnasium: Distribution of damage from the earthquake

Figure 1-5: Seismic damage to Lushan gymnasium's domed roof [7]

(d) Damage to non-structural elements: Every recent major earthquake has severely

damaged ceilings and non-structural elements, such as suspended lights and partition walls. Figure 1-6 illustrates typical damage patterns caused by the asymmetric roof response [2], [7], [21], [22].

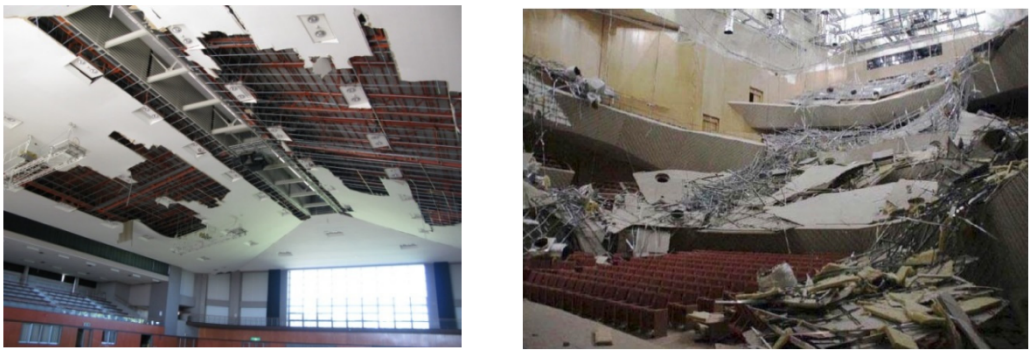

Figure 1-6: Ceiling damage and collapse [7]

1.4 Seismic response evaluation methods

Before the early 1900s, the conventional design approach was to design the roof to remain elastic, and the horizontal seismic loads were considered by adopting a horizontal base shear at the base of the roof and distributing it along the roof [7], [8], [23]. Following this approach, many medium or short-span domed structures were designed to remain elastic while considering the effect of horizontal seismic forces. The current proposal of considering anti-symmetric vertical loads from horizontal seismic input (the primary focus of this thesis) may therefore be applied to such structures to quickly check the capacity of existing domes, particularly before the 1980s when the computational capacity of digital computers was limited, without conducting the time- and data-intensive NLRHA.

After the 1995 Kobe earthquake, studies on the dynamic behaviour of large-scale structures began rapidly [8], [23]. Recent years have also seen numerous research efforts been directed towards the study of seismic response of dome systems. Selected work is reviewed and summarised in this section which is categorised as follows. The first subsection introduces the studies on elastic response of a simple arch, followed by those on the medium-span domes. The following subsections discuss the valuation methods for estimating the linear response for domes with single-storey substructures, and is followed by the subsection on nonlinear response evaluation methods. The nonlinear response is focused on substructures with braces (which is the focus of this thesis). Finally, the response of an elastic multistorey substructure is discussed and a summary of the current response evaluation methods for a domed roof is presented.

1.4.1 Response of a simple arch

Study conducted by Jung et al. [24] was among the earliest studies to develop static seismic forces for the design of arches. Simple arch models with varying parameters were constructed as shown in Figure 1-7.

They observed that the peak acceleration response in both the horizontal and vertical directions mainly consisted of the first and second dominant asymmetric and symmetric mode shapes. Further, simple equations to represent the equivalent horizontal and vertical

static seismic forces were proposed as shown in Figure 1-8 for aches with half-subtended angle greater than 45°. Among the four response parameters that consist of the maximum acceleration, displacement, extreme fiber stress and the reaction force response, the static load coefficients obtained from the maximum acceleration response were adopted as they showed the highest amplitude.

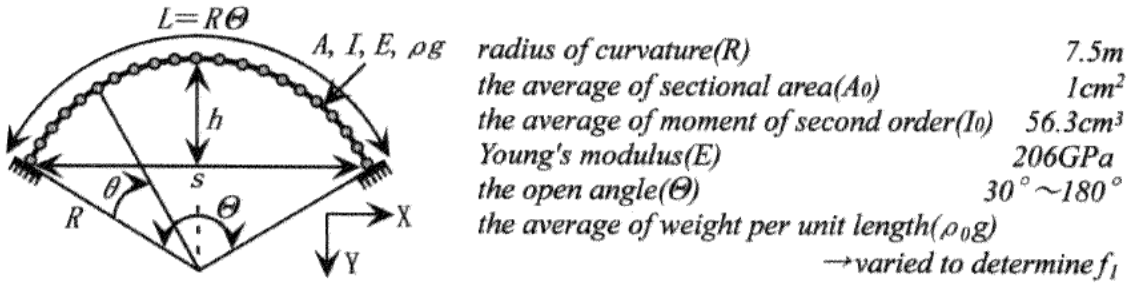

Figure 1-7: Geometry and Parameters of arch model [24]

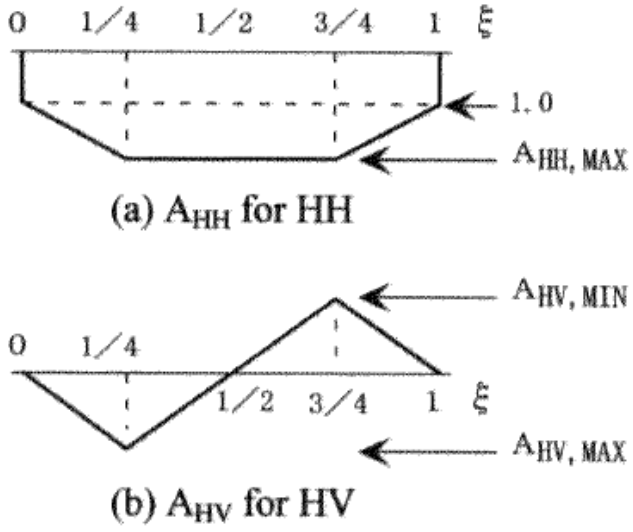

Figure 1-8: Seismic intensity distribution function to evaluate seismic loads in the horizontal and vertical directions [24]

Amplification factor approach

Takeuchi et al. [25] studied the seismic response of a simple-arch model to quantify the anti-symmetric response. The arch model shown in Figure 1-9 has three masses, spring hinges and rigid axial stiffness, which captures the asymmetric out-of-plane mode shape that generally governs the dynamic response. The modal participation factor (β_{R1}) and effective mass (M_{R1}) of the asymmetric out-of-plane mode are expressed in Equations 1.1a and 1.2b, where m is the diagonal nodal mass matrix and I_x is the identity vector with the x components. The in-plane effective mass (M_{R2}) is then given by Equation 1.3. This captures the modal mass of the axial vibration modes, but since the axial stiffness is assumed to be infinite [25], the spectral acceleration of these modes is identical to the input ground acceleration ($S_{A2} = S_{Ag}$).

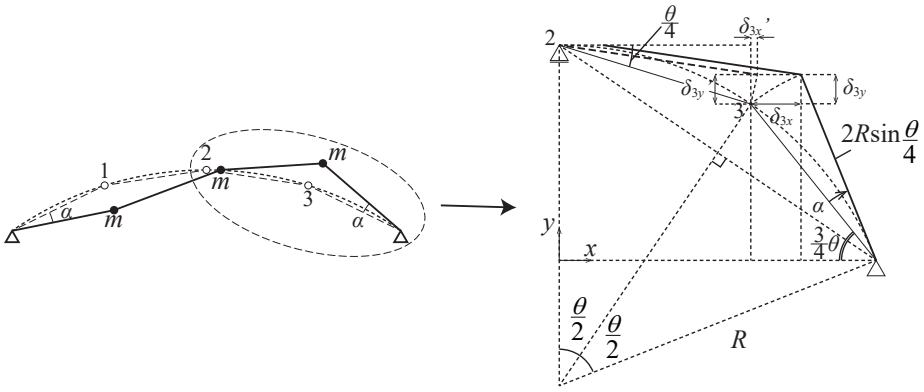

Figure 1-9: Asymmetric mode of the 2-d arch model [25]

$$u^T = u\left[\sin\frac{3}{4}\theta, -\cos\frac{3}{4}\theta, 2\sin\frac{\theta}{4}, 0, \sin\frac{3}{4}\theta, \cos\frac{3}{4}\theta\right] \tag{1.1a}$$

$$u = 2R\alpha\sin\frac{\theta}{4} \tag{1.1b}$$

$$\beta_{R1} = \frac{u^T m I_x}{u^T m u} = \frac{\sin\frac{3}{4}\theta + \sin\frac{\theta}{4}}{u\left(1+2\sin^2\frac{\theta}{4}\right)} \tag{1.2a}$$

$$M_{R1} = \frac{\left(u^T m I_x\right)^2}{u^T m u} = \frac{2m\left(\sin\frac{3}{4}\theta + \sin\frac{\theta}{4}\right)^2}{1+2\sin^2\frac{\theta}{4}} \tag{1.2b}$$

$$M_{R2} = M_R - M_{R1} = 3m\left(1 - \frac{2\left(\sin\frac{3}{4}\theta + \sin\frac{\theta}{4}\right)^2}{3\left(1+2\sin^2\frac{\theta}{4}\right)}\right) \tag{1.3}$$

The out-of-plane modal mass M_{R1} increases with the half-subtended angle θ, which corresponds to a greater contribution from the asymmetric out-of-plane mode, while M_{R1} reduces to zero when $\theta = 0$. The maximum response of the roof can thus be expressed by combining the base ground motion and out-of-plane mode's response. The response amplification factors are defined as the response of roof divided by the base acceleration, which is equal to the peak ground acceleration S_{Ag}. Assuming the asymmetric mode T_R lies on the constant acceleration region of the spectrum such that $S_{A1} = S_{AP}$ [25], the amplification factors F_H and F_V may be derived as the horizontal and vertical components of F in Equation 1.4a. These equations have been validated using CQC and linear response history analyses [25].

$$A_R = \sqrt{(S_{A1}\beta_{R1}u)^2 + \left(S_{A2}I_x\left(\frac{M_{R2}}{M_R}\right)\right)^2} \tag{1.4a}$$

$$F = \frac{A_R}{S_{Ag}} = \sqrt{\left(\frac{S_{AP}}{S_{Ag}}\beta_{R1}u\right)^2 + \left(I_x\left(\frac{M_{R2}}{M_R}\right)\right)^2} \tag{1.4b}$$

1.4.2 Response of medium-span domes

Study conducted by Ogawa et al. [26] was among the earliest studies to have revealed that in addition to horizontal accelerations, medium spanned domed roofs with some rise are subjected to large anti-symmetric vertical accelerations even under horizontal earthquake motions (Figure 1-10). This is mainly due to their inherent shell-like geometry which depends on the rise of the dome and the horizontal span.

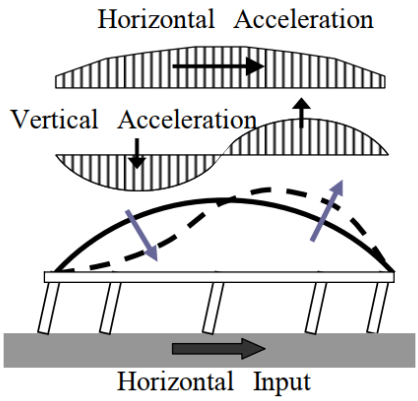

Figure 1-10: Excited roof response under horizontal seismic input

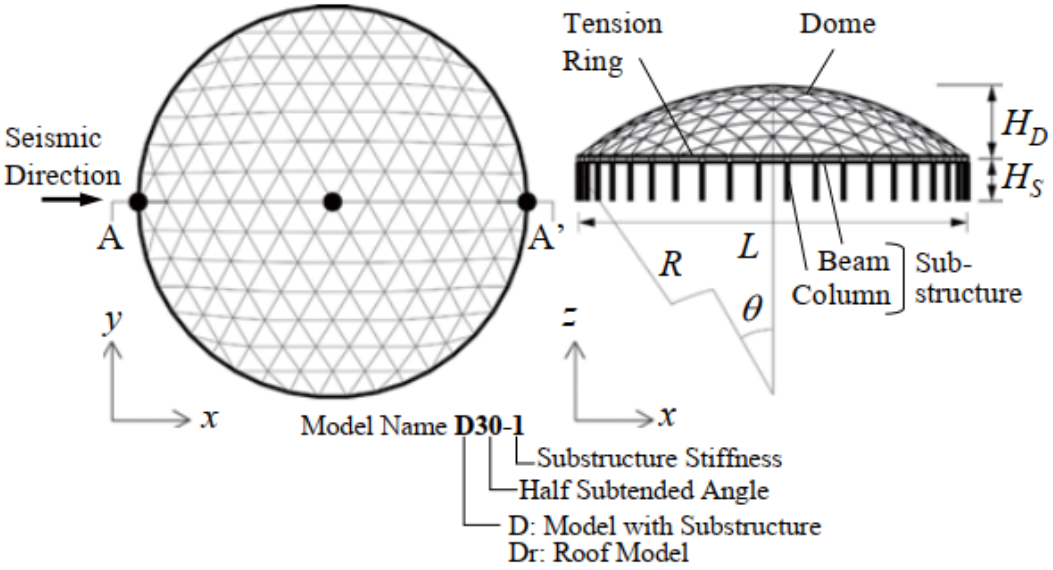

Figure 1-11: Lattice Dome model with Single-storey substructure [27]

The seismic response characteristics were found to be complicated as the dome exhibits a large number of parallel vibration modes. A parametric study for three types of single layer lattice domes (span of about 60m) as shown in Figure 1-11 with various half subtended angles was conducted. The response values were evaluated using the SRSS method and the CQC method, and compared with those of the time history response analyses. It was concluded that, in the half subtended angle from 20 to 40, the trends of the distribution of the maximum response are similar. In addition, the results from the response spectrum analyses including a combined mass participation of 90% were found to be are nearly equal to those at 100% participation (Figure 1-12).

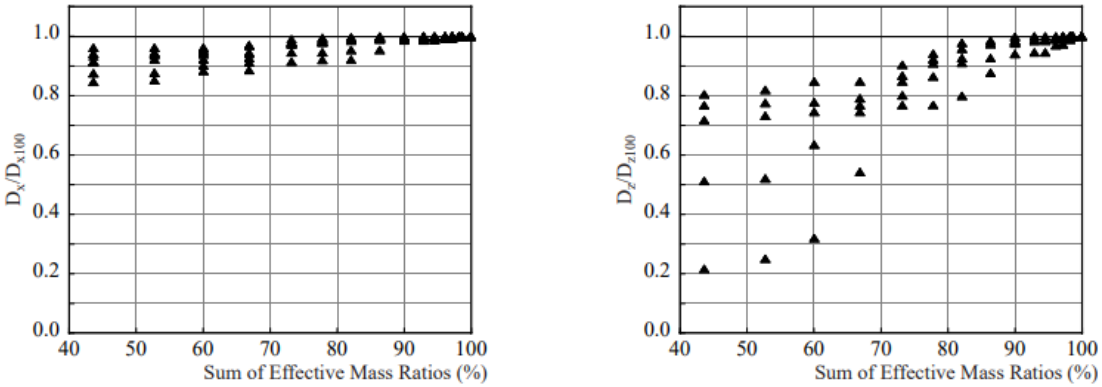

(a) Horizontal Displacements (b) Vertical Displacements

Figure 1-12: Effect of Combined Mass participation ratio on the response accuracy [26]

Kato et al. [28] studied the seismic response of single-layer 60m spanned domes of various configurations with different rises and dead loads subjected to horizontal ground motions as shown in Figure 1-13(a). Elasto-plastic dome members were modelled to capture post-yield behaviour and estimate the peak accelerations that lead to collapse.

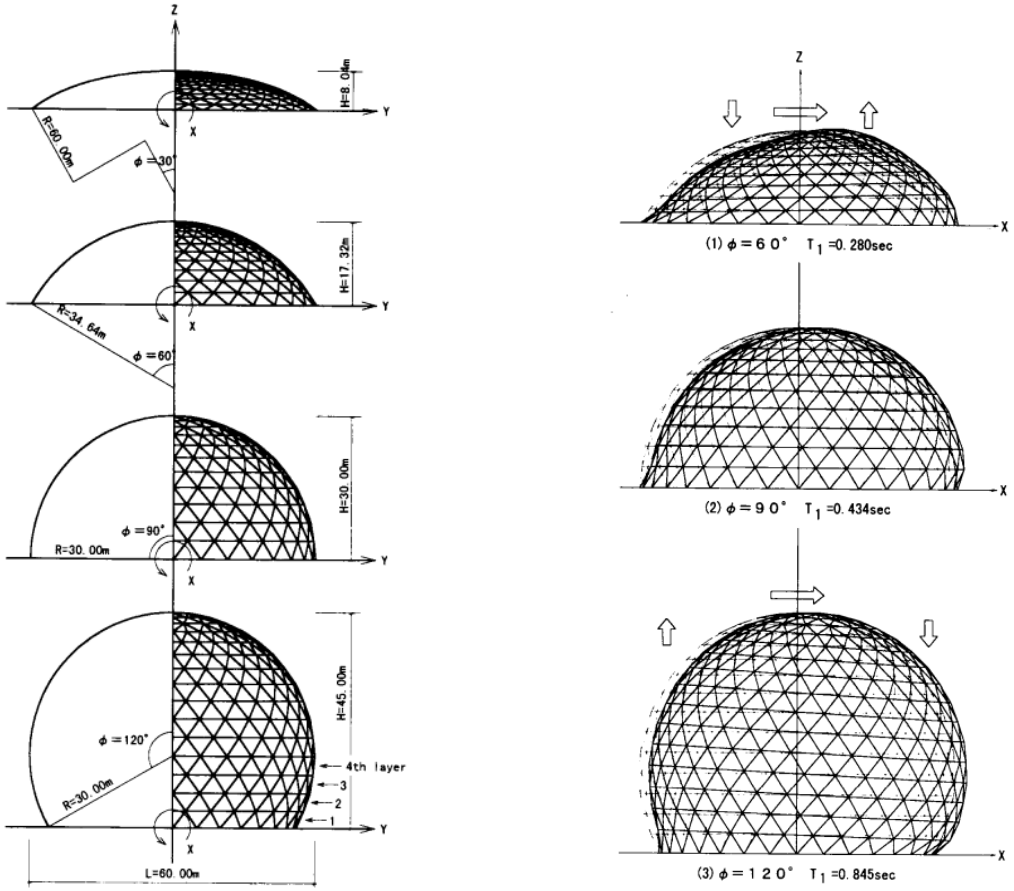

(a) Analytical models (b) Dominant fundamental modes in high-rise domes

Figure 1-13: Single-layer domes studied by Kato et al. [28]

It was found that in low-rise domes, the vertical response was equal to or greater than the horizontal response . However, multiple modes contributed to the overall response and no single predominant mode was identified. Nevertheless, equivalent seismic coefficients were proposed based on linear response history analyses and obtaining the peak nodal accelerations at the time when a selected roof member reaches its peak response value [28].

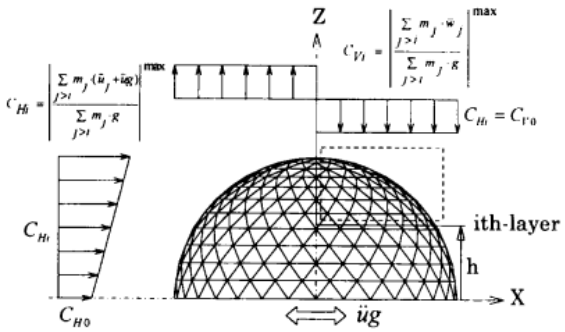

Figure 1-14: Derivation of shear coefficients in high-rise single-layer domes [28]

For single-layer domes with higher rises, Kato et al. [28] found that the fundamental mode as shown in Figure 1-13(b) was the governing mode in determining the overall response. The peak accelerations at the nodal points obtained from the linear response history analyses were used to formulate the horizontal (C_{Hi}) and vertical (C_{Vi}) shear coefficients as given below in Equations 1.5-1.8, where $\beta(\phi)$, $\alpha(\phi)$ and $\gamma(\phi)$ are empirical functions of the half-subtended angle ϕ, and H and h correspond to the height of the top and the height of the i^{th} layer, respectively. It was observed that the vertical coefficient C_{Vi} was constant along the height while the horizontal coefficient C_{Hi} varied linearly along the height. Note that these equations have been proposed and verified for high-rise domes with half-subtended angles in the range of 60°-120°.

$$C_{Hi} = C_{Ho}(1+\beta(\phi)h/H) \tag{1.5}$$

$$C_{Ho} = \alpha(\phi)S_a(T_1)/g \tag{1.6}$$

$$C_{Vi} = C_{Vo} \tag{1.7}$$

$$C_{Vo} = \gamma(\phi)C_{Ho} \tag{1.8}$$

Dominant modes in single- and double-layered domes

Takeuchi et al. [27] also carried out studies to understand the response characteristics of medium sized domes (span=60m). In the case of single-layer lattice domes, the first mode (the fundamental mode) is not necessarily dominant, and so many higher roof modes with similar periods tend to participate in the overall response as shown in Figure 1-15. Furthermore, the number of modes required to achieve an effective mass ratio of 90% is also quite large [26], [27]. Note that the proposed amplification factor approach in this thesis (Chapter-3 and Chapter-4) may not efficiently capture all these local higher roof modes' responses and lead to underestimation, if used directly on single-layer domes.

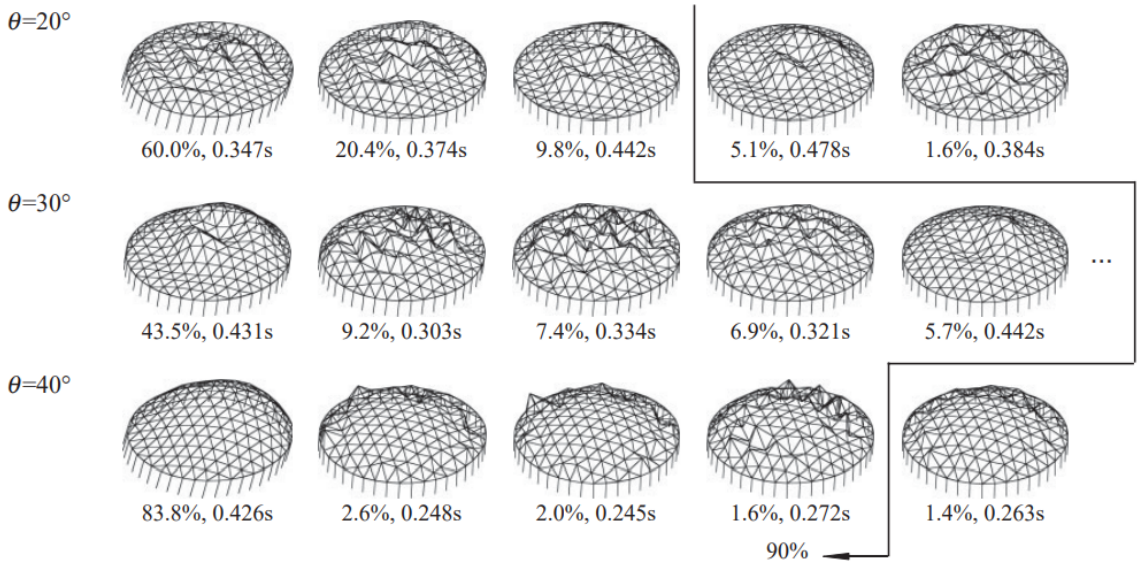

Figure 1-15: Single-layer domes: participating modes and the mass participation ratio (effective mass in %) [27]

It was observed that the number of modes required for a combined mass participation of 90% decreased drastically when the out of plane stiffness increased from R1 to R100 as shown in Figure 1-16 and Figure 1-17 [27]. Such domes with sufficient out-of-plane stiffness are termed as double-layered domes. These modes were found to consist primarily of four prominent mode shapes: asymmetrical 1 wave (O1), asymmetrical 2 wave (O2), asymmetrical 2.5 wave (O2.5), and an in-plane (I) wave as shown in Figure 1-18. It was concluded that the response characteristics are considered to be simpler when the out-of-

plane stiffness of the members of the roof is relatively large. This is typically observed in roofs with a double-layer of members separated by a distance to obtain additional out-of-plane stiffness.

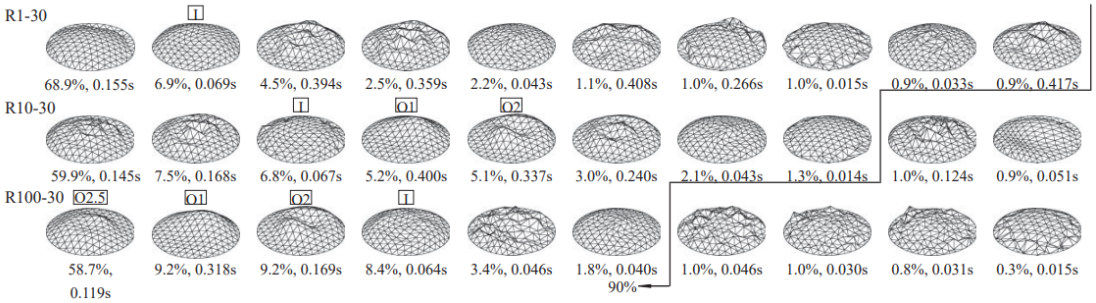

Figure 1-16: Relationship between out-of-plane stiffness and major modes (θ =30 deg.) [27]

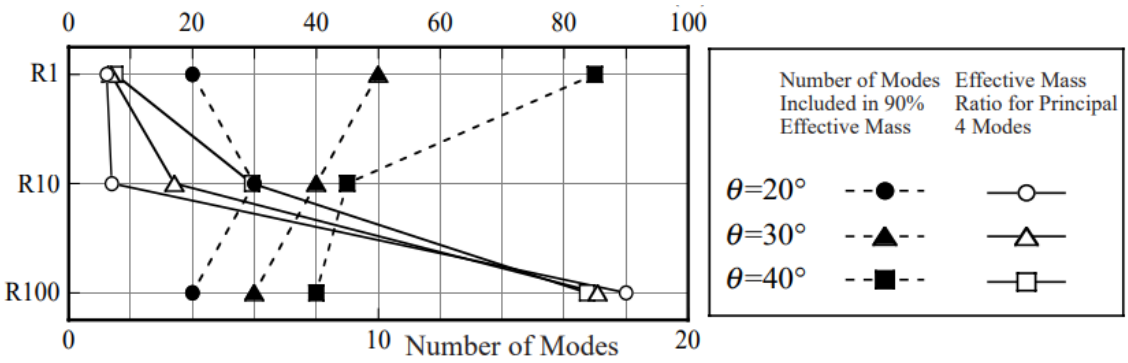

Figure 1-17: Required no. of modes vs out-of-plane stiffness [27]

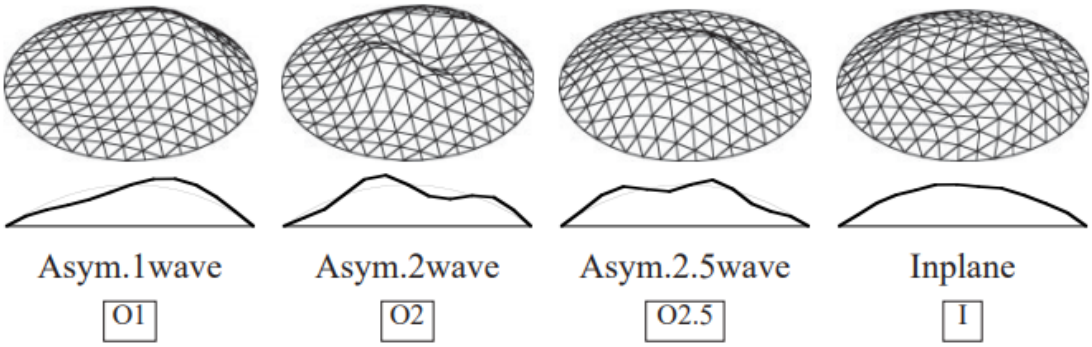

Figure 1-18: Four dominant roof modes of double-layered domes [27]

1.4.3 Linear response estimation: Domes with single-storey substructures

Amplification factor approach

The amplification factor approach in Section 1.4.1 was then extended to more complex 3-d domes and cylindrical roofs with single-storey substructures using 3-d models modelled using beam elements. Takeuchi et al. [25], [27] studied 60m spanned domes and cylindrical gridshells and varied the substructure stiffness to understand the dominant roof modes as shown in Figure 1-19. The peak ridgeline acceleration response was then investigated using response-spectrum analyses using the four dominant modes combined using the CQC method. It was confirmed that the the sway mode governs the response from soft or flexible substructure (F0.1-30), where the horizontal acceleration envelope is almost flat and there is negligible vertical response as shown in Figure 1-20. Furthermore, in F10 and F1 models with increased substructure stiffness, the dome roof and the substructure modes interact with each and the peak response can be evaluated using response-spectrum analyses considering just the combination of the principal 4 modes. For example, the two peaks appearing in the vertical acceleration response in the F10-30 model can be explained by a combination of the O2 and O2.5 mode response, and the O1 mode governs the response of the F1 model. Response spectrum analyses considering only the predominant or principal modes were found to sufficient to obtain the overall envelope, thus simplifying the complex response characteristics of domes with substructures.

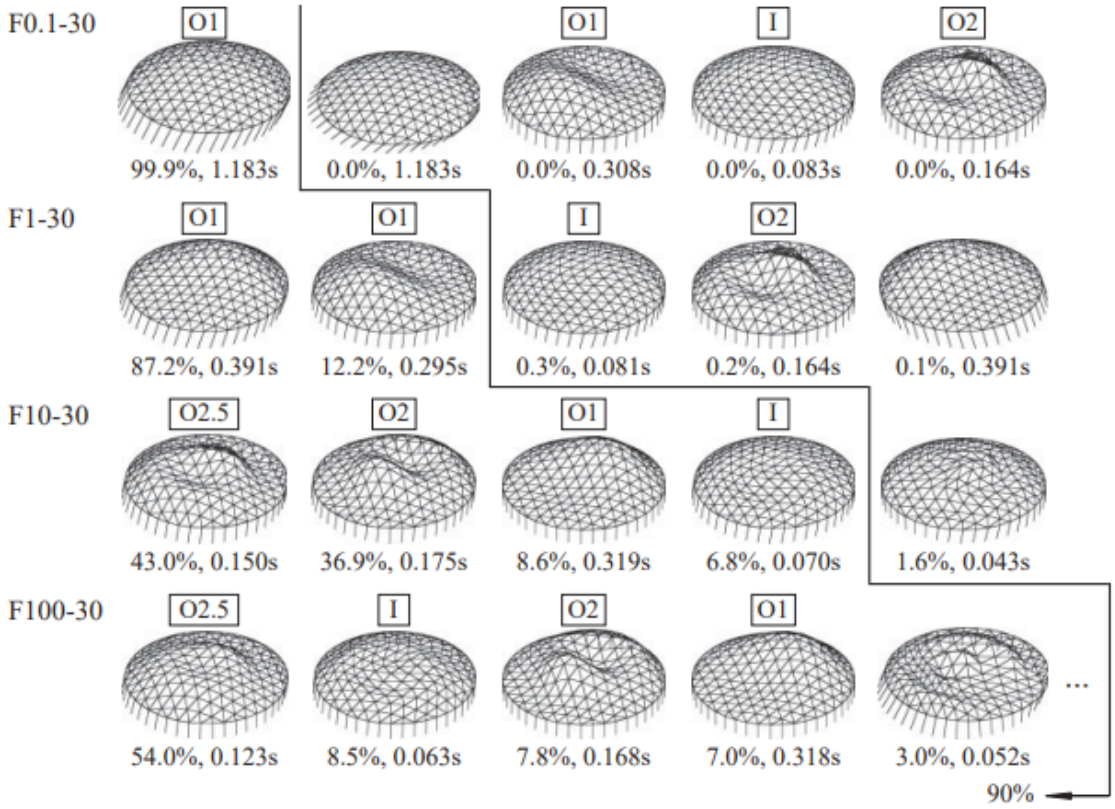

Figure 1-19: Single-storey analysis models and dominant modes [27]

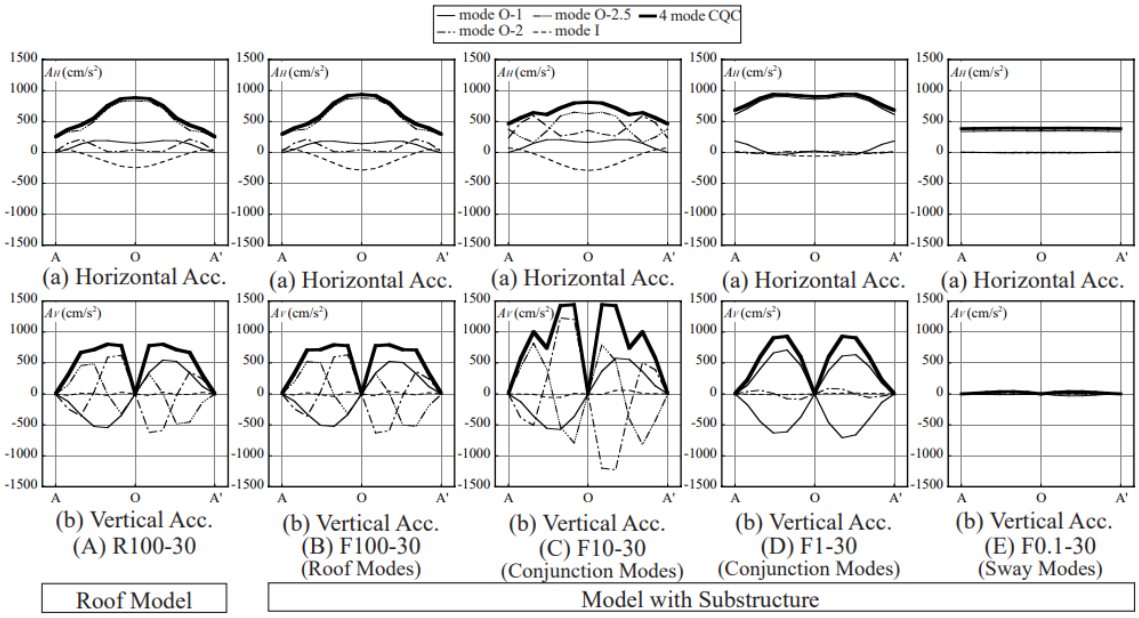

Figure 1-20: Effect of substructure stiffness on the peak acceleration response [27]

The substructure-roof representation is depicted in Figure 1-21 [25]. Since multiple roof modes (O1, O2, O2.5 and I) contribute to the overall response, the amplification factors were obtained using results directly obtained from the response spectrum analyses. Simple horizontal and vertical amplification factor curves were proposed by dividing the peak roof response by the peak substructure response [25]. The amplification factors for these cases were derived using Equation 1.9, which replaces the ground acceleration with the maximum acceleration at the top of the substructure A_{Heq} and S_{A1} with the spectral acceleration of the out-of-plane modal roof mass M_{R1} ($S_{A1} = S_{AR1}$) [25].

$$F = \frac{A_R}{A_{Heq}} = \sqrt{\left(\frac{S_{AR1}}{A_{Heq}}\beta_{R1}u\right)^2 + \left(I_x\left(\frac{M_{R2}}{M_R}\right)\right)^2} \tag{1.9}$$

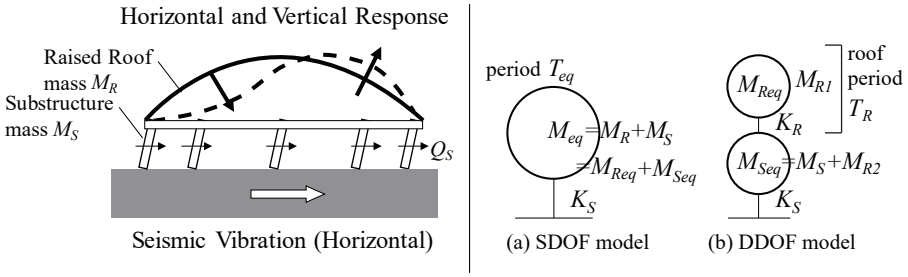

Figure 1-21: Raised roof response and combined model as an equivalent DDOF model [25]

Mass and period ratios

The amplification factors arising from the roof-substructure interaction mainly depend on the ratios of mass (R_M) and period (R_T) [25] defined in Equation 1.10. These are formulated as ratios of the effective mass (M_{eq}) and period (T_{eq}) of the substructure SDOF model (Figure 1-21(a)), which includes the roof mass, relative to the total roof mass (M_R) and the period of the dominant O1 roof mode (T_R) (Figure 1-21(b)). Therefore, a larger R_M or R_T ratio represents a heavier and more flexible substructure, such that both ratios increase as storeys are added.

$$R_M = \frac{M_{eq}}{M_R}, \quad R_T = \frac{T_{eq}}{T_R} \tag{1.10}$$

Roof amplification factors

Equations 1.11 and 1.12 define the proposed amplification factors F_H and F_V for the horizontal and vertical directions and are compared with the obtained amplification factors derived using Equation 1.9 in Figure 1-23; where θ is the dome's half subtended angle, R_T in Equation 1.10 is the ratio of equivalent period of the SDOF model (Figure 1-21(a)) to that of the roof O1 mode, R_M in Equation 1.10 is the ratio of SDOF model to roof mass. The influence of half-subtended angle was also studied by analysing the peak roof response normalised by the peak acceleration of the spectrum S_{AP} (Figure 1-22) using roof models without substructures and a vertical calibration factor C_V of 1.88 was proposed [25].

$$F_H = \begin{Bmatrix} 3 & (0 < R_T \leq 5/16) \\ \sqrt{5/(4R_T)} & (5/16 < R_T \leq 5/4) \\ 1 & (5/4 < R_T) \end{Bmatrix} \tag{1.11}$$

$$F_V = \begin{Bmatrix} 3C_V\theta & (0 < R_T \leq 5/16) \\ (\sqrt{5/R_T} - 1)C_V\theta & (5/16 < R_T \leq 5) \\ 0 & (5 < R_T) \end{Bmatrix} \tag{1.12}$$

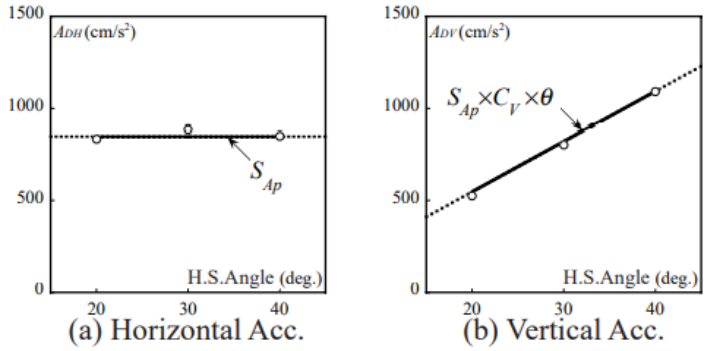

Figure 1-22: Calibration factor to account for the influence of half-subtended angle [27]

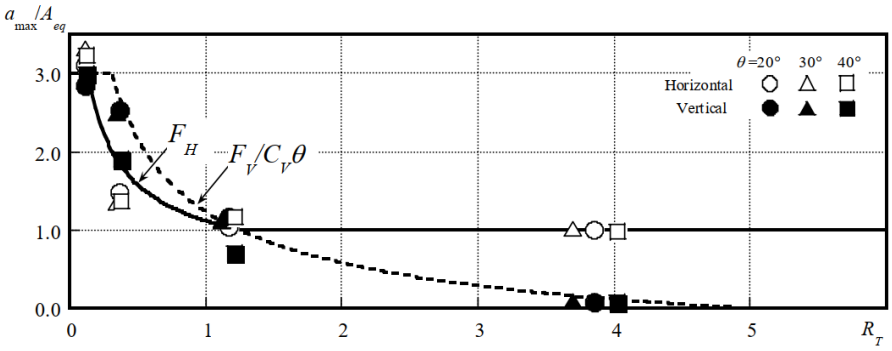

Figure 1-23: Horizontal and vertical amplification factors [25], [27]

Peak roof response

Equations 1.13-1.14 were then used to obtain the acceleration distributions A_H and A_V across the dome using the peak acceleration of the SDOF model A_{Heq} (Figure 1-21); where x and y are the coordinates of roof nodes with $\{x,y\} = \{0,0\}$ as the centre and L is the span of the dome. The equivalent static loads were then validated against response spectrum analyses results as shown in Figure 1-24 [27].

1. Horizontal acceleration distribution

   The envelope of the horizontal acceleration response was defined using the O1 modeshape as follows:

$$A_H(x,y) = A_{Heq}\{1 + (F_H - 1)\cos\frac{\pi\sqrt{x^2+y^2}}{L}\} \tag{1.13}$$

2. Vertical acceleration distribution

   As observed by researchers in the studies discussed in previous sections [7], [29], [30] and shown in Figure 1-20, the vertical acceleration distribution is sensitive to the shape of the contributing modes with distinct modeshapes. The equation for the proposed vertical acceleration distribution was formulated based on the dominant O1 mode [25].

$$A_V(x,y) = A_{Heq}F_V\frac{x}{\sqrt{x^2+y^2}}\sin\frac{2\pi\sqrt{x^2+y^2}}{L} \tag{1.14}$$

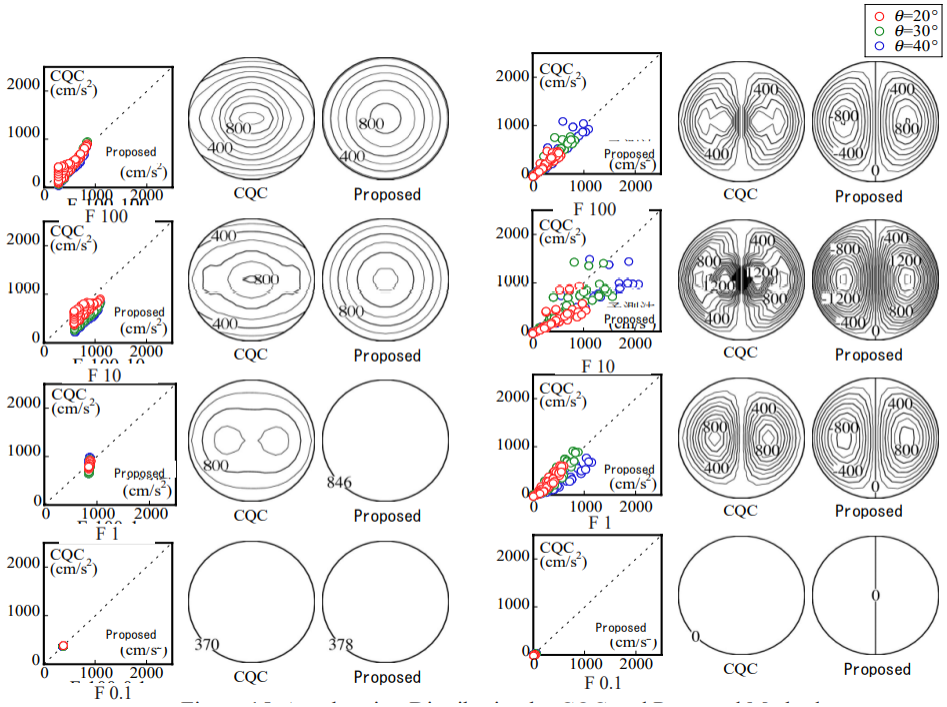

Figure 1-24: Peak acceleration contour distribution
obtained using RSA (CQC) and Proposed Method [27]

Modelling double-layer lattice as an equivalent single-layer lattice

In all the research studies by Takeuchi and Ogawa group [25], [26], [29], [31]–[33], the double-layer truss lattice has been modelled using an equivalent single-layer beam model.

This concept was first explained and validated by Takeuchi et al. [34]. A double-layer lattice model (labelled as D model) and an equivalent single-layer lattice dome (labelled as F model) with a single-storey substructure were constructed as shown in Figure 1-25. The idea is to equate the cross sectional area of the double-layer lattice with that of the single-layer model, and modify the single-layer model's bending stiffness by increasing the moment of inertia to equate it to the corresponding double-layer lattice's bending stiffness. This implies that the web members of the double-layer lattice and the corresponding shear deformation is not accounted for in this equivalent single-layer beam model. However, it was found that, as is commonly observed in deep H beams, the out-of-plane stiffness was not affected by neglecting the web members. The eigenvalue results are shown in Figure 1-26. It may be seen that the fundamental periods (O1) modes and their mass participation

values are nearly equal. The difference in periods was around 2% which was accounted to the effect of the shear deformation. The prominent modes that govern the seismic response in both the cases were the O1, O2 and I modes. This confirms that the equivalent single-layer is a simple way to efficiently capture the stiffness and seismic characteristics of the double-layer model.

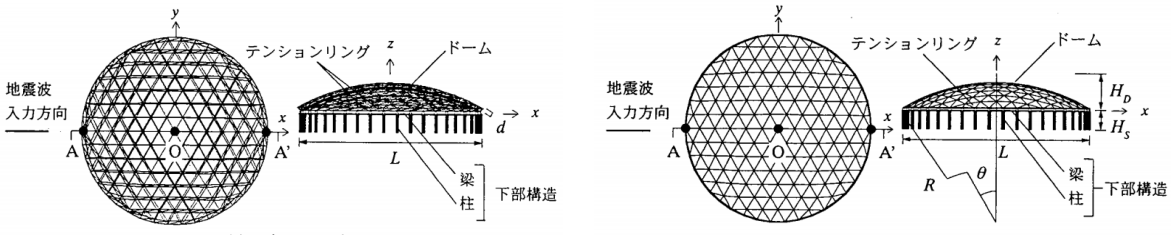

(a) Double-layer dome model (D) (b) Equivalent single-layer dome model (F)

Figure 1-25: Analysis models for comparison [34]

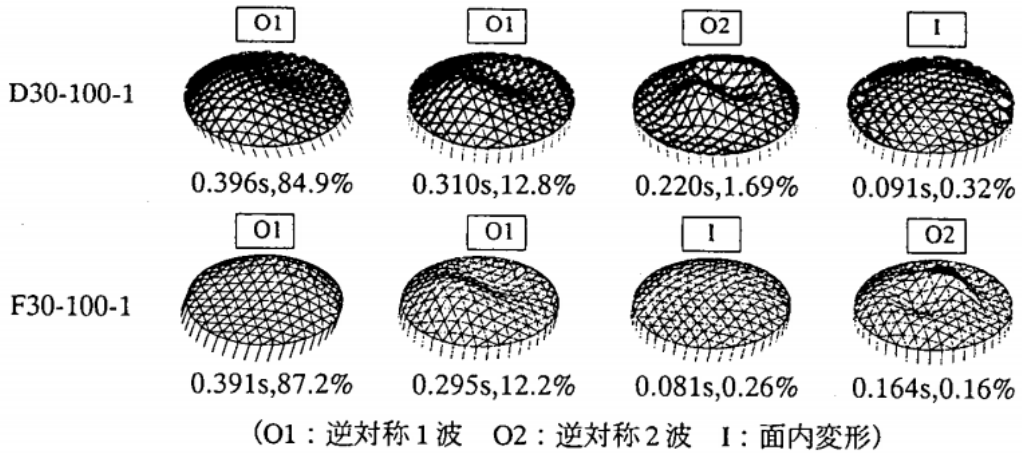

Figure 1-26: Prominent modes and periods of the two models [34]

The seismic response of the two models from response spectrum analysis using the CQC rule, were also compared in detail as shown in Figure 1-27. The peak horizontal and vertical accelerations were in good agreement for both the models. The ridgeline forces and moments also showed good agreement although there was some disagreement around the ends. Takeuchi et al. [34] concluded that the double-layer lattice model may have an overall roof force distribution that may be different from the simplified single-layer model as the

distribution of stress may vary with the geometry of members, for all practical preliminary design purposes, the overall peak response is captured well by the single-layer model. It was recommended to use the single-layer model to estimate the periods and compute the peak accelerations and equivalent static loads, and then apply it to the double-layer model to obtain a more accurate estimate of the member forces.

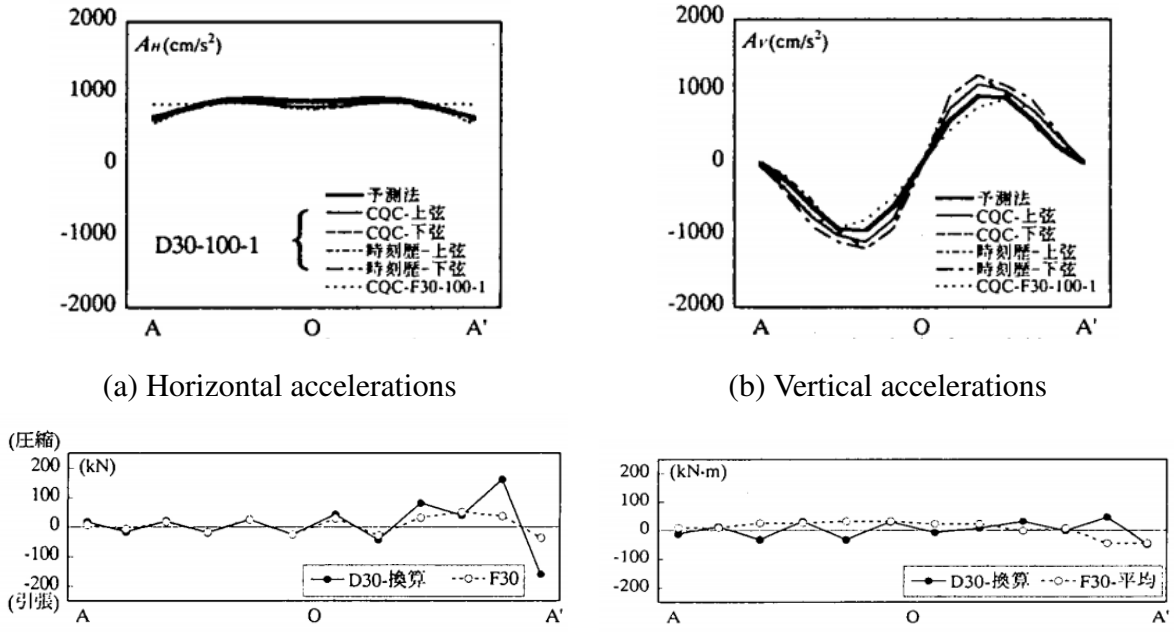

(a) Horizontal accelerations

(b) Vertical accelerations

(c) Axial forces along ridgeline

(b) Bending moment along ridgeline

Figure 1-27: Comparison of seismic response [34]

1.4.4 Nonlinear response estimation: Domes with single-storey braced substructures

Domed roof structures with large open spaces, widely used for indoor stadiums, gymnasiums, and other entertainment complexes, are often designated emergency shelters after a large earthquake. This implies that these structures need to be designed to prevent not only collapse and structural damage but also to meet the immediate occupancy criteria so as to ensure a safe place for refugees. To enable this, several domed roofs with substructures that employ response control devices have been built in countries with high seismic hazards, such as Japan, China, and the United States [7], [35]. One efficient solution to limit the roof seismic demand by decreasing the peak substructure response is to add damping devices such as the hysteretic buckling-restrained braces (BRB) to the substructure frames [3]. This lowered demand enables engineers to design roofs such that they remain elastic and the reduced roof acceleration also ensures the seismic performance of acceleration sensitive non-structural components such as ceilings and lighting equipment. Practical applications of employing passive-control devices include the Toyota stadium [36], Shimokita dome [37] and other seismic-retrofit projects of high-school gymnasiums [35], [38]. The response estimation of nonlinear single-storey substructures has been studied [30], [33], [39], [40] using Kasai's equivalent linearisation method [41], [42] and are discussed in the following subsections.

Inelastic response of single-layer roofs with BRB frames

Kato and Nakazawa [39] investigated the response of a single-layer reticular dome, 100m in span, half-subtended angle of 40 degrees and relatively thick (with depth-to-span ratio exceeding 1/100) and supported by a single-storey substructure. The dome members were designed for a dead load of 1.5 kPa as shown in Figure 1-28. The substructure consisted of braces and columns with pin connections. For a level-2 Japanese earthquake, large vertical and horizontal accelerations were observed in the roof members. The envelope of the elastic accelerations consisted of ripples, and the vertical maximum accelerations far exceeded the horizontal maximum accelerations, as shown in Figure 1-30(a).

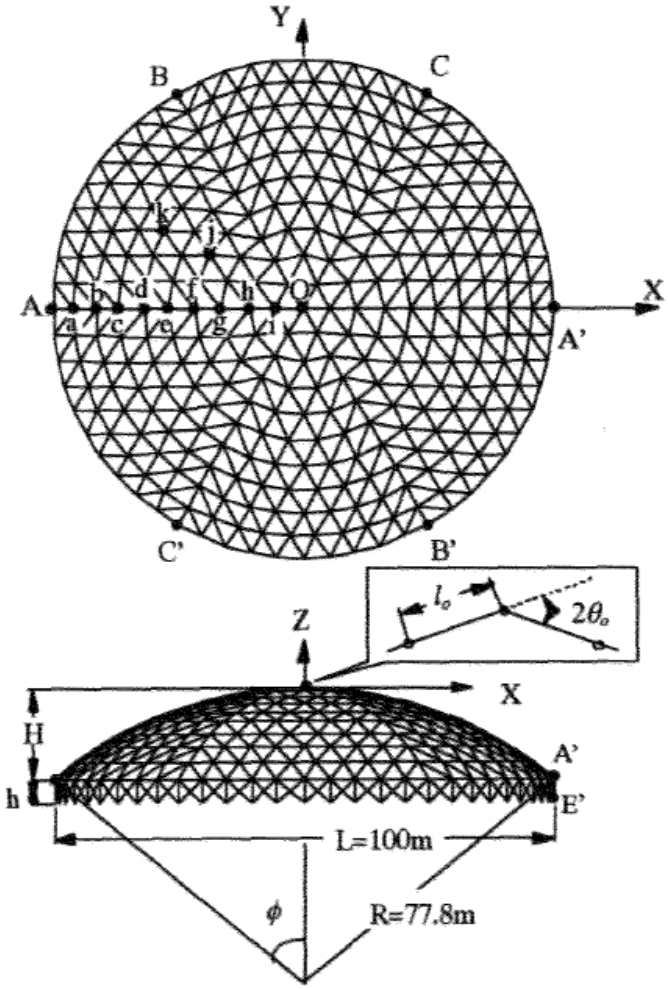

Figure 1-28: Analysis model [39]

Braces with bi-linear hysteresis model shown in Figure 1-29 were added to the

substructure as a measure to control the response of the dome. Introducing energy dissipating dampers in the substructure proved to be effective in suppressing the response of the dome as shown in Figure 1-30.

The study observed that the first two dominant modes for the analysed models had a cumulative mass participation of more than 90%. This study was among the first to present equivalent static loads for nonlinear substructures considering maximum deformation of the braces in the sway mode. They concluded that the design procedure using a two-mode based equivalent linearisation concept can accurately predict the response of a certain class of domes with single-storey substructures exhibiting large sway.

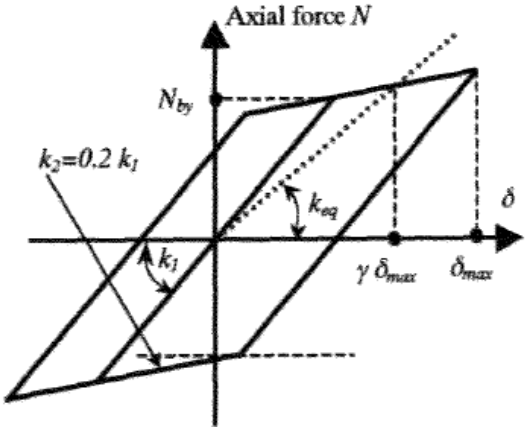

Figure 1-29: Hysteresis of Brace [39]

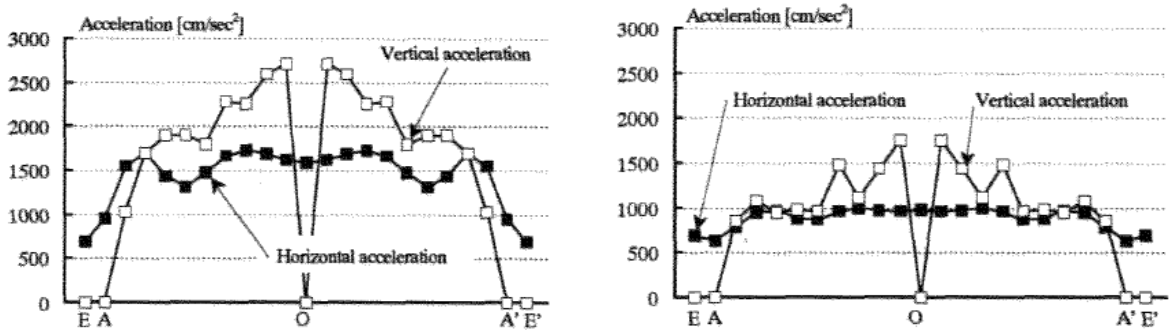

(a) Linear Response

(b) Nonlinear Response
(Brace allowed to yield)

Figure 1-30: Acceleration along the ridge line [39]

Roof as a series of lumped masses with springs

To further estimate the response of these domes, Kato et al. [43] developed a two-mode based response evaluation method. The analysed dome was supported by a single-storey substructure which was assumed to exhibit a bi-linear hysteresis. Figure 1-31 shows the estimation of equivalent stiffness of the deformed substructure using ductility μ.

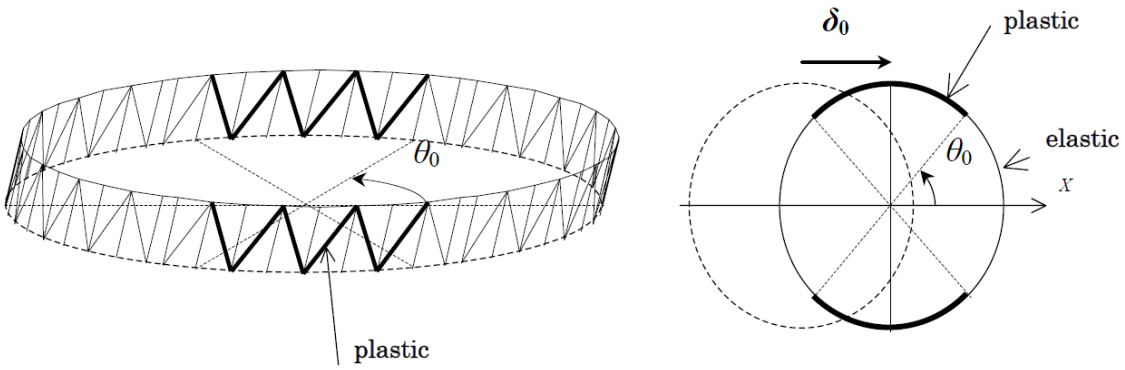

$$\kappa = \frac{K_{eq}}{K_0} = \frac{Q_B/\delta_0}{Q_y/\delta_y} = \frac{\alpha}{\mu}$$
$$= \left\{ \frac{2\theta_0}{\pi}(1-r) - \frac{1-r}{\pi}\sin 2\theta_0 + r \right\} + \frac{4(1-r)\cos\theta_0}{\pi\mu}$$

Figure 1-31: Estimation of the plastic region of the substructure to estimate equivalent stiffness K_{eq} using base shear at yield Q_y [43]

To incorporate the contribution from higher modes, the dome was simplified as a series of parallel lumped masses with elastic springs as shown in Figure 1-32. Each mass at the top represents the contribution of the mass in that mode and is obtained using a mode decoupling method [43]. The modes are selected in decreasing order of mass participation until they have a cumulative mass participation of over 90%. In this study, two modes of the substructure and 30 modes of the dome were considered. In the proposed method, the displacements of the structure after the substructure yields are obtained from the modified vibration modes using an adaptive method (similar to the iterative inverse power method) [44]. The displacements are used to obtain the base shears for each mode, which are then used to calculate the static forces for pushover analysis.

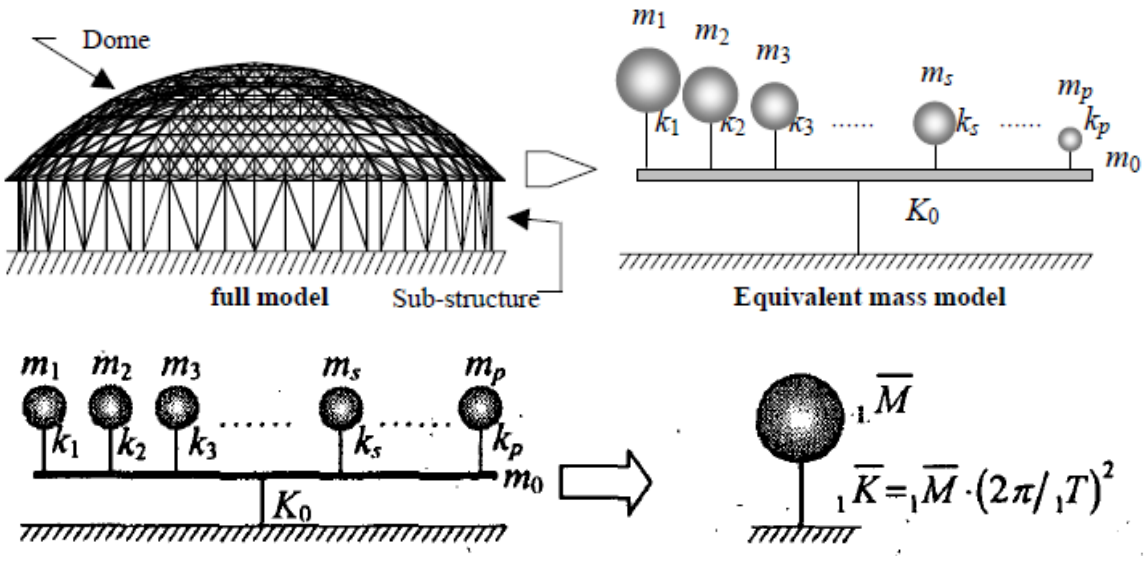

Figure 1-32: Simplification of analysis model
(from 3-d model to equivalent mass model and SDOF model) [43]

This method provided an efficient numerical method to obtain the response of the dome. However, this method is numerically complex and computationally intensive and an extension of this method to be applicable for multistorey substructures has not yet been investigated.

Pushover analyses using nonlinear equivalent static loads based on equivalent linearisation and RSA

Excessive strength in the substructures often leads to an amplified response of the roof. To mitigate the seismic input to the roof, Kato et al. [45] investigated the response of a long-span double layered dome supported by ductile substructure. The substructure consists of a single storey of earthquake-resistant bracing members, as shown in Figures 1-33. The hysteresis of the substructure was assumed to be bi-linear with a post-yield stiffness of 2%.

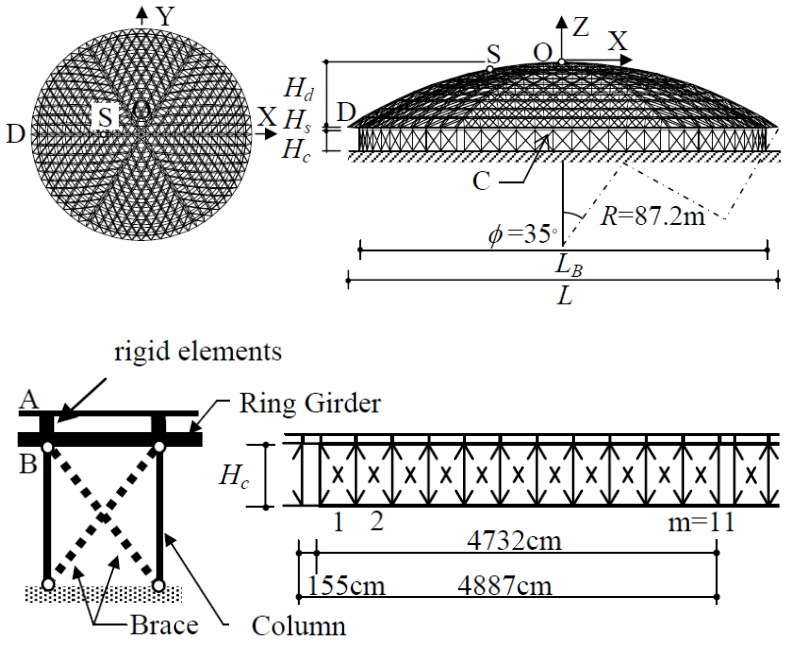

Figure 1-33: 3-d Model and brace in substructure [45]

The displacements and related equivalent seismic loads were calculated based on the response spectrum analysis using the obtained mode shapes of the first two dominant modes and the equivalent linearisation method to account for the yielding while considering the full 3d structural model. This approach is different from other researchers as in this method, the combined structure (dome and substructure) is analysed simultaneously. The method proposes nonlinear equivalent static seismic loads (for pushover analyses) corresponding to three intensity levels - serviceability level, repair level, and ultimate limit state .

In contrast to the method proposed earlier [43], in this study, contributions from two dominant modes of the structure toward the overall response were considered. The effective

mass participation of the structure from the first O1 mode and the sway mode was found to be generally more than 85%. This implies that the higher roof mode contributions were found to be less significant. The response of the dome to the ground motions corresponding to ultimate intensity level are shown in Figure 1-34. The maximum axial forces for each member of the dome are obtained for each of these seismic intensity levels. The sectional areas for each member of the dome are then obtained using allowable stress design.

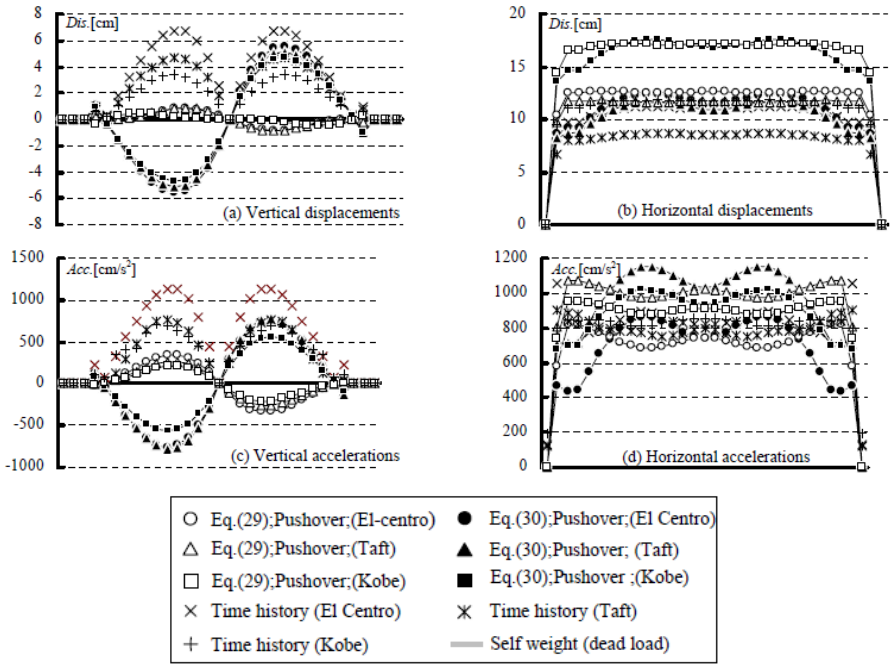

Figure 1-34: Response of dome to earthquakes corresponding to ultimate seismic intensity level [45]

This method being almost entirely numerical, is complex and intensive as it requires several cycles of iteration and requires the designer to obtain the full mass and stiffness matrices. Nevertheless, the nonlinear static loads used in the pushover analyses were found to be accurate in estimating the stresses in the roof and are a positive step towards performance-based design for spatial structures. An important assumption in this study is that the damping matrix was fixed for all models using the fundamental period of 0.6s and the second mode period was assumed at 0.15s. Since the overall response of domes are sensitive to the excited modes, this assumption may not be applicable for other long-span domes. This study assumes that nonlinearity in the structure is concentrated in the

energy-dissipating braces in the substructure. Therefore, there is a requirement to extend this study to propose a more general and numerically less intensive method applicable for all substructures.

Equivalent static loads using amplification factors and RSA based equivalent linearisation

Section 1.4.3 discussed the method of estimation of the seismic response for medium-span domes developed by Ogawa et al. [26] and Takeuchi et al. [25] using roof amplification factors. However, these studies were focused on structures confined in the elastic region and post-yield behaviour was not considered. Therefore, extending the research on estimating the seismic response of domes using amplification factors, Kumagai et al. [33] studied a medium-span dome supported by a yielding substructure. It was proposed to reduce the response of the dome by introducing elasto-plastic hysteretic dampers in the substructure (Figure 1-35).

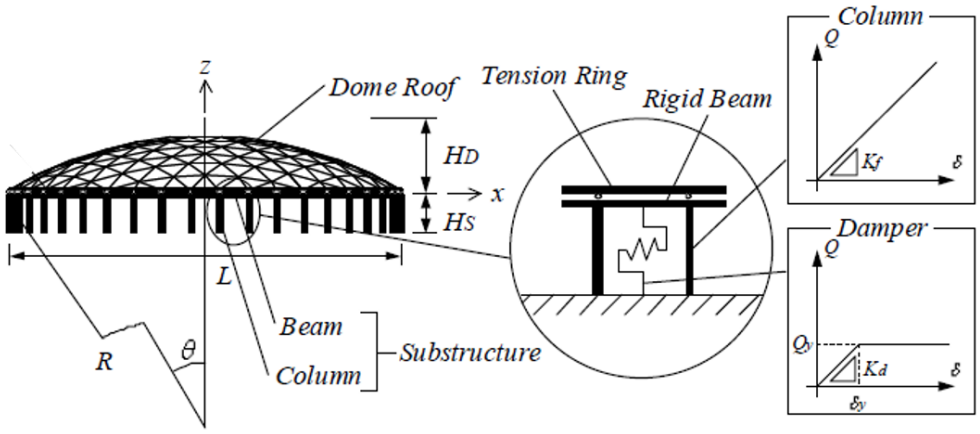

Figure 1-35: Hysteretic dampers in the substructure [33]

Amplification factors were proposed [33] to derive a numerical analysis method using response spectrum analysis and equivalent linearization procedure. The substructure is simplified as an SDOF model assuming that the roof is a rigid mass, and its response is obtained using the first mode using the response spectrum analysis design acceleration spectrum. This is followed by equivalent linearization to obtain the peak inelastic response of the substructure. The calculated amplification factors are then multiplied by the peak

substructure response to obtain the dome response. In this study, the dominant mode of the roof and substructure was used to estimate the response of the dome.

Figure 1-36 shows the results of the response history analysis subjected to ground input motions spectrally matched to the level-2 design spectrum. Maximum accelerations along the ridge line of the dome with a natural period lying in constant acceleration region of the spectrum are shown, which are in good agreement with the proposed accelerations. A significant reduction in the response of the roof can be observed, which is due to the effective energy dissipation by the yielding dampers. However, the applicability of this method to larger domes or substructures with higher modes was not verified.

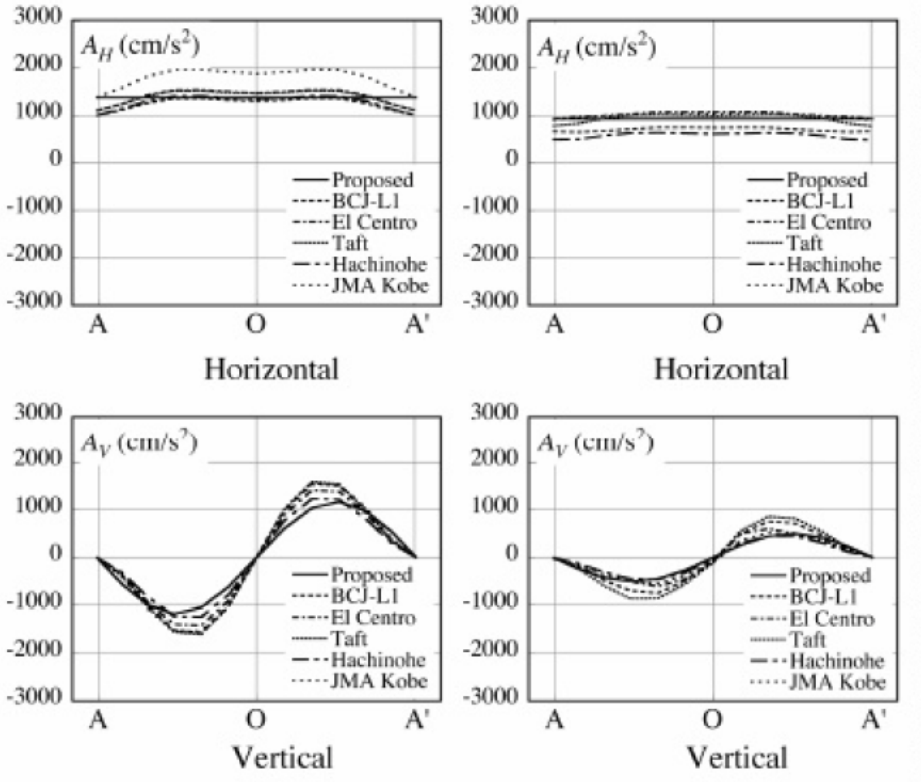

(a) Linear Response (b) Nonlinear Response

Figure 1-36: Reduction of accelerations along the ridge line of dome [33]

Response in cylindrical gridshells

Similar studies for raised single-layer and double-layer cylindrical gridshells have also been carried out to present simplified design approaches. Studies by Cedron et. al. [46], Takeuchi et al. [25], and Shen et al. [47] have indicated that their dynamic characteristics are also similar to domes due to the inherent geometric similarities and the seismic responses are highly influenced by the rise-to-span ratio, length-to-span ratio and the fundamental anti-symmetric mode. Therefore, as the design approaches for domes may be extended to cylindrical gridshells to an extent, their behaviours are not discussed separately here and is beyond the scope of this thesis.

Response to vertical input ground motions

Domes and curved gridshell roofs, because of their inherent curved arch forms, are efficient in carrying uniformly distributed vertical loading. The response and behaviour of gridshells against the vertical earthquake loading are similar to that against the long-term vertical loads. Therefore, as the roofs have been designed conservatively for static loads (safety factor of 1.5 (or more if heavy snow loads are considered [48], [49])), the resistance to vertical earthquakes is expected to be inherently high and it is expected that these domed roofs may sustain vertical earthquakes up to a maximum intensity of 0.5g.

As per the international guide to earthquake design of metal spatial structures [7], the vertical earthquake intensity at far-field sites (assumed in this research) is approximately 0.5 times the horizontal component although the vertical component may exceed the horizontal component at near-fault sites. In such cases, the vertical component of earthquake motions may also lead to large vertical accelerations and may need to be considered when it is significant to the overall vertical response. However, the response from vertical ground motion input (using the vertical component's response spectra) is outside the scope of this research. Nevertheless, the methodology in this study may be extended in future to consider the response from vertical seismic motions, and propose additional amplification factors to quantify the additional response from vertical ground motions.

1.4.5 Response from multistorey substructures

In contrast to the literature available on roofs with single-storey substructures, as such, research on the dynamic characteristics of roofs with multistorey substructures are limited.

Amplification factor approach

The approach of using a 3-mass arch model was also extended to evaluate the response of raised medium-span lattice roofs supported by multistorey substructures in a study by Takeuchi et al. [32]. The amplification factors (Figure 1-37) were multiplied with the response at the top floor of the substructure to obtain the response of the roof. The response evaluation procedure is shown in Figure 1-38.

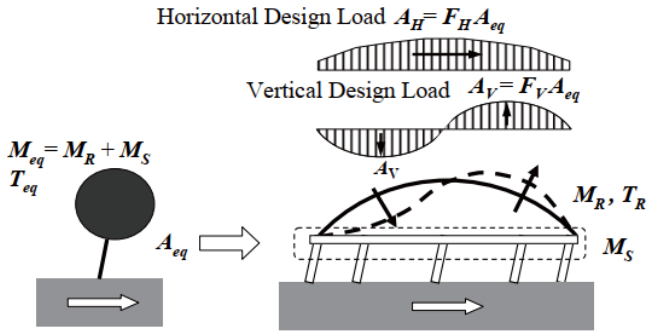

Figure 1-37: Response evaluation using amplification factors [25]

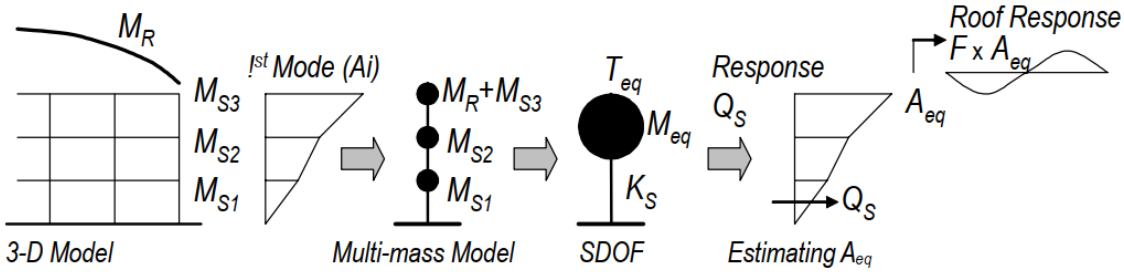

Figure 1-38: Response evaluation for dome with multistorey substructure [32]

The response evaluation is divided in two main parts which are as follows:

Part 1: Peak substructure response

Step 1 Obtain the substructure periods.

From the eigenvalue analysis, obtain the fundamental period of the substructure model (T_1).

Step 2 Obtain the peak elastic roof acceleration of the substructure.

Use the *Ai* distribution (as per the Japanese code [50]) and the design acceleration spectrum (Figure 1-38) to obtain the maximum elastic acceleration distribution of the substructure. The acceleration at the top storey is adopted as the peak elastic acceleration A_{Heq}.

Part 2: Peak roof response

After obtaining the peak response of the substructure, the next step is to calculate the horizontal and vertical amplification factors.

Step 3 Calculate the roof amplification factors.

Use Equations 1.11 and 1.12 to estimate the amplification factors F_H and F_V for the horizontal and vertical directions. θ is the dome's half subtended angle, R_T=T_{eq}/T_R is the ratio of the equivalent period of the SDOF model (equal to the fundamental period of the substructure with rigid roof in Figure 1-38) to that of the O1 mode of the roof (equal to the fundamental period of the roof), R_M=M_{eq}/M_R is the ratio of SDOF model to roof mass (Figure 1-38) and the calibration factor C_V is taken as 1.88 [25]. Note that only the fundamental substructure mode and its period are considered in this method.

Step 4 Calculate the modified amplification factors to consider harmonic resonance.

When $R_M > 2$ and $R_T < 1.5$, harmonic resonance must be taken into account [32]. Harmonic excitation of the roof is expected to occur when the O1 mode of the roof coincides with the substructure period and the substructure is much heavier than the roof. In such cases, the modified amplification factors $F_H{}'$ and $F_V{}'$ for the substructure period (T) is calculated using Equations 1.15 and 1.16.

$$F_H{}' = \sqrt{{F_H}^2 + \frac{1}{\left(1-{R_T}^2\right)^2 + \left(1/R_M\right)^{\theta}}} \tag{1.15}$$

$$F_V{}' = \sqrt{{F_V}^2 + \frac{1}{\left(1-{R_T}^2\right)^2 + \left(1/R_M\right)}} \tag{1.16}$$

Step 5 Obtain the peak roof acceleration distributions.

Compute the acceleration distributions A_H and A_V using the calculated amplification factors; where x and y are the coordinates of the roof nodes with $\{x,y\} = \{0,0\}$ as the centre and L is the span of the dome (Equations 1.13-1.14).

Case study for validation

A three storey building resembling a typical school gymnasium in Japan was modelled as shown in Figure 1-39 to validate the proposed method. Cylindrical and dome roof geometries of span 60m were considered with a fundamental O1 mode period of about 0.3s. The substructure was designed to have a uniform storey drift against a gravity floor loading of 5kPa as per Japanese code[32]. Eigenvalue analyses revealed that more than 80% of the mass participation was composed of the roof's O1 mode with the substructure's T1 mode vibrating in- and out-of-phase with each other as shown in Figure 1-40.

The results from the proposed method are compared with the results obtained using RSA and combined using the CQC modal combination rule are shown in Figure 1-41. The accuracy of the results, when compared with the CQC results, was lesser than that observed for the study of single-story substructures [25], [32]. This was explained to be because of the effects of higher vibration modes which were ignored in the estimations. However, the proposed method was found to be much more accurate than the conventional method of only considering horizontal loads (Figure 1-41) on the roof.

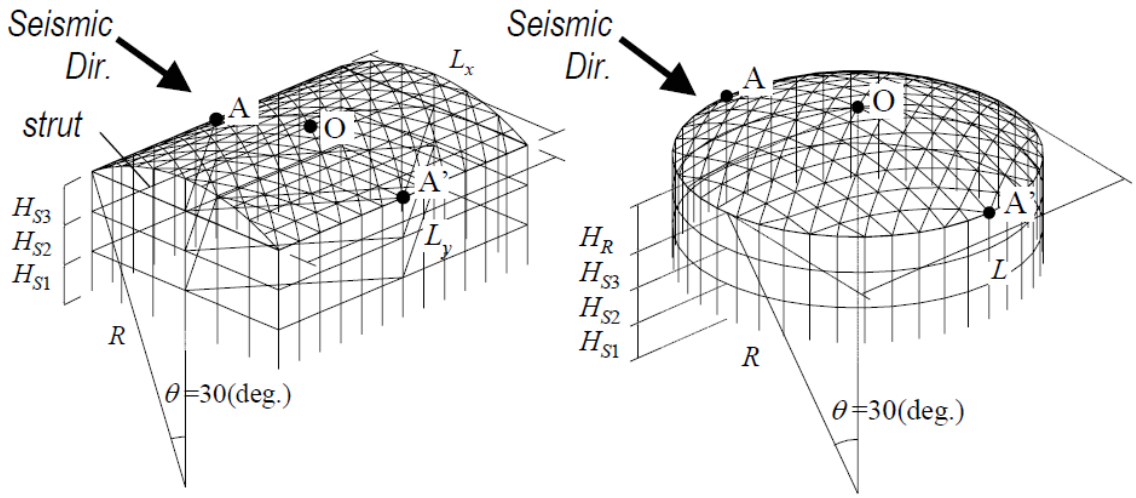

Figure 1-39: Cylindrical and Dome gridshell roof with a 3-storey substructure [32]

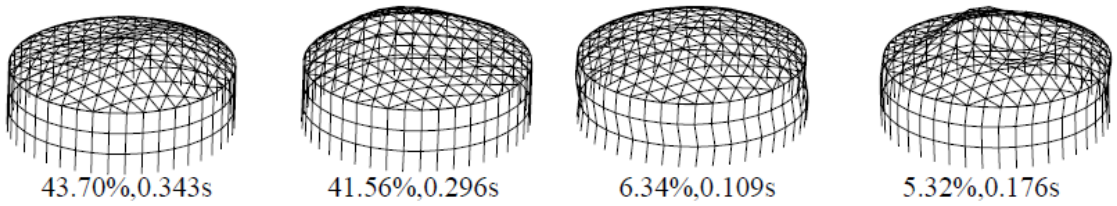

Figure 1-40: Dominant modes of the domed roof with 3-storey substructure [32]

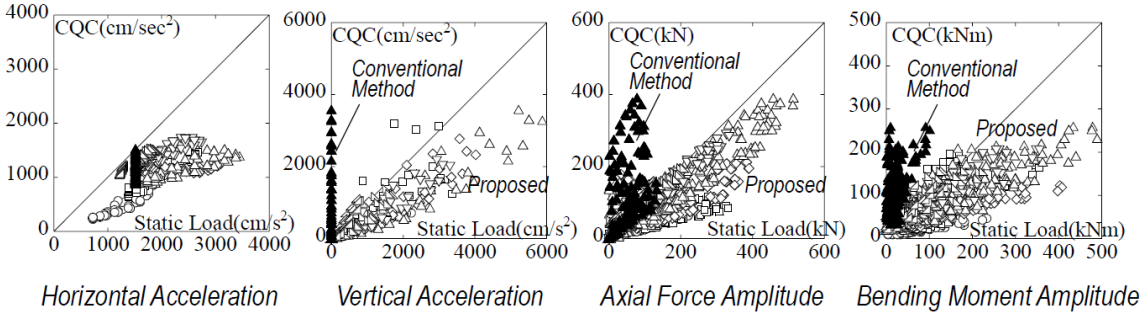

Figure 1-41: Comparison of results from the equivalent static loads and RSA [32]

1.4.6 Summary

From the literature review, the response estimation procedure of domes may be broadly summarised as shown in the flowchart below:

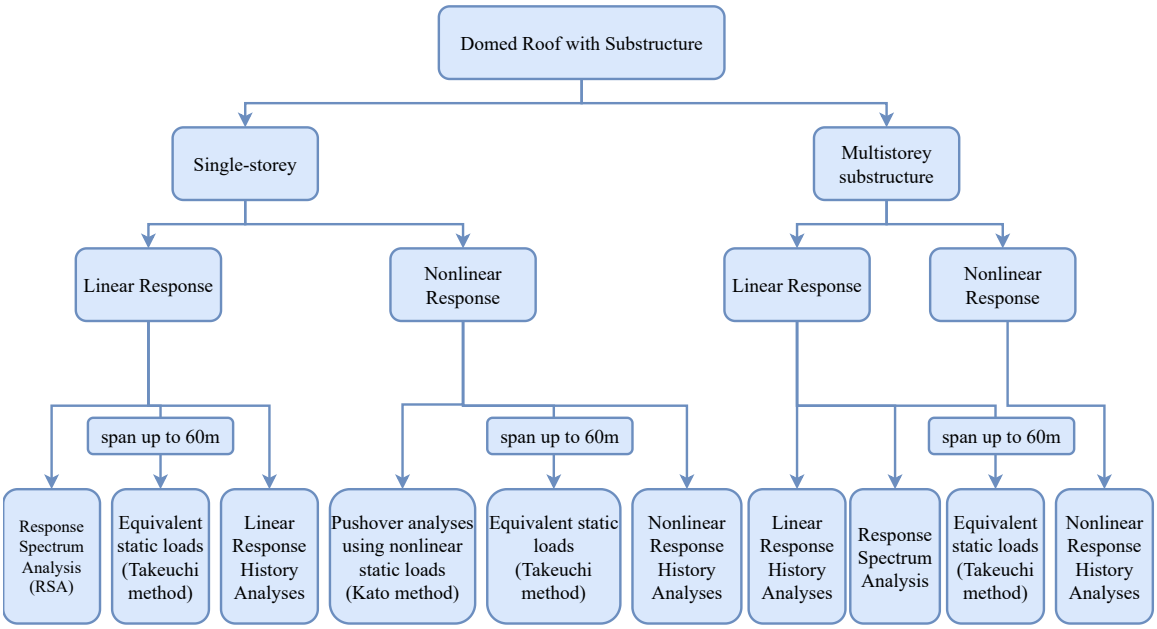

Figure 1-42: Seismic response analysis methods for domes

For domes supported by single-storey substructures or short-period substructures, several response estimation methods are available. To estimate the linear response, response spectrum analysis using the full 3d model is the most efficient way to obtain the peak responses.

For substructures with additional damping devices or significant yielding, pushover analyses using nonlinear static loads have been proposed, as discussed in Section 1.4.4, which have proved to be an efficient alternative to the nonlinear response history analysis method. Equivalent static loads using the amplification factor approach are also an alternative as they only require linear static analyses and the substructure may be simplified as a lumped mass model (with the roof modelled as a rigid mass), significantly reducing the required computational and modelling effort.

On the contrary, for roofs with multistorey substructures, there are relatively few studies available in the literature, as discussed in Section 1.4.5. For linear structures, modal RSA using an appropriate combination rule accurately captures the complex

dynamic characteristics. However, RSA requires a high degree of expertise because of the complex, closely spaced modes and the sensitivity of the substructure-roof interaction to the precise modelling assumptions. Equivalent static loads using the amplification factors were found to be an efficient alternative for domes with spans of up to 60m. However, for the design of nonlinear multistorey substructures, alternatives to nonlinear response history analyses do not exist or have not been investigated.

1.5 Equivalent static loads for multistorey buildings

As opposed to the complex response characteristics of curved gridshells, the seismic behaviour of a regular multistorey building may be simplified into a lumped mass model and a first-mode dominant horizontal response. Therefore, a simpler equivalent static lateral force procedure is available and often forms the precedent for seismic design of (regular) nonlinear multistorey buildings as prescribed by most design codes such as ASCE-7-16 [51], NZS1170.5 [52], Eurocode 8 [53] and the Building Standard Law of Japan [50]. Equivalent lateral forces are formulated to represent the internal forces generated by dynamic response to earthquake ground motions. The forces are set at a magnitude to allow elastic analysis and design, and to provide an elastic lateral strength that will control response at full design ground motions to acceptable ductility and drift levels.

Consider the equivalent lateral force procedure in ASCE-7 that is based on the ideology of representing an MDOF building in an SDOF system. Furthermore, it is assumed that the nonlinear response of the building can be represented by an elastoplastic relationship (or negligible post-yield stiffness). The idealised base shear-roof displacement relationship is used to replace the actual relationship shown by the dashed line in Figure 1-43 as explained by Whittaker et al. [54]. The response of the idealised nonlinear (or yielding) frame is given by the intersection point of the capacity curve and the demand curve in the figure (point I in Figure 1-43), where the demand curve is represented by a normalised acceleration response spectrum in the acceleration-displacement space. Assuming that the structure has unlimited strength and therefore can remain elastic for the earthquake characterised by the demand

spectrum, the response of the frame may be given by point E in Figure 1-43. The base shear and the corresponding roof displacement at the formation of the first plastic hinge in the frame are V_s and Δ_s respectively, the yield strength and the yield displacement of the idealised building frame are V_y and Δ_y respectively; the required elastic strength and the maximum elastic displacement are V_e and Δ_e, respectively. Furthermore, the base shear V_s is adopted as the design base shear that is given by V_e divided by the response modification factor R. The maximum inelastic displacement is Δ_i and is obtained using the displacement amplification factor C_d and the deformation Δ_s.

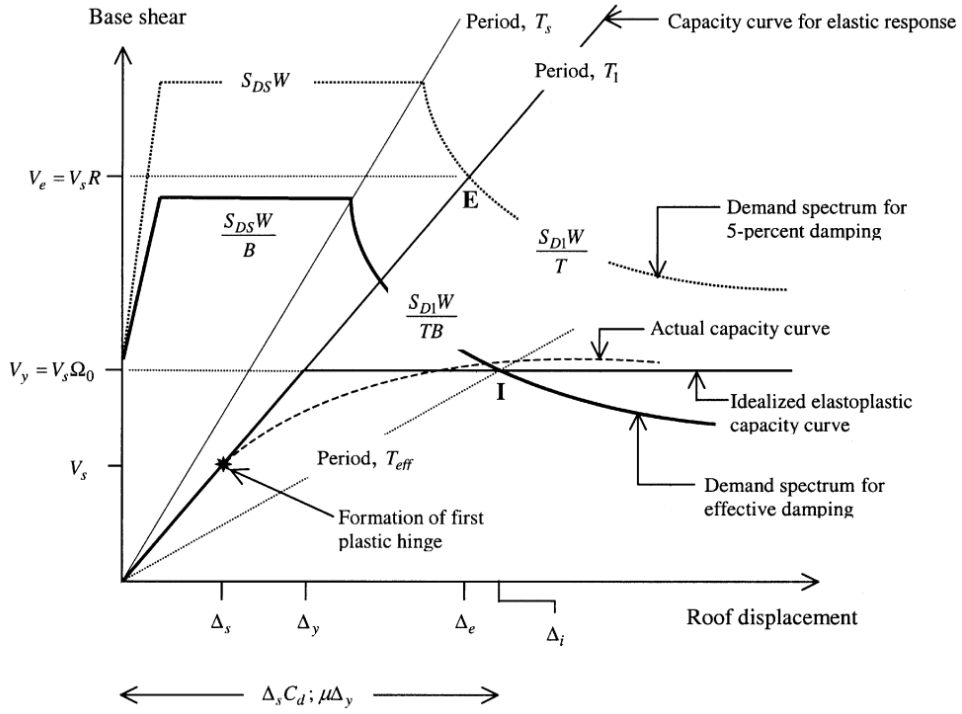

Figure 1-43: Base-shear and roof displacement relation (Capacity curve) and demand curves [54]

The equivalent static analysis procedure (with examples from ASCE-7[51]) consists of the following steps:

1. Compute or estimate an approximate first mode period of the building using code prescribed formulas.

2. Use the specific design response spectra to determine the design lateral base shear of the complete building consistent with the level of post-yield (ductility) response

assumed. For example, the ASCE-7-16 provides response reduction factors (R-factors [51]), to estimate the design base shear and the horizontal storey forces based on the type of buildings.

3. Distribute the base shear between the various lumped mass levels usually based on an inverted triangular shear distribution or parabolic distribution to allow for higher mode effects. For example, the shear force distribution in ASCE-7 is dominated by the first mode shape. However, the deformed shape is controlled by a factor k to account for higher mode effects that contribute to the behaviour of the deformed shape.

4. Analyse the resulting structure under the assumed distribution of strength-level design earthquake forces and determine the member forces and displacements.

5. Determine the overall structural response using the inter-storey drifts assessed for the elastically responding structure. For the assessment of the post-yield deformation, design standards typically magnify the elastic deformed shape using a displacement amplification factor (C_d in ASCE-7 shown in Figure 1-44) to determine the overall maximum deformation.

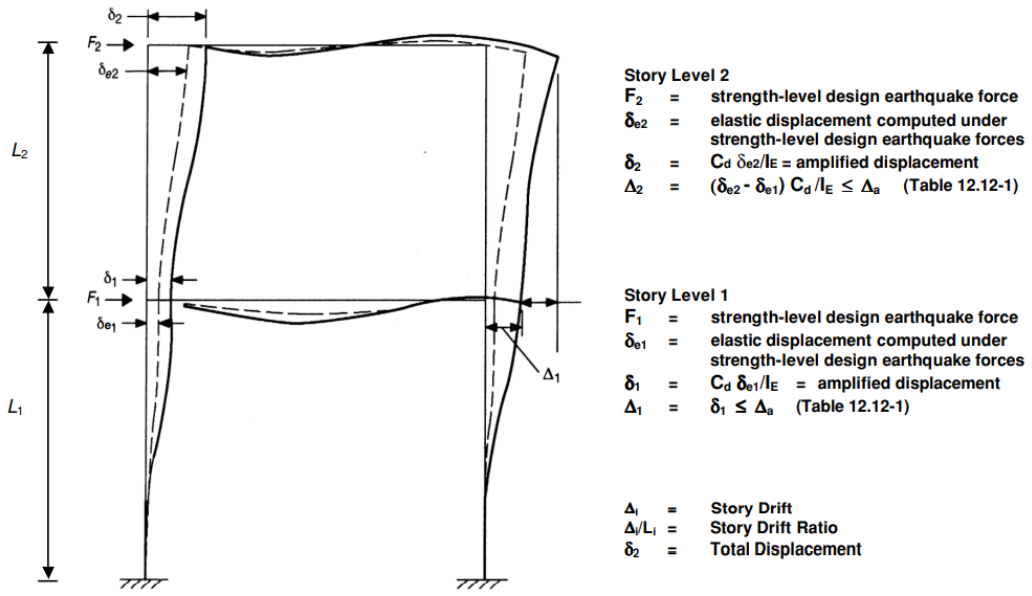

Figure 1-44: Design storey drift determination from equivalent static loads [51]

However, gridshells are often treated as irregular or special structures owing to the complex roof-substructure interaction and closely-spaced multiple participating modes [7], [9] and therefore require advanced analyses. Furthermore, while there exist well-established response reduction factors for design and estimation of the inelastic design spectra of conventional multistorey braced frames [55], [56], their application to the substructures of curved gridshell roofs has not yet been explored. Therefore, as neither reliable static load procedures nor realistic *R* factors are available for such structural systems, iterative time- and data-intensive nonlinear response history analyses (NLRHA) as shown in Figure 1-42 are often the only design route.

Main objective of the thesis

To summarise, the literature review suggests that there is a need to develop effective yet simple design strategies for the design of domed roofs with multistorey substructures in areas of high-seismic hazard. While significant advances have been made over the past decade, seismic design codes and manuals fail to provide quantitative guidance on the seismic design of long-span domes or domes with multistorey substructures. Furthermore, the higher-mode effects of multistorey substructures on the seismic response of the roof

have not yet been captured. Gridshell roofs are often used in school gymnasiums or community centres, which are expected to be functional as shelters even after a big earthquake in countries of high seismic hazard such as Japan. Seismic design codes and specifications typically prescribe increasing the seismic base shear for designated important structures [7], [51]. However, increasing the structural seismic demand while designing the structure to remain elastic even during a major earthquake leads to larger roof accelerations that have caused significant ceiling and other non-structural damage in past recent earthquakes rendering these structures non-functional as emergency shelters. Consequently, it becomes important to design such structures with seismic response control strategies. Therefore, this thesis aims to develop generalised but simple equivalent static loads for domes supported by multistorey substructures that may provide the basis for incorporating seismic demands in the preliminary design of gridshell roofs.

1.6 Organisation of the thesis

This dissertation is composed of seven chapters which are organised as follows.

1. Chapter 1: This chapter provides the background of metal domed gridshells, their seismic response characteristics, summarises the prior studies on the seismic response estimation methods for domes with substructures, and discusses the equivalent static loads procedure for conventional multistorey structures. Based on the literature review, the main objective of the thesis is presented.

2. Chapter 2: This chapter discusses a case study carried out on a 150m span dome supported by a 6-storey substructure. The analysed models are chosen to represent a large-scale stadium in a high-seismic hazard country and mainly explores the modal and seismic response characteristics of long-span domes with multistorey substructures subjected to design-level earthquake loading. To investigate the effects of additional damping to mitigate the roof response, analysis models with two types of response-control systems are studied and the applicability of the previously proposed amplification factor approach using the substructure first mode is discussed. This chapter also investigates the segmented spine frame system as a measure to mitigate the higher mode response of the structure.

3. Chapter 3: This chapter explores the roof-substructure interaction in medium- and long-span gridshell domes with 60, 100 and 150m spans and supported by single-storey and six-storey substructures. Parametric studies are carried out to investigate the effect of substructure stiffness and mass ratios on the dominant substructure and roof modes using response spectrum analysis. The contribution of each substructure mode to the overall roof response is characterised by a newly proposed dominance response ratio.

4. Chapter 4: This chapter quantifies the interaction between the higher substructure mode and dominant roof modes using amplification factors. These factors were used to develop equivalent static loads for domes with multistorey substructures, and the

improvement in response estimation (from the current methodology of using only the substructure first mode) was measured using median response ratios.

5. Chapter 5: This chapter applies the proposed equivalent static loads to nonlinear structures by including ductility-based reduction factors (labelled as the 'R-factor approach') and an alternative equivalent linearisation approach to estimate the peak substructure response using response-spectrum analysis for buckling-restrained braced frames. The roof response of single-storey substructures subjected to serviceability, design-basis and maximum considered earthquake loading are studied, and the response from equivalent static loads (from both R-factor approach and equivalent linearisation approach) are compared against those from nonlinear response history analyses (NLRHA).

6. Chapter 6: This chapter investigates the applicability of the proposed R-factor approach for 60m and 150m spans with two-storey and six-storey (multistorey) BRBFs with different post-yield stiffnesses. The roof response from the substructures higher mode is estimated using the proposed T2 mode amplification factors and the combined envelope of response (and member forces) from the R-factor approach and equivalent linearisation approach are compared and verified against the NLRHA response. Finally, the scope of application of the proposed equivalent static loads is discussed.

7. Chapter 7: This chapter provides a summary of the results obtained in each chapter, along with the main conclusions. A list of journal publications and conference papers published in conjunction with this thesis is also appended in the end for reference.

References

[1] W. G. 8, "Guide to buckling load evaluation of metal reticulated roof structures," *International Association for Shell and Spatial Structures*, 2014.

[2] T. Sasaki, A. Aoi, K. Kajiwara, H. Tagawa, and D. Sato, "Collapse mechanism of wide-area suspended ceiling in school gymnasium," in *Proceedings of IASS Annual Symposia*, International Association for Shell and Spatial Structures (IASS), vol. 2016, 2016, pp. 1–10.

[3] T. Takeuchi, S. D. Xue, S. Nakazawa, and S. Kato, "Recent applications of response control techniques to metal spatial structures," *Journal of the IASS*, vol. 53, no. 2, pp. 99–110, 2012.

[4] J.-W. Kim and L. Schmidt, "Test of deployable dome-shaped space truss," in *Computing in Civil and Building Engineering (2000)*, 2000, pp. 66–73.

[5] A. Kaveh and M. I. Ghazaan, "Optimal design of dome truss structures with dynamic frequency constraints," *Structural and Multidisciplinary Optimization*, vol. 53, no. 3, pp. 605–621, 2016.

[6] *AIJ Recommendation for Design of Latticed Shell Roof Structures (in Japanese)*. Architectural Institute of Japan, 2016.

[7] *Guide to Earthquake Response Evaluation of Metal Roof Spatial Structures*. Working Group 8,International Association for Shell and Spatial Structures (IASS), 2019.

[8] M. Kawaguchi and S. Kato, "Metal space structures," *Journal of the IASS*, vol. 42, pp. 21–26, 2001.

[9] S. Nakazawa, S. Kato, T. Takeuchi, S.-D. Xue, and C. Lázaro, "State-of-the-art of seismic response evaluation methods for metal roof spatial structures," *Journal of the IASS*, vol. 53, pp. 117–130, 2012.

[10] N. Sahashi, T. Hisatoku, Y. Hangai, and M. Yamada, "Structural design of large-span single layer latticed dome," *IABSE REPORTS*, pp. 731–736, 1998.

[11] K. Hara, "Design and construction of osaka dome," *Structural engineering international*, vol. 8, no. 1, pp. 25–27, 1998.

[12] Y. Tanno, Y. Sasaki, and M. Nakai, "Fukuoka dome, japan," *Structural Engineering International*, vol. 4, no. 3, pp. 151–153, 1994.

[13] R. S. Pfaffmann, "Memory & renewal," *Western Pennsylvania History: 1918-2018*, 2010.

[14] R. K. Otani, H. Jungjohann, D. Reynolds, and A. G. Puyol, "Adaptive stadia roof structures," in *Structures Congress 2015*, pp. 1695–1706.

[15] R. S. Pfaffmann, "The pittsburgh civic arena: Memory and renewal," in *The Challenge of Change: Dealing with the Legacy of the Modern Movement*, IOS Press, 2008, pp. 159–165.

[16] Yoshito Isono, *Nagoya dome*, https://structurae.net/photos/108219-nagoya-dome, 2008.

[17] KENPEI, GFDL, Creative Commons Attribution ShareAlike 2.1 Japan License, *Osaka dome*
, https://commons.wikimedia.org/wiki/File:Kyocera_Dome_Osaka1.jpg, 2007.

[18] User id: Mmry0241, *Fukuoka yafuoku! dome*, https://commons.wikimedia.org/wiki/File:FUKUOKA_DOME.JPG, Access Date = March 12, 2019, 20 August 2008.

[19] T. Takeuchi, "Retrofit of damaged gymnasia according to response control concept," in *Proceedings of IASS Annual Symposia*, International Association for Shell and Spatial Structures (IASS), vol. 2013, 2013, pp. 1–8.

[20] T. Takeuchi, Y. Terazawa, S. Inanaga, and R. Matsui, "Collapse analysis of damaged space-frame gymnasiums in the 2016 kumamoto earthquake," in *Proceedings of IASS Annual Symposia*, International Association for Shell and Spatial Structures (IASS), vol. 2018, 2018, pp. 1–7.

[21] K. Kawaguchi, “Damage to non-structural components in large rooms by the japan earthquake,” in *Structures Congress 2012*, 2012, pp. 1035–1044.

[22] T. Takeuchi, “Buckling-restrained brace: History, design and applications,” in *Key Engineering Materials*, Trans Tech Publ, vol. 763, 2018, pp. 50–60.

[23] Y. Tsuboi, “Historical outline of space structures in japan,” *Journal of the International Association for Shell and Spatial Structures*, vol. 42, no. 1-2, pp. 9–14, 2001.

[24] C. Jung, Y. Shinohara, and M. Yamada, “A study on the static seismci force for the design of the arch,” in *Proceedings - International Symposium on Theory, Design and Realization of Shell and Spatial Structures : IASS 2001*, Nagoya, Japan, Oct. 2001, TP080.

[25] T. Takeuchi, T. Ogawa, and T. Kumagai, “Seismic response evaluation of lattice shell roofs using amplification factors,” *Journal of the IASS*, vol. 48, pp. 197–210, 2007.

[26] T. Ogawa, T. Takeuchi, M. Nakagawa, and T. Kumagai, “Seismic response analysis of single layer lattice domes,” in *IASS-APCS 2003: Proceedings of the International Symposium on New Perspectives for Shell and Spatial Structures*, Taipei, Taiwan, Oct. 2003, pp. 110–111.

[27] T. Takeuchi, T. Ogawa, M. Nakagawa, and T. Kumagai, “Response evaluation of medium-span lattice domes with substructures using response spectrum analysis,” in *IASS 2004: Proceedings of the International Symposium “Shell and Spatial Structures from Models to Realization”*, Montpellier, France, Sep. 2004, pp. 205–206.

[28] S. Kato, T. Ueki, and Y. Mukaiyama, “Study of dynamic collapse of single layer reticular domes subjected to earthquake motion and the estimation of statically equivalent seismic forces,” *International Journal of Space Structures*, vol. 12, no. 3-4, pp. 191–203, 1997.

[29] T. Takeuchi, T. Ogawa, M. Nakagawa, and T. Kumagai, “Response evaluation of medium-span lattice domes with substructures using response spectrum analysis,” in *IASS2004 Symposium, Montpellier, 9*, 2004.

[30] S. Kato, S. Nakazawa, and K. Saito, “Two-mode based estimation of equivalent seismic loads and static estimation of dynamic response of reticular domes supported by ductile substructures,” *Journal of the IASS*, vol. 47, pp. 35–52, 2006.

[31] T. Takeuchi, T. Ogawa, and T. Kumagai, “State-of-arts views on response control technologies on metal space structures,” in *Proceedings of IASS 2009*, Valencia, Spain, Sep. 2009.

[32] T. Takeuchi, T. Kumagai, H. Shirabe, and T. Ogawa, “Seismic response evaluation of lattice roofs supported by multistory substructures,” in *Shell and Spatial Structures: Structural Architecture - Towards the future looking to the past. IASS Symposium*, Venice, Italy, Dec. 2007, p. 362.

[33] T. Kumagai, T. Takeuchi, T. Ogawa, A. Nakama, and E. Sato, “Seismic response evaluation of latticed domes with elasto-plastic substructures using amplification factors,” in *Proceedings of IASS 2005*, Bucharest, Romania, Sep. 2005, pp. 383–390.

[34] T. Takeuchi, T. Ogawa, T. Kumagai, A. Nakama, and E. Sato, “Applicability of response evaluation method for lattice domes with substructures,” *Journal of structural engineering. B*, no. 52, pp. 53–61, Mar. 2006, ISSN: 09108033.

[35] T. Takeuchi, T. Tsutsumi, T. Ogawa, and T. Kumagai, “Seismic retrofit of steel-structure school gymnasia with energy dissipation braces,” in *Proceedings of IASS 2010*, Shanghai.

[36] K. Kaneda, “Endeavors to control the vibration on long span structure,” in *Proc. of International Symposium on Theory, Design and Realization of Shell and Spatial Structures, Nagoya, Oct., 2001*, 2001.

[37] O. Hosozawa and T. Mizutani, “Structural design of Simokita Dome,” in *Proceedings of IASS 2005*, Bucharest, 2005, p. 707.

[38] T. Takeuchi, T. Ogawa, T. Suzuki, T. Kumagai, and C. Yamagata, "A basic study on damage-controlled design concept for truss frame structures," *Journal of Structural and Construction Engineering (Transactions of AIJ)*, vol. 51, pp. 31–37, 2005.

[39] S. Kato and S. Nakazawa, "Seismic design method to reduce the responses of single layer reticular domes by means of yielding of substructure under severe earthquake motions," in *Proceedings of IASS 2001*, Nagoya, Japan, Oct. 2001, TP077.

[40] D. Nair, Y. Terazawa, B. Sitler, and T. Takeuchi, "Seismic response of long-span domes supported by multi-storey substructures," *Journal of the IASS*, vol. 61, pp. 140–157, 2020.

[41] K. Kasai, H. Ito, and A. Watanabe, "Peak response prediction rule for a SDOF elasto-plastic system based on equivalent linearization technique," *Journal of Structural and Construction Engineering (Transactions of AIJ)*, vol. 68, no. 571, pp. 53–62, 2003.

[42] K. Kasai and H. Ito, "JSSI manual for building passive control technology. Part. 8 Peak response evaluation and design for elastoplastically damped system," in *13th World Conference on Earthquake Engineering, Vancouver, Canada. Paper*, 2004.

[43] S. Kato, Y. Konishi, and S. Nakazawa, "Pushover analysis and static estimation of seismic response of large steel space structures," *Proceedings of the IASS-APCS 2003*, pp. 54–55, 2003.

[44] S. Kato and Y. Konishi, "A study on seismic response estimation based on push-over analysis applied to reticular domes : Investigation in case of domes with one predominant vibration mode," *Journal of Structural and Construction Engineering (Transactions of AIJ)*, vol. 67, no. 561, pp. 153–160, 2002. DOI: 10.3130/aijs.67.153_2.

[45] S. Kato, S. Nakazawa, and K. Saito, "Two-mode based estimation of equivalent seismic loads and static estimation of dynamic response of reticular domes supported by ductile substructures," *Journal- International Association for Shell and Spatial Structures*, vol. 47, pp. 35–52, 2006.

[46] F. Cedrón and A. Elghazouli, "Seismic performance of single layer steel cylindrical lattice shells," *Journal of Constructional Steel Research*, vol. 163, p. 105 772, 2019.

[47] S. Shen, J. Xing, and F. Fan, "Dynamic behavior of single-layer latticed cylindrical shells subjected to seismic loading," *Earthquake Engineering and Engineering Vibration*, vol. 2, no. 2, pp. 269–279, 2003.

[48] S. Kato and T. Iwamoto, "Buckling and reliability analysis of single layer grid dome with diagonal brace under snow load," *Journal of the International Association for Shell and Spatial Structures*, vol. 58, no. 3, pp. 207–225, 2017.

[49] S. Kato, T. Yoshino, Y. Niho, and S. Nakazawa, "Discussions on loads factor for reticulated shells under snow load," in *Proceedings of IASS Annual Symposia*, International Association for Shell and Spatial Structures (IASS), vol. 2018, 2018, pp. 1–8.

[50] *The Building Standard Law of Japan on CD-ROM*. The Building Center of Japan, 2016.

[51] *Minimum Design Loads for Buildings and Other Structures*. ASCE Standard–ASCE/SEI 7–16: American Society of Civil Engineers (ASCE), 2016.

[52] *NZS 1170.5: 2004, Structural Design Actions Part 5: Earthquake actions-New Zealand*. Wellington, New Zealand: Standards New Zealand, 2004.

[53] *Design of Structures for Earthquake Resistance*. British Standard–Eurocode 8: Part-1, 2005.

[54] A. S. Whittaker, M. C. Constantinou, O. M. Ramirez, M. W. Johnson, and C. Z. Chrysostomou, "Equivalent lateral force and modal analysis procedures of the 2000 nehrp provisions for buildings with damping systems," *Earthquake Spectra*, vol. 19, no. 4, pp. 959–980, 2003.

[55] L. A. Fahnestock, R. Sause, and J. M. Ricles, "Seismic response and performance of buckling-restrained braced frames," *Journal of Structural Engineering*, vol. 133, no. 9, pp. 1195–1204, 2007.

[56] T. Güner and C. Topkaya, "Performance comparison of BRBFs designed using different response modification factors," *Engineering Structures*, vol. 225, p. 111 281, 2020.

Chapter 2

Case study of a long-span dome with multistorey substructures

Contents

2.1 Introduction

Since literature has very few studies on large-scale spatial structures (in areas of high seismic hazard) with long-span domes, in this chapter, the seismic response of a large-scale dome (150m span) with a multistorey substructure is explored. The choice of the models are inspired from the recent trend of large scale realised indoor stadiums or sports arenas with seating capacities of around 20,000 people. The substructure frame was modelled based on the preliminary substructure design of the K-arena project realised in Yokohama, Japan [1]. The detailed parametric studies on multistorey substructures are summarised later in Chapters 3 and 4.

2.2 Types of substructures

Assuming the location to be in Japan, a region of high seismic hazard, two types of response control strategies are considered for the substructure. The first type is the conventional steel braced frame - the buckling restrained braced frame [2]. As these framed structures are prone to weak-story failure mechanisms owing to large inelastic deformations, an alternative response control method- the damped spine frame (also referred to as the rocking frame [3] or steel concentrically braced frame (CBFs) [4]) is adopted for the second substructure. These systems are increasingly being adopted to control story drifts in taller buildings and mitigate post-earthquake structural damage and associated losses.

2.2.1 Buckling restrained braced frames

The first type of substructure (labelled as the 'Sub-BRB-MF') consists of a moment resisting frame (MRF) enveloping 16 pairs of braced frames, spaced equidistant around the perimeter (Figure 2-1a). These braced frames (BRBF) employ energy-dissipating braces called buckling-restrained braces BRBs (Figures 2-2-2-3) [5] arranged in a v-configuration (Figure 2-1c (i)). The substructure has 6 storeys below the roof and has a total height of 32m (Figure 2-1).

The 3-D analysis benchmark models were constructed in ETABS [5] and high-strength

steel material ($f_y = 345$MPa) was adopted for all frame and roof members. The substructure moment frame members were adopted from the preliminary design of the K-arena project [1]. This type of braced substructure is widely used to design buildings in countries of high seismic hazard, such as Japan. Recent years have seen BRBF being increasingly applied to large-scale indoor stadiums and arenas, an example of which is the Toyota stadium shown in Figure 2-4. The design shear force distribution was calculated using a peak ground acceleration of 0.97g and the BRBs were designed using seismic design shear forces and Ai distribution defined in the Japanese code [6]. The frame sections and mass distribution are summarised in Tables 2.1 and 2.2. For analysis, the BRBs were modelled as links. When a single truss element replaces both the core and the connections, an equivalent elastic axial stiffness can be used [2] which were used as input parameters to define the links for the models. The simplified modelling parameters are illustrated in Figure 2-2 and the hysteresis curve is shown in Figure 2-3. The axial force-displacement of the BRBs were determined assuming a post-yield tangent stiffness modulus E_t as 2% of initial modulus E. The effective stiffness (K_{eq}) can be determined using the parameters- total length (L_t), axial force (N_y), core-to-elastic area ratio (A_c/A_e) and plastic-to-work point length ratio (L_p/L_0) as shown in Equation 2.1. It is assumed that the member degradation is prevented by the debonding mechanism and the strong restrainer, hence a simple bi-linear hysteresis model (Figure 2-3(b)) was adopted composed of elastic stiffness, compressive (N_c) and tensile yield strengths (N_y or P_y), and post-yielding stiffness ($p = 2\%$) and a compression adjustment factor ($\beta = 1.1$, $N_c = 1.1 \times N_y$). The specifications of the employed BRBs for both the substructures are summarised in Table 2.3. The floors are modelled as membrane elements [5] to represent mass of each floor. These elements essentially transfer the entire loads directly to the structural objects.

Table 2.1: Frame Sections Data

Member	Section Shape	Section Size (mm)
Roof Member	CHS	ϕ500 t12
Tension Ring	CHS	ϕ1500 t24
MF Column	SHS	600×600×25
MF Beam	I/Wide Flange	588×300×12×20
RF Brace	I/Wide Flange	600×600×19×19

Table 2.2: Model Mass Data

Storey	Height (m)	Weight (kN)
RFL	32	54018
6FL	21	18304
5FL	17.5	28507
4FL	14	28507
3FL	10.5	41121
2FL	7	41121
M2FL	3.5	41121

Table 2.3: Specifications for BRBs in substructure

Name	N_y (kN)	L_t (m)	K_{eq} (kN/m)	σ_y (MPa)	A_c/A_e	L_p / L_0
BRC	3000	5.5	685285	225	0.5	0.4
BRC	3000	7.0	685285	225	0.4	0.3
BRB-RFL	1200	6.6	233578	245	0.5	0.3
BRB-Lower	1500	5.1	380587	245	0.5	0.3

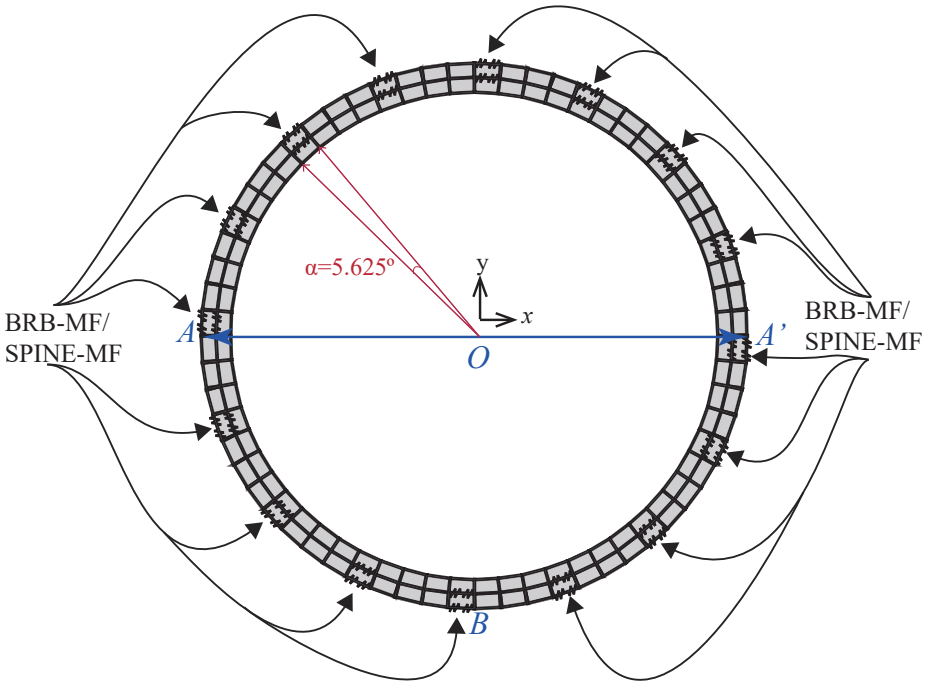

(a) Plan view: location of BRB-MF/Spine-MF

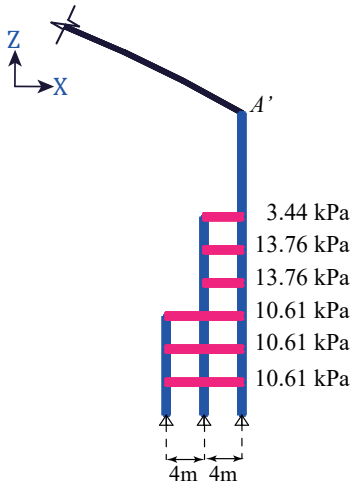

(b) Elevation view OA': Mass distribution per floor

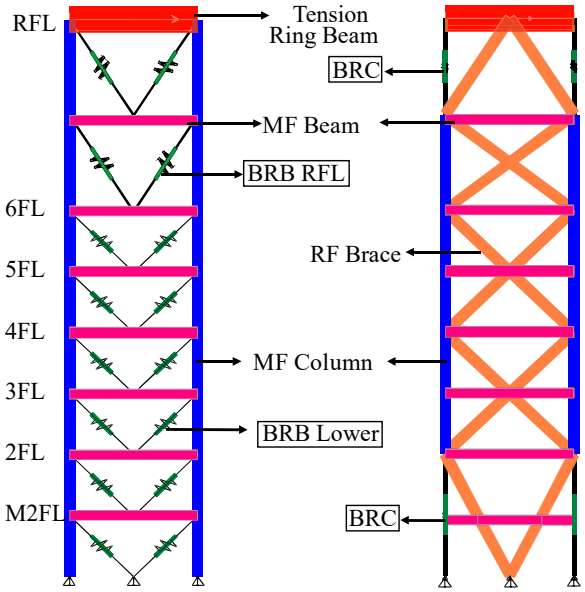

(i) BRB-MF (ii) Spine-MF

(c) Elevation view illustrating frame section properties

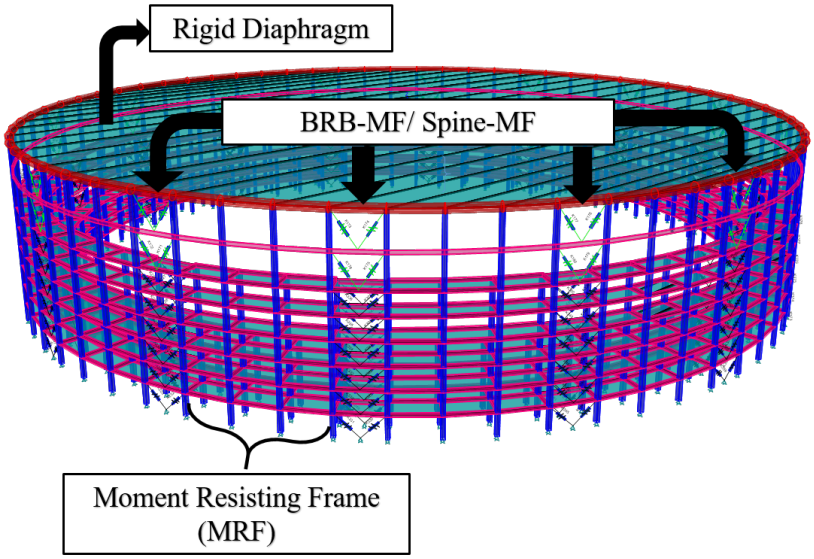

(d) 3-D view of substructure

Figure 2-1: Analysis models for case study

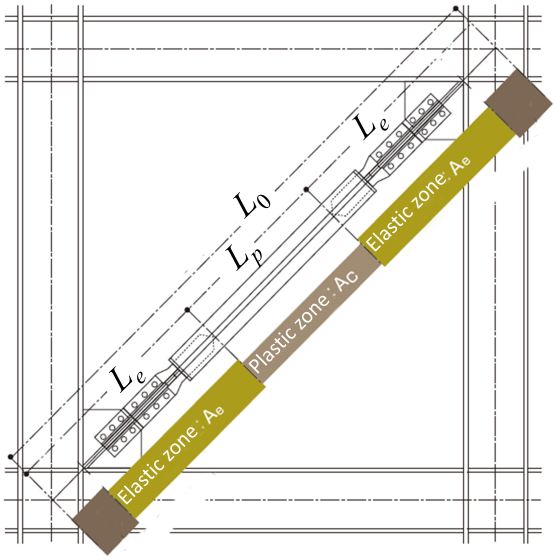

Figure 2-2: Simplified modelling parameters of BRB [2]

$$K_{eq} = \frac{EA_c}{L_0} \cdot \frac{1}{\frac{L_p}{L_0} + 2\frac{L_e}{L_0}\frac{A_c}{A_e}} \tag{2.1}$$

where,

Yield axial force : $N_y = A_c \cdot \sigma_y$

Yield axial deformation : $\delta_y = N_y / K_{eq}$

L_p : length of plastic zone

L_e : length of reinforced elastic zone

A_c : area of core in plastic zone

A_e : area of core in reinforced elastic zone

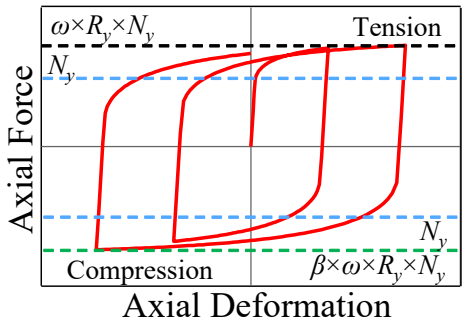

R_y: Overstrength Factor

ω : Strain Hardening Factor

β : Compression Strength Adjustment Factor (1.1~1.3)

(a) General hysteresis curve of a BRB

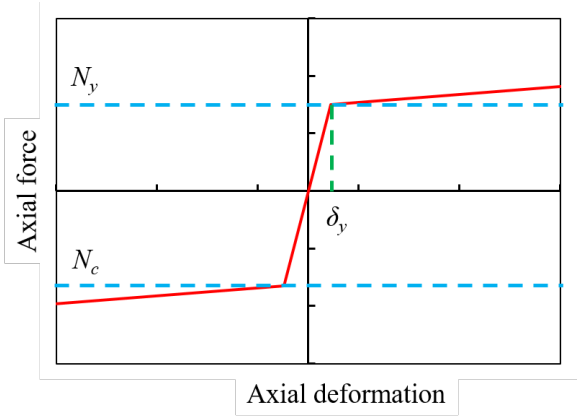

(b) Bi-linear model with kinematic hardening

Figure 2-3: BRB backbone curve for analysis

Figure 2-4: Application of BRBF in substructure of Toyota stadium [7]

2.2.2 Damped spine frames

The second substructure considered (Sub-Spine-MF) consists of spine frames in place of the braced frames (Figures 2-1(c -ii) and 2-1(d)). The spine frame utilises a stiff elastic braced steel frame with replaceable energy-dissipating members inserted vertically (here, the BRBs are referred to as buckling restrained columns (BRC)).

The spine frame is composed of an elastic truss that provides a strong vertical backbone and rocks upon its foundation during an earthquake while the BRCs dissipate energy. The spine frames engage every story in a pivoting displaced shape and thereby prevent damage concentration while the enveloping MRF provides self-centering force and reduces residual drifts [3]. This further facilitates faster recovery of the structure post-earthquake and minimises the economical costs of repair.

This substructure was designed to have a similar initial stiffness and yield deformation as the equivalent Sub-BRB-MF. The BRC specifications are given in Table 2.3. The spine frame was designed to stay elastic which was confirmed by performing NLRHA analysis on the combined model using ground motions specified in Section 2.7.2 to check the member forces against their capacity design strength as per the guidelines in AISC 360-16 [8]. In both the substructure models, the floors are assumed to be rigid and a rigid diaphragm is assigned to the roof.

Both the substructure models employ MRF with rigidly jointed beam-column connections although two additional models with pinned beam-column connections are also included (labelled as Sub-Spine-P and Sub-BRB-P) to investigate the effects of low post-yield stiffness of the substructure. The contribution of the MRF towards the lateral stiffness is negligible in the Sub-Spine-P and Sub-BRB-P models.

2.3 Modal analysis of substructures

The first two vibration modes (in order of decreasing mass participation factors $\Gamma_i(\%)$) of the substructure models are given in Table 2.4 and the mode shapes are shown in Figure 2-5. The first mode of both substructures is a translational sway mode and this has a mass participation factor of less than 80%.

In the case of Sub-Spine-MF, the modal displacements increase continuously from the base to the top. Therefore, the maximum displacements and accelerations can be expected to occur at the top storey. The first mode shape of Sub-BRB-MF is slightly irregular, but the maximum displacements are still observed at the top storey. As seen in Figure 2-5, the second mode shape has an inflection point, implying that the maximum acceleration may not always occur at the top storey due to higher mode effects. In the case of Sub-BRB-MF, the stories at mid height exhibit the maximum modal displacement. Thus, the simplified first mode based shear distributions proposed by several codes (like the Japanese *Ai* distribution or the ASCE-7 prescribed equivalent lateral force distribution) may not always be accurate in such cases when the contribution of the higher mode or the mass participation towards the overall response is significant.

Table 2.4: Periods of the substructure models

Model Name	Mode	T (s)	Γ (%)
Sub-BRB-MF	1	0.91	55
	2	0.39	35
Sub-Spine-MF	1	0.91	67
	2	0.30	25

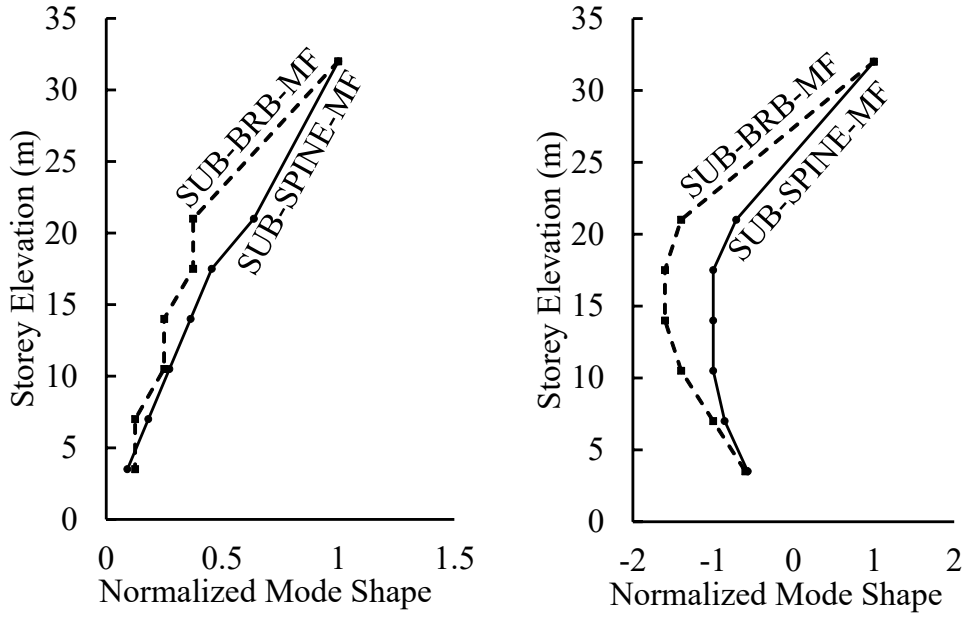

(a) Mode 1 (b) Mode 2

Figure 2-5: Mode shapes of the substructures

2.4 Inelastic response of substructure

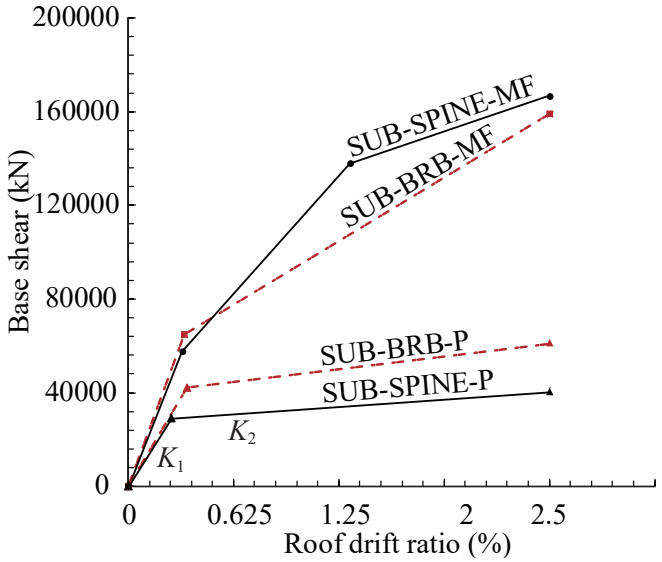

Figure 2-6: Simplified first modal pushover curve for the substructure models

Nonlinear pushover analysis (derived from the fundamental mode shape) was performed on the global substructure model (with the roof as a rigid diaphragm and mass), allowing the beam ends of the moment frame beam and the BRBs to yield. To better understand the major yielding points, the first-mode curves were bilinearised by matching the areas at 2.5% roof drift (Figure 2-6). The Sub-Spine-MF is better simplified as a trilinearised curve to mark the two distinct yield points which correspond to yielding of the spine frame and yielding of the moment frame beams [3]. For this study, it was observed that the moment frame did not yield in the level-2 earthquake and were modelled as elastic for the later sections to decrease analysis time. The ratio of post-yield stiffness to the elastic stiffness (K_{2i}/K_{1i}) for all models from the bi-linearised curves were also computed and the initial stiffness in the first (K_{11}) and second mode (K_{12}) are listed in Table 2.5.

Table 2.5: Base Shear vs Roof Displacement: stiffness in each mode (kN/mm)

Model	K_{11}	K_{11}/K_{21}	K_{12}	K_{12}/K_{22}
BRB-MF	615	4.5	4600	1
Spine-MF	562	2.2	5896	1
BRB-P	381	14	2820	1
Spine-P	354	22	4160	1

NLRHA was also performed for the substructure models to study the seismic behaviour of the substructures (Figure 2-1). All isolated buildings and tall buildings in Japan are always subjected to the same three earthquakes or the "golden set". These earthquakes are El Centro NS 1940, Taft EW 1952 and Hachinohe EW 1968 [9]. Therefore, these three input earthquake ground motions were selected and spectrally matched to the target design spectrum (BRI-L2) corresponding to a Level-2 Japanese earthquake defined by the Building Research Institute [6], [10]. The spectrum was adjusted to an inherent damping ratio h_o=2% using Equation 2.3 (Figure 2-7) [11]. In addition, the artificial ground motion BCJ-L2 was also used as an input ground motion for analysis. A Rayleigh damping ratio of 2% was assigned to the first two modes for analysis. The base shear time history for all four waves and the story shear force distributions for El-Centro wave for the two models

are shown in Figures 2-8-2-9. The larger shear forces in the Sub-Spine-MF model (Figure 2-9) are a result of a higher post-yield stiffness.

The interstorey drifts for all four input ground motions are also compared in Figure 2-10. The Sub-Spine-MF model exhibits a near-uniform storey drift distribution, while the sub-BRB-MF model tends to concentrate damage at the top storey. In contrast, the stiff spine frames effectively engage the neighbouring MRF to produce an even storey drift distribution.

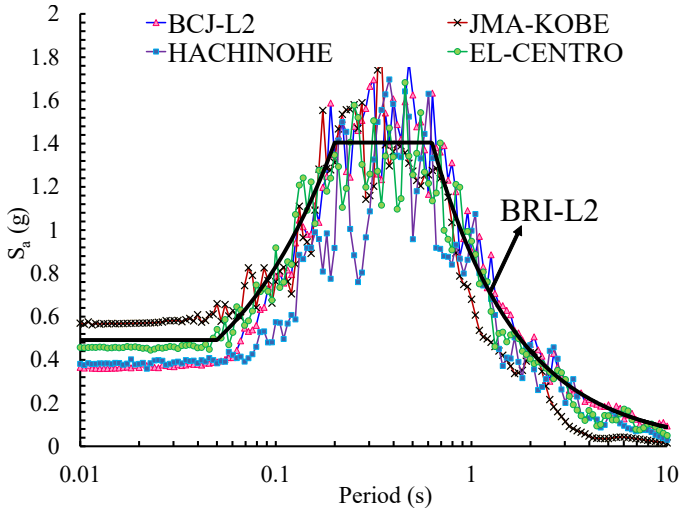

Figure 2-7: Design acceleration spectrum for level-2 earthquake (h_o=0.02)

$$S_a(T) = \left\{ \begin{array}{cc} 350D_h & (T \leq 0.05) \\ 350D_h(T/0.05)^{(1+log(5/7)log4)} & (0.05 < T \leq 0.2) \\ 1000D_h & (0.2 < T < \pi/5) \\ 1000D_h/(T/2\pi) & (\pi/5 \leq T) \end{array} \right\} \tag{2.2}$$

$$D_h = \sqrt{(1+75h_b)/(1+75h_o)} \tag{2.3}$$

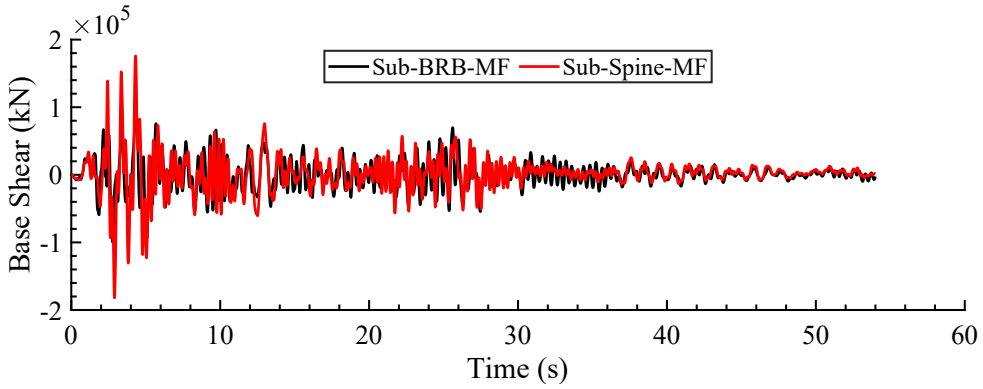

(a) El-Centro

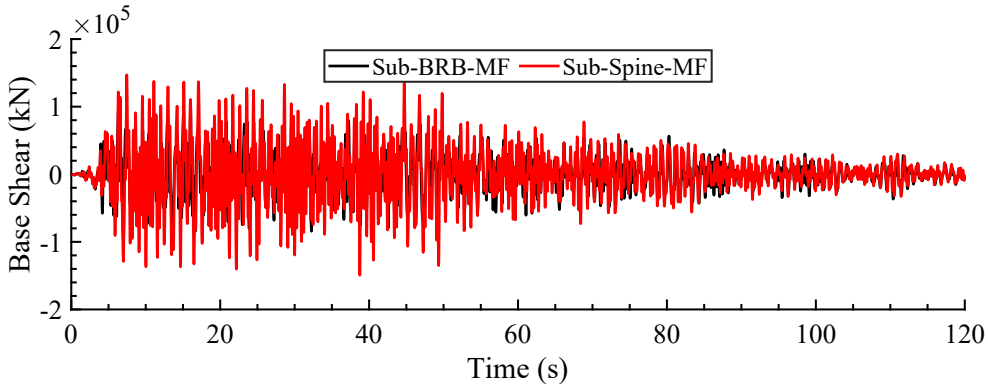

(b) BCJ-L2

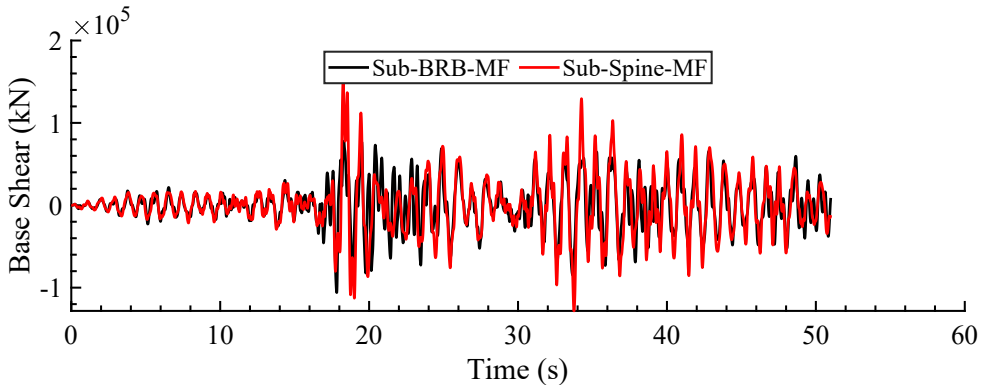

(c) HACHINOHE

Base Shear Force in substructure model (contd.)

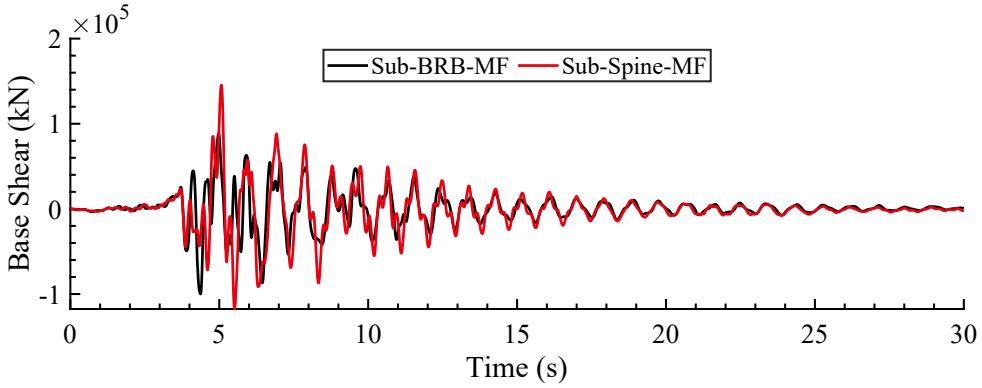

(d) JMA-KOBE

Figure 2-8: Base Shear Force in substructure model

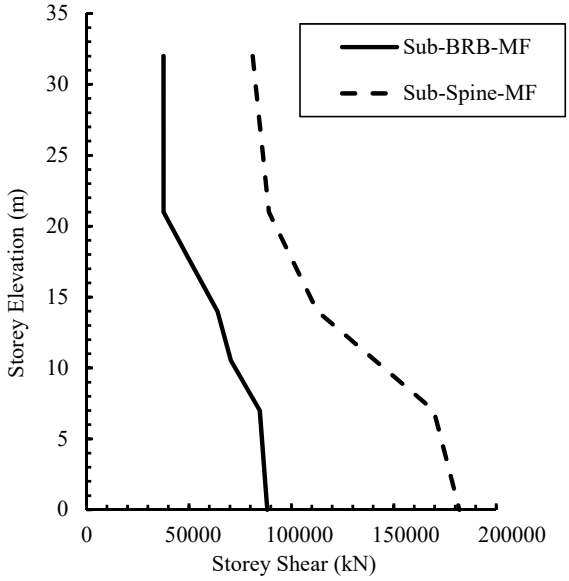

Figure 2-9: Maximum shear force distributions for substructure models

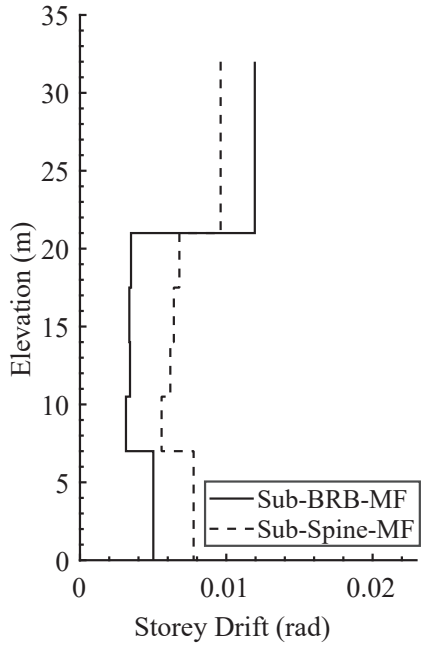

(a) El-Centro

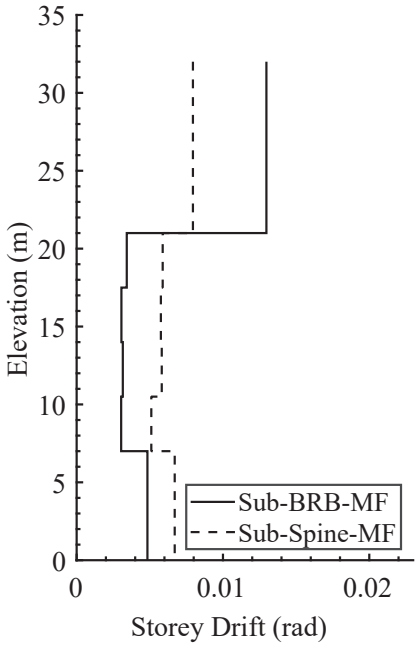

(b) BCJ-L2

Maximum storey drifts for substructure models (contd.)

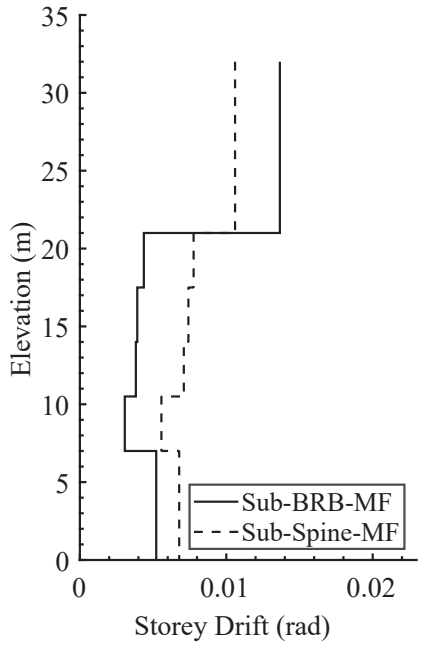

(c) HACHINOHE

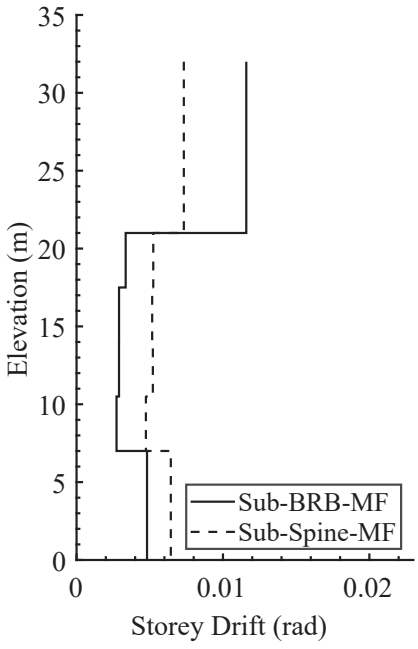

(d) JMA-KOBE

Figure 2-10: Maximum storey drifts for substructure models

2.5 Roof model

A double-layered steel dome was designed for a span of 150m and a half subtended angle (θ) of 30°. The size of the lattice members and the vertical offsets (d) between the centre lines of the section are listed in Table 2.6. All roof members were assigned the same size of members for simplicity. The design of the roof members was performed using a trial and error approach using an assumed section size proposed by the engineer's judgement and was checked by performing NLRHA analysis on the combined model using ground motions specified in Section 2.7.2 to check the forces of the members against their design strength according to the guidelines in AISC 360-16 [8]. An example of the design check for the roof's ridgeline members is summarised in Table 2.7. For simplicity, the double-layer lattice was modelled using equivalent beams (Figure 2-12 (a)) with out-of-plane stiffness modification factors [12] with moment connections and pinning the roof lattice perimeter nodes.

The roof geometry was modelled in *Grasshopper* [13] and imported to ETABS [5] using the *GeometryGym* [14] plugin for analysis. GeometryGym is a tool for parametrically defining and developing ETABS models using Grasshopper. First, a 2d triangular grid was constructed using an equivalent triangulation method using a suitable edge length of 5m as shown in Figure 2-11(a,b). The 2d grid was trimmed at the edges using the base circumferential curve. Finally, the 2d grid was projected vertically onto the spherical surface to obtain the 3d dome model as shown in Figure 2-11(c). After importing, the roof member beams in ETABS were modelled as 'frame' objects which are general three-dimensional beam elements [15]. The dead load on the roof was then uniformly loaded on the nodes as point loads. This dome model was used to identify the roof modes and is denoted as the 'roof model'.

Table 2.6: Roof models: Member section sizes ($f_y = 345$ MPa)

Model	Dead Load (DL) (kPa)	Double-layer beam (mm)	offset d (m)	Single-layer beam (roof member) (mm)	m
$L150$	3	$2\times(\phi)407t7.2$	2.8	$(\phi)500t12^*$	64.3

* ϕ =Outer Diameter, t =Thickness of circular hollow section
m = Out-of-plane stiffness modification factor

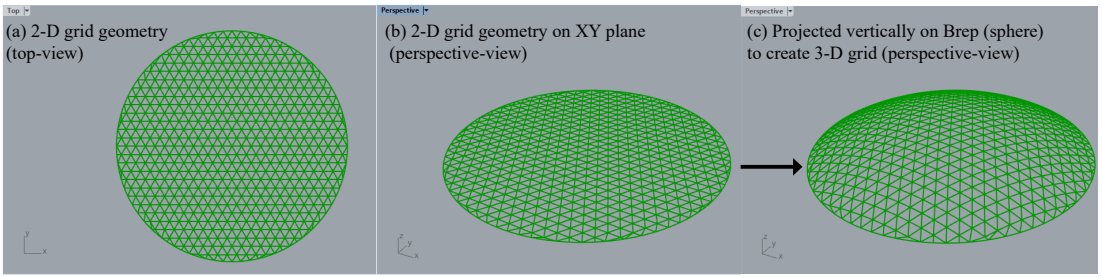

Figure 2-11: Building the 3d geometry of dome in *Grasshopper*

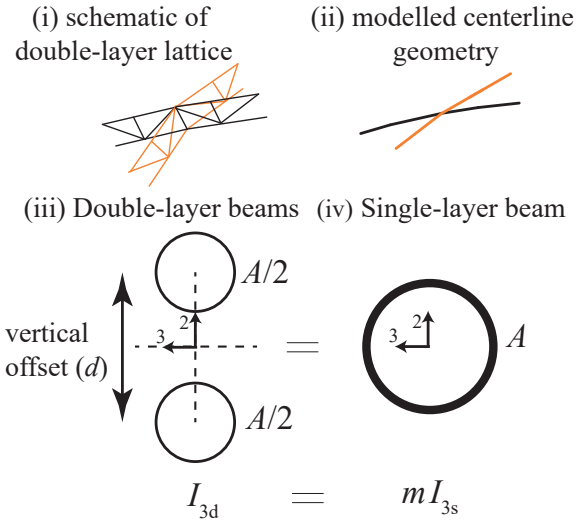

Figure 2-12: Equivalent single-layer beam modelling

The first few vibration modes of the dome are shown in Figure 2-13. The fundamental period of the roof (T_R) was found to be 0.5s with the roof exhibiting the anti-symmetric O1 mode shape [16], [17]. The mode with the highest participation was a higher mode denoted as O3.5 mode followed by the O1 mode.

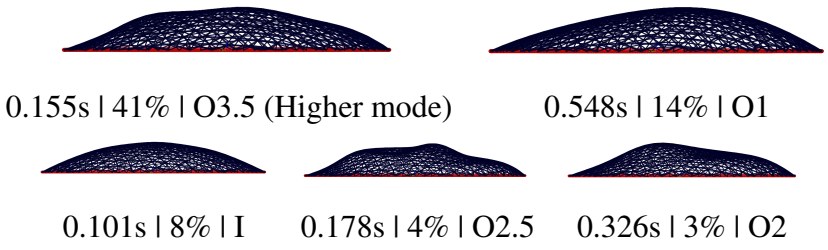

Figure 2-13: First few dominant modes of the dome:
Periods and Mass participation (%)

Table 2.7: Axial forces design check for ridgeline roof members (AISC-360 [8])

Member	Max TC	Min TC	Max BC	Min BC	A	λ	P_{dt}	P_{dc}	F_e	$P_{dt} > P_t$	$P_{dc} > P_c$	$P_{dt} > P_t$	$P_{dc} > P_c$
	kN	kN	kN	kN	cm^2		kN	kN	MPa	TC	TC	BC	BC
m2352	-644	-1083	572	-1076	90	47	2807	2405	934	TRUE	TRUE	TRUE	TRUE
m2388	-581	-973	381	-1030	90	46	2807	2415	960	TRUE	TRUE	TRUE	TRUE
m2426	-590	-793	316	-1067	90	45	2807	2423	981	TRUE	TRUE	TRUE	TRUE
m2464	-443	-866	342	-1091	90	45	2807	2429	999	TRUE	TRUE	TRUE	TRUE
m2503	-321	-934	317	-1052	90	45	2807	2434	1014	TRUE	TRUE	TRUE	TRUE
m2544	-249	-956	243	-984	90	44	2807	2438	1024	TRUE	TRUE	TRUE	TRUE
m2585	-215	-849	38	-896	90	44	2807	2440	1032	TRUE	TRUE	TRUE	TRUE
m2626	-266	-658	-248	-735	90	44	2807	2441	1035	TRUE	TRUE	TRUE	TRUE
m2690	-268	-648	-243	-735	90	44	2807	2441	1035	TRUE	TRUE	TRUE	TRUE
m2725	-212	-834	52	-890	90	44	2807	2440	1032	TRUE	TRUE	TRUE	TRUE
m2766	-237	-935	265	-971	90	44	2807	2438	1024	TRUE	TRUE	TRUE	TRUE
m2807	-297	-900	349	-1030	90	45	2807	2434	1014	TRUE	TRUE	TRUE	TRUE
m2845	-393	-808	381	-1063	90	45	2807	2429	999	TRUE	TRUE	TRUE	TRUE
m2883	-523	-726	344	-1049	90	45	2807	2423	981	TRUE	TRUE	TRUE	TRUE
m2920	-484	-869	382	-1001	90	46	2807	2415	960	TRUE	TRUE	TRUE	TRUE
m2954	-497	-927	619	-1075	90	47	2807	2405	934	TRUE	TRUE	TRUE	TRUE
m2249	-195	-1517	152	-1732	90	50	2807	2342	798	TRUE	TRUE	TRUE	TRUE
m2267	-554	-1560	543	-1625	90	49	2807	2362	837	TRUE	TRUE	TRUE	TRUE
m2291	-794	-1383	689	-1338	90	48	2807	2379	873	TRUE	TRUE	TRUE	TRUE
m2320	-774	-1242	693	-1195	90	47	2807	2393	906	TRUE	TRUE	TRUE	TRUE
m2983	-610	-1078	783	-1131	90	47	2807	2393	906	TRUE	TRUE	TRUE	TRUE
m3011	-650	-1248	767	-1247	90	48	2807	2379	873	TRUE	TRUE	TRUE	TRUE
m3033	-398	-1495	672	-1565	90	49	2807	2362	837	TRUE	TRUE	TRUE	TRUE
m3049	-38	-1334	359	-1484	90	50	2807	2342	798	TRUE	TRUE	TRUE	TRUE

where BC= bottom chord, TC=top chord, $\lambda = L_c/r$ is the member slenderness ratio,

A=BC/TC member gross area, $F_e = \pi^2 E/\lambda^2$ = elastic buckling stress, $E = 205,000$ MPa,

$P_{dt} = \phi_t P_{nt}$ and $P_{dc} = \phi_t P_{nc}$ are the design tensile and compressive strength respectively, $\phi = 0.90$ (LRFD)

P_t and P_c are the maximum tensile and compressive forces from NLRHA (load combination of 1.2DL+E [18]),

P_{nt} and P_{nc}= nominal tensile and compressive strength, respectively, as per Chapters D and E of AISC [8]

2.6 Combined models

The combined analysis models were then constructed by adding the dome roof model (Section 2.5) to the multistorey substructure models (Section 2.2). The combined models are denoted as Spine-MF and BRB-MF and their first two dominant mode shapes are shown in Figure 2-14. Both of these models employ MRF with rigidly jointed beam-column connections although two additional models with pinned beam-column connections are also included (labelled as Spine-P and BRB-P) to investigate the effects of low post-yield stiffness of the substructure. The contribution of the MRF towards the lateral stiffness is negligible in the Spine-P and BRB-P models.

2.6.1 Modal analysis

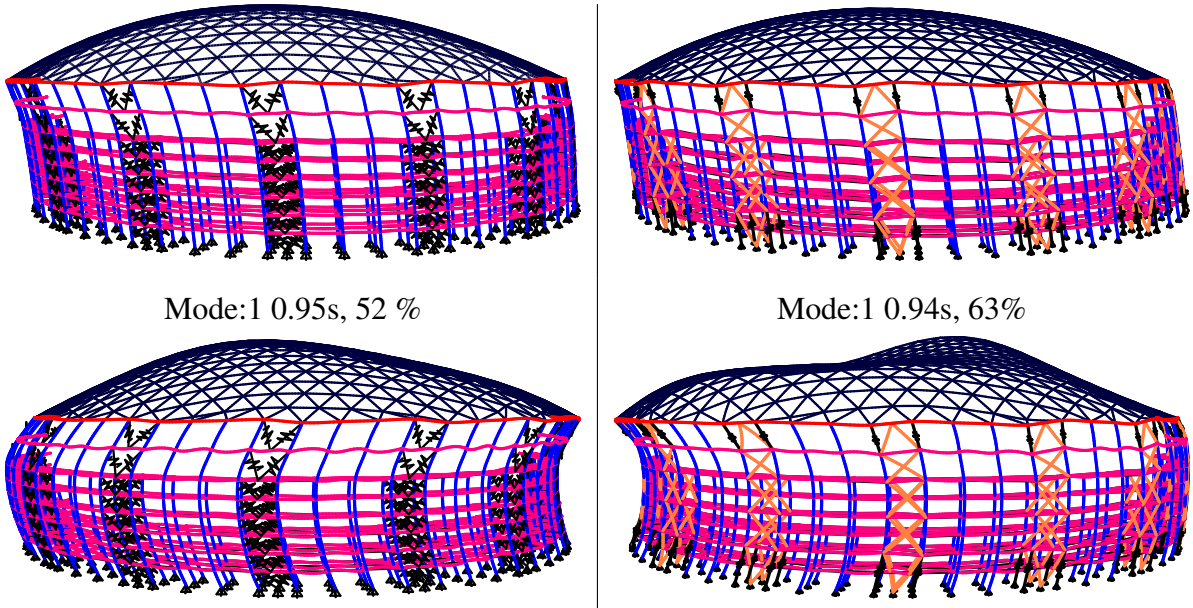

Mode:1 0.95s, 52 %

Mode:1 0.94s, 63%

Mode:2 0.41s, 36 %

Mode:2 0.34s, 25%

(a) BRB-MF

(b) Spine-MF

Figure 2-14: Two dominant modes of combined models

The first two periods of all the four combined models and substructure models are summarised in Figure 2-15. The periods of the first two modes are very close to the corresponding periods of their substructure models and the mass participation factors are nearly

equal. The slight difference in the periods is due to the rigid roof assumption in the sub-structure model with infinite in-plane stiffness as opposed to the large but finite stiffness from the lattice members.

For the combined models (Figure 2-14), the first mode is essentially a combination of the translational sway mode of the substructure and the roof's O1 mode. The second mode of the two models is slightly different. This is because Spine-MF is slightly stiffer than BRB-MF in the second mode. The substructure in both the models vibrates in its respective (translational) second mode. In the second mode of Spine-MF model, the O2 roof mode (higher mode) is excited as the period 0.34s coincides with the roof's O2 mode (Section 2.5). For the BRB-MF case, the second mode lies between the O2 and the O1 mode of the roof, but since it's closer to the O1 mode, the roof appears to vibrate in its O1 mode. As opposed to the medium-span domes, the first mode of the long-span domes generally lies on the constant-velocity region of the design acceleration spectrum while the second mode lies on the constant acceleration region of the design spectrum as shown in Figure 2-7. This implies a greater contribution of the higher modes to the overall response.

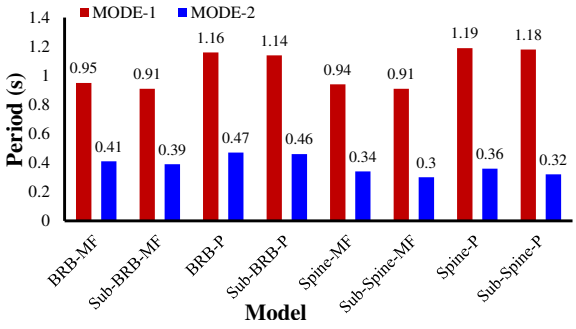

(a) Periods of two dominant modes

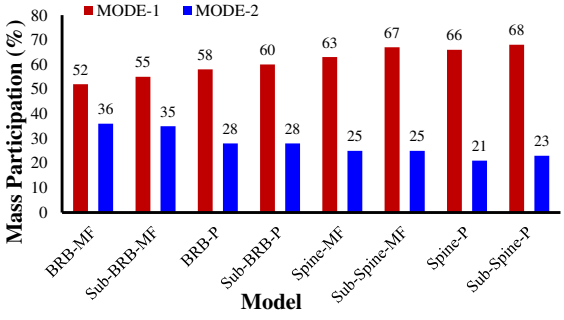

(b) Mass participation of two dominant modes

Figure 2-15: Modal analysis results

2.7 Linear and nonlinear response history analysis

LRHA and NLRHA were performed on all the four models (Figure 2-15) permitting the BRCs and BRBs to yield. Four input ground motions (El-Centro, Hachinohe, BCJ-L2 and JMA-Kobe) were used, each were spectrally matched to the BRI-L2 design spectrum (Figure 2-7). Response history analysis was implemented using the fast non-linear analysis method (FNA) developed by Wilson et al. [5]. This method has proven to be extremely efficient, particularly for structural systems which are primarily linear elastic and have predefined nonlinear elements. The beams and columns were confirmed to remain elastic [19] up to the design drifts using nonlinear pushover analysis. 2% Rayleigh damping was applied to the first two dominant modes. It should be noted that geometric non-linearity, P-delta secondary effects and wave-passage effects are outside the scope of the present study.

2.7.1 Elastic response

LRHA was performed with the BRBs, BRCs and the MRF assigned elastic properties. The acceleration distributions along the ridge line *A-O-A'* are given in Figures 2-16-2-19. The response was also estimated using the amplification factor approach discussed in Sections 1.3.4-1.3.5.

As an example, the peak elastic acceleration calculation for Spine-MF model is shown in Table 2.8. It can be observed that the roof accelerations are nearly double of the base acceleration.

Table 2.8: Spine-MF: Using *Ai* distribution to obtain peak elastic acceleration of substructure

Storey	Storey Weight (kN)	Cumulative Weight (kN)	α_i	A_i	Shear Force Q_i (kN)	Acceleration A_{eq} (g)
RFL	54018	54018	0.21	1.95	102230	1.89
6FL	18304	72323	0.29	1.77	124341	1.72
5FL	28507	100830	0.40	1.58	154312	1.53
4FL	28507	129336	0.51	1.43	179690	1.39
3FL	41121	170457	0.67	1.26	209153	1.23
2FL	41121	211578	0.84	1.12	230825	1.09
M2FL	41121	252699	1.00	1.00	245118	0.97

The LRHA response was then compared with the computed response using the Equations 1.10-1.16, which only considers the first mode of the substructure (with Γ_1 equal to 100%). These plots are labelled as 'PREVIOUS'. From the plots, it can be seen that the proposed accelerations well cover the elastic horizontal response underestimating the peak responses by about 20%. The proposed vertical response reasonably covers the obtained response but the envelope shape is different from the obtained responses for the Spine-MF and Spine-P models. The obtained envelope indicates that the O2 mode of the roof and not the fundamental O1 mode governs the response for these models. This indicates that the assumed O1 modeshape may not be accurate for structures where the higher roof modes are dominant. It may also be concluded that the roof higher modes are sensitive to the substructure modal characteristics and can significantly influence the envelope roof response.

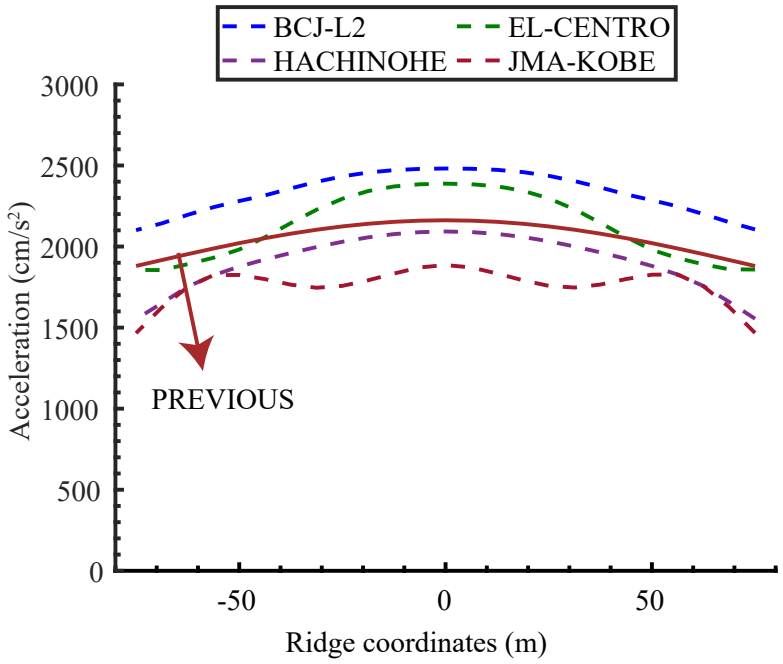

(a) Horizontal accelerations

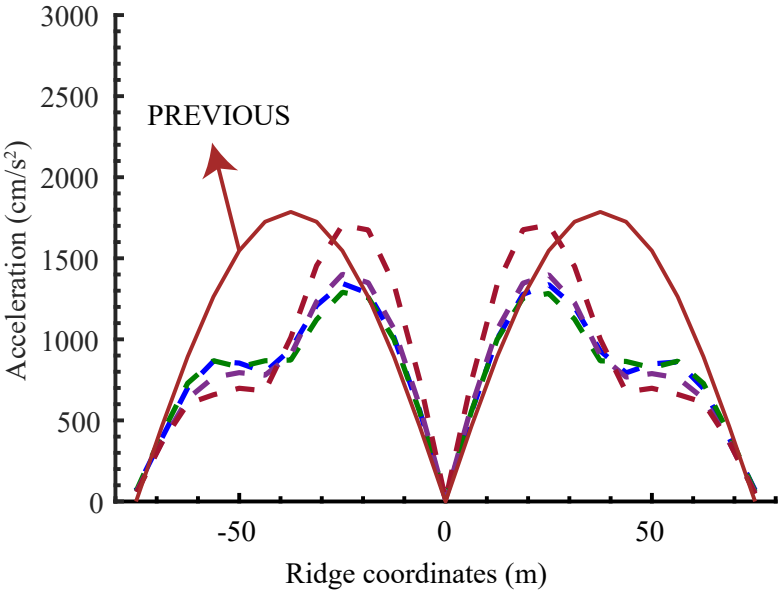

(b) Vertical accelerations

Figure 2-16: Elastic response: Spine-MF

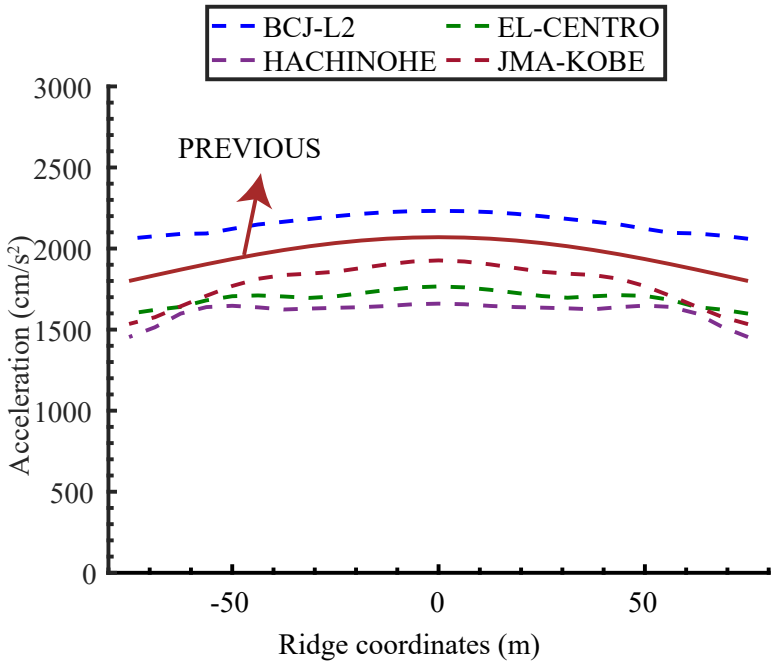

(a) Horizontal accelerations

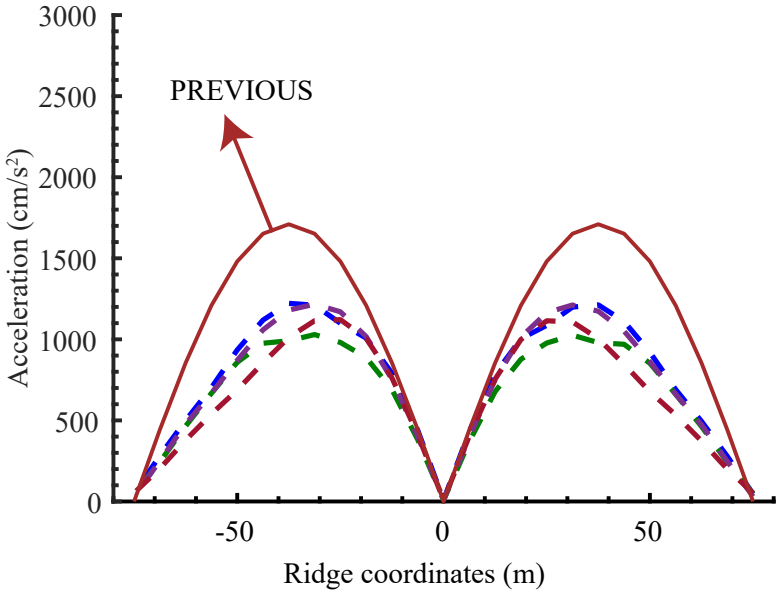

(b) Vertical accelerations

Figure 2-17: Elastic response: BRB-MF

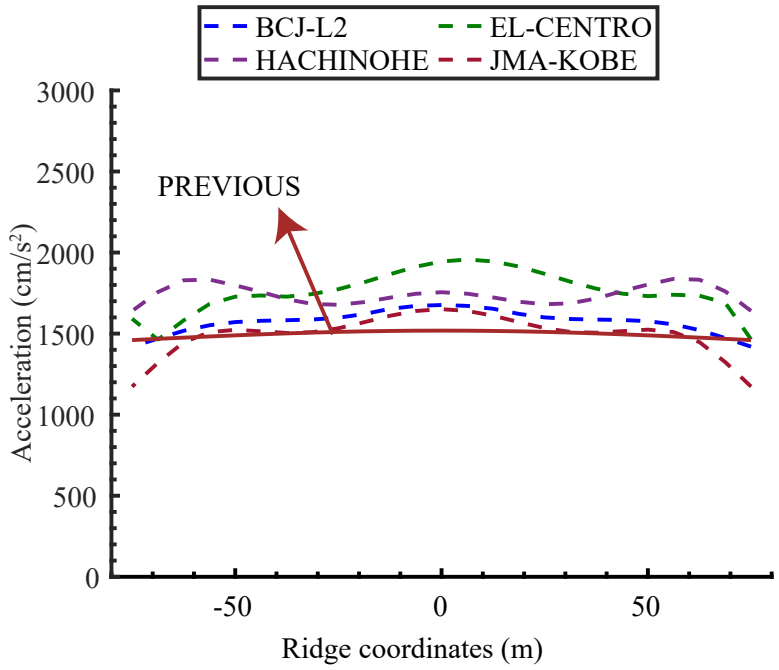

(a) Horizontal accelerations

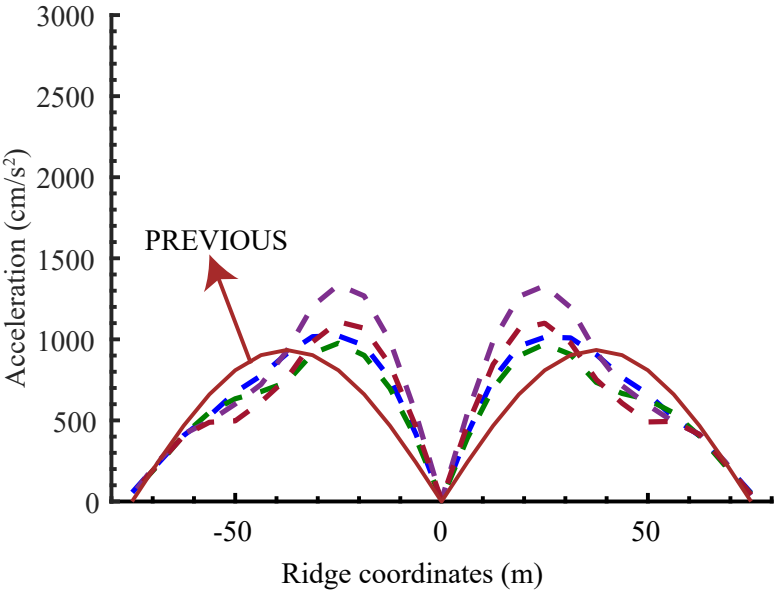

(b) Vertical accelerations

Figure 2-18: Elastic response: Spine-P

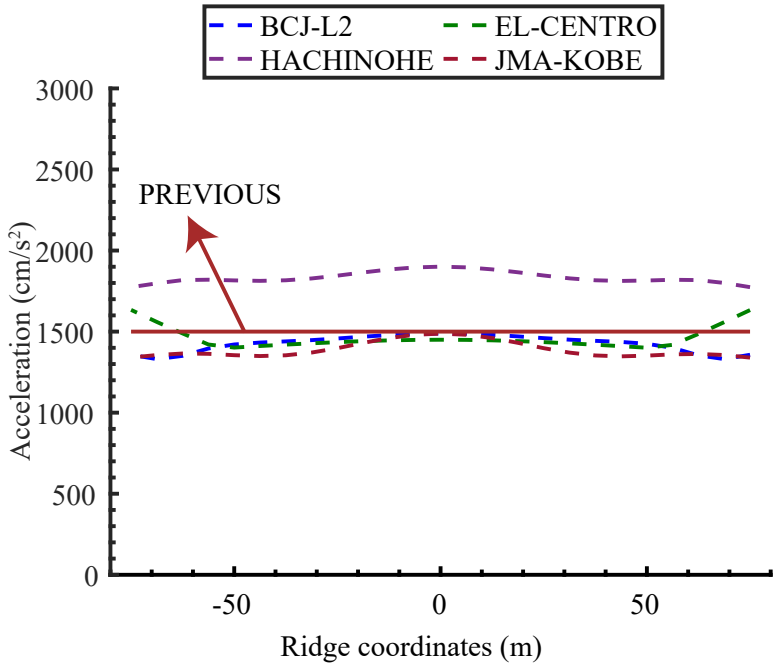

(a) Horizontal accelerations

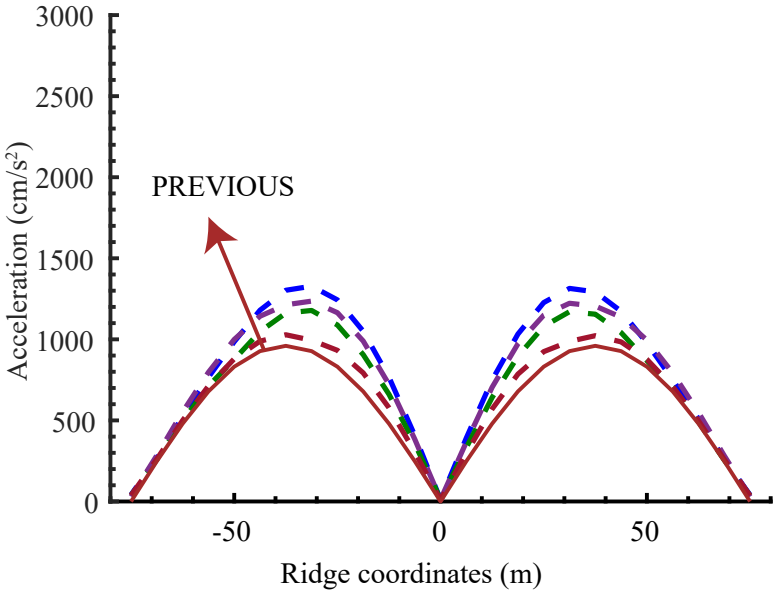

(b) Vertical accelerations

Figure 2-19: Elastic response: BRB-P

2.7.2 Inelastic roof response estimation

To apply the procedure in Section 1.3.5 which was proposed to estimate the peak elastic roof response, the peak inelastic substructure response was computed as follows to estimate the peak inelastic roof response referring to the inelastic substructure studies by Kumagai [10], [20] using equivalent linearisation approach by Kasai [11].

Peak substructure response Estimation

Step 1 Obtain the substructure periods.

From the eigenvalue analysis, obtain the fundamental period of the substructure model (T_1).

Step 2 Obtain the peak elastic roof acceleration of the substructure.

Use the Ai distribution (as per the Japanese code [6]) and the design acceleration spectrum to obtain the maximum elastic acceleration distribution of the substructure. The acceleration at the top storey is adopted as the peak elastic acceleration A_{Heq}.

Step 3 Obtain the yield point and post-yield stiffness of the substructure.

Allowing the moment frame beams and BRBs to yield, perform nonlinear pushover analysis on the substructure models using the force distributions as per the first mode. Calculate the ratio of the post-yield stiffness to the elastic stiffness K_2/K_1 for all the models from the bi-linearized curves (Figure 2-6).

Step 4 Obtain the equivalent damping ratio and response reduction factor.

The equivalent stiffness (K_{eq}) and equivalent damping ratio (h_{eq}) are obtained using the equivalent linearization procedure proposed by Kasai et al. [11], which estimates the peak response of elasto-plastic systems. For each of the modes, assume a starting value of ductility ratio μ and iterate h_{eq} and K_{eq}/K_1 using Equations 2.4-2.7 until μ converges, where the subscript (j) is the jth step of the iteration. In case of Spine-MF models where peak roof drift falls in the third region of the pushover curve, K_{eq} can be calculated using the equivalent linearization procedure given by Chen et al. [3].

$$K_{eq}/K_1 = 1/\mu + (1 - 1/\mu)K_2/K_1 \tag{2.4}$$

$$h_{eq} = h_o + \frac{2(K_1/K_2)}{\pi\mu} \ln \frac{K_1/K_2 + \mu - 1}{(K_1/K_2)\,\mu^{K_2/K_1}} \tag{2.5}$$

$$D_h = \sqrt{(1+25\,h_o)/(1+25h_{eq})} \tag{2.6}$$

$$\mu_{(j)} = \mu_{(1)}\,D_{h(j-1)}/\sqrt{K_{eq(j-1)}/K_1} \tag{2.7}$$

Step 5 Calculate the equivalent periods and inelastic peak roof accelerations of the substructure.

Calculate the equivalent (secant) period T_{eq} and the peak accelerations A_{Heq1} and A_{Veq1} of the SDOF model using Equations 2.8-2.10. A_{Heq1} and A_{Veq1} are the peak horizontal and vertical inelastic accelerations of the SDOF model (Figure 1-31).

$$T_{eq1} = T_1\sqrt{K_1/K_{eq}} \tag{2.8}$$

$$A_{Heq1} = A_{eq}\,D_h\sqrt{K_{eq}/K_1} \tag{2.9}$$

$$A_{Veq1} = A_{eq}\sqrt{K_{eq}/K_1} \tag{2.10}$$

These substructure accelerations were then used in Equations 1.13-1.16 to obtain the peak roof response using period ratios obtained from the substructure's equivalent period T_{eq1}.

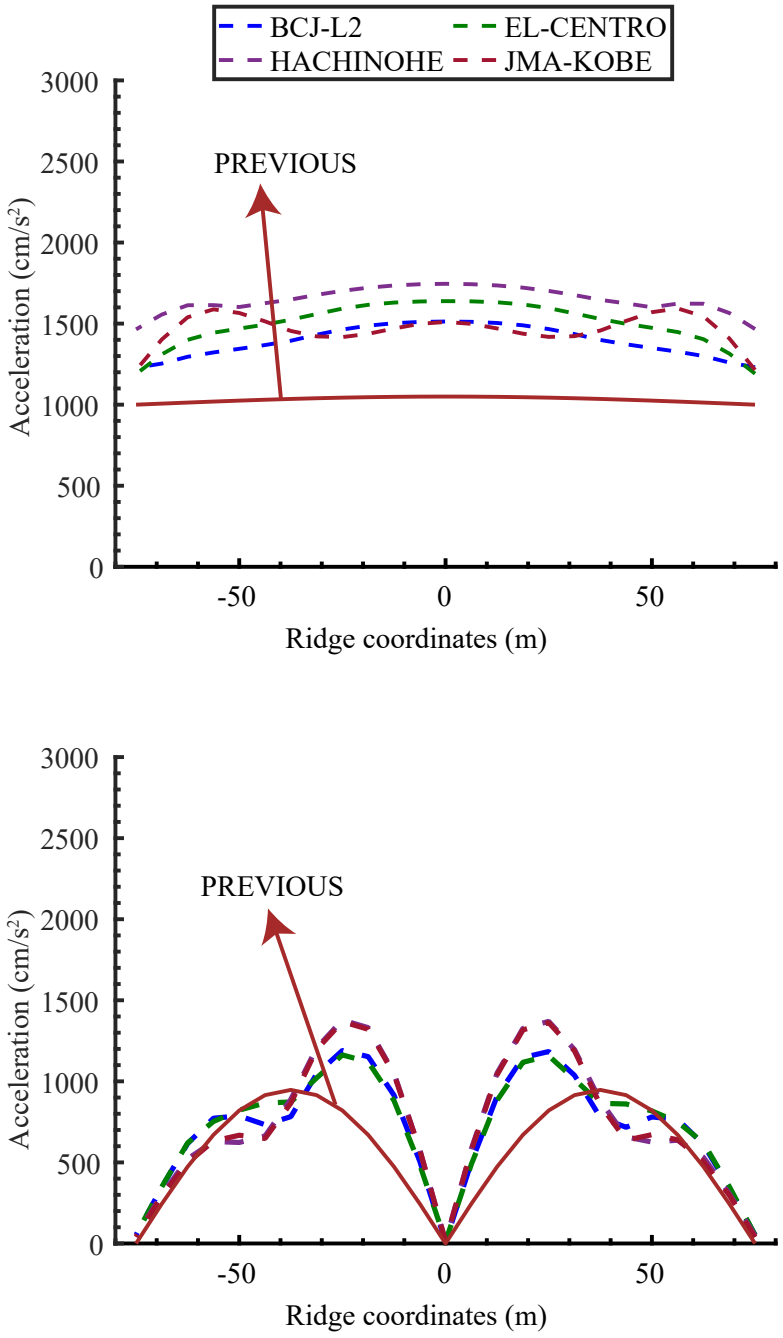

Figure 2-20: Inelastic response: Spine-MF

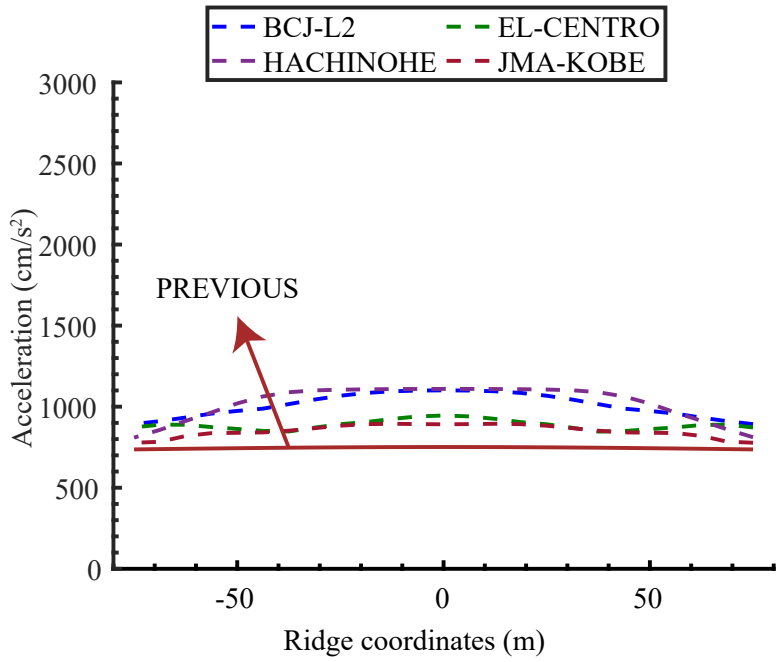

(a) Horizontal accelerations

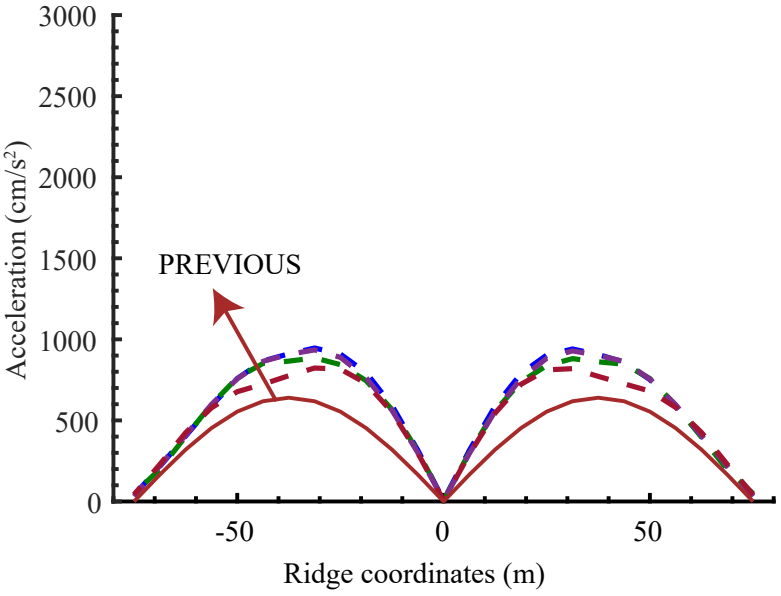

(b) Vertical accelerations

Figure 2-21: Inelastic response: BRB-MF

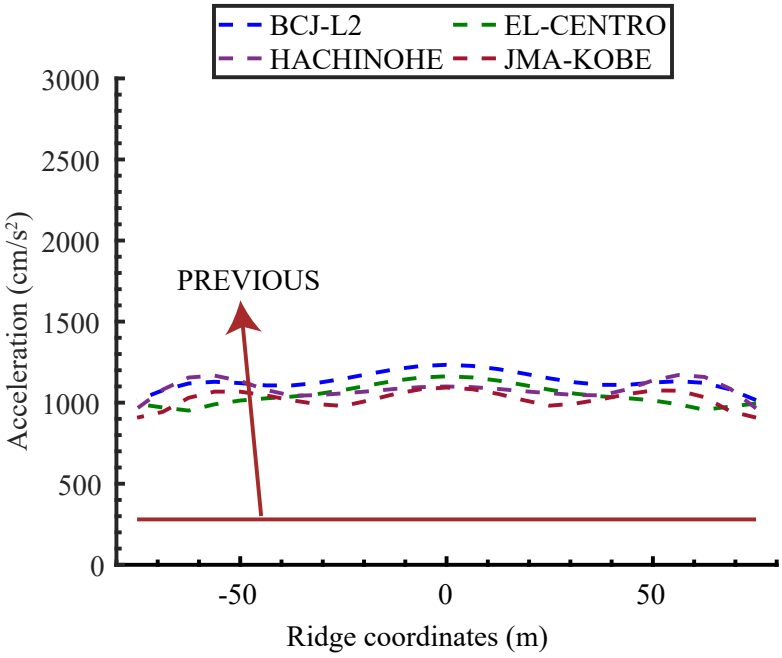

(a) Horizontal accelerations

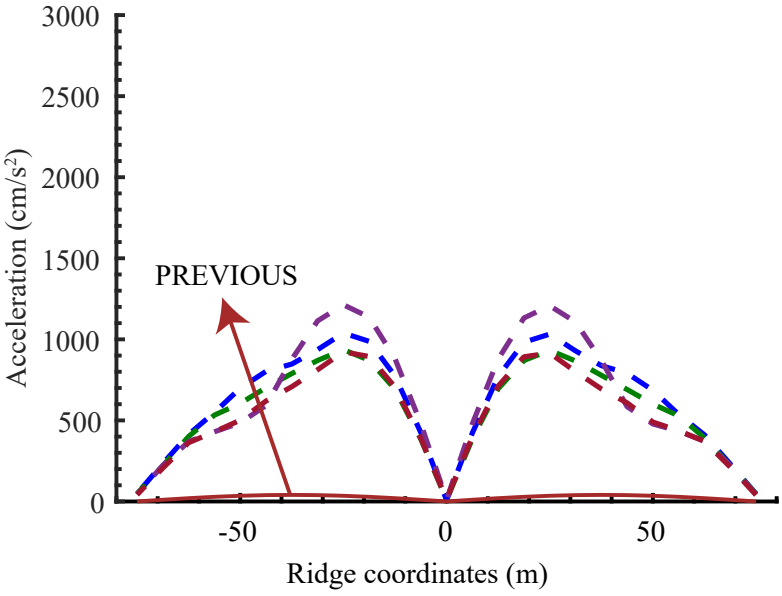

(b) Vertical accelerations

Figure 2-22: Inelastic response: Spine-P

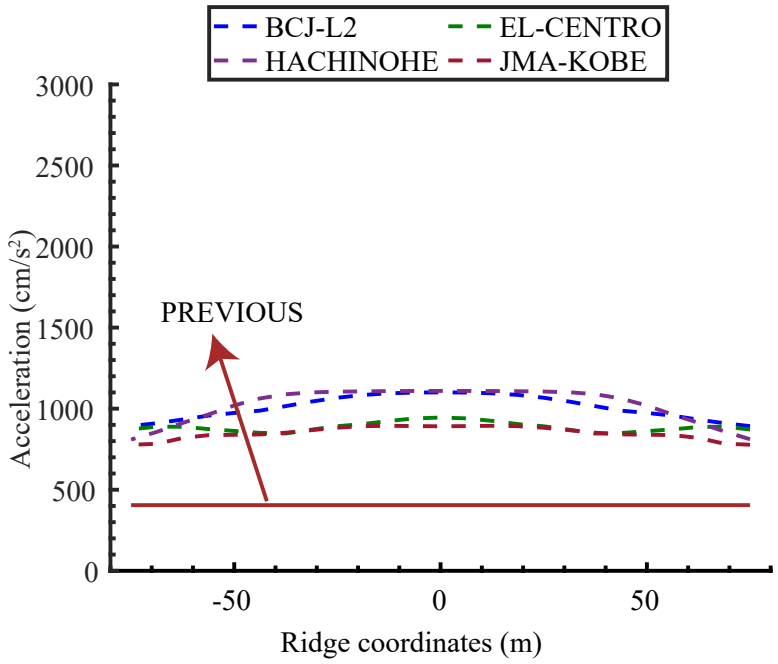

(a) Horizontal accelerations

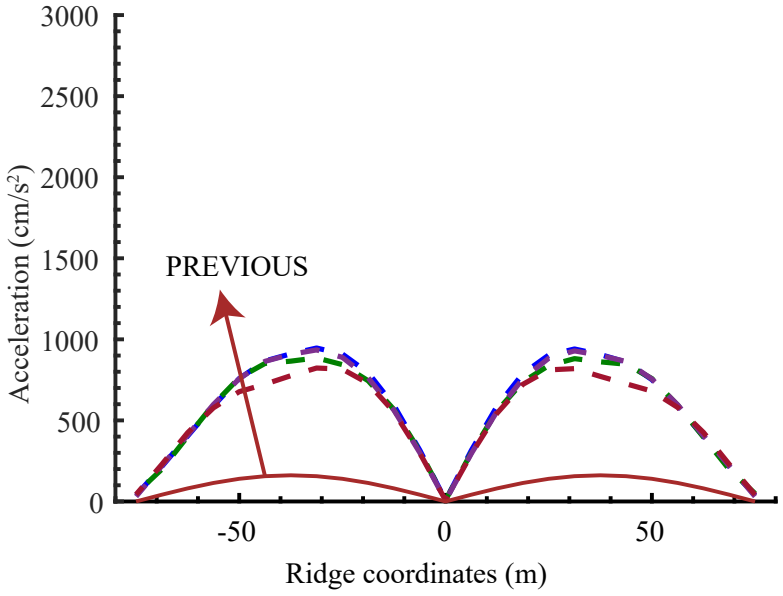

(b) Vertical accelerations

Figure 2-23: Inelastic response: BRB-P

The peak acceleration distributions along the ridge line *A-O-A'* are given in Figures 2-20-2-23. The excitation of the O2 mode in the Spine-MF model is evident from the dual peaks appearing in the distribution of vertical acceleration. The substructure yields for all models in the first mode, significantly reducing the contribution of the first mode to the overall response, evident from the reduced values A_{Heq1} and A_{Veq1} in Table 2.9. A reduction of about 40-50% was observed for the horizontal accelerations and about 20-30% for the vertical accelerations if compared to the elastic response where BRBs remained elastic. The reduction was more in the BRB-MF model compared to the Spine-MF model due to the lower post-yield stiffness of the substructure (i.e., a lower value of K_{21}/K_{11} in Table 2.5). The reductions in vertical acceleration values due to the added dampers are found to be lesser than those in the horizontal accelerations. Similar observations were made by Takamatsu et al. [21] while studying seismically isolated domes where the reduction in vertical acceleration was mainly due to the elongated period.

In the case of the simply supported BRB-P and Spine-P models (Figures 2-22-2-23), the 'PREVIOUS' response, which is computed using only the substructure's first mode, severely underestimates the overall response. This is because the post-yield modal stiffness of the substructure is negligible as evident from the near elastic-perfectly-plastic pushover curve (Figure 2-6). This results in longer equivalent periods (T_{eq1}) and larger response reductions ($D_h \sim 0.5$) explaining the low values of peak accelerations. However, the higher substructure's mode lie on the maximum acceleration region of the response spectrum which may correspond to high A_{Heq2} and A_{Veq2} values. However, this second mode response is not considered in the proposed method. Therefore, the results for BRB-P and Spine-P shown in Figures 2-18-2-19 confirm that only considering the substructure's first mode for response may severely underestimate the peak accelerations of structures with significant yielding in first-mode and near-elastic higher modes. This also suggests that there is a need to introduce response control strategies that can effectively reduce the response not only of the first mode but also of the significant higher modes, particularly for spine framed systems.

The energy dissipation curves of the four models for the input ground motion BCJ-L2 are shown in Figure 2-24. It was observed that the input energy of the models with spine

frames was slightly less than the models with BRBF. However, the energy dissipated due to hysteretic damping as a percentage of input energy was slightly less in spine frame models (around 50%-60% in Spine-MF and Spine-P compared to 60%-70% in BRB-MF and BRB-P). The reduction in values of the maximum axial forces along the members of the ridgeline are summarised in Table 2.10. The maximum axial forces for the inelastic response were about 20% lower than those observed for the elastic response. It was observed that the distribution of axial forces Figure 2-25 was sensitive to the input ground motion and model parameters and hence no general trend could be inferred. From the plots, it can be seen that the reduction in the axial forces was more for the models with BRBF. In addition, the reductions in axial forces are not proportional to the reductions in accelerations. This is also in accordance with the energy dissipation results.

Table 2.9: Main Parameters of equivalent linearisation method [17]

Model	Mode i	T_1 (s)	D_h	K_{eq}/K_1	μ	T_{eq1} (s)	A_{Heq1} (cm/s^2)	A_{Veq1} (cm/s^2)
BRB-MF	1	0.91	0.57	0.47	3.14	1.33	750	1300
Spine-MF	1	0.91	0.68	0.64	3.61	1.13	1100	1600
BRB-P	1	1.14	0.48	0.31	3.91	2.05	400	860
Spine-P	1	1.18	0.41	0.20	5.98	2.61	280	700

Table 2.10: Maximum reduction in axial forces

Model	Reduction in Maximum Axial Force (%)			
	BCJ-L2	EL-CENTRO	HACHINOHE	JMA-KOBE
Spine-MF	21	20	12	13
BRB-MF	27	25	26	32
Spine-P	12	12	18	11
BRB-P	33	30	31	11

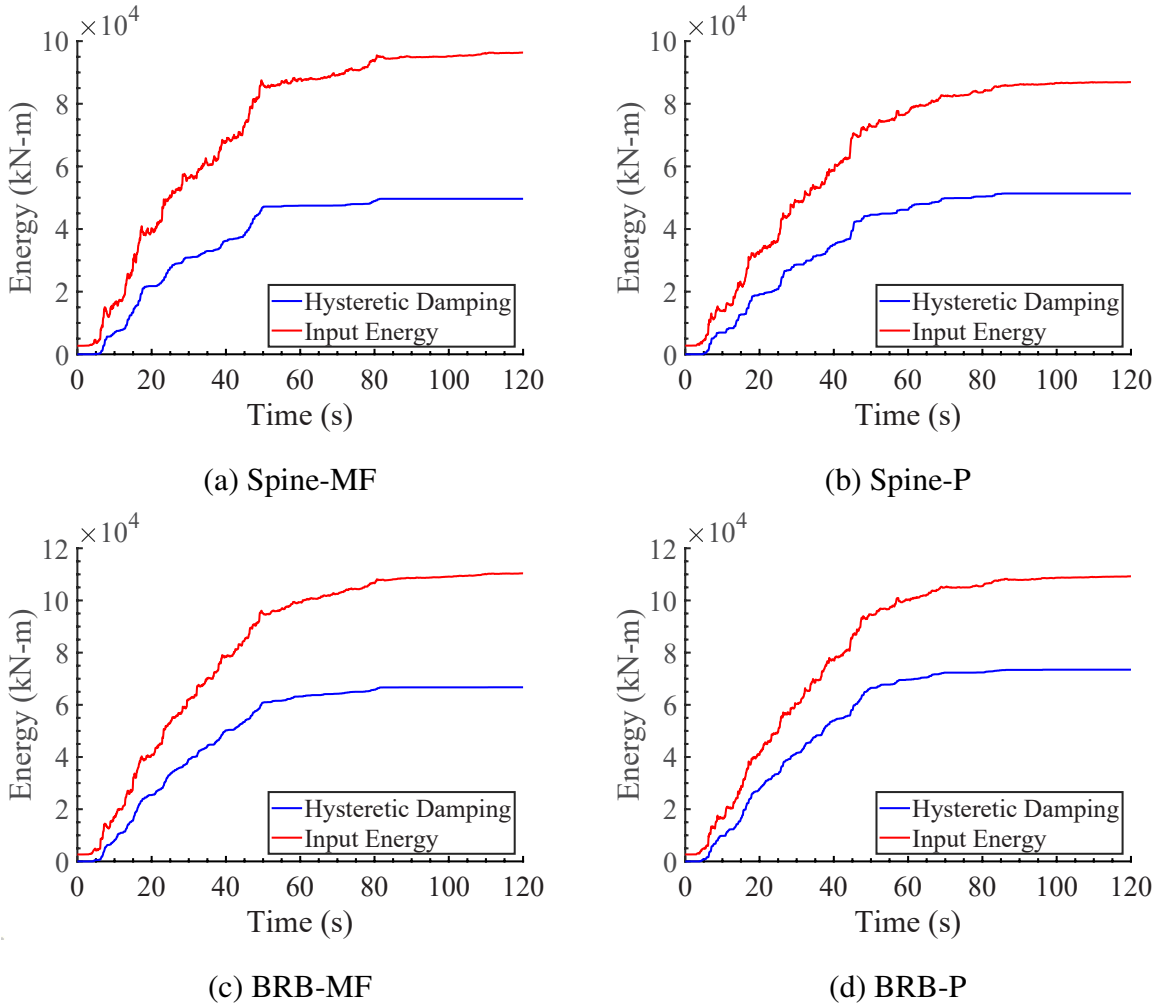

(a) Spine-MF

(b) Spine-P

(c) BRB-MF

(d) BRB-P

Figure 2-24: Energy dissipation as a function of time
for BCJ-L2 input ground motion

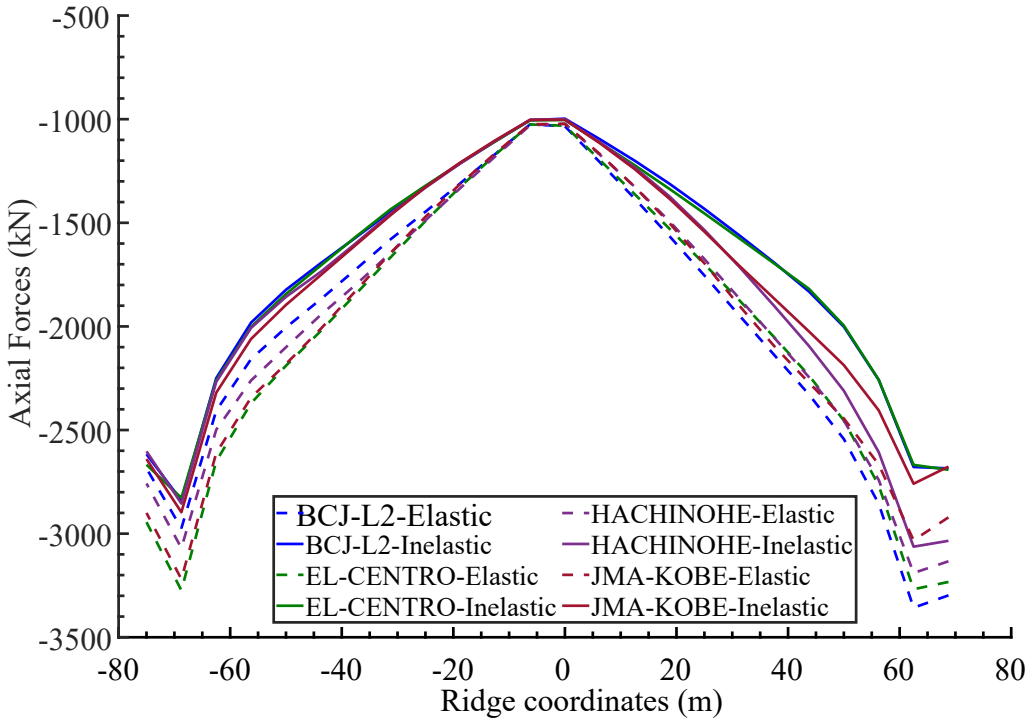

(a) Spine-MF

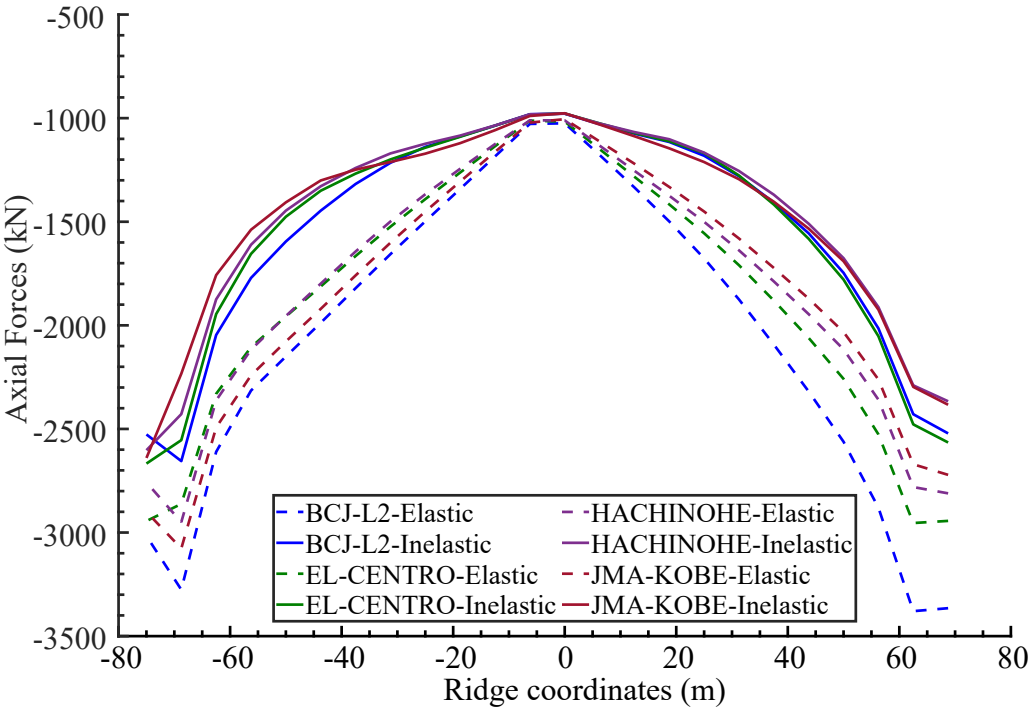

(b) BRB-MF

Figure 2-25: Combined models: Reduction in maximum axial forces

2.8 2-Segmented spine frames

The previous section established a need to explore response control strategies for strong-back or spine frames that can reduce the response of the long-span dome due to the sub-structure higher modes. This chapter investigates the effects of the addition of 2-segmented damped spine frames as a measure to mitigate the higher-mode response.

Chen et al. [22] proposed segmented spine systems as shown in Figure 2-26 to control the near-elastic higher mode response of high-rise structures with 1-segmented spine frames. The behaviour of the 1-segmented spine frame is limited to yielding in the first mode. The 2-segmented spine systems segment the stiff elastic frame at mid heights to enable the yielding of ductile BRBs in the higher mode, which effectively reduces the response of high-rise buildings by providing additional energy dissipation capacity, compared to the 1-Segmented spine system. It was shown that considering only the first mode for the response could result in large errors for high-rise structures with significant participation from higher modes.

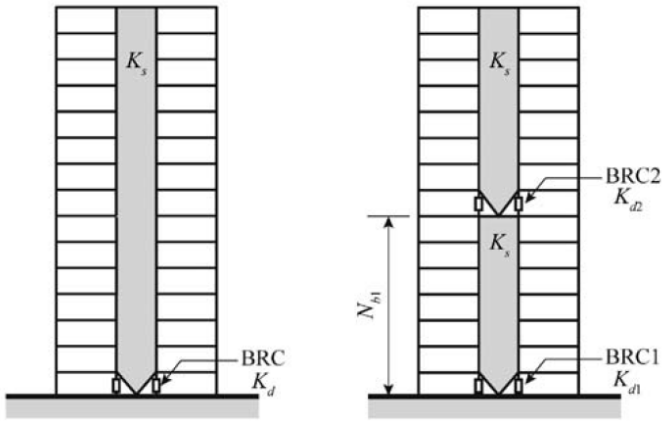

Figure 2-26: 1-segmented spine frame vs 2-segmented spine frame (Chen et al. [22])

Segmented spine frames are essentially two or three spine frames arranged in series along the height of the structure. All of these are pin-connected at the boundaries. These systems were found to effectively reduce base shear for high-rise buildings compared to the performance of a 1-segmented spine system [22]. Therefore, additional substructure models with 2-segmented spine frames were constructed and the effects of the 2-segmented

spine frame on the roof response were investigated.

2.8.1 Analysis models

3-d models with substructures employing 2-segmented spine frames instead of the conventional 1-segmented spine frames (formerly the Spine-MF model) were constructed (Figure 2-27). The spine frames employ BRCs as energy dissipating devices that are inserted vertically. The location of added BRCs (BRC-MID) are as shown in Figure 2-28. The deformed shape of the frame in the higher mode is also shown in Figure 2-29. The floor at which the next segment was to be added was determined as per the floor with maximum modal displacement observed in the higher mode (in this case, the second mode) of the Sub-Spine-MF model (Figure 2-5).

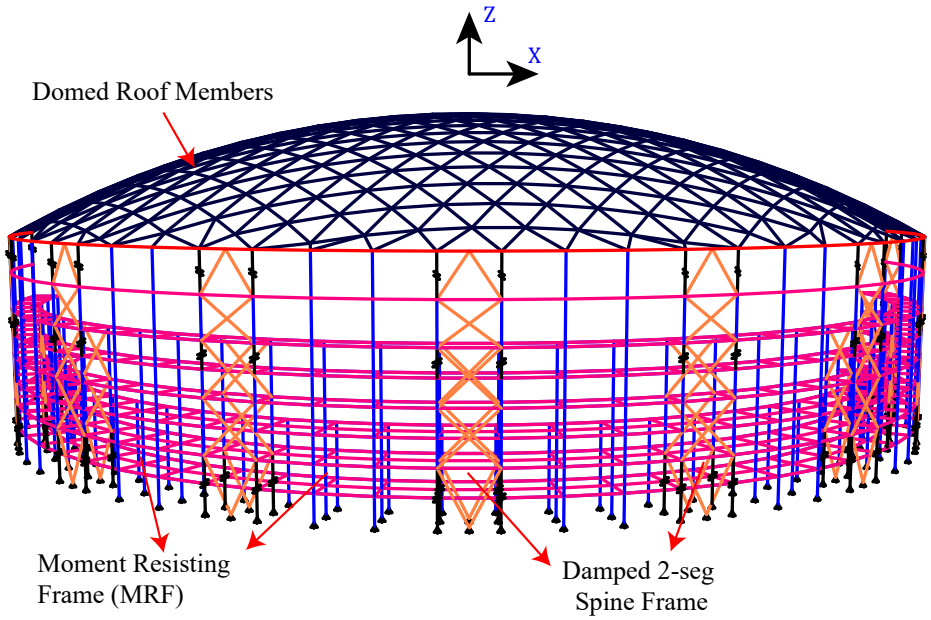

Figure 2-27: 3-D view of combined analysis model

Two substructure models were considered by varying the stiffness of the added BRCs. They are labelled as 2-Seg-A and 2-Seg-B respectively, as shown in Table 2.11. In this study, the material properties of the added BRCs (BRC-MID) are kept the same as the original BRC-Bottom (as explained in Section 2.2.2: Table 2.3). The specifications of the BRCs are given in Table 2.12.

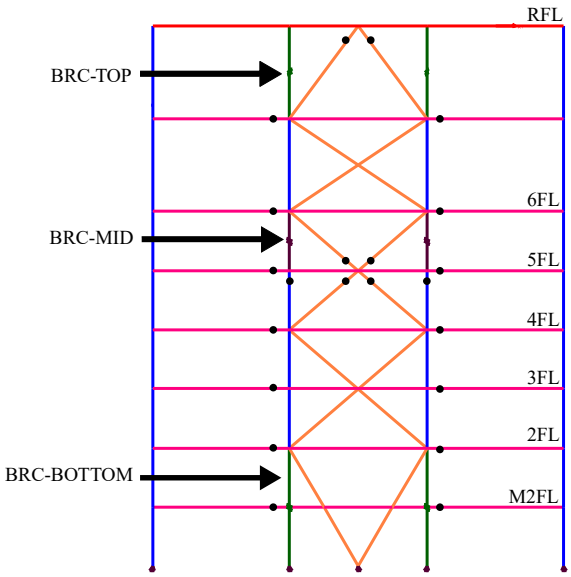

Figure 2-28: 2-segmented spine frame: Location of BRCs

Table 2.11: Model Nomenclature

BRB position	Stiffness Variable	Stiffness ratio (K_2/K_1)	Model Name
BRC-TOP	K_1	–	1-Seg
BRC-MIDDLE	K_2	1	2-Seg-A
BRC-BOTTOM	K_1	0.5	2-Seg-B

Table 2.12: BRC Specifications in 2-Segmented Spine Frame Models

	Model	N_y (kN)	L (m)	A_c (mm^2)	k_{eff} (kN/m)	A_c/A_e	L_p/L_o
BRC-Mid	2-Seg-A	1710	3.5	7597	685285	0.5	0.3
BRC-Bottom	2-Seg-A/B	3000	7	13330	685285	0.4	0.3
BRC-Mid	2-Seg-B	855	3.5	3799	342642	0.5	0.3

The frame section properties of other structural elements (MF Beam, MF Column, and RF Brace) and the mass distribution along the structure height in the analysis models are kept the same as those defined previously in the 1-Seg model (reproduced here in Tables 2.13 and 2.14).

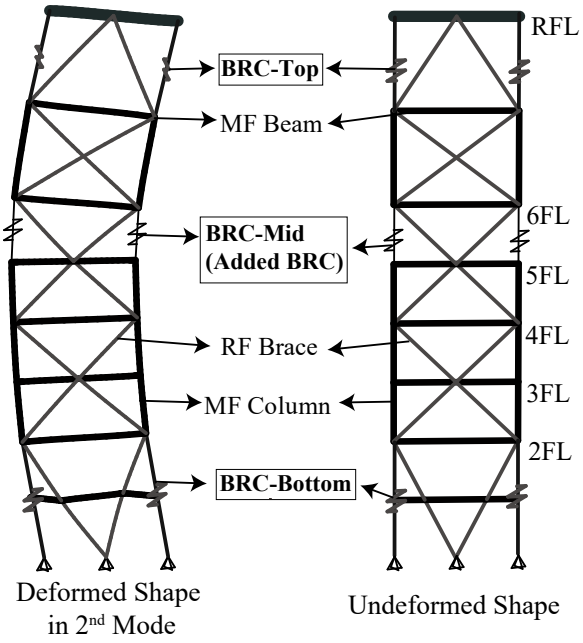

Figure 2-29: Schematic view of 2-seg frame in higher mode

Table 2.13: Frame Sections Data

Member	Section Shape	Section Size (mm)
Roof Member	CHS	ϕ500 t12
Tension Ring	CHS	ϕ1500 t24
MF Column	SHS	600×600×25
MF Beam	I/Wide Flange	588×300×12×20
RF Brace	I/Wide Flange	600×600×19×19

Table 2.14: Model Mass Distribution

Storey	Height (m)	Weight (kN)	Cumulative Weight (kN)
RFL	32	54018	54018
6FL	21	18304	72323
5FL	17.5	28507	100830
4FL	14	28507	129336
3FL	10.5	41121	170457
2FL	7	41121	211578
M2FL	3.5	41121	252699

2.8.2 Modal analysis results

Eigenvalue analysis was performed on the analysis models to compare the dynamic characteristics of the 2-seg models with the 1-seg models.

Comparisons of the first two dominant modes for the two combined models 1-Seg and 2-Seg-A are shown in Figure 2-30 and their corresponding mode shapes are shown in Figure 2-31. The mode shapes are also nearly identical with a slightly more even distribution observed for the 2-Seg-A model due to the added BRC-MID. The first mode for both models is a translational sway mode. As observed in the 1-seg models in Section 2.6.1, the roof appears to vibrate in the O2 mode in the second mode of the models. However, the heights of troughs and crests observed in the roof of the 2-Seg-A model are smaller.

The periods of all the combined models are compared in Figure 2-32. From the plots, it can be observed that, among the two segmented models, 2-Seg-B has slightly longer periods which is accompanied by a lower first mode participation and a slightly larger second mode participation.

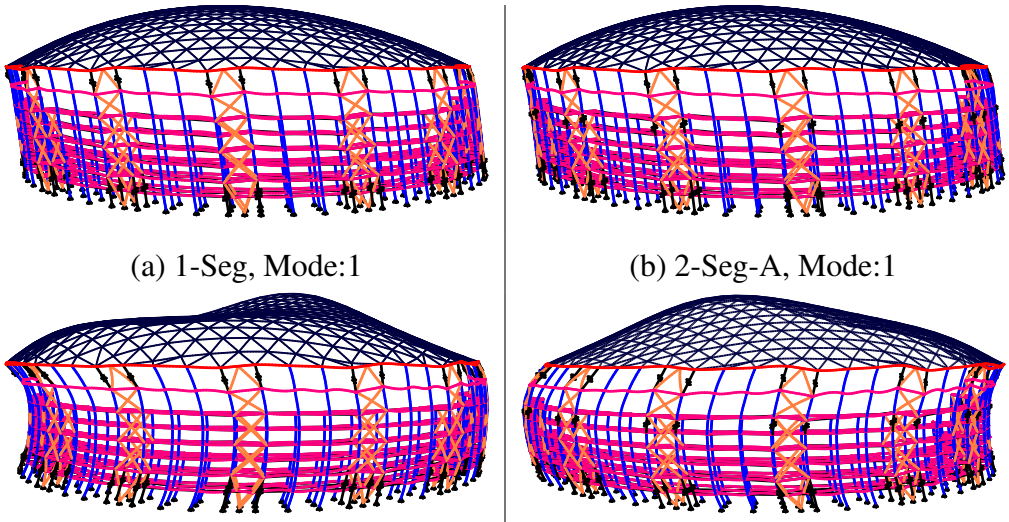

(a) 1-Seg, Mode:1 (b) 2-Seg-A, Mode:1

(a) 1-Seg, Mode:2 (b) 2-Seg-A, Mode:2

Figure 2-30: Comparison of first two dominant modes: Periods: Mode shapes

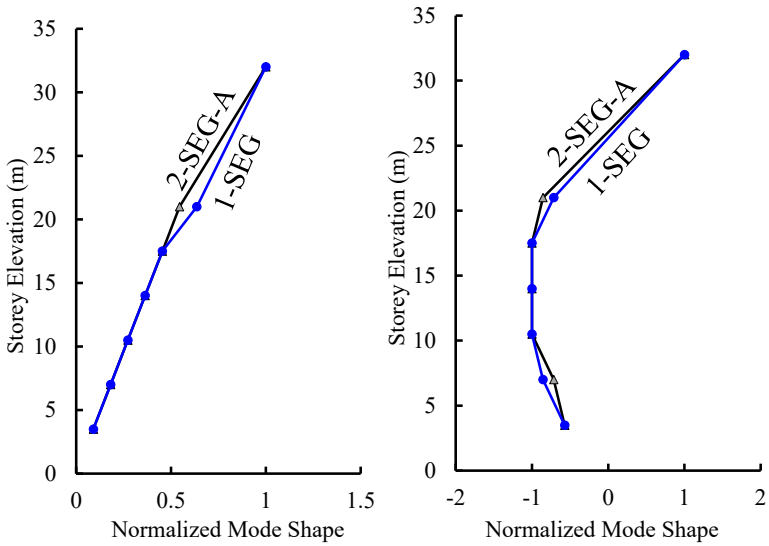

(a) Mode 1 (b) Mode 2

Figure 2-31: Mode shapes of substructures

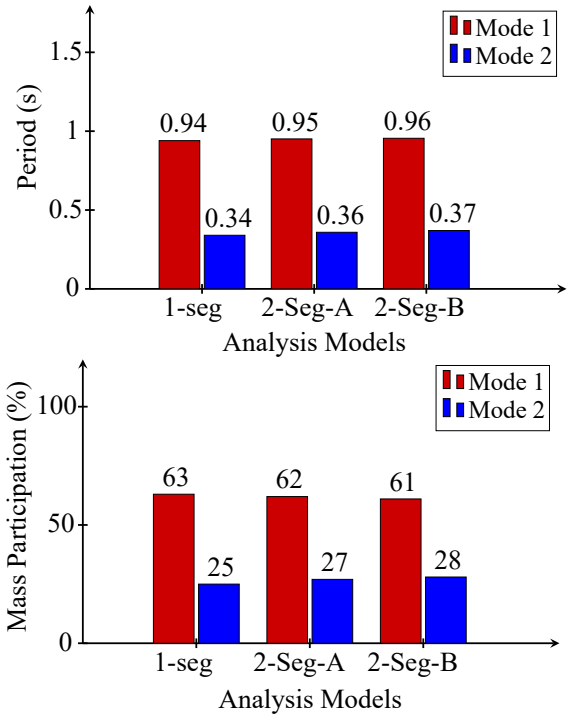

Figure 2-32: Comparison of first two dominant modes: Periods and Mass Participation

2.9 Inelastic response of substructure

NLRHA was performed for the substructure models to study the seismic behaviour of the substructures (Figure 2-1). The input earthquake ground motions were spectrally matched to the target design spectrum (BRI-L2) corresponding to a Level-2 earthquake as per the Japanese Building Code [6]. The spectrum was adjusted to an inherent damping ratio h_o=2% using Equation 2.3 (Figure 2-7) [11]. Rayleigh damping of 2% was assigned to the first two modes for analysis.

The maximum storey drift responses along the height of the substructure for a selected frame at $x = -75m$ for the 1-seg and 2-Seg-A models are shown in Figure 2-33. The storey drifts in the substructure of 2-Seg-A are slightly more than those of the 1-Seg model. The distribution of storey drift varies with the input ground motion. The distribution is most uniform for the El-Centro case and the least uniform for the JMA-Kobe case. However, the storey drift values were generally found to be generally within 1%.

Similar comparisons have been made for the two segmented models as well.

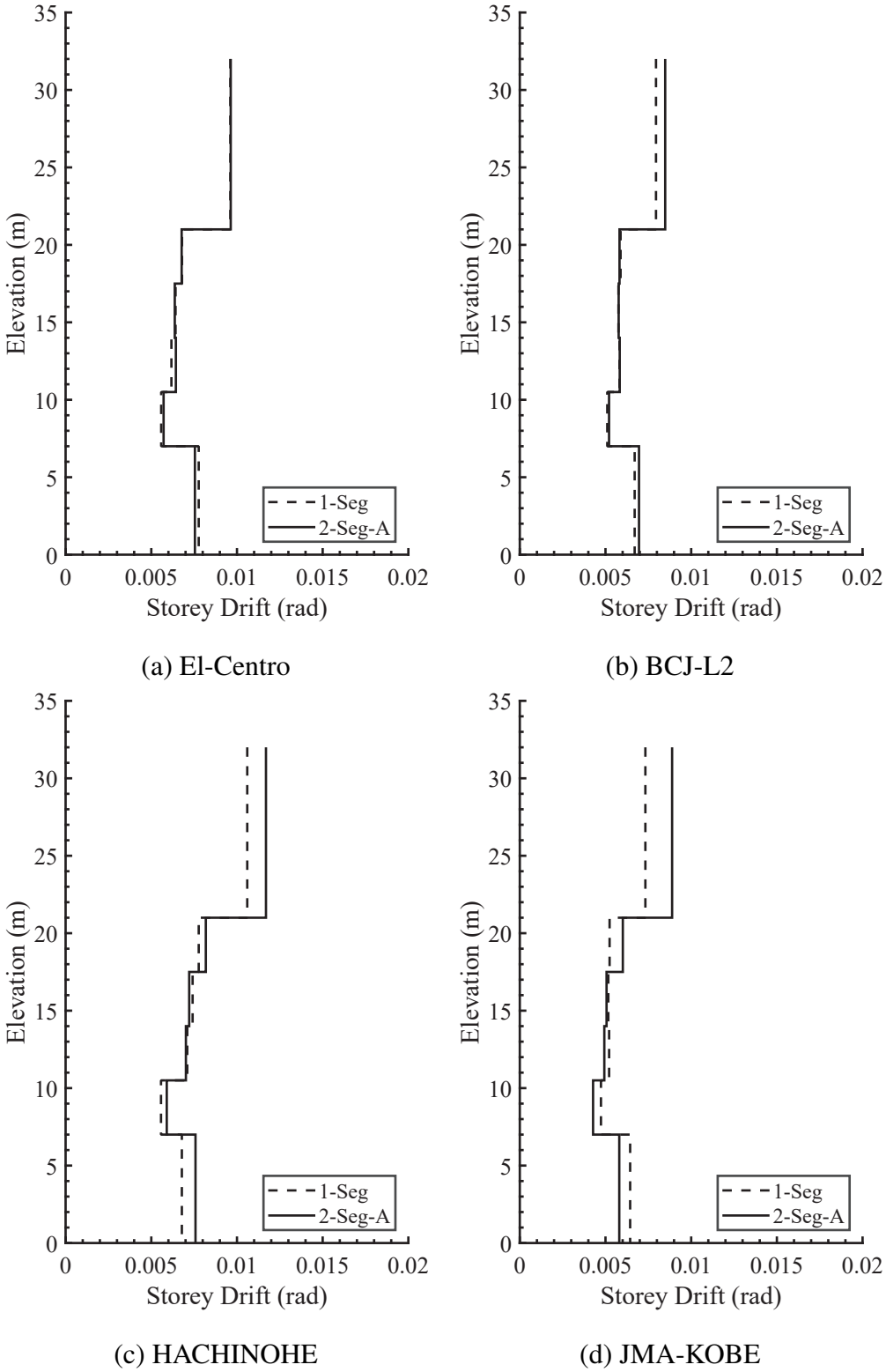

(a) El-Centro (b) BCJ-L2

(c) HACHINOHE (d) JMA-KOBE

Figure 2-33: Comparison of maximum storey drifts for spine models

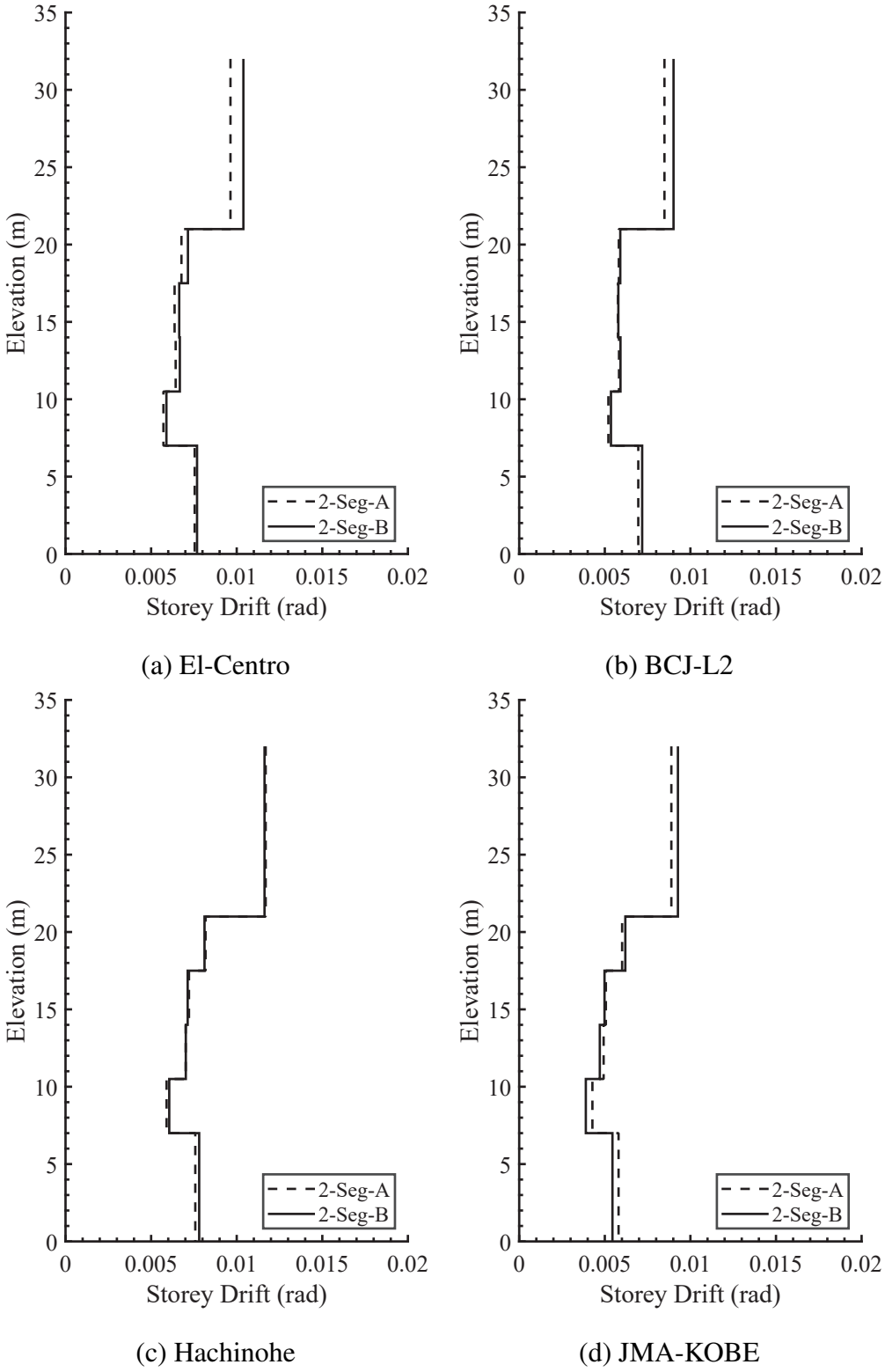

(a) El-Centro

(b) BCJ-L2

(c) Hachinohe

(d) JMA-KOBE

Figure 2-34: Comparison of maximum storey drifts for 2-seg models

2.10 Effects of 2-segmented spine frames on roof response

Following the modal analysis, NLRHA was performed on the analysis models (Figure 2-30) to investigate the effects of segmented spine frames on the roof response.

The peak inelastic responses of the combined models along the ridge line are shown in Figures 2-35 and 2-36. The average peak accelerations of the segmented models and the 1-seg model (Spine-MF model) are also shown for comparison. It can be seen that the average peak accelerations for 2-seg spine models are lower than the 1-seg spine model. The reduction in average response for the 2-Seg-B model was slightly more than that observed for the 2-Seg-A model.

The shape of the peak horizontal acceleration distribution for a particular ground motion generally remained the same for both 1-seg and 2-seg spine models. This indicated that the higher modes are still influential. However, the segmented spine frames present lower peaks that can be attributed to higher modes. For example, the peaks in JMA-Kobe and Hachinohe response observed in the horizontal acceleration plot of 1-seg model smoothen in the 2-seg models.

Further, an overall comparison of the average response of 1-Seg and 2-Seg-A models are shown in Figure 2-37. The change in the shape of the envelope of the average vertical acceleration distribution from 1-Seg to 2-Seg spine model indicates a transition towards the predominance of the first mode (O1 mode) of the roof. This confirms that implementing response control strategies for substructure higher modes can be employed to suppress the higher mode effects to a certain extent.

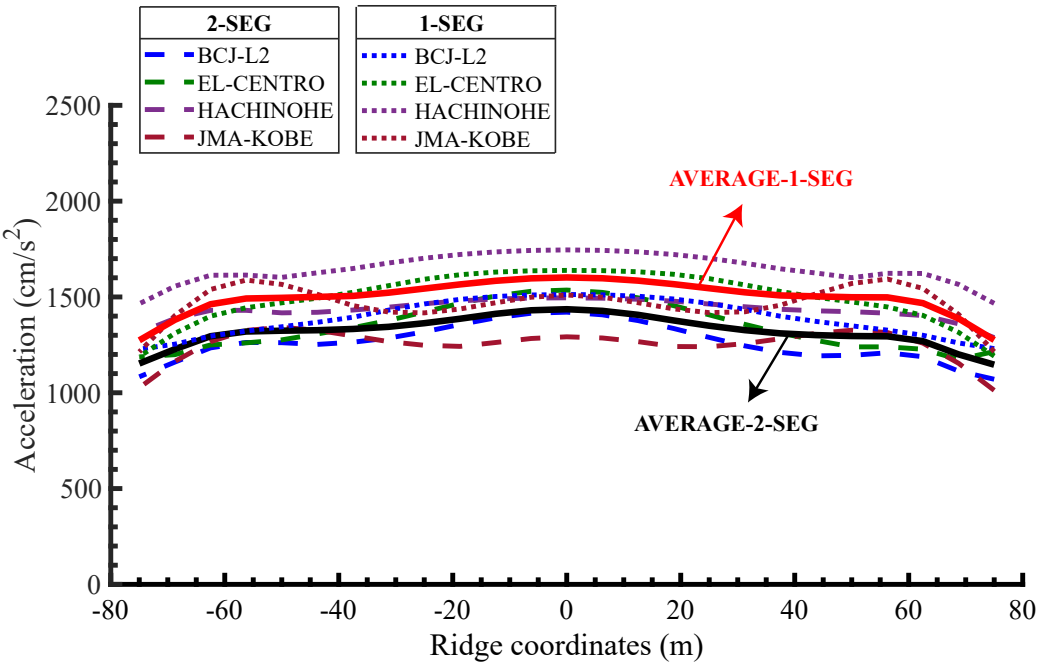

(a) Horizontal accelerations

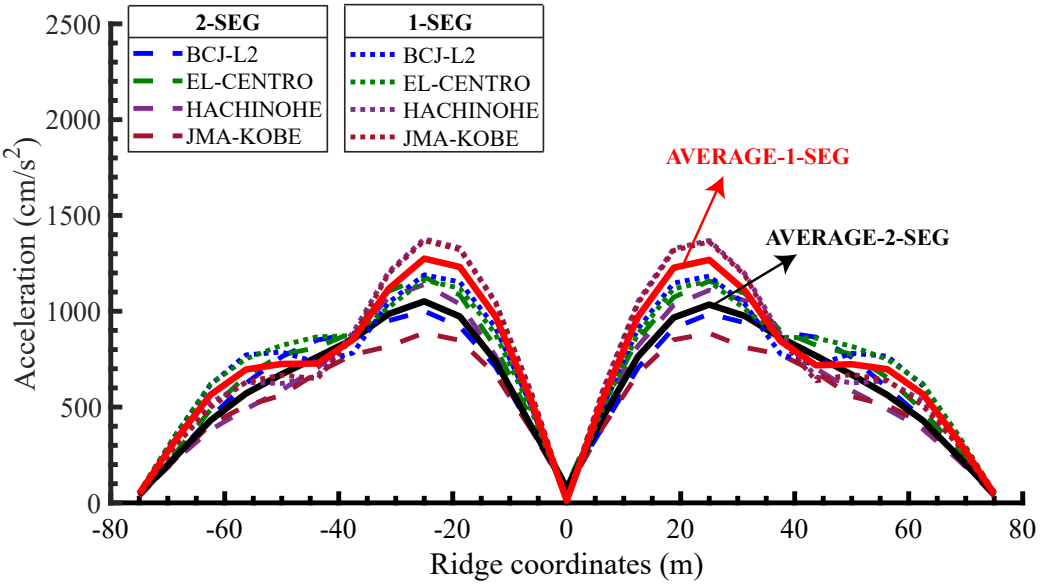

(b) Vertical accelerations

Figure 2-35: Inelastic Response of 2-Seg-A

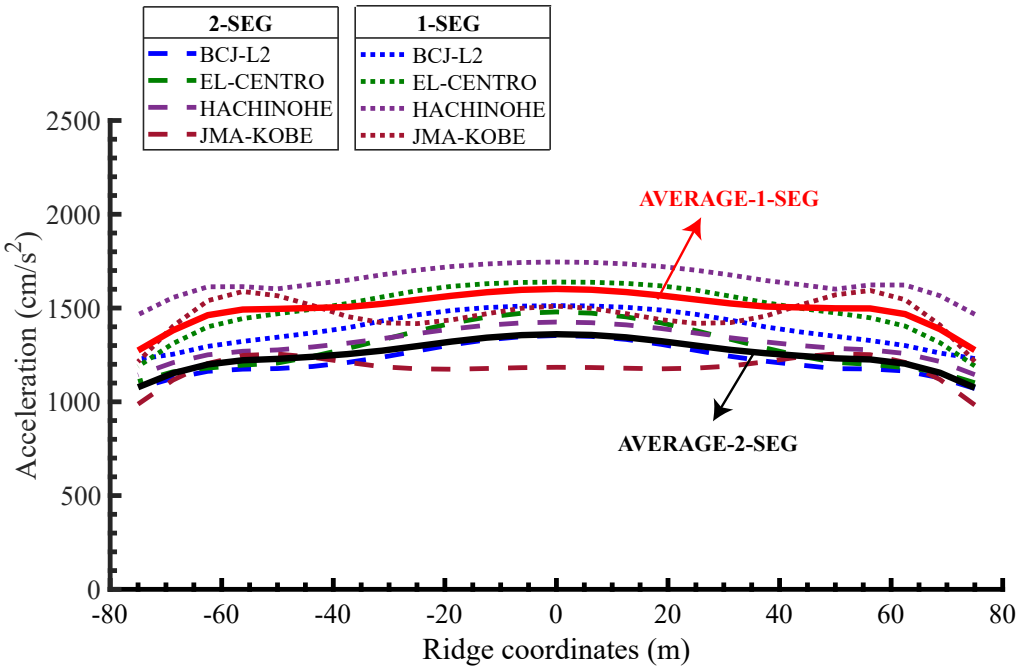

(a) Horizontal accelerations

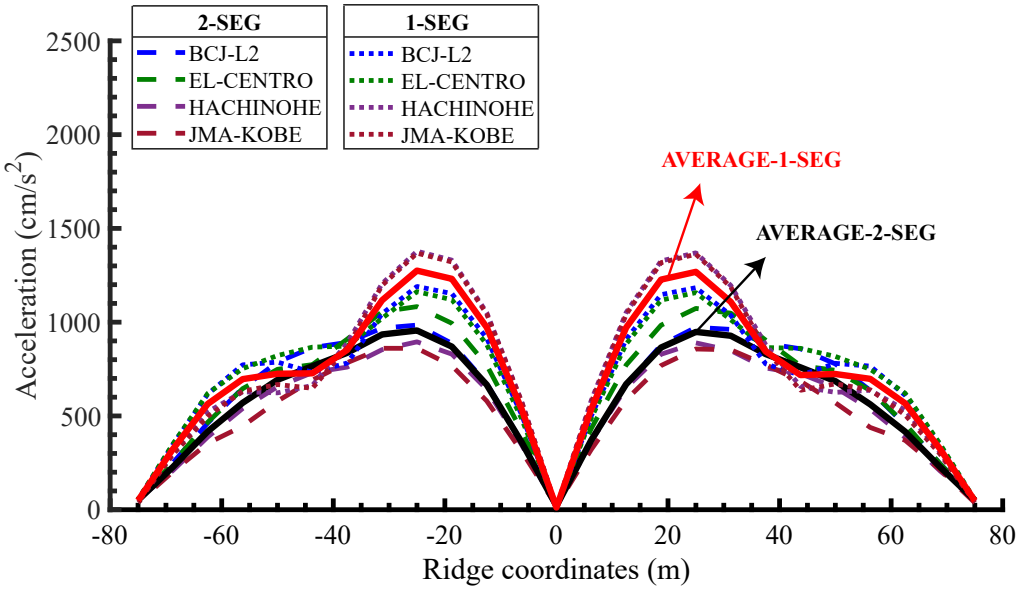

(b) Vertical accelerations

Figure 2-36: Inelastic Response of 2-Seg-B

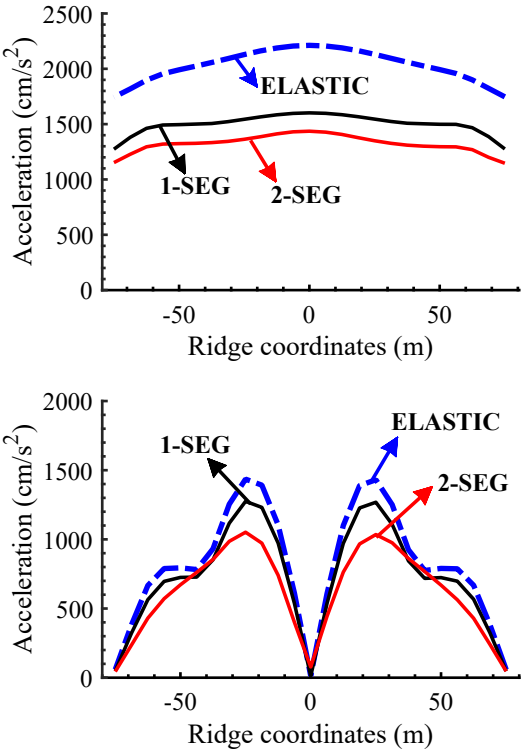

Figure 2-37: Average Response of 2-Seg-A and 1-Seg:
Horizontal (top figure) and Vertical (bottom figure) acceleration

2.11 Conclusions

The following conclusions were drawn from this chapter.

1. The magnitude of the roof excitation in long-span domes may be significant despite the elongated natural periods. For substructures with higher modes lying on the constant acceleration region of the design spectrum, the higher modes may contribute significantly and may even govern the overall response of the roof. Therefore, it is important to consider the roof's higher modes as well that may combine with the substructure higher modes.

2. For substructures lacking MRF, significant reduction in accelerations is expected when judged from the first modal response due to the near elastic-perfectly-plastic pushover curves. However, the higher modes are still in the elastic range and hence significantly contribute to the overall response, resulting in the large combined roof accelerations.

3. The distribution of the overall roof response may be different for two structures having similar periods and mass distribution and the distribution of vertical acceleration was found to be sensitive to the modeshape of the roof in the participating substructure modes.

4. Adding spine frames in the substructure proved to be effective in reducing the roof response while producing uniform storey drifts. However, this was limited to the response derived from the substructure first mode. Incorporating a two segmented spine frame system in the substructure was found to be an effective response control strategy to reduce the response due to the substructure's higher mode.

5. Despite reducing the roof response associated with the fundamental substructure mode, the higher substructure modes interacted with the roof and significantly amplified the response. The current AIJ/IASS proposed equivalent static loads using substructure first mode and the corresponding roof amplification factors underestimated this higher mode response.

References

[1] Y. Terazawa, T. Takeuchi, and M. Fujishima, "Brb design optimization for a large arena structure based on generalized response spectrum analysis," in *Proceedings of the 17th World Conference on Earthquake Engineering*, 2020.

[2] T. Takeuchi and A. Wada, *Buckling-restrained braces and applications*. Japan Society of Seismic Isolation, 2017.

[3] X. Chen, T. Takeuchi, and R. Matsui, "Simplified design procedure for controlled spine frames with energy-dissipating members," *Journal of Constructional Steel Research*, vol. 135, pp. 242–252, 2017.

[4] R. Sause, J. Ricles, D. Roke, N. Chancellor, and N. Gonner, "Seismic performance of a self-centering rocking concentrically-braced frame," in *Proceeding of the 9th US National and 10th Canadian conference on earthquake engineering*, 2010, pp. 25–29.

[5] *Analysis reference manual for SAP2000, ETABS, SAFE and CSIBridge*. Computers and Structures, Inc., Berkeley, CA, USA, 2015.

[6] *The Building Standard Law of Japan on CD-ROM*. The Building Center of Japan, 2016.

[7] T. Takeuchi, "Buckling-restrained brace: History, design and applications," in *Key Engineering Materials*, Trans Tech Publ, vol. 763, 2018, pp. 50–60.

[8] *Specification for Structural Steel Buildings (ANSI/AISC 360–16)*. American Institute of Steel Construction (AISC), 2016.

[9] T. Becker, S. Furukawa, S. Mahin, and M. Nakashima, "Comparison of us and japanese codes and practices for seismically isolated buildings," in *Structures Congress 2010*, 2010, pp. 2330–2338.

[10] T. Kumagai, T. Takeuchi, T. Ogawa, A. Nakama, and E. Sato, "Seismic response evaluation of latticed domes with elasto-plastic substructures using amplification factors," in *Proceedings of IASS 2005*, Bucharest, Romania, Sep. 2005, pp. 383–390.

[11] K. Kasai, H. Ito, and A. Watanabe, "Peak response prediction rule for a SDOF elasto-plastic system based on equivalent linearization technique," *Journal of Structural and Construction Engineering (Transactions of AIJ)*, vol. 68, no. 571, pp. 53–62, 2003.

[12] D. Nair, K. Ichihashi, Y. Terazawa, B. Sitler, and T. Takeuchi, "Higher mode effects of multistorey substructures on the seismic response of double-layered steel gridshell domes," *Engineering Structures*, vol. 243, p. 112 677, 2021.

[13] D. Rutten, *Grasshopper3d*, 2015.

[14] J. Mirtschin, *Geometry gym bim*, 2016.

[15] E. L. Wilson, *Three-dimensional static and dynamic analysis of structures*. Computers and Structures, 2002.

[16] T. Takeuchi, T. Ogawa, and T. Kumagai, "Seismic response evaluation of lattice shell roofs using amplification factors," *Journal of the IASS*, vol. 48, pp. 197–210, 2007.

[17] D. Nair, Y. Terazawa, B. Sitler, and T. Takeuchi, "Seismic response of long-span domes supported by multi-storey substructures," *Journal of the IASS*, vol. 61, pp. 140–157, 2020.

[18] *Minimum Design Loads for Buildings and Other Structures*. ASCE Standard–ASCE/SEI 7–16: American Society of Civil Engineers (ASCE), 2016.

[19] ASCE-41, "Seismic evaluation and retrofit of existing buildings," American Society of Civil Engineers, 2014.

[20] *Guide to Earthquake Response Evaluation of Metal Roof Spatial Structures*. Working Group 8,International Association for Shell and Spatial Structures (IASS), 2019.

[21] K. Takamatsu, T. Takeuchi, T. Kumagai, and T. Ogawa, "Response evaluation of seismically isolated lattice domes using amplification factors," in *Proceedings of IASS 2009*, Valencia, Spain, Sep. 2009.

[22] X. Chen, T. Takeuchi, and R. Matsui, "Seismic performance and evaluation of controlled spine frames applied in high-rise buildings," *Earthquake Spectra*, vol. 34, no. 3, pp. 1431–1458, 2018.

Chapter 3

Roof-substructure interaction in multistorey substructures

Contents

3.1 Introduction

The previous chapter investigated the seismic response of 150m long-span domes with multistorey substructures, which alternatively incorporated spine frames and buckling-restrained braces. Despite reducing the roof response associated with the fundamental substructure mode, the higher substructure modes interacted with the roof and significantly amplified the roof response. The previously proposed equivalent static loads using substructure first mode and the corresponding roof amplification factors underestimated this higher mode response. Furthermore, a wide range of ratios between the higher substructure and roof modes are conceivable, and the previously developed amplification factor curves [1] may need to be refined to avoid a gross overestimation or underestimation of the roof response.

Therefore, this chapter investigates the interaction between the different roof and substructure modes in detail for dome gridshell roofs with multistorey substructures. A parametric study is performed for linear 60, 100 and 150m double-layered domes featuring a range of substructure stiffness and roof-substructure mass ratios using response spectrum analysis. The overall response contribution of the dominant substructure mode, which need not be the fundamental substructure mode, was investigated using a new 'dominance response ratio' that provides insight into the dynamic roof-substructure interaction. Finally, the applicability of the previously proposed amplification factors (for T1-roof interactions) are investigated for the different multistorey substructures, and the extent is quantified using the period ratios.

3.2 Benchmark analysis models and design parameters

Prototype medium- and long-span double-layered dome roofs were selected, as double-layered lattices exhibit less complex dynamic characteristics than the single-layer lattices and are ubiquitous in high seismic regions. Double-layered domes with depth-to-span (d/L where d is the vertical offset and L is the span) ratios exceeding 1/50 [1] exhibit four primary modes, with the three primary out-of-plane modes denoted 'O1', 'O2' and 'O2.5', and the in-plane mode 'I' (Figure 2-13).

Three roof models (Table 3.1) with 60, 100 and 150m spans and a half subtended angle (θ) of 30° were designed using steel ($f_y = 325$MPa) for three different dead loads (2, 2.44 and 3kPa), respectively (Figure 3-2(a)). The roof dead loads were determined considering a structural weight of about 1kg/m^2 for every meter of span [2], a 15% allowance for the connections, and 1.3kPa nonstructural dead load, such as purlins, cladding, ceilings, mechanical and electrical. The double-layer lattice member sizes and vertical offsets (d) between the section centerlines are listed in Table 3.1. All roof members were assigned the same member size for simplicity. As explained in Section 2.5, for simplicity, the double-layer lattice truss (Figure 2-12) was modelled using equivalent beams with out-of-plane stiffness modification factors and moment connections (Figure 2-12) [3].

3.2.1 Modelling double-layer lattice using single-layer beams

The basic idea of modelling the parallel double-layer truss lattice using single-layer beams is to accurately capture the out-of-plane stiffness and the axial stiffness of the double-layer lattice shell to simplify the modelling and increase the analysis speed. This is done using the truss-beam analogy shown in Figure 2-12 where the top and bottom chords can be thought of as the flanges of a beam and the vertical or diagonal members as the web. This analogy has also been studied by Giltner (Method-2 of Reference [4]) by using the parallel-axis theorem and neglecting the inertia of vertical and diagonal members. The equivalent beam sizes were determined as shown in Figure 2-12 such that the area of the beam (A) equals the combined area of the two sections of the double-layer lattice ($2 \times A/2$). The moment of inertia of the equivalent beam in the out-of-plane direction I_{3s} was then

increased by a modification factor m to match the moment of inertia of the double-layer lattice about the centerline I_{3d}. This approach was also validated by Takeuchi [3] using 3d models of double-layer roofs with moment connections and single-storey substructures.

All roof members were modelled as elastic beam elements, which is consistent with the common design philosophy where the roof lattice is designed to remain elastic [5]. Partial models omitting the substructure and pinning the roof lattice perimeter nodes were used to identify the roof modes and are denoted as 'roof models'. The roof geometry was modelled in *Grasshopper* [6] and imported to ETABS [7] for analysis. The roof member beams in ETABS were modelled as 'frame' objects which are general three-dimensional beam elements [8] including axial, biaxial shear, torsion and biaxial bending deformation [9].

Table 3.1: Roof models: Member section sizes

Model	Dead Load (DL) (kPa)	Double-layer beam (mm)	offset d (cm)	Single-layer beam (roof member) (mm)	m	Tension beam (mm)
$L60$	2	2× I250×125×6×9**	150	ϕ307.5 t7.5*	53.3	ϕ809 t9
$L100$	2.44	2× I250×250×9×14	200	ϕ414.5 t14.5	50.7	ϕ1020 t10
$L150$	3	2× ϕ511 t11	350	ϕ715.5 t15.5	51	ϕ2525 t25

**I=I beam section, Dimensions: Height×Breadth×Web thickness×Flange thickness

* ϕ =Outer Diameter, t =Thickness of circular hollow section

Validation using arch model

For verification of this equivalent single-layer model, a simple example of a parallel double-layer 2d arch model was constructed for $L150$ roof model as shown below. The double-layer lattice is modelled as truss elements that carry axial forces only. The double-layer lattice and single-layer beam model for 150m dome ($L150$ sections according to Table 3.1) are shown in Figure 3-1. All diagonal and vertical members are also assigned the same section for simplicity, but in practice, the sections can be reduced as required. The vertical offset between AB and CD is $d = 3.5$m (Table 3.1).

The eigenvalue analysis results of both models are shown in Table 3.2. The periods confirm that the stiffness of both models is reasonably similar even if the vertical members

(shear deformation) are ignored.

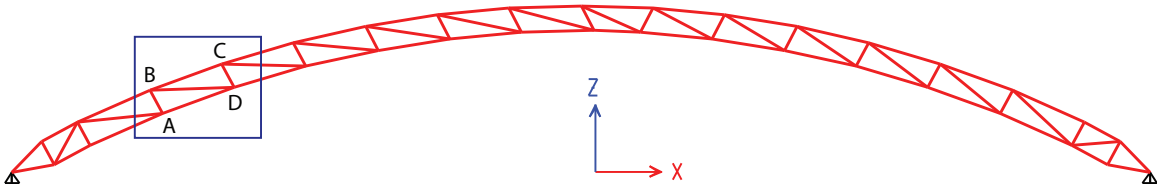

(a) Double-layer truss model

(b) Single-layer beam model

Figure 3-1: *L*150: 2d arch models

Table 3.2: Comparison of natural (eigenvalue) periods

Property	Double-layer	Single-layer
Seismic weight	4040kN	4040kN
Mode 1 (O1)	1.77s	1.71s
Mode 2	0.22s	0.22s

3.2.2 Substructure models

The lateral force resisting system of the substructure consisted of a two-way moment-resisting frame (MRF) enveloping 24 circumferential bays of buckling-restrained braced frames (BRBFs) spaced equidistantly along the perimeter, as shown in Figure 3-2(b). The substructure was designed to keep the MRF elastic, with the maximum inter-storey drift limited to 1% under a Japanese level-2 [10] earthquake (comparable to the design basis earthquake, DBE) on the West Coast, US [11]). Therefore, the beams and columns were modelled using elastic beam elements with the section sizes listed in Table 3.3(b). The BRBs (arranged in a single-diagonal configuration for the shorter beam spans of the 60m and 100m models and chevron configuration for the longer beam spans of the 150m models) were proportioned using Kasai's damper distribution method [12], which targets a uniform inelastic storey drift (assumed to be 1/150) up the building height using a target BRB yield drift ratio of 1/750 giving a target yield ratio of around 5. For design checks, the substructure BRBs were modelled in ETABS using links with axial stiffness given in Table 3.3(a) and a post-yield stiffness of 2% as explained in Chapter-2.

Finally, the substructure floors were modelled as membrane elements and assigned as rigid diaphragms [7]. A 7kPa uniform load was applied to all floors, giving the storey seismic weights listed in Table 3.3(a). To isolate the effect of the horizontal substructure acceleration on the roof response, a tension ring beam was included along the roof perimeter and pinned connections provided to both the substructure framing members and roof lattice, eliminating the local bending moments that would otherwise occur (Figure 3-2(c)). Furthermore, the cantilever columns at the top storey were braced in the radial direction to avoid a soft storey.

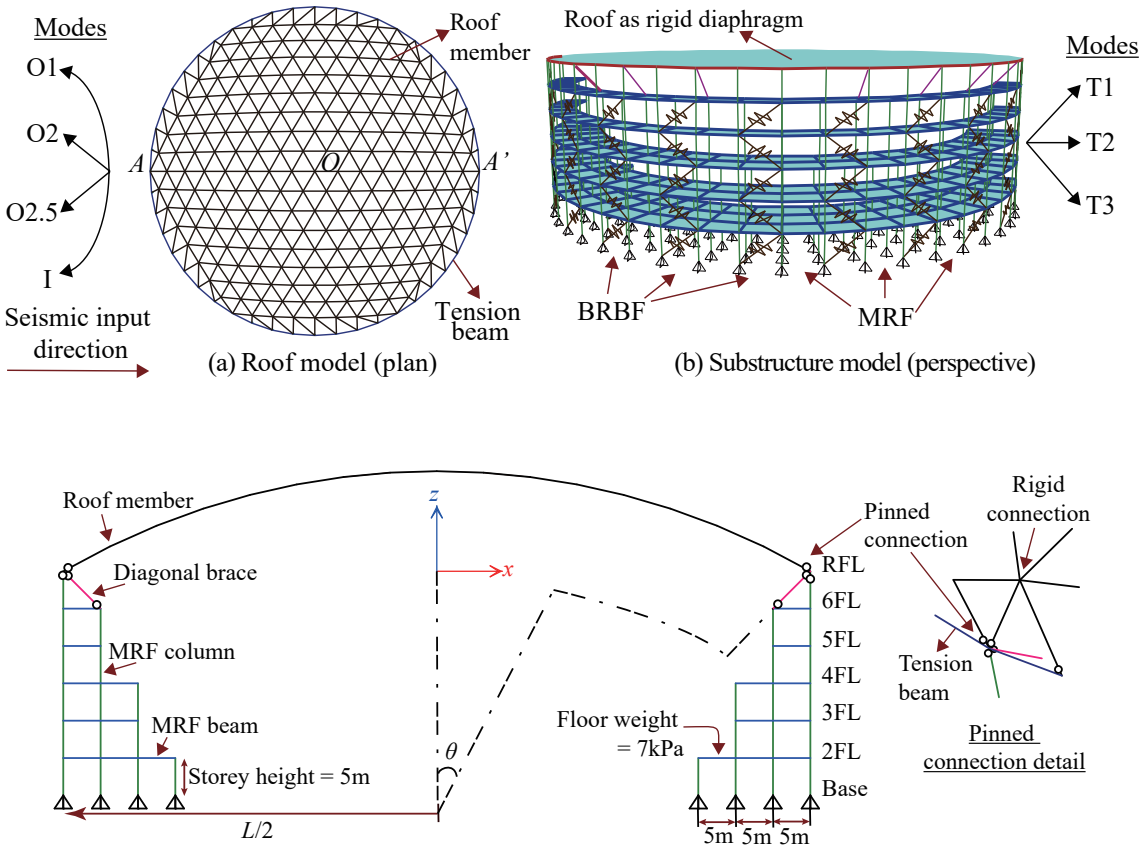

(c) Combined model (elevation)

Figure 3-2: Multistorey models

As a complement to the 'roof model', a 'substructure model' was analysed where the roof gridshell was replaced with a rigid diaphragm and lumped mass (Figure 3-2(b)). A third 'combined model' was then constructed that includes both the roof gridshell and substructure (Figure 3-2(c)). The two partial models were solely used to obtain the independent modal properties of the roof and substructure, while the combined model was used to obtain the seismic response and validate the analytical procedure.

Note that this chapter is focused on the general dynamic substructure-roof interaction and so the complexities of a yielding substructure were omitted. Therefore, for the parametric studies discussed in this chapter (Section 3.3 onward), BRBs were modelled as elastic link elements using the initial axial stiffness (Table 3.3(a)). Although yielding may reduce the substructure response and elongate the first mode, this is an acceptable simplification as each roof-substructure mode pair is analysed separately and the

parametric study includes flexible substructures which may represent such substructures with an elongated first mode. The focus of this study is to quantify the roof amplification where multiple substructure modes contribute to the response, and inelasticity is outside the scope of the present study. Nevertheless, it is anticipated that the proposed amplification factors will remain valid for a yielding multistorey substructure as well.

Table 3.3: Substructure model data

(a) Storey weight distribution and BRB stiffness

Storey	Height (m)	Seismic weight (kN)			BRB axial stiffness (kN/m)		
		L=60	L=100	L=150	L=60	L=100	L=150
RFL	30	6063	20581	56840	108989	-	-
6FL	25	6032	10420	15904	80057	101373	271382
5FL	20	6032	10420	15904	118111	225316	314543
4FL	15	10968	19742	30710	149529	318357	252994
3FL	10	10968	19742	30710	287434	442784	367798
2FL	5	10968	27968	44420	472209	598652	626060
Total		51031	108873	194488			

(b) MRF section sizes

Member	Section shape	Section sizes (mm)		
		L=60	L=100	L=150
MRF column	SHS*	450×450×25	600×600×32	650×650×32
MRF beam	I/Wide flange**	340×250×9×14	450×300×10×16	550×400×20×25
Diagonal brace	SHS*	350×350×15	350×350×16	200×200×8

*SHS=square hollow section, Dimensions: Height×Breadth×Thickness

**I=I section, Dimensions: Height×Breadth×Web thickness×Flange thickness

3.2.3 Dominant modes of roof models

The major vibration modes of the roof models and corresponding periods and mass participation factors are shown in Figure 3-3. The fundamental or natural periods of all the roof models was found to be the O1 mode. This is expected as the out-of-plane stiffness of the designed double-layer domes are high such that the depth to span ratios are more than 1/50 [1], [3]. The first mode of the dome is a higher mode O2.5 followed by the O1 and O2 modes. The mass participation of the modes remain consistent across all four models. The modeshapes of the dominant asymmetric roof modes are shown in Figure 3-4 and can be defined as follows.

1. Asymmetric mode O1: This mode is the fundamental mode of the roof, and the vertical modeshape can be represented with one cycle (one trough and one crest) of a sine wave of wavelength equal to the roof span. (Figure 3-4) This modeshape with (x,y)=(0,0) as the centre and span = L is simplified as a sine wave [1], [3] as shown in Equation 3.1:

$$u_z(x,y) = \frac{x}{\sqrt{x^2+y^2}} \sin \frac{2\pi\sqrt{x^2+y^2}}{L} \tag{3.1}$$

2. Asymmetric mode O2: This mode is the next mode of the roof, and the vertical modeshape can be represented with sine waves of two peaks in one cycle (two troughs and two crests) [13] of wavelength equal to half of the span as shown in Equation 3.2:

$$u_z(x,y) = \left\{ \begin{array}{cc} d & (|x| \le L/4) \\ 0.5d & (|x| > L/4) \end{array} \right\}; \quad d = \frac{x}{\sqrt{x^2+y^2}} \sin \frac{2\pi\sqrt{(2x)^2+(2y)^2}}{L} \tag{3.2}$$

3. Asymmetric mode O2.5: this mode is the next higher mode of the roof, and the vertical modeshape can be represented with sine waves of two and a half (2.5) peaks in one cycle (2.5 troughs and 2 crests or vice versa) of wavelength equal to half of the span (Figure 3-4). The modeshape has not been defined in literature as it has a more complex wave formulation but may be better expressed using a simple sum of

two sine waves as shown in Equation 3.3:

$$u_z(x,y) = \frac{0.5x}{\sqrt{x^2+y^2}}\left(\sin\frac{8\pi\sqrt{x^2+y^2}}{5L} - \sin\frac{6\pi\sqrt{x^2+y^2}}{L}\right) \tag{3.3}$$

4. Inplane mode I: In this mode, the roof vibrates in the in-plane direction and has negligible out-of-plane modeshape. There are several in-plane modes but the first in-plane mode is called the I mode and has the shortest period, so becomes significant only when the substructure is very stiff (Figure 1-19) [1].

As the span increases, the natural periods shift towards the right. As shown in Figure 3-5, O1 mode in all the models lies on the maximum acceleration region of the spectrum. In case of R100 and R150 models, the O2 and O2.5 modes correspond to larger spectral accelerations but for R60, the corresponding accelerations are lower.

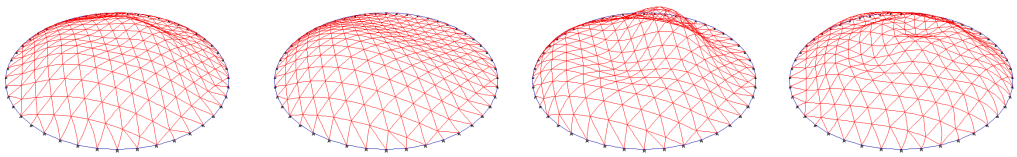

R60	0.059s | 56% | O2.5	0.223s | 18% | O1	0.111s | 6% | O2	0.047s | 5% | I

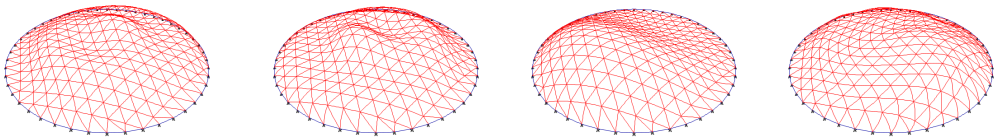

R100	0.111s | 30% | O2.5	0.119s | 27% | O2	0.390s | 17% | O1	0.077s | 6% | I

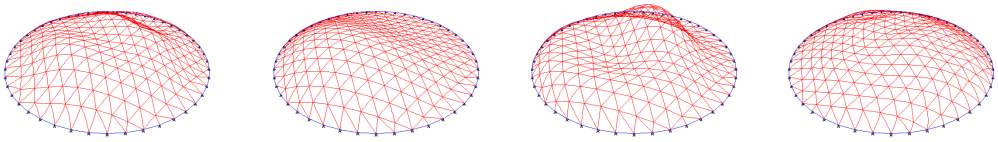

R150	0.171s | 53% | O2.5	0.562s | 18% | O1	0.290s | 6% | O2	0.115s | 6% | I

Figure 3-3: Periods & mass participation along the x-direction of dominant modes

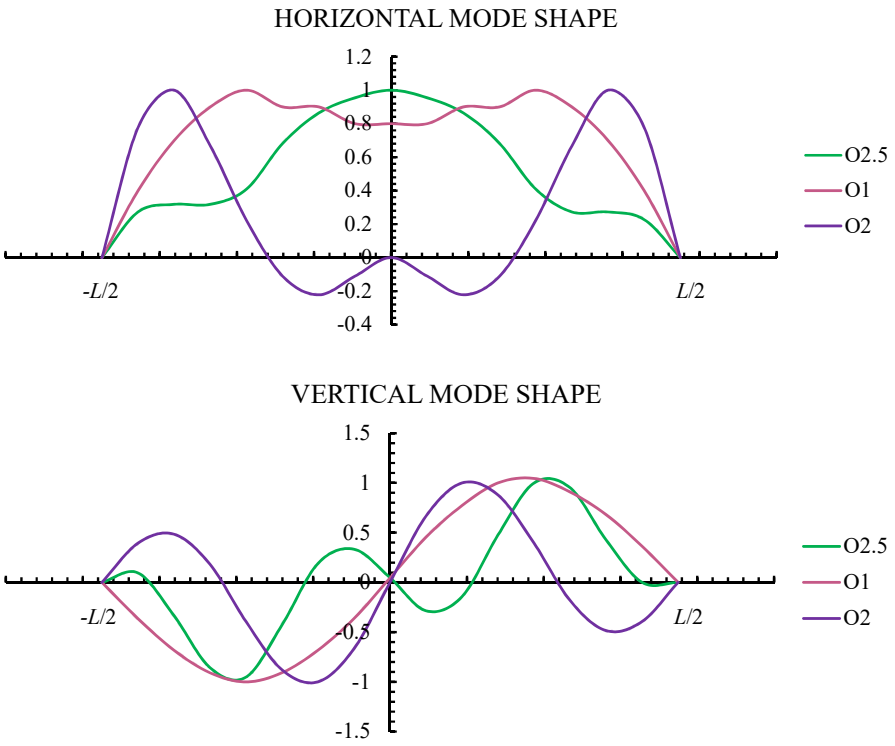

Figure 3-4: (Normalised) asymmetric roof mode shapes

3.2.4 Seismic response of roof models

The benchmark roof models (pinned at the base) were also analysed using response spectrum analysis based on the BRI-L2 spectrum as the input and the modal responses were combined using the CQC method.

The peak horizontal and vertical acceleration response along the ridgeline is shown in Figure 3-6. The horizontal response increases with the increase in span and seismic weight which leads to longer natural periods and increasing spectral accelerations (Figure 3-5). The magnitude of peak horizontal and vertical responses are nearly equal indicating that the vertical response is indeed significant and can not be neglected. Furthermore, it can be seen that the R60 model's vertical response has an envelope governed by the O1 mode whereas a combination of O1, O2 or O2.5 make up the peak vertical response envelope for R100 and R150 models. This is because the O2.5 modes have the highest mass participation for the roof models and for longer span models, the corresponding spectral

accelerations are larger than those of the R60 model. In the R60 model, O2.5 mode has a very low spectral acceleration (Figure 3-5), and thus, the fundamental O1 mode with the high spectral acceleration governs the response even though the mass participation is lesser than the O2.5 mode.

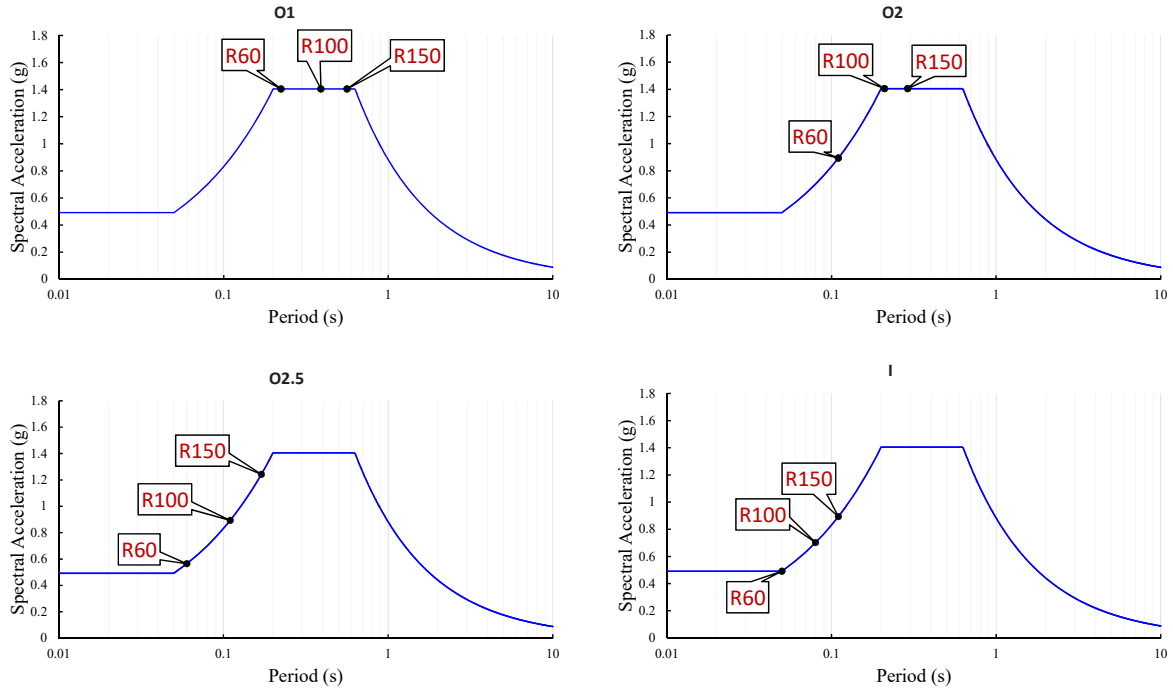

Figure 3-5: Roof modes mapped on the target design spectrum

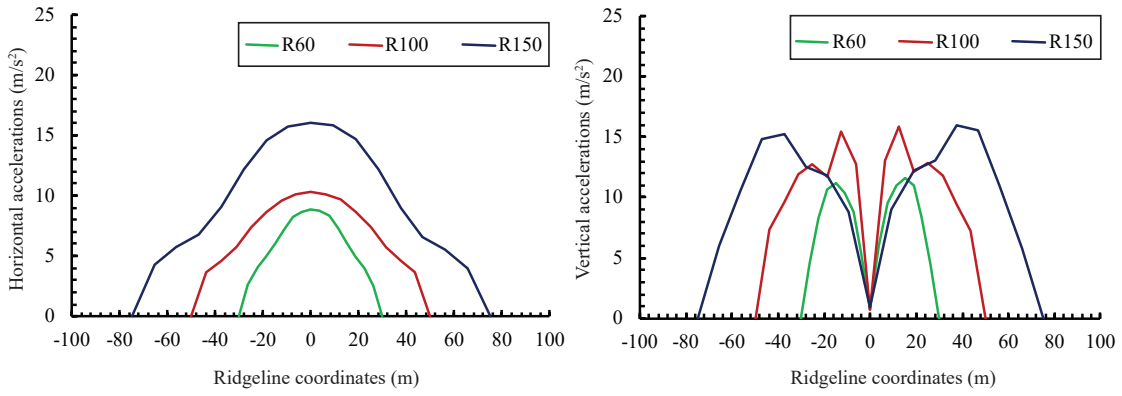

Figure 3-6: Peak acceleration envelope of benchmark roof models

3.2.5 Mass and period ratios

The mass and period ratio formulations are repeated below to aid in the following sections. The mass ratios are formulated as ratios of the effective modal mass (${}_sM_{eqi}$) and period (${}_sT_i$) of the i^{th} mode of the substructure model, which includes the roof mass, relative to the total roof mass (${}_rM_R$) and period of the dominant O1 roof mode (${}_rT_R$). Therefore, a larger R_M or R_T ratio represents a heavier and more flexible substructure, such that both ratios increase as storeys are added. For completeness, the effective modal mass, mass participation factor (Γ_i) and modal participation factor (β_i) are given by Equation 3.5, where m is the mass matrix and ϕ_i is the mode shape vector. (Note that the preceding subscripts r, s and c are used in this thesis to refer to the roof, substructure and combined models (Figure 3-2 and 3-8), respectively.)

$$R_{Mi} = \frac{{}_sM_{eqi}}{{}_rM_R}, \quad R_M = \sum_{i=1}^{n} R_{Mi}, \quad R_{Ti} = \frac{{}_sT_i}{{}_rT_R} \tag{3.4}$$

$$\beta_i = \frac{{\phi_i}^T m\{1\}}{{\phi_i}^T m\phi_i}; \quad {}_sM_{eqi} = \frac{\left({\phi_i}^T m\{1\}\right)^2}{{\phi_i}^T m\phi_i}; \quad \Gamma_i = \frac{{}_sM_{eqi}}{\sum_{i=1}^{n} {}_sM_{eqi}} \tag{3.5}$$

3.2.6 Substructure model characteristics

The natural periods of the three substructure models are given in Table 3.4. The fundamental periods (T1) of all the models was about 0.7s with less than 75% mass participation, and that of T2 mode was about 0.2s giving a T1/T2 ratio of about 3. The roof period ratios R_{T1} are quite large and decrease with increasing span. This implies a higher amplification factor from the first mode for longer span models. Furthermore, R_{T2} values are smaller and vary from 0.4 to 1. Since the T2 modes are very close to the roof modes, significant contribution can be expected from the T2 mode to the overall roof response.

Table 3.4: Benchmark substructure models: Periods (s) and mass participation (%)

Roof DL (kPa)	span L(m)	T_1 and Γ_1 (%)	T_2 and Γ_2 (%)	R_{T1}	R_{T2}
2	60	0.67s, (75%)	0.24s, (17%)	3.00	1.09
2.44	100	0.68s, (69%)	0.25s, (21%)	1.75	0.69
3	150	0.66s, (71%)	0.24s, (20%)	1.17	0.42

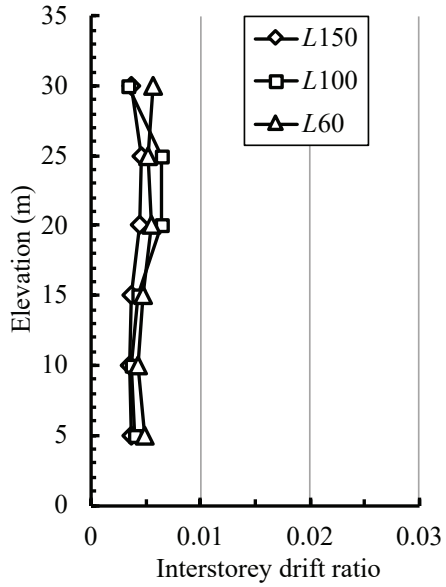

Figure 3-7: Design storey drifts for benchmark substructure models

The storey drift for the benchmark substructure models obtained from NLRHA subjected to design level earthquake BCJ-L2 are shown in Figure 3-7. Rayleigh damping of $h_o = 2\%$ was assigned to the first and second modes and Newmark-β method was adopted as the integration method. The uniform peak storey drift distribution is confirmed facilitating near-uniform yielding in all storeys.

3.3 Roof-substructure interaction in single-storey substructures

Before investigating the response of the multistorey models, the first-mode response characteristics were confirmed using single-storey substructure models to benchmark the response.

3.3.1 Effects of substructure stiffness

The effect of the mass (R_M) and period (R_T) ratios on the dynamic response are investigated in this section using the 100m span models with single-storey substructures and a braced mezzanine (Figure 3-8). The storey heights, seismic weight and frame sections are listed in Tables 3.5, 3.6 and 3.7. The total seismic weights were calculated using the surface areas and dead loads (DL) applied to the roof which was varied from 1 to 3kPa producing the roof periods listed in Table 3.7. Several different substructure stiffnesses were investigated by modifying the moment of inertia of the MRF beams and columns by a scale factor α, such that a higher α equates to a stiffer substructure. The periods and the mass participation factors of the first two substructure modes are given in Table 3.8. Here, the period ratio R_{T1} is the ratio of the first (T1) substructure mode's period (ranked in decreasing order of mass participation) to the roof's O1 period. Note that T2 includes all of the translational modes with a single inflection point, while T1 refers to the translational sway modes. However, T1 or T2 modes about all axes have identical periods for the dome models considered in this study due to symmetry.

Increasing the substructure stiffness decreased the fundamental periods of the combined model, but did not affect the cumulative mass participation factor of the modes featuring translational substructure sway, which was about 99% for most models (Table 3.8). This suggests that for first-mode dominated substructures, the roof response may be obtained from the peak acceleration at the substructure roofline (${}_sA_{Heq}$) generated solely from the first substructure mode, and that higher substructure modes need not be considered.

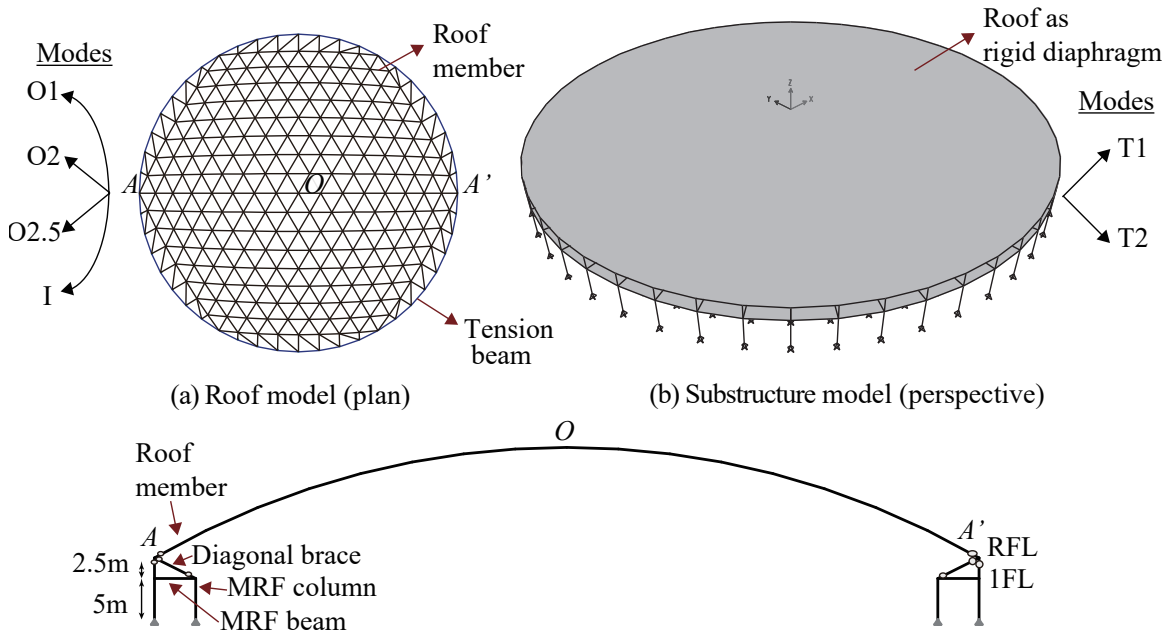

Figure 3-8: Single-storey models

Table 3.5: *L*100 : Single-storey substructure model data (a)

(a) Storey heights and seismic weights

Storey	Height (m)	Weight (kN)
RFL (3kPa)		25,230
RFL (2kPa)	2.5	16,820
RFL (1kPa)		8,410
1FL	5	10,420

Table 3.6: *L*100 : Single-storey substructure model data (b)

(b) MRF section sizes

Member	Section Shape	Section Size (mm)
MRF column	SHS	600×600×32
MRF beam	I/Wide flange	450×300×10×16
Diagonal brace	SHS	350×350×16

Table 3.7: $L100$ roof models: Seismic weights, periods (s) and mass participation (%)

Roof dead load (kPa)	Weight (kN)	O1 ($_rT_R$)	O2	O2.5	I
1	8410	0.25s, (18%)	0.14s, (5%)	0.07s, (57%)	0.05s, (6%)
2	16820	0.35s, (18%)	0.20s, (5%)	0.11s, (57%)	0.07s, (6%)
3	25230	0.43s, (18%)	0.24s, (5%)	0.13s, (57%)	0.09s, (6%)

Table 3.8: Single-storey $L100$ substructure models: Periods (s) and mass participation (%)

Roof dead load (kPa)	R_M	α	T_1 and Γ_1 (%)	T_2 and Γ_2 (%)	R_{T1}
1	2.24	1/6	0.7s, (99%)	0.05s, (0.003%)	3.00
		1	0.3s, (99%)	0.04s, (0.5%)	1.40
		6	0.2s, (98%)	0.03s, (1.5%)	0.80
2	1.62	1/6	0.9s, (99%)	0.06s, (0.003%)	2.58
		1	0.4s, (99%)	0.05s, (0.5%)	1.22
		6	0.2s, (98%)	0.03s, (1.1%)	0.71
3	1.41	1/6	1.0s, (99%)	0.06s, (0.003%)	2.41
		1	0.5s, (99%)	0.05s, (0.4%)	1.15
		6	0.3s, (98%)	0.03s, (0.7%)	0.68

Dominant modes in combined models

The target design acceleration (S_a(cm/s^2)) spectrum defined using Equations 2.2-2.3 was adopted (where D_h is the reduction factor to adjust the damping ratio from the base damping ratio h_b=5%). The spectrum was adjusted to an inherent damping ratio h_o=2% (for steel structures) using Equation 2.3 [10]. Mapping the periods of the roof and substructure models on the spectrum provides insight into their interaction (Table 3.9). The fundamental substructure mode always interacts with the nearest roof mode. For example, the fundamental substructure mode is much longer than all roof modes for the combined model with $R_M = 2.2$ (1kPa) and α=1/6 (Table 3.9), and so the substructure T1 sway mode dominates while only mildly interacting with the roof's O1 mode (Table 3.10). Increasing the stiffness to α=1 brings the substructure and roof periods closer together

and produces a strong interaction between the substructure T1 and roof O1 modes. This interaction manifests as two modes in the combined model, with the T1 and O1 modes interacting in and out of phase (denoted as O1+T1 and O1-T1 in Table 3.10). Increasing the substructure stiffness by α=6 once again produced dominant O1+T1 and O1-T1 modes, although the cumulative participation factor of the O1+T1 and O1-T1 modes reduced slightly to 93%, with another 5% participation coming from the next closest roof mode (O2) to the substructure sway mode (T1). Thus, the roof-substructure interaction is strongly influenced by the relative proximity of their fundamental periods, and the response of roofs with single-storey substructures may be explained solely from the interaction of a sequential subset of roof modes with the substructure T1 mode.

Table 3.9: Single-storey L100 models: Roof and substructure periods

DL (kPa)	Substructure stiffness scale factor α		
	α=1/6	α=1	α=6
L = 100m 1	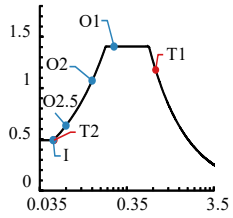	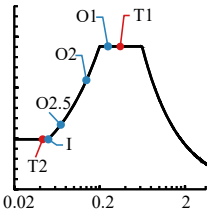	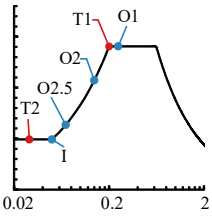
L = 100m 2	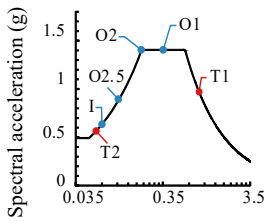	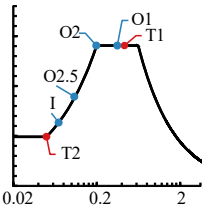	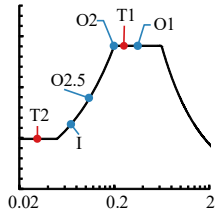
L = 100m 3	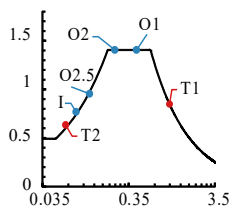	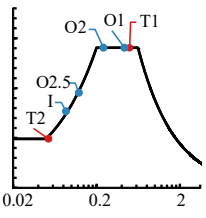	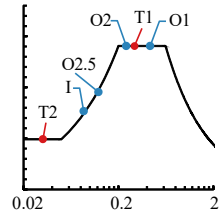

Table 3.10: Single-storey combined models:
Periods (s), mass participation (%) and mode shapes

DL (kPa)	R_M	α	L=100m, Mode shapes		
1	2.2	1/6	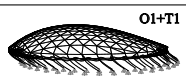	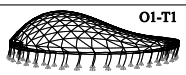	
			0.8s, (97%)	0.3s, (1%)	-
		1	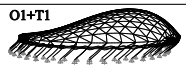	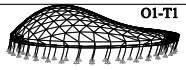	
			0.4s, (89%)	0.2s, (10%)	-
		6	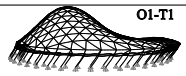	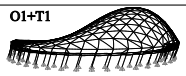	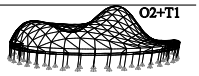
			0.2s, (54%)	0.3s, (39%)	0.1s, (5%)
2	1.6	1/6	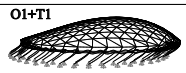	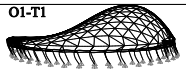	
			1.0s, (97%)	0.4s, (2%)	-
		1	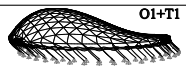	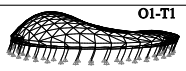	
			0.5s, (83%)	0.3s, (15%)	-
		6	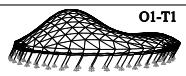	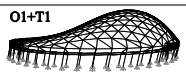	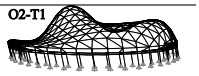
			0.2s, (55%)	0.4s, (35%)	0.2s, (4%)
3	1.4	1/6	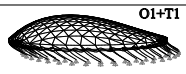	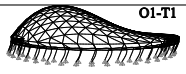	
			1.2, (97%)	0.5s, (2%)	-
		1	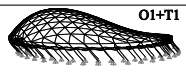	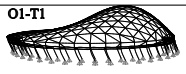	
			0.6s, (80%)	0.4s, (18%)	-
		6	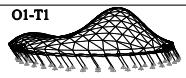	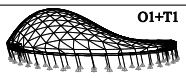	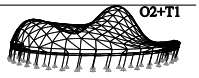
			0.3s, (54%)	0.5s, (35%)	0.2s, (5%)

3.3.2 Dominant roof modes

Terazawa and Nair et al. [14] have also investigated the dominance of the four prominent roof modes (O1, O2, O2.5 and I) in single and multistorey structures varying parameters like the dome's half-subtended angle, period and the substructure stiffness. Response spectrum analysis (RSA) was conducted for each combined model using the elastic BRI-L2 design spectrum [10] adjusted to a constant damping ratio of 2%. The influence of each roof mode (in combination with the substructure T1 mode) to the overall roof's acceleration response was studied using a 'dominance ratio' defined in Equation 3.6. As the response is sensitive to the selected location, the horizontal and vertical ratios are reported at the node producing the maximum combined resultant response (usually a node near the quarter points). The dominance ratios in the horizontal and vertical directions were calculated using the critical node's acceleration results following Equation 3.6 and plotted in Figure 3-9.

The horizontal dominance ratios were evenly divided between the O1, O2 and O2.5 modes for stiff shorter period substructures with $R_{T1} < 1$, while the dominant O1+T1 mode dominated the flexible substructures where $1 < R_{T1} < 2$. The O1+T1 mode for more flexible substructures ($R_{T1} > 2$) is also referred to as the sway mode as there is negligible roof amplification leading to a flat envelope of the horizontal response (with magnitude equal to that of the peak substructure response) and negligible vertical response. Furthermore, the vertical and horizontal O1+T1 dominance ratio *DR* peaked at almost 100% for stiff substructures with $R_{T1} \sim 1$ such that the T1+O1 interactions governed, but reduced for cases with $1 < R_{T1}$ due to the increasing contribution of the O2+T1 and O2.5+T1 interactions and finally became negligible for flexible substructures with $R_{T1} >> 2$, as the substructure period was too long for significant interaction. To summarise, the peak roof response with single-storey substructures is a complex combination of the four roof modes' interactions with the T1 mode for $1 << R_{T1}$, and becomes dominated by the O1+T1 interactions for $1 < R_{T1} < 2$, and the roof-substructure becomes negligible for longer period substructures $R_{T1} >> 2$.

$$DR_i = \frac{{}_cA_i{}^2}{\left(\sqrt{\sum_{i=1}^{n} {}_cA_i{}^2}\right)^2} = \frac{{}_cA_i{}^2}{{}_cA_{SRSS}{}^2} \tag{3.6}$$

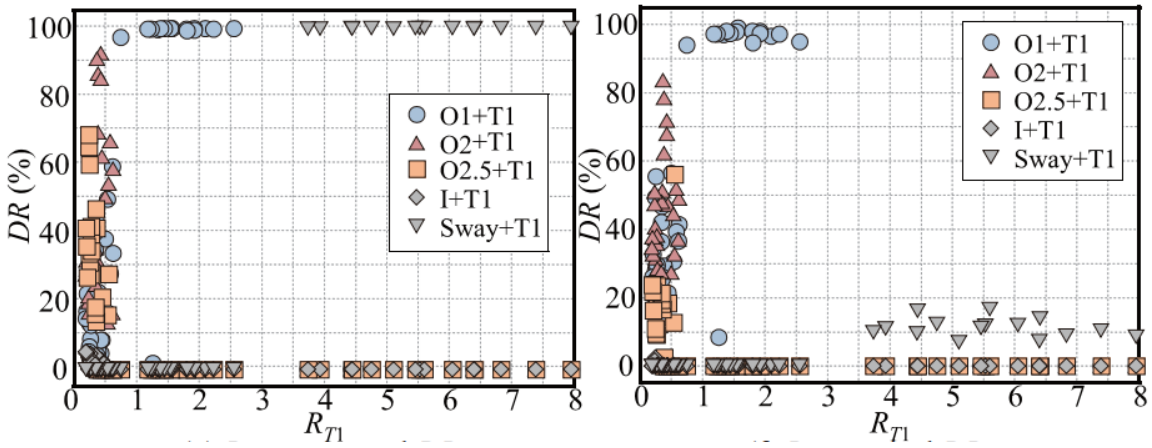

(a) Horizontal *DR* (b) Vertical *DR*

Figure 3-9: Single-storey models: Dominance ratios of the four roof modes [14]

Effects of the roof half-subtended angle

The effects of roof half-subtended angle on the overall peak roof responses have been studied for medium-span domes in the past [1], [15]. To investigate the effects of half-subtended angle on the peak acceleration response, Terazawa et al. [14] carried out parametric studies for longer 100m spanned domes and varying the substructure stiffness. The fundamental (O1 mode) periods of the 100m spanned roof models designed for a dead load of 2kPa with half-subtended angles of 20°, 30° and 40° were found to be 0.25s, 0.22s, and 0.18s respectively [14]. RSA was conducted for each combined model using the elastic BRI-L2 design spectrum [10] adjusted to a constant damping ratio of 2% (Figure 2-8). The peak horizontal and vertical roof accelerations are compared among the roofs with three different half-subtended angles (20°, 30° and 40°) designed for three roof dead loads (2kPa to 3kPa), using bar-plots as shown in Figures 3-10(a) and (b).

It was observed that the horizontal peak response was same across models of the same stiffness (same *k* values) and the half-subtended angle had no (or negligible) effect on the

peak responses. Therefore, the horizontal response was confirmed to be independent of the half-subtended angle. In the case of vertical response, the peak response was found to change with the half-subtended angle and the distribution of the response among the four roof modes also varied. The vertical response is sensitive to the governing roof mode (that is the mode closest to the substructure T1), particularly for stiff substructures ($k >= 10$ and $R_T < 1$ or $T_1 < 0.2s$) as observed in the previous section. For flexible substructures ($k < 1$ and $R_T > 1.5$ or $T_1 > 0.4s$), the dominant O1+T1 governed both the horizontal response and vertical response for all the models, and the magnitude changed slightly with the increase in half-subtended angle as the period ratio R_T increased leading to different vertical amplification factors (as F_V is a function of the half-subtended angle [15]). In contrast, the horizontal response was constant in all the models for flexible substructures as the horizontal amplification factor is constant ($F_H = 1$) in this range ($k < 1$ and $R_T > 1.25$).

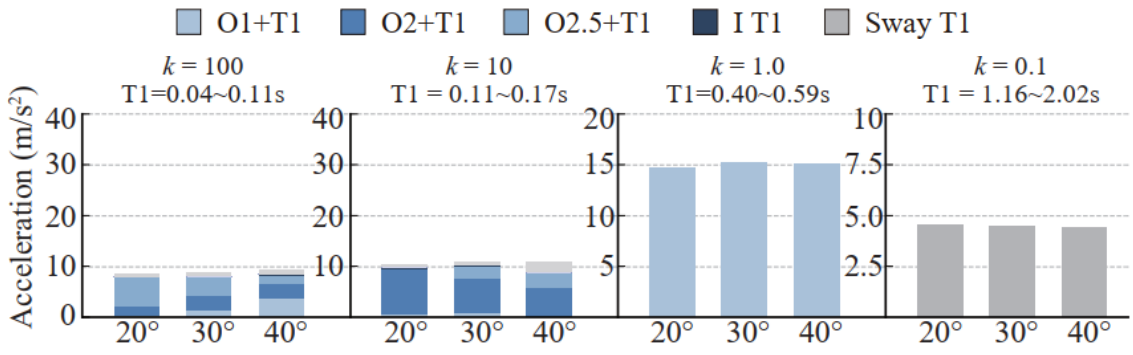

(a) Peak Horizontal Accelerations

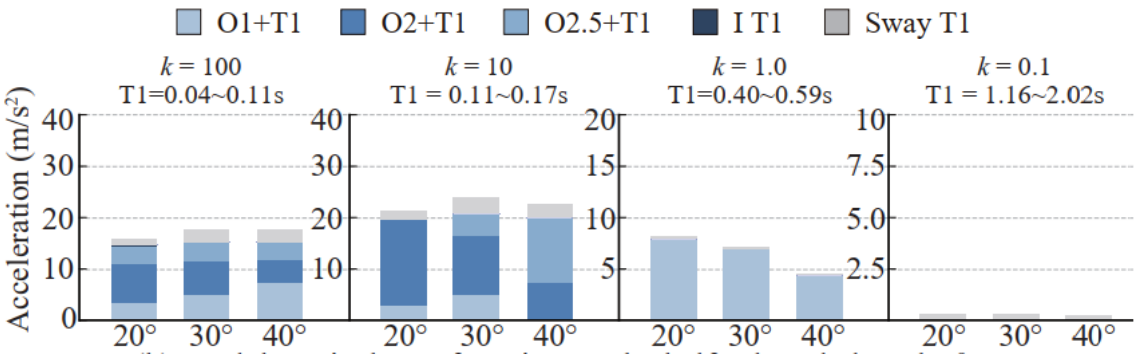

(b) Peak Vertical Accelerations

Figure 3-10: Single-storey 100m models: Effects of half-subtended angle [14]

3.3.3 Effects of high mass ratio

In the study of medium span domes [1], additional excitation around $R_{T1} = 1$ was observed when the mass ratio $R_M = M_{eq}/M_R$ (Figure 3-11) exceeded 2. This is expected to occur when the substructure is made of reinforced concrete and is relatively heavy while the roof is lightweight and made of steel. This additional excitation was attributed as the 'harmonic resonance effect' between the roof and substructure's dominant fundamental modes. Therefore, the amplification factors for such cases were modified as given in Equations 1.15-1.16 to account for the increased amplification significant in the region where $R_M > 2$ and $R_T < 1.5$.

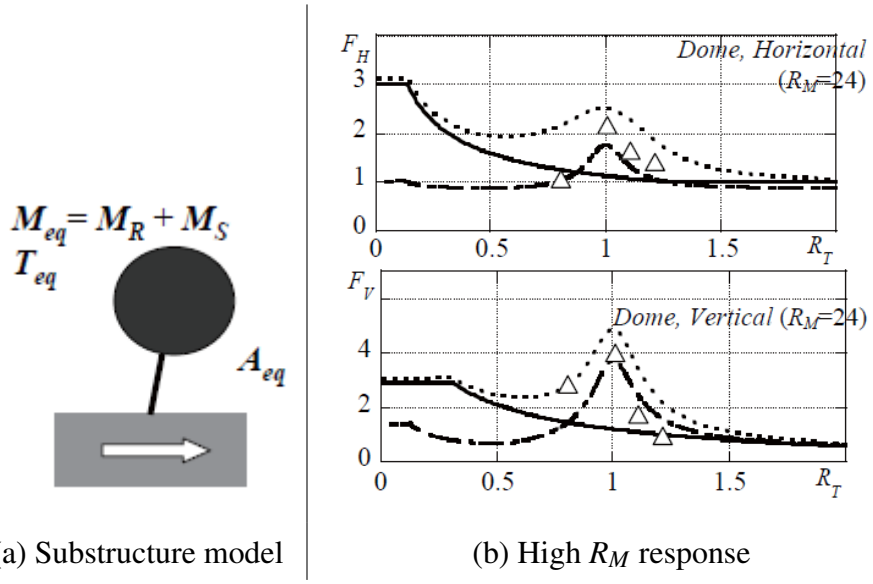

(a) Substructure model (b) High R_M response

Figure 3-11: Effect of high mass ratio in 60m single-storey domed structures [1]

To confirm this phenomenon for long-span domes and compare with that of the medium-span domes, additional single storey models of 60m, 100m and 150m were constructed. The benchmark analysis models as explained in Section 3.2 (Figure 3-8) and the frame sections are adopted. To increase the mass ratios, the dead load on the roof (Figure 3-8) was changed and kept fixed at 1kPa and the substructure floor weight was increased to 40 kPa for the 150m model, and 20kPa for the 60m model and 100m models, respectively, and the substructure stiffness was varied to vary the period ratios as shown in Table 3.11. RSA was performed using the BRI-L2 spectrum (defined in Section 2.4) and

the amplification results from RSA using the CQC combination methods were obtained using Equations 3.7 and 3.8, and compared with the previously proposed amplification factors calculated to the results using the Equations 1.15-1.16 [1], plotting both against the T1 period ratios as depicted in Figure 3-12.

$$F_H = \frac{{}_cA_{H\max}}{{}_sA_{Heq1}}, \quad F_V = \frac{{}_cA_{V\max}}{{}_sA_{Heq1}} \tag{3.7}$$

where

$${}_sA_{Heqi} = {}_s\beta_{is} S_{ais} \phi_i \tag{3.8}$$

Table 3.11: High mass ratio single-storey model parameters

Span (m)	R_M	T_1 (s)	T_R (s)	R_T	${}_sA_{Heq}$ (m/s^2)
60	7	0.18	0.16	1.12	16
60	7	0.19	0.16	1.18	17
60	7	0.27	0.16	1.12	16
100	5	0.27	0.25	1.07	16
100	5	0.48	0.25	1.93	15
100	5	1.06	0.25	4.24	8
150	6	0.34	0.33	1.05	14
150	6	0.72	0.33	2.21	12

The amplification around $R_{T1} = 1$ is evident even in the case of long-span domes for heavy substructures as shown in Figure 3-12. This is a result of resonance between the fundamental period of substructure and the dominant O1 mode of roof. This confirms that the resonance effects are prominent even in the case of long-span domes.

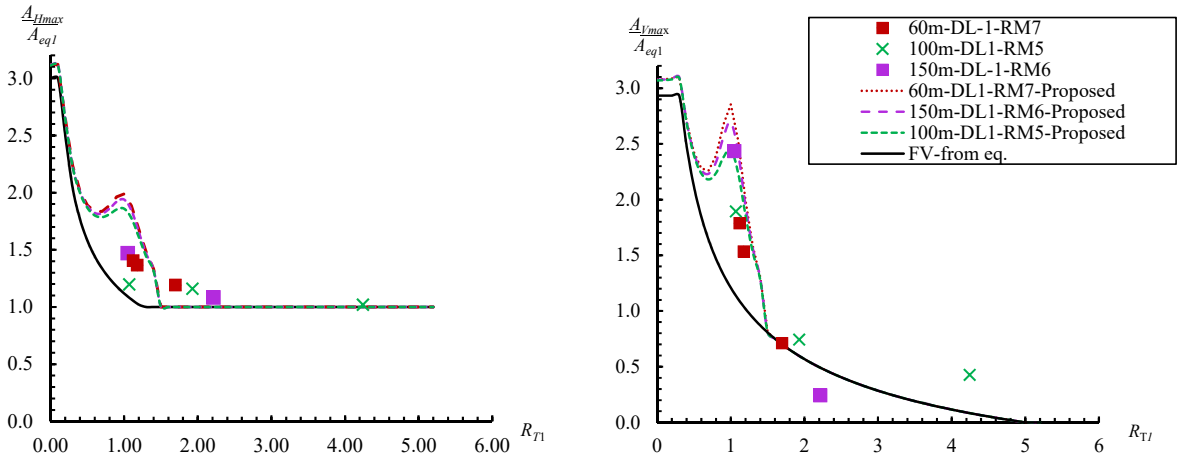

(a) Horizontal amplification (b) Vertical amplification

Figure 3-12: Effect of high mass ratios-single storey models

Dominant modes in combined models, $R_T \sim 1$

Since very few models were analysed to propose amplification accounting for resonance effects in previous studies, these resonance effects are further investigated in this section. Additional models with single-storey substructures were constructed using the benchmark single-storey models. The substructure mass and stiffness of frame members was varied such that the period ratios were very close to 1 and the mass ratios were higher than 2 as given in Table 3.12. Similar to the previous sections, RSA was performed on the models using the BRI-L2 design spectrum and the modal responses were combined using the CQC combination method.

In all these models, the substructure had a first-mode (T1) dominant response with T1 constituting all of the mass participation. However, in the combined models, the mass participation is split between two dominant modes- Mode 1, where the O1 mode of the roof and substructure are in phase (labelled as 'O1+T1'), and Mode 2, where the two modes are out of phase (labelled as 'O1-T1'). The periods of both these modes are slightly apart. The fundamental mode with the longest period is always the O1+T1 mode and the O1-T1 acts as a higher mode. The substructure stiffness in both these modes are comparable to the stiffness of the substructure only model. These two modes and their effects on the combined response are further discussed in the next two subsections.

Table 3.12: Combined Models: Period Ratios (R_T), Mass Participation (%) and Mode Shapes

Span (m)				
	R_M	R_T	${}_cR_T$ & mode shapes	
			Mode 1	Mode 2
60	4	0.88	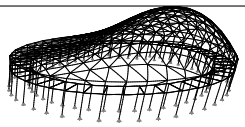	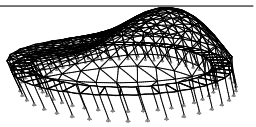
			1.11, (43%)	0.83, (52%)
	7	1.12	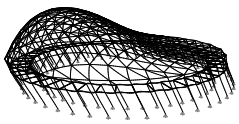	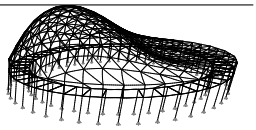
			1.24s, (79%)	0.95, (18 %)
	7	0.77	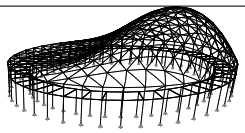	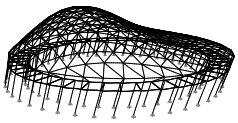
			1.04, (18%)	0.76, (77%)
	15	1.13	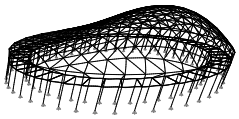	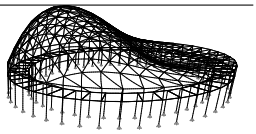
			1.19, (84%)	0.97, (15%)
	29	1.06	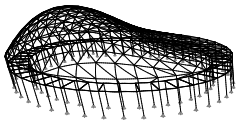	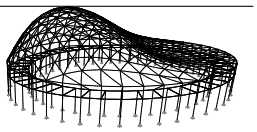
			1.10, (75%)	0.97, (24%)
100	5	0.74	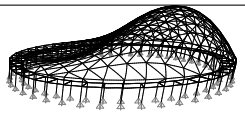	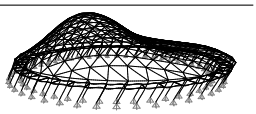
			1.05, (19%)	0.73, (73%)
	5	1.07	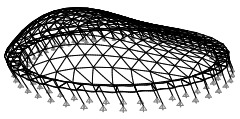	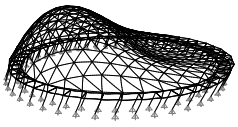
			1.23, (71%)	0.92, (26%)
150	6	1.06	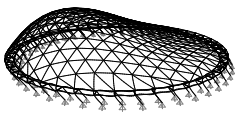	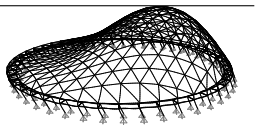
			1.12, (75%)	0.95, (21%)

Case 1: R_T<1

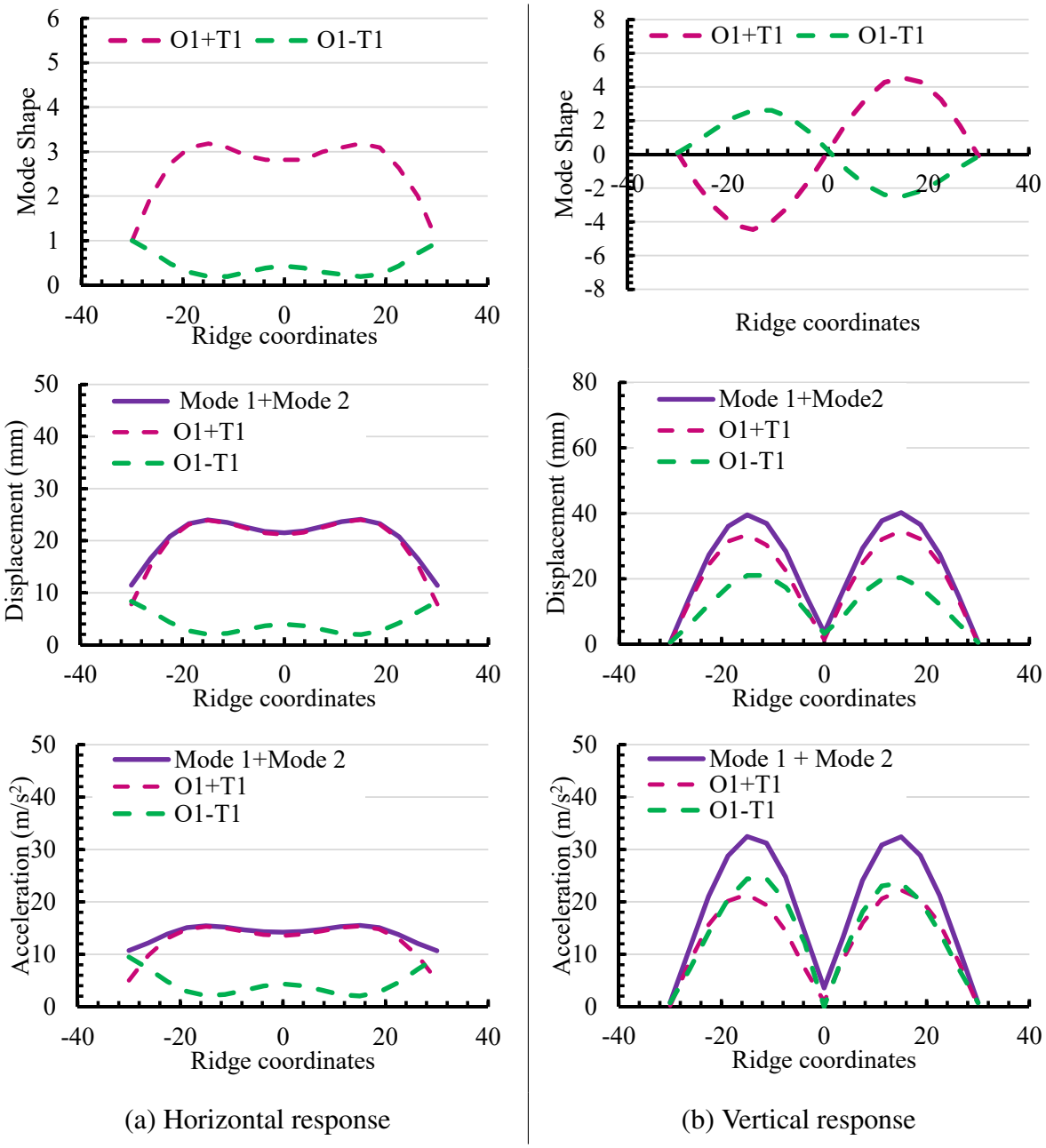

(a) Horizontal response

(b) Vertical response

Figure 3-13: Interaction of O1 and T1 modes:
Response of a single-storey 60m model, $R_M = 4$, $R_T = 0.88$

When R_{T1}<1, the mass participation of the mode O1-T1 becomes higher (Table 3.12) than that of the O1+T1 mode as can be seen in Figure 3-13(a) with higher peak response values in the horizontal response, even though the participation of the latter is smaller. The peak

substructure response (A_{Heq}) of the O1+T1 is smaller as the participation is less which implies that the horizontal amplification in this mode is very high. On the other hand, the O1-T1 mode has very little horizontal amplification and some models exhibit peak response at the base of the ridge indicating negative amplification. As a result, the mass participation of the O1+T1 mode is low but the horizontal amplification is higher than the O1-T1 mode. Thus, the overall peak horizontal response after combining the two modes often flattens decreasing the overall horizontal amplification. In the case of vertical response, both the modes have identical mode shapes and the overall envelope is obtained by combining the two contributions.

Case 2: R_T>1

When R_T>1, the mass participation of the mode O1+T1 is higher (Figure 3-14) than the O1-T1 mode. Thus, the peak substructure response of the O1+T1 is larger as the participation is more. As a result, the mass participation and horizontal amplification is higher than the O1-T1 mode. On the other hand, the O1-T1 mode has little contribution and so, after combining the two modal contributions, the peak roof response is still governed by the O1+T1 mode shape explaining the amplified arch-like shape of the envelope. In the case of vertical response, like in the previous case, both the modes seem to contribute equally to the overall response.

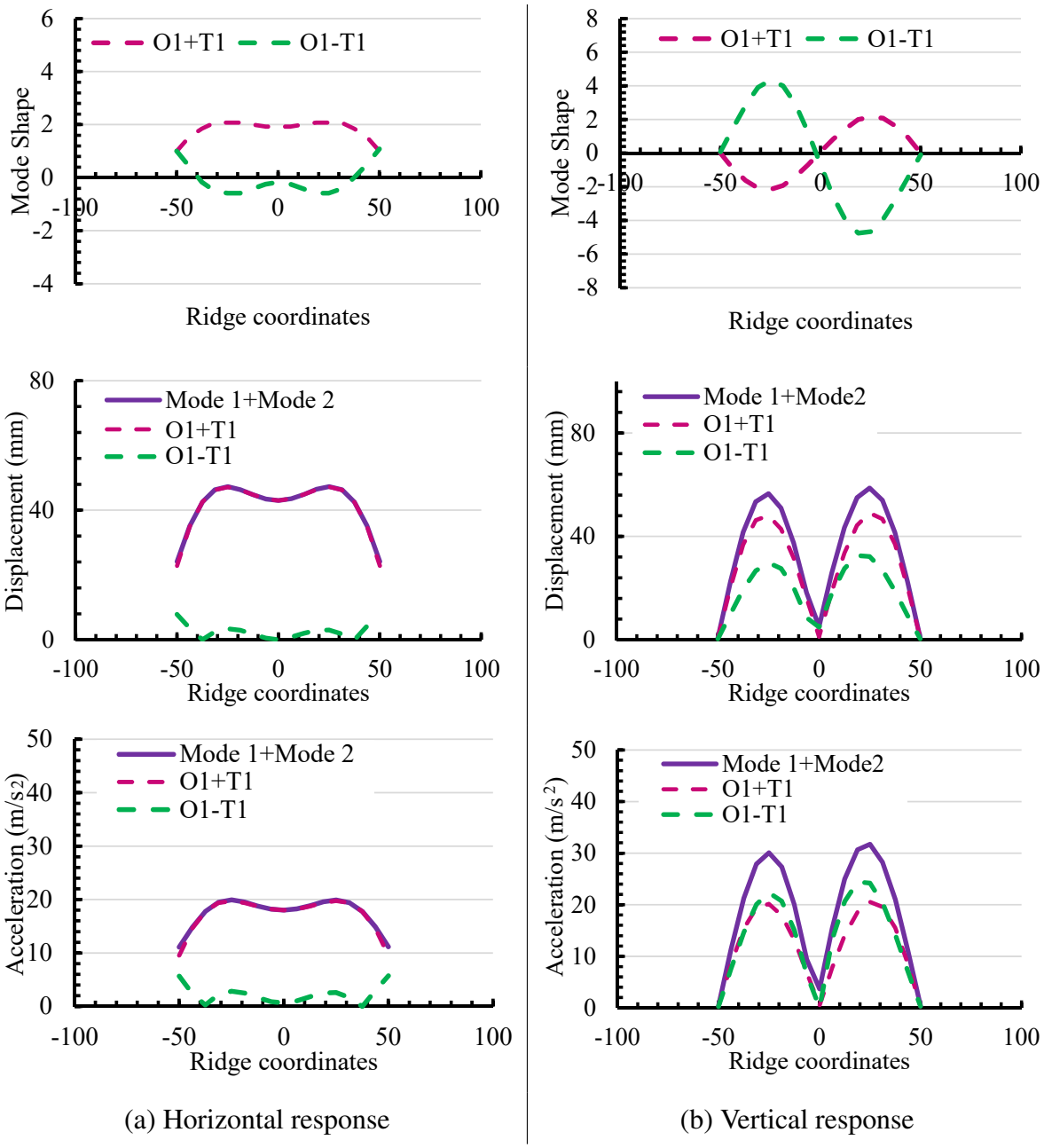

Figure 3-14: Interaction of O1 and T1 modes:
Response of a single-storey 100m model, $R_M = 5$, $R_T = 1.07$

3.3.4 Proposed response considering resonance

The response obtained from RSA for the analysis models given in Table 3.12 was compared with the proposed response results computed using the modified amplification factors given in Equations 1.15-1.16 (Figure 3-15). The participation of other higher roof modes was found to be negligible as can be seen from the plots where 'CQC all' and 'CQC Mode $1+2$' lines coincide.

Due to the differences in mass participation and periods of the two modes (O1+T1 and O1-T1) in the combined model, the peak substructure response calculated from the substructure model (assuming 100% participation from the T1 mode only) often overestimates the actual peak substructure response which is obtained from a modal combination (CQC) of the peak response in the two modes.

For each model, the proposed response was calculated with (labelled as 'Proposed Res' in Figure 3-15 and without (labelled as 'Proposed No Res' in Figure 3-15 considering resonance effects. The modified horizontal amplification factors tend to overestimate the peak roof response in all the models. The overestimation of horizontal response was found to be higher in cases when $R_T < 1$. However, not considering modified amplification factors (see 'Proposed No Res' results in Figure 3-15) also underestimates the overall peak response. Therefore, it is proposed to consider modified amplification factors for cases when period ratios are less than 1.5 and the mass ratio is more than 2 even though it leads to a conservative estimate.

		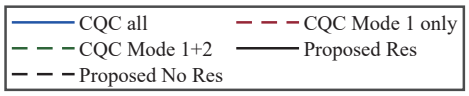	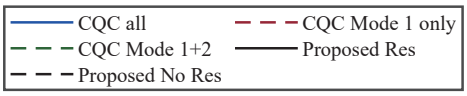
60m	0.88	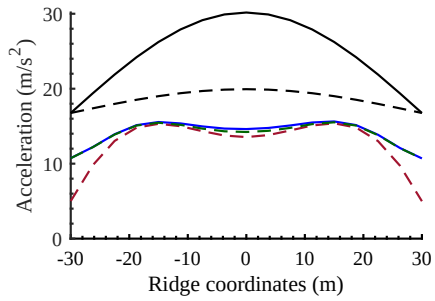	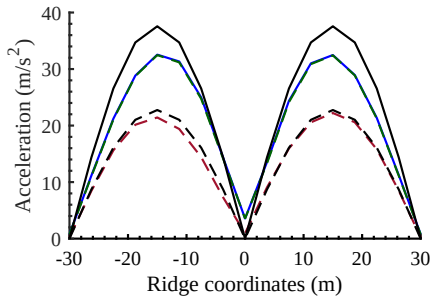
60m	1.12	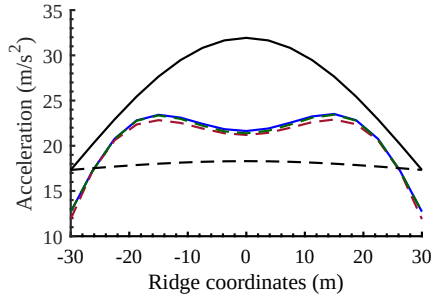	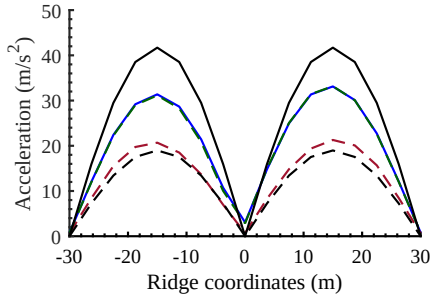
60m	0.77	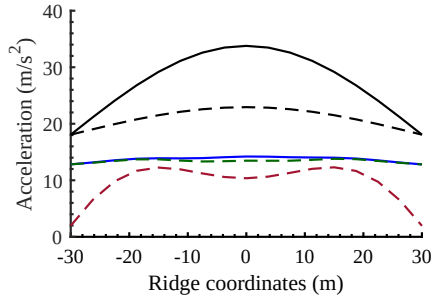	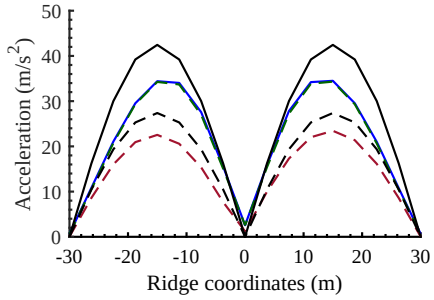
60m	1.13	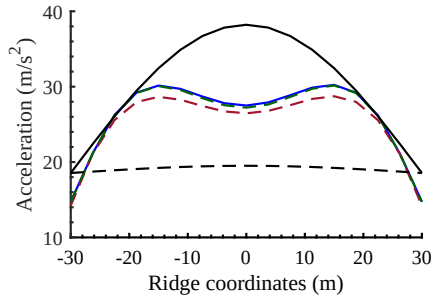	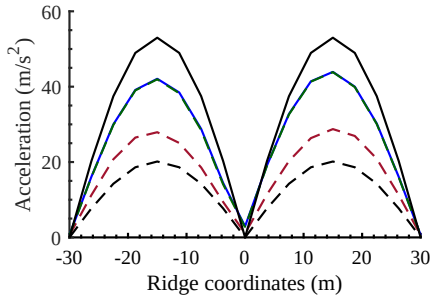

60m	1.06	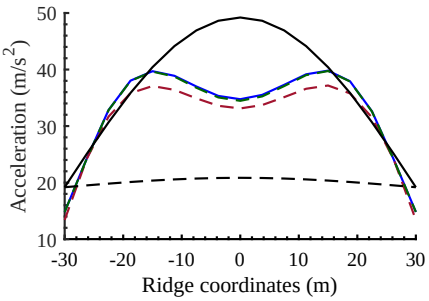	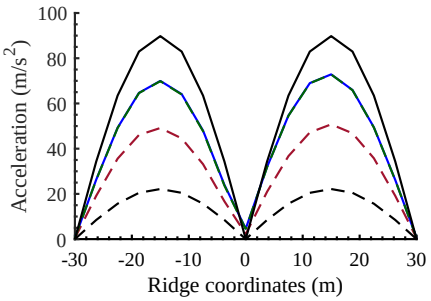
100m	0.73	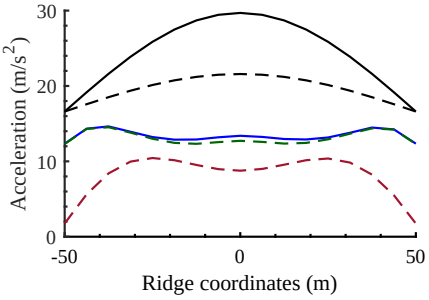	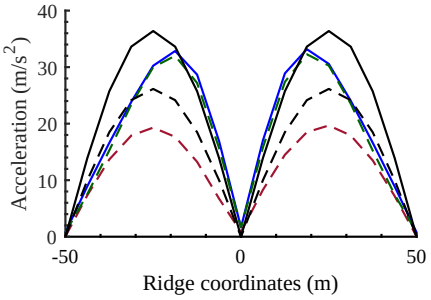
100m	1.07	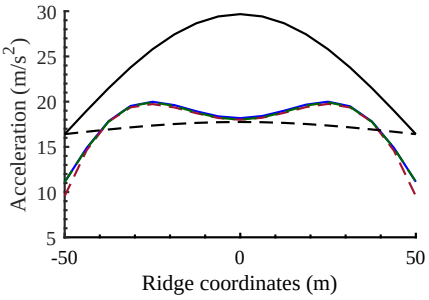	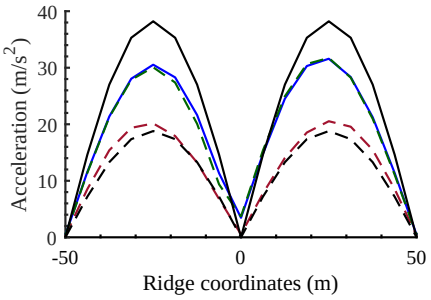
150m	1.06	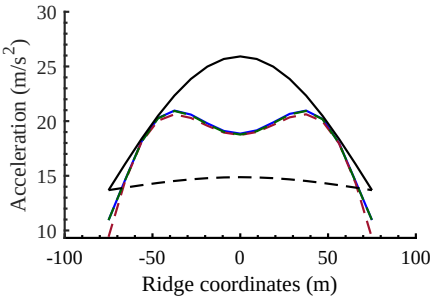	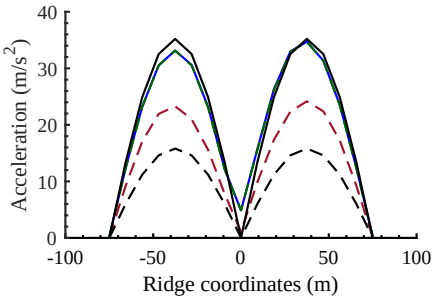

Figure 3-15: CQC Analysis results: Comparison of response with and without considering resonace

3.3.5 Dominance ratios

Dominance ratio D_{Ri} is defined as the square of the ratio of the peak modal response to the total peak response. This ratio identifies the acceleration response contribution of the i^{th} mode ($_cA_i$) to the overall peak roof acceleration ($_cA_{CQC}$) calculated using the CQC modal combination rule (Equations 3.9-3.10). This ratio is however, sensitive to the location of the nodal coordinate chosen as the reference. In this study, the node at which peak occurs (usually a node located midway between the centre and the perimeter) (labelled as 'Peak-Roof') and the node at the base of the ridge (labelled as 'Peak-Sub') are selected as reference points for calculating the dominance ratio in the horizontal direction. In the vertical direction, the peak node suffices as the response is negligible at the ridge base (or the peak substructure). The dominance ratios are plotted as bar graphs in Figures 3-15.

$$D_{Rhi} = (\frac{A_{hmaxi}}{A_{hmax}})^2 = \frac{{}_cA_{hi}{}^2}{{}_cA_{hCQC}{}^2} \tag{3.9}$$

$$D_{Rvi} = (\frac{A_{vmaxi}}{A_{vmax}})^2 = \frac{{}_cA_{vi}{}^2}{{}_cA_{VCQC}{}^2} \tag{3.10}$$

It was observed that, in all the models, the vertical response had a nearly equal contribution ($D_{Rvi} \approx 0.5$) from both the O1+T1 and O1-T1 modes with the O1-T1 mode having a slightly higher dominance ratio. In contrast, the horizontal dominance ratio was found to be quite sensitive to the node selected for computation. For most of the models, the O1+T1 mode governed the response and had a large dominance ratio ($D_{Rh1} > 0.8$) in the peak-roof response and a very small D_{Rh2}. However, for the peak substructure response, the dominance ratio was found to be sensitive to the period ratio R_T. When $R_T < 1$, the O1-T1 mode dominated the horizontal substructure response ($D_{Rh1} > 0.8$) and the O1+T1 mode had a very small contribution. Consequently, When $R_T > 1$, the O1+T1 mode dominated the horizontal substructure response ($D_{Rh1} > 0.8$) and the O1-T1 mode had a very small contribution.

60m	0.88	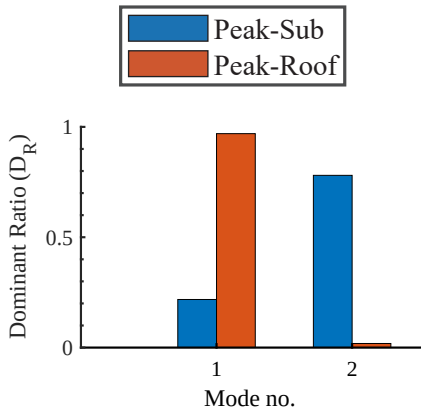	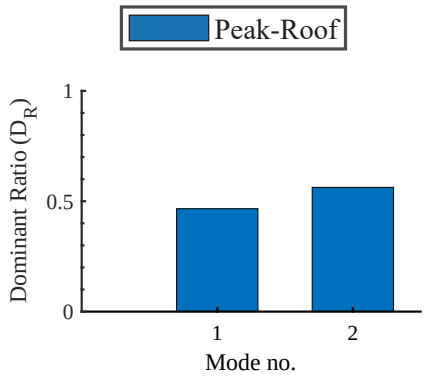
60m	1.12	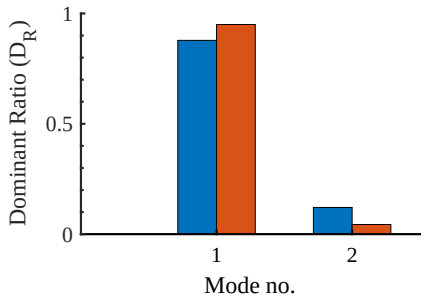	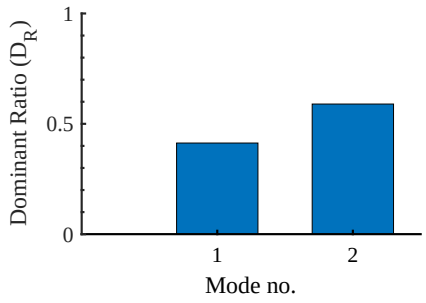
60m	0.77	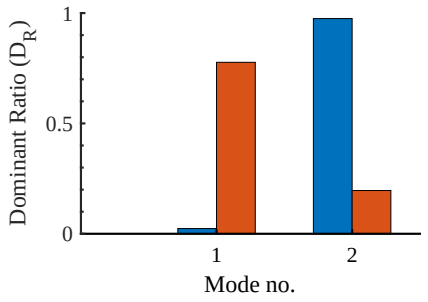	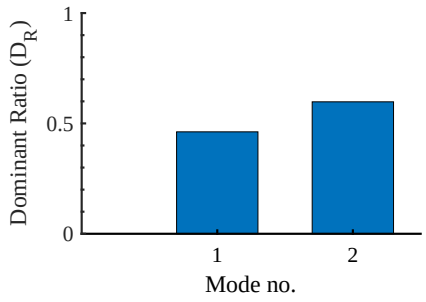
60m	1.13	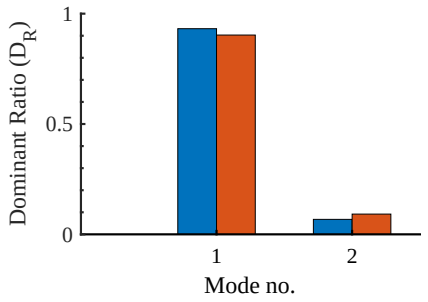	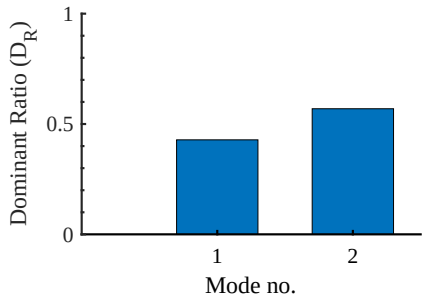

60m	1.06	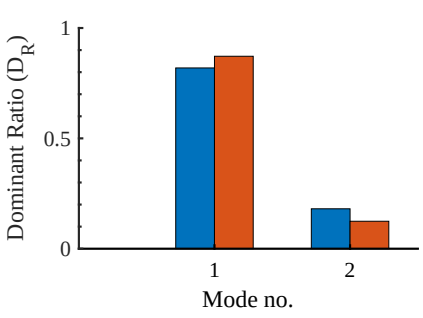	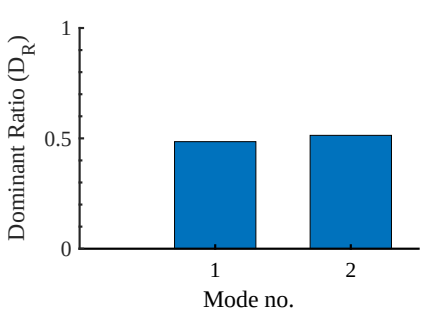
100m	0.73	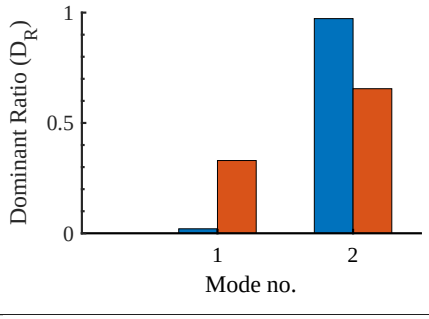	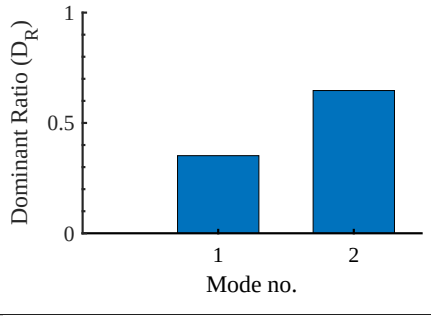
100m	1.07	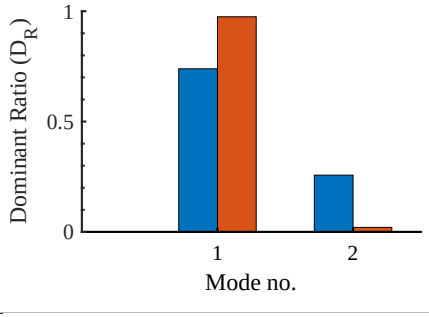	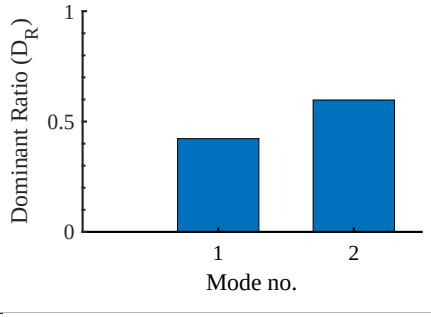
150m	1.06	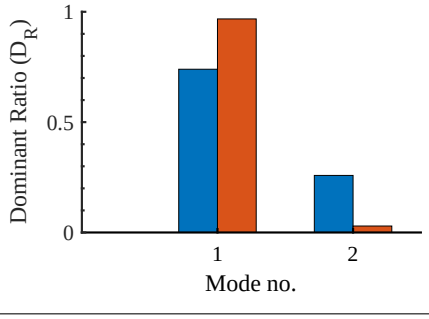	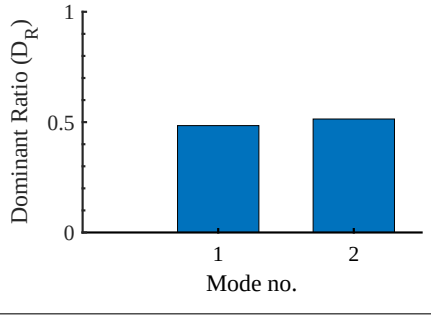

Figure 3-15: CQC Analysis results: Comparison of dominance ratios of O1+T1 and O1-T1 modes

3.3.6 Amplification factors accounting for resonance

RSA was performed using the BRI-L2 spectrum (defined in Section 2.4) and the amplification results from RSA using the CQC combination method were obtained using Equations 3.7 and 3.8, and compared with the previously proposed amplification factors calculated from the results using the Equations 1.15-1.16 [1], plotting both against the T1 period ratios as depicted in Figure 3-16. The amplification factors obtained by dividing the peak roof response A_{Hmax} or A_{Vmax} by the peak substructure response ${}_sA_{Heq}$ (as calculated from the SDOF substructure model using Equation 3.13) are labelled as 'F_H CQC' or 'F_v CQC'. In all cases, the proposed factors overestimate the actual amplification factors, implying that both F'_H and F'_V are conservative estimates of the actual amplification. Considering the responses from Figures 3-12 and 3-16, the overestimation of the horizontal and vertical response is significantly higher for models where $R_T < 1$. Nevertheless, for the sake of simplicity, the previously proposed modified amplification factors (Equations 1.15-1.16) are adopted in this study for $R_T < 1.5$ and $R_M > 2$ models, as the focus of this thesis is to obtain a conservative initial response estimate and the obtained accuracy is considered to be sufficient for an initial estimate.

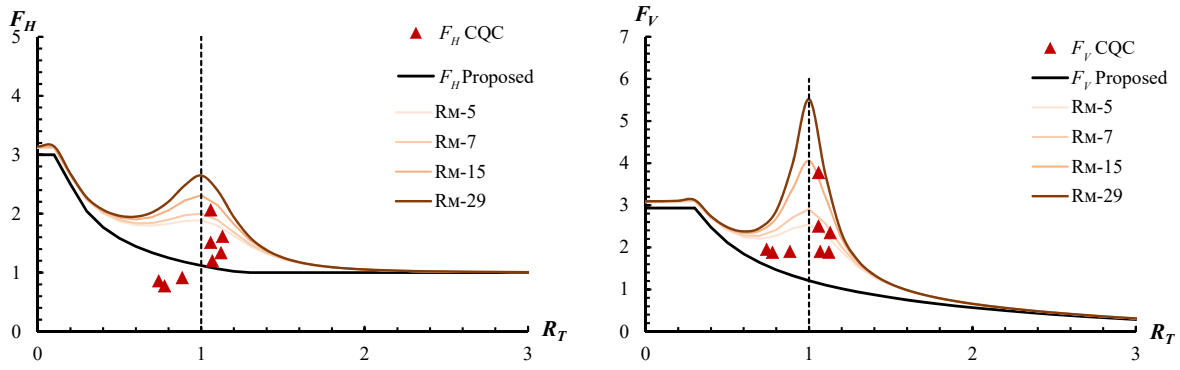

Figure 3-16: Effects of harmonic resonance: Amplification factors from RSA compared with proposed equations

3.4 Proposed roof response

Response Spectrum Analyses were performed on the single-storey combined models using the level-2 design acceleration spectrum BRI-L2 (Figure 2-8 and Equations 2.2-2.3) and the modal responses were combined using the CQC rule. For the analyses, a constant damping of 2% was assumed for all modes. The peak roof responses are shown in Figure 3-17.

For roofs with soft and flexible substructures (α =1/6), the response is governed by the translational sway mode of the substructure and the roof's O1 mode characterised by the flat horizontal response and mild amplification in the vertical response. On the other hand, domes with slightly stiffer substructures (α =1) are governed by the strong interaction between the roof and substructure's dominant modes. In these cases, the second dominant mode can be seen as oscillating in a phase opposite to that of the first dominant mode. Hence, even though the period ratio is close to 1, the resonance effect is reduced by this opposing mode. This effect has been discussed later in Section 3.3.3. For models with stiffer substructures (α =6), the roof's response is further amplified as the substructure periods are in the same range as the roof's modes. However, the mass participation in such cases comes from more than one dominant roof mode resulting in higher roof amplifications. Although the horizontal accelerations for the three stiffness models are comparable, the vertical accelerations are significantly different. This implies that the vertical response is more sensitive to the substructure stiffness.

The accelerations along the ridgeline obtained from CQC and those calculated following the IASS guidebook's recommended method (labelled as 'Previous') using the Equations 1.12-1.17, are also compared in Figure 3-17. The results are in good agreement with the CQC results except for cases with α =6 where the horizontal accelerations are overestimated by the equations.

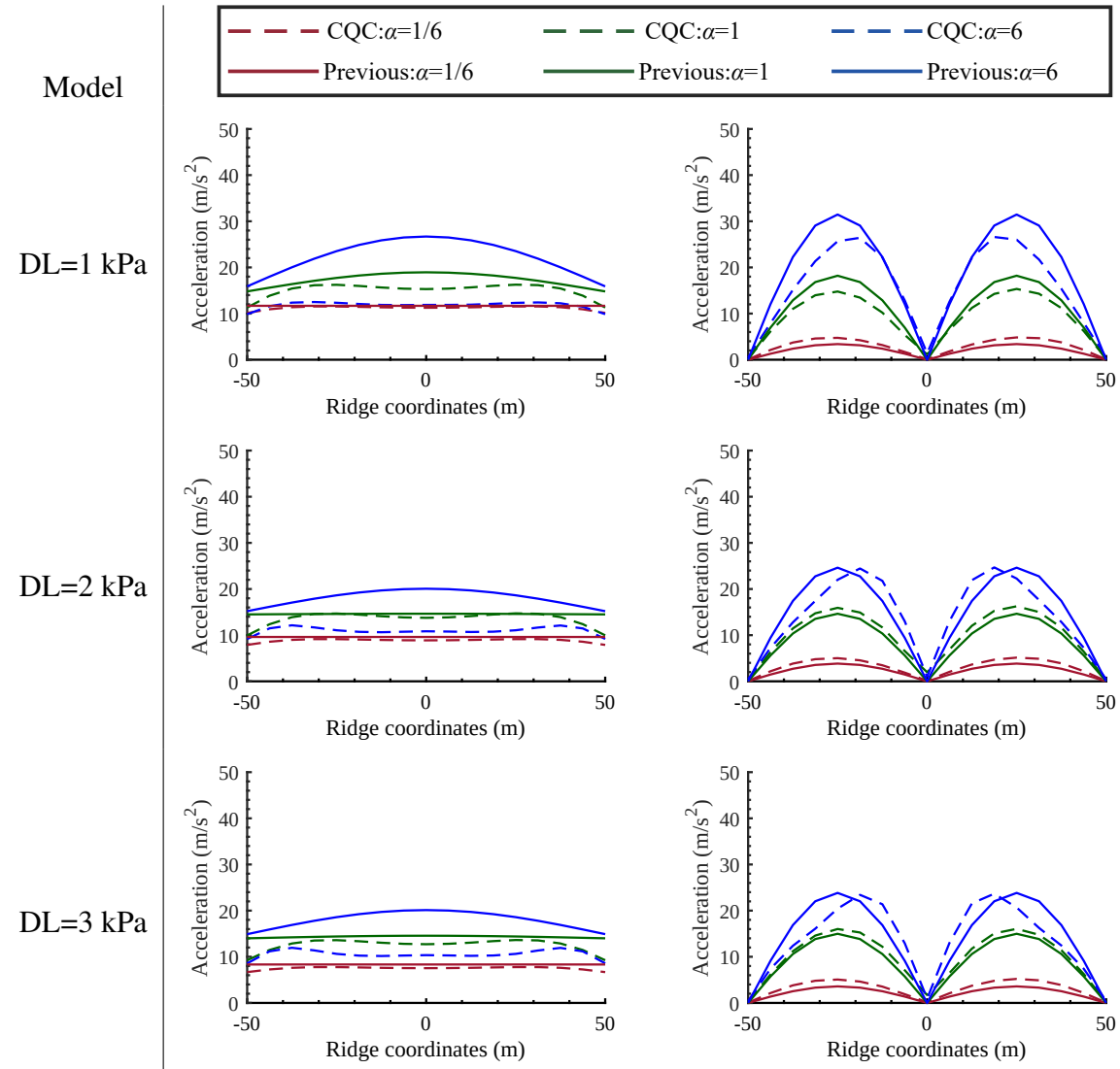

Figure 3-17: CQC results and Previously proposed accelerations [1]

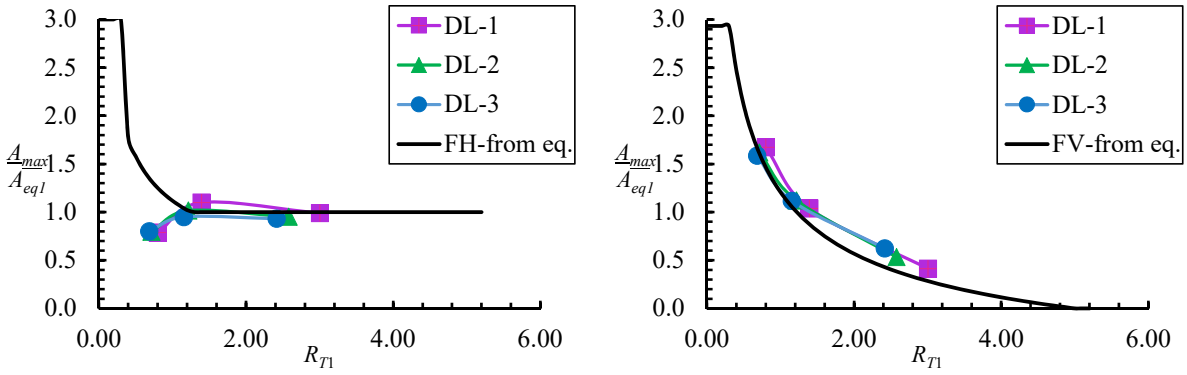

(a) Horizontal amplification factors (b) Vertical amplification factors

Figure 3-18: Comparison with proposed amplification factors

The horizontal and vertical amplification factors, which have been adopted in the guide to earthquake response evaluation for metal spatial structures are multiplied by A_{eq} to obtain the roof accelerations. The amplification factors are in good agreement with those obtained from the equations proposed in the guide. In Figure 3-18, it can be seen that when R_{T1} is in the range of 1 (α =1), resonance effect is not observed. This occurs when the substructure's first mode and roof's O1 mode coincide with each other. This leads to dominance of two modes in the combined model- the first where the substructure and roof interact strongly with each other and the second mode where the roof vibrates independent of the substructure as the substructure remains largely stationery. The second mode thus has a mild cancelling effect on the overall response. This suggests that the proposed response estimation method conservatively covers the peak horizontal and vertical response of roofs with single-storey substructures.

3.5 Multistorey models: Higher substructure mode effects

3.5.1 Roof-substructure interaction

The multistorey substructure models defined in Section-3.2 are investigated in this section. As discussed in Section 3.3, the roof dead load ranged from 1 to 3kPa, while the substructure loads were held constant and the substructure stiffness was adjusted by modifying the moment of inertia of MRF members and the axial stiffness of the BRBs by a scale factor α. Each model was labelled L-DL-κ where κ denotes the roof dead load (kPa).

Effects of mass ratio

First, the effects of mass ratio on the dominant roof and substructure modes are investigated in this section using the L-100 model series. The dead load on the dome was varied from 1 kPa to 3 kPa as shown in Table 3.7, and the corresponding periods of the four modes of the roof only model where the roof ends were pinned, and their mass participation factors (Γ (%)) and the trends are illustrated in Figure 3-19. It can be seen that the periods of the modes generally decrease with increasing mass ratio as the roof mass is decreasing, and so are the periods when the stiffness remains constant. The reduction in the fundamental periods (O1 modes) is the largest whereas the higher mode periods reduce more gradually (Figure 3-19(a)). The mass participation of the O2.5 mode is the highest as the roof ends are pinned and therefore represents a case when the substructure is very rigid. In combined models with substructures of finite stiffness, the fundamental mode, which is the O1 mode in all the roof models, is expected to be the most dominant. Furthermore, it was observed that varying the mass ratios did not change the participation factors of these four periods and the contribution from the individual modes remained rather constant throughout as can be seen in Figure 3-19(b).

The same exercise was repeated for the substructure model (with the roof modelled as a rigid diaphragm) keeping the mass of the lower floors (2FL-6FL) constant and the results are shown in Table 3.13 and Figure 3-20. The period ratios are calculated as per Equation 3.4. The effect of mass ratio has a direct correlation to the fundamental periods

of the substructure (Figure 3-20(a)). However, the periods of the higher mode period were relatively less affected. As observed in the roof model, varying the mass ratio did not change the contributions from the individual modes (Figure 3-20(b)). Similarly, varying the mass ratios had a larger influence on R_{T1} which decreased with increasing R_M than on R_{T2} which decreased more gradually.

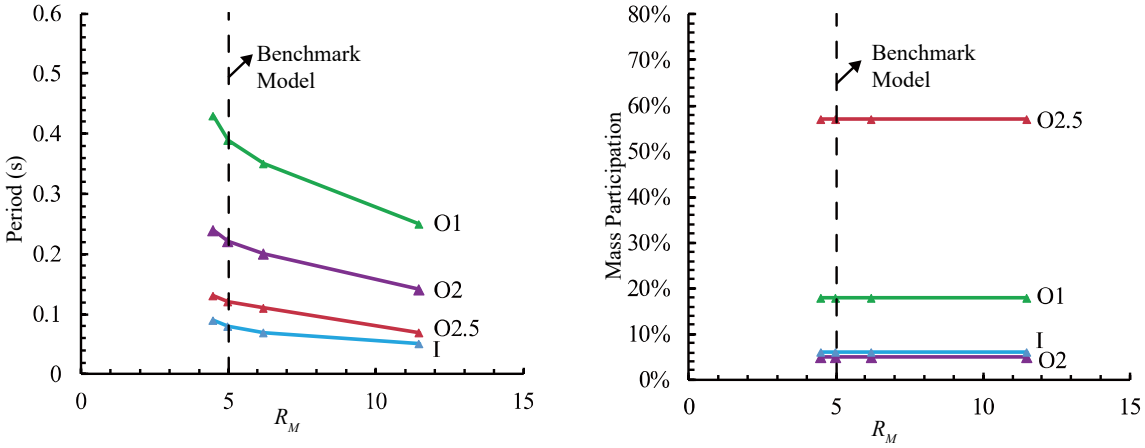

(a) Roof periods (b) Mass participation of the four modes

Figure 3-19: Effects of R_M on the dominant modes of the roof model

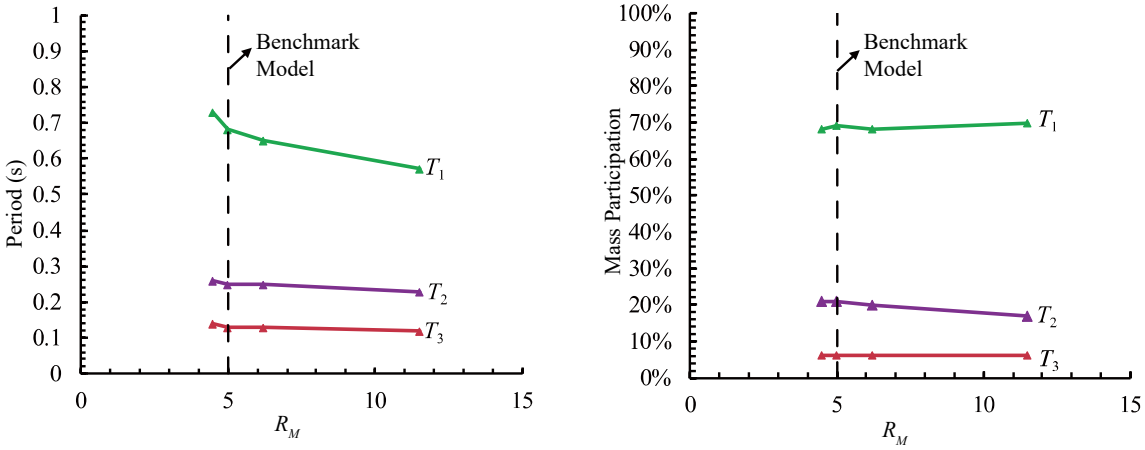

(a) Substructure periods (b) Mass participation

Figure 3-20: Effects of R_M on the dominant modes of the substructure model

Table 3.13: $L100$ substructure periods: Effects of R_M

Roof dead load (kPa)	R_M	T_1	T_2	T_3	R_{T1}	R_{T2}
1	11	0.57s, (70%)	0.23s, (17%)	0.12s, (6%)	2.3	0.9
2	6	0.65s, (68%)	0.25s, (20%)	0.13s, (6%)	1.8	0.7
3	4	0.73s, (68%)	0.26s, (21%)	0.14s, (6%)	1.7	0.6

Effects of substructure stiffness

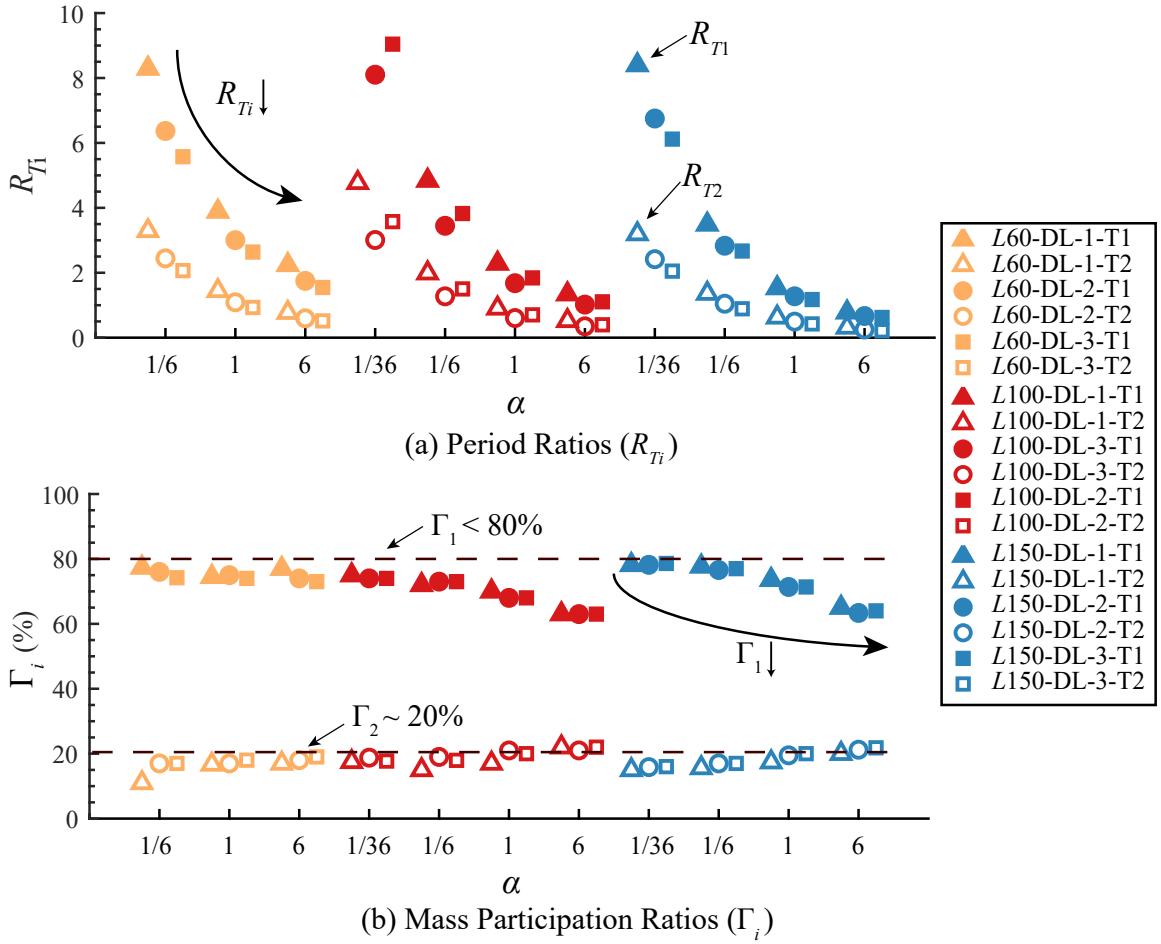

(a) Period Ratios (R_{Ti})

(b) Mass Participation Ratios (Γ_i)

Figure 3-21: Multistorey models: Effects of varying the mass and substructure stiffness

The period ratios (R_{Ti}) and combined model mass participation factors (Γ_i) for the first two translational substructure mode shapes are plotted in Figure3-21. Here, the period ratios R_{T1} and R_{T2} are the ratios of the first (T1) and second (T2) substructure periods

(ranked in decreasing order of mass participation) to the roof's fundamental O1 mode ($_rT_R$ in Table 3.7). Note that the substructure modes are denoted by the mode shape, where T1 is a sway mode, while T2 and T3 feature increasing numbers of inflection points. Increasing the substructure stiffness decreased the period and participation factor of the first mode, indicating an increased contribution from the higher roof and substructure modes. The T1 modes have a mass participation factor of around $\Gamma_1 = 60 - 80\%$, with the remaining participation coming from the higher substructure modes. This implies that the peak acceleration of the substructure ($_sA_{Heq}$) cannot be obtained solely from the substructure T1 mode (as proposed by various design guidelines for the design of regular multi-storey buildings[5], [16]), and that it may be important to include the contributions of the higher substructure modes, specifically those needed to achieve a minimum cumulative participation factor of 90% [16], [17].

The roof and substructure periods are mapped on the design spectrum in Tables 3.14 and 3.15. The dominant modes and their mode shapes for all the combined models are also shown in Figures 3.16-3.18. Unlike the single-storey cases, both the substructure T1 and T2 modes interact with the nearest roof mode. For example, consider the mode shapes of the 100m combined models shown in Table 3.17. For the combined model L100-DL-3 α=1/6, the first substructure mode (T1) is much longer than the roof modes (Table 3.15) and only weakly interacts with the roof O1 mode, as shown in Table 3.17. However, the substructure T2 mode strongly interacts with the roof O1 mode. Increasing the substructure stiffness to α=1 results in increased interaction between the substructure T1 and roof O1 modes, as well as between the substructure T2 and roof O2 modes, which have nearly identical periods. The third mode features the roof O1 mode mildly interacting with the substructure T1 mode. This trend is further accentuated for the stiffer α=6 model, with the first and second modes exhibiting a strong interaction between the substructure T1 and roof O1 modes, but with a lower mass participation than the α=1/6 and 1 cases. The third mode features the substructure T2 mildly interacting with the roof's higher O2.5 mode.

Therefore, the dynamic characteristics of roofs with flexible multistorey substructures (α=1/6 and α=1/36) are governed by the dominant roof mode O1 interacting with the closest substructure mode and the higher roof modes remain unexcited. On the other hand,

when the T1 and T2 modes of stiffer multistorey substructures (α=1 and α=6) are closer to the O1 roof mode, the roof-substructure interaction is far more complex, exciting the O1, O2, O2.5 and I roof modes. Although the interacting pairs depend on the proximity of the respective substructure and roof modes, combinations of the fundamental roof (O1 and O2) and substructure (T1 and T2) modes (e.g. O1+T1, O2+T2 and O1+T2) tend to dominate. Furthermore, each substructure mode tends to be split into multiple combined modes, for example O1+T1, O1-T1 and I+T1, each attracting a portion of the mass participation of the underlying substructure mode.

Table 3.14: Multistorey models: Roof and substructure periods (*L*60 models)

DL (kPa)		Substructure stiffness scale factor α		
		α=1/6	**α=1**	**α=6**
***L* = 60m**	**1**	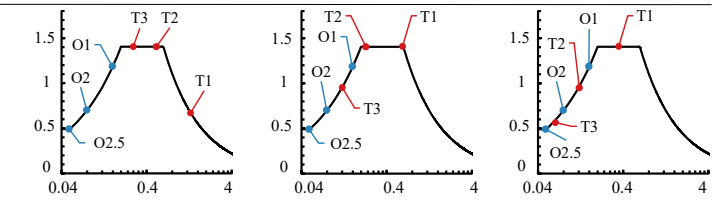		
	2	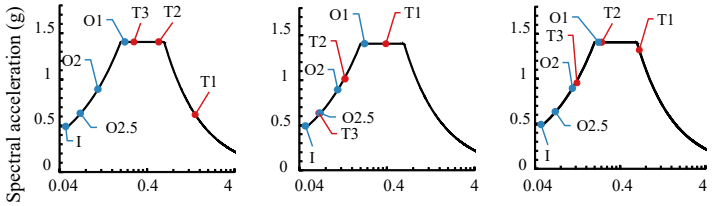		
	3	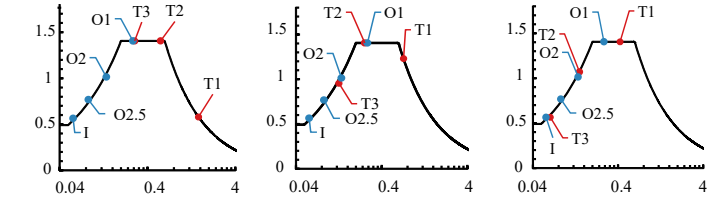		

Table 3.15: Multistorey models: Roof and substructure periods ($L100$ and $L150$ models)

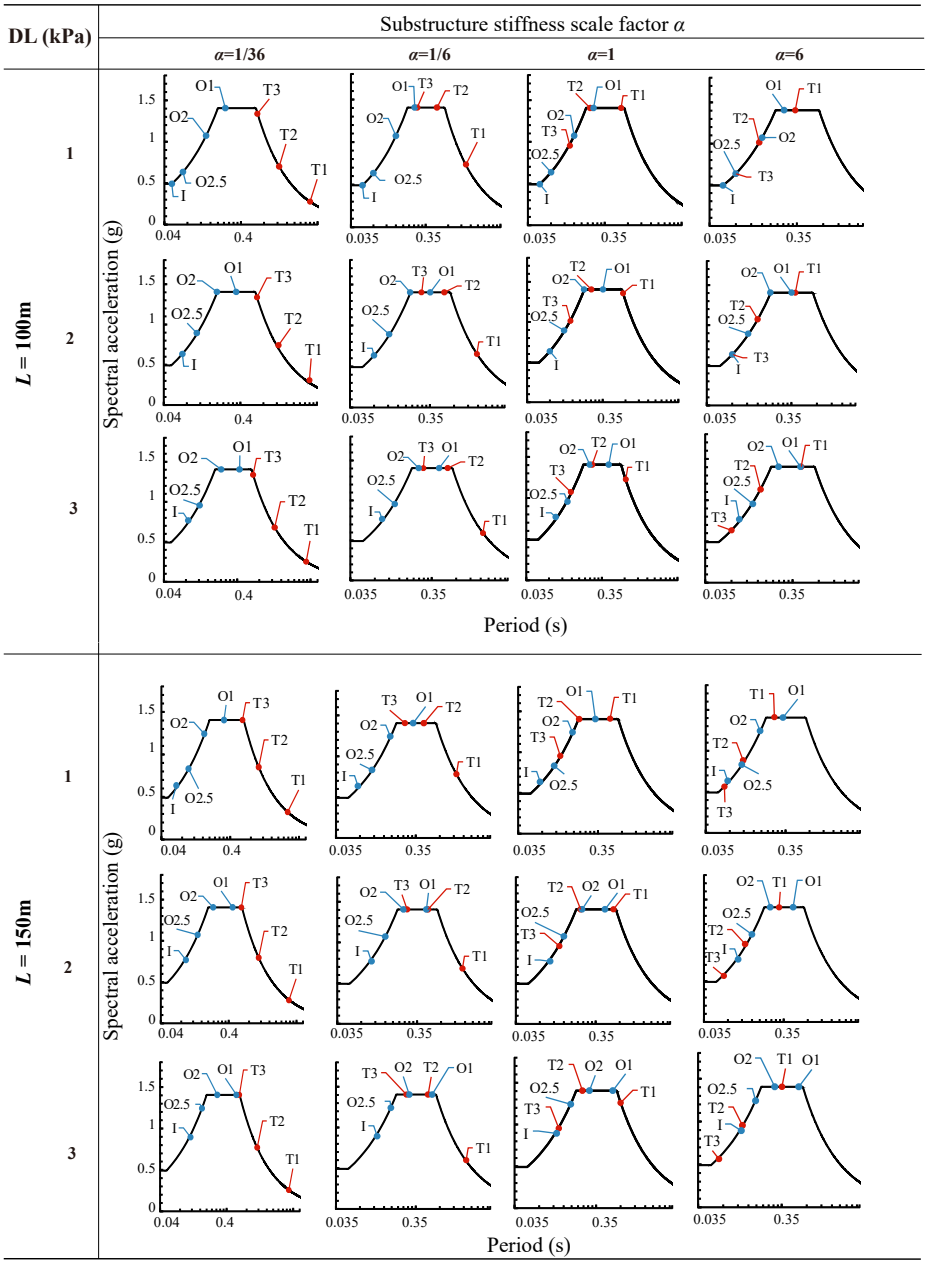

Table 3.16: Multistorey models: Periods (s), mass participation (%) and mode shapes

DL	R_M	α	L=60m, Mode shapes		
1	16	1/6	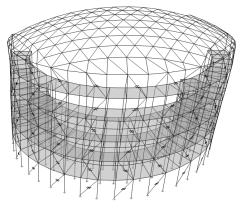 O1+T1, 1.3s, (75%)	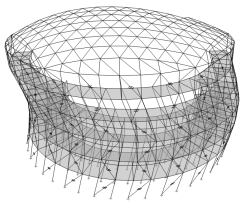 O1+T2, 0.5s, (15%)	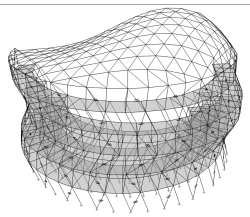 O1+T3, 0.3s, (5%)
		1	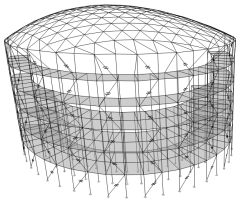 O1+T1, 0.6s, (75%)	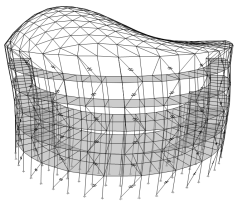 O1+T2, 0.2s, (16%)	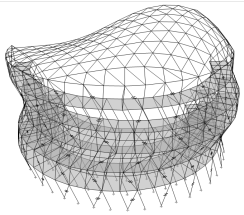 O1-T3, 0.1s, (5%)
		6	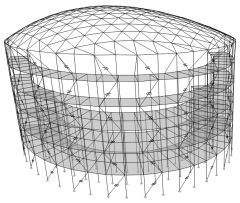 O1+T1, 0.4s, (80%)	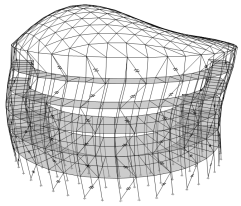 O2-T2, 0.1s, (6%)	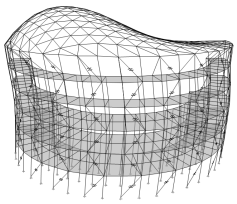 O2+T2, 0.2s, (6%)
2	8	1/6	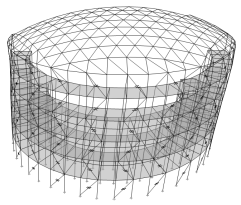 O1+T1, 1.4s, (75%)	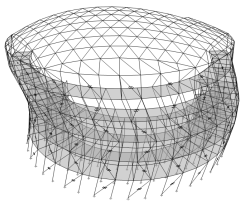 O1+T2, 0.5s, (17%)	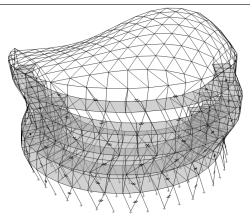 O1+T3, 0.3s, (5%)
		1	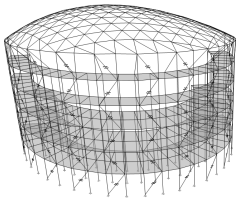 O1+T1, 0.7s, (73%)	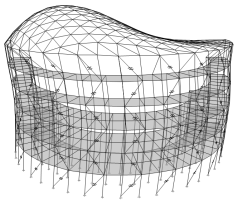 O1+T2, 0.3s, (13%)	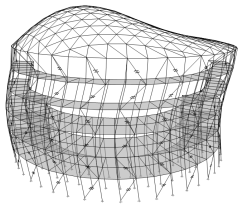 O1-T2, 0.2s, (5%)
		6	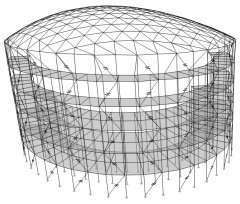 O1+T1, 0.5s, (78%)	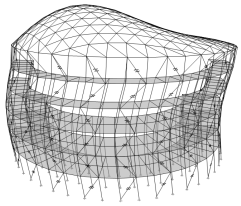 O1-T2, 0.2s, (13%)	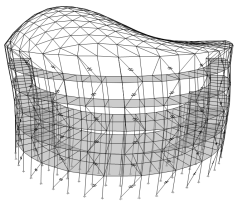 O1+T2, 0.2s, (3%)

DL	R_M	α	L=60m, Mode shapes		
3	6	1/6	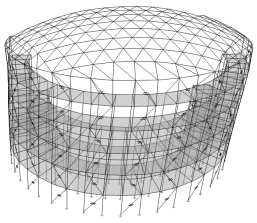	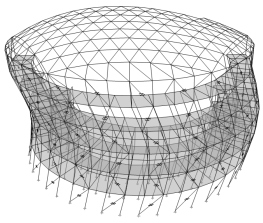	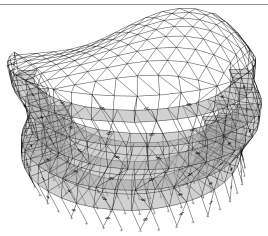
			O1+T1, 1.5s, (74%)	O1+T2, 0.6s, (17%)	O1+T3, 0.3s, (3%)
		1	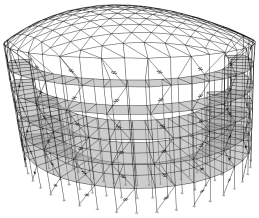	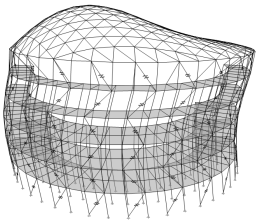	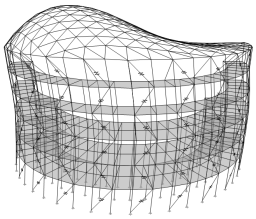
			O1+T1, 0.7s, (72%)	O1-T2, 0.24s, (11%)	O1+T2, 0.3s, (6%)
		6	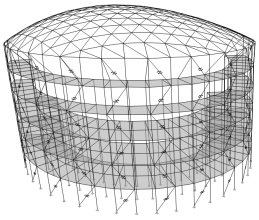	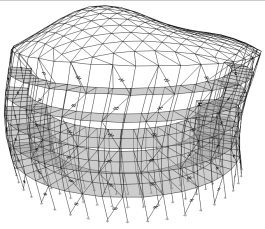	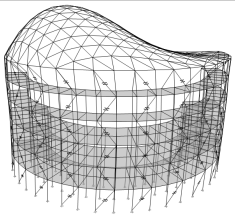
			O1+T1, 0.5s, (76%)	O2+T2, 0.2s, (13%)	O1-T1, 0.3s, (4%)

Table 3.17: Multistorey combined models: Periods (s), mass participation (%) and mode shapes

DL	R_M	α	L=100m, Mode shapes		
1	11.5	1/6	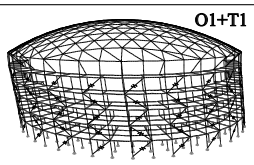 1.2s, (73%)	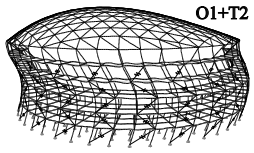 0.5s, (18%)	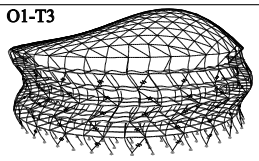 0.2s, (5%)
		1	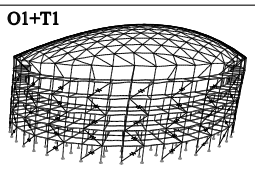 0.5s, (68%)	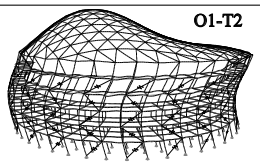 0.2s, (15%)	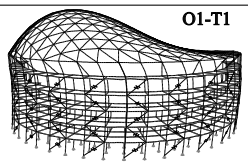 0.3s, (8%)
		6	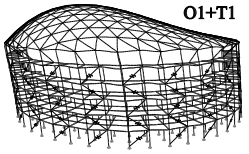 0.3s, (49%)	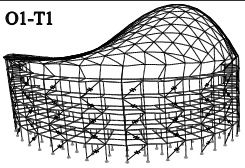 0.2s, (14%)	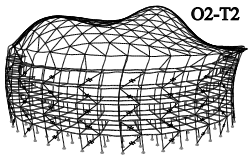 0.1s, (12%)
2	6.2	1/6	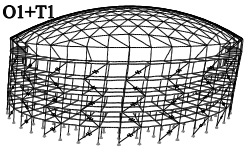 1.3s, (72%)	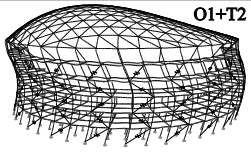 0.5s, (18%)	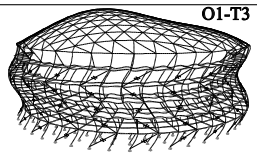 0.3s, (6%)
		1	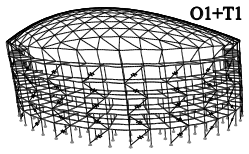 0.6s, (62%)	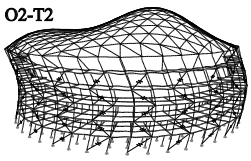 0.2s, (17%)	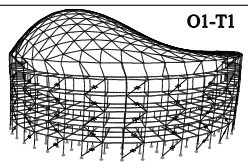 0.4s, (9%)
		6	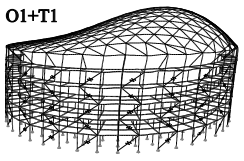 0.4s, (30%)	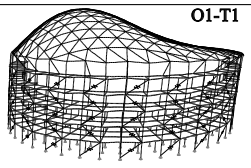 0.3s, (29%)	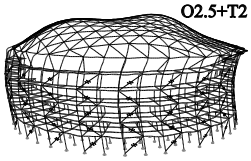 0.1s, (19%)

DL	R_M	α	L=100m, Mode shapes		
3	4.5	1/6	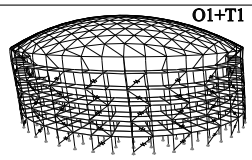	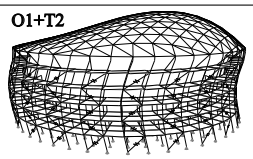	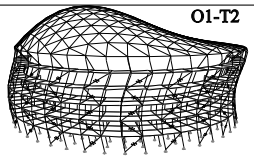
			1.5s, (71%)	0.6s, (16%)	0.5s, (6%)
		1	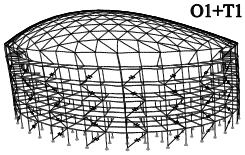	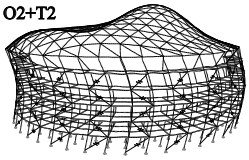	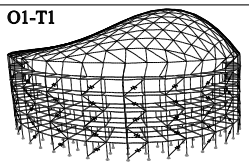
			0.7s, (59%)	0.3s, (17%)	0.5s, (10%)
		6	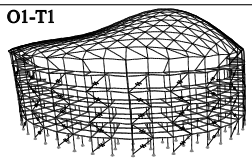	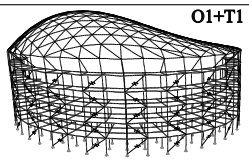	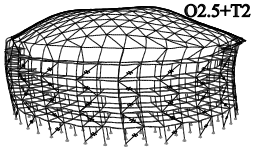
			0.4s, (32%)	0.5s, (25%)	0.2s, (21%)

Table 3.18: Multistorey combined models: Periods (s), mass participation (%) and mode shapes

DL	R_M	α	L=150m, Mode shapes		
1	8.3	1/6	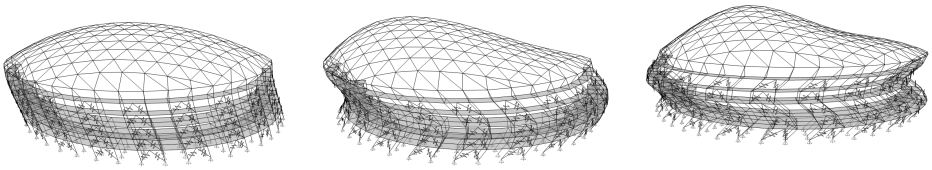		
			O1+T1, 1.2s, (73%)	O1+T2, 0.5s, (18%)	O1+T3, 0.2s, (5%)
		1	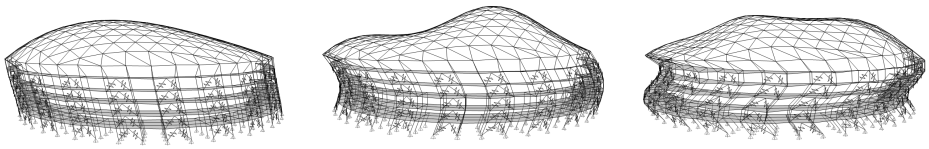		
			O1+T1, 0.5s, (68%)	O2+T2, 0.5s, (15%)	O2.5+T3, 0.2s, (7%)
		6	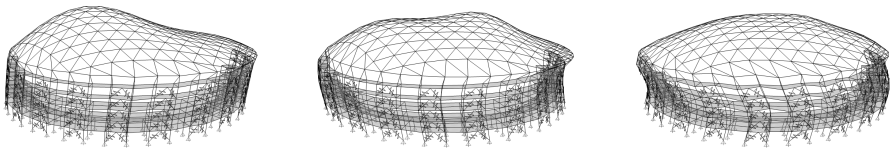		
			0.3s, (49%)	0.2s, (14%)	0.1s, (12%)
2	4.6	1/6	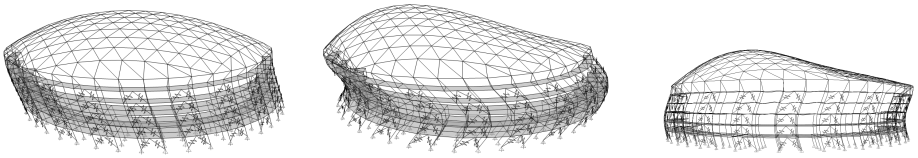		
			O1+T1, 1.36s, (75%)	O1+T2, 0.53s, (13%)	O1-T2, 0.43s, (6%)
		1	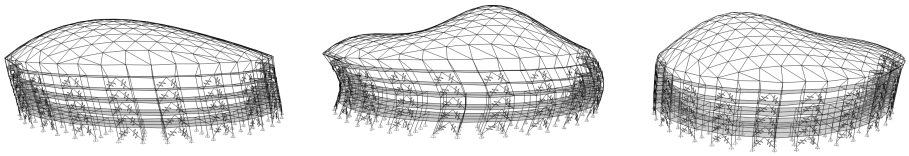		
			O1+T1, 0.63s, (59%)	O2+T2, 0.24s, (13%)	O1-T1, 0.44s, (12%)
		6	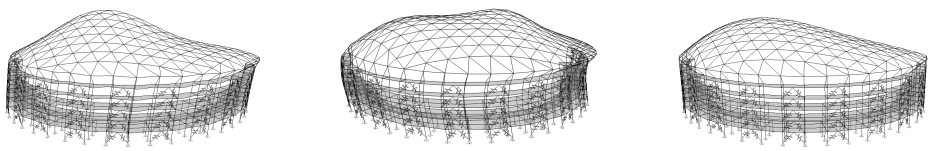		
			O1-T1, 0.32s, (41%)	O2.5+T2+I, 0.15s, (13%)	O1+T1, 0.48s, (9%)

DL	R_M	α	L=150m, Mode shapes		
3	8.3	1/6	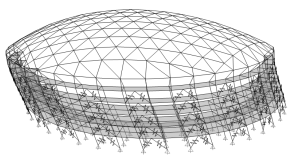	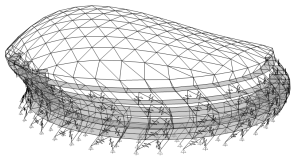	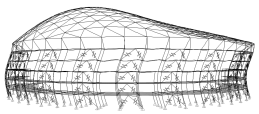
			O1+T1, 1.5s, (75%)	O1+T2, 0.48s, (12%)	O1-T2, 0.6s, (7%)
		1	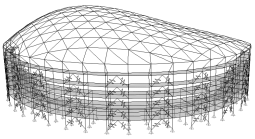	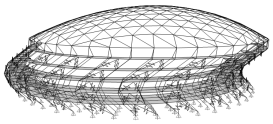	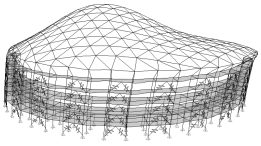
			O1+T1, 0.73s, (42%)	O2+T2, 0.25s, (18%)	O1-T1, 0.52s, (15%)
		6	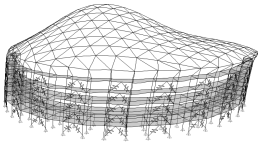	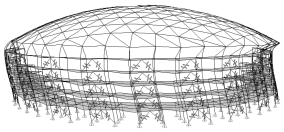	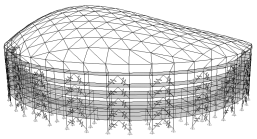
			O1-T1, 0.4s, (42%)	I+T2, 0.2s, (22%)	O1+T1, 0.6s, (12%)

The seismic response of domes with multistorey substructures may therefore be interpreted as a combination of response from both T1-roof and T2-roof interactions. These interactions are further quantified in the following subsection.

3.5.2 Dominance Response Ratio

To distinguish the contributions of the substructure T1 and T2 modes to the peak response, dominance response ratio DR_i introduced in the Section 3.3.5 was computed for each substructure mode. This ratio identifies the acceleration response contribution of the i^{th} substructure mode ($_cA_i$) to the overall peak roof acceleration ($_cA_{SRSS}$) calculated using the SRSS modal combination rule (Equation 3.11) such that the sum of DR_i from the three substructure modes equals to 1 (100% of the response). As the response is sensitive to the selected location, the horizontal and vertical ratios are reported at the node producing the maximum combined resultant response (usually a node near the quarter points). Therefore, DR_1, DR_2 and DR_3 represent the combined response contribution of all modes

exhibiting a substructure T1, T2 and T3 mode, respectively.

$$DR_i = \frac{{}_cA_i{}^2}{\left(\sqrt{\sum_{i=1}^{n} {}_cA_i{}^2}\right)^2} = \frac{{}_cA_i{}^2}{{}_cA_{SRSS}{}^2} \tag{3.11}$$

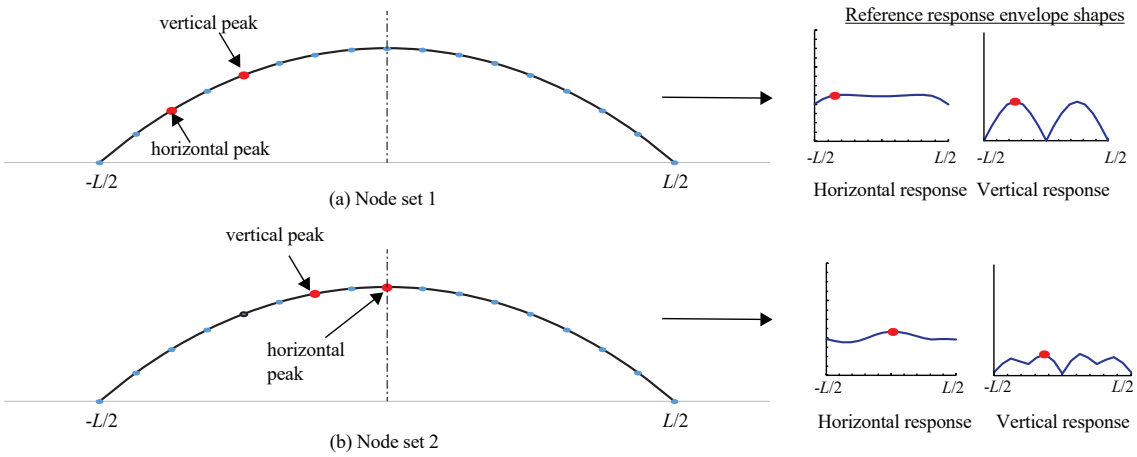

Figure 3-22: Chosen nodes for computing dominance ratios

Response spectrum analysis (RSA) was conducted for each combined model using the elastic BRI-L2 design spectrum [10] adjusted to a constant damping ratio of 2%. The dominance ratios in the horizontal and vertical directions were calculated using the critical nodes' acceleration results following Equation 3.11. Since the dominance ratio values are sensitive to the selected node, two sets of critical nodes along the ridgeline were considered as shown in Figure 3-22. The nodes were adopted from the two most common response envelopes (reference envelopes) and the respective peaks were selected and are marked with red labels in Figure 3-22. The peak response envelope considered for the Node set 1 is the most common and is usually observed when the O1 mode primarily governs the response. The Node set 2 consist of the nodes located near the centre of the ridgeline and the reference envelope of this set (Figure 3-22(b)) is observed when the higher roof modes O2 and O2.5 govern the peak response envelope. In this study, this envelope was commonly observed in the higher substructure modes response when the T2 mode was in close proximity with the O2 and O2.5 modes.

The dominance ratios for each substructure mode (T1, T2 and T3) for all the combined models are plotted in Figures 3-23-3-28. Consider the models of $L-100$-DL-2 series in Figure 3-24. The horizontal dominance ratios are dominated by the T1 mode for all cases and the next dominant mode is the T2 mode. The dominance of the T1 mode decreases with decrease in the substructure stiffness (or as α decreases). This trend is similar to that of a response of a conventional multistorey building where the base shear and forces are primarily governed by the fundamental mode with increasing contributions from higher modes as the fundamental period increases. However, in the case of the vertical response, one particular substructure mode governs the overall response. When the substructure is very stiff ($\alpha = 6$), the vertical dominance ratio from T1 is the highest at 0.9 and almost no contribution from T2 mode. As the substructure gets stiffer the contribution of T1 mode drops to 0 and the contribution of T2 mode shoots up to more than 0.9 for $\alpha = 1/6$. As the substructure stiffness further reduces, the vertical response from T1 and T2 drop to 0 and the only contribution is from the mild T3-O1 interaction although the absolute value of this vertical response is low as the mass participation of T3 mode is low. In contrast, the horizontal dominance is still governed by the T1 mode. Thus, the vertical response is highly sensitive to the proximity of the substructure modes to the roof's dominant asymmetric modes (O1, O2 and O2.5) and resonance of any substructure mode with these roof modes makes that substructure mode govern the vertical roof response. On the other hand, the horizontal response is not as sensitive to the location of the substructure modes with respect to the roof modes and the T1 mode is always the maximum contributing mode to the horizontal response.

Similar trends were observed for the dominance ratios computed using the Node set-2 in Figures 3-26-3-28. For cases where T2 interacts with the roof's higher modes like the $L-150$-DL-1 $\alpha = 6$ case where T2 is close to O2.5 (Table 3.15), the horizontal dominance ratio of T2 mode was significantly higher for the Node set 2 ($DR_2 = 0.40$ in Figure 3-28) if compared to the corresponding horizontal ratio computed for Node set 1 ($DR_2 = 0.15$ in Figure 3-25). Thus, the horizontal dominance ratio is sensitive to the selected node for cases when T2 mode contributes to the overall response and so the contribution of higher modes should not be judged based on the dominance ratios from a single set of critical

nodes. Nevertheless, the horizontal response was dominated by the T1 mode for both node sets and the T2 mode's contribution to horizontal response gradually increased as the substructure stiffness decreased. The vertical dominance ratios for both node sets were similar to those computed from node set 1 with minor differences when the T2 interacted significantly with roof's higher modes. The vertical response was generally governed by the T1 and T2 modes for stiff substructures ($\alpha >= 1$) and a singular mode (the T2 or T3 mode) governed the response for flexible substructures ($\alpha <= 1/6$).

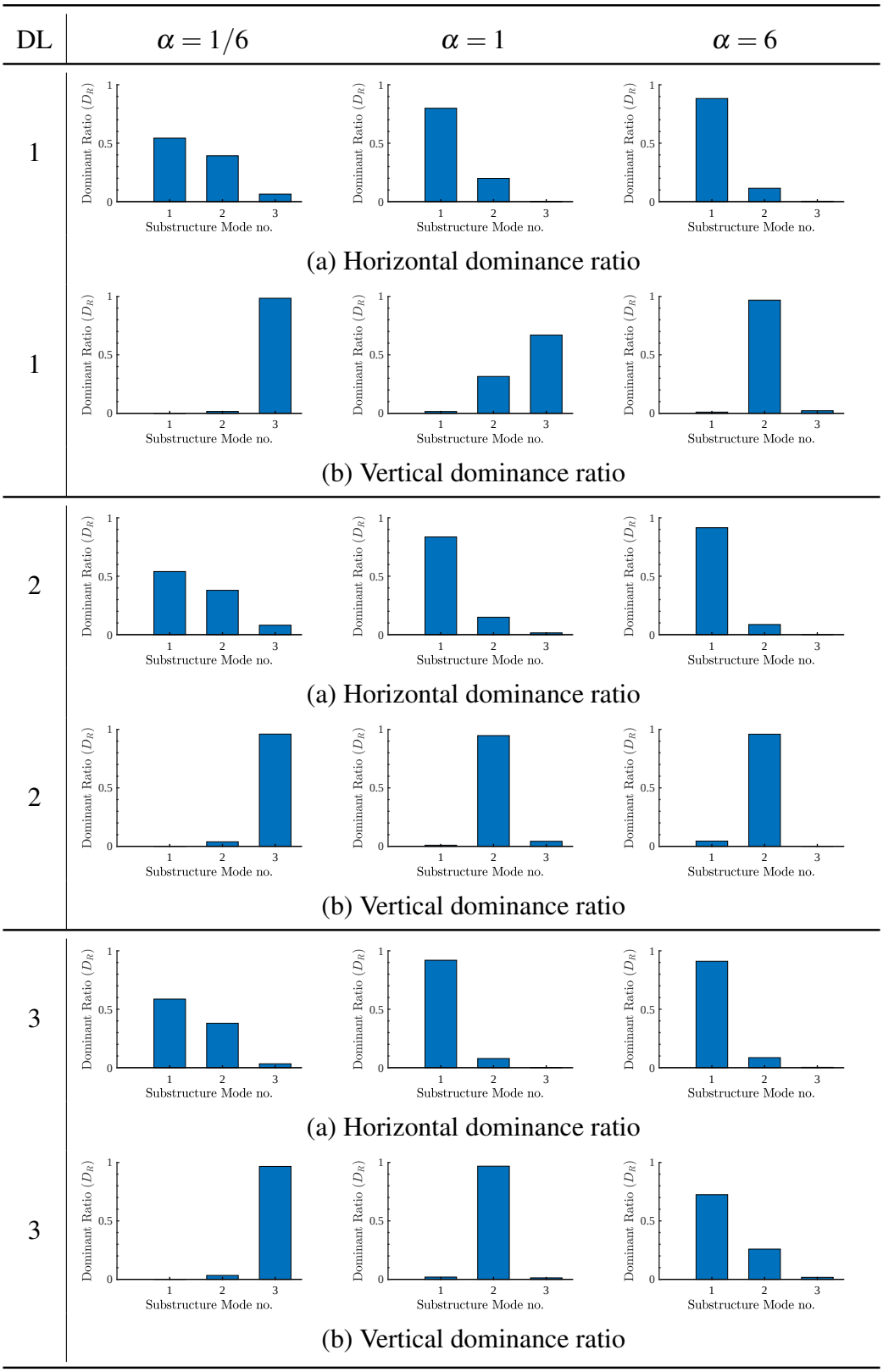

Figure 3-23: $L-60$ models: Dominance ratio of each substructure mode at Node set-1

DL	$\alpha = 1/36$	$\alpha = 1/6$	$\alpha = 1$	$\alpha = 6$
1	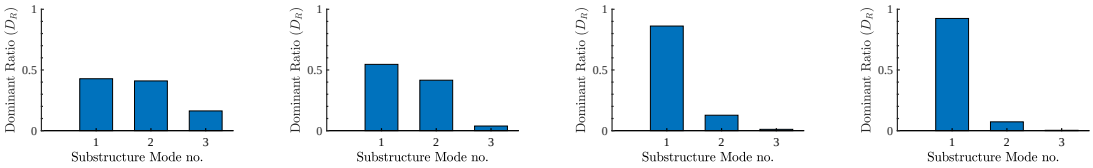			
	(a) Horizontal dominance ratio			
1	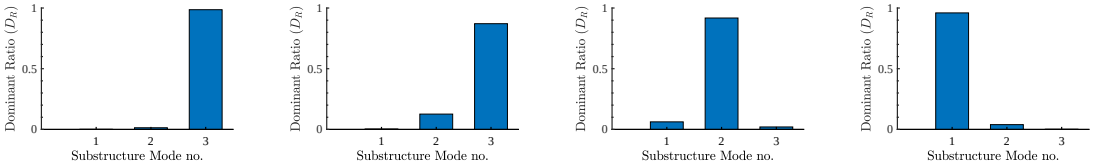			
	(b) Vertical dominance ratio			
2	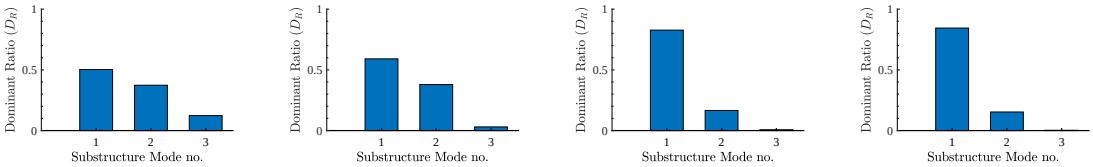			
	(a) Horizontal dominance ratio			
2	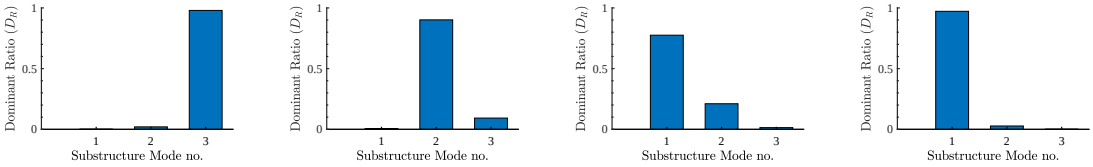			
	(b) Vertical dominance ratio			
3	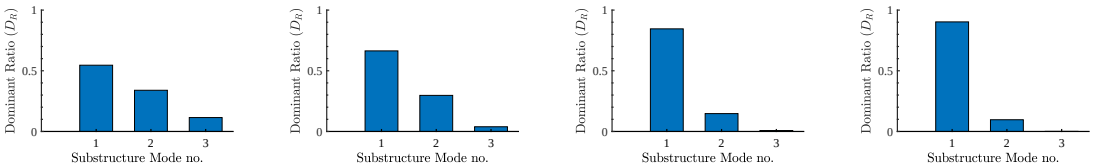			
	(a) Horizontal dominance ratio			
3	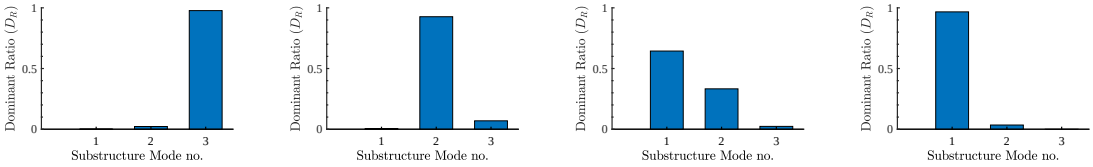			
	(b) Vertical dominance ratio			

Figure 3-24: $L-100$ models: Dominance ratio of each substructure mode at Node set-1

DL	$\alpha = 1/36$	$\alpha = 1/6$	$\alpha = 1$	$\alpha = 6$
1	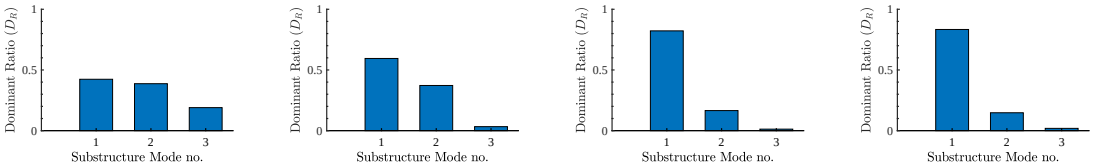			
	(a) Horizontal dominance ratio			
1	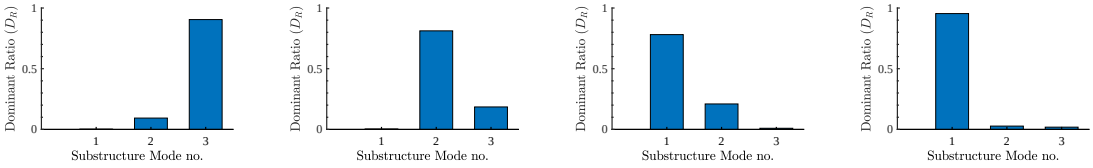			
	(b) Vertical dominance ratio			
2	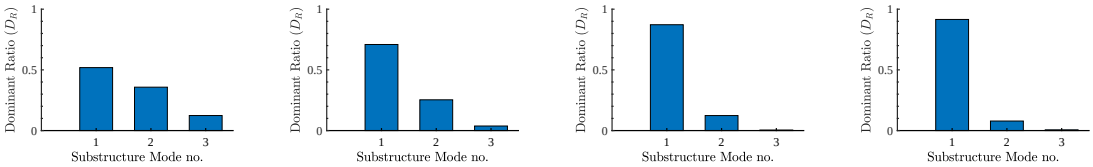			
	(a) Horizontal dominance ratio			
2	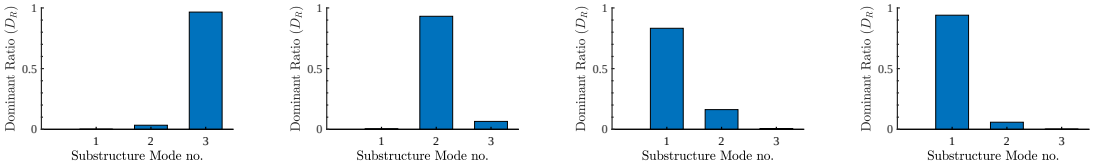			
	(b) Vertical dominance ratio			
3	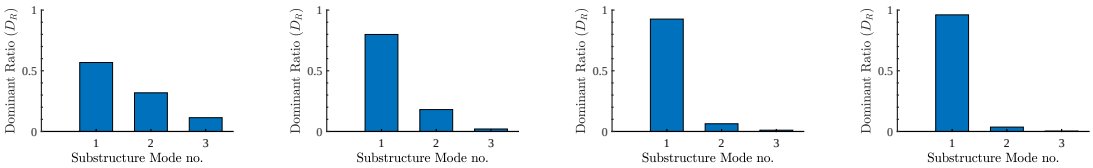			
	(a) Horizontal dominance ratio			
3	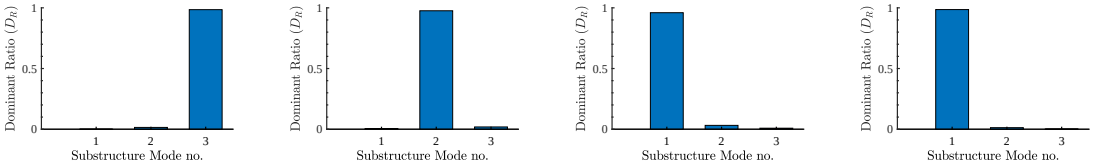			
	(b) Vertical dominance ratio			

Figure 3-25: $L-150$ models: Dominance ratio of each substructure mode at Node set-1

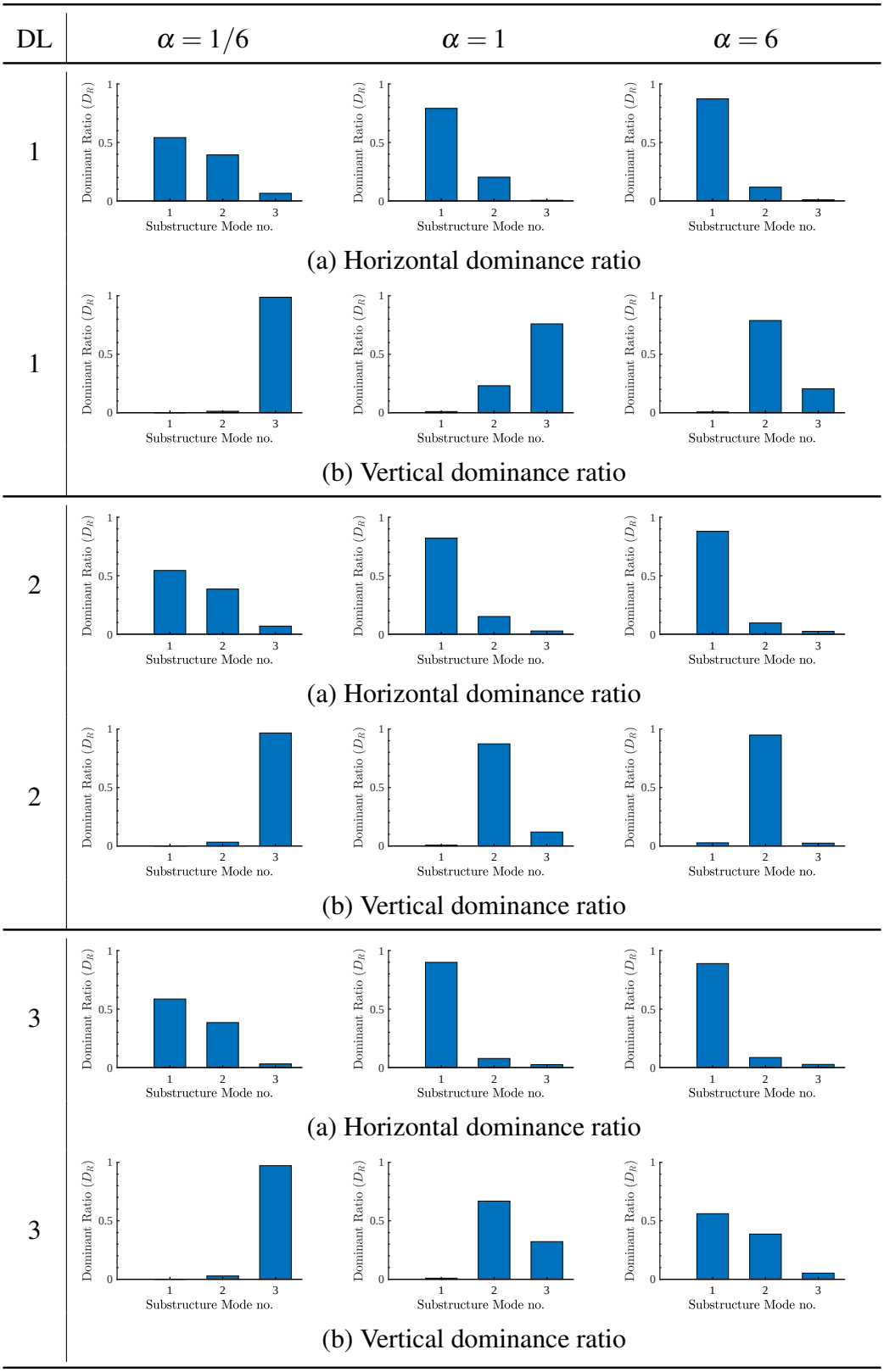

Figure 3-26: $L-60$ models: Dominance ratio of each substructure mode at Node set-2

DL	$\alpha = 1/36$	$\alpha = 1/6$	$\alpha = 1$	$\alpha = 6$
1	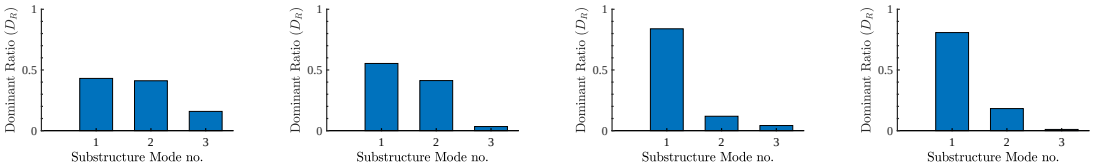			
	(a) Horizontal dominance ratio			
1	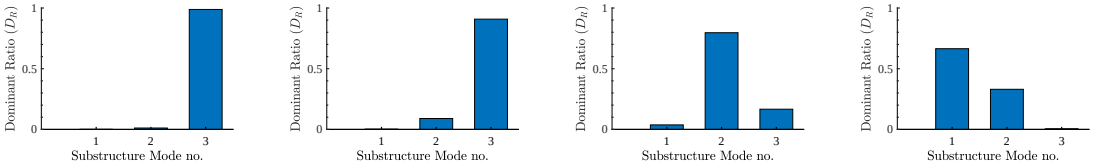			
	(b) Vertical dominance ratio			
2	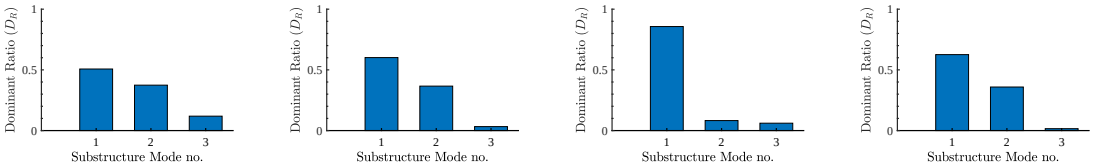			
	(a) Horizontal dominance ratio			
2	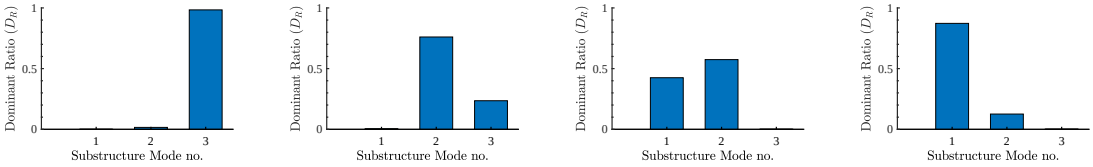			
	(b) Vertical dominance ratio			
3	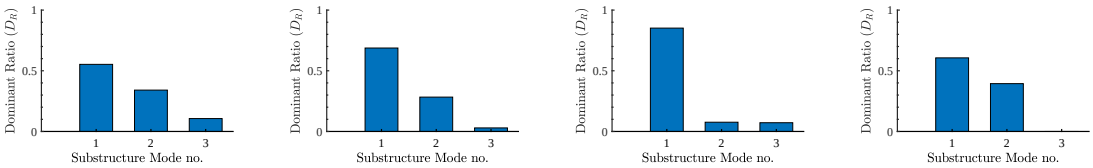			
	(a) Horizontal dominance ratio			
3	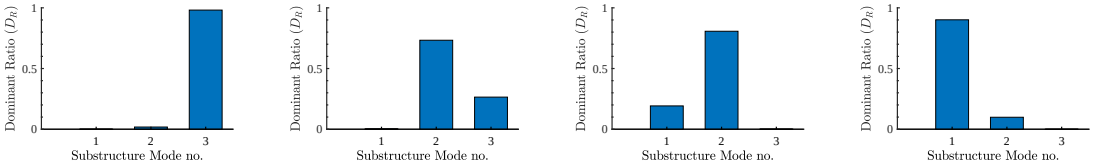			
	(b) Vertical dominance ratio			

Figure 3-27: $L-100$ models: Dominance ratio of each substructure mode at Node set-2

DL	$\alpha = 1/36$	$\alpha = 1/6$	$\alpha = 1$	$\alpha = 6$
1	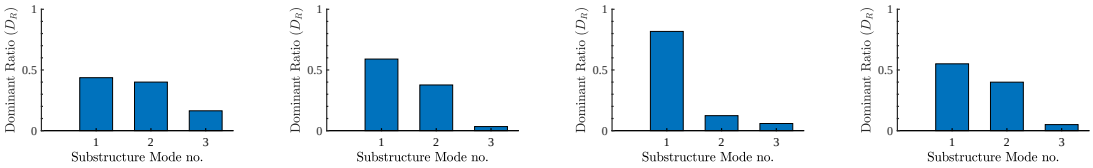			
	(a) Horizontal dominance ratio			
1	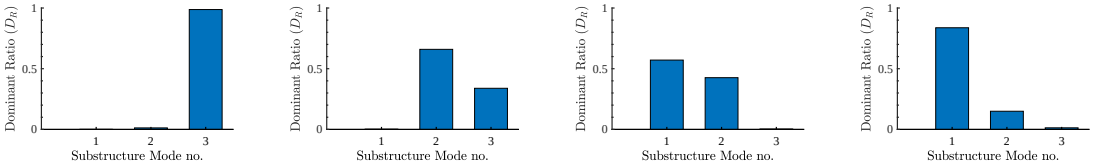			
	(b) Vertical dominance ratio			
2	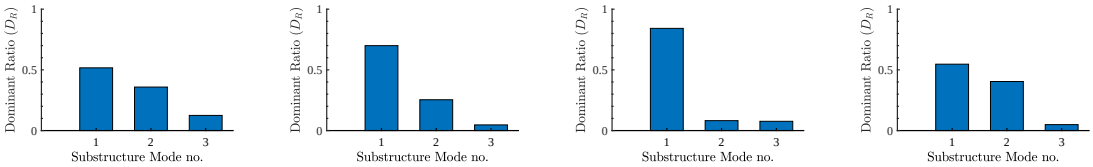			
	(a) Horizontal dominance ratio			
2	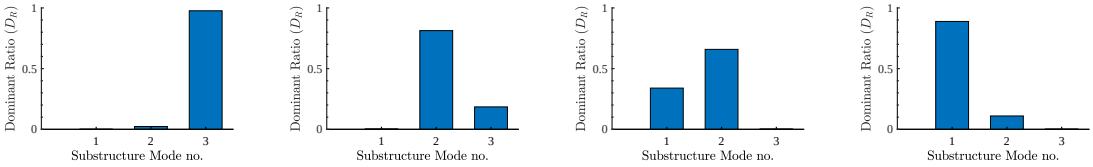			
	(b) Vertical dominance ratio			
3	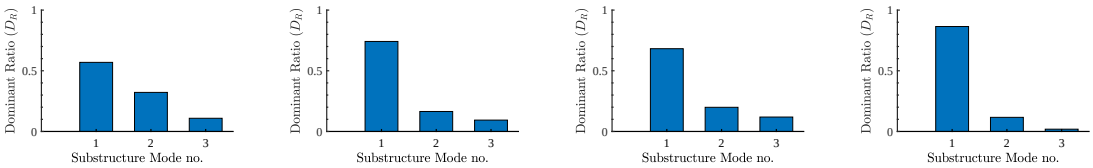			
	(a) Horizontal dominance ratio			
3	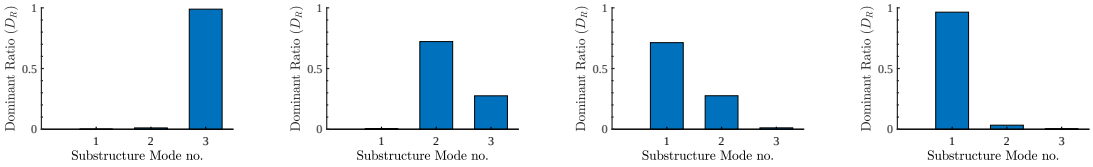			
	(b) Vertical dominance ratio			

Figure 3-28: $L-150$ models: Dominance ratio of each substructure mode at Node set-2

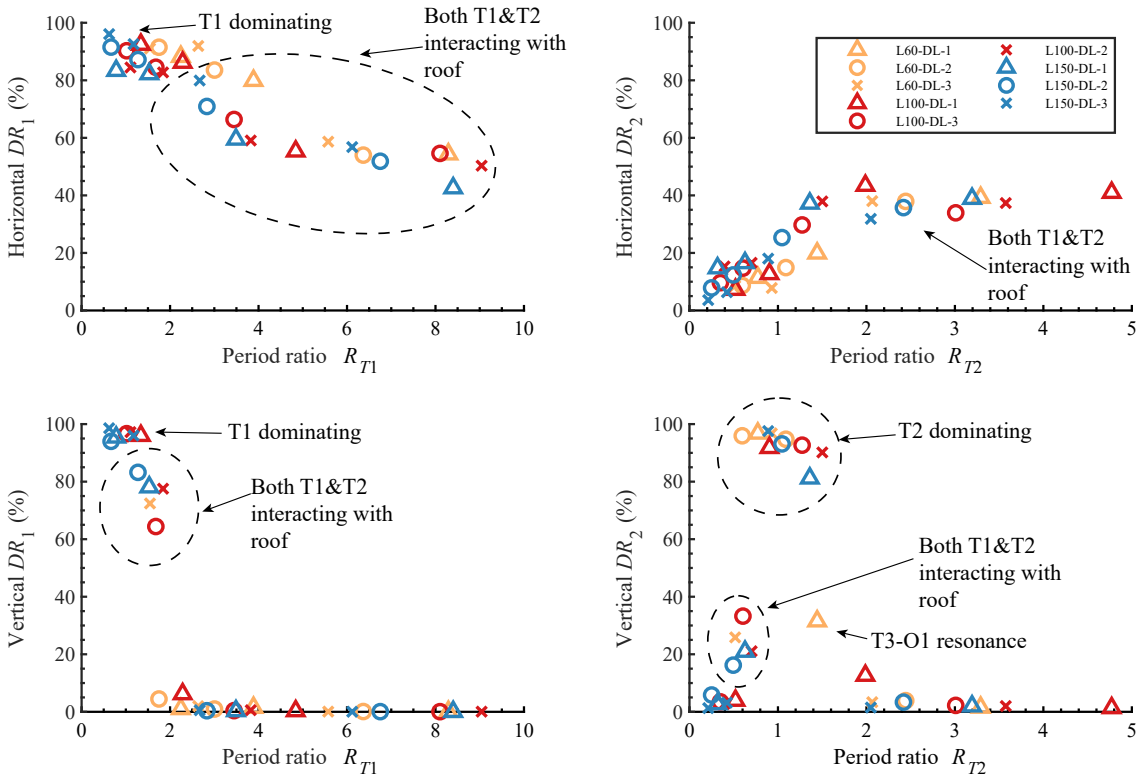

Figure 3-29: Dominance response ratios as a function of the period ratios

The dominance ratios for the Node set-1 are further summarised and plotted as a function of the period ratios in Figure 3-29. The horizontal dominance ratios were evenly divided between the T1 and T2 modes for longer period substructures, while the T1-roof interaction dominated for stiff substructures with $R_{T1} < 2$, with a horizontal T1 dominance ratio of $DR_1 > 80\%$. Furthermore, the vertical T1 dominance ratio DR_1 peaked at almost 100% for stiff substructures with $R_{T1} < 1$ such that the T1-roof interactions governed, but reduced for cases with $1 < R_{T1} < 2$ due to the increasing contribution of the T2-roof interactions and finally became negligible for flexible substructures with $R_{T1} >> 2$, as the substructure period was too long for significant interaction. Similarly, the vertical T2 dominance ratio DR_2 peaked at almost 100% for $R_{T2} \approx 1$ and became negligible for longer substructure periods with $R_{T2} >> 2$. This suggests that the vertical response contributions are more sensitive to the period ratios for multistorey structures and the vertical roof response is primarily a result of the T1-roof and T2-roof interactions for all but the most flexible multistorey substructures ($R_{T1} >> 2$). For flexible substructures,

the vertical T2 dominance ratio occasionally dropped due to resonance of higher substructure modes (e.g. T3) with the roof O1 mode. To summarise, the peak horizontal response is always a combination of the T1-roof and T2-roof interactions, while the peak vertical response is primarily governed by the T1-roof interaction for extremely stiff structures, followed by a combination of the T1-roof and T2-roof interactions for moderately stiff substructures and negligible interaction for flexible substructures.

3.6 Roof amplification in multistorey substructures

Before quantifying the T2-roof interactions in Chapter-4, the following section reviews the previously proposed amplification factors for T1-roof interactions.

3.6.1 Substructure T1 mode amplification factor

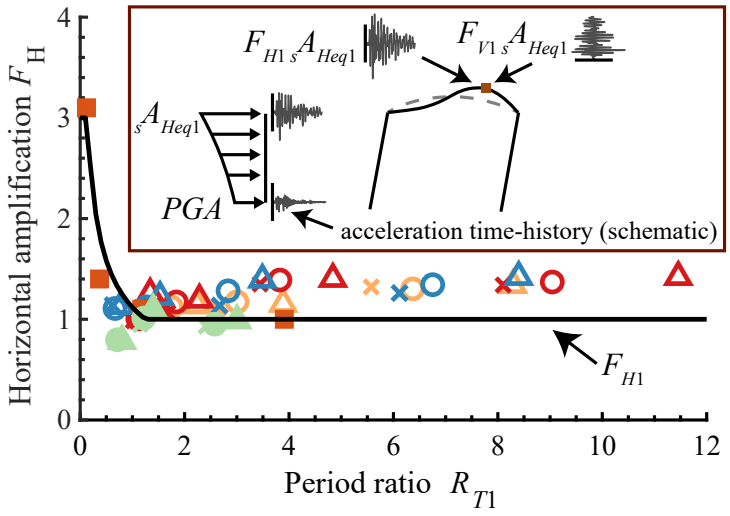

(a) Horizontal amplification factors

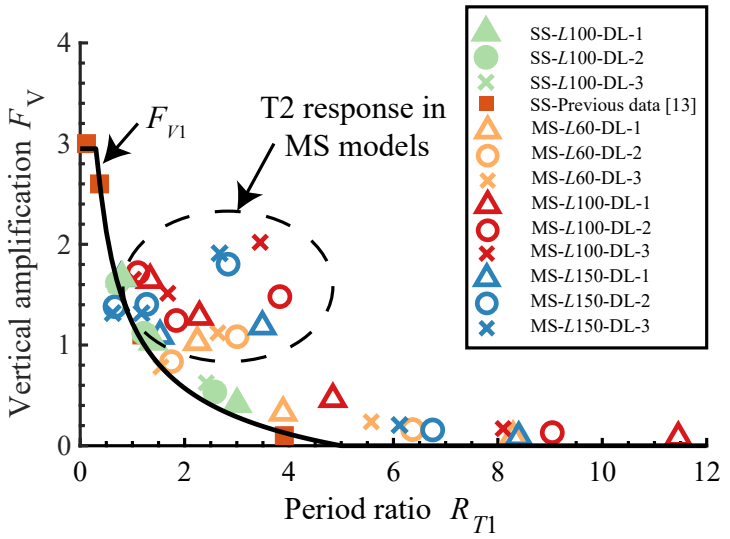

(b) Vertical amplification factors

Figure 3-30: *L*100 single-storey(SS) and multistorey(MS) models' response compared to the previous proposal

$$F_H = \frac{{}_cA_{H\max}}{{}_sA_{Heq1}}, \quad F_V = \frac{{}_cA_{V\max}}{{}_sA_{Heq1}} \tag{3.12}$$

where,

$${}_sA_{Heqi} = {}_s\beta_{is} S_{ais} \phi_i \tag{3.13}$$

The T1-roof interactions are characterised by the amplification factors F_{H1} and F_{V1} [1] given by Equations 1.13-1.14 in Chapter 1. To investigate the effect of the T2 modes on the overall amplification of the roof, the previously proposed amplification factors were compared with the overall amplification defined in Equations 3.12 obtained using the peak response ${}_sA_{Heq1}$ of the first mode T1 calculated using Equation 3.13 and Equation 3.5, and plotted both against the ratios of the period T1 in Figure 3-30. Although the amplification of single-storey models (labelled as 'SS') agrees well with the previous proposal (Figure 3-30), the multistorey (labelled as 'MS') models exhibit significantly higher overall amplification factors, especially in the vertical direction for $R_{T1} > 1.5$. This excess response may be attributed to the amplification arising from the substructure T2 mode, which is close to the predominant modes of the roof in this region (Figure 3-29). This reiterates the need to characterise the T2-roof interactions and incorporate them in the amplification factor for multistorey substructures.

3.7 Conclusions

1. The response of 60m, 100m and 150m double-layer roof models were investigated and was found to be governed by the three dominant asymmetric modes: the O1, the O2.5 and the O2 mode. The O2.5 has the largest mass participation for roof models while the fundamental mode is the O1 mode. Therefore, the roof's response envelope is a combination of all the three modes and depends on the location of the three modes on the acceleration spectrum. The roof response envelope was found to be dominated by the O2.5 mode for the longer span models (R100 and R150) and by the O1 mode for the shorter medium span models (R60).

2. For domed roofs with single-storey substructures, the peak roof response may be explained from the interaction of a sequential subset of the dominant roof modes with the substructure mode.

3. In the case of single-storey substructures, the horizontal and vertical dominance ratios were evenly divided between the O1, O2 and O2.5 modes for stiff shorter periods ($R_{T1} < 1$), with the dominance for O1+T1 modes peaking at almost 100% for $R_{T1} \approx 1$ and the O1+T1 mode continued to dominate the response of flexible substructures ($1 < R_{T1} < 2$) before converging into the sway mode for even flexible substructures ($R_{T1} > 2$) as the roof-substructure interaction becomes negligible for longer period substructures.

4. When the fundamental mode of the substructure resonates with the fundamental O1 mode of the roof, additional vertical and horizontal amplification was observed for all models when the substructure is heavy ($R_M > 2$). The modified previously proposed amplification factors (F'_{H1} and F'_{V1}) account for this additional amplification although the proposed curves overestimate the actual amplification for $R_{T1} < 1$. This was found to be primarily due to the effect of O1-T1 mode cancelling some of the resonance amplification from O1+T1 mode.

5. For roofs with multistorey substructures, the dominant modes were found to depend on the proximity of the dominant substructure and roof mode periods, with the

substructure T1 and T2 modes typically combining with the nearest roof mode. The vertical response of flexible multistorey substructures (α=1/6 and α=1/36) were governed by the roof O1 mode interacting with the closest substructure mode, while the higher roof modes remained unexcited. Stiffer multistorey substructures (α=1 and α=6) with the T1 and T2 modes close to the roof O1 mode exhibit complex roof-substructure interaction, with significant excitation of the O1, O2, O2.5 and I roof modes.

6. The relative contributions of the substructure T1 and T2 modes to the combined acceleration response were investigated using a dominance response ratio, which includes both the spectral acceleration and mass participation effects. Although the dominance ratio was found to be sensitive to the critical node of computation, the influence of T2 mode on the vertical acceleration response was found to peak when period ratio $R_{T2} \approx 1$ as T2 dominance ratio DR_2 peaked at almost 100% and became negligible for longer substructure periods with $R_{T2} >> 2$. The contribution to horizontal response was investigated using the horizontal dominance ratios which were more evenly divided between the T1 and T2 modes for longer period substructures, while the T1-roof interaction dominated for stiff substructures with $R_{T1} < 2$, achieving a horizontal T1 dominance ratio of $DR_1 > 80\%$.

7. Single-storey substructures and first-mode dominated substructures (with mass participation from T1 mode of over 90%) may obtain the peak roof response solely from the first substructure mode (the current IASS/AIJ method), but neglecting higher substructure modes underestimated the peak horizontal and vertical accelerations for all the multistorey substructures with a significant T2 mode ($\alpha < 6$ or $R_{T1} > 1.5$).

References

[1] T. Takeuchi, T. Ogawa, and T. Kumagai, "Seismic response evaluation of lattice shell roofs using amplification factors," *Journal of the IASS*, vol. 48, pp. 197–210, 2007.

[2] M. King, W. Whitby, and G. Hanshaw, "Design of the Singapore Sports Hub Roof with high strength niobium steel," in *IABSE Symposium Report*, International Association for Bridge and Structural Engineering, vol. 101, 2013, pp. 1–8.

[3] T. Takeuchi, T. Ogawa, T. Kumagai, A. Nakama, and E. Sato, "Applicability of response evaluation method for lattice domes with substructures," *Journal of structural engineering. B*, no. 52, pp. 53–61, Mar. 2006, ISSN: 09108033.

[4] B. Giltner and A. Kassimali, "Equivalent beam method for trusses," *Practice Periodical on Structural Design and Construction*, vol. 5, no. 2, pp. 70–77, 2000.

[5] *Guide to Earthquake Response Evaluation of Metal Roof Spatial Structures*. Working Group 8,International Association for Shell and Spatial Structures (IASS), 2019.

[6] D. Rutten, *Grasshopper3d*, 2015.

[7] *Analysis reference manual for SAP2000, ETABS, SAFE and CSIBridge*. Computers and Structures, Inc., Berkeley, CA, USA, 2015.

[8] E. L. Wilson, *Three-dimensional static and dynamic analysis of structures*. Computers and Structures, 2002.

[9] K.-J. Bathe and E. L. Wilson, "Numerical methods in finite element analysis," 1976.

[10] *The Building Standard Law of Japan on CD-ROM*. The Building Center of Japan, 2016.

[11] T. Becker, S. Furukawa, S. Mahin, and M. Nakashima, "Comparison of us and japanese codes and practices for seismically isolated buildings," in *Structures Congress 2010*, 2010, pp. 2330–2338.

[12] T. Takeuchi and A. Wada, *Buckling-restrained braces and applications*. Japan Society of Seismic Isolation, 2017.

[13] D. Nair, Y. Terazawa, B. Sitler, and T. Takeuchi, "Seismic response of long-span domes supported by multi-storey substructures," *Journal of the IASS*, vol. 61, pp. 140–157, 2020.

[14] Y. Terazawa, D. Nair, K. Ichihashi, and T. Takeuchi, "Equivalent static seismic load for middle to large span latticed domes considering roof antisymmetric mode amplified by substructure second mode," *Journal of Structural and Construction Engineering (in Japanese)*, vol. 87, no. 792, pp. 194–204, 2022. DOI: 10.3130/aijs.87.194.

[15] T. Takeuchi, T. Ogawa, M. Nakagawa, and T. Kumagai, "Response evaluation of medium-span lattice domes with substructures using response spectrum analysis," in *IASS 2004: Proceedings of the International Symposium "Shell and Spatial Structures from Models to Realization"*, Montpellier, France, Sep. 2004, pp. 205–206.

[16] *Minimum Design Loads for Buildings and Other Structures*. ASCE Standard–ASCE/SEI 7–16: American Society of Civil Engineers (ASCE), 2016.

[17] *Design of Structures for Earthquake Resistance*. British Standard–Eurocode 8: Part-1, 2005.

Chapter 4

Roof amplification factors for substructure higher mode

Contents

4.1 Introduction

The previous chapter explored the roof-substructure interaction in multistorey models and its effects on the overall roof amplification factors. The roof substructure interaction was concluded to be a combination of the T1-roof and T2-roof response. The T1-roof response has been quantified using T1 mode amplification factors [1]. This chapter extends this methodology and proposes amplification factors to quantify this additional response from the substructure higher mode (the T2 mode) combining with the roof modes. Horizontal and vertical amplification factors were proposed to estimate the roof response generated by higher multistorey substructure modes. The proposed amplification factors were then applied to obtain combined roof accelerations, which may be used to design acceleration-sensitive non-structural components.

A generalised static approach for developing equivalent static loads for domes with multistorey substructures was then proposed and validated for linear models with varying substructure stiffness using linear RSA (CQC combination), comparing against the member forces.

4.2 Substructure T2 mode amplification factor

The amplification factors F_{H2} and F_{V2} quantify the horizontal and vertical roof response from modes where the substructure exhibits the T2 mode. To define the relationship between amplification factors F_{H2} and F_{V2} and the substructure T2 mode's period ratio R_{T2} (obtained following Equation 3.1), the higher mode amplification factors were back-calculated by subtracting the fundamental substructure T1 mode response ($F_{H1s}A_{Heq1}$ and $F_{V1s}A_{Heq1}$) from the combined peak responses ($_cA_{H\max}$ and $_cA_{V\max}$) obtained from RSA. The CQC rule was adopted for the RSA and a sufficient number of modes were considered to achieve at least a 90% combined translational modal mass participation. To accurately capture the response only from the T2 mode, participation from higher substructure T3 or T4 modes were not considered. This excess response was then divided by the peak response of the substructure T2 mode ($_sA_{Heq2}$), as given by

Equations 4.1-4.2. The peak substructure responses ${}_sA_{Heq1}$ and ${}_sA_{Heq2}$ were calculated using the spectral accelerations S_{ai} and Equation 3.10.

The resulting horizontal and vertical amplification factors obtained from Equations 4.1-4.2 for all multistorey models ($L60, L100$ and $L150$ series) are plotted in Figure 4-1(a) and (b). The proposed substructure T2 mode amplification factors were then empirically formulated, as given in Equations 4.3-4.4 as a function of the period ratio R_{T2} to define the excess response. The horizontal response amplifications F_{H1} were sufficiently conservative to cover the mild amplification arising from the substructure T2 mode and so a constant amplification factor of $F_{H2} = 1$ is proposed. However, significant amplification is observed in the vertical direction, which may be interpreted as the F_{V1}-R_{T1} distribution (Figure 3-29(b)) shifted to the right. The plateau region of this curve is primarily attributed to the substructure T2 mode interacting with the roof O1 or O2 modes as the period ratio is close to 1. For extremely stiff substructures with $R_{T2} < 0.2$, F_{V1} tends to cover the mild T2-roof interactions, and so it is proposed to set the vertical amplification of the substructure T2 mode to zero in this region and gradually increase to a peak at $R_{T2} \approx 1$. This may also be related to the dominance ratios seen in Figure 3-28, where the vertical DR_2 reduces to zero and the vertical DR_1 almost reaches unity for $R_{T1} < 1$, indicating a dominant substructure T1 response. For a longer R_{T2}, F_{V2} gradually decreases to zero as the T2 mode and roof modes spread further apart, decreasing the T2 mode's interaction with the roof and consequently, the associated amplification.

$$F_{H2} = \frac{{}_cA_{H\max} - F_{H1}\,{}_sA_{Heq1}}{{}_sA_{Heq2}} \tag{4.1}$$

$$F_{V2} = \frac{{}_cA_{V\max} - F_{V1}\,{}_sA_{Heq1}}{{}_sA_{Heq2}} \tag{4.2}$$

$$F_{H2} = 1 \tag{4.3}$$

$$F_{V2} = \left\{ \begin{array}{cc} 0 & R_{T2} \le 1/5 \\ 6C_V\theta(R_{T2} - 1/5) & 1/5 < R_{T2} < 7/10 \\ 3C_V\theta & 7/10 \le R_{T2} \le 21/16 \\ \sqrt{5/(R_{T2}-1)} - 1)C_V\theta & R_{T2} > 21/16 \end{array} \right\} \tag{4.4}$$

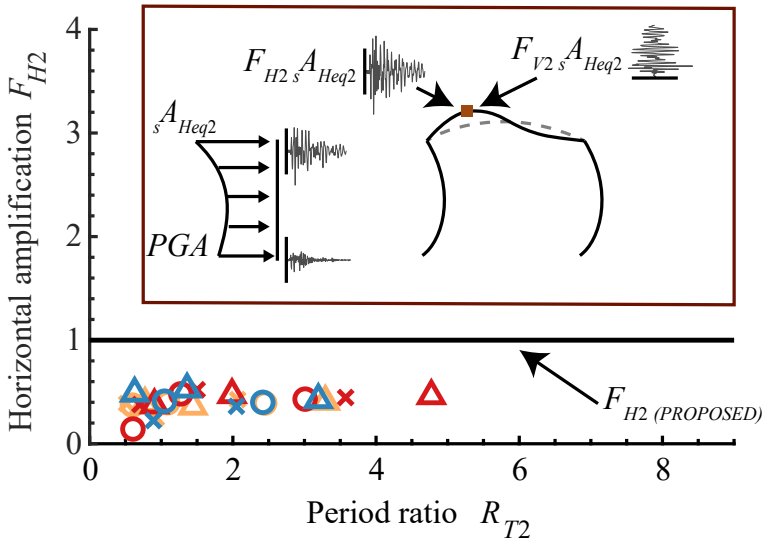

(a) Horizontal amplification factors

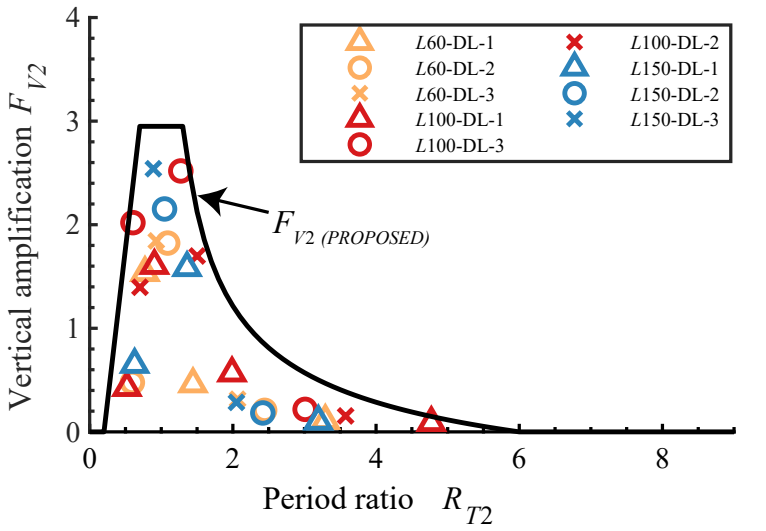

(b) Vertical amplification factors

Figure 4-1: Proposed amplification factors for substructure T2 mode

4.3 T2-O1 resonance in heavy substructures

Large-scale gymnasiums and auditoriums are typically designed with steel roofs and reinforced concrete substructures, which tend to be heavier than steel frames, resulting in larger substructure mass ratios R_M. Heavy substructures with $R_{T1} < 1.5$ produce significant resonant amplification between the T1 and O1 modes, increasing both the horizontal and vertical responses, as noted by Takeuchi et al. [1]. This has been accounted for by modifying the amplification factors to F'_{H1} and F'_{V1} when $R_{M1} > 2$, as given by Equations 4.5-4.6 as discussed in Section 1.3.5 [1].

$$F'_{H1} = \sqrt{{F_{H1}}^2 + \frac{1}{\left(1-{R_{T1}}^2\right)^2 + \left(1/R_{M1}\right)^{\theta}}} \tag{4.5}$$

$$F'_{V1} = \sqrt{{F_{V1}}^2 + \frac{1}{\left(1-{R_{T1}}^2\right)^2 + \left(1/R_{M1}\right)}} \tag{4.6}$$

Domes with multistorey substructures have even heavier substructures, which result in larger mass (typically $R_{M1} > 4$) and period ratios (typically $R_{T1} > 2$) than single-storey substructures. This implies that the substructure T1 and roof O1 modes are farther apart, reducing the potential for resonance with the substructure T1 mode. However, the substructure T2 mode is closer to the roof modes and the ratio R_{T2} may be close to 1, suggesting that the substructure T2 mode may be in resonance with the roof O1 mode. To investigate the T2-O1 resonance effects in structures with heavy substructures, three additional long-span ($L = 100$ or $L = 150$) models were constructed with the substructure floor loads increased to 20 (L100-DL-1-R_{M2}-6), 30 (L150-DL-1-R_{M2}-7) or 60kPa (L150-DL-1-R_{M2}-13), which resulted in mass ratios of about $R_{M1} = 23$, 25 and 49 for the substructure T1 modes, and $R_{M2} = 6$, 7 and 13 for the substructure T2 modes, respectively.

The back-calculated substructure T2 mode amplification factors from Equations 4.1-4.2 are compared to Equations 4.3-4.4 in Figure 4-2. For $R_{T2} \approx 1$, the proposed curves (Equations 4.3-4.4) are conservative enough to cover the mild T2-O1 resonance effects arising in the high R_{M2} models. Therefore, it was concluded that additional amplification for T2-O1 resonance is not required for domes with multistorey substructures and high

mass ratios.

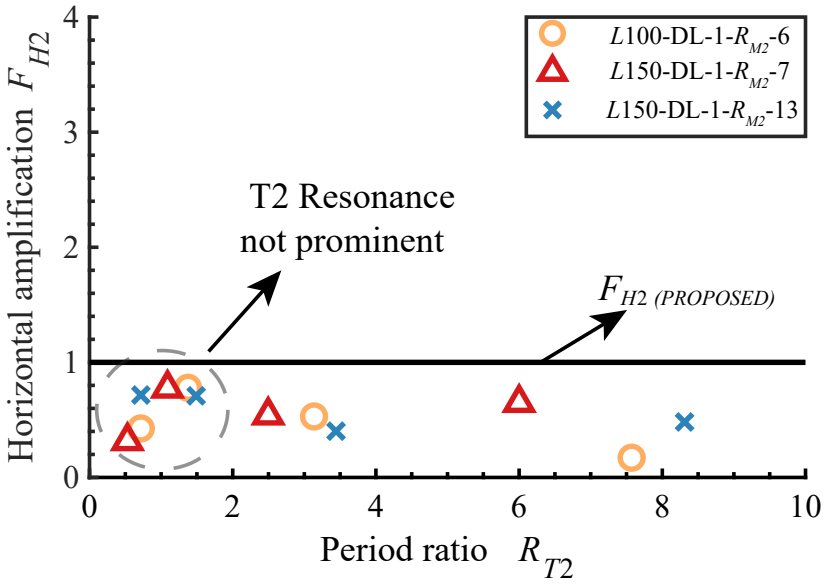

(a) Horizontal amplification factors

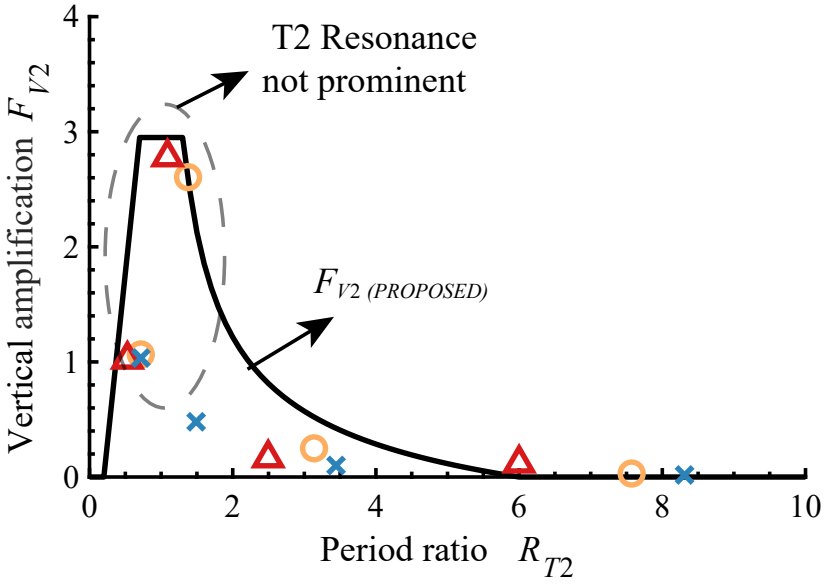

(b) Vertical amplification factors

Figure 4-2: Effect of high mass ratio R_{M2} on higher mode amplification

4.4 Proposed static approach: Equivalent static loads

This section summarises the proposed static design procedure (Figure 4-3) to obtain the peak roof accelerations and equivalent static forces using the proposed amplification factors in Section 4.1 for the preliminary seismic design of roofs with multistorey substructures.

1. Perform eigenvalue analysis of the substructure model (or combined model) and roof model (Figures 3-1(a) and (b)) to obtain the substructure T1 and T2 modes and roof O1 mode. The cumulative mass participation (Γ_1 in Equation 3.2) from the first two substructure modes should be at least 90%. If the mass participation from the first substructure mode exceeds 90%, the effect of T2-roof interactions need not be considered (i.e. ${}_sA_{Heq2}$ may be taken as 0).

2. Calculate the peak accelerations (${}_sA_{Heqi}$) for the two substructure modes using Equation 3.10, where 'i' is the substructure mode number.

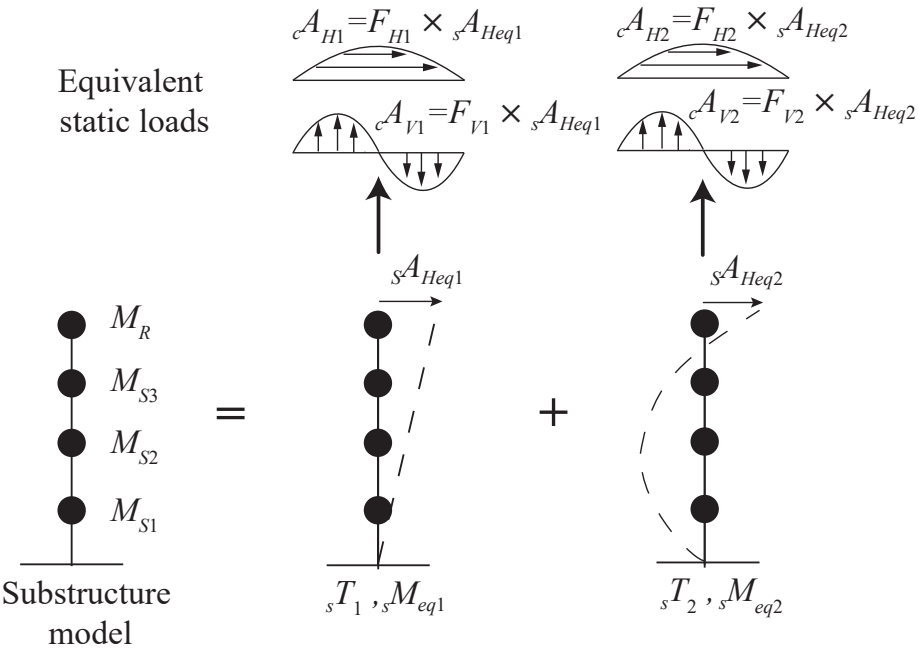

Figure 4-3: Simplified method to estimate static loads for domes

3. Calculate the period (R_{T1}, R_{T2}) and mass (R_{M1}, R_{M2}) ratios from Equation 3.1. Apply these ratios to compute the roof amplification factors F_{H1} (or F'_{H1} for $R_{M1} > 2$ and

$R_{T1} < 1.5$), F_{H2}, F_{V1} (or F'_{V1} for $R_{M1} > 2$ and $R_{T1} < 1.5$) and F_{V2} using Equations 1.13-1.14, 4.3-4.4 and 1.15-1.16.

4. Compute the roof horizontal (${}_cA_{Hi}$) and vertical (${}_cA_{Vi}$) according to the mode-specific distributions. The dominant roof O1 mode is adopted for the envelope, which has the distributions given by (Equations 4.7-4.8) [1], where x and y are the coordinates of roof nodes, the roof center is located at $\{x,y\} = \{0,0\}$ and L is the span of the dome.

$$ {}_cA_{Hi}(x,y) = {}_sA_{Heqi}\{1 + (F_{Hi} - 1)\cos\frac{\pi\sqrt{x^2+y^2}}{L}\} \tag{4.7} $$

$$ {}_cA_{Vi}(x,y) = {}_sA_{Heqi}F_{Vi}\frac{x}{\sqrt{x^2+y^2}}\sin\frac{2\pi\sqrt{x^2+y^2}}{L} \tag{4.8} $$

5. Combine the modal accelerations at each node using Equations 4.9-4.10 to obtain the combined horizontal and vertical response envelope. This study uses an absolute summation rule. The equivalent static horizontal and vertical seismic forces for each node may then be computed from the nodal mass m_k and the corresponding acceleration (horizontal ${}_cA_H(x,y)$ and vertical ${}_cA_V(x,y)$) at position (x,y) using Equations 4.11-4.12.

$$ {}_cA_H(x,y) = \sum_{i=1}^{2} |{}_cA_{Hi}(x,y)| \tag{4.9} $$

$$ {}_cA_V(x,y) = \sum_{i=1}^{2} |{}_cA_{Vi}(x,y)| \tag{4.10} $$

$$ f_H(x,y) = m_{kc}A_H(x,y) \tag{4.11} $$

$$ f_V(x,y) = m_{kc}A_V(x,y) \tag{4.12} $$

4.5 Accuracy of the proposed method

4.5.1 Comparison of peak acceleration response

The proposed method was applied to obtain the overall peak response for each model of the series *L*-60, *L*-100 and *L*-150. The detailed ridgeline roof accelerations for all the combined models are compared in Figures 4-4-4-6. The individual modal contributions from the response spectrum analyses (labelled 'RSA T1' and 'RSA T2') are also compared with the proposed equivalent static responses (labelled 'Proposed T1' and 'Proposed T2').

Consider the example of the *L*-100 series models in Figure 4-5. Models with flexible substructures (α=1/36) produced relatively small roof responses due to the long substructure periods. The flat horizontal response envelope indicates minimal amplification, while the vertical response is almost negligible. Thus, the horizontal acceleration input from the substructure is more significant in these cases. Note that the models with $R_{T2} > 2$ have fundamental periods of around 3s (Table 3.14), which is unusual for shorter or medium-height multistorey substructures but may occur for taller buildings supporting roofs at height. Models with slightly less flexible substructures (α=1/6) exhibited a horizontal and vertical roof response dominated by the T2 mode interaction. These are representative of yielded substructures with an elongated first mode T1 but a nearly elastic higher T2 mode. Models with stiffer substructures (α=1) generated larger horizontal and vertical responses combining the substructure T1 and T2 modes with the T1 mode generally dominating the horizontal response and the T2 mode or T1 mode (depending on the period ratios and location on the design spectrum) dominating the vertical response. In these two cases, the exclusion of the T2 mode will underestimate the response. As the substructure stiffness is further increased (α=6), the vertical response becomes much larger and the response is dominated by T1 mode, while retaining a modest contribution from the substructure T2 mode. The proposed method is thus in good agreement with the actual response over this full range of substructure stiffness.

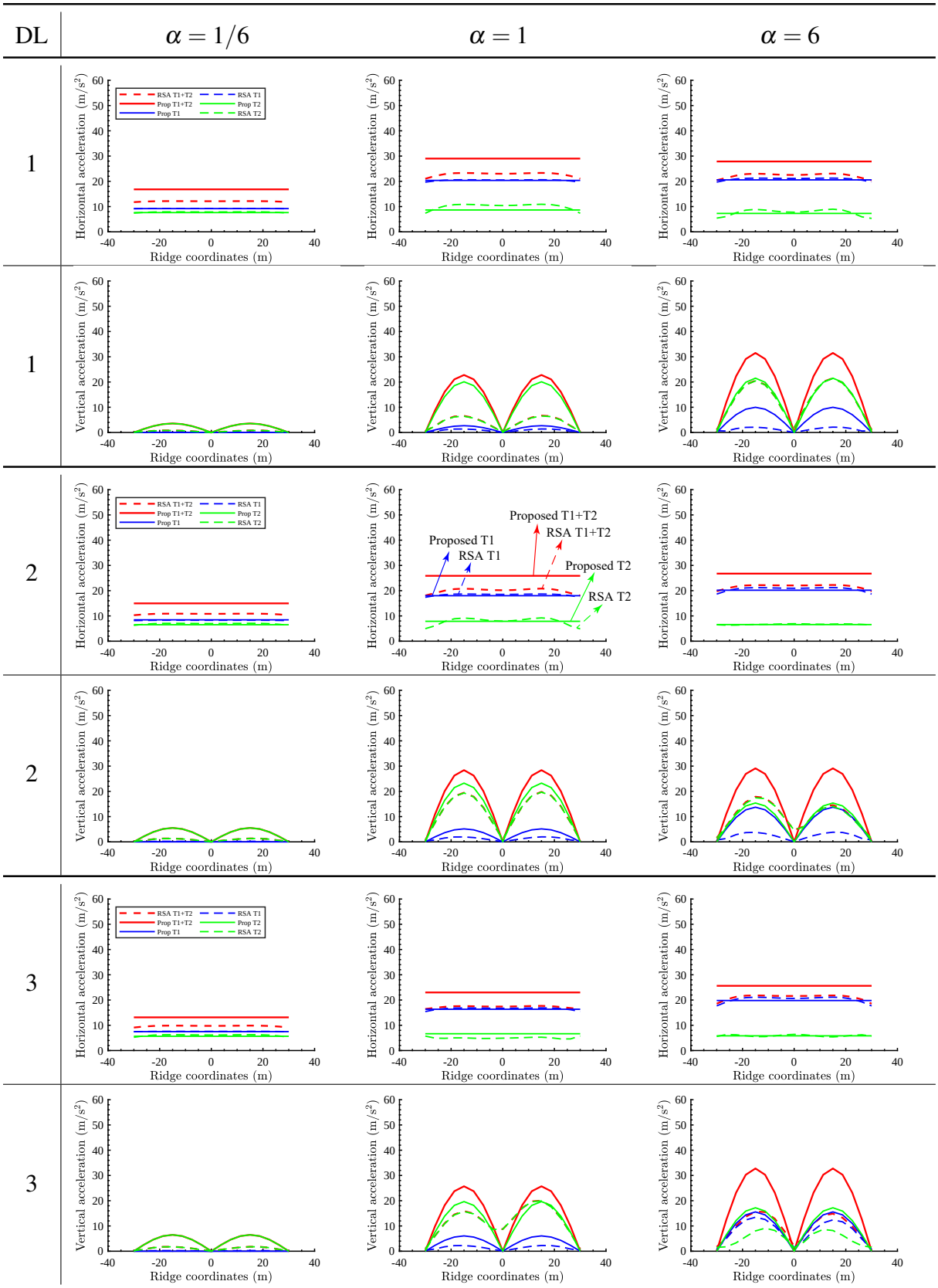

Figure 4-4: $L-60$ series: Comparison with proposed horizontal and vertical ridgeline accelerations

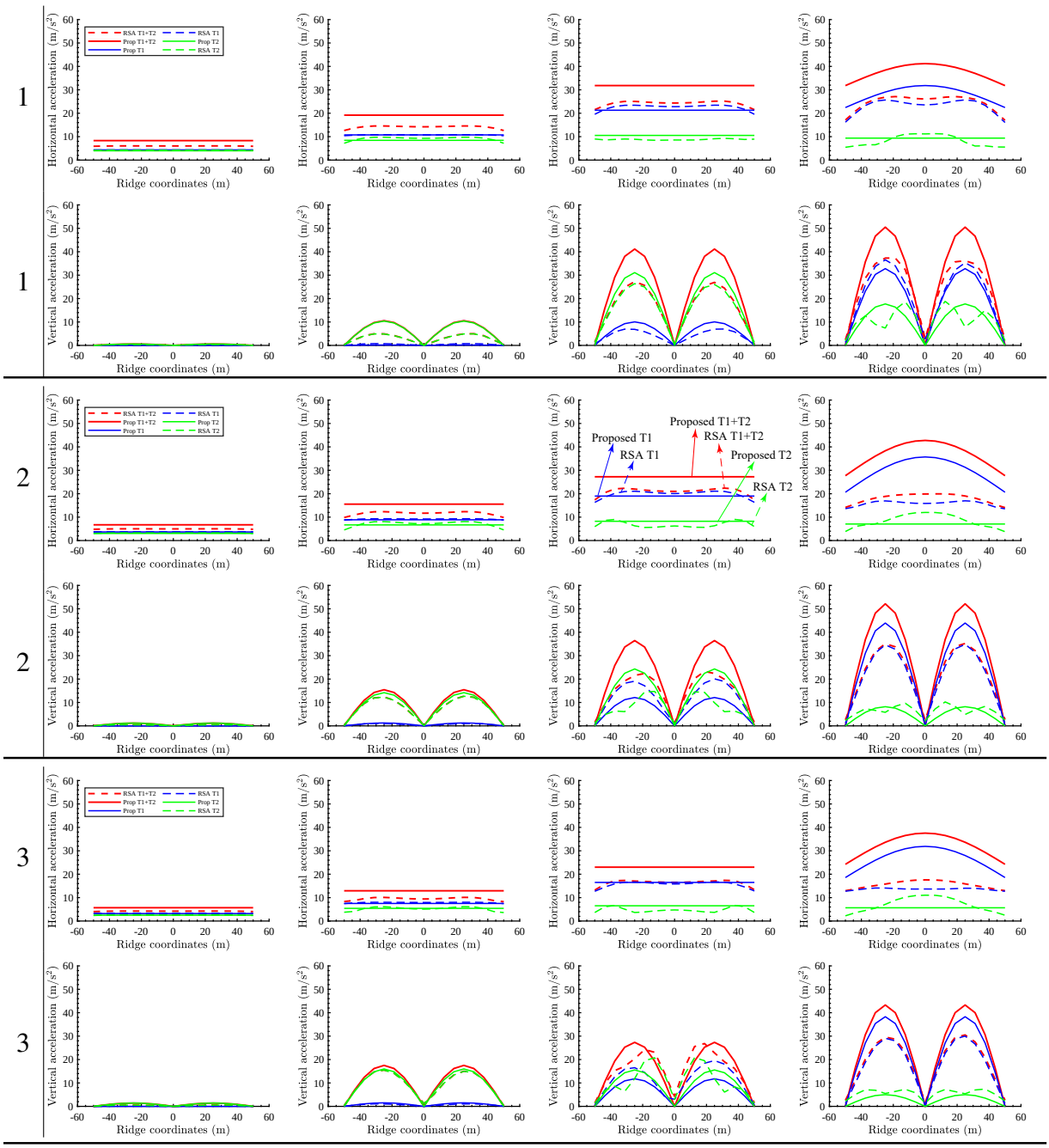

Figure 4-5: $L-100$ series: Comparison with proposed horizontal and vertical ridgeline accelerations

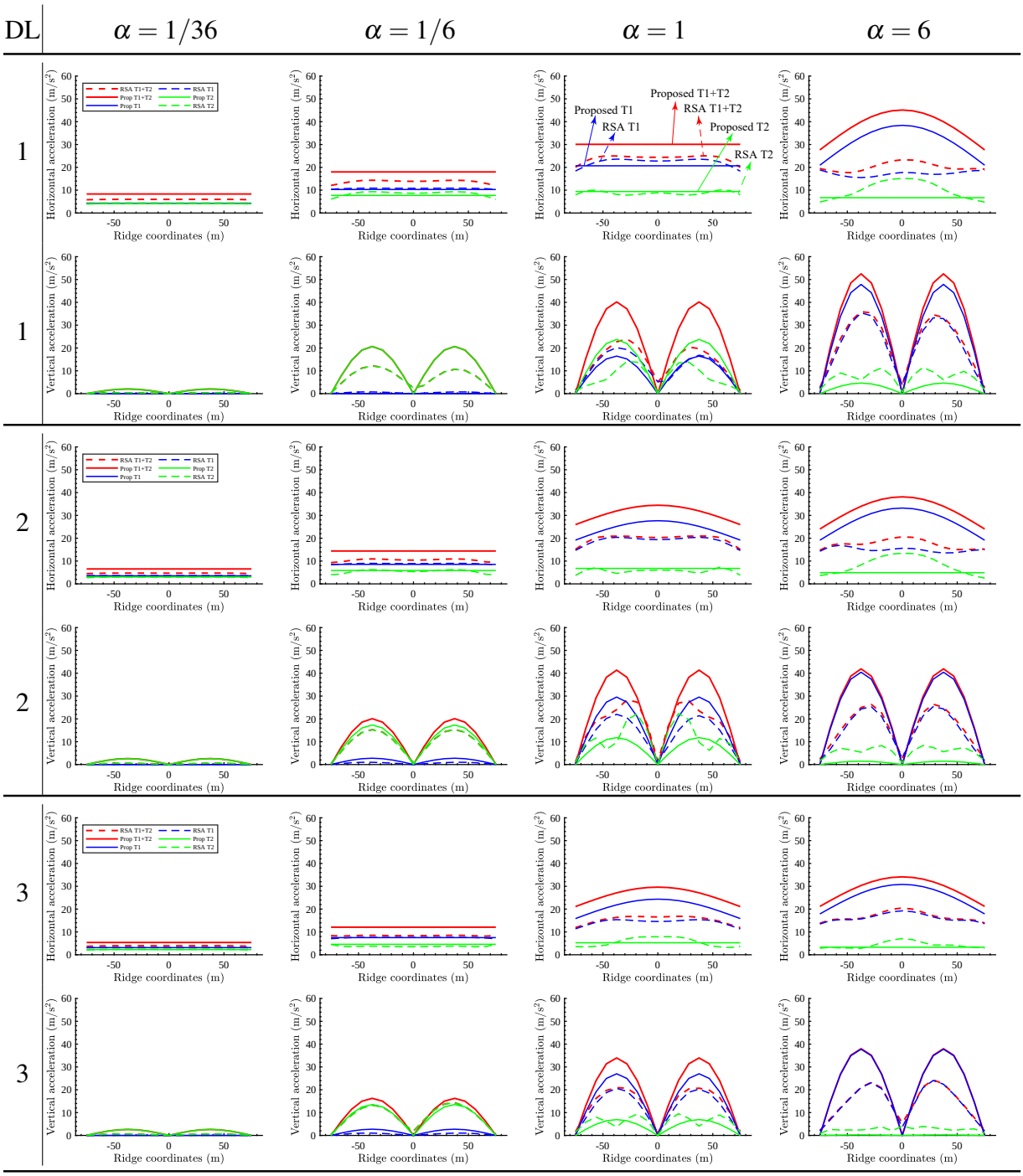

Figure 4-6: $L-150$ series: Comparison with proposed horizontal and vertical ridgeline accelerations

Contour maps of the acceleration distribution

The proposed acceleration distribution for the entire roof nodes are also compared with the response from RSA by plotting contour maps of the horizontal and vertical accelerations as shown in Figures 4-7-4-24. Consider the example of *L*-100-DL-1 series of models in Figures 4-13-4-14. Note that the contour maps for obtained RSA responses were externally plotted using the MATLAB Mathworks toolbox [2] function named 'scatteredInterpolant' which extrapolates contour surfaces from the actual scattered data set and therefore there is some noise along the radial edges and along the centre (x=0 lines) of the contours due to the interpolation and extrapolation of data and the inbuilt algorithm.

For most cases, the proposed horizontal accelerations are constant across the domed roof as the amplification factors F_{H1} and F_{H2} are both equal to 1. The RSA contours indicate some horizontal amplification that is centred along the quarter points on the ridgelines of the dome which indicates the dominance of roof O1 mode as the contour map resembles the roof O1 mode's horizontal mode shape (Figure 3-3). These horizontal amplifications further increase as the substructure stiffness increases to α=6 and the horizontal contour maps for α=6 varies with each model as the response in this range is a complex interaction of T1-roof and T2-roof modes. Even so, the response was found to be highest at the centre of the dome for all models with α=6. The blanket response envelope proposed covers these amplifications conservatively. On the other hand, the vertical contour maps for all models in all ranges of substructure stiffnesses were found to be mainly governed by the roof's O1 mode and therefore the contour map shapes observed are generally similar to the contour map shapes of the proposed vertical accelerations (which are obtained using the roof's O1 mode shape) with peaks centred at the quarter-points of the ridgeline, except for a few cases where the O2 mode dominates (as seen in *L*-100-DL-3 $\alpha = 1$ case in Figure 4-18 and the peaks in these cases shift towards the centre of the dome).

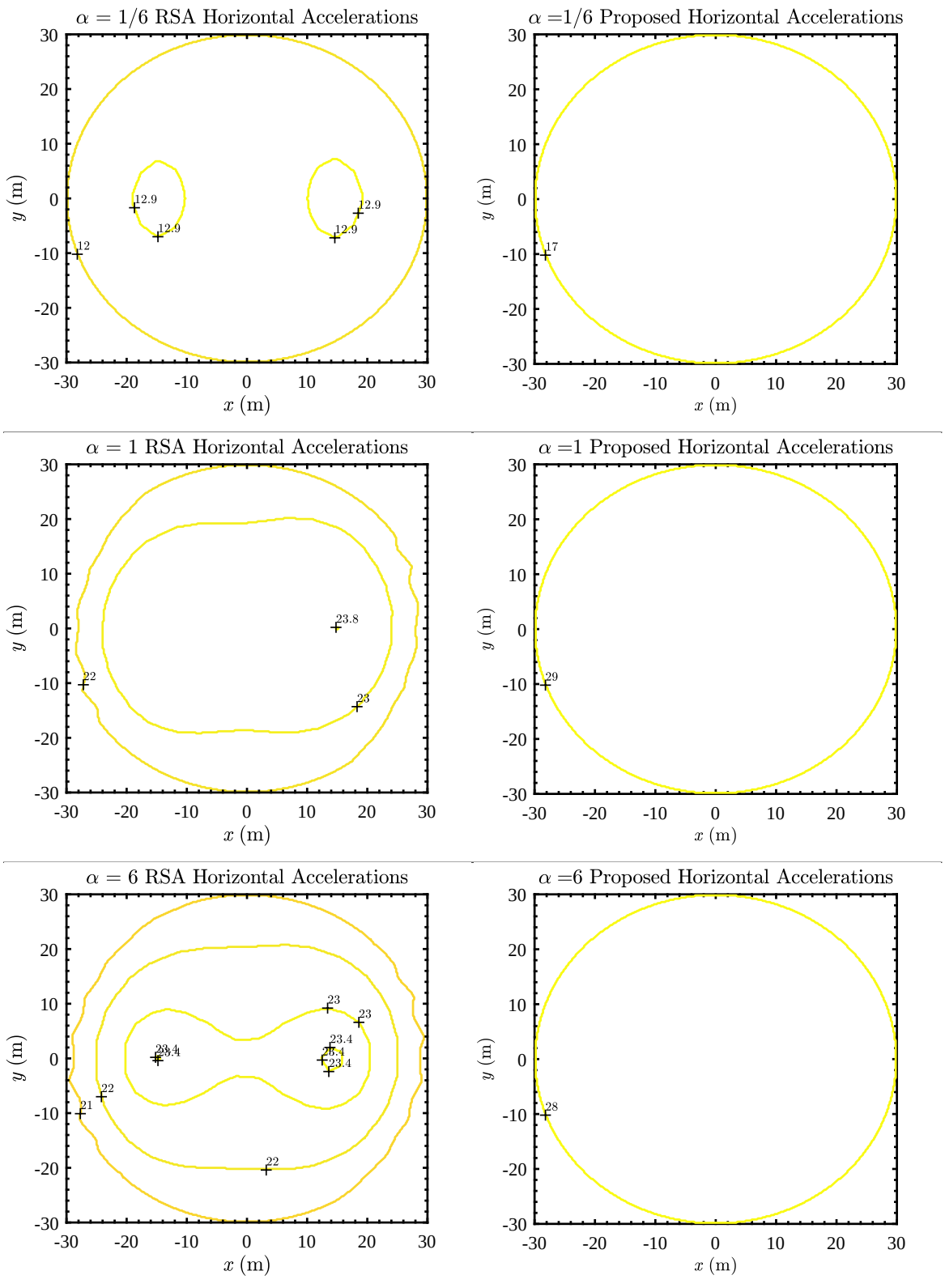

Figure 4-7: *L*-60-DL-1 model: Contour plots comparing the proposed horizontal accelerations (values in m/s^2)

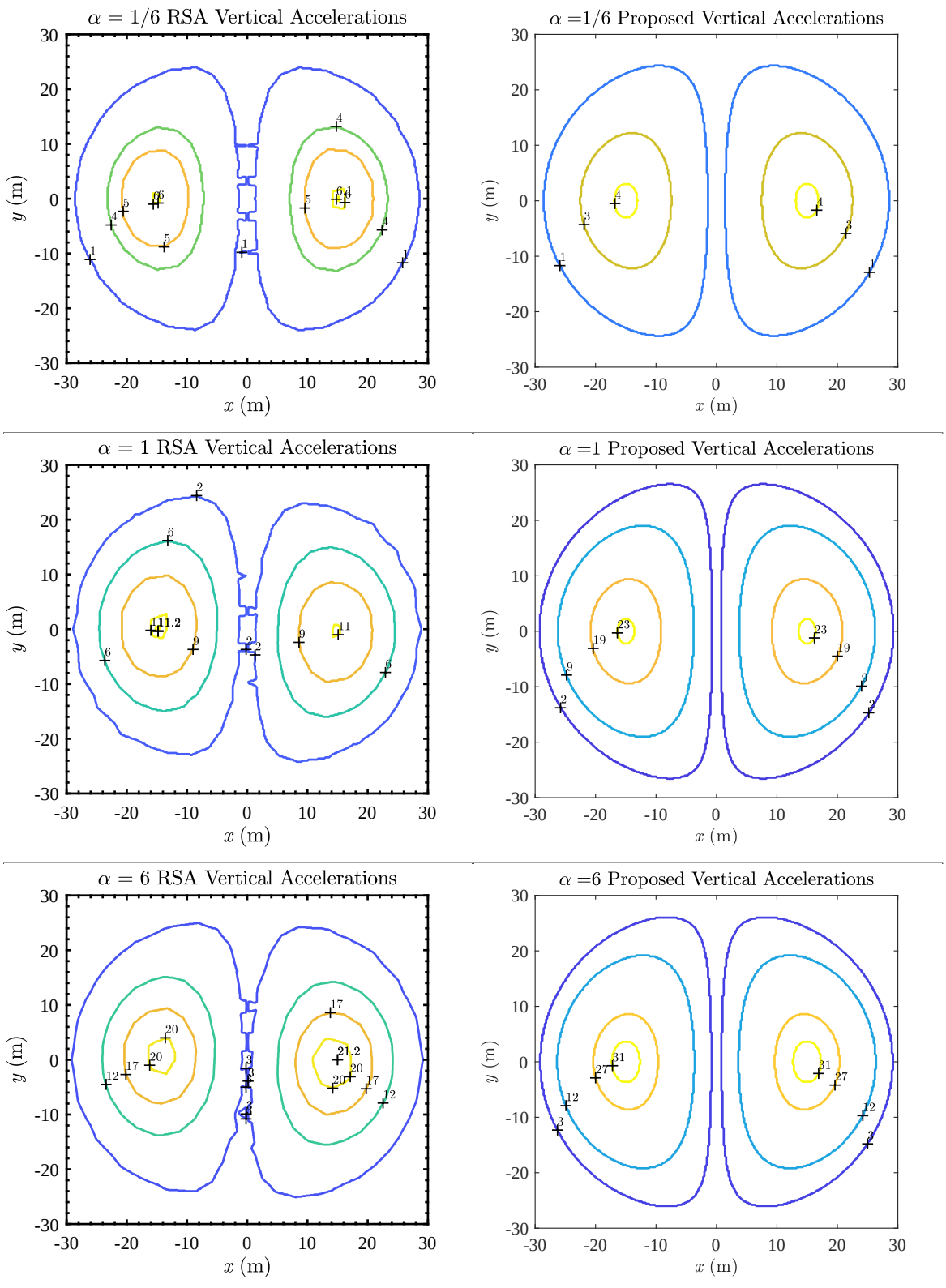

Figure 4-8: *L*-60-DL-1 model: Contour plots comparing the proposed vertical accelerations (values in m/s^2)

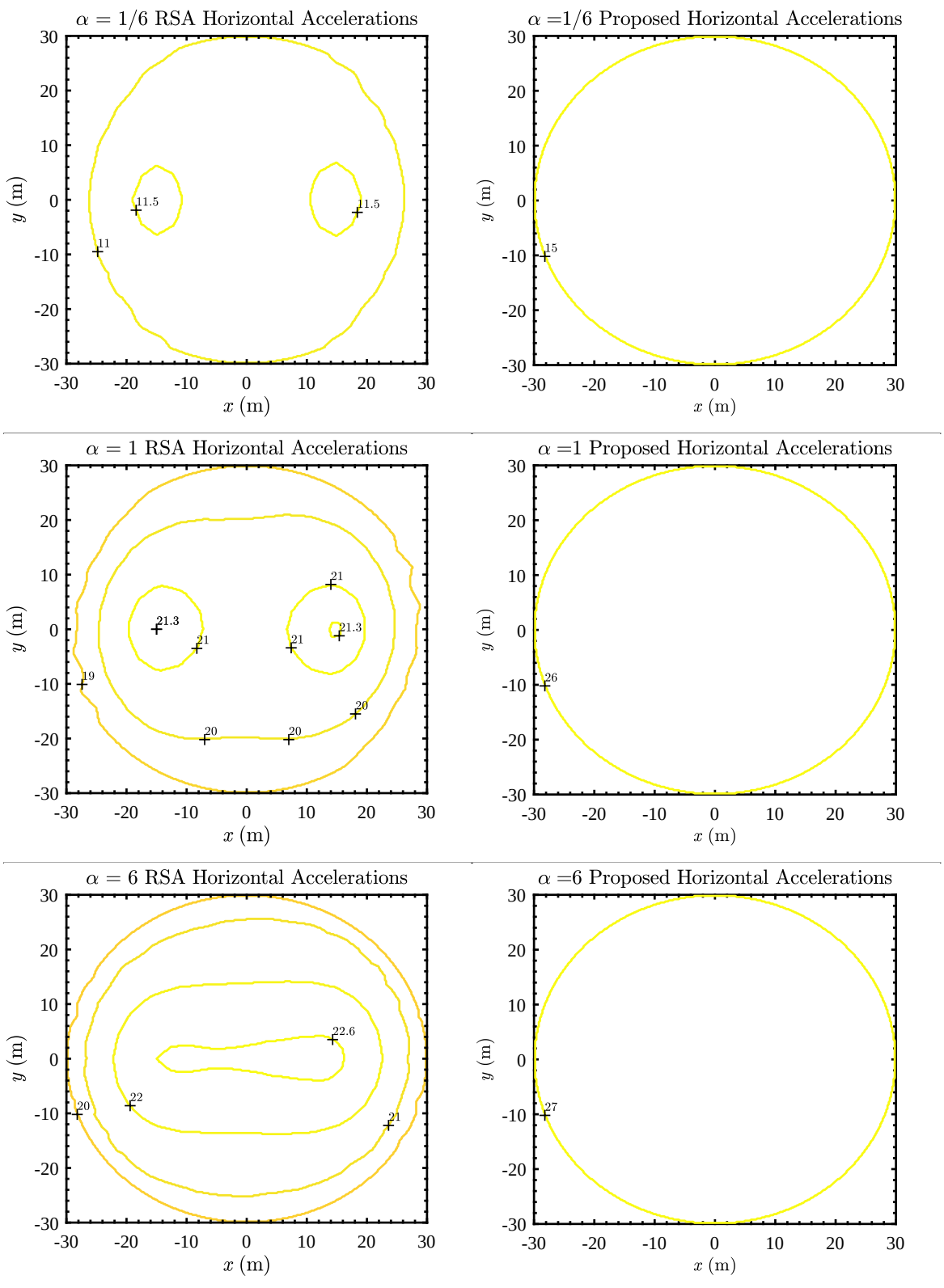

Figure 4-9: *L*-60-DL-2 model: Contour plots comparing the proposed horizontal accelerations (values in m/s^2)

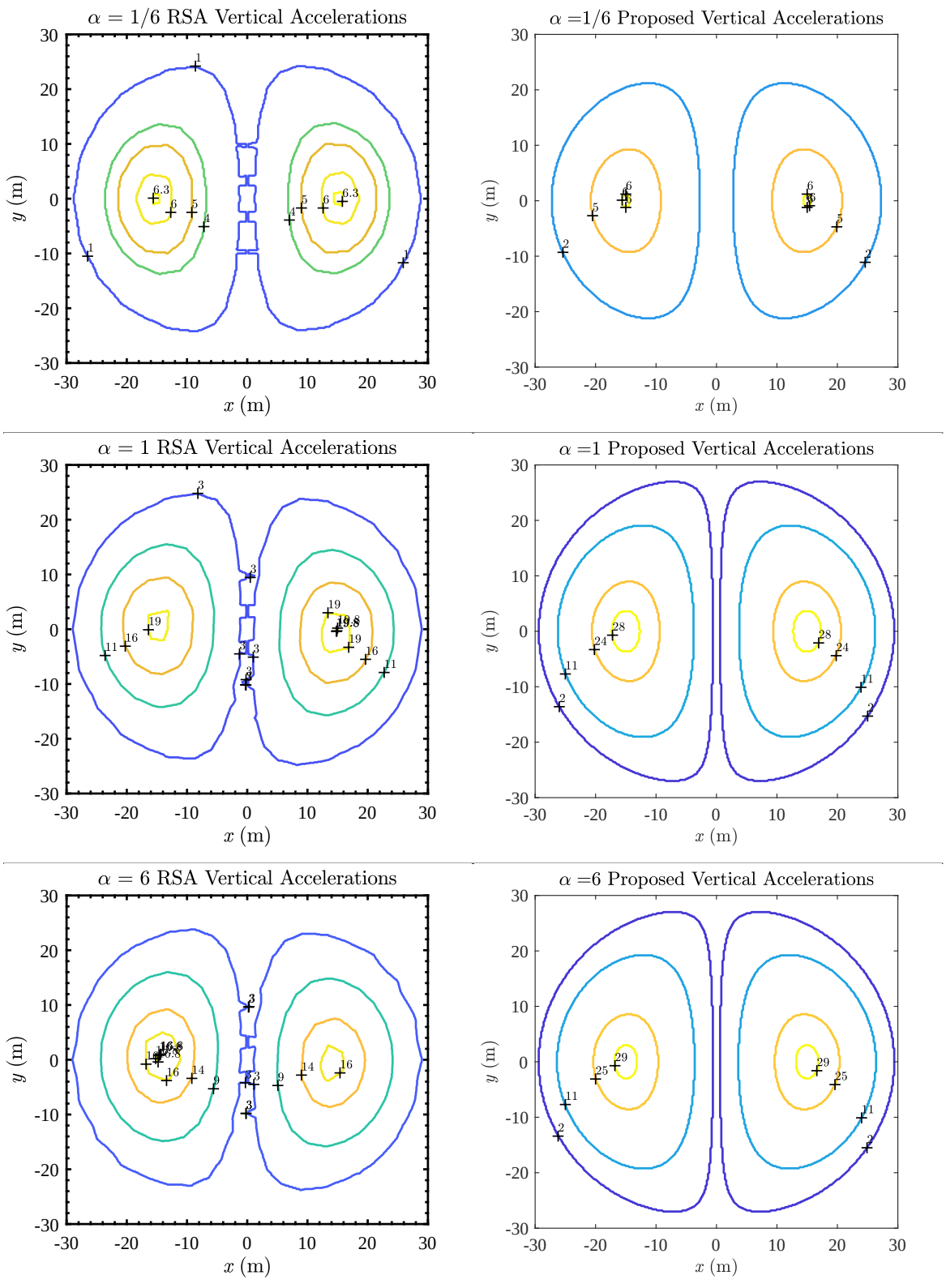

Figure 4-10: *L*-60-DL-2 model: Contour plots comparing the proposed vertical accelerations (values in m/s^2)

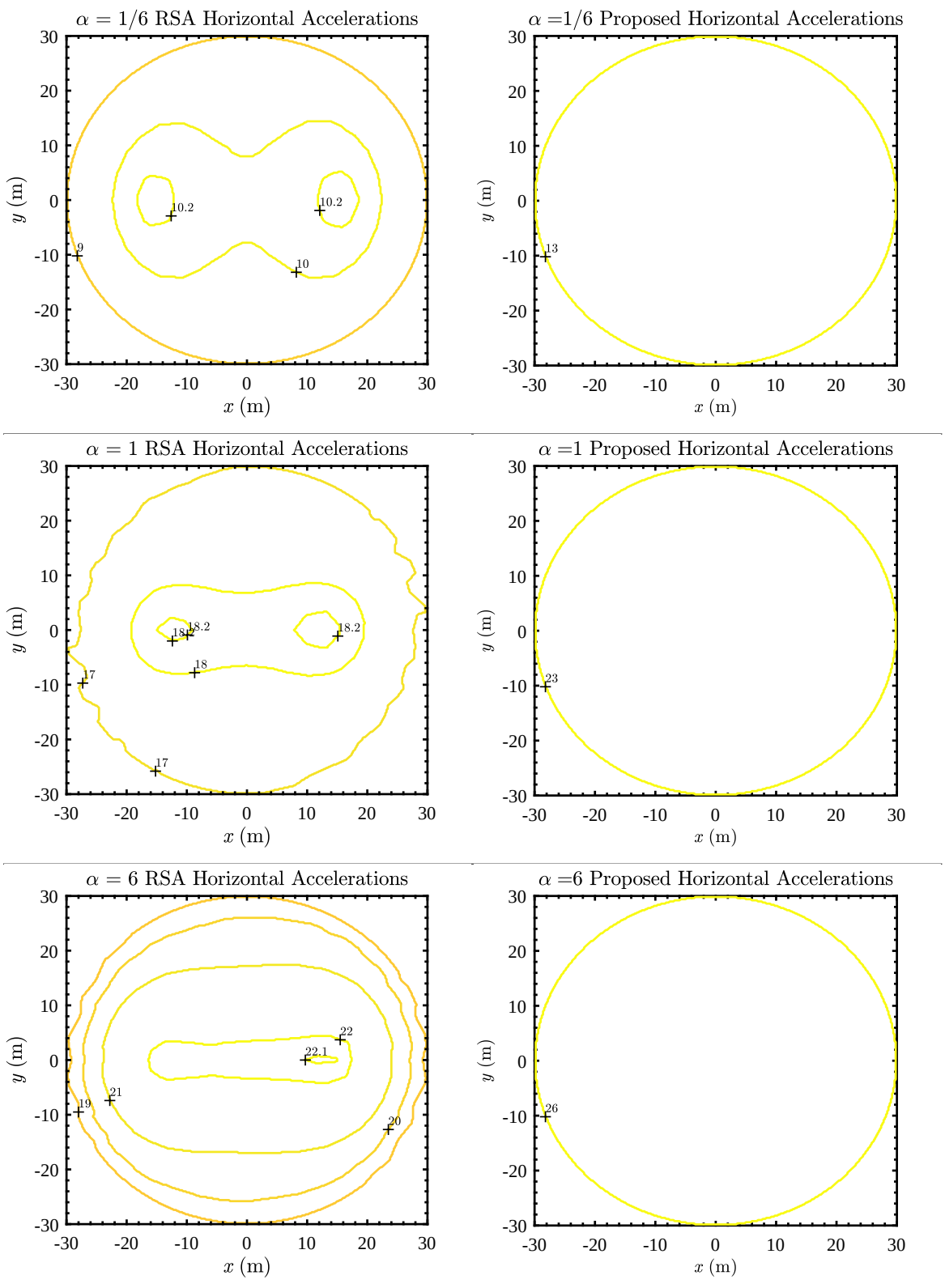

Figure 4-11: *L*-60-DL-3 model: Contour plots comparing the proposed horizontal accelerations (values in m/s^2)

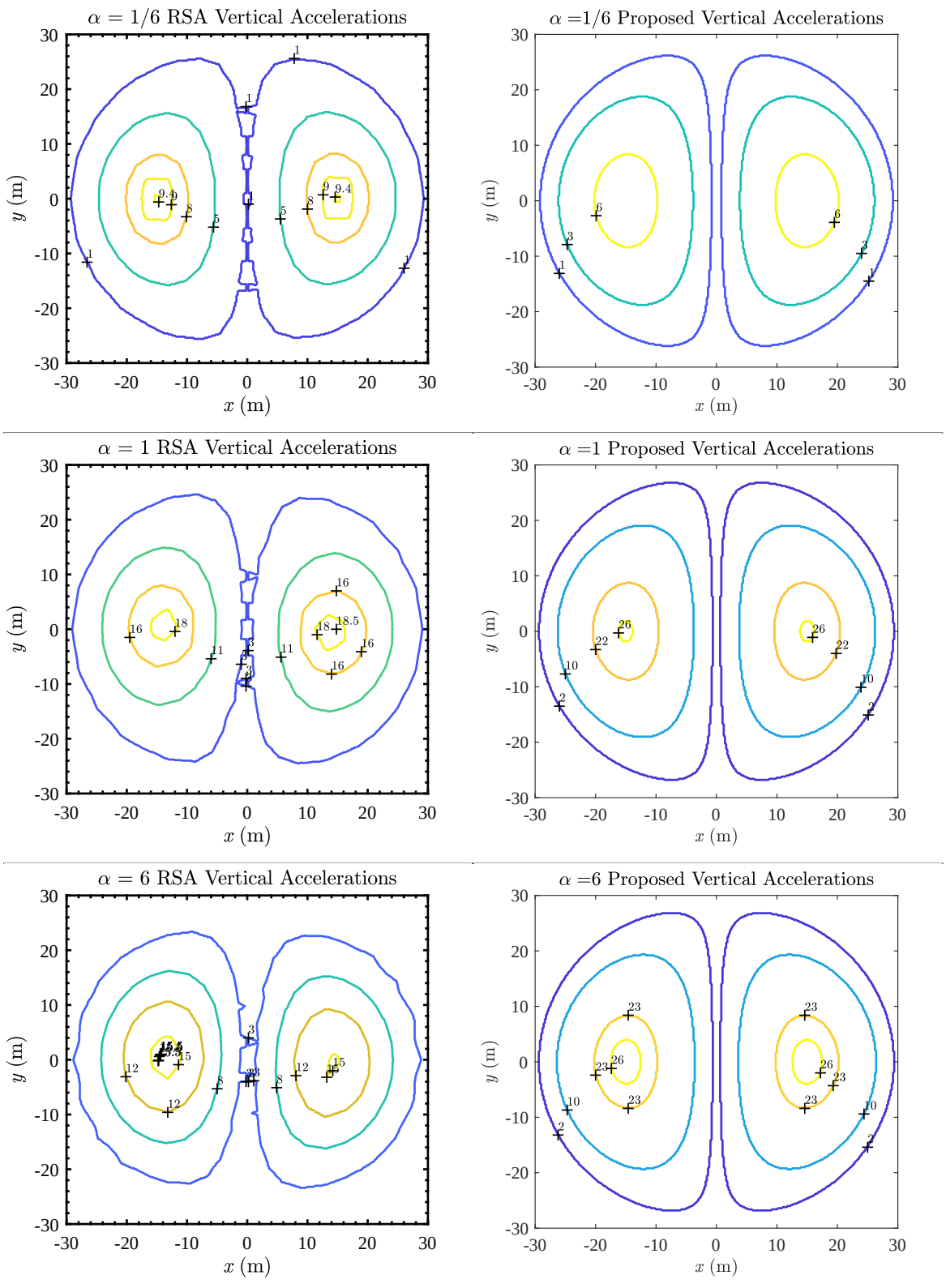

Figure 4-12: *L*-60-DL-3 model: Contour plots comparing the proposed vertical accelerations (values in m/s^2)

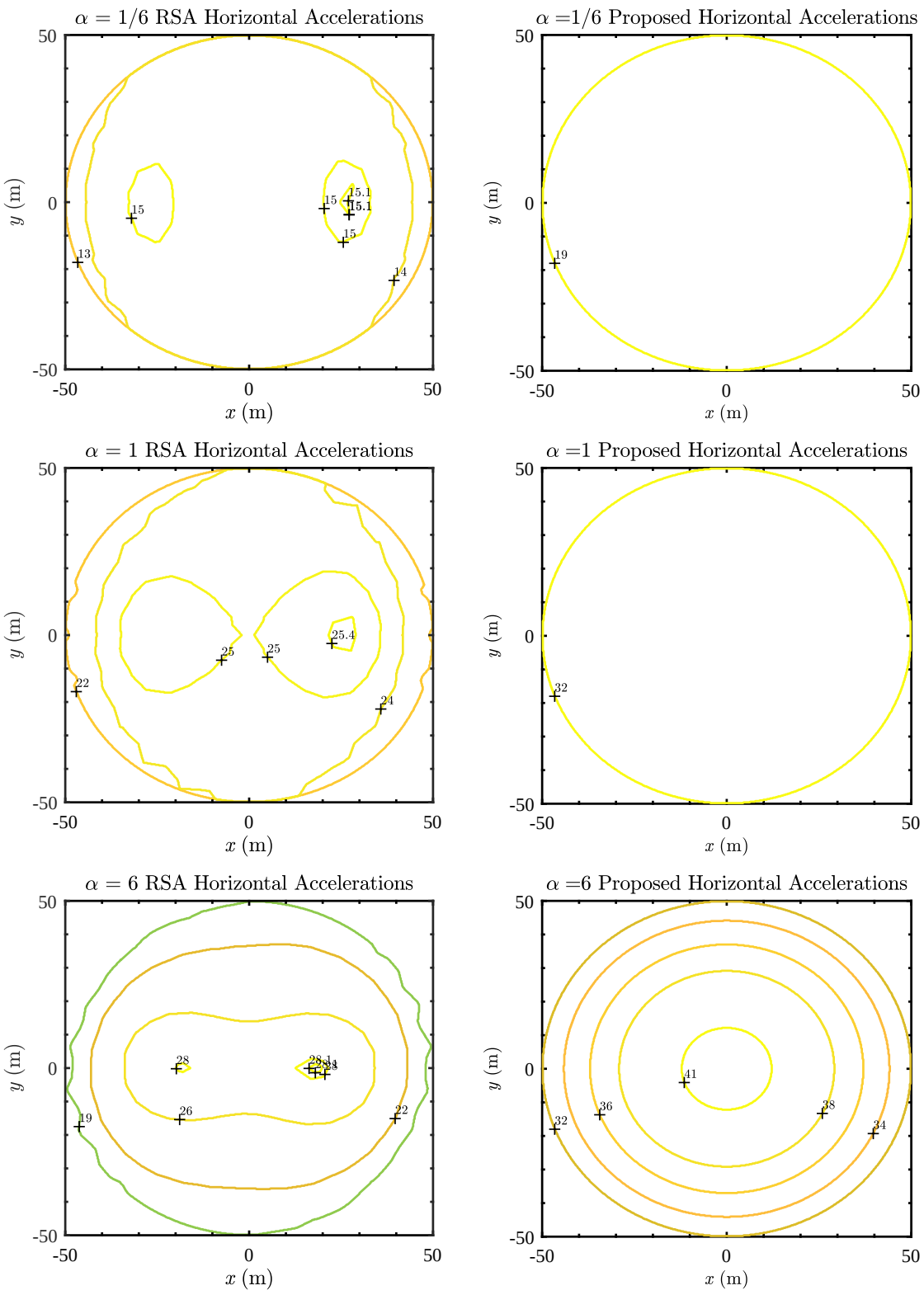

Figure 4-13: *L*-100-DL-1 model: Contour plots comparing the proposed horizontal accelerations (values in m/s^2)

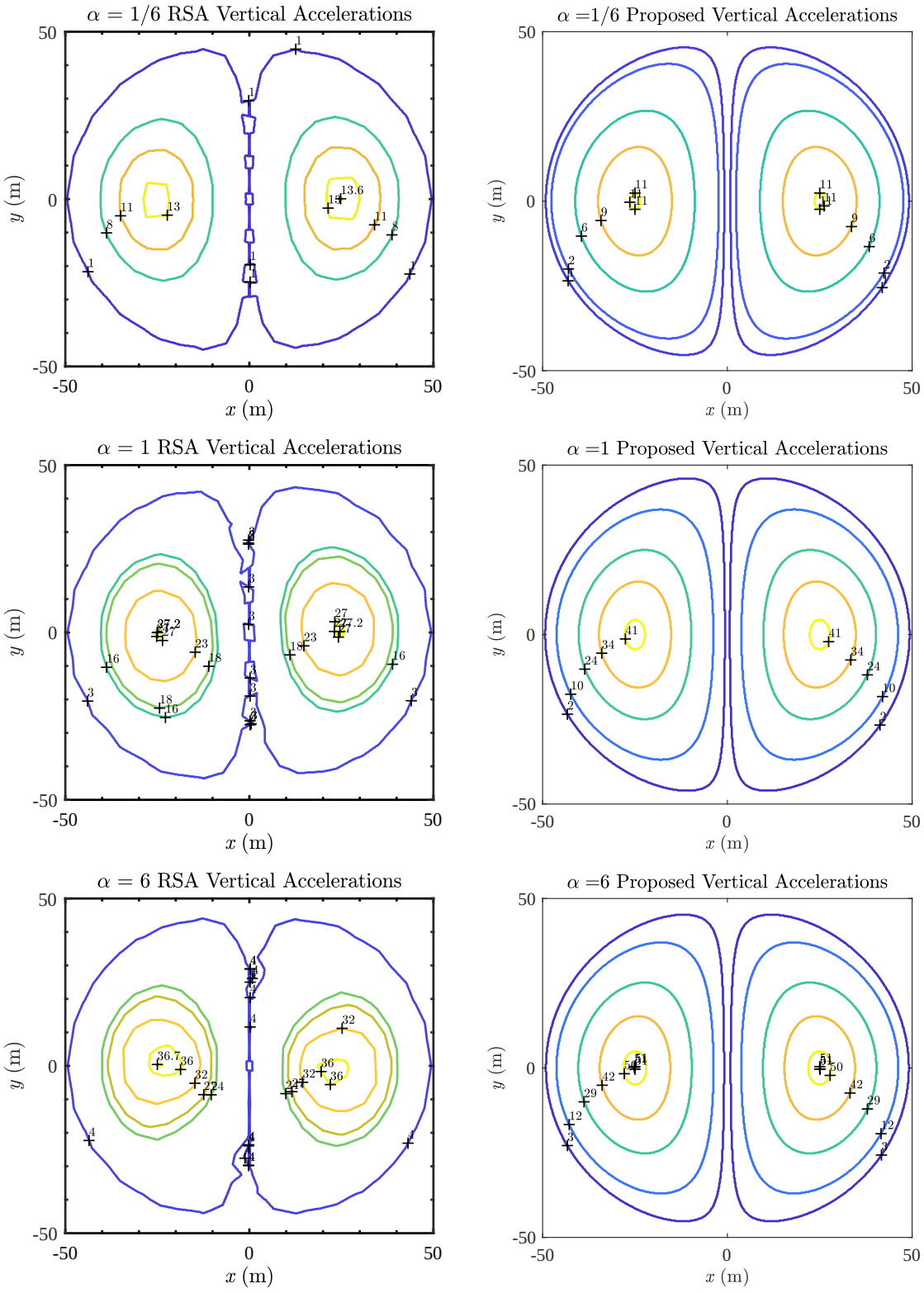

Figure 4-14: *L*-100-DL-1 model: Contour plots comparing the proposed vertical accelerations (values in m/s^2)

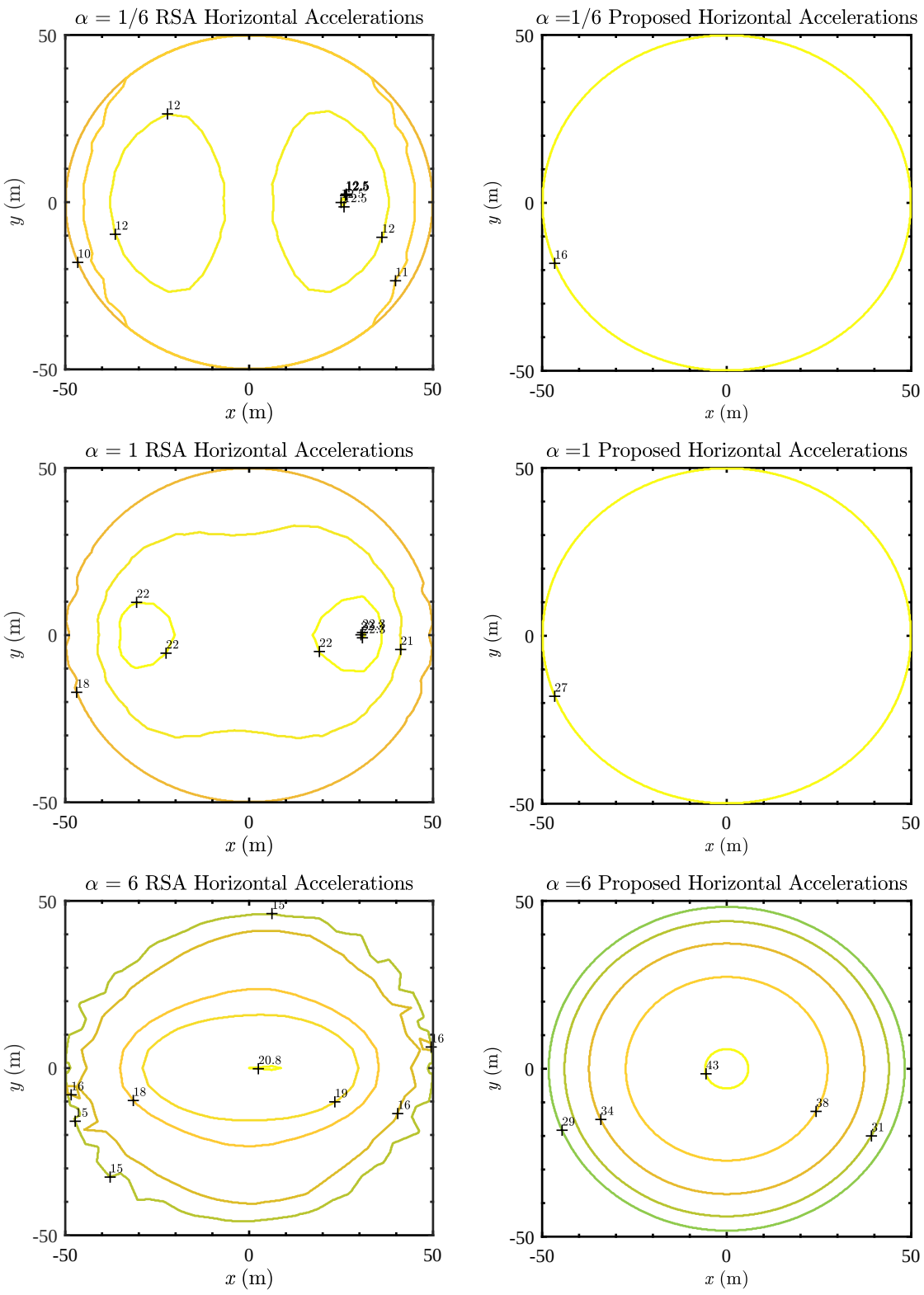

Figure 4-15: *L*-100-DL-2 model: Contour plots comparing the proposed horizontal accelerations (values in m/s^2)

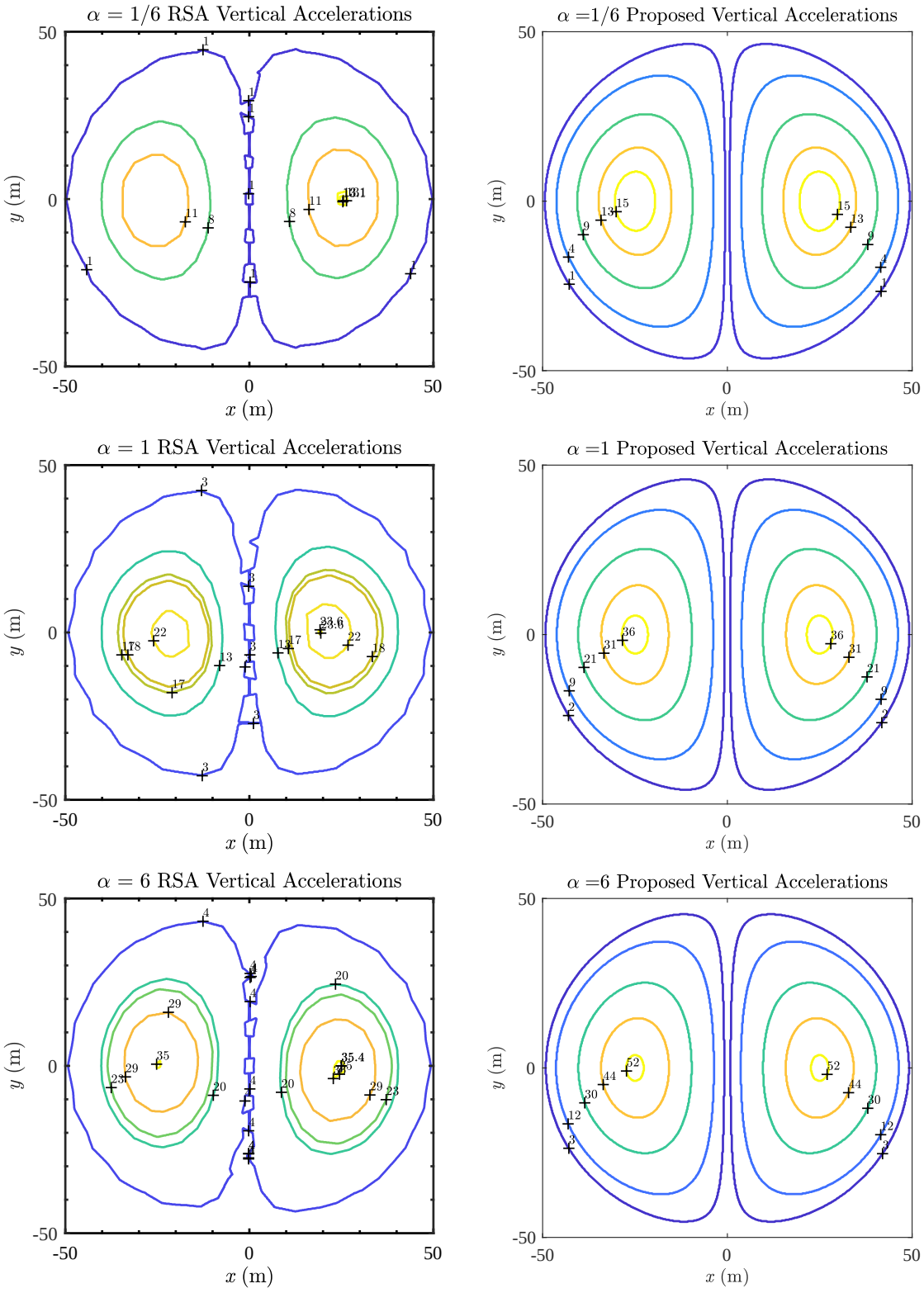

Figure 4-16: *L*-100-DL-2 model: Contour plots comparing the proposed vertical accelerations (values in m/s^2)

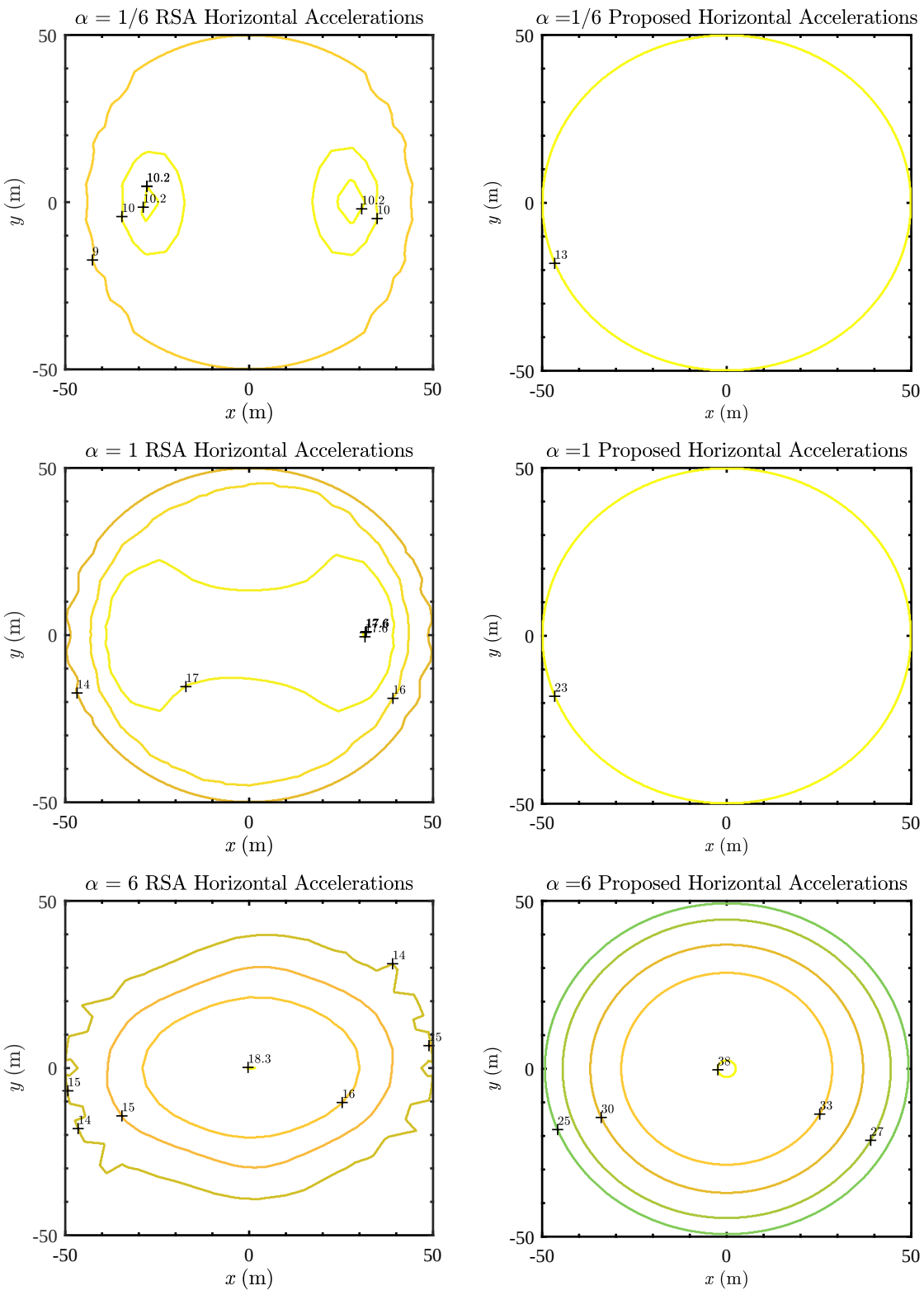

Figure 4-17: *L*-100-DL-3 model: Contour plots comparing the proposed horizontal accelerations (values in m/s^2)

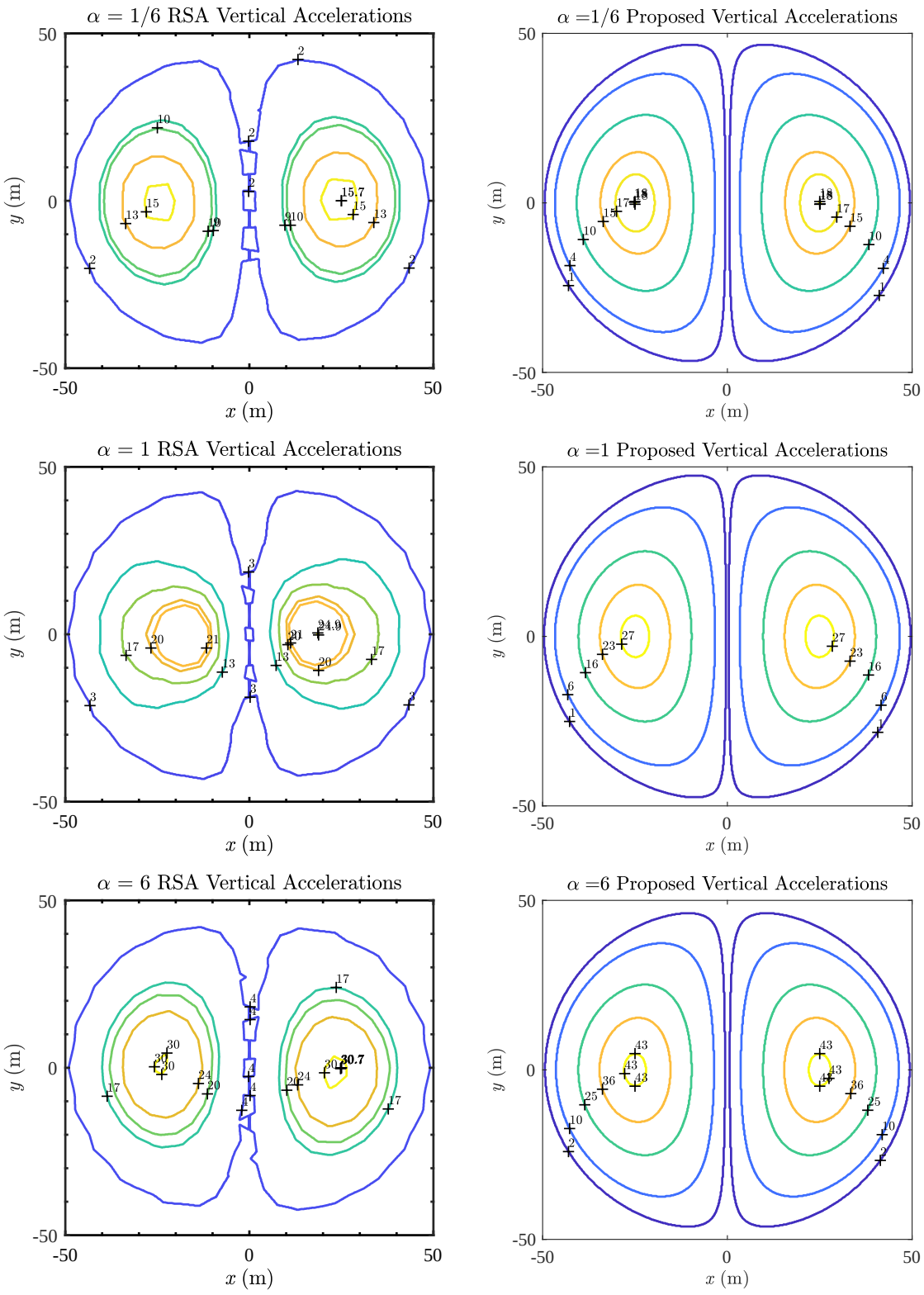

Figure 4-18: *L*-100-DL-3 model: Contour plots comparing the proposed vertical accelerations (values in m/s^2)

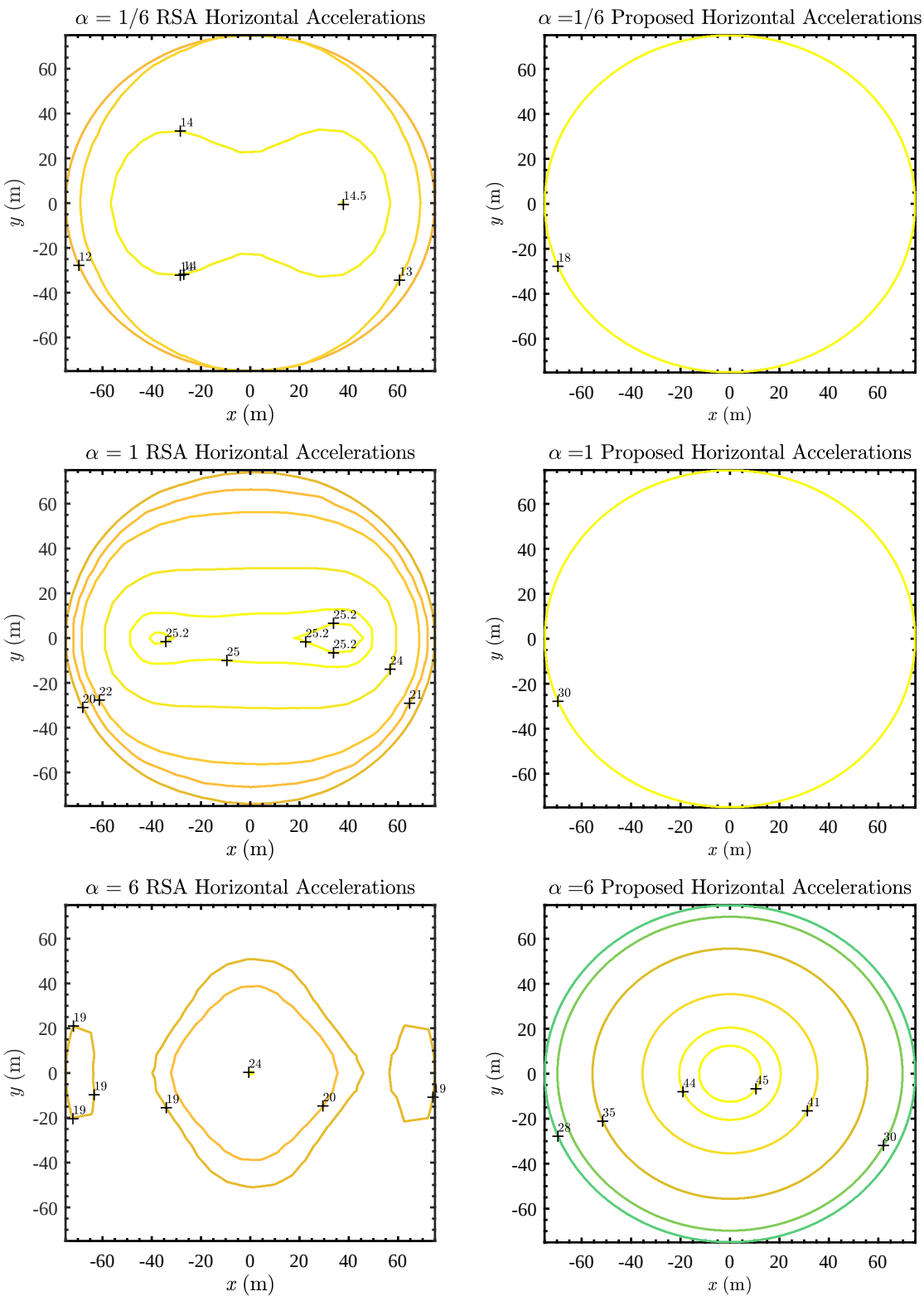

Figure 4-19: *L*-150-DL-1 model: Contour plots comparing the proposed horizontal accelerations (values in m/s^2)

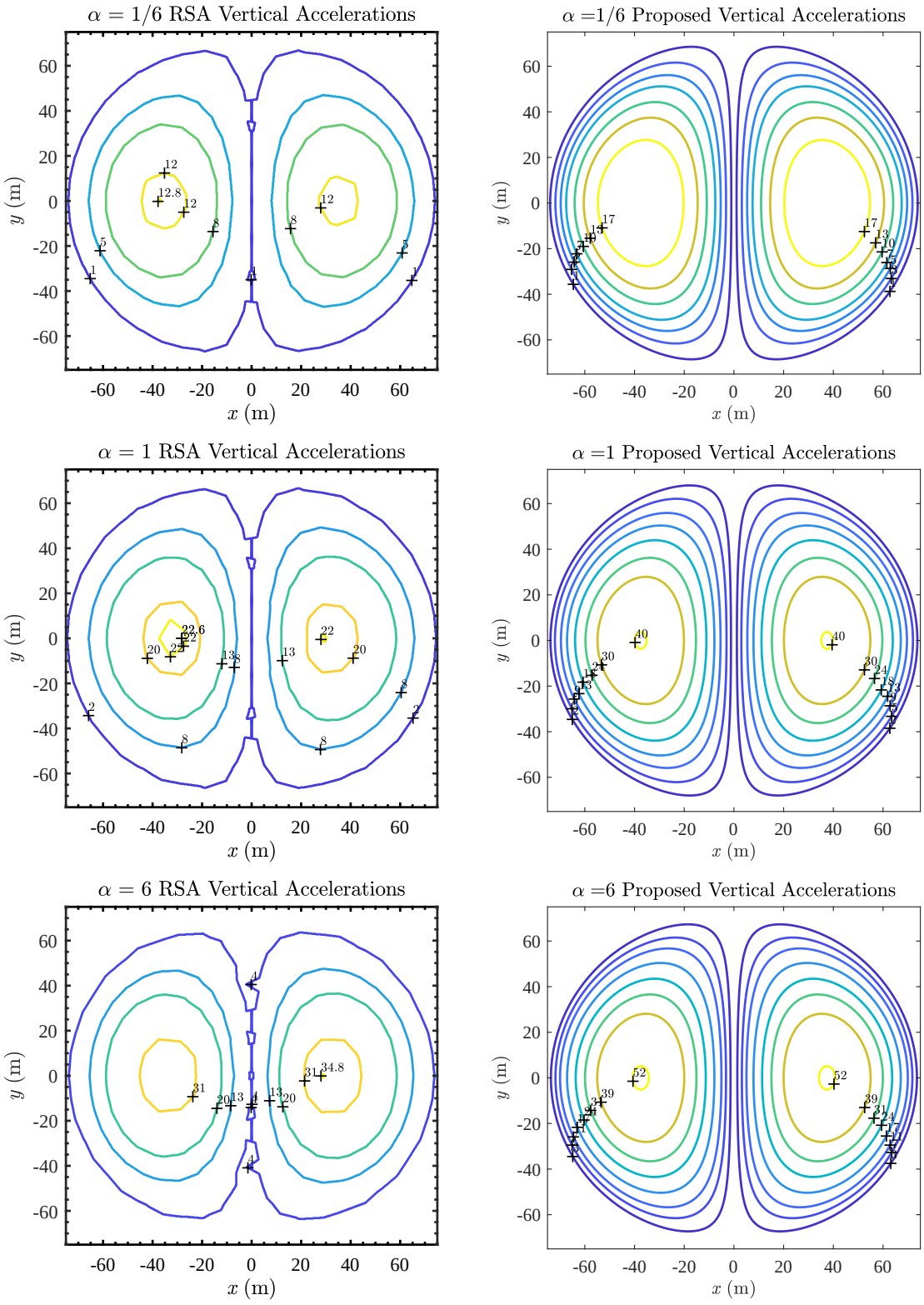

Figure 4-20: *L*-150-DL-1 model: Contour plots comparing the proposed vertical accelerations (values in m/s^2)

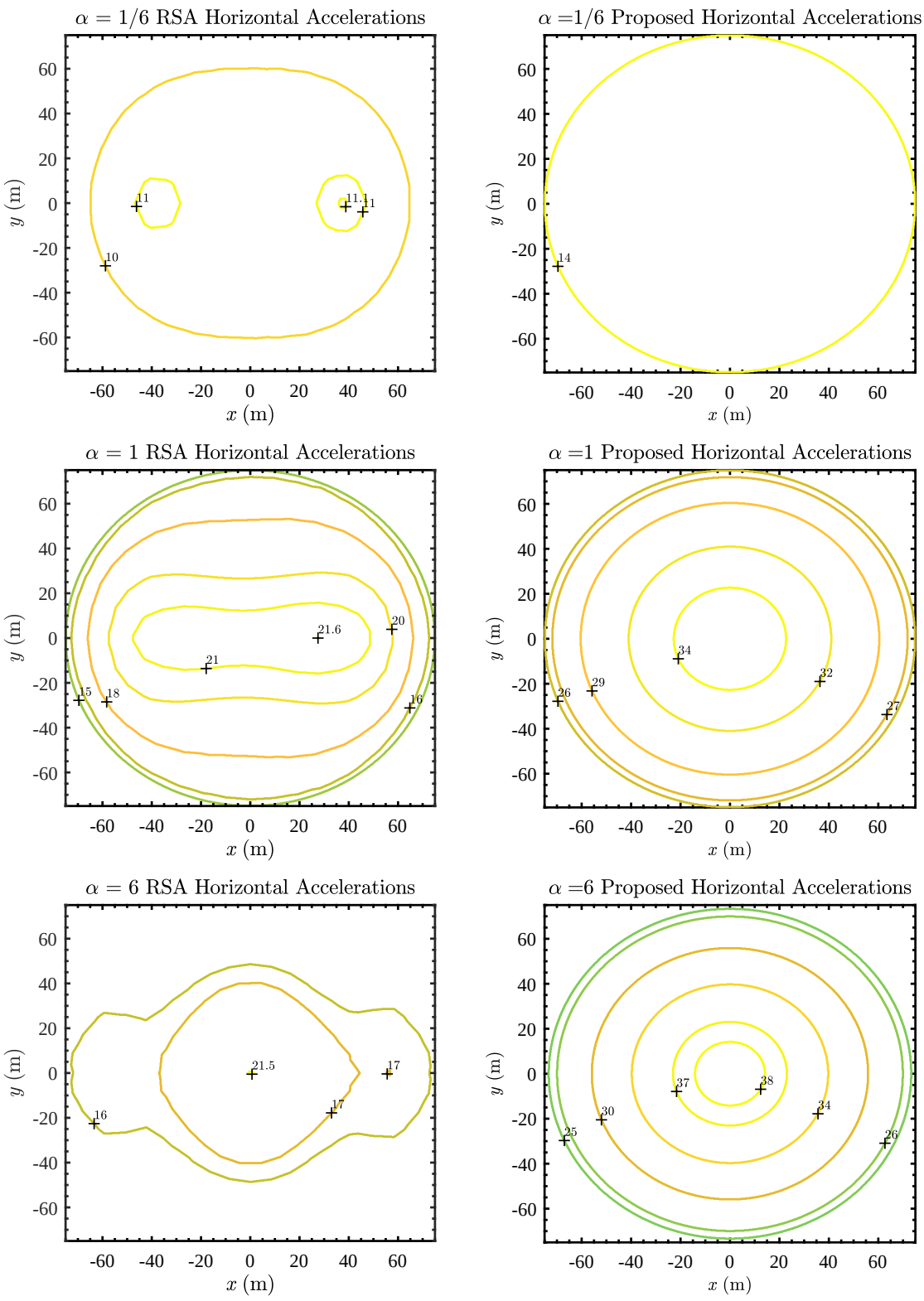

Figure 4-21: *L*-150-DL-2 model: Contour plots comparing the proposed horizontal accelerations (values in m/s^2)

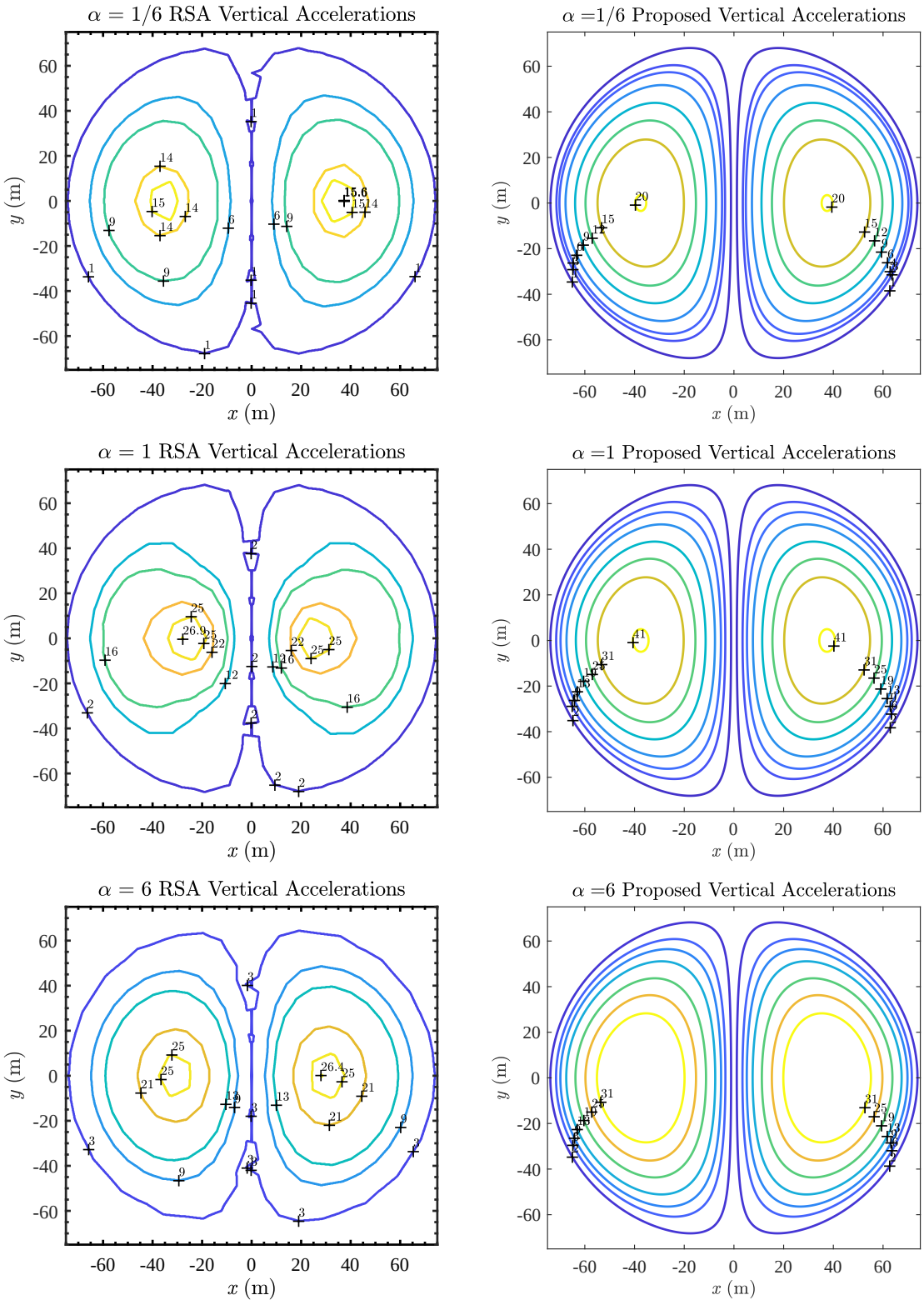

Figure 4-22: *L*-150-DL-2 model: Contour plots comparing the proposed vertical accelerations (values in m/s^2)

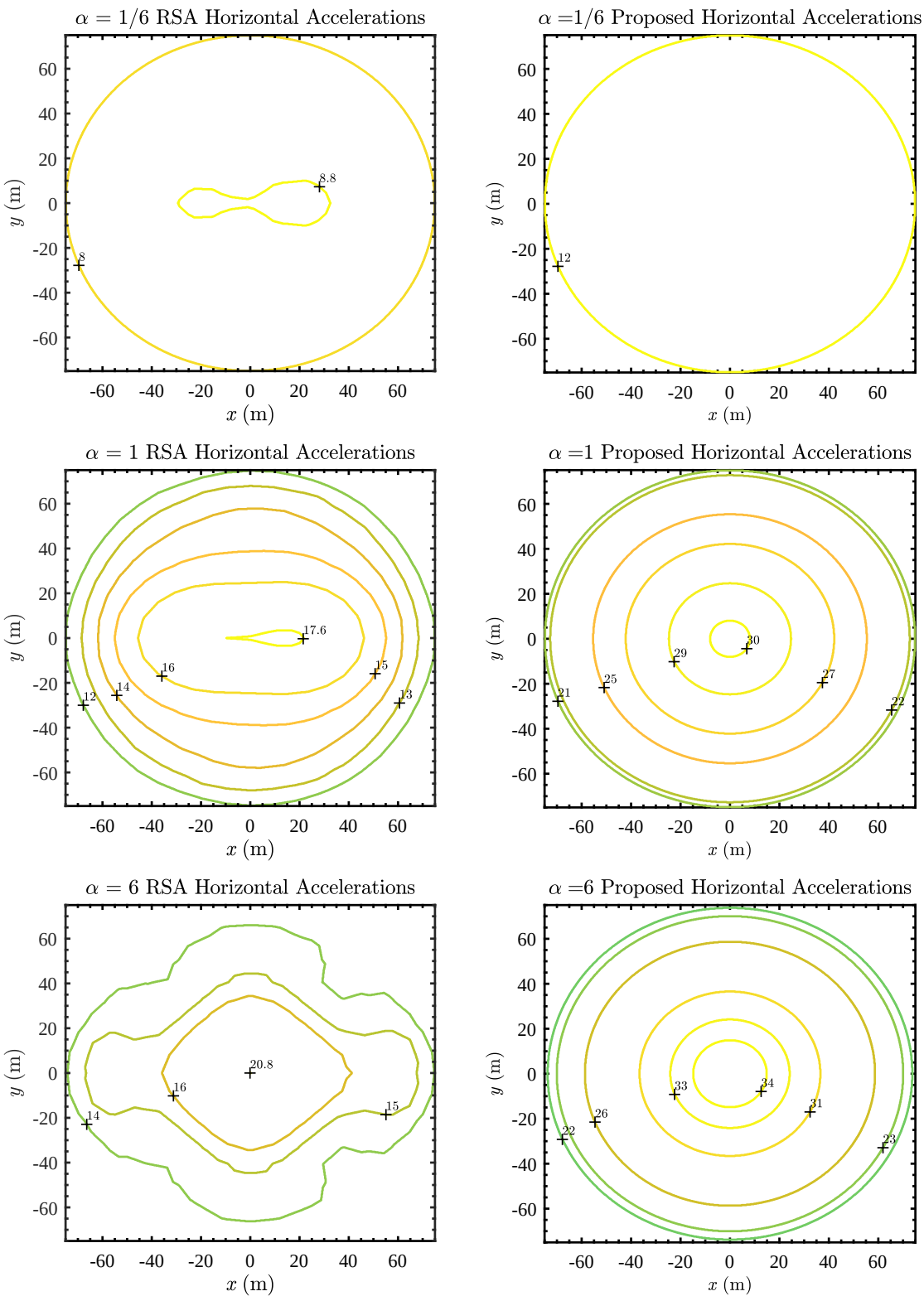

Figure 4-23: *L*-150-DL-3 model: Contour plots comparing the proposed horizontal accelerations (values in m/s^2)

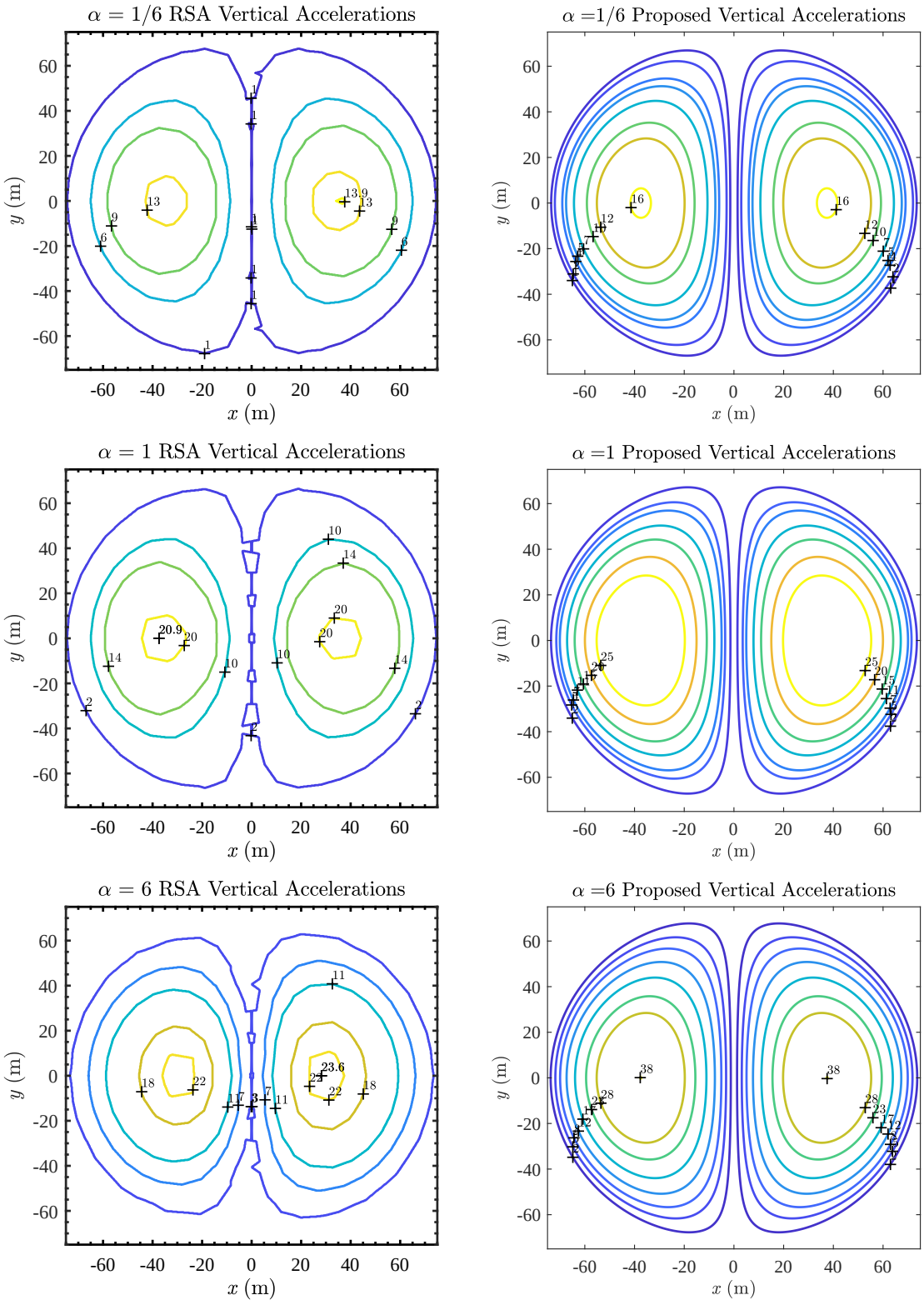

Figure 4-24: *L*-150-DL-3 model: Contour plots comparing the proposed vertical accelerations (values in m/s^2)

4.5.2 Comparison of roof member forces

The proposed peak roof accelerations were then used to compute the corresponding equivalent static loads using Equations 4.11-4.12. Static analyses were performed by applying the obtained vertical and horizontal loads simultaneously to the roof nodes of the combined models in each of the patterns (corresponding to the roof's dominant anti-symmetric mode shape O1 expressed by Equations 4.9 and 4.10) as shown in Figure 4-25 [3]. The maximum response (absolute values of the axial force N and out-of-plane bending moment M) in each member from the four static load cases may be considered as the preliminary seismic demand.

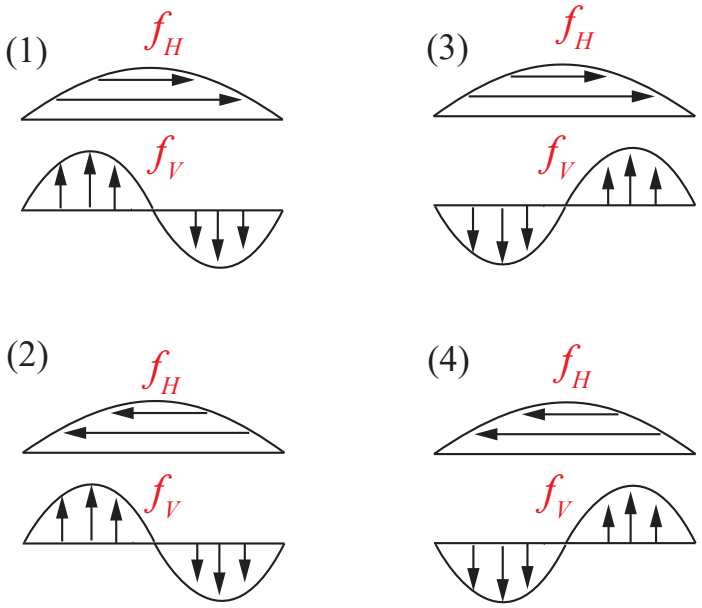

Figure 4-25: Static Load Patterns

The detailed response results for all the analysed models are compared with the RSA response in Figures 4-26-4-28. For comparison, results accounting only for the substructure T1 mode (${}_sA_{Heq1}$) with the corresponding roof amplification factors (F_{H1} and F_{V1}) are also shown and labelled 'T1'. This is also representative of the method presented in the current IASS design guideline [4] (and was previously proposed for medium-span domes with substructures where the fundamental substructure mode governs the response [1], [5]), which estimates the equivalent static loads from the roof's interactions with the first substructure mode alone. The results including the higher mode contributions using

the proposed methodology in 4.3 are labelled as 'T1+T2'. The detailed results comparing the underestimation in the member axial forces are shown in Tables 4.1-4.3. Note that, to directly compare the accuracy of the proposed method in estimating the seismic demands, the member forces and bending moments are compared only from the seismic loading and the response from dead loads are not included.

Consider the example of $L-100$-DL-2 model. As was observed in the results of peak ridgeline accelerations (Figure 4-5), the maximum benefit in including the T2 mode's contribution was observed for the $\alpha = 1/6$ and $\alpha = 1$ models (Figure 4-27(ii) and (iii). Further, adding the contribution of T2 mode reduced the number of members with underestimation in the forces. For $\alpha = 1/6$, omitting the effect of T2 mode underestimated the forces for 100% of the roof members 4.2 and considering the T2 mode significantly increased the accuracy and underestimated the forces of just 1% of the roof members. Even for the stiffer $\alpha = 1$ model, considering just the T1 mode underestimated the axial forces of 84% of the roof members and bending moments of 99% of the members. The current proposal of combining T1 and T2 showed major improvements in these values with just 2% and 4% of the members with underestimated axial forces and bending moments respectively. For very stiff substructures where $\alpha = 6$, the T1 mode dominates the response and the current existing guideline of using only the T1 mode also results in sufficiently conservative response estimates with just about 3% of members with underestimated axial forces. Considering the relatively small contribution of T2 mode resulted in minor improvements and slightly more conservative estimates of the member responses. Thus, including the higher substructure T2 mode ($_sA_{Heq2}$) using the corresponding roof amplification factors (F_{H2} and F_{V2}) significantly increases the accuracy of the member responses by providing a more conservative response, especially for models with $1/36 < \alpha < 1$ (Figures 4-27-4-28), which is the expected range for realistic multistorey substructures for design.

Response ratios

The improvement in estimation may also be measured by comparing the parameters ${}_rf_{T1}$ and ${}_rf_{T1+T2}$ which are defined as the medians of the ratios of the responses obtained from the static analyses by the proposed method (r_{T1} and r_{T1+T2}) to the responses obtained from the response spectrum analyses (r_{RSA}) calculated for all the roof members. ${}_rf < 1$ suggests that the response obtained from the equivalent static loads underestimate the actual response and similarly, ${}_rf > 1$ indicates a conservative estimate of the response. Note that, to directly compare the accuracy of the proposed method in estimating the seismic demands, the member forces and bending moments are compared only from the seismic loading and the response from dead loads are not included. The median response values for all the models are compared in bar-plots for the maximum (absolute) of the axial forces and the bending moment parameters as shown in Figures 4-29-4-31.

$$ {}_rf_{T1} = median\left(\frac{r_{T1}}{r_{RSA}}\right) \tag{4.13}$$

$$ {}_rf_{T1+T2} = median\left(\frac{k_{T1+T2}}{k_{RSA}}\right) \tag{4.14}$$

where r is the response parameter: N=Axial force and M=Bending moment.

It was observed that only considering T1 mode severely underestimates the responses for all cases with ${}_rf_{T1}$ around 0.5 (Figures 4-29-4-31) for $\alpha = 1/6$ and $\alpha = 1/36$ models where the T2 mode governs the responses. Consequently, ${}_rf_{T1} > 1$ for stiffer models with $\alpha = 6$ where the substructure first mode dominates the response and ${}_rf_{T1} > 1$. The bending moments were also equally underestimated. Adding the T2 mode's contribution improved these values by as much as 200% for the flexible $\alpha = 1/6$ models and minor improvements of around 30% were observed for the stiff $\alpha = 6$ models with the responses for all the cases generally conservative (${}_rf_{T1+T2} > 1$).

Table 4.1: $L-60$ series: Number of frames with underestimated axial forces N (in %) from seismic loads

	$\alpha = 1/6$		$\alpha = 1$		$\alpha = 6$	
Model	T1	T1+T2	T1	T1+T2	T1	T1+T2
DL-1	99%	23%	86%	13%	77%	6%
DL-2	100%	8%	91%	6%	25%	3%
DL-3	100%	11%	86%	4%	16%	2%

Table 4.2: $L-100$ series: Number of frames with underestimated axial forces N (in %) from seismic loads

	$\alpha = 1/36$		$\alpha = 1/6$		$\alpha = 1$		$\alpha = 6$	
Model	T1	T1+T2	T1	T1+T2	T1	T1+T2	T1	T1+T2
DL-1	100%	31%	100%	10%	92%	2%	14%	4%
DL-2	100%	20%	100%	1%	84%	2%	3%	2%
DL-3	100%	25%	100%	1%	68%	1%	2%	2%

Table 4.3: $L-150$ series: Number of frames with underestimated axial forces N (in %) from seismic loads

	$\alpha = 1/36$		$\alpha = 1/6$		$\alpha = 1$		$\alpha = 6$	
Model	T1	T1+T2	T1	T1+T2	T1	T1+T2	T1	T1+T2
DL-1	100%	11%	100%	4%	54%	5%	3%	3%
DL-2	100%	4%	100%	2%	2%	1%	5%	4%
DL-3	100%	35%	100%	3%	1%	1%	2%	2%

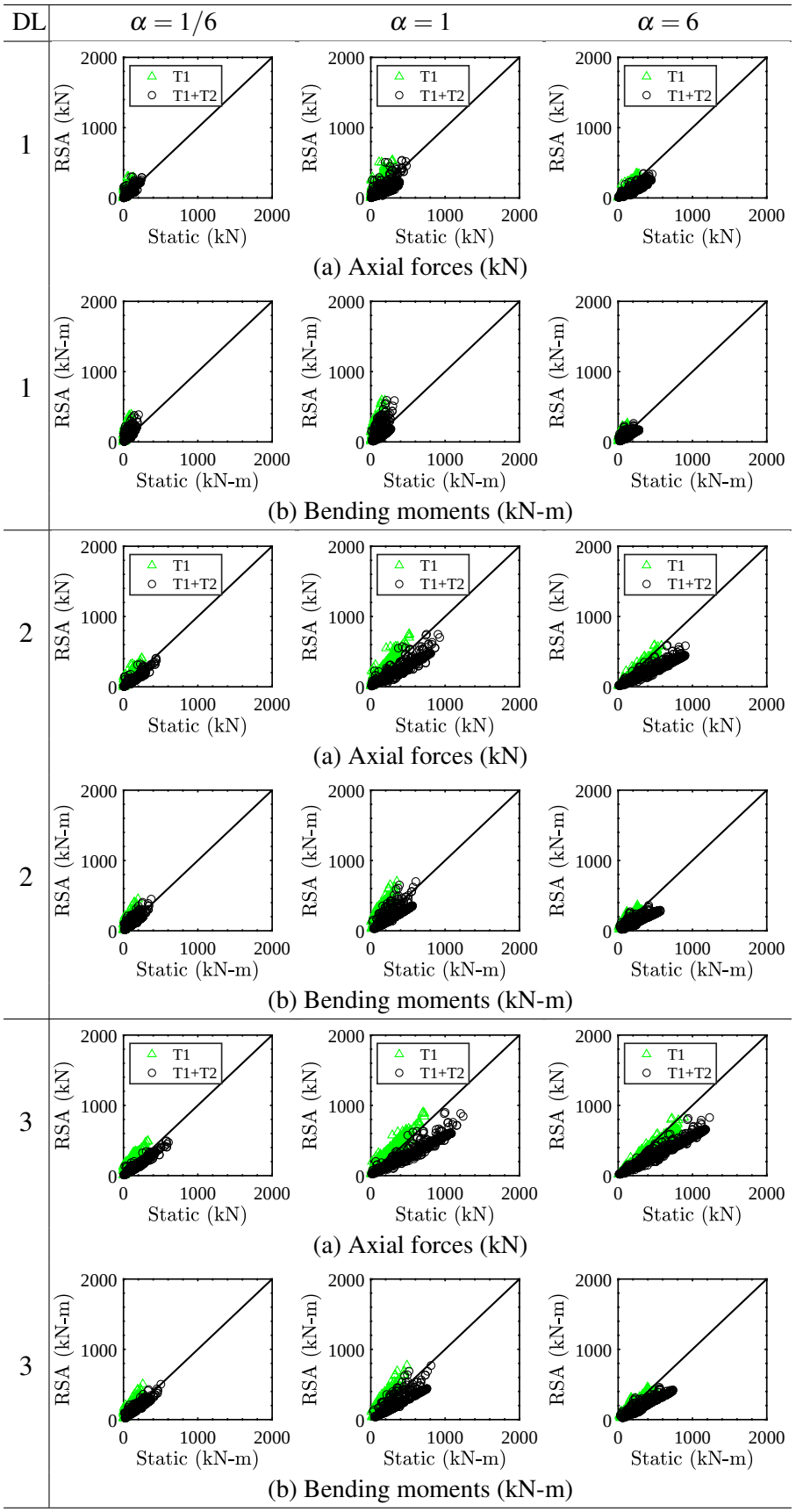

Figure 4-26: *L*-60 models: Comparison of proposed response

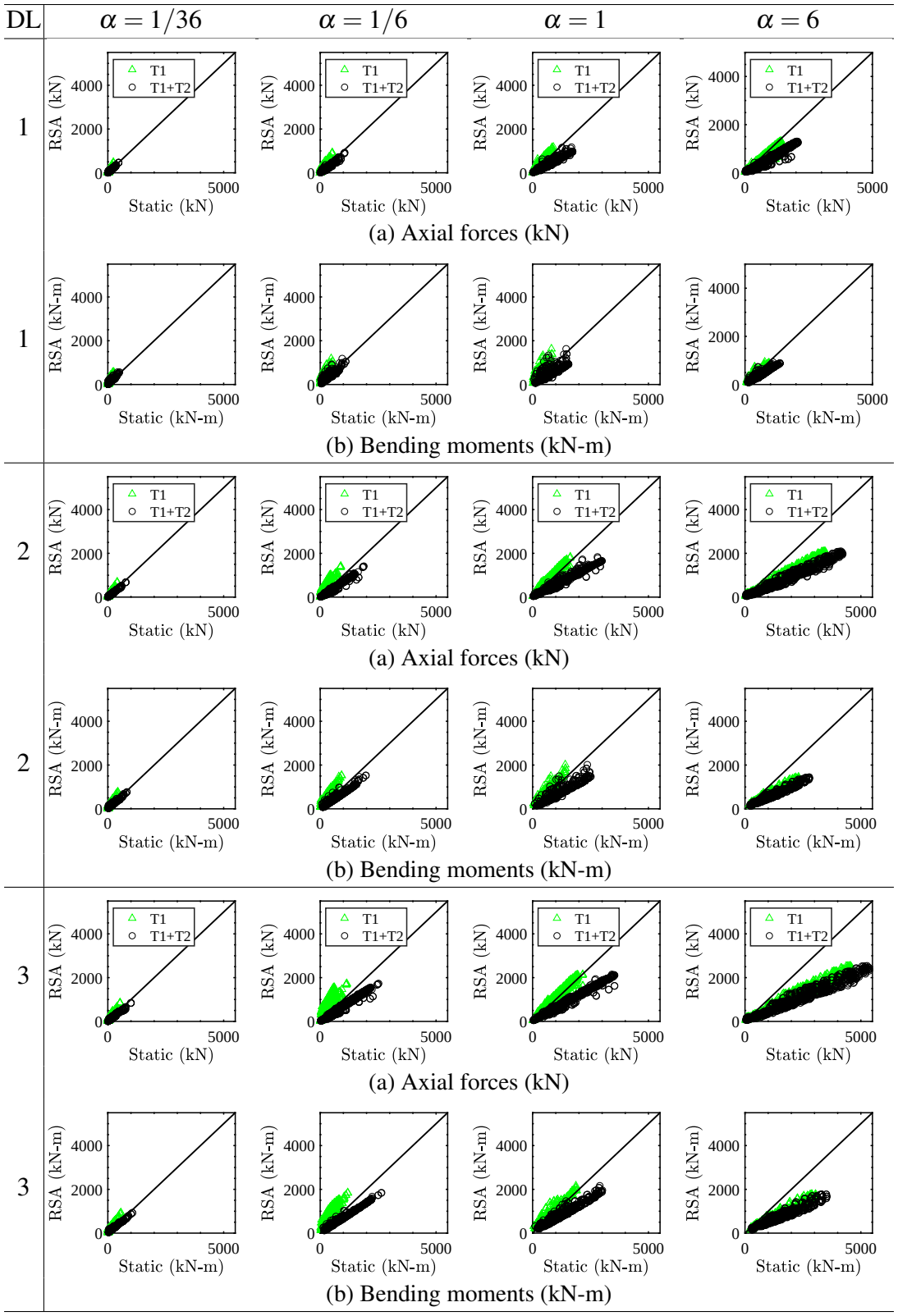

Figure 4-27: $L-100$ series: Comparison of proposed response with and without higher mode effects

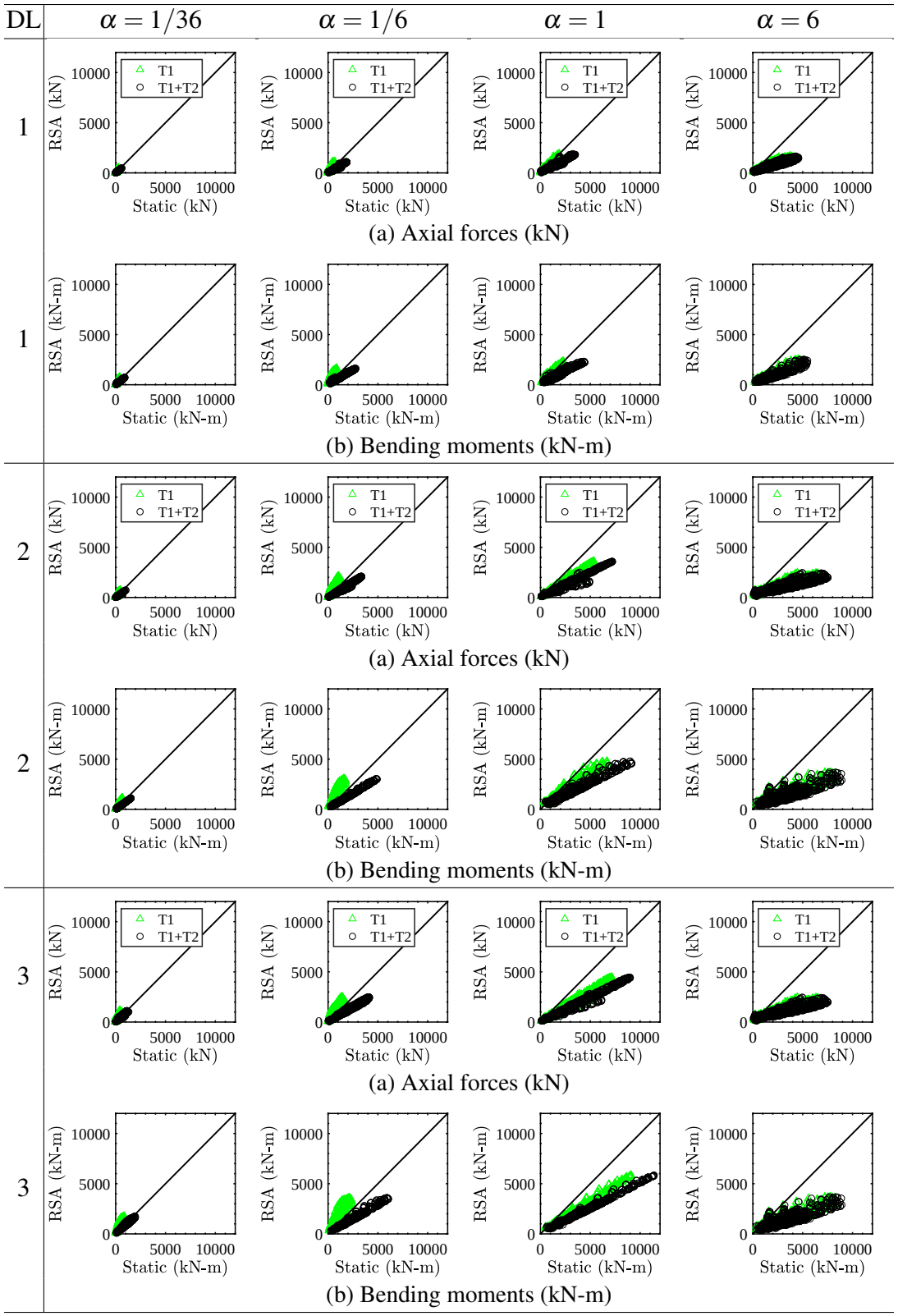

Figure 4-28: $L-150$ series: Comparison of proposed response with and without higher mode effects

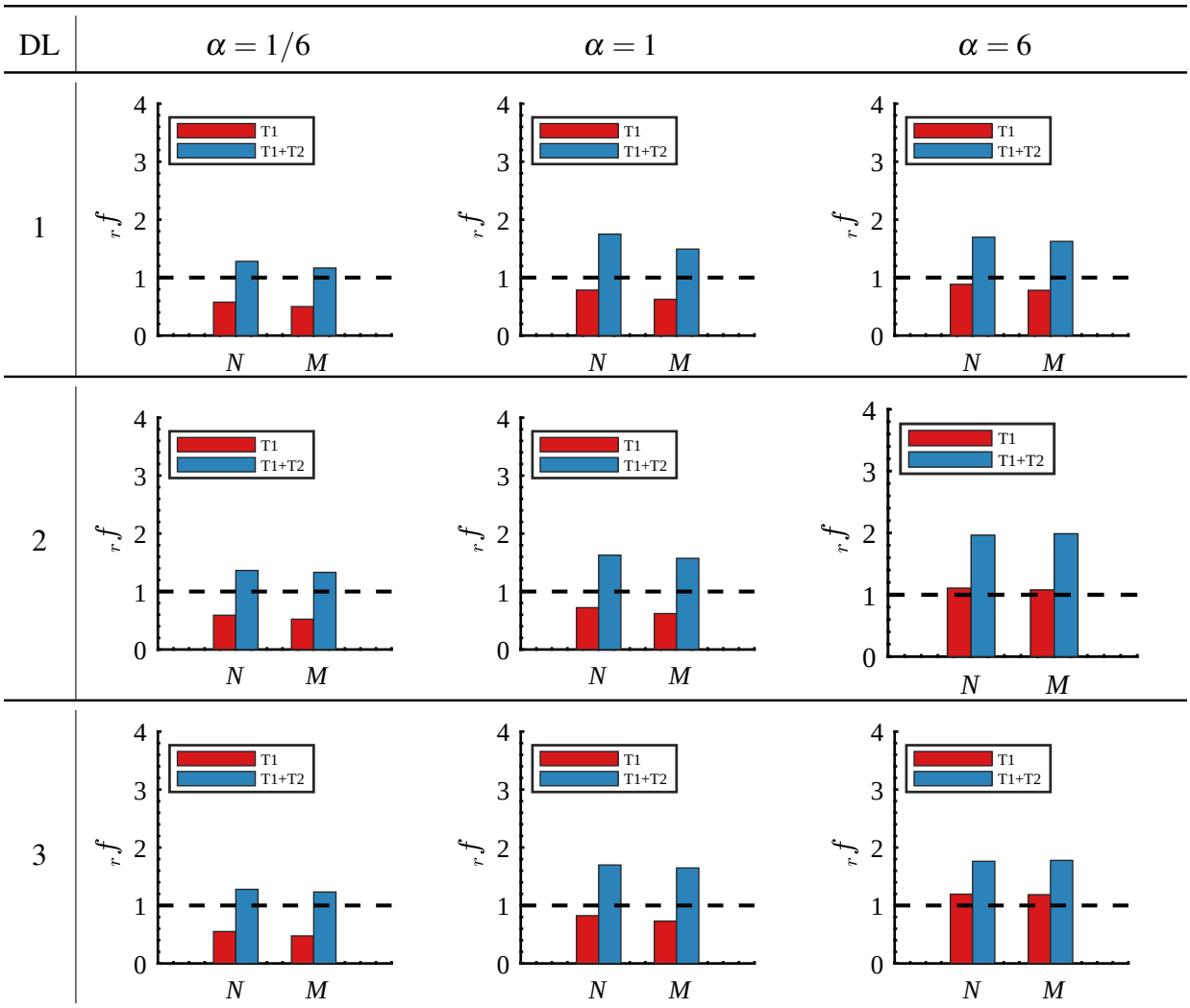

Figure 4-29: $L-60$ series: Improvement in median response ratios of forces (labelled as N) and bending moments (labelled as M)

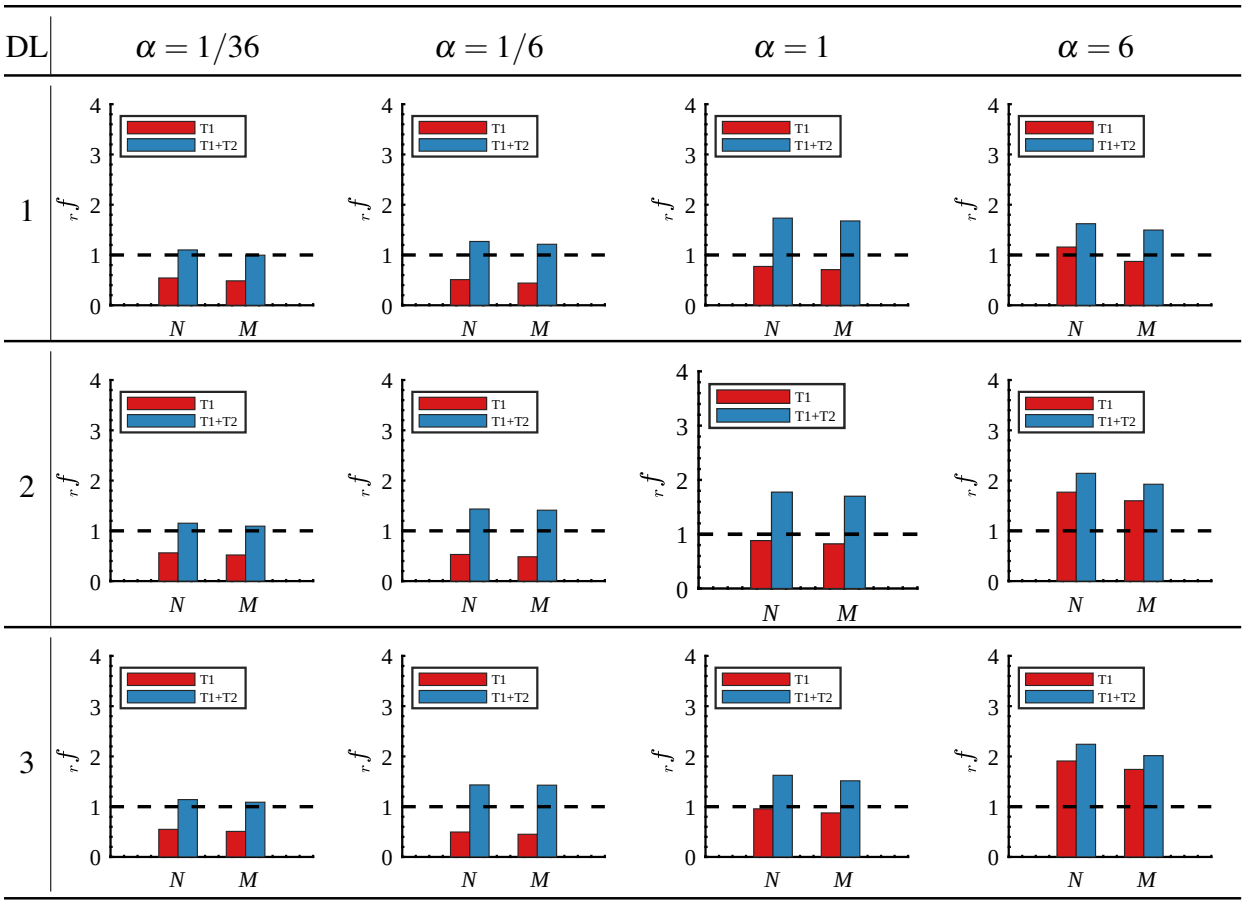

Figure 4-30: $L-100$ series: Improvement in median response ratios of forces (labelled as N) and bending moments (labelled as M)

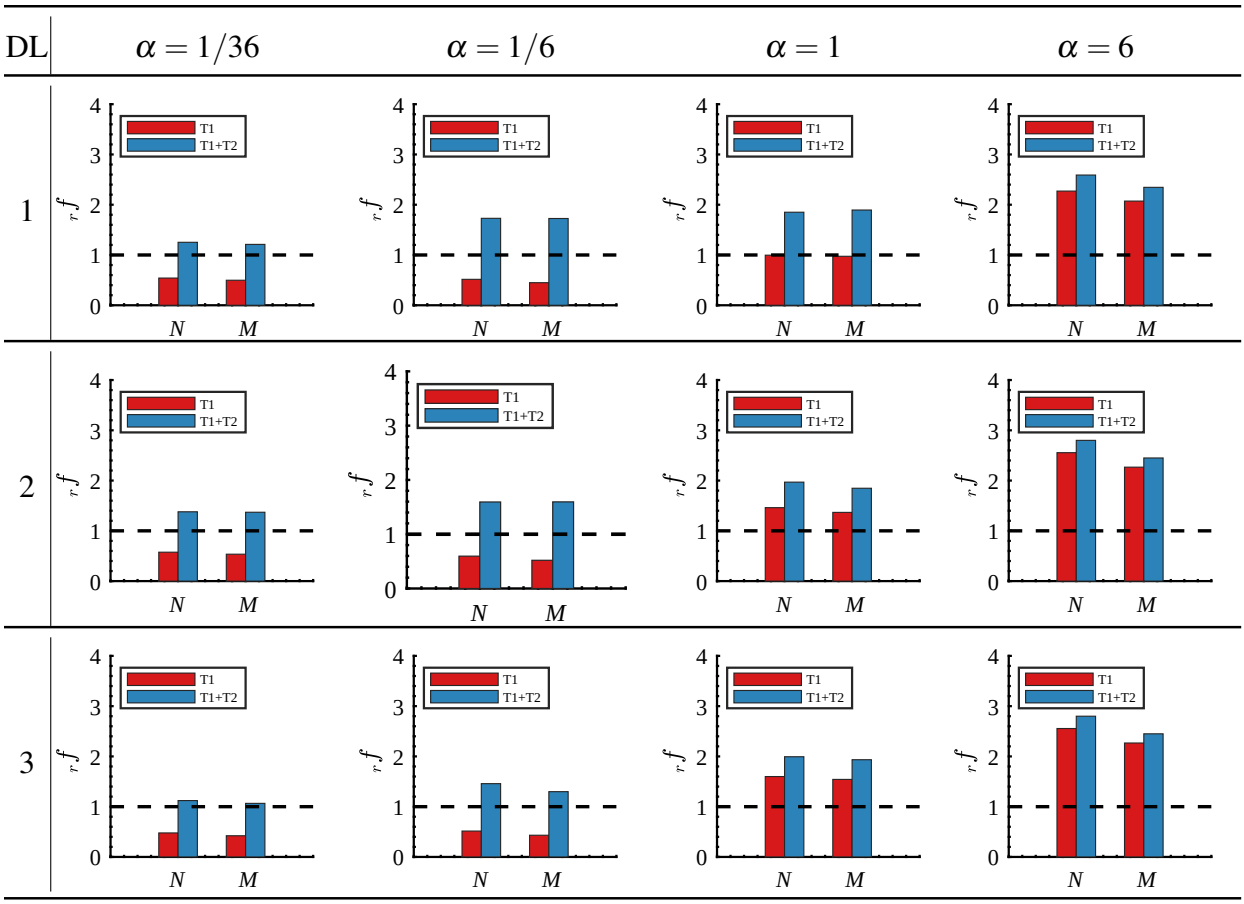

Figure 4-31: $L-150$ series: Improvement in median response ratios of forces (labelled as N) and bending moments (labelled as M)

4.6 Conclusions

The following conclusions were drawn from this investigation.

1. Simple equations were proposed to account for the amplification induced by the substructure T2 mode based on the T2-roof period ratios and to obtain equivalent static loads for preliminary seismic design, significantly improving upon the current IASS/AIJ method for domes with multistorey substructures.

2. According to the peak ridgeline acceleration results, models with flexible substructures (α=1/36) produced relatively small roof responses due to the long substructure periods. Models with slightly less flexible substructures (α=1/6) exhibited a generally flat horizontal response and a vertical roof response dominated by the T2 mode. These are representative of yielded substructures with an elongated first mode (T1) and an elastic higher mode (T2). Models with stiffer substructures (α=1) generated amplified peak response envelopes combining the substructure T1 and T2 modes. In these two cases, the exclusion of the T2 mode will underestimate the response. As the substructure stiffness is further increased (α=6), the vertical response becomes much larger and the response is dominated by T1 mode, while retaining a modest contribution from the substructure T2 mode. The proposed method was found to be in good agreement with the actual acceleration response over this full range of substructure stiffness.

3. The vertical response amplification was found to be sensitive to the period ratios of the T1 and T2 modes to the roof O1 mode (R_{T1} and R_{T2}) with peak amplification from the T2 mode F_{V2} reaching up to a value of 3 as R_{T2} approached 1. The horizontal response amplification (F_H) was primarily a result of the substructure T1 interacting with the roof's predominant modes (F_{H1}) while the peak amplification contribution from T2 mode towards the horizontal response (F_{H2}) was found to around 1 and a flat horizontal response envelope was proposed.

4. The RSA contours indicate some horizontal amplification that is centred along the quarter points on the ridgelines of the dome for substructure stiffness in the range

α<6 which indicates the dominance of roof O1 mode as the contour map resembles the roof O1 mode's horizontal mode shape. These horizontal amplifications further increase as the substructure stiffness increases to α=6 and the horizontal contour maps for α=6 varies with each model as the response in this range is a complex interaction of T1-roof and T2-roof modes. On the other hand, the vertical contour maps for all models in all ranges of substructure stiffnesses were found to be mainly governed by the roof's O1 mode and therefore the contour map shapes observed are generally similar to the contour map shapes of the proposed vertical accelerations (which are obtained using the roof's O1 mode shape) with peaks centred at the quarter-points of the ridgeline

5. The improvement in response estimation may be measured by comparing the parameters ${}_{r}f_{T1}$ and ${}_{r}f_{T1+T2}$ which are defined as the medians of the ratios of the responses obtained from the static analyses by the proposed method (r_{T1} and r_{T1+T2}) to the responses obtained from the response spectrum analyses (r_{RSA}) calculated for all the roof members. Significant improvement was observed for the models with high contribution from T2 modes ($1/36 <= \alpha <= 1$) with $r_{T1} < 1$ and $r_{T1+T2} > 1$, while for stiffer first mode dominated substructures (α=6 models), r_{T1} was generally close to or more than 1 for most of the models.

6. The greatest benefit from the proposed methodology was for substructures with dominant T2 modes ($1/6 <= \alpha <= 1$ in the period range $0.2 < R_{T2} < 2$)), with the percentage of roof members with underestimated forces up to around 99% when considering only the T1 mode reducing to just 1% when considering both T1+T2 modes. The method saw the least improvement for stiffer first mode dominated substructures (α=6), where the T1 mode's contribution alone produced a conservative response estimate leading to similar accuracy even after considering the T2 mode.

References

[1] T. Takeuchi, T. Ogawa, and T. Kumagai, "Seismic response evaluation of lattice shell roofs using amplification factors," *Journal of the IASS*, vol. 48, pp. 197–210, 2007.

[2] MATLAB, *Academic version R2019a*. Natick, Massachusetts: The MathWorks Inc., 2019.

[3] D. Nair, Y. Terazawa, B. Sitler, and T. Takeuchi, "Seismic response of long-span domes supported by multi-storey substructures," *Journal of the IASS*, vol. 61, pp. 140–157, 2020.

[4] *Guide to Earthquake Response Evaluation of Metal Roof Spatial Structures*. Working Group 8,International Association for Shell and Spatial Structures (IASS), 2019.

[5] T. Kumagai, T. Takeuchi, T. Ogawa, A. Nakama, and E. Sato, "Seismic response evaluation of latticed domes with elasto-plastic substructures using amplification factors," in *Proceedings of IASS 2005*, Bucharest, Romania, Sep. 2005, pp. 383–390.

Chapter 5

Equivalent static loads in single-storey substructures: the R-factor approach

Contents

5.1 Introduction

Gridshell roofs are often employed in school gymnasiums or public community centres with large open spaces that are expected to function as emergency shelters even after a large earthquake in countries of high seismic hazard like Japan. In such a major event where numerous residential buildings collapse, these structures may be appropriated out to provide longer-term shelter. Consequently, it becomes important to design such structures so that immediate occupancy performance criteria are achieved to ensure a safe and accessible space for refugees.

Seismic design codes and specifications typically prescribe increasing the seismic base shear for designated important structures [1], [2]. However, increasing the structural seismic demand while designing the structure to remain elastic even during a major earthquake leads to larger roof accelerations that have caused significant ceiling and other non-structural damage in past recent earthquakes rendering these structures non-functional as emergency shelters [3]. Therefore, one efficient solution to limit the roof seismic demand by decreasing the peak substructure response is to add damping devices such as the hysteretic buckling-restrained braces (BRB) to the substructure frames [4] and the response estimation of such systems have also been studied [5]–[8] using Kasai's equivalent linearisation method [9], [10]. This lower demand enables engineers to design the roofs so that they remain elastic, and the reduced roof acceleration also ensures the seismic performance of acceleration sensitive nonstructural components such as ceilings and lighting equipment. Practical applications of employing passive-control devices include the Toyota stadium [11], Shimokita dome [12] and other seismic-retrofit projects of high-school gymnasiums [13], [14]. While there exists well-established response-reduction factors for design and estimation of the inelastic design spectra of conventional BRB frames [15], [16], their application to substructures of curved gridshell roofs has not yet been explored. Therefore, as neither reliable static load procedures nor realistic R-factors are available for such structural systems, time- and data-intensive nonlinear response history analyses (NLRHA) are often the only design route.

In the previous chapter, equivalent elastic horizontal and vertical equivalent static

seismic forces were proposed for domes with elastic multistorey substructures considering the effects of higher substructure mode. The roof loads are determined from the input horizontal acceleration at the substructure's (top storey's roof) level, an assumed acceleration distribution, nodal roof masses and amplification factors derived from the dynamic characteristics of the dome and substructure. To extend this methodology to nonlinear substructures (with displacement-dependent damping devices), this chapter investigates the applicability of ductility reduction factors (or R_μ factors) to estimate the inelastic response spectra and an alternative equivalent linearisation approach to compute the peak horizontal acceleration of multistorey substructures with buckling-restrained braces. This is achieved by modelling the curved roof as a rigid mass for the substructure model and using its idealised base shear-roof displacement relationship obtained using modal pushover analyses. The peak horizontal acceleration of the substructure is then used to obtain the equivalent static loads of the curved roof using the proposed amplification factors and the accuracies are verified against the results from nonlinear response history analyses. In this chapter, the response of simpler single-storey substructures are first studied. The response estimation methods from the R-factor approach are compared with the equivalent linearisation approach while verifying all responses against those from nonlinear response history analyses.

5.2 Peak substructure response

This section discusses two R-factor approaches (Section 5.2.1) and an equivalent linearisation approach (Section 5.2.2) to estimate the peak substructure acceleration of a yielding substructure.

The peak substructure roof acceleration (A_{Heq}) is the seismic input to the dome and is the first step in the proposed equivalent static load procedure for linear double-layered domes with elastic substructures as discussed in Section 4.4 [17], [18]. The substructure is modelled as a simple lumped-mass model as shown in Figure 4-3 with the roof modelled as a rigid mass (M_R) and the peak substructure acceleration is computed using response-spectrum analysis. The substructure acceleration for each participating mode is then multiplied by the corresponding horizontal and vertical amplification factors to obtain the maximum acceleration distributions of the dome using an assumed mode shape (in this study, the dominant mode O1) [18], [19]. The amplification factors quantify the roof-substructure interaction defined by the substructure to roof period and mass ratios [8], [18], [19]. These roof horizontal and vertical accelerations (Figure 4-3) are then multiplied by the nodal masses to obtain the equivalent static inertial forces.

5.2.1 Inelastic accelerations: RSA & R-factor

For regular multistorey buildings, a simpler equivalent static lateral force procedure is available and often forms the precedent for seismic design of (regular) nonlinear multistorey buildings as prescribed by most design codes like the ASCE-7-16 [2], NZS1170.5 [20], Eurocode 8 [21] and the Building Standard Law of Japan [22]. The equivalent lateral forces are formulated to represent the internal forces generated by the dynamic response to earthquake ground motions. The forces are set at a magnitude to allow elastic analysis and design, and to provide an elastic lateral strength that will control response at full design ground motions to acceptable ductility and drift levels.

The total force reduction factor (or the response modification factor R) for idealised bilinear systems is derived as shown in Equation 5.1 and Figure 5-1, as per Uang [23], where R_μ is the ductility reduction factor and Ω is the structural overstrength factor. R_μ

accounts for the reduction in the elastic design force because of the energy dissipation capacity, and the reserve strength that exists between the actual structural yield level and the first yield level is defined as the overstrength factor Ω [23]. R_μ is therefore defined as the ratio of the elastic strength demand to the inelastic strength demand (Equations 5.1-5.2), where $\mu_s = \Delta_{max}/\Delta_y$ is the structural ductility (Figure 5-1). Note that the yield strength level (C_y in Figure 5-1) refers to the structural collapse level, not the level of first significant yielding. A 5% equivalent viscous damping ratio is usually considered in the computation of this reduction factor [23]. R_μ is therefore used to derive the inelastic seismic acceleration spectrum. Note that this R_μ factor has, by definition, the same usage and may be considered equivalent to the D_s factor used for specifying the required ultimate structural strength for the Level-2 design as per the Japanese design code BSL [22].

It was also observed that both the R and C_d factors are functions of structural overstrength factor, structural ductility factor, and damping ratio—the effect of damping is generally included in the ductility reduction factor R_μ. Furthermore, the definitions of these factors in Equations 5.1-5.2 show that it may be misleading to call R_μ the ductility reduction factor as the structural overstrength Ω may play an equally vital role to the global ductility in these factors [23].

$$R = R_\mu \Omega \tag{5.1}$$

$$R_\mu = \frac{F_y(\mu = 1)}{F_y(\mu = \mu_s)} \tag{5.2}$$

The following three subsections discuss on the three different formulations for this ductility reduction factor that will be used in the latter sections to obtain the peak inelastic acceleration of the substructure.

(i) Newmark-Hall methodology:

The Veletsos-Newmark-Hall methodology [24] (labelled and referred to as the *'Newmark'* method hereon) is one of the earliest and commonly used methods to derive the inelastic seismic design spectra (Figure 5-2(a)), where the 5 percent damped spectrum for the

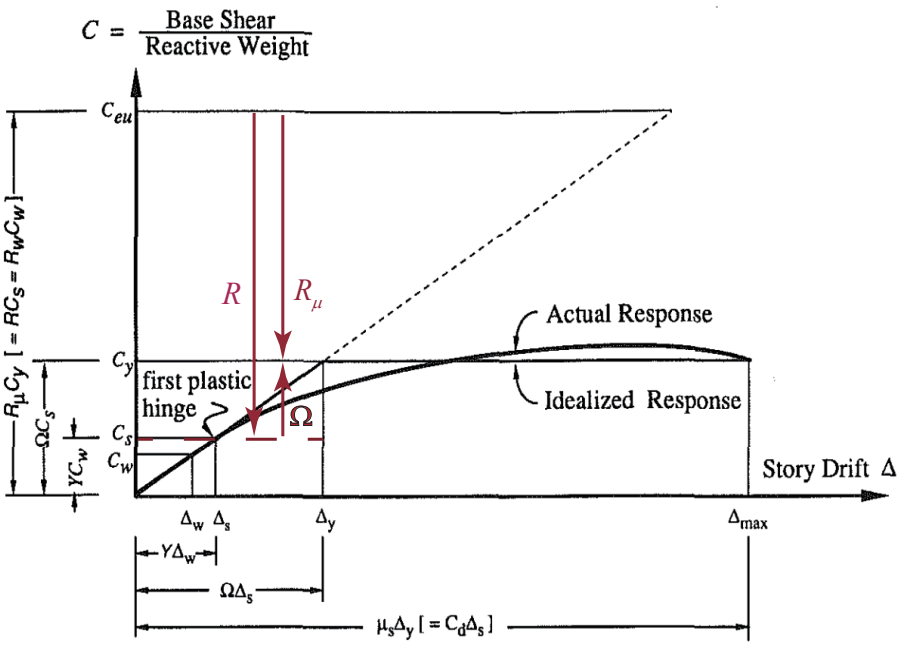

Figure 5-1: Idealisation of structural response & *R* factors, Picture taken from Uang. [23]

elastoplastic system is obtained by drawing a curve similar to that of the elastic system but displaced downward by the reduction factor. An elastoplastic resistance-displacement relationship was used as the response spectra for such a case can be drawn in generally the same way as the spectra drawn for elastic conditions. The reduction factor proposed depends on the position of the period on the spectrum.

Figure 5-2(a) shows a schematic of the elastic design spectrum with frequency on the abscissa where the frequency values for points I', J', M', and N' are only illustrative and need to be adjusted according to the seismic region and the geotechnical conditions at the site. From L' to the left, the inelastic design spectrum is obtained by dividing the elastic spectrum by μ (i.e. according to the equal displacement rule), L' is obtained by dividing the ordinate at L by $\sqrt{2\mu - 1}$ (i.e. according to the equal energy rule), and the construction is completed with transition lines. Their studies also showed that the equal displacement rule is conservative from K' to the left, but unconservative in the velocity-sensitive region (K'L') for damping larger that 2% and ductility factors larger than 2 or 3; in turn, the equal energy rule applicable to the acceleration-sensitive region (L'M') is unconservative for damping larger than 5% [24]. The design spectrum methodology has been the basis for

designing special facilities that require more rigorous design criteria than those applicable to buildings, with regard to both the definition of the earthquake hazard and the acceptable extent of inelastic deformations, depending on the performance requirements [24].

These ductility reduction factors Figure 5-2(b) were adopted by Uang [23] and are defined as follows, and are applied to a design spectrum (from ASCE-7 defined later) in Figure 5-3:

1. For constant-acceleration region of the spectrum ($T < T_c$) where the equal energy rule applies [23], and the area under the load-deformation diagram up to the maximum deformation is equated with that of an elasto-perfectly plastic system :

$$R_\mu = \sqrt{2\mu - 1} \tag{5.3}$$

2. For constant-velocity region of the spectrum ($T > T_c$) where the equal displacement rule applies (Figure 5-3) [23]:

$$R_\mu = \mu \tag{5.4}$$

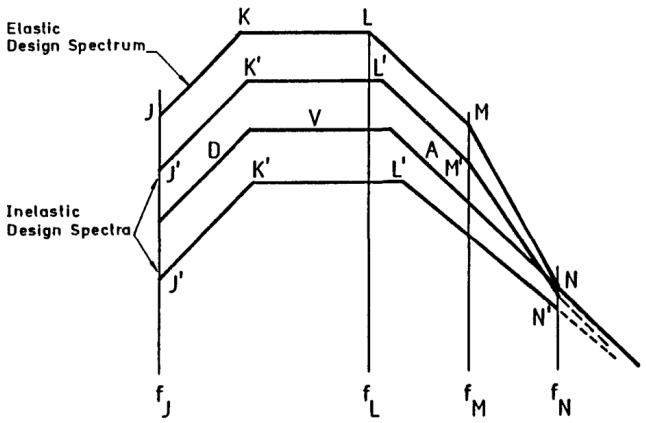

(a) Construction of design velocity spectra

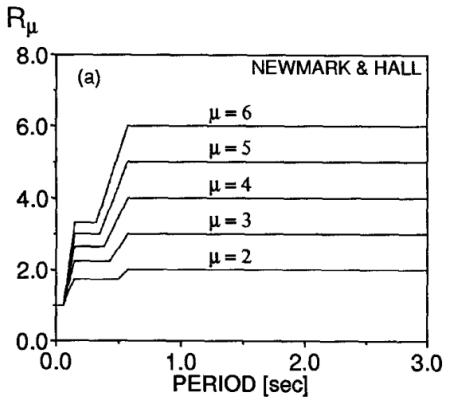

(b) Ductility reduction factors vs T

Figure 5-2: Newmark-Hall proposal: Pictures (a) taken from Riddell et al. [25] and (b) from Miranda [26]

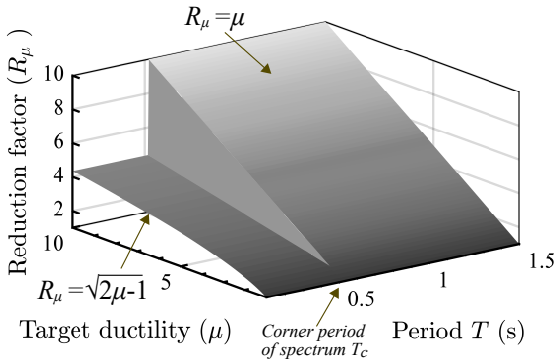

Figure 5-3: Newmark's $R - \mu - T$ relationship applied to ASCE-7 design spectrum [23] (Figure 5-9)

(ii) Nassar & Krawinkler :

Adopting the same ideaology, this study by Nassar and Krawinkler [27] aimed to define displacement as the basic design parameter in determining the demand versus capacity diagram. The main objective of this study was to estimate the required lateral load capacity of the structure in order to limit the global ductility to a pre-determined target value so that the local member ductility demands are limited to their corresponding capacities.

To estimate the inelastic strength demands, strength reduction factors R_μ were derived as a function of the target ductility ratio μ and the period T, using a least squares fit regression analysis for a single degree of freedom system with post-yield stiffness ratios (p) of 0, 2 and 10 % subjected to 39000 time history analyses for T= 0.1-4.0 s, μ=1-8 for a damping of 5% [27] as shown in Figures 5-4-5-3. given in Equations 5.5-5.6 (labelled and referred to as the 'N&K' method hereon)

$$R_\mu = [c(\mu - 1) + 1]^{1/c} \tag{5.5}$$

$$c = \frac{T^a}{T^a + 1} + \frac{b}{T} \tag{5.6}$$

where $a = 1$ for p <=2%, $a = 0.8$ for p =10% and $b = 0.42, 0.37$ and 0.29 for p =0, 2 and 10% respectively.

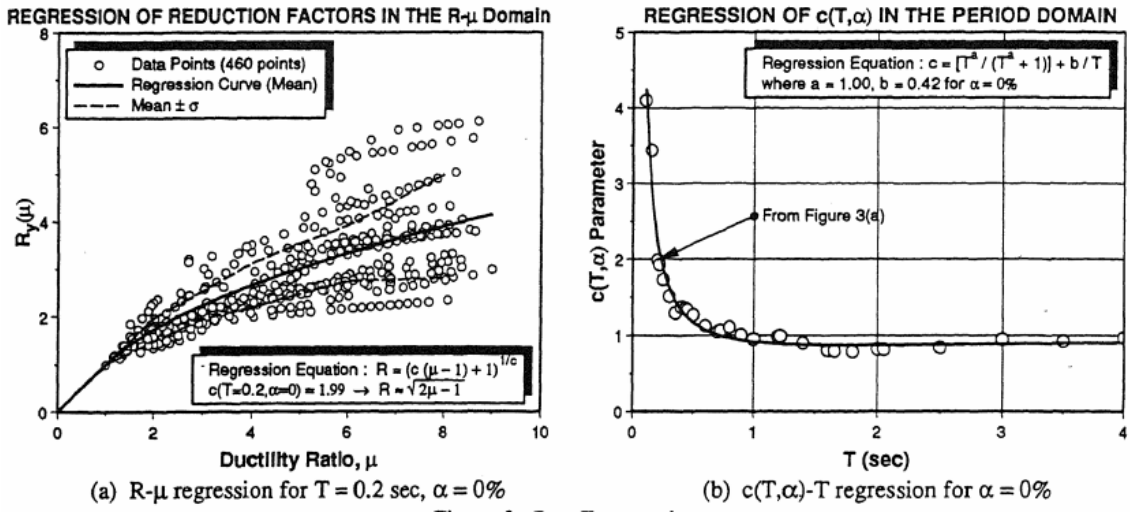

Figure 5-4: Derivation of $R - \mu - T$ relationship through regression
Picture taken from Nassar & Krawinkler [27]

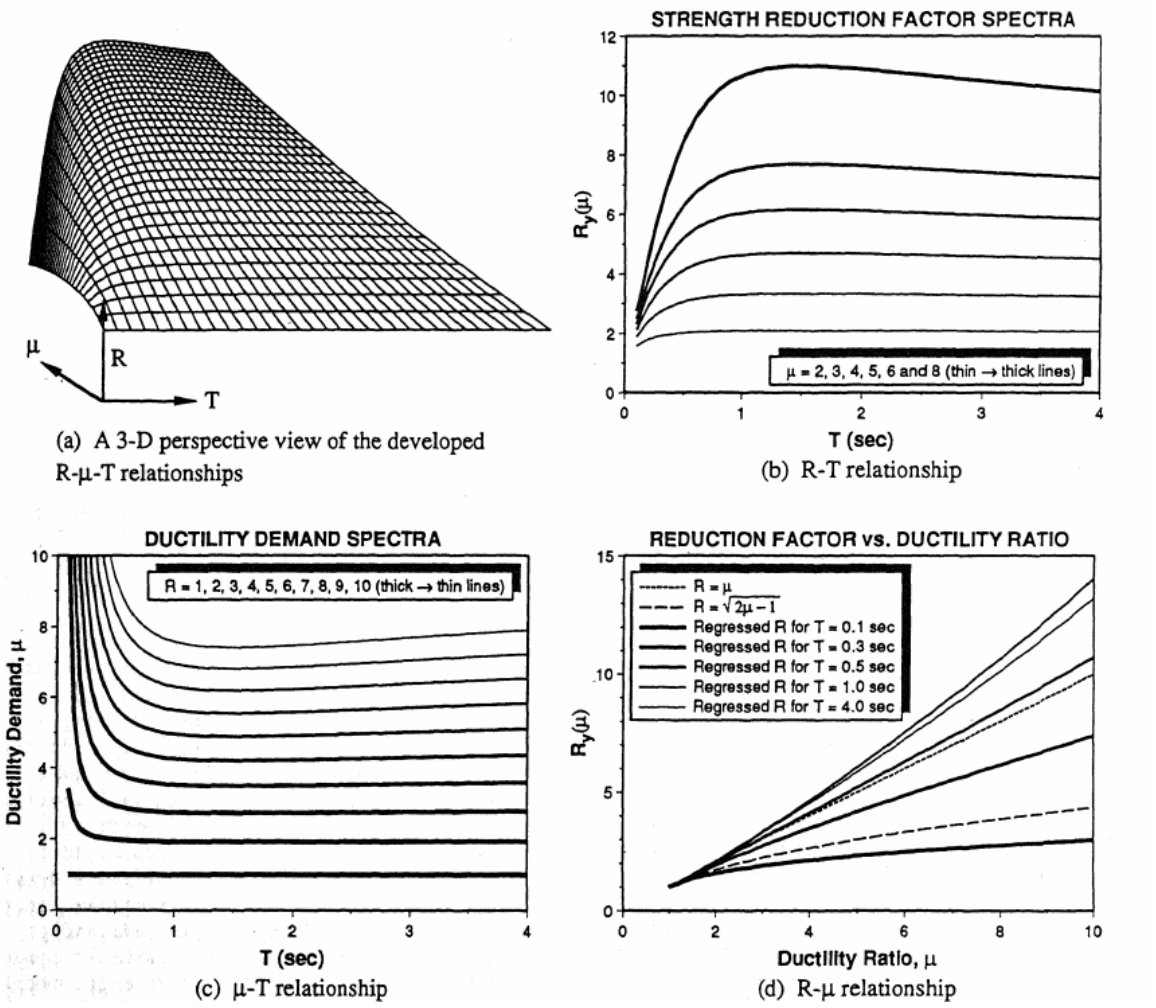

Figure 5-5: Proposed $R - \mu - T$ relationships for elastoplastic models
Picture taken from Nassar & Krawinkler [27]

It was observed that, for the bilinear models considered, the strength assessment results were not very sensitive to the hysteretic model used [27], although this formulation has not been verified for models with strength-degrading hysteretic behaviour. Furthermore, Nassar and Krawinkler and Miranda [26] studied the influence of earthquake magnitude and epicentre distance on the R_μ factors. Both studies concluded that the effects of both parameters are negligible on the R_μ factor [28].

(iii) Lee & Han:

Lee & Han [28] further studied the reduction factors for different hysteretic models and proposed R_μ as a function of the period and ductility using a two-stage regression analysis. For the statistical study, 40 earthquake ground motions are used for nonlinear time history analyses on SDOF systems [28]. Target ductility ratios of 1, 2, 3 ,4 ,5, and 8 were considered and natural periods of the SDOF systems were in the range of 0.05s to 3s. The following equations for elasto-perfectly plastic models given in Equations 5.7-5.8 were proposed through regression. Figure 5-6 compares the regressed values against the NLRHA results for elastoplastic models.

$$R_\mu = A_0\{1-\exp(-B_0 \times T)\} \tag{5.7}$$

$$A_0 = 0.99 \times \mu + 0.15; \quad B_0 = 23.69 \times \mu^{-0.83} \tag{5.8}$$

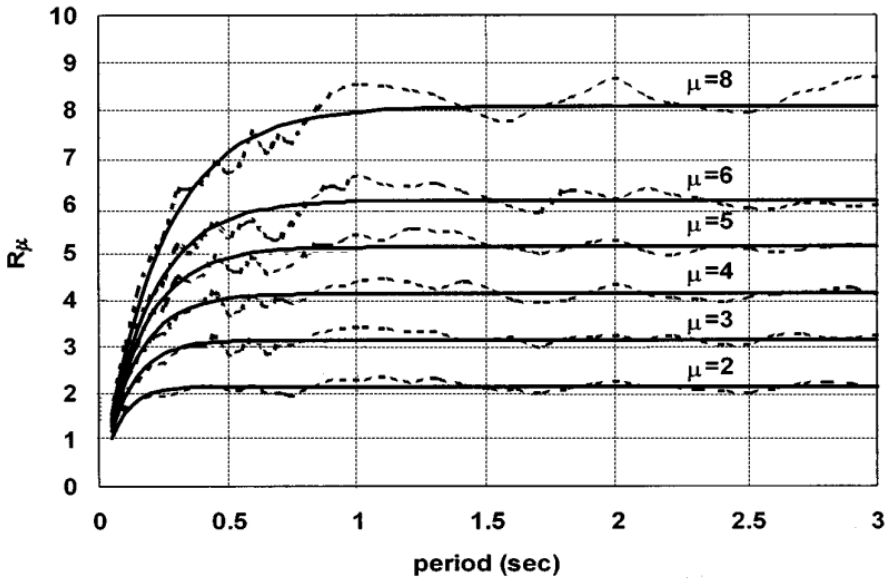

Figure 5-6: Fitness of the regressed $R-\mu$ relationship for elastoplastic models
Picture taken from Lee & Han [28]

Comparison

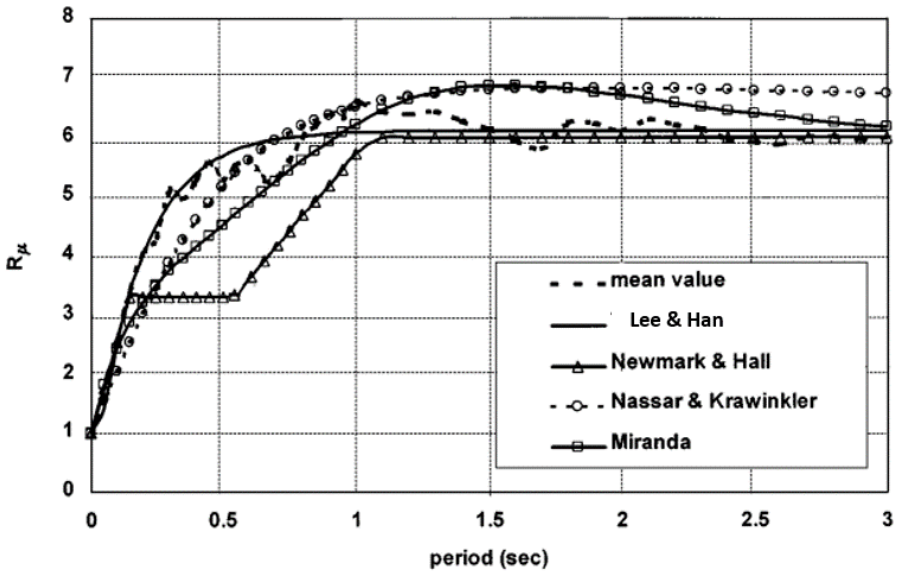

Figure 5-7: Comparison of R_μ functions for a constant target ductility $\mu = 6$
Picture taken from Lee & Han [28]

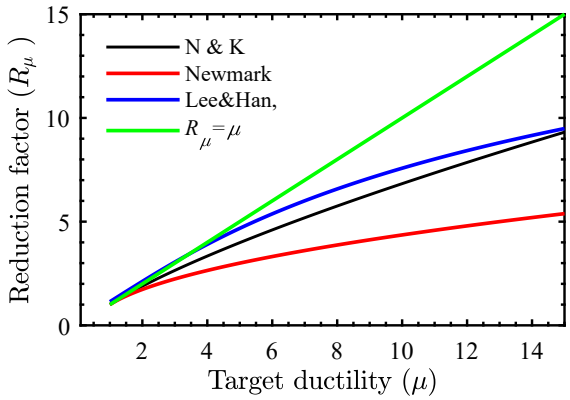

Figure 5-8: T=0.4s, Reduction factor as a function of target ductility

The three proposals were compared by Lee & Han and are reproduced in the Figure 5-7. The variation in the formulations in the short period region (period range of 0.2-0.6s, also referred to as the constant acceleration region) was found to be the largest. The period 0.4s lies in between the two endpoints. Furthermore, this region is also the region where the fundamental period (=0.4s) of the benchmark substructure model (Model-B in Section 5.2

(Table 1)) lies. Therefore, for comparison, this period was chosen as an example to compare the different formulations as a function of the target ductility which is a varying parameter in this chapter of the thesis. The reduction factors obtained from the three methods are plotted in Figure 5-8 considering a fundamental period as 0.4s and elastoplastic hysteretic behaviour. From both the figures, it may be concluded that the Newmark method provides the smallest estimates of the reduction factors throughout the period range and ductility ranges considered.

Summary

While these ductility reduction factors were proposed to develop the inelastic response spectra to estimate the design base shear for elastoplastic models, in this study, these ductility reduction factors are used to estimate the approximate peak spectral acceleration of the substructure as a function of the obtained period and the target roof displacement ductility. The acceleration reduction ratio R_a is defined as the ratio of the peak inelastic acceleration to the peak elastic acceleration which can be computed using the inverse of the ductility reduction ratio [24] as shown in Equations 5.9-5.10. For this study, from hereon, the two most conservative methods -Newmark and N&K methods (Figure 5-8) are considered and discussed for the estimation of peak substructure acceleration using the R-factor approach.

$$R_a = \frac{A_{eq1}}{A_1} \tag{5.9}$$

$$R_a = \frac{1}{R_\mu} \tag{5.10}$$

5.2.2 Inelastic accelerations: RSA & Equivalent linearisation

An alternative simplified theory for estimation of the peak inelastic response of any bilinear system is the equivalent linearisation method proposed by Kasai et al. [9], [10]. It uses mathematical expressions as a function of the dynamic properties of the system to consider the effect of period shift as well as the effect of damping by evaluating the dissipated energy. The multistorey building is idealised as an SDOF (single-degree of freedom) model and the target ductility is iterated to obtain a more accurate ductility value which is a function of the achieved damping and the secant stiffness ratio which in turn is a function of the ductility. The proposed reduction in displacement R_d and acceleration (or force) R_a depends on the stiffness of the frame, braces and the energy dissipation devices.

The equivalent stiffness (K_{eq}) and equivalent damping ratio (h_{eq}) of the system are obtained using the equivalent linearisation procedure. For each of the participating modes (where i = mode number), a starting value of ductility ratio (target ductility) μ_{ti} is assumed and h_{eqi} and the equivalent stiffness ratio K_{eqi}/K_{1i} are iterated using Equations 5.11-5.14 until μ_i converges, where K_{1i} is the initial stiffness, D_h is the reduction factor to adjust the damping ratio from the base damping ratio h_{oi} (5% in this study) for periods less than 2s, and the subscript (j) is the jth step of the iteration [5], [9]. The equivalent (secant) period T_{eqi} is then computed using Equation 5.15 [9].

$$K_{eqi}/K_{1i} = 1/\mu_i + (1 - 1/\mu_i)K_{2i}/K_{1i} \tag{5.11}$$

$$h_{eqi} = h_{oi} + \frac{2(K_{1i}/K_{2i})}{\pi\mu_i} \ln \frac{K_{1i}/K_{2i} + \mu_i - 1}{(K_{1i}/K_{2i})\mu_i^{K_{2i}/K_{1i}}} \tag{5.12}$$

$$D_{hi} = \sqrt{(1+25h_{oi})/(1+25h_{eqi})} \tag{5.13}$$

$$\mu_{i(j)} = \mu_{ti(1)} D_{hi(j-1)} / \sqrt{K_{eqi(j-1)}/K_{1i}} \tag{5.14}$$

$$T_{eqi} = T_i \sqrt{K_{1i}/K_{eqi}} \tag{5.15}$$

For each of the participating modes, the reduction in displacement R_d can then be computed as a function of the periods T_{eqi} and T_i using Equations 5.16-5.18 [9] depending on the regions of the spectrum the periods lie. This method is labelled and referred to as the 'Kasai' method hereon.

1. For T_i and T_{eqi} in the constant acceleration region:

$$R_{di} = D_{hi}\frac{T_{eqi}}{T_i}\left(\frac{T_{eqi}+T_i}{2T_i}\right) \tag{5.16}$$

2. For T_i in the constant acceleration region and T_{eqi} in the constant velocity region, where T_c is the corner period (in this study, T_c=0.52s as described later in Section 5.3.1):

$$R_{di} = D_{hi}\frac{T_{eqi}}{T_i}\left[\frac{T_c}{T_i} - \frac{(T_c/T_i - 1)^2}{2(T_{eqi}/T_i - 1)}\right] \tag{5.17}$$

3. For T_i and T_{eqi} in the constant velocity region:

$$R_{di} = D_{hi}\frac{T_{eqi}}{T_i} \tag{5.18}$$

The reduction in acceleration may then be computed using Equation 5.19 [9], [10]. For comparison of response with the other methods based on the R-factor approach, $R_{\mu i}$ from this method may then be defined as the inverse of the reduction in acceleration as given in Equation 5.20.

$$R_{ai} = R_{di}\left(\frac{T_i}{T_{eqi}}\right)^2 \tag{5.19}$$

$$R_{\mu i} = \frac{1}{R_{ai}} \tag{5.20}$$

5.3 Analysis models: Single-storey substructures

First, the peak substructure response of simple 60m spanned single-storey analysis models are discussed in this section to compare the response from each of the response estimation methods introduced in Section 5.2.1 and Section 5.2.2.

5.3.1 Design acceleration response spectrum

As the R-factor approach is primarily practised in the USA, a site with high seismic hazard from the southern California region was chosen to develop a 5% damped DBE (design basis earthquake) acceleration spectrum (Figure 5-10) using the ASCE 7-16 Section 11.4 procedure [2]) with a short period spectral acceleration (as shown in Figure 5-9 and defined below) $S_{DS} = 1.4g$ adopted from the weighted mean specified in Table C22-2 of ASCE 7-16 [2], and a spectral response acceleration at a period of 1s $S_{D1} = 0.73g$ adopted from the weighted mean specified in Table C22-3 of ASCE 7-16 [2], and a long-period transition period $T_L = 8s$ obtained from the Figure 22-14 of ASCE 7-16 [2]).

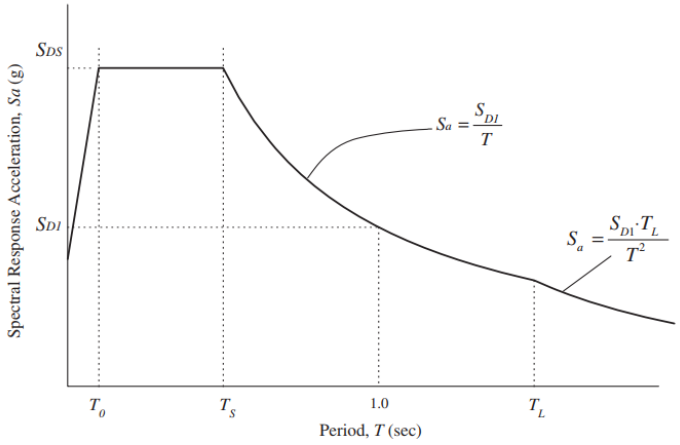

Figure 5-9: Defining the design response spectrum as per ASCE-7 [2]

where,

S_{DS} = the design spectral response acceleration parameter at short periods;

S_{D1} = the design spectral response acceleration parameter at a 1s period;

$T_0 = 0.2(S_{D1}/S_{DS})$;

$T_S = S_{D1}/S_{DS} = 0.52$s;

T_L = long-period transition period;

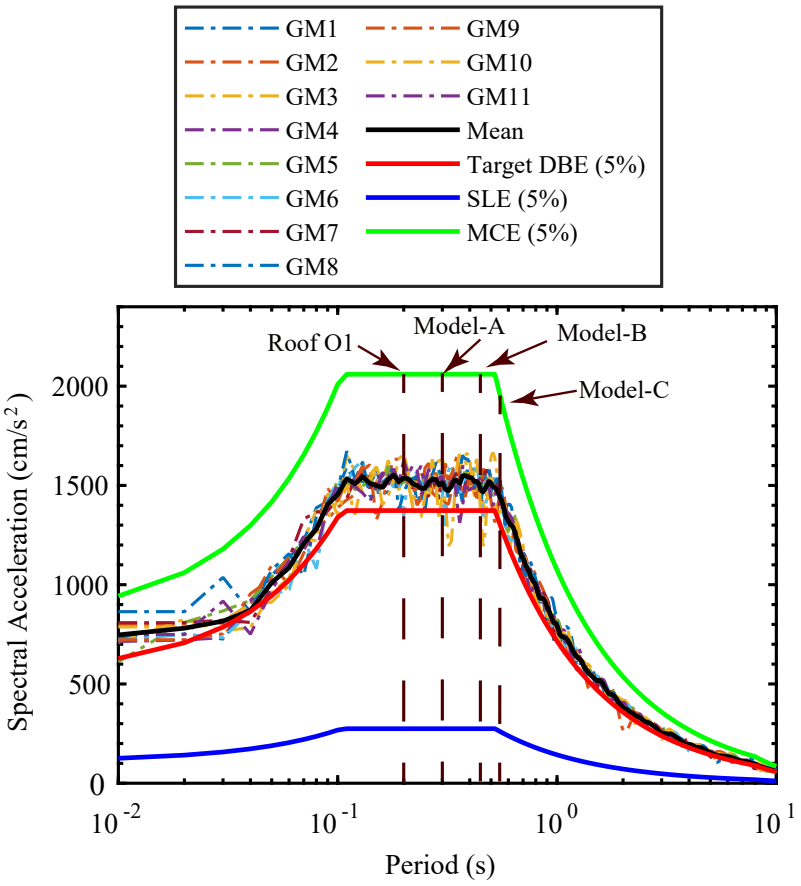

Figure 5-10: Target design spectrum and earthquake levels & fundamental periods of single-storey combined models

5.3.2 BRBF substructure model

The 60m spanned substructure has one storey 5m high and the roof dead load was assumed to be 2kPa (considering a structural weight of about 1kg/m^2 for every meter of span [29], a 15% allowance for the connections, and 1.3kPa nonstructural dead load). It was assumed that all the lateral forces are resisted by the buckling-restrained braces (BRBs [30]) placed along the perimeter in a diagonal configuration, and so in the 3-d ETABS [31] analysis substructure model shown in Figure 5-11(a), all the beams and columns were modelled using elastic beam and column elements with the section sizes listed in Table 5.1. The roof is modelled as a rigid mass in the substructure model. The BRBs for the substructure (Figure 5-11) were designed for the vertically distributed forces obtained as per ASCE 7-16 [2], where h_x is the height from base to level x and k is taken as 1 (Equation 5.23), S_a is the design acceleration obtained for the code-defined approximate fundamental period $T_a = C_t \times h_n^x$ ($C_t = 0.073$ and $x = 0.75$ for steel BRBFs as per Table 12.8.1 of ASCE 7-16 [2]), R was taken as 8 (as recommended for BRBFs as per Table 12.2.1 of ASCE 7-16 [2]) in Equation 5.21, I_e was assumed as 1, giving a base shear ratio $C_b = 0.2$, V_x is the storey shear, BRB V_x is the storey shear resisted by the BRBs (in this study 100%) and BRB V_{ix} is the storey shear resisted by each BRB as given in Table 5.2.

$$V = \frac{S_a W}{R/I_e} \tag{5.21}$$

$$F_x = C_{vx} V \tag{5.22}$$

$$C_{vx} = \frac{w_x {h_x}^k}{\sum_{i=1}^{n} w_i {h_i}^k} \tag{5.23}$$

Three combined models were designed to include substructures with different BRB design yield displacements. Note that for design of the substructure frame sections and the BRBs, the substructure models were adopted to represent the 3-d combined model as a lumped mass SDOF model shown in Figure 5-11(a). This idealisation enables the substructures of gridshell domes to be designed using the same code based simplified design procedures as prescribed for regular multistorey buildings. The substructure model for Model-B (benchmark model) is shown in Figure 5-11(a) and was designed with a

standard BRB yield drift ratio of 1/750 [30]. A second model (Model-A) was designed for the same design base shear with a shorter BRB yield displacement of 0.06% such that the fundamental period is shorter and lies in the constant-acceleration region of the spectrum (Figure 5-10) and a third model (Model-C) was designed with a longer BRB yield displacement of 0.2% with the fundamental period in the constant-velocity region as given in Table 5.2. The axial force-displacement of BRBs were determined following the design guidelines by Takeuchi and Wada [30] and the BRB parameters are given in Table 5.2. In the analysis FE model, the BRBs have been modelled as links [31], [32] with bilinear hysteretic characteristics and a post-yield stiffness ratio (p) of 2% typical of BRBFs [30], [33].

In US design practise, BRBFs are typically modeled with columns that are continuous over the frame height and with the idealisations that columns have pinned bases and that beams and braces have pinned end connections. Nevertheless, these beam end connections do have the potential for significant moment transfer, especially when gusset plates are present to connect the BRBs to the column and beam joints [33]. However, the portion of the shear force of the storey that is resisted by these mechanisms is generally small in the elastic range but can contribute to a post-yield stiffness of 5-10%. On the other hand, in countries such as Japan, due to the relatively cheap fabrication costs of moment resisting frames (MRFs) using box columns and high-strength steel [30], moment frames are often adopted as lateral force resisting systems (also known as dual systems) that remain elastic even after the dampers yield. Consequently, the post-yield stiffness of such substructures are much higher than those of BRBFs designed using pinned connections in the USA. Therefore, to investigate and validate response estimation methods for models with high post-yield stiffness, additional substructure models with p=10% and 25% were created, keeping the yield displacements the same in all models in the same series. The $p = 25\%$ models are representative of BRBF substructures in Japan [30] that adopt rigid moment connections in the supporting frames such that the stiffness provided by the damper to the stiffness of the supporting moment frame ratio (referred to as the 'K_d/K_f' ratio [30]) has a typical value of '$K_d/K_f = 3$' [7], [30]. The $p = 10\%$ models are representative of substructures with post-yield stiffness in between the $p = 2\%$ and $p = 25\%$ models. These

are typically seen in substructures without MRFs but with additional post-yield stiffness contributions from connections, gusset plates (as discussed in the previous paragraph) and other non-structural components like the parapets. Additional models with $p = 0\%$ were also constructed to validate and confirm the approaches proposed for elastoplastic SDOF systems in Section 5.2.1.

Table 5.1: $L60$: Substructure model data

(a) Storey heights and seismic weights

Storey	Height (m)	Weight (kN)
RFL	5	6064

(b) Section sizes (σ_y=325MPa)

Member	Section Shape	Section Size (mm)
Column	SHS	450×450×25

Table 5.2: Equivalent Lateral Forces: Proportioning BRBs using $R = 8$

Storey	h (m)	kN W_x	kN V_x	kN BRB V_x	kN BRB P_i	mm δ_y	kN/m BRB K_{eqi}	(m) L_t	MPa σ_y	mm^2 A_c
Model-A ($T_1 = 0.3s$)										
RFL	5	6064	1061	1061	54	1.85	29160	6.4	90	600
Model-B ($T_1 = 0.4s$)										
RFL	5	6064	1061	1061	54	4.12	13125	6.4	235	230
Model-C ($T_1 = 0.5s$)										
RFL	5	6064	1061	1061	54	6.17	8748	6.4	235	230

where P_i=Yield axial force, δ_y=Yield axial deformation,K_{eqi}=Equivalent axial stiffness, L_t=total BRB length and A_c=Area of core in plastic zone [30]

5.3.3 Roof model

The double-layered dome was designed for a span of 60m and a half subtended angle (θ) of 30°. The lattice member sizes and vertical offsets (d) between the section centerlines are listed in Table 5.3. For simplicity, the double-layer lattice (Figure 5-11 (b)) was modelled using equivalent beams with out-of-plane stiffness modification factors [18] with moment connections and pinning the roof lattice perimeter nodes. As discussed in Chapters 2, 3 and 4, this dome model was used to identify the roof modes and is denoted as the 'roof model'. The fundamental period of the roof (T_R) was found to be 0.22s with the roof exhibiting the anti-symmetric O1 mode shape [8], [19].

Table 5.3: 60m roof models: Member section sizes (σ_y=325MPa)

Dead Load (DL) (kPa)	Double-layer beam (mm)	offset d (cm)	Single-layer beam (roof member) (mm)	m	Tension beam (mm)
2	$2\times\phi 165.2\ t7.1^*$	150	$\phi 307.5\ \ t7.5^*$	50.1	$\phi 816\ \ t16$

* m = Out-of-plane stiffness modification factor

5.3.4 Modes of combined models

The combined analysis models were then constructed combining the roof model and substructure model. As discussed in the design example of Section 2.5, the design of roof members were checked by performing NLRHA analysis on the combined model using the load combination of 1.2DL+EQ (as per Section 2.3.6 of ASCE-7-16 [2]) and ground motions specified in Section 5.3.5 to check the member forces against their design strength as per the guidelines in AISC 360-16 [34]. The roof geometry was modelled in *Grasshopper* [35] and imported to ETABS [31] for analysis. The roof member beams in ETABS were modelled as 'frame' objects which are general three-dimensional beam elements [32].

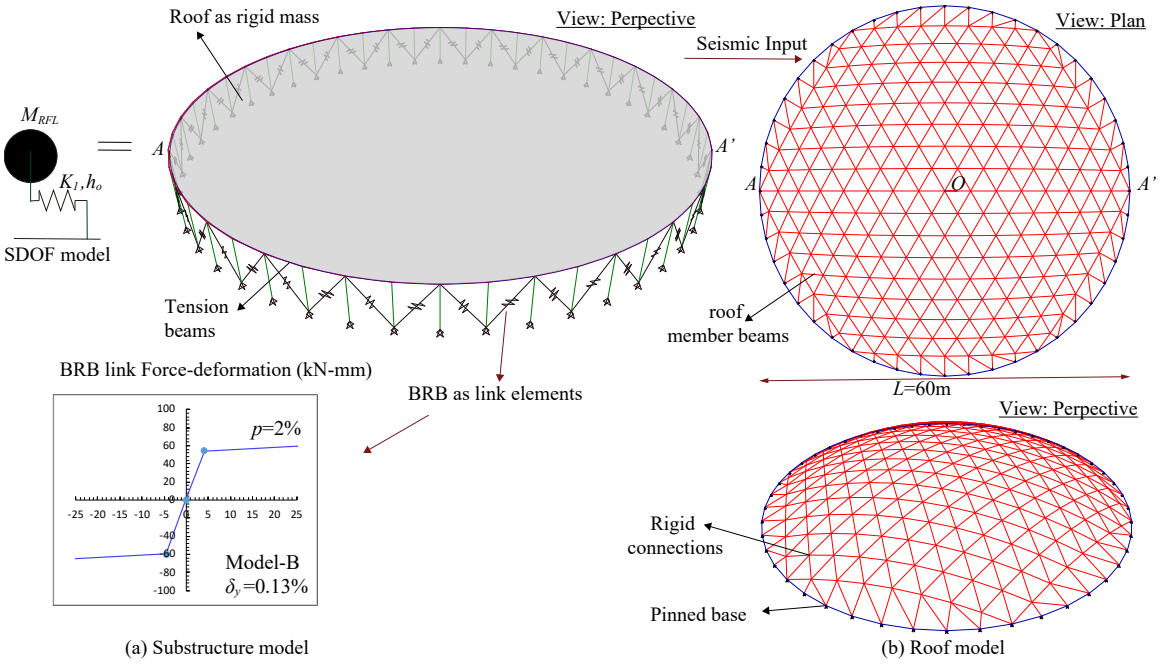

Figure 5-11: Single-storey substructure model and roof model

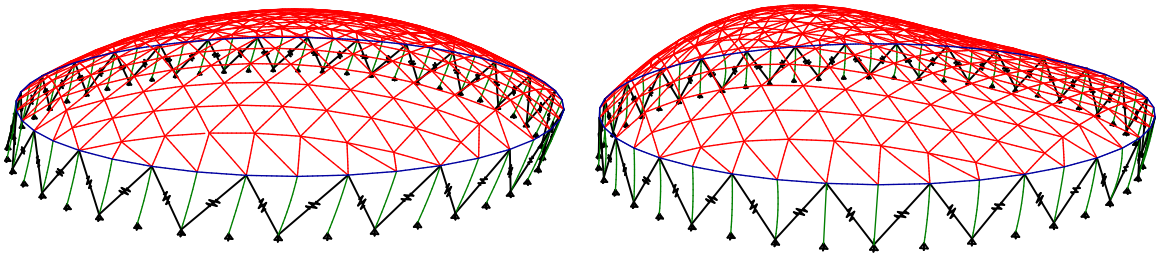

Mode-1: O1+T1 (0.47s), Γ_{x1}=99.5%

Mode-2: O1-T1 (0.22s), Γ_{x1}=0.4%

Figure 5-12: Model-B: Combined model mode shapes

The periods and mass participation of the first two modes (Γ_x in the direction of seismic input) of the combined model (Model-B) are shown in Figure 5-12. The first mode is the substructure T1 mode oscillating in-phase (labelled as 'O1+T1') with the roof's dominant O1 mode [19]. The second mode exhibits the two modes oscillating out-of-phase (labelled as 'O1-T1') . This implies that only the O1 roof mode governs the dynamic response and the contribution of higher roof modes (like the O2, O2.5 or I mode is negligible. This is due to the fact that the substructure period ratio is long and therefore has interaction with only the roof's dominant O1 mode. The effects of substructure stiffness and period ratio on the dominant modes have been discussed in detail in previous studies [18], [19].

5.3.5 Input ground motions

11 natural ground motions were selected from the Pacific Earthquake Engineering Center strong motion database [36]. An initial suite was obtained using a standard search criteria of minimum magnitude of 6.5, a maximum magnitude of 7.5, and maximum shear velocity of 400m/s. 11 of the selected ground motions (Horizontal-1 direction) listed in Table 5.4 were then spectrally matched to the design spectrum (in accordance with Section 16.2 of ASCE 7-16 [2]) such that the average of the spectra for the suite equals or exceeds 110% of the 5% target design spectrum over the period range of 0.2T1-1.5T1 where T1 was considered as 0.4s (the fundamental period of benchmark Model-B). The response spectra of the 11 matched ground motions and the average of their spectra (labelled as 'Mean') are shown in Figure 5-10.

Table 5.4: Input ground motions from PEER database [36]

No.	Earthquake*	Year	Station name	M	R_{jb} (km)	PGA (g)
1	Trinidad	1980	Rio Dell Overpass E-Ground	7.20	76.06	0.16
2	Spitak Armenia	1988	Gukasian	6.77	23.99	0.20
3	Loma Prieta	1989	Emeryville; Pacific Park	6.93	76.87	0.25
4	Loma Prieta	1989	Fremont - Emerson Court	6.93	39.66	0.19
5	Loma Prieta	1989	Hayward - BART Sta	6.93	54.01	0.16
6	Loma Prieta	1989	Sunnyvale - Colton Ave.	6.93	23.92	0.21
7	Northridge-01	1994	LA - 116th St School	6.69	36.39	0.21
8	Northridge-01	1994	LA - Baldwin Hills	6.69	23.50	0.24
9	Northridge-01	1994	LA - Cypress Ave	6.69	28.98	0.22
10	Northridge-01	1994	LA - N Faring Rd	6.69	12.42	0.28
11	Northridge-01	1994	LA - Obregon Park	6.69	35.43	0.36

R_{jb} = closest horizontal distance between the vertical projection of the rupture plane and recording station, M = moment magnitude,

PGA = unscaled peak ground acceleration

*These records were obtained from the NGA-West2 online ground motion database tool

For NLRHA performed on the combined models using these spectral matched waves, Rayleigh damping of 5% was assigned to the first and second mode and the analysis was performed using the integration approach using the Hilber-Hughes-Taylor (HHT) method [31], [32]. Two additional levels of ground motion intensity were considered to investigate the response at maximum-considered earthquake (MCE) level (1.5 $\times$ DBE level as prescribed by the ASCE-7 [2]) and the serviceability level (SLE = 0.2 $\times$ the DBE level). As ASCE does not have a defined SLE design level, for this study, the SLE spectrum spectrum was defined by retaining the shape of the DBE spectra as is common practice in countries like Japan and New Zealand, and then scaling it by 0.2 (following the average ratio between the SLE and DBE design spectra of typical seismic codes as reviewed by Chandler et. al. [37]).

5.3.6 Storey Drifts

The mean peak inter-storey drifts and mean residual inter-storey drifts for the substructure models are given in Figure 5-13. For structures having four stories or less, Table 12.12-1 [2] prescribes an allowable storey drift of 2.5% for DBE level and 4% for MCE level. When the initial damping ratio h_o =5% is assigned, the obtained mean storey drifts are within the permissible ASCE limits for both EPP models as well as for models with post-yield stiffness. The EPP models show significant residual deformations under the design-based excitations. Typical values of mean residual drift are about 1% for EPP models and 0.4% for p=2% models under the DBE level. These values increase to 2.5% and 0.6% under the MCE level. If 0.5% residual drift is assumed to be the limit beyond which the structures are no longer practically usable [38], then the design of EPP structures according to ASCE 7-16 may result in structures that do not meet this immediate occupancy performance level under DBE level excitation.

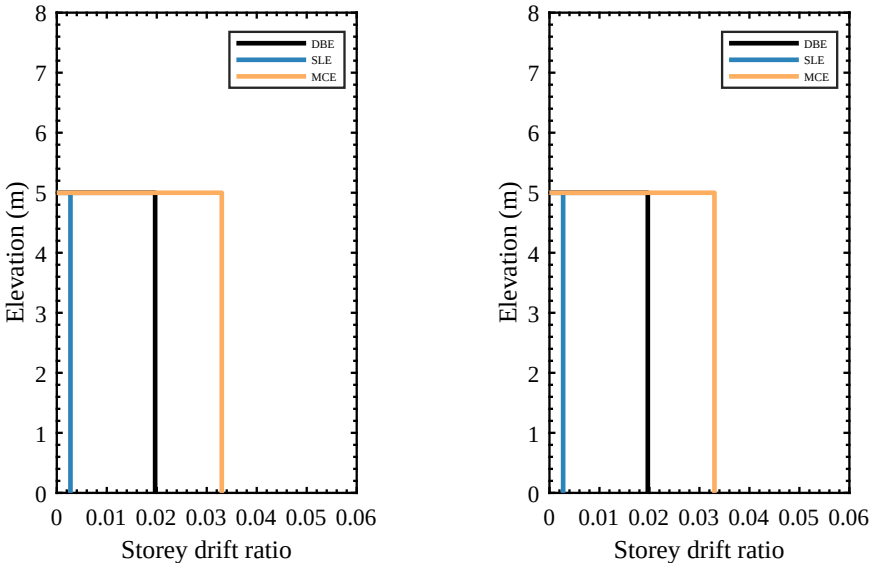

(a) p=0% (b) p=2%

(i) Mean Peak Inter-storey drift ratios

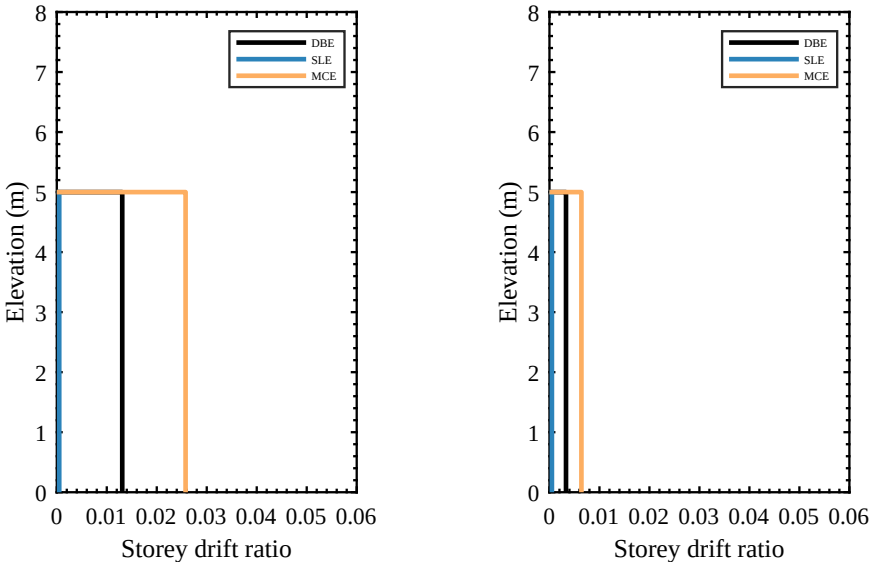

(a) p=0% (b) p=2%

(ii) Mean Residual storey drift ratio

Figure 5-13: Substructure drifts of benchmark model (Model-B)

5.3.7 BRB ductility demands

As the BRBs are the only source of lateral resistance in the substructure, to confirm the BRBs' performance and design, the maximum ductility demands of a lower BRB oriented almost completely in the input x-direction was computed as the maximum negative displacement divided by the yield displacement. The ductility demands for benchmark Model-B were within expected ductility demand for DBE level earthquake around 25 [39]. The ductility demands for Model-A were higher and may not be practically realistic. Nevertheless, the analyses were performed to investigate the performance of short-period substructures with alternative dampers, such as oil dampers with shorter yield displacements in large-ductility regimes.

$$\mu_{BRB} = \frac{\delta_{link}}{\delta_y} \tag{5.24}$$

Table 5.5: Maximum BRB ductility demands (p=2% models)

	μ_{BRB}		
	SLE	DBE	MCE
$h_o = 5\%$			
Model-B ($\delta_y = 0.13\%$)	2	15	25
Model-A ($\delta_y = 0.06\%$)	2	25	44
Model-C ($\delta_y = 0.2\%$)	2	11	19

5.3.8 Comparison of peak substructure response

For each of the three substructure models, the elastic design spectral acceleration (S_{a1}) was used to obtain the elastic base shear (V_1) and then extrapolate the maximum elastic substructure roof displacement (D_1) at the substructure roof level (point A of Figure 5-11(a)) from the initial stiffness (K_1) as shown in Equation 5.25. The initial stiffness was calculated using the idealised bilinear base-shear and roof displacement relationship obtained from the modal pushover analysis using the fundamental mode. This relationship for the elastoplastic models are shown in Figure 5-14.

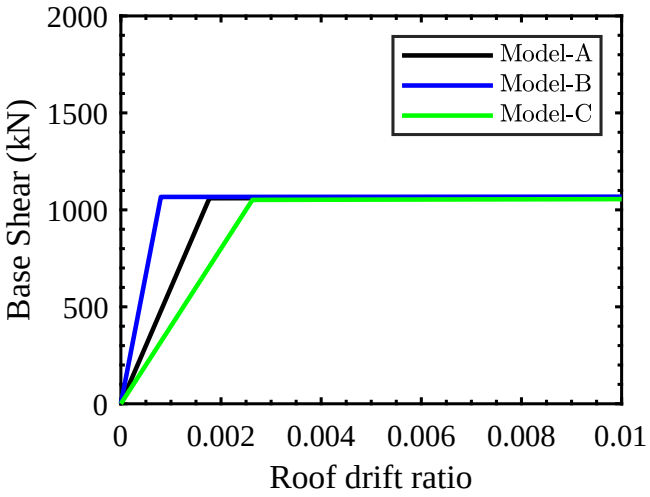

Figure 5-14: Idealised base shear and roof drift ratio relationship

The maximum acceleration at the roof level (point A of Figure 5-11(a)) A_1 of the substructure is then obtained from the corresponding roof displacement and the fundamental period and the response spectrum (S_{a1}) as shown in Equation 5.25. The reduction factors (R_μ and R_a) were then computed following Equations 5.3-5.6 from the target ductility μ_t using Equations 5.26 and Equations 5.10. For the equivalent linearisation approach, Equations 5.11-5.20 were used. The mean responses obtained from the NLRHA performed on the combined models were also used to obtain the mean displacement ductility and the reduction factor using Equations 5.27-5.28.

$$V_1 = M_1 S_{a1} \quad D_1 = V_1/K_1 \quad A_1 = D_1 \omega^2 \tag{5.25}$$

$$\mu_t = D_1/D_y \tag{5.26}$$

$$\mu_{NLRHA} = D_{mean}/D_y \tag{5.27}$$

$$R_{\mu-NLRHA} = V_1/V_{mean} \tag{5.28}$$

To compare the peak substructure responses from all the methods against the NLRHA results, the reduction in acceleration $R_a = A_{eq}/A_1$ and R_μ is plotted against the displacement ductility μ_{NLRHA} for Model-B in Figure 5-15. When the structure is subjected to SLE level earthquakes, the obtained ductility values are close to 2 with a small reduction in response. When the intensity of the earthquake is increased to DBE level, the mean ductility values increase to a range of 8-14 depending on the post-yield stiffness. For MCE levels, the values increase further to 15-20, but the reduction in response (R_a) is not linearly proportional to the increase in ductility. The results in Figure 5-15 exhibit a nonlinear relationship between R_μ and μ that is similar to the nonlinear R_μ and μ curve proposed by Newmark for short-period structures in Figure 5-8. The results also suggest that for short period structures, the actual ductility reduction factors (from NLRHA) do not strictly follow either the equal energy (Equation 5.3) or the equal displacement rule (Equation 5.4) but lie between the two Newmark factors as can be seen from the dotted lines in Figures 5-15(a) and (b). Therefore, for short-period models with low post-yield stiffness ($p < 10\%$), the Newmark method provides the most conservative estimates of the acceleration if compared to those obtained from the NLRHA.

For a detailed comparison between the estimation methods, the errors in estimation of the response against the NLRHA response for the DBE levels for the benchmark substructure model (Model-B) have been shown in Table 5.6. As the post-yield stiffness increased, the reduction ratio R_a obtained from the NLRHA and Kasai method increased but the R-factor methods estimated lower peak accelerations assuming an elastoplastic response. The errors can be attributed to the underlying assumptions of elastoplastic models in the R-factor methods. Furthermore, the target ductility value (Equation 5.26) used in the R-factor approaches may not be equal to the achieved ductility value (Equation 5.27) which further contributes to the errors. For the N&K method, even though modified formulas exist for higher post-yield stiffness models (Equation 5.6 for $p = 10\%$, the

resulting values severely underestimated the reduction factor. The main aim behind the N&K proposed formulations is to estimate the reduction in elastic base shear to achieve the target ductility. Therefore, as the post-yield stiffness increases, a smaller yield strength and a larger reduction in the base shear are proposed to achieve the same target ductility. However, in this study, the yield strength was kept constant using a single reduction factor of $R = 8$. In such cases, an increase in post-yield stiffness leads to an increased acceleration and the N&K method, therefore, does not accurately estimate the peak inelastic response for models with higher post-yield stiffness $p > 2\%$ in this study.

The Newmark method is conservative for short-period structures with elastoplastic response (with 39% overestimation of the R_a value for $p = 0\%$ in Table 5.6), the Newmark method remained conservative for models with higher post-yield stiffness as well (Figure 5-15(b) and (c) and Table 5.6). As the post-yield stiffness further increased to 25%, the Newmark method estimates became unconservative with the error increasing to 31%. This confirms that even though Newmark method has been proposed for elastoplastic systems, it may be applied for short-period structures with post-yield stiffness of up to 10%. Finally, among the discussed estimation methods, Kasai's approach provides the most accurate estimate of the response to that obtained from NLRHA for all cases as this approach is more mathematical and less empirical making it applicable to any bilinear system. The actual ductility values and damping ratios are estimated as given in Tables 5.7-5.10, leading to better accuracy in response estimation.

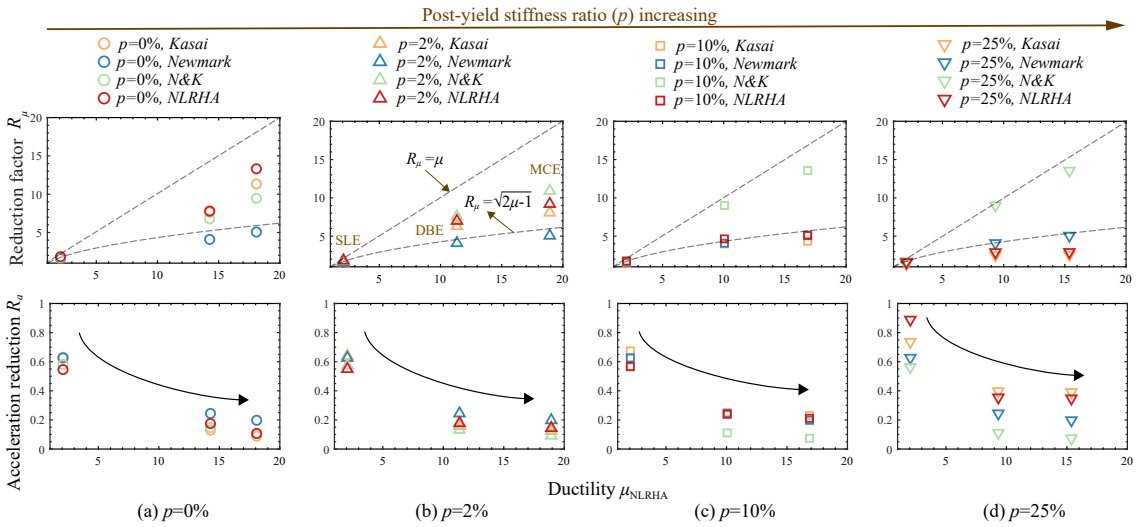

Figure 5-15: Substructure of Model-B: Reduction factors R_μ and R_a as functions of achieved displacement ductility μ_{NLRHA}

Table 5.6: Substructure of Model-B: Errors in estimation of DBE response

	% error in R_μ estimation				% error in R_a estimation			
Method	$p=0\%$	$p=2\%$	$p=10\%$	$p=25\%$	$p=0\%$	$p=2\%$	$p=10\%$	$p=25\%$
Newmark	-47	-41	-12	+40	+39	+37	+2	-31
N&K	-13	+8	+93	+200	-16	-26	-53	-68
Kasai	-2	-10	-14	-13	-25	-10	+5	+12

where a $+$ve % error indicates the estimated value is more than the NLRHA value.

Table 5.7: Substructure models: Kasai method's equivalent linearisation results, *p=0%*

	h_{eq1}	K_{eq1}/K_1	D_h	R_d	R_a	μ_{t1}	T_1	T_{eq1}	T_R
Model-A-SLE	0.12	0.57	0.75	1.16	0.66	1.8	0.30	0.40	0.23
Model-A-DBE	0.51	0.08	0.41	2.34	0.18	8.8	0.30	1.08	0.23
Model-A-MCE	0.58	0.04	0.38	3.17	0.13	13.2	0.30	1.51	0.23
Model-B-SLE	0.12	0.57	0.75	1.11	0.63	1.8	0.45	0.60	0.23
Model-B-DBE	0.51	0.08	0.41	1.66	0.13	8.9	0.45	1.61	0.23
Model-B-MCE	0.58	0.04	0.38	2.20	0.09	13.3	0.45	2.25	0.23
Model-C-SLE	0.11	0.59	0.77	1.00	0.59	1.7	0.55	0.72	0.23
Model-C-DBE	0.49	0.09	0.41	1.40	0.12	8.4	0.55	1.88	0.23
Model-C-MCE	0.56	0.04	0.39	1.83	0.08	12.7	0.55	2.61	0.23

Table 5.8: Substructure models: Kasai method's equivalent linearisation results, *p=2%*

	h_{eq1}	K_{eq1}/K_1	D_h	R_d	R_a	μ_{t1}	T_1	T_{eq1}	T_R
Model-A-SLE	0.12	0.58	0.76	1.15	0.67	1.76	0.30	0.40	0.23
Model-A-DBE	0.44	0.10	0.43	2.15	0.22	8.82	0.30	0.94	0.23
Model-A-MCE	0.47	0.07	0.42	2.70	0.18	13.23	0.30	1.18	0.23
Model-B-SLE	0.12	0.58	0.75	1.11	0.64	1.77	0.45	0.59	0.23
Model-B-DBE	0.44	0.10	0.43	1.55	0.16	8.87	0.45	1.41	0.23
Model-B-MCE	0.47	0.07	0.42	1.90	0.12	13.31	0.45	1.77	0.23
Model-C-SLE	0.11	0.60	0.78	1.00	0.60	1.69	0.55	0.71	0.23
Model-C-DBE	0.44	0.11	0.43	1.31	0.14	8.43	0.55	1.67	0.23
Model-C-MCE	0.46	0.07	0.42	1.60	0.11	12.64	0.55	2.09	0.23

Table 5.9: Substructure models: Kasai method's equivalent linearisation results, *p=10%*

	h_{eq1}	K_{eq1}/K_1	D_h	R_d	R_a	μ_{t1}	T_1	T_{eq1}	T_R
Model-A-SLE	0.11	0.62	0.78	1.13	0.69	1.76	0.30	0.39	0.23
Model-A-DBE	0.31	0.19	0.51	1.78	0.33	8.82	0.30	0.70	0.23
Model-A-MCE	0.30	0.15	0.51	2.06	0.31	13.23	0.30	0.78	0.23
Model-B-SLE	0.11	0.61	0.77	1.10	0.67	1.78	0.45	0.58	0.23
Model-B-DBE	0.31	0.19	0.51	1.34	0.25	8.88	0.45	1.04	0.23
Model-B-MCE	0.30	0.15	0.51	1.52	0.23	13.31	0.45	1.16	0.23
Model-C-SLE	0.10	0.64	0.79	1.00	0.63	1.69	0.55	0.69	0.23
Model-C-DBE	0.31	0.19	0.51	1.15	0.22	8.43	0.55	1.25	0.23
Model-C-MCE	0.30	0.16	0.51	1.30	0.20	12.64	0.55	1.40	0.23

Table 5.10: Substructure models: Kasai method's equivalent linearisation results, *p=25%*

	h_{eq1}	K_{eq1}/K_1	D_h	R_d	R_a	μ_{t1}	T_1	T_{eq1}	T_R
Model-A-SLE	0.10	0.68	0.82	1.09	0.74	1.76	0.30	0.37	0.23
Model-A-DBE	0.20	0.33	0.61	1.44	0.48	8.79	0.30	0.52	0.23
Model-A-MCE	0.19	0.30	0.63	1.61	0.48	13.19	0.30	0.55	0.23
Model-B-SLE	0.10	0.68	0.81	1.08	0.74	1.77	0.45	0.55	0.23
Model-B-DBE	0.20	0.33	0.61	1.20	0.40	8.87	0.45	0.78	0.23
Model-B-MCE	0.19	0.30	0.63	1.31	0.39	13.30	0.45	0.82	0.23
Model-C-SLE	0.09	0.70	0.83	0.99	0.69	1.69	0.55	0.66	0.23
Model-C-DBE	0.21	0.34	0.61	1.05	0.35	8.43	0.55	0.95	0.23
Model-C-MCE	0.19	0.30	0.62	1.13	0.34	12.64	0.55	1.00	0.23

5.4 Peak roof response

As discussed in the previous chapters, the substructure-roof interactions for single-storey structures are defined by the amplification factors F_{H1} and F_{V1} [19] that depend on the mass (R_M) and period (R_T) ratios [19] given in Equation 3.1. These are characterised as ratios of the effective modal mass (M_{eq}) and fundamental period (T_1) of the substructure model, which includes the roof mass, relative to the total roof mass (M_R) and period of the (dominant) fundamental roof O1 mode (T_R) [18], [19].

5.4.1 Inelastic T1 mode period ratios

In previous studies [5], [8], for Kasai's equivalent linearisation approach, the period ratios were computed using the substructure's inelastic periods R_{Teq1} [8] and the rationale behind this assumption has not been confirmed yet. Therefore, to investigate the relationship between the amplification factors and the inelastic period ratios, the vertical amplification factors computed from the mean NLRHA response divided by the peak substructure acceleration $F_V = {}_cA_{Vmax}/{}_sA_{Heq}$ have been plotted against the elastic (R_{T1} in Equation 5.29) and inelastic (R_{Teq1}) period ratios (Equation 5.30).

$$R_{T1} = \frac{{}_sT_1}{{}_rT_R} \tag{5.29}$$

$$R_{Teq1} = \frac{{}_sT_{eq1}}{{}_rT_R} \tag{5.30}$$

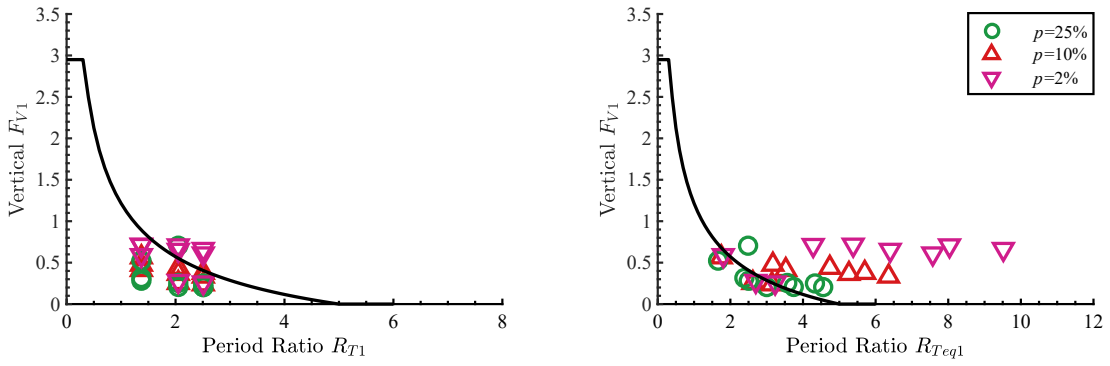

(a) Period ratio calculated using T_1 (b) Period ratio calculated using T_{eq1}

Figure 5-16: Vertical amplification factors w.r.t period ratios

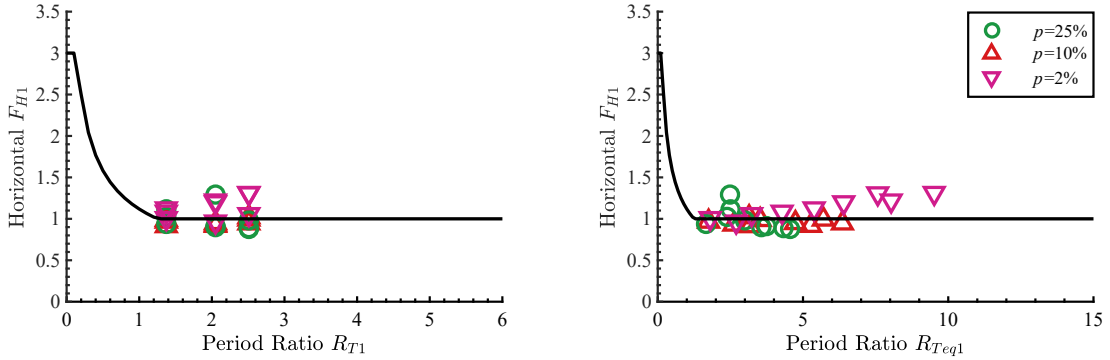

(a) Period ratio calculated using T_1 (b) Period ratio calculated using T_{eq1}

Figure 5-17: Horizontal amplification factors w.r.t period ratios

It was observed that the obtained amplification factors plotted against the elastic period ratios (Figures 5-16(a) and 5-17(a)) are in better agreement as opposed to the plots against the inelastic period ratios (Figures 5-16(b) and 5-17(b)). The largest errors between the proposed curves and the obtained factors were observed for the $p = 2\%$ and $p = 10\%$ models as can be seen in Figure 5-16(b). As the post-yield stiffness increases, the more conservative the proposed factor becomes. The horizontal amplification factors have also been plotted for comparison as $F_H = {}_cA_{Hmax}/{}_sA_{Heq}$. In case of horizontal amplification, the errors in the calculation remain the same as the horizontal amplification factor becomes constant at 1 ($F_{H1} = 1$) for all period ratios larger than 1.25 ($R_{T1} > 1.25$). Therefore, in this study, the more accurate elastic period ratios (Equation 5.29) are adopted for the computation of the amplification factors.

5.4.2 Direct-R method

The 'Modal response spectrum analysis' method in ASCE-7-16 [2] recommends calculation of design level force-related parameters by dividing the elastic response directly by R/I_e (=8 in this study). Therefore, another straightforward method of estimating the DBE-level response is to divide the peak elastic roof response directly by the R-factor as shown in Equation 5.31. However, there is no explicit commentary on modification of this factor for models with post-yield stiffness. Furthermore, employing a single reduction factor for all modes to estimate the peak accelerations may underestimate the overall response as the actual reduction in acceleration depends on the achieved target ductility and additional modal damping. The higher substructure modes may not achieve such high levels of ductility as assumed in this approach. In addition, since the method is fundamentally derived from the 'equal-displacement rule' (assuming the structures are in the constant-velocity region), the applicability of this method to models with fundamental periods in the constant-acceleration region (or short-period range) has not been proven yet. Therefore, to illustrate the applicability of this method, it is also used for computing DBE level response (using a reduction factor of $R = 8$) for comparison and is labelled as the 'Direct-R' method hereon.

$$R_a = \frac{1}{R} \tag{5.31}$$

5.4.3 Roof acceleration time history

Few of the past studies on seismically isolated roofs that proposed peak response estimates for seismically isolated structures with elastoplastic dampers using amplification factors had noted that the vertical response peaks early and the effects of damping (the shift of damping ratio from h_o to h_{eq}) are not significant, as reported in the review article by Takeuchi et al. [40]. It was concluded that the vertical response is excited initially before yielding and for the estimation of the peak substructure response A_{eq}, only the effect of period shift (from T_o to T_{eq}) was considered [40], [41]. However, this hypothesis has not been confirmed for roofs that employ other types of response control strategy, such as braced substructures. To further investigate the times at which peak of the horizontal and vertical response occur for braced substructures, the absolute of the acceleration time history of a node near the quarter points of the roof's ridgeline (where the maximum response is expected to occur) for Model-B is plotted for each ground motion alongside the BRB hysteresis (BRB chosen such that it is nearly parallel to the direction of seismic input in the global $x-$direction) until the peak of that node's acceleration is reached.

It was found that the time at which the peak of the vertical acceleration was reached was very close to the corresponding time for the horizontal acceleration. This implies that significant additional damping was achieved by the time both peaks were reached. For all the 11 ground motions, the horizontal acceleration peaked when the BRB was yielding. Similarly, for 9 out of the 11 ground motions, the vertical acceleration peaked when the BRB was yielding. This confirms the effectiveness of the BRBs in reducing both the horizontal and vertical response. According to the the results from NLRHA, the trends in the horizontal and vertical accelerations were found to be very similar. Therefore, in this study, for the estimation of both the horizontal and vertical response, the peak inelastic substructure response A_{Heq} is considered as defined in Equation 5.19 that includes the effects of both the period shift (T_o to T_{eq} in Equation 5.15) as well as the damping (the increase in damping ratio from h_o to h_{eq}) as quantified by the factor D_h in Equation 5.13.

GM	BRB hysteresis (until peak)	Acceleration time history
GM-1	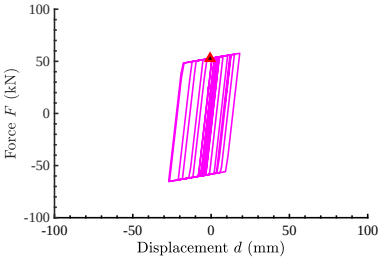	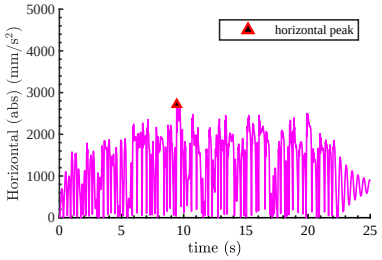
	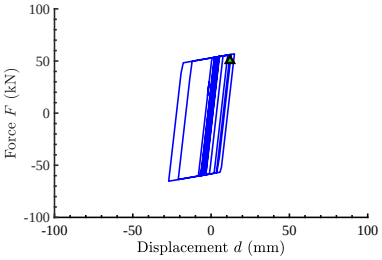	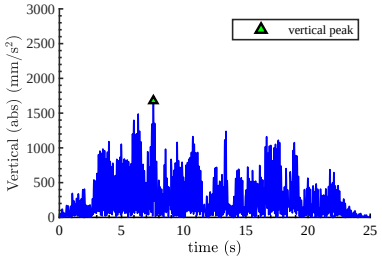
GM-2	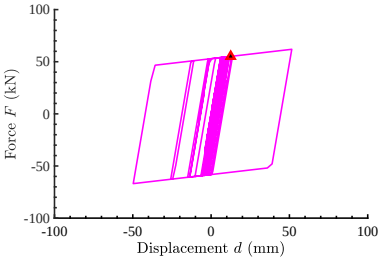	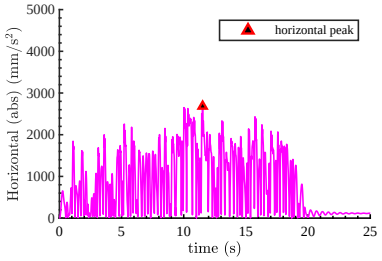
	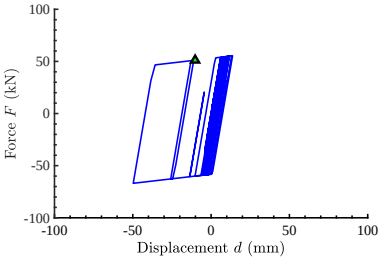	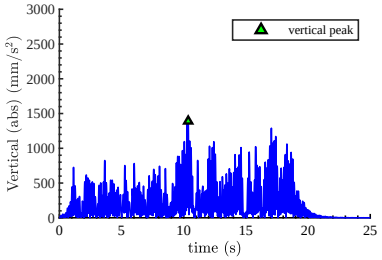
GM-3	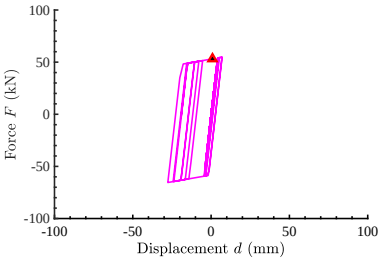	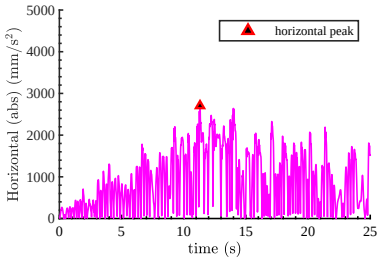
	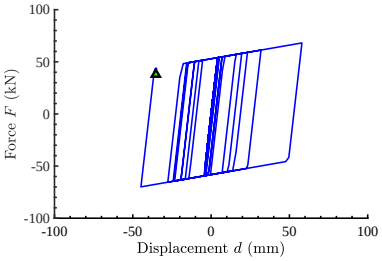	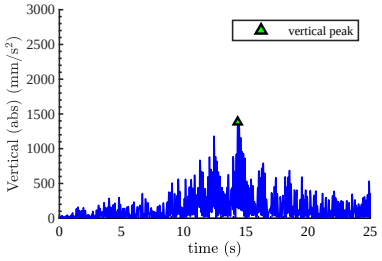

GM	BRB hysteresis (until peak)	Acceleration time history
GM-4	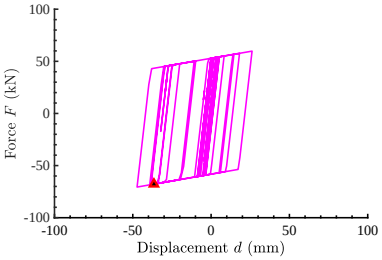	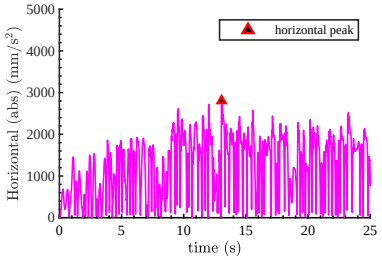
	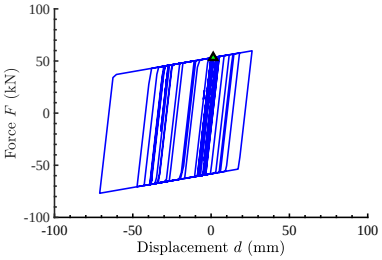	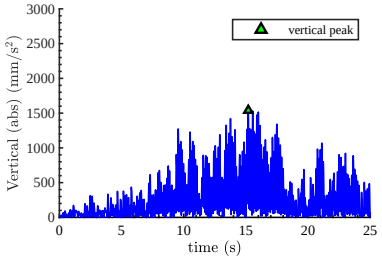
GM-5	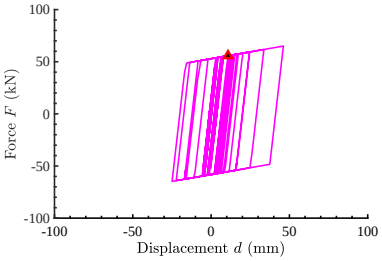	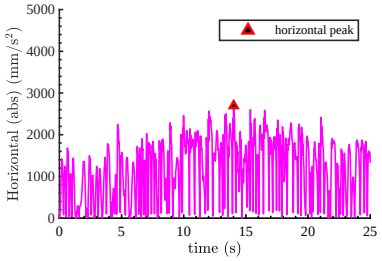
	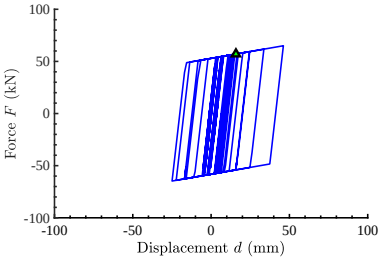	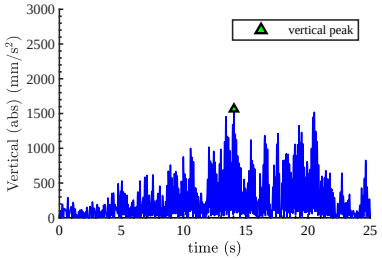
GM-6	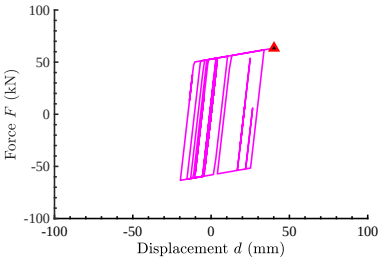	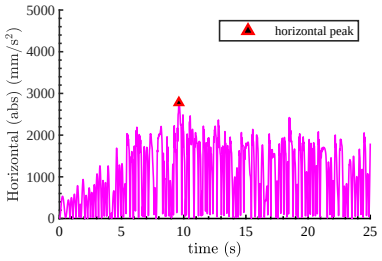
	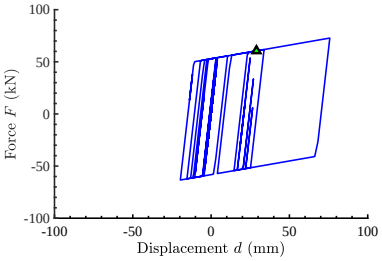	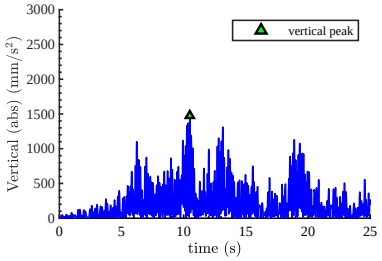

GM	BRB hysteresis (until peak)	Acceleration time history
GM-7	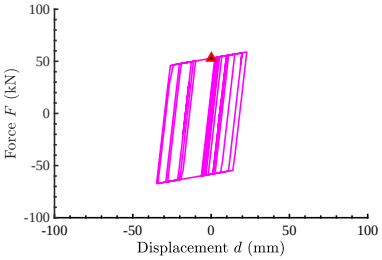	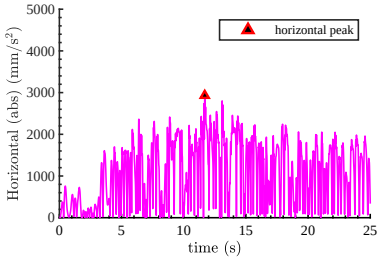
	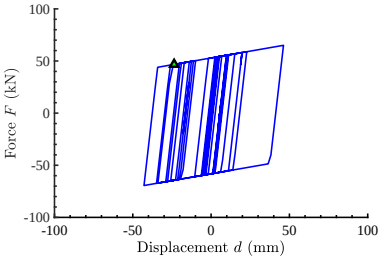	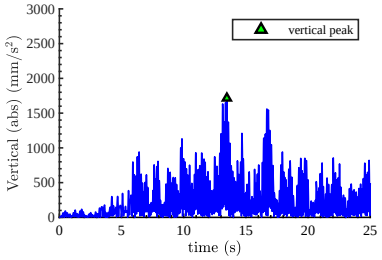
GM-8	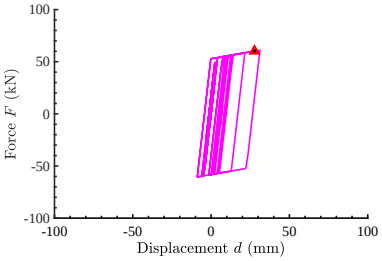	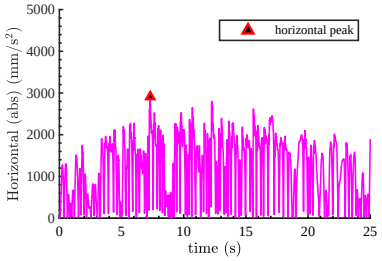
	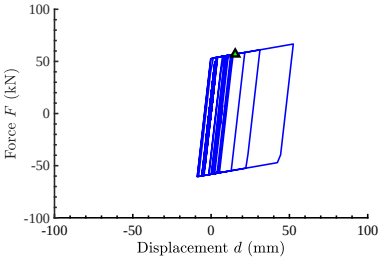	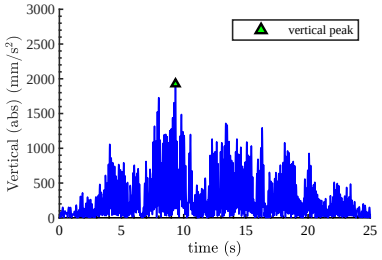
GM-9	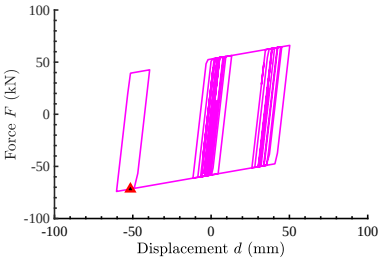	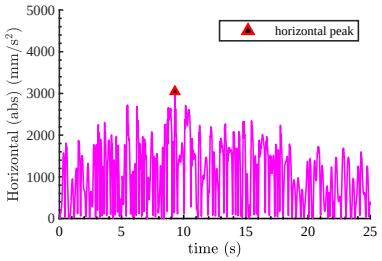
	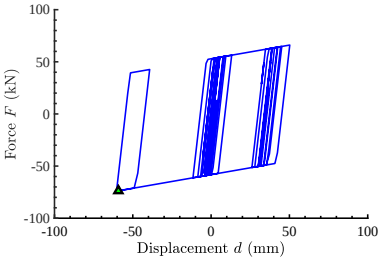	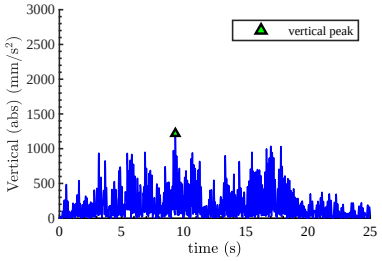

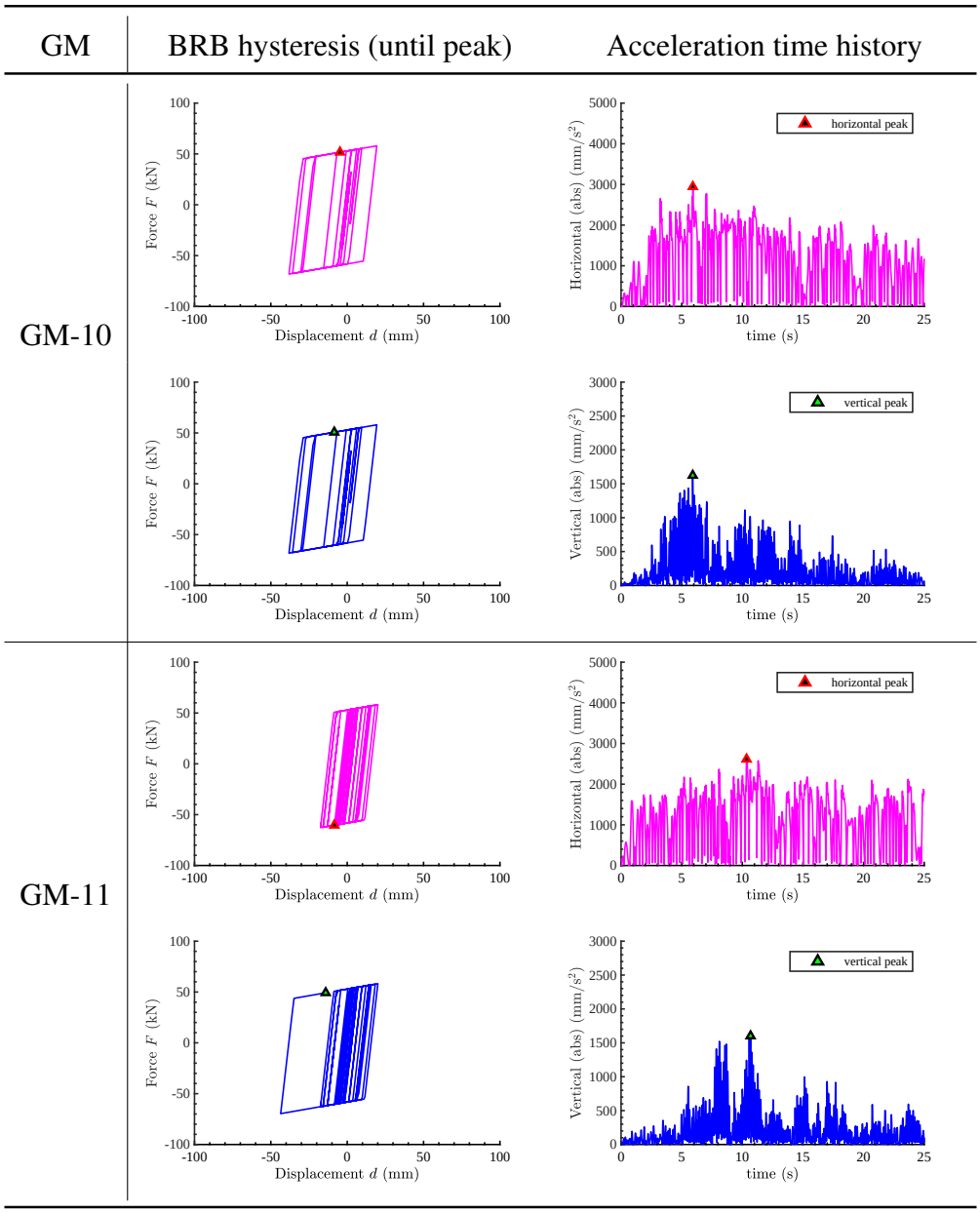

Figure 5-18: Model-B p=2%: Roof nodal acceleration time-history with peaks mapped to the BRB hysteresis

5.4.4 Comparison of peak roof response

The peak roof accelerations for the Model-A, Model-B, and Model-C were calculated using the first mode amplification factors in Equations 1.13-1.14 and are given in Table 5.11. For the equivalent linearisation approach, ${}_sA_{Heqi}$ was calculated considering the effect of both the period shift and the damping [8] using Equations 5.11-5.19. For the methods of the R factor approach, the acceleration of the maximum substructure was obtained using Equations 5.9-5.10. The proposed ridgeline *A-O-A'* (Figure 5-11) accelerations are compared with the mean NLRHA results in Figures 5-20-5-21.

When the post-yield stiffness ratio (p) is low (Figure 5-20), the peak substructure accelerations for Model-C in the constant velocity region obtained from the Newmark and N&K method were nearly equal to the peak accelerations obtained from Kasai's method leading to similar accuracy in the overall roof response. Model A exhibited the highest amplifications in both horizontal and vertical directions, as the substructure periods were closest to the roof period (smallest period ratio R_T) among the three models. In the small ductility regions (Figure 5-20 SLE results), all methods give reasonably accurate results. In large ductility regimes like the DBE and MCE levels, for structures with fundamental periods in the constant velocity region (Model-C), all R-factor methods estimate the DBE response with reasonable accuracy although the Kasai method is the most conservative, and the Newmark method presents the most conservative response estimates for models in the constant acceleration region (Model-A and Model-B). The differences in the Newmark and Kasai methods may be further understood by considering the example of Models A and B and their MCE response in Figures 5-20(a) and (b). Both models have periods in the constant acceleration region and therefore have the same horizontal elastic accelerations ($A_1 \approx 23\text{m/s}^2$). In addition, both models have nearly the same target ductility value for MCE levels ($\mu_t \approx 13$), and so the Newmark method gives $R_\mu = 5$ (following Equation 5.3) for both models, resulting in identical peak substructure acceleration ($A_{Heq1} \approx 4.5\text{m/s}^2$ as can be seen from the 'Newmark' horizontal response). However, the A_{Heq1} from the NRLHA and Kasai method differ for the two models. This illustrates the shortcoming of the Newmark method, which considers the effect of

ductility, while the effect of energy dissipation is implicitly accounted for by the backbone elastoplastic curve using the equal energy rule, and therefore may not always be accurate in estimating the maximum response values. The iterative equivalent linearisation approach better captures the energy dissipation by considering the equivalent viscous damping as well as the effect of period elongation which is quantified in Equations 5.16-5.18 by the Kasai method [9], [10] and is different in the two models.

Table 5.11: Estimated roof amplification factors

Model	R_{T1}	R_{M1}	F_{H1}	F_{V1}
Model-A	1.34	1.00	1.00	0.92
Model-B	2.00	1.00	1.00	0.57
Model-C	2.45	1.00	1.00	0.42

When the post-yield stiffness ratio (p) is large (Figure 5-21), the peak substructure accelerations for all models were underestimated by the Newmark and the N&K method (Figure 5-15 in Section 5.3.8). These errors increase as the intensity level increases from SLE to MCE. In addition, all methods give reasonably accurate results in small regions of ductility (Figure 5-21 SLE results) as the structure is largely in the elastic range. As observed for the low post-yield ratio models, Model-A exhibited the largest amplifications in both the horizontal and vertical directions. Kasai's relatively rigorous equivalent linearisation method accurately estimates the substructure response (Figure 5-15) and therefore presents a conservative roof response envelope (Figure 5-21) for models in both the constant acceleration and velocity regions. Therefore, it is recommended to use the equivalent linearisation approach when p is greater than 2%.

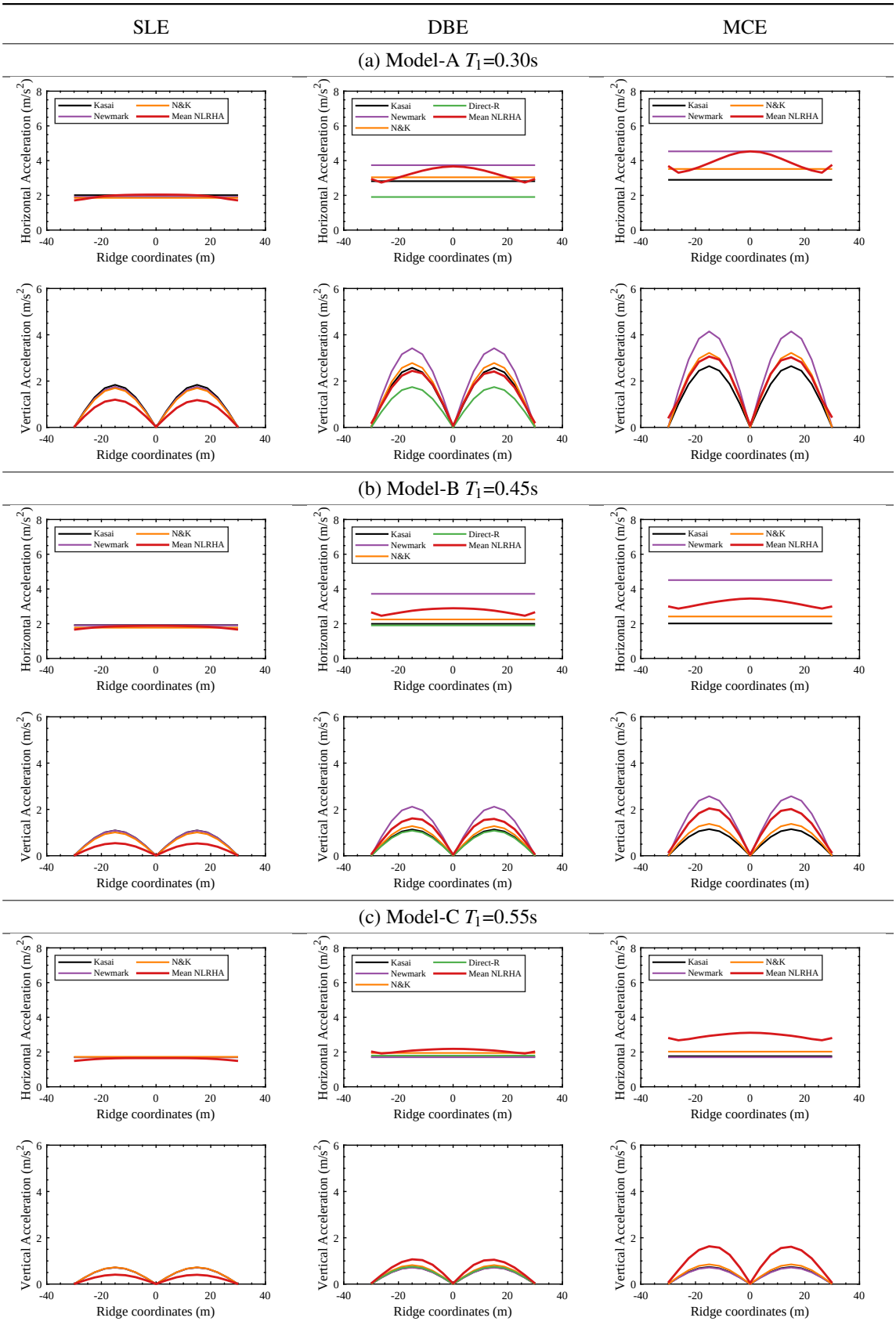

Figure 5-19: Roof ridgeline accelerations ($p = 0\%$, elastoplastic cases)

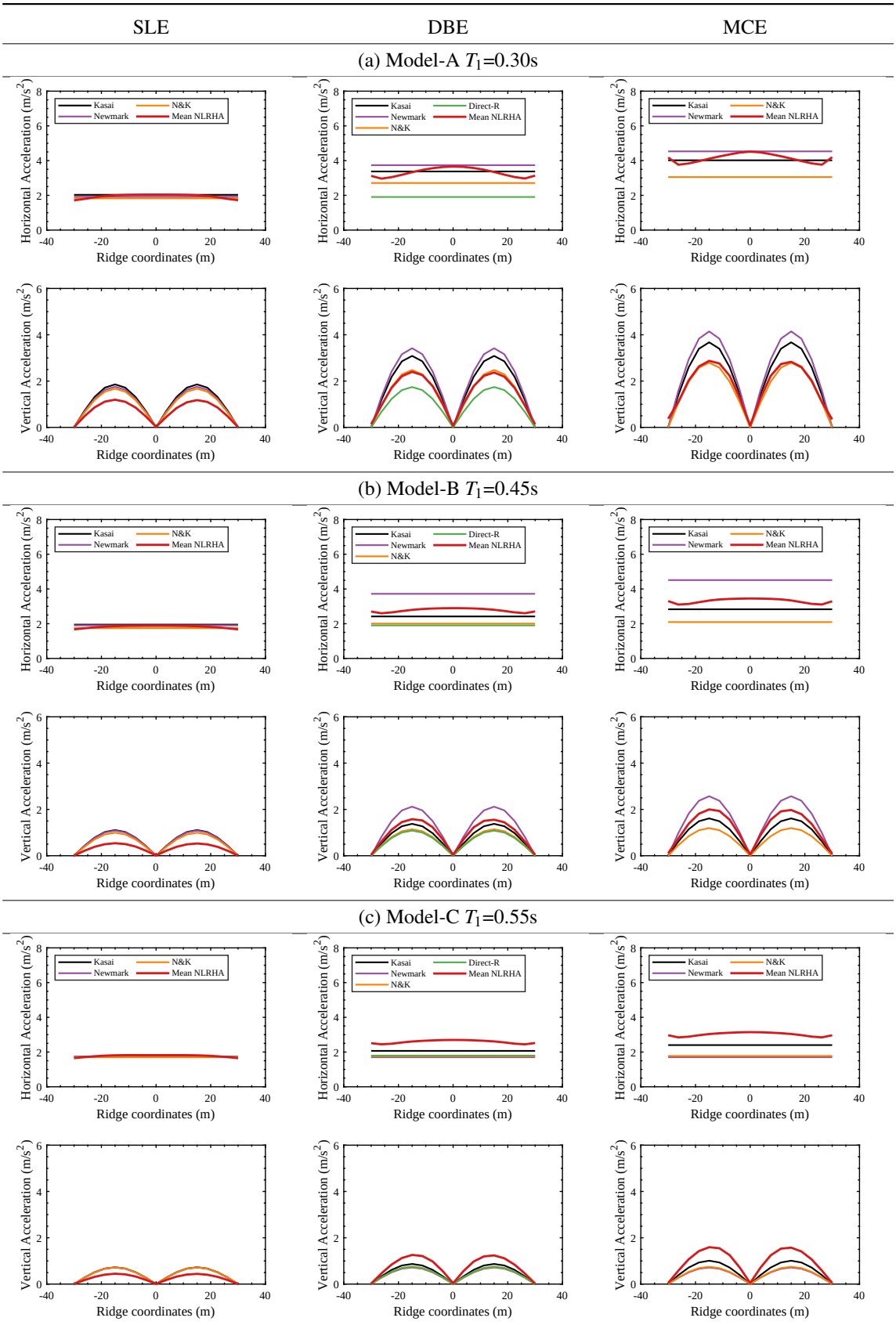

Figure 5-20: Roof ridgeline accelerations (post-yield stiffness ratio $p = 2\%$)

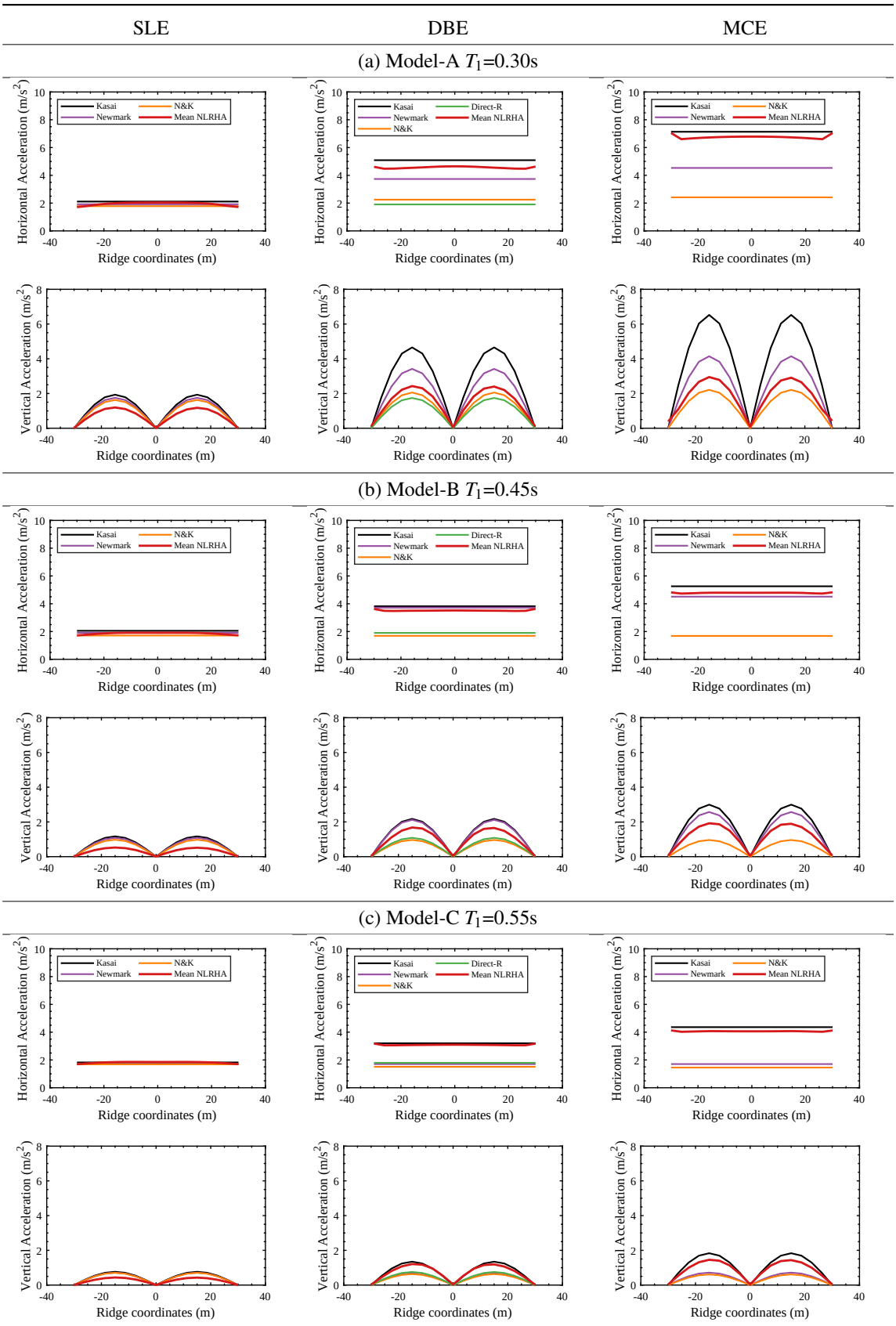

Figure 5-21: Roof ridgeline accelerations (post-yield stiffness ratio $p = 10\%$)

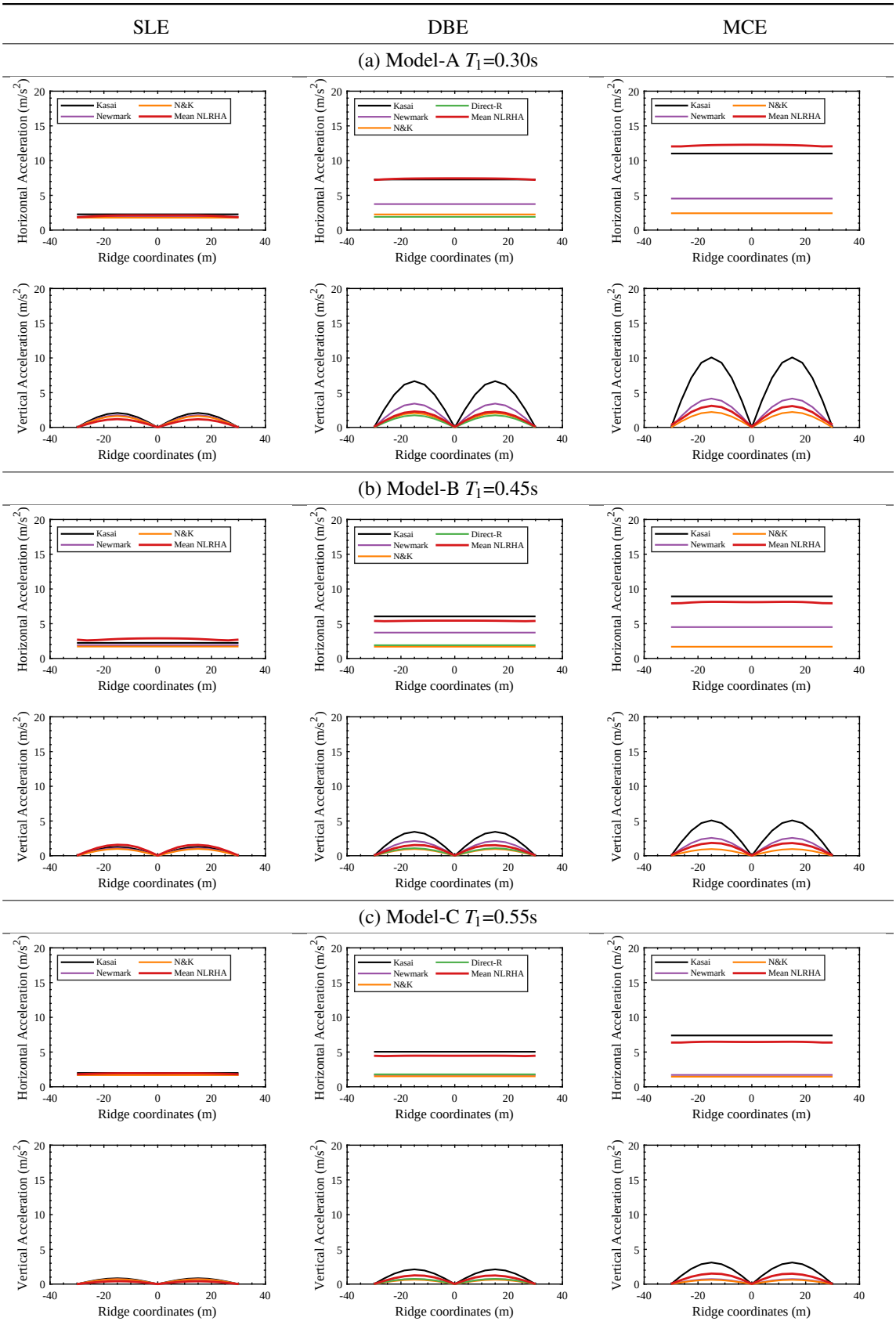

Figure 5-22: Roof ridgeline accelerations (post-yield stiffness ratio $p = 25\%$)

5.5 Comparison of roof member forces

The proposed peak roof accelerations were then used to compute the corresponding equivalent static loads using Equations 4.11-4.12. Static analyses were performed by applying the obtained vertical and horizontal loads simultaneously to the roof nodes of the combined model in each of the patterns (corresponding to the roof's dominant anti-symmetric mode shape O1 expressed by Equations 4.7 and 4.8) as shown in Figure 4-25 [8].

The detailed results for the single-storey models are compared with the mean NLRHA response in Figures 5-26-5-28. The proposed fit lines are also shown using dashed lines along the median ratios. For each of the roof members, since each NLRHA load case was run after applying dead loads, the response from the dead loads (N_{DL} and M_{DL}) is deducted from the mean NLRHA response ($N_{NLRHA+DL}$ and $M_{NLRHA+DL}$) to obtain the response only from the earthquake motions (N_{NLRHA} and M_{NLRHA}) using Equations 5.32 and 5.33. Similarly, the seismic demand from only the equivalent static loads were obtained using Equations 5.34 and 5.35.

$$N_{NLRHA} = N_{NLRHA+DL} - N_{DL} \tag{5.32}$$

$$M_{NLRHA} = M_{NLRHA+DL} - M_{DL} \tag{5.33}$$

$$N_{static} = N_{static+DL} - N_{DL} \tag{5.34}$$

$$M_{static} = M_{static+DL} - M_{DL} \tag{5.35}$$

For Model-A and Model-B (with T1 mode in the constant acceleration region), the Newmark method followed by the Kasai method presents the most conservative response among the investigated estimation methods while the Kasai method is the most conservative for Model-C in the constant-velocity region where all the R-factor methods present near-identical response. As the post-yield stiffness increases to $p = 10\%$, the R-factor methods become more unconservative althought the Newmark method is still conservative for Model-A and Model-B in the constant acceleration region as can be seen

in Figure 5-27. As the post-yield stiffness is further increased to $p = 25\%$, the errors in the R-factor methods are more evident in all the models (Figure 5-28) where the Kasai method (shown in black markers) exhibits a much more conservative DBE and MCE level axial forces and bending moments when compared to the NLRHA method. As discussed in Sections 5.3.8 and 5.4.4, this is due to the underlying assumptions of R-factor approaches which were proposed considering idealised elastoplastic (or low post-yield stiffness) backbone behaviour and thus are recommended for models with relatively low post-yield stiffness.

The accuracy of the methods is further compared by listing the number of roof members (in percentage) with axial forces and bending moments underestimated by more than 10% in Tables 5.12-5.13. It was observed that, for models with $p <= 2\%$, Kasai and Newmark have excellent accuracy for Model-A and Model-B in the constant acceleration region with less than 10% of the roof members' response underestimated. The Newmark method remains conservative for models in the constant acceleration region up to a post-yield stiffness of $p = 10\%$. The iterative Kasai's equivalent linearisation approach presents the best accuracy for Model-C in the constant velocity region across all ranges. The Direct-R method underestimates the seismic axial and bending moment demand of more than 90% of the roof members in all ranges of post-yield stiffness. As was observed in the peak acceleration response, the errors in the R-factor approaches increase as the post-yield stiffness increases, and the Kasai method is thus recommended for models with $p > 2\%$, as it maintained excellent accuracy in all ranges.

Table 5.12: % of roof members with more than 10% underestimation in N

Roof members with $N_{static} < 0.9 \times N_{NLRHA}$ (%)						
Model	Level	p	Kasai	Newmark	N&K	Direct-R
Model-A	SLE	2	2	2	3	
Model-B	SLE	2	2	2	3	
Model-C	SLE	2	3	3	3	
Model-A	DBE	2	0	0	3	80
Model-B	DBE	2	3	0	15	39
Model-C	DBE	2	8	99	87	72
Model-A	MCE	2	0	0	4	
Model-B	MCE	2	2	0	69	
Model-C	MCE	2	11	100	100	
Model-A	SLE	10	0	2	2	
Model-B	SLE	10	0	2	2	
Model-C	SLE	10	1	2	2	
Model-A	DBE	10	0	2	85	100
Model-B	DBE	10	0	0	100	100
Model-C	DBE	10	0	100	100	100
Model-A	MCE	10	0	19	99	
Model-B	MCE	10	0	0	100	
Model-C	MCE	10	0	100	100	
Model-A	SLE	25	0	0	2	
Model-B	SLE	25	0	0	1	
Model-C	SLE	25	0	0	1	
Model-A	DBE	25	8	71	100	100
Model-B	DBE	25	0	32	100	100
Model-C	DBE	25	0	100	100	100
Model-A	MCE	25	0	85	100	
Model-B	MCE	25	0	75	100	
Model-C	MCE	25	0	100	100	

Table 5.13: % of roof members with more than 10% underestimation in M

Roof members with $M_{static} < 0.9 \times M_{NLRHA}$ (%)						
Model	Level	p	Kasai	Newmark	N&K	Direct-R
Model-A	SLE	2	0	0	0	
Model-B	SLE	2	0	0	0	
Model-C	SLE	2	0	0	0	
Model-A	DBE	2	0	0	1	96
Model-B	DBE	2	4	0	48	76
Model-C	DBE	2	46	100	98	96
Model-A	MCE	2	0	0	2	
Model-B	MCE	2	11	0	92	
Model-C	MCE	2	52	100	100	
Model-A	SLE	10	0	0	0	
Model-B	SLE	10	0	0	0	
Model-C	SLE	10	0	0	0	
Model-A	DBE	10	0	0	35	99
Model-B	DBE	10	0	0	100	99
Model-C	DBE	10	0	100	100	100
Model-A	MCE	10	0	1	99	
Model-B	MCE	10	0	0	100	
Model-C	MCE	10	0	100	100	
Model-A	SLE	25	0	0	0	
Model-B	SLE	25	0	0	0	
Model-C	SLE	25	0	0	0	
Model-A	DBE	25	5	28	100	100
Model-B	DBE	25	0	1	100	100
Model-C	DBE	25	0	100	100	100
Model-A	MCE	25	0	29	100	
Model-B	MCE	25	0	12	100	
Model-C	MCE	25	0	100	100	

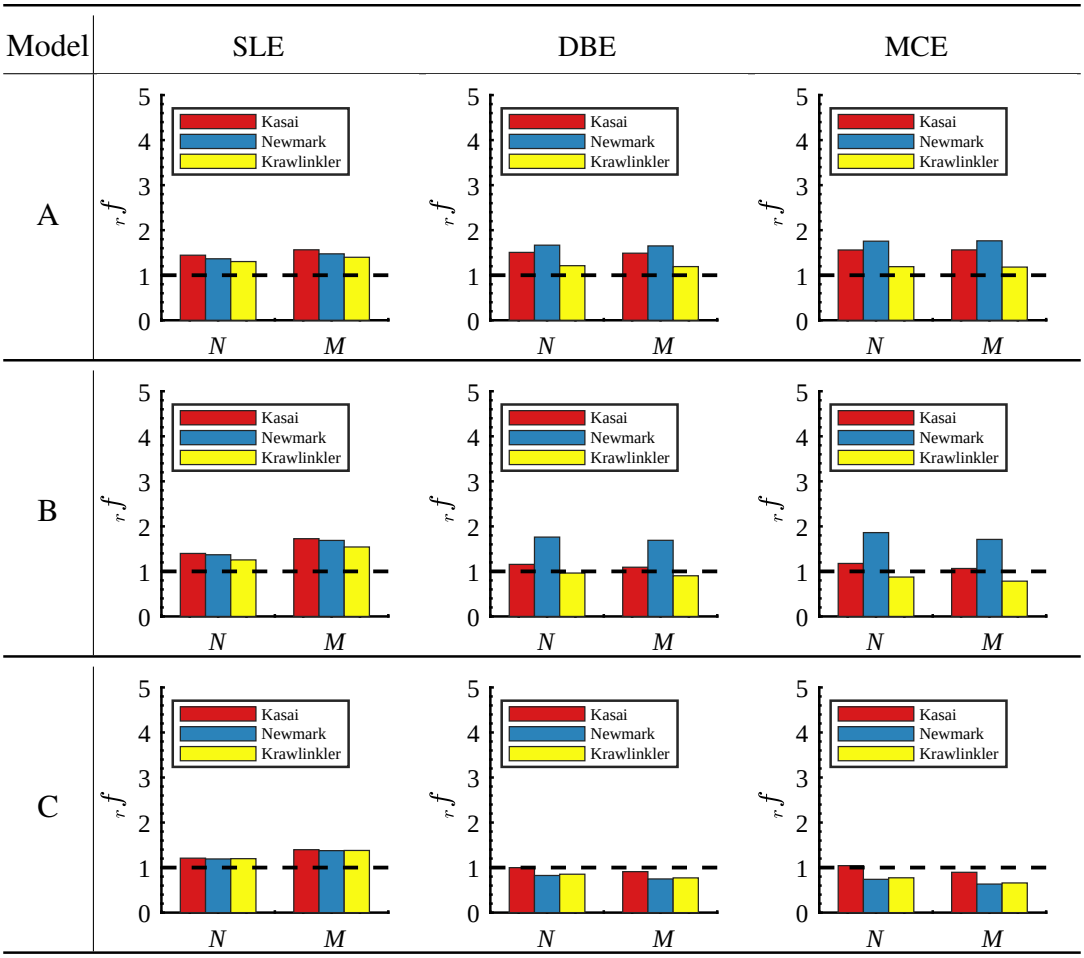

Figure 5-23: Single-storey $p = 2\%$ models: median response ratios

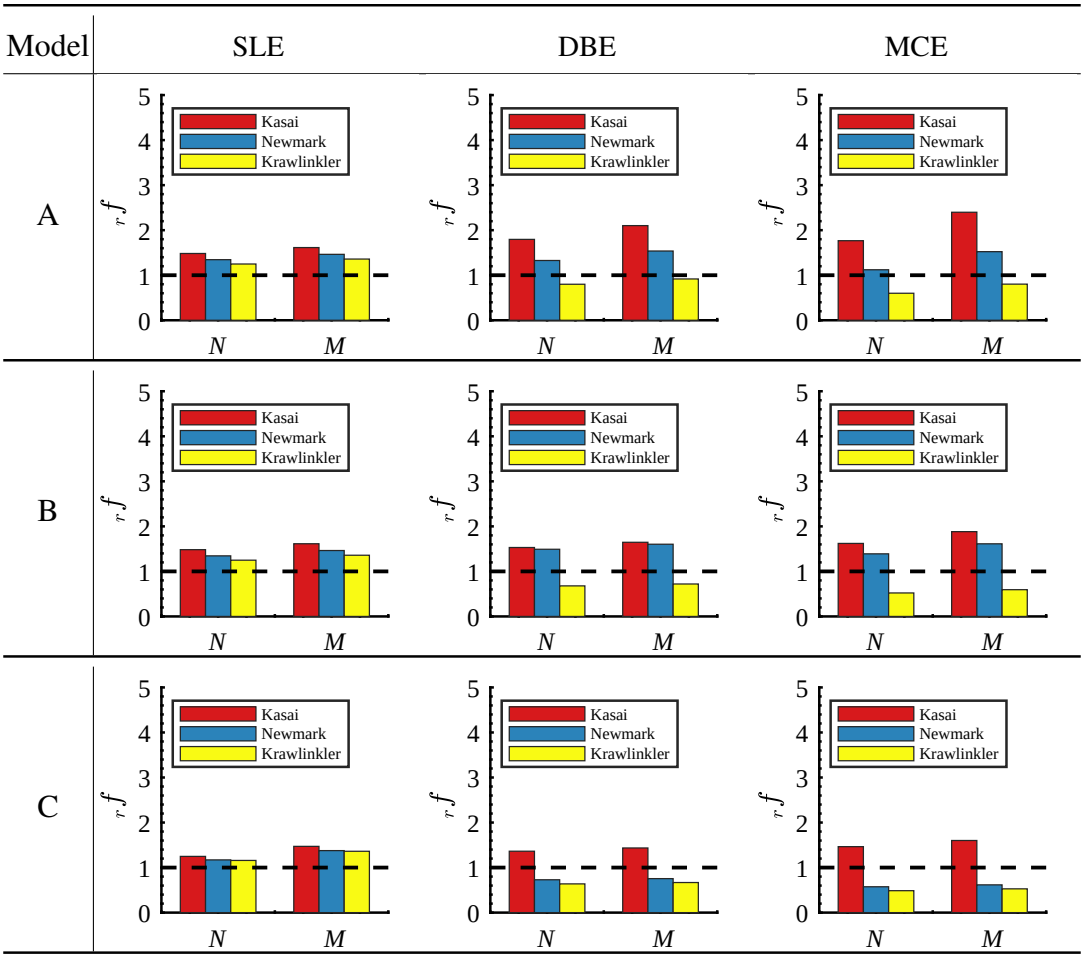

Figure 5-24: Single-storey $p = 10\%$ models: median response ratios

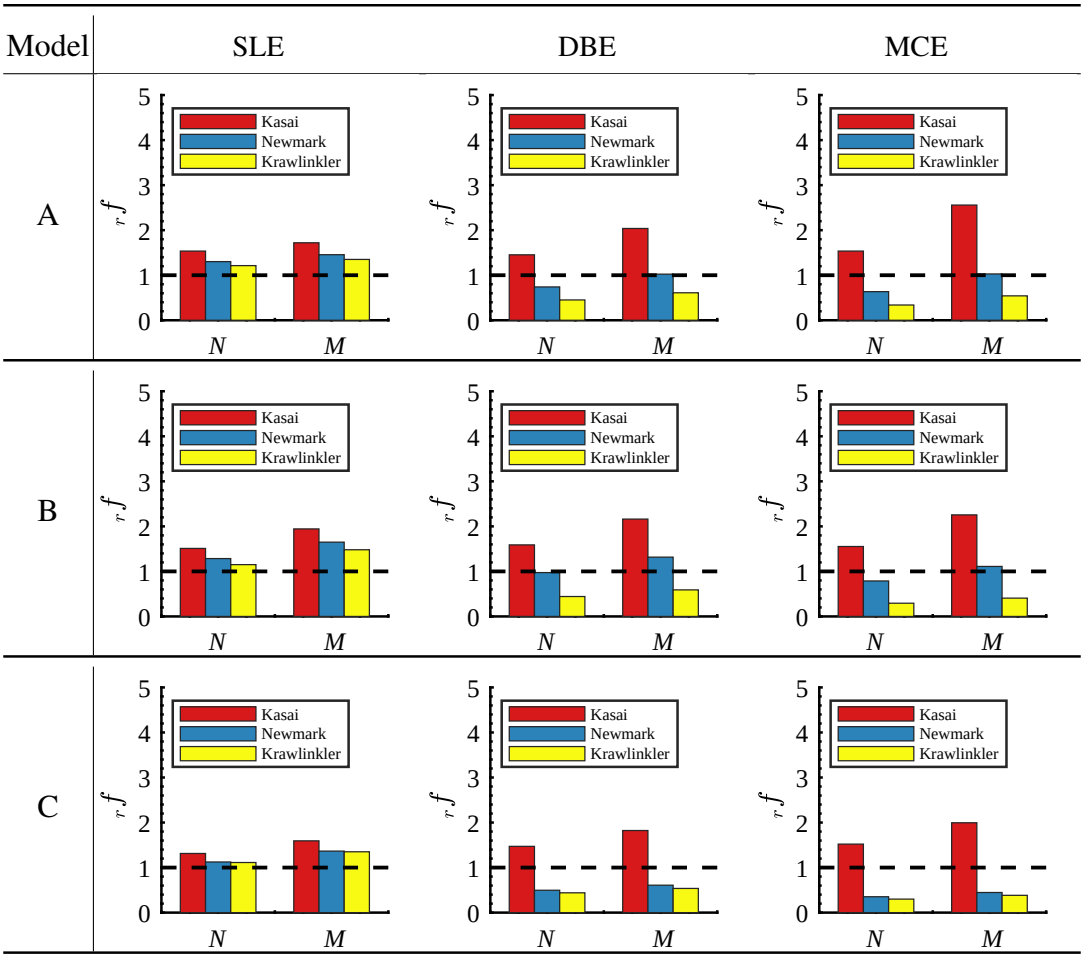

Figure 5-25: Single-storey $p = 25\%$ models: median response ratios

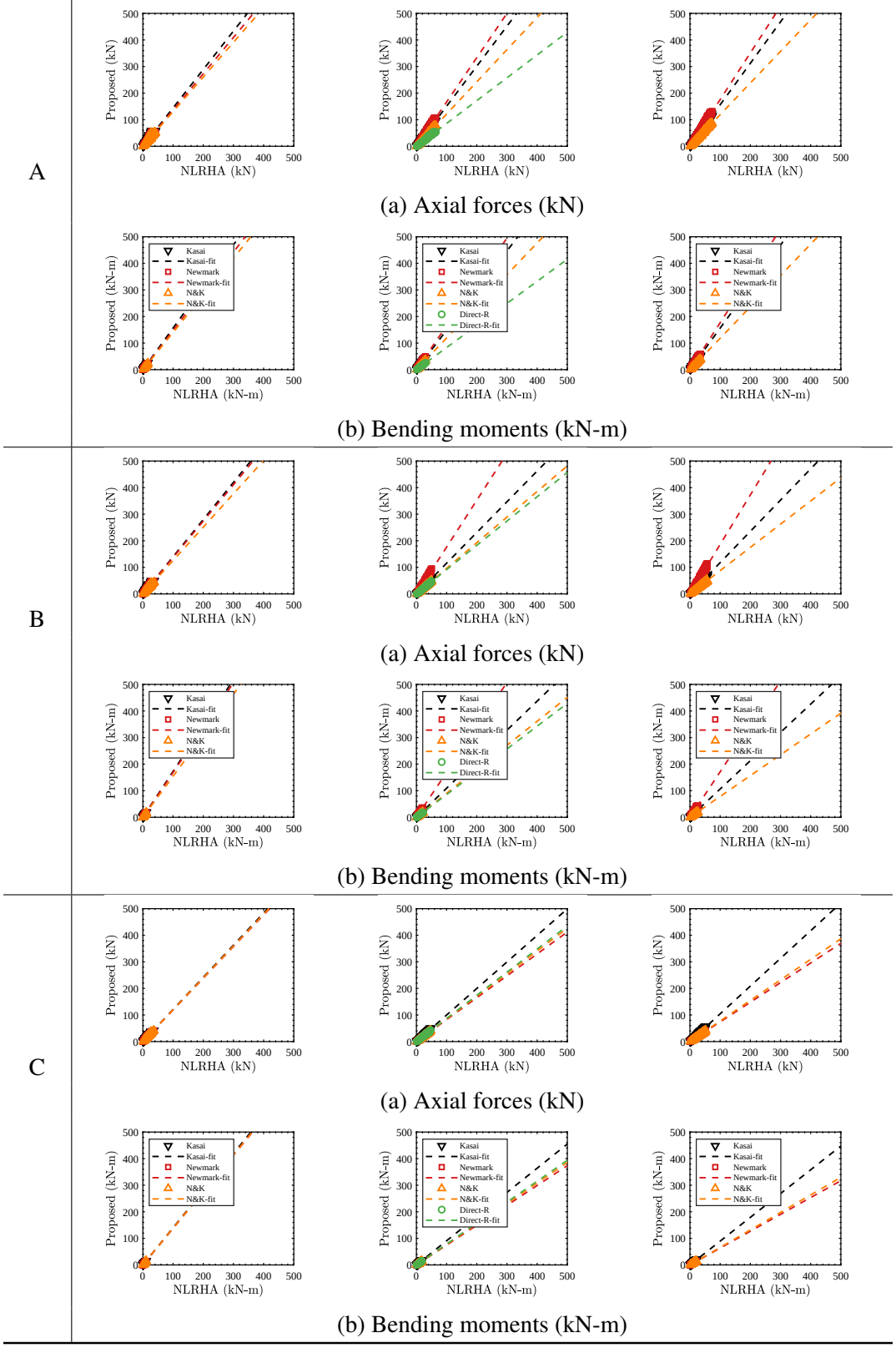

Figure 5-26: Single-storey $p = 2\%$ models: Comparison of member axial forces and bending moments

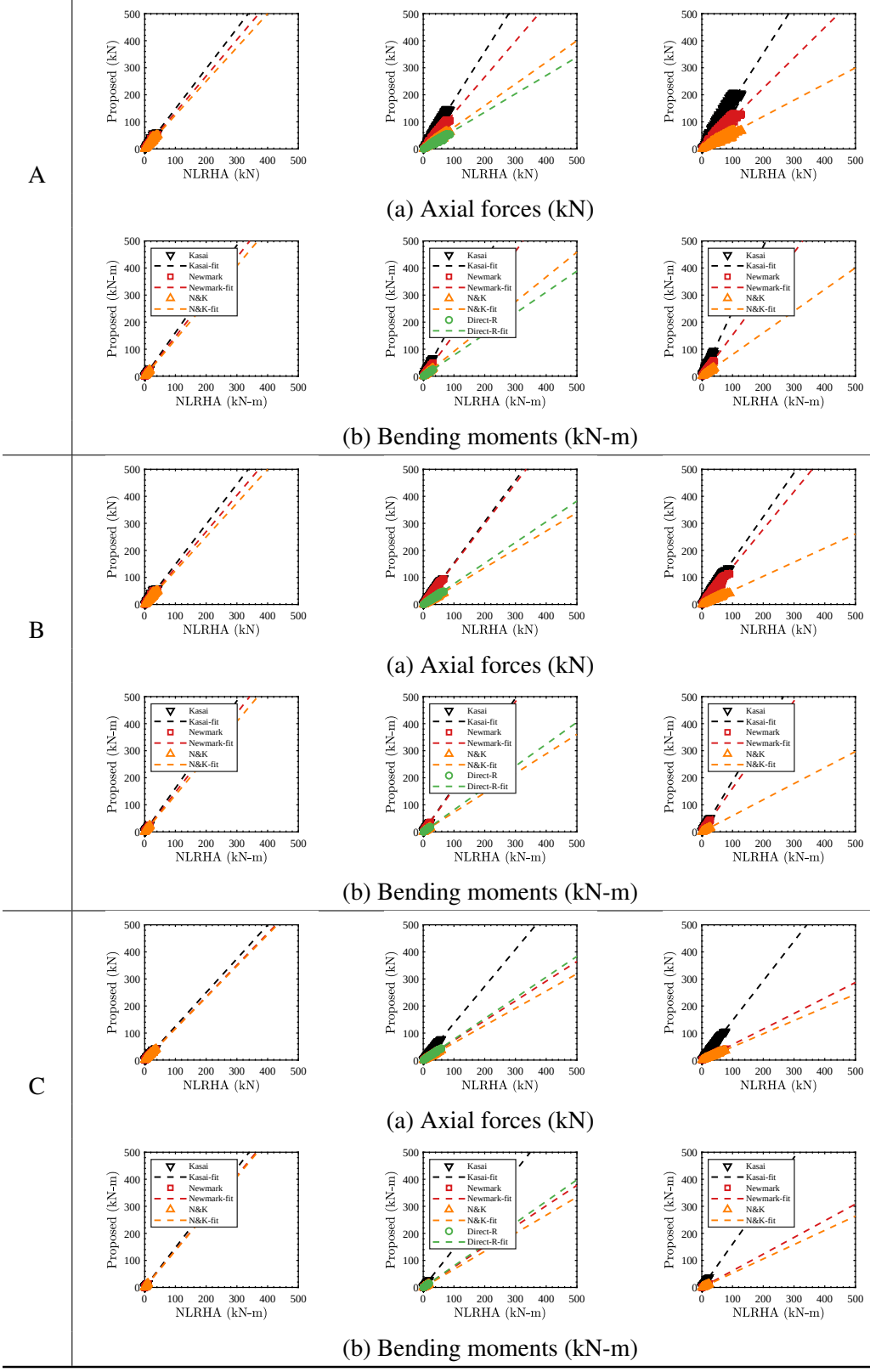

Figure 5-27: Single-storey $p = 10\%$ models: Comparison of member axial forces and bending moments

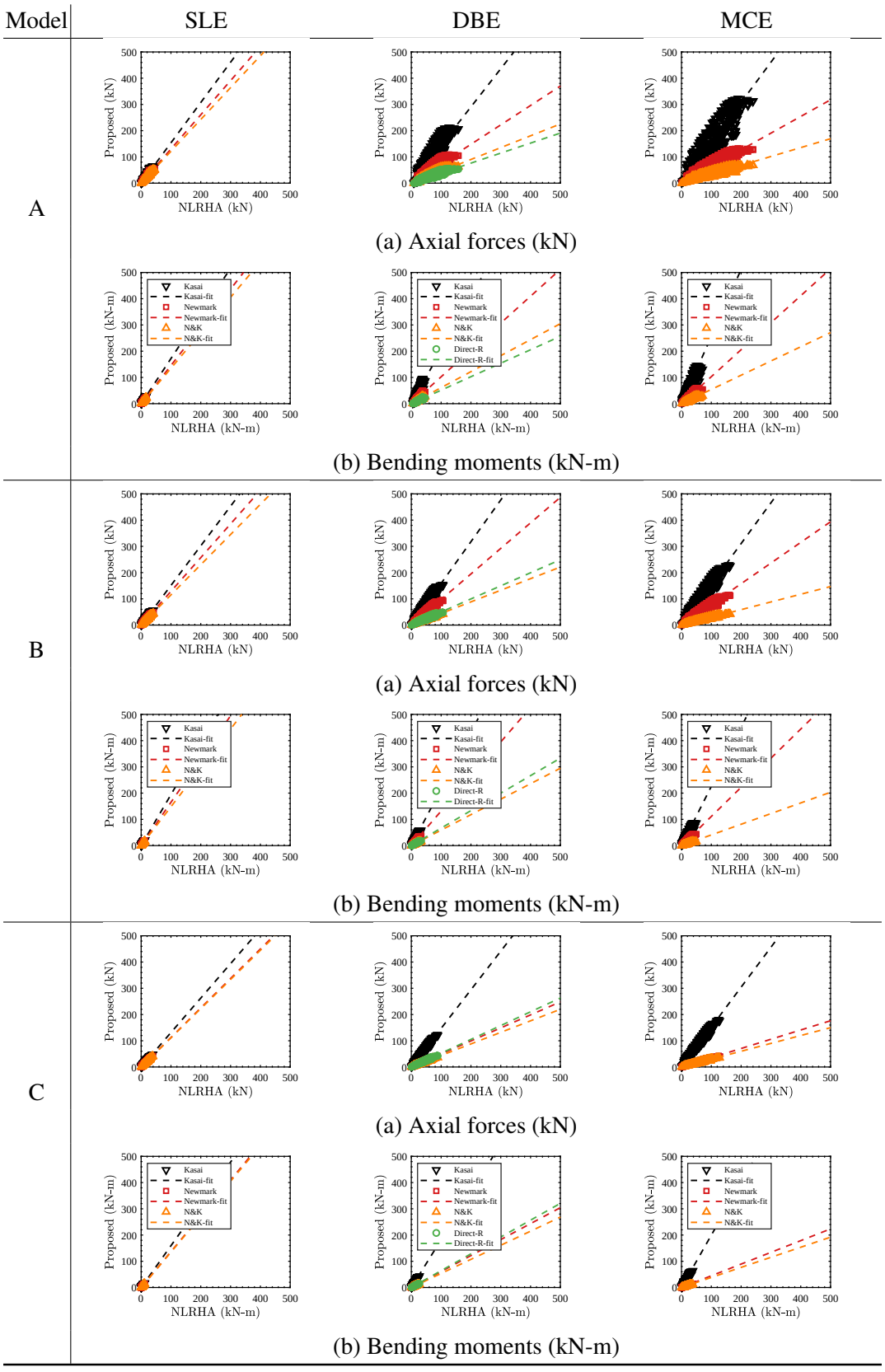

Figure 5-28: Single-storey $p = 25\%$ models: Comparison of member axial forces and bending moments

5.6 Conclusions

The following conclusions were drawn from this investigation.

1. The RSA based amplification factor approach proposed for elastic structures was extended for practical yielding BRBF substructures designed using an *R*-factor of 8 and varying the post-yield stiffness. Target ductility based reduction factors (R-factor approach) were incorporated to account for the nonlinearity of the buckling restrained braced substructure.

2. It was found that the time at which the peak of the vertical roof acceleration was reached was very close to the corresponding time for the horizontal acceleration. It was confirmed that significant additional damping was achieved by the time peaks of both horizontal and vertical acceleration were reached. Therefore, the effectiveness of the BRBs in reducing both the horizontal and vertical response was confirmed.

3. It was observed that the peak inelastic roof acceleration was highly influenced by the post-yield stiffness (p) of the substructure, and so adopting the same *R*-factor (=8) for obtaining the inelastic force demands (as in the 'direct-R' method) severely underestimated the peak roof responses for models with $p > 2\%$. This also lead to the forces and bending moments being underestimated for all roof members and is not recommended for estimation of the seismic demand for the roof members.

4. Kasai's equivalent linearisation method estimated the substructure response with accuracies very similar to the NLRHA for all the studied models. This method used in combination with the proposed amplification factor approach is an efficient alternative to the NLRHA method to estimate a conservative envelope of the peak accelerations and the equivalent static loads for the preliminary design of the dome.

5. For single-storey structures, both the R-factor methods- 'Newmark' and 'Nassar&Krawinkler' apply simple ductility reduction factor formulations to estimate the peak substructure responses and the accuracies are comparable to those from the NLRHA for structures with low post-yield stiffness ratios ($p <= 2\%$). The

Newmark method formulated based on the equal energy rule was found to have the best accuracy among the R-factor approaches for short-period structures with fundamental periods in the constant acceleration region of the design acceleration spectrum and is recommended for models with post-yield stiffness of up to 10% ($p <= 10\%$).

6. For models designed as per the US code with low post-yield stiffness and fundamental periods in the constant-acceleration region, the simpler Newmark method presented good accuracy for models and is recommended for models with $p <= 10\%$.

7. The accuracies of the R-factor methods in estimating the peak substructure response was low for single-storey structures with high post-yield stiffness ratios ($p = 25\%$) in large ductility regimes due to the underlying assumptions behind the formulations. Therefore, for structures with higher post-yield stiffness ratios ($p >= 25\%$) typically found in countries like Japan with moment connections, it is recommended to adopt the more accurate Kasai method in combination with the amplification factors to obtain the peak envelope roof response. These may then be used to obtain the equivalent static loads on the roof for preliminary member sizing.

References

[1] *Guide to Earthquake Response Evaluation of Metal Roof Spatial Structures*. Working Group 8,International Association for Shell and Spatial Structures (IASS), 2019.

[2] *Minimum Design Loads for Buildings and Other Structures*. ASCE Standard–ASCE/ SEI 7–16: American Society of Civil Engineers (ASCE), 2016.

[3] T. Sasaki, A. Aoi, K. Kajiwara, H. Tagawa, and D. Sato, "Collapse mechanism of wide-area suspended ceiling in school gymnasium," in *Proceedings of IASS Annual Symposia*, International Association for Shell and Spatial Structures (IASS), vol. 2016, 2016, pp. 1–10.

[4] T. Takeuchi, S. D. Xue, S. Nakazawa, and S. Kato, "Recent applications of response control techniques to metal spatial structures," *Journal of the IASS*, vol. 53, no. 2, pp. 99–110, 2012.

[5] T. Kumagai, T. Takeuchi, T. Ogawa, A. Nakama, and E. Sato, "Seismic response evaluation of latticed domes with elasto-plastic substructures using amplification factors," in *Proceedings of IASS 2005*, Bucharest, Romania, Sep. 2005, pp. 383–390.

[6] S. Kato and S. Nakazawa, "Seismic design method to reduce the responses of single layer reticular domes by means of yielding of substructure under severe earthquake motions," in *Proceedings of IASS 2001*, Nagoya, Japan, Oct. 2001, TP077.

[7] S. Kato, S. Nakazawa, and K. Saito, "Two-mode based estimation of equivalent seismic loads and static estimation of dynamic response of reticular domes supported by ductile substructures," *Journal of the IASS*, vol. 47, pp. 35–52, 2006.

[8] D. Nair, Y. Terazawa, B. Sitler, and T. Takeuchi, "Seismic response of long-span domes supported by multi-storey substructures," *Journal of the IASS*, vol. 61, pp. 140–157, 2020.

[9] K. Kasai, H. Ito, and A. Watanabe, "Peak response prediction rule for a SDOF elasto-plastic system based on equivalent linearization technique," *Journal of Structural and Construction Engineering (Transactions of AIJ)*, vol. 68, no. 571, pp. 53–62, 2003.

[10] K. Kasai and H. Ito, "JSSI manual for building passive control technology. Part. 8 Peak response evaluation and design for elastoplastically damped system," in *13th World Conference on Earthquake Engineering, Vancouver, Canada. Paper*, 2004.

[11] K. Kaneda, "Endeavors to control the vibration on long span structure," in *Proc. of International Symposium on Theory, Design and Realization of Shell and Spatial Structures, Nagoya, Oct., 2001*, 2001.

[12] O. Hosozawa and T. Mizutani, "Structural design of Simokita Dome," in *Proceedings of IASS 2005*, Bucharest, 2005, p. 707.

[13] T. Takeuchi, T. Ogawa, T. Suzuki, T. Kumagai, and C. Yamagata, "A basic study on damage-controlled design concept for truss frame structures," *Journal of Structural and Construction Engineering (Transactions of AIJ)*, vol. 51, pp. 31–37, 2005.

[14] T. Takeuchi, T. Tsutsumi, T. Ogawa, and T. Kumagai, "Seismic retrofit of steel-structure school gymnasia with energy dissipation braces," in *Proceedings of IASS 2010*, Shanghai.

[15] L. A. Fahnestock, R. Sause, and J. M. Ricles, "Seismic response and performance of buckling-restrained braced frames," *Journal of Structural Engineering*, vol. 133, no. 9, pp. 1195–1204, 2007.

[16] T. Güner and C. Topkaya, "Performance comparison of BRBFs designed using different response modification factors," *Engineering Structures*, vol. 225, p. 111 281, 2020.

[17] T. Takeuchi, T. Kumagai, H. Shirabe, and T. Ogawa, "Seismic response evaluation of lattice roofs supported by multistory substructures," in *Shell and Spatial Structures: Structural Architecture - Towards the future looking to the past. IASS Symposium*, Venice, Italy, Dec. 2007, p. 362.

[18] D. Nair, K. Ichihashi, Y. Terazawa, B. Sitler, and T. Takeuchi, "Higher mode effects of multistorey substructures on the seismic response of double-layered steel gridshell domes," *Engineering Structures*, vol. 243, p. 112 677, 2021.

[19] T. Takeuchi, T. Ogawa, and T. Kumagai, "Seismic response evaluation of lattice shell roofs using amplification factors," *Journal of the IASS*, vol. 48, pp. 197–210, 2007.

[20] *NZS 1170.5: 2004, Structural Design Actions Part 5: Earthquake actions-New Zealand*. Wellington, New Zealand: Standards New Zealand, 2004.

[21] *Design of Structures for Earthquake Resistance*. British Standard–Eurocode 8: Part-1, 2005.

[22] *The Building Standard Law of Japan on CD-ROM*. The Building Center of Japan, 2016.

[23] C.-M. Uang, "Establishing R (or R_w) and C_d factors for building seismic provisions," *Journal of Structural Engineering*, vol. 117, no. 1, pp. 19–28, 1991.

[24] R. Riddell, "Inelastic response spectrum: Early history," *Earthquake Engineering & Structural Dynamics*, vol. 37, no. 8, pp. 1175–1183, 2008.

[25] R. Riddell, P. Hidalgo, and E. Cruz, "Response modification factors for earthquake resistant design of short period buildings," *Earthquake Spectra*, vol. 5, no. 3, pp. 571–590, 1989.

[26] E. Miranda, "Site-dependent strength-reduction factors," *Journal of Structural Engineering*, vol. 119, no. 12, pp. 3503–3519, 1993.

[27] A. Nassar, J. Osteraas, and H. Krawinkler, "Seismic design based on strength and ductility demands," in *10th World Conference on Earthquake Engineering*, vol. 10, 1992, pp. 5861–5866.

[28] L. H. Lee, S. W. Han, and Y. H. Oh, "Determination of ductility factor considering different hysteretic models," *Earthquake Engineering & Structural Dynamics*, vol. 28, no. 9, pp. 957–977, 1999.

[29] M. King, W. Whitby, and G. Hanshaw, "Design of the Singapore Sports Hub Roof with high strength niobium steel," in *IABSE Symposium Report*, International Association for Bridge and Structural Engineering, vol. 101, 2013, pp. 1–8.

[30] T. Takeuchi and A. Wada, *Buckling-restrained braces and applications*. Japan Society of Seismic Isolation, 2017.

[31] *Analysis reference manual for SAP2000, ETABS, SAFE and CSIBridge*. Computers and Structures, Inc., Berkeley, CA, USA, 2015.

[32] E. L. Wilson, *Three-dimensional static and dynamic analysis of structures*. Computers and Structures, 2002.

[33] R. A. Kersting, W. A. Lopez, L. A. Fahnestock, *et al.*, "Nehrp seismic design technical brief no. 11: Seismic design of steel buckling-restrained braced frames," 2015.

[34] *Specification for Structural Steel Buildings (ANSI/AISC 360–16)*. American Institute of Steel Construction (AISC), 2016.

[35] D. Rutten, *Grasshopper3d*, 2015.

[36] Pacific Earthquake Engineering Research Center, *PEER ground motion database*, 2020. [Online]. Available: https://ngawest2.berkeley.edu/.

[37] A. M. Chandler and X. Duan, "Performance of asymmetric code-designed buildings for serviceability and ultimate limit states," *Earthquake Engineering & Structural Dynamics*, vol. 26, no. 7, pp. 717–735, 1997.

[38] J. Erochko, C. Christopoulos, R. Tremblay, and H. Choi, "Residual drift response of SMRFs and BRB frames in steel buildings designed according to ASCE 7-05," *Journal of Structural Engineering*, vol. 137, no. 5, pp. 589–599, 2011.

[39] L. A. Fahnestock, R. Sause, J. M. Ricles, and L.-W. Lu, "Ductility demands on buckling-restrained braced frames under earthquake loading," *Earthquake Engineering and Engineering Vibration*, vol. 2, no. 2, pp. 255–268, 2003.

[40] T. TAKEUCHI, T. OGAWA, and T. KUMAGAI, “State-of-arts views on response control technologies on metal space structures,” in *Symposium of the International Association for Shell and Spatial Structures (50th. 2009. Valencia)*, 2009.

[41] T. Takeuchi, K. Takamatsu, T. Kumagai, and T. Ogawa, “Response evaluation of lattice domes supported by substructures with seismic isolation system,” *Journal of Structural and Construction Engineering*, vol. 74, no. 641, pp. 1259–1266, 2009.

Chapter 6

Equivalent static loads in multistorey substructures: the R-factor approach

Contents

6.1 Introduction

The previous chapter investigated the applicability and effectiveness of two formulations of ductility-based reduction factors in estimating the peak inelastic accelerations of the substructure. Single storey buckling restrained braced frames with varying post-yield stiffness were studied and the accuracy of the amplification factor-based equivalent static loads (using the inelastic substructure accelerations) in estimating the seismic demands of the roof were discussed.

To extend this methodology to nonlinear multistorey substructures, in this chapter, 60m spanned two-storey and six-storey buckling restrained braced substructures are constructed. The BRBF substructures are designed for base shears using a force reduction factor of $R = 8$ (as per ASCE-7), and have longer fundamental periods and low-post yield stiffness. The higher mode effects of multistorey substructures are investigated using the proposed amplification factors for two-storey and six-storey analysis models with different post-yield stiffnesses to discuss the extent of applicability of the amplification factor-based equivalent static loads on domes with multistorey substructures. The accuracies of the proposed R-factor approach were then verified for longer 150m spanned domes with buckling-restrained frames and for the case study models defined in Chapter-2. Finally, the scope of application of the proposed methodology is discussed.

6.2 Inelastic response of 2-storey BRBF

To investigate the applicability of the approach of using R-factors for substructures with higher modes, the single-storey substructure was replaced with a two-storey substructure. As in the single-storey models, the first storey and the roof level are each 5m high and the first storey has a floor weight of 7kPa and the roof dead load is assumed to be 2kPa (Section 5.3.2). The substructure model is shown in Figure 6-1 and the section sizes of the gravity frame have been adopted from the single-storey model given in Table 6.1. The BRBs for the 2-storey substructure models were designed using the same design procedure as outlined in Section 5.3 and the properties of the BRBs and design storey shears are given in Table 6.2. The combined analysis models A, B and C were then constructed combining the 60m roof model introduced in Section 3.1 (*L*60-DL-2 roof model) and the substructure models.

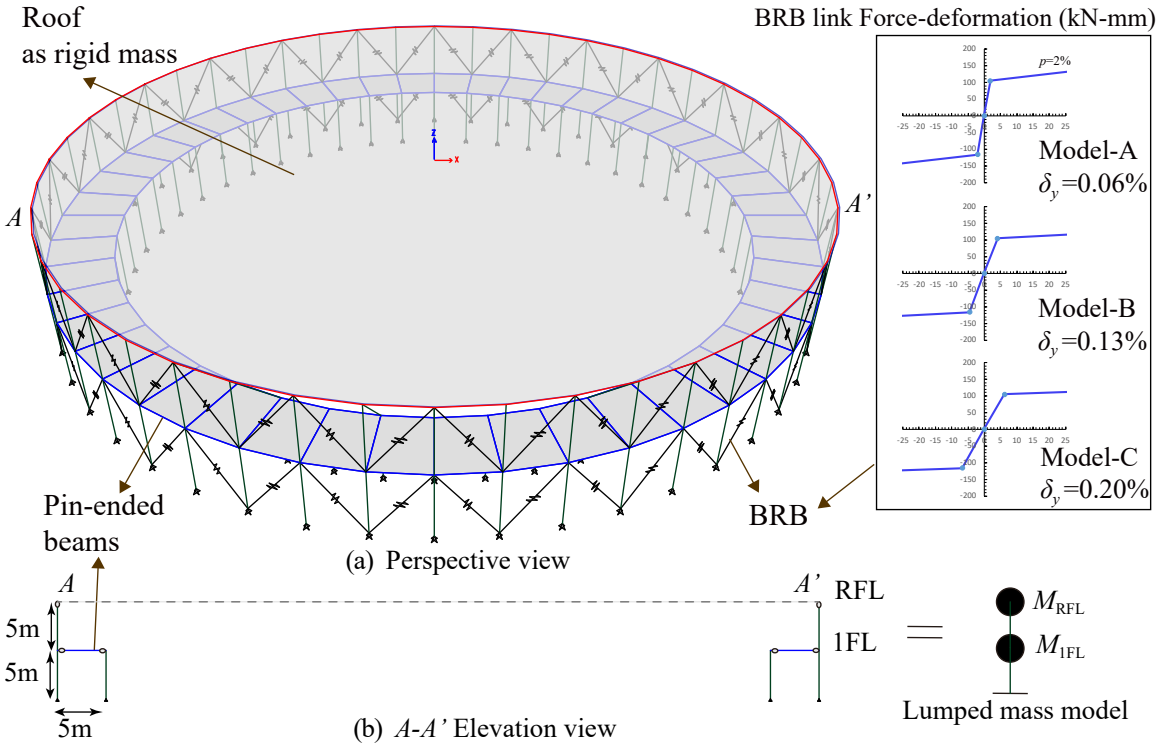

Figure 6-1: 60m Substructure model and modelling assumptions

The seismic response of domes with multistorey substructures may be interpreted as a combination of responses from T1-roof and T2-roof interactions [1]. Both the substructure T1 and T2 modes interact with the nearest roof mode and the contribution of each of these modes to the overall response is directly proportional to their mass participation values. The substructure periods and roof periods are mapped on the design spectrum in Figure 6-2. Model-B and Model-C have fundamental periods (first substructure mode (T1)) in the constant velocity region, and Model-A with a stiffer substructure has a relatively shorter fundamental period in the constant acceleration region. The fundamental periods (T1) for all models contribute to a mass participation ratio (in the direction of seismic input i.e. the x-direction) of about 90% and the remaining 10% came from the higher T2 mode which lies in the constant acceleration region for all models. This implies a higher spectral acceleration value from the T2 modes. The substructure T2 modes are also in close proximity to roof dominant O1 and O2 modes giving rise to second mode period ratios $R_{T2} = T_2/T_R$ in the range of 1 (where T_2 is the substructure T2 mode period and T_R is the roof's O1 mode as defined previously by the authors [1]). Consequently, in these models, the vertical amplification factors that quantify the T2 roof interactions are larger and more significant than those of the T1 roof interactions with the longer R_{T1} period ratios [1].

Table 6.1: 2-storey substructure model data

(a) Storey heights and seismic weights

Storey	Height (m)	Weight (kN)
RFL	10	6064
1FL	5	6032

(b) Section sizes

Member	Section Shape	Section Size (mm)
Column	SHS	450×450×25
Beam	I beam	340×250×9×14

Table 6.2: Equivalent Lateral Forces: Proportioning BRBs ($\sigma_y = 235, 205$MPa)

Model-A ($T_1 = 0.38s, T_2 = 0.15s,$)

Storey	h (m)	kN W_x	kN V_x	kN BRB V_x	kN BRB V_{ix}	kN BRB P_i	mm δ_y	kN/m BRB K_{eqi}	mm^2 A_c
RFL	10	6064	1414	1414	40	70	1.85	37770	341
1FL	5	6032	2117	2117	60	105	1.85	56558	511

Model-B ($T_1 = 0.56s, T_2 = 0.23s,$)

Storey	h (m)	kN W_x	kN V_x	kN BRB V_x	kN BRB V_{ix}	kN BRB P_i	mm δ_y	kN/m BRB K_{eqi}	mm^2 A_c
RFL	10	6064	1414	1414	40	70	4.12	16997	298
1FL	5	6032	2117	2117	60	105	4.12	25451	446

Model-C ($T_1 = 0.69s, T_2 = 0.28s,$)

Storey	h (m)	kN W_x	kN V_x	kN BRB V_x	kN BRB V_{ix}	kN BRB P_i	mm δ_y	kN/m BRB K_{eqi}	mm^2 A_c
RFL	10	6064	1414	1414	40	70	6.17	11331	298
1FL	5	6032	2117	2117	60	105	6.17	16967	446

where P_i=Yield axial force in each BRB, δ_y=Yield axial deformation

K_{eqi}=BRB equivalent axial stiffness, A_c=Area of core as defined in Takeuchi[2]

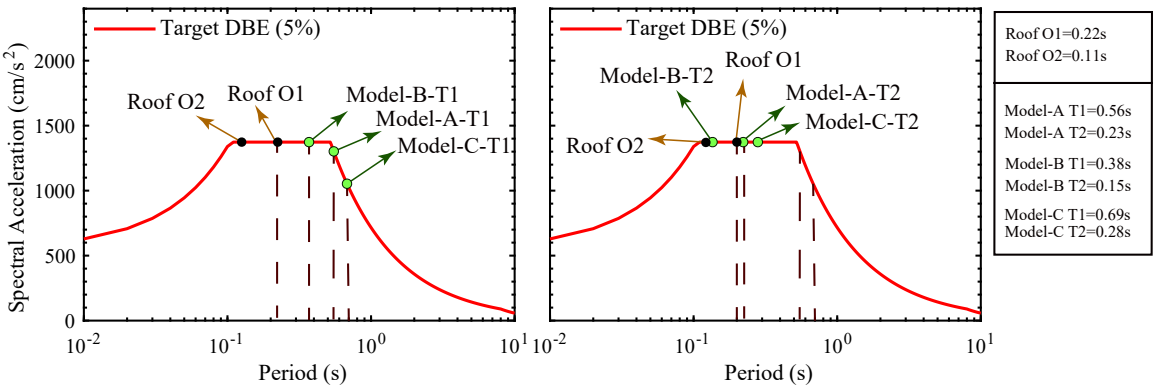

Figure 6-2: Substructure and roof periods on the design acceleration spectrum

6.2.1 Inter-storey drifts

The mean peak substructure inter-storey drifts and mean residual inter-storey drifts obtained from the NLRHA (using the spectrally matched input ground motions in Section 5.3.5) of the combined models are shown in Figure 6-3. For structures having four storeys or less, ASCE-7 [3] prescribes an allowable storey drift of 2.5% for the level of DBE. The obtained mean storey drifts are within the permissible ASCE limits for all models. Typical values of mean residual drift are about 0.3% for p=2% models under the DBE level. These values increase to 0.6% under the MCE level. If 0.5% residual drift is assumed to be the limit beyond which the structures are no longer practically usable [4], then the models with less than or equal to 2% post-yield stiffness ratio may not meet this immediate occupancy performance level under MCE level excitation.

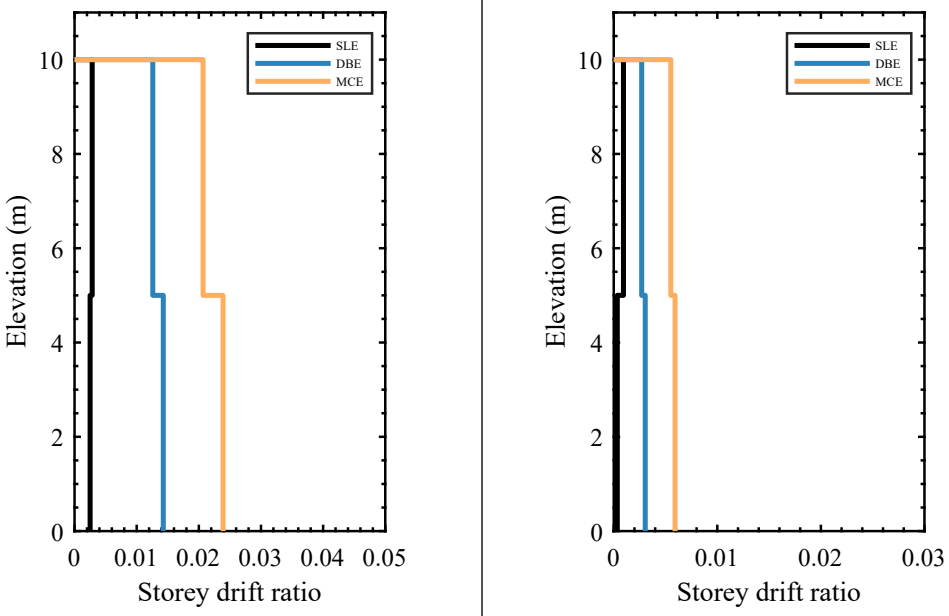

(a) Storey drift ratio

(b) Residual drift ratio

Figure 6-3: Model-B $p = 2\%$: Mean of peak storey drift ratios of substructure

6.2.2 Peak substructure response

For each of the three substructure models, modal pushover analyses corresponding to the first and second translational modes were performed to obtain the initial base shear to roof displacement stiffness (K_{1i}) as shown in Equation 5.25. The elastic design spectral accelerations of the first and second modes (S_{a1} and S_{a2}) were used to obtain the elastic base shears (V_i) and then extrapolate the maximum elastic substructure roof displacement (D_i) at point A of Figure 6-1(a) from the initial stiffness (K_{1i}) as shown in Equation 5.25. The peak elastic RFL level acceleration A_i of the substructure is also obtained from the corresponding roof displacement and the fundamental period and the response spectrum as shown in Equation 5.25. The reduction factors ($R_{\mu i}$ and R_{ai}) were then computed for both T1 and T2 modes following Equations 5.3-5.6 from the target ductility μ_{ti} using Equation 5.26 and 5.10. For the equivalent linearisation approach, Equations 5.11-5.20 were used. The peak inelastic base shear and roof acceleration of the substructure model were then obtained by combining the modal base shears using the SRSS modal combination rule using Equations 6.1 and 6.2.

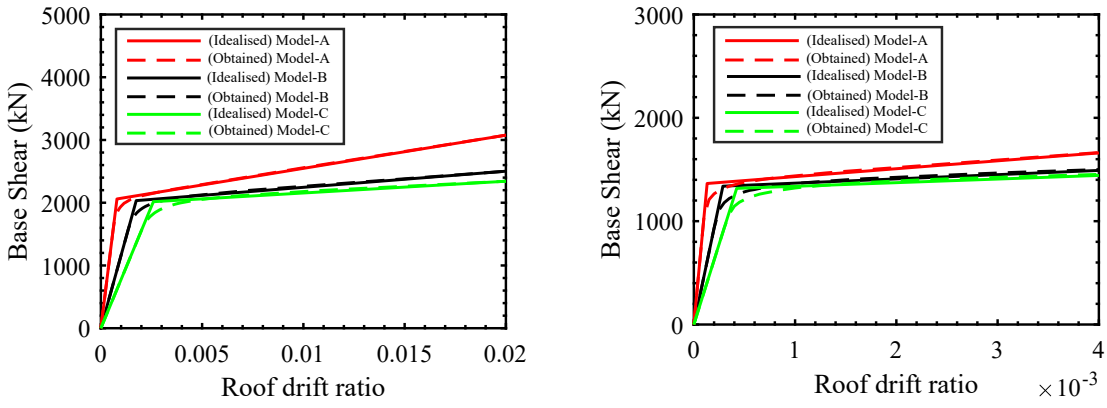

(a) First mode (b) Second mode

Figure 6-4: Modal pushover curves and idealisation of structural response ($p = 2\%$ models)

$$ {}_sV = \sqrt{\left(\frac{V_1}{R_{\mu 1}}\right)^2 + \left(\frac{V_2}{R_{\mu 2}}\right)^2} \tag{6.1} $$

$$ {}_sA_{eq} = \sqrt{\left(\frac{A_1}{R_{\mu 1}}\right)^2 + \left(\frac{A_2}{R_{\mu 2}}\right)^2} \tag{6.2} $$

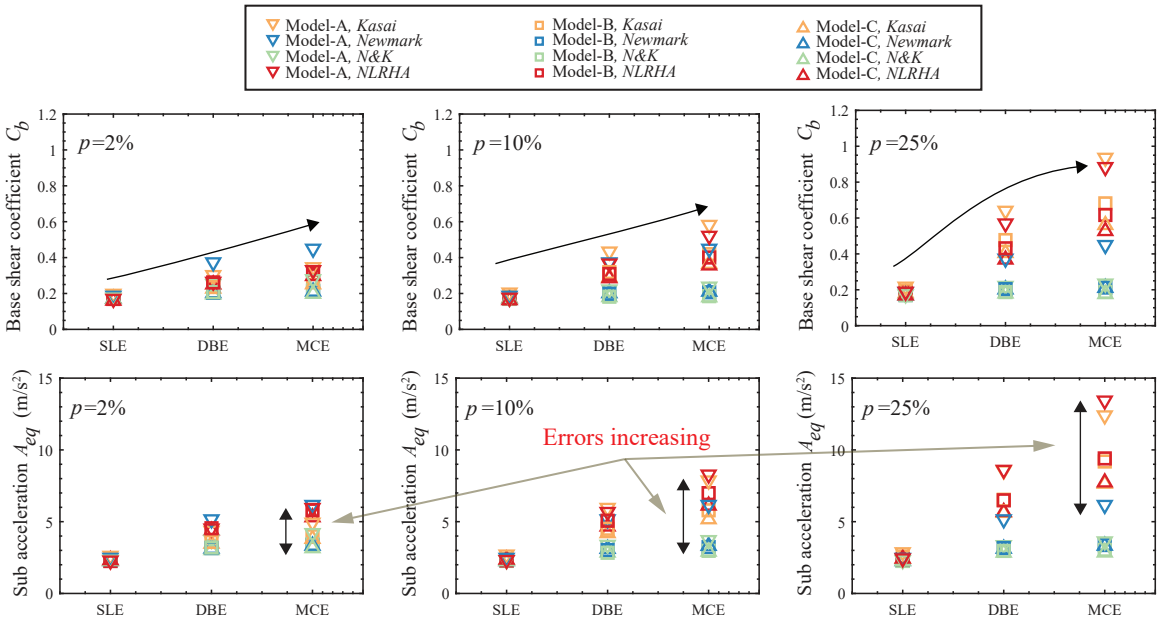

Figure 6-5: Base shear ratios and peak substructure (RFL) acceleration

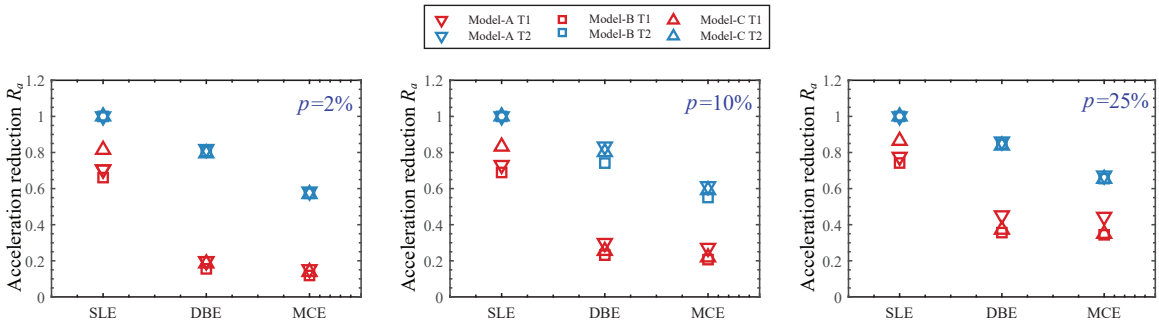

Figure 6-6: Kasai method: Reduction in substructure modal acceleration

The peak substructure accelerations ${}_sA_{eq}$ and the base shear ratio C_b (=${}_sV/W$ where W is the seismic weight) for all models are compared with the mean NLRHA response in Figure 6-5. The typical base shear ratios at the DBE level are low around 0.3 and increase to 0.35 for the MCE level for $p = 2\%$ models. These values further increase with increasing post-yield stiffness with Model-A with the lowest reduction and the highest base shear ratio at about 0.9. As observed for single-storey models, the R factor methods estimate base shear and accelerations with good accuracy for $p = 2\%$, with Newmark's method being the most

conservative of all estimation methods in the short period range. As the post-yield stiffness ratio increases ($p = 25\%$), Kasai method is the most accurate if compared with the mean NLRHA response. For the SLE level response and low-ductility regimes, all methods are equally accurate.

The achieved damping, reduction ratios and the periods corresponding to Kasai's evaluation method (Section 5.2.2) are also shown in Tables 6.3-6.8. To compare the reduction in acceleration for each mode across models with different post-yield stiffness, the reduction in peak substructure acceleration $R_{ai} = A_{eqi}/A_i$ obtained from the Kasai method is plotted for modes T1 and T2 for Model-A, Model-B and Model-C in Figure 6-6. For models with $p = 2\%$, the reduction in T1 mode is the lowest for the SLE level with typical R_{a1} values around 0.7. These values reduced further to 0.2 for the DBE level and 0.1 for MCE level. As the post-yield stiffness increases to $p = 10\%$, the reduction ratio increases to 0.3 for the DBE level and 0.2 for the MCE level. The models with $p = 25\%$ therefore exhibit the lowest reductions in acceleration with typical R_{a1} values at around 0.8 for the SLE level, 0.4 for the DBE level and 0.3 for the MCE level. However, for the T2 mode response, the increase in post-yield stiffness has a relatively minor effect on the reduction ratios as the additional damping is lesser and the ductility values are smaller in the higher mode (Tables 6.4 and 6.8). Therefore, substructures designed with a high post-yield stiffness can achieve reduced residual inter-storey drifts (Figure 6-17b) but the corresponding gridshell roofs may have to be designed for higher design forces due to increased seismic input.

Table 6.3: $p = 2\%$ models: Peak substructure First-mode (T1) parameters

	h_{eq1}	K_{eq1}/K_1	D_h	R_d	R_a	μ_{t1}	T_1	T_{eq1}	T_R
Model-A-SLE	0.10	0.62	0.79	1.14	0.71	1.63	0.38	0.48	0.23
Model-A-DBE	0.43	0.11	0.44	1.74	0.20	8.14	0.38	1.12	0.23
Model-A-MCE	0.47	0.07	0.42	2.15	0.15	12.21	0.38	1.41	0.23
Model-B-SLE	0.09	0.65	0.82	1.01	0.66	1.53	0.56	0.69	0.23
Model-B-DBE	0.42	0.12	0.44	1.25	0.16	7.66	0.56	1.59	0.23
Model-B-MCE	0.46	0.08	0.43	1.52	0.12	11.48	0.56	2.00	0.23
Model-C-SLE	0.07	0.78	0.92	1.04	0.81	1.24	0.69	0.77	0.23
Model-C-DBE	0.38	0.16	0.46	1.14	0.19	6.18	0.69	1.70	0.23
Model-C-MCE	0.44	0.10	0.43	1.36	0.14	9.27	0.69	2.15	0.23

Table 6.4: $p = 2\%$ models: Peak substructure Second-mode (T2) parameters

	h_{eq2}	K_{eq2}/K_2	D_h	R_d	R_a	μ_{t2}	T_2	T_{eq2}	T_R
Model-A-SLE	0.05	1.00	1.00	1.00	1.00	1.00	0.15	0.15	0.23
Model-A-DBE	0.08	0.73	0.88	1.12	0.82	1.37	0.15	0.18	0.23
Model-A-MCE	0.15	0.49	0.69	1.19	0.58	2.06	0.15	0.22	0.23
Model-B-SLE	0.05	1.00	1.00	1.00	1.00	1.00	0.23	0.23	0.23
Model-B-DBE	0.08	0.72	0.87	1.12	0.81	1.40	0.23	0.27	0.23
Model-B-MCE	0.16	0.49	0.68	1.18	0.57	2.10	0.23	0.33	0.23
Model-C-SLE	0.05	1.00	1.00	1.00	1.00	1.00	0.28	0.28	0.23
Model-C-DBE	0.08	0.71	0.86	1.13	0.80	1.42	0.28	0.33	0.23
Model-C-MCE	0.16	0.47	0.67	1.20	0.57	2.13	0.28	0.41	0.23

Table 6.5: $p = 10\%$ models: Peak substructure First-mode (T1) parameters

	h_{eq1}	K_{eq1}/K_1	D_h	R_d	R_a	μ_{t1}	T_1	T_{eq1}	T_R
Model-A-SLE	0.10	0.65	0.81	1.12	0.73	1.63	0.38	0.47	0.23
Model-A-DBE	0.31	0.20	0.51	1.51	0.30	8.14	0.38	0.85	0.23
Model-A-MCE	0.30	0.16	0.51	1.72	0.27	12.21	0.38	0.95	0.23
Model-B-SLE	0.09	0.68	0.83	1.01	0.69	1.53	0.56	0.68	0.23
Model-B-DBE	0.31	0.21	0.51	1.12	0.23	7.66	0.56	1.23	0.23
Model-B-MCE	0.31	0.16	0.51	1.26	0.21	11.48	0.56	1.38	0.23
Model-C-SLE	0.06	0.80	0.93	1.04	0.83	1.24	0.69	0.76	0.23
Model-C-DBE	0.29	0.24	0.52	1.06	0.25	6.18	0.69	1.40	0.23
Model-C-MCE	0.31	0.19	0.51	1.18	0.22	9.27	0.69	1.59	0.23

Table 6.6: $p = 10\%$ models: Peak substructure Second-mode (T2) parameters

	h_{eq2}	K_{eq2}/K_2	D_h	R_d	R_a	μ_{t2}	T_2	T_{eq2}	T_R
Model-A-SLE	0.05	1.00	1.00	1.00	1.00	1.00	0.15	0.15	0.23
Model-A-DBE	0.07	0.75	0.89	1.11	0.83	1.37	0.15	0.18	0.23
Model-A-MCE	0.14	0.52	0.71	1.17	0.61	2.06	0.15	0.21	0.23
Model-B-SLE	0.05	1.00	1.00	1.00	1.00	1.00	0.23	0.23	0.23
Model-B-DBE	0.10	0.67	0.81	1.10	0.74	1.58	0.23	0.28	0.23
Model-B-MCE	0.17	0.48	0.65	1.14	0.55	2.37	0.23	0.33	0.23
Model-C-SLE	0.05	1.00	1.00	1.00	1.00	1.00	0.28	0.28	0.23
Model-C-DBE	0.08	0.71	0.87	1.13	0.80	1.44	0.28	0.33	0.23
Model-C-MCE	0.15	0.49	0.70	1.21	0.59	2.15	0.28	0.40	0.23

Table 6.7: $p = 25\%$ models: Peak substructure First-mode (T1) parameters

	h_{eq1}	K_{eq1}/K_1	D_h	R_d	R_a	μ_{t1}	T_1	T_{eq1}	T_R
Model-A-SLE	0.09	0.71	0.84	1.09	0.78	1.63	0.38	0.45	0.23
Model-A-DBE	0.21	0.34	0.60	1.33	0.45	8.14	0.38	0.65	0.23
Model-A-MCE	0.19	0.31	0.62	1.45	0.44	12.20	0.38	0.68	0.23
Model-B-SLE	0.08	0.74	0.86	1.01	0.74	1.53	0.56	0.65	0.23
Model-B-DBE	0.21	0.35	0.61	1.03	0.36	7.65	0.56	0.95	0.23
Model-B-MCE	0.20	0.31	0.62	1.11	0.34	11.48	0.56	1.01	0.23
Model-C-SLE	0.06	0.84	0.94	1.03	0.86	1.24	0.69	0.75	0.23
Model-C-DBE	0.20	0.37	0.61	0.99	0.37	6.18	0.69	1.12	0.23
Model-C-MCE	0.20	0.33	0.61	1.06	0.35	9.27	0.69	1.20	0.23

Table 6.8: $p = 25\%$ models: Peak substructure Second-mode (T2) parameters

	h_{eq2}	K_{eq2}/K_2	D_h	R_d	R_a	μ_{t2}	T_2	T_{eq2}	T_R
Model-A-SLE	0.05	1.00	1.00	1.00	1.00	1.00	0.15	0.15	0.23
Model-A-DBE	0.07	0.79	0.91	1.09	0.86	1.37	0.15	0.17	0.23
Model-A-MCE	0.12	0.60	0.76	1.11	0.67	2.06	0.15	0.20	0.23
Model-B-SLE	0.05	1.00	1.00	1.00	1.00	1.00	0.23	0.23	0.23
Model-B-DBE	0.07	0.79	0.90	1.08	0.85	1.40	0.23	0.26	0.23
Model-B-MCE	0.13	0.61	0.74	1.08	0.66	2.10	0.23	0.29	0.23
Model-C-SLE	0.05	1.00	1.00	1.00	1.00	1.00	0.28	0.28	0.23
Model-C-DBE	0.07	0.76	0.90	1.11	0.84	1.42	0.28	0.32	0.23
Model-C-MCE	0.12	0.56	0.75	1.16	0.65	2.13	0.28	0.37	0.23

6.2.3 Comparison of peak roof accelerations

After obtaining the peak substructure response, the peak roof accelerations for the combined models were calculated for each of the modes from the inelastic response ${}_sA_{Heqi}$ and the corresponding first and second mode amplification factors using the proposed method as discussed in Chapter-4 and outlined in Section 4.1.4. For the equivalent linearisation approach, as discussed in the previous section, the substructure's peak modal response ${}_sA_{Heqi}$ was computed considering the effect of both the period shift and the damping [5]. For the R-factor approach methods, the peak acceleration of the inelastic substructure for each mode was obtained using Equation 5.10. For comparison, the DBE level response was also computed using the Direct-R method (Section 5.4.2) and a reduction factor $R = 8$ for both the modes.

The proposed ridgeline *A-O-A'* (Figure 5-10) accelerations are compared with the mean NLRHA results in Figures 6-7-6-9. For comparison, results accounting only for the substructure T1 mode (${}_sA_{Heq1}$) with the corresponding roof amplification factors (F_{H1} and F_{V1}) are also shown and labelled 'T1' and for the substructure T2 mode (${}_sA_{Heq2}$) response obtained with the corresponding roof amplification factors (F_{H2} and F_{V2}) are also shown and labelled 'T2'.

The ductility ratios of the first mode T1 are large, resulting in longer secant periods (Tables 6.3 and 6.7) and thereby smaller substructure accelerations from the first mode, as depicted by the dotted T1 lines in Figures 6-7-6-9. The second mode accelerations achieve smaller ductility ratios (Tables 6.4 and 6.8) resulting in near-elastic peak substructure (${}_sA_{Heq2}$) response. Furthermore, the T2 mode exhibits shorter period ratios (R_{T2}) leading to larger vertical roof amplification factors, and therefore, the higher mode contribution to the overall vertical roof response is much larger than the first mode, although the mass participation of the higher mode is small. However, for $p = 10\%$, both N&K and Newmark methods present near identical responses for Model-B and Model-C (with T1 modes in the constant-velocity region) and conservatively capture the mean DBE level NLRHA vertical response but underestimate the horizontal response (Figure 6-8(b) and (c)). For Model-A (with T1 mode in the constant acceleration region), the Newmark

method presents the most conservative horizontal and vertical response among the proposed R-factor approaches. For DBE level response results using direct-R factor method, the accuracy is relatively low as it assumes much larger force reduction factors in both the modes and may not be realistic for multistorey structures with significant second mode contributions. For structures with higher post-yield stiffness like the $p = 25\%$ models, the peak substructure response is underestimated by the R-factor methods leading to unconservative overall peak roof responses (Figure 6-9) in all models. These errors increase as the level of the intensity increases from SLE to MCE with increasing ductility values. The more accurate Kasai method is therefore recommended for estimating responses of structures with higher post-yield stiffness ratios.

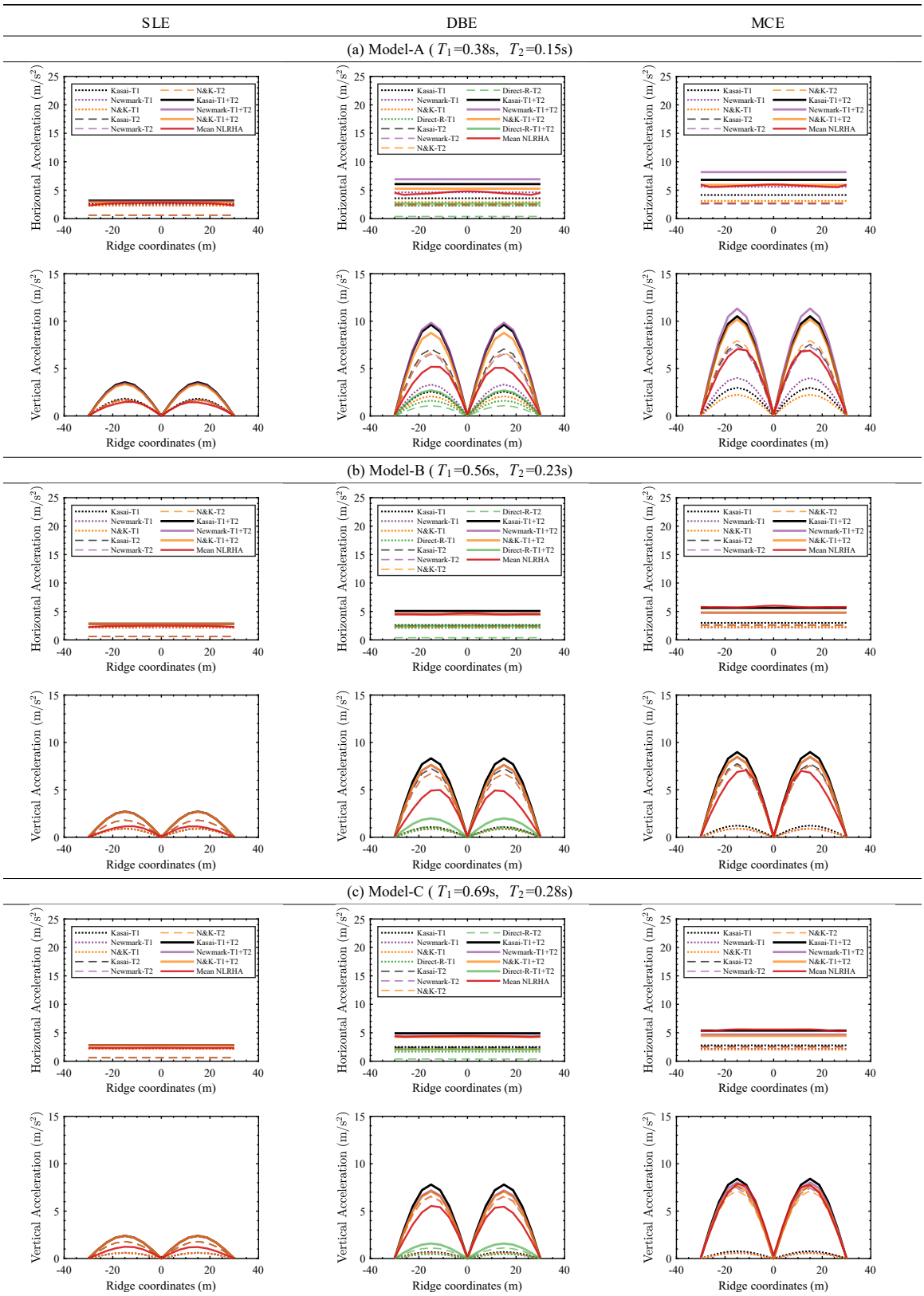

Figure 6-7: $p = 2\%$ 2-storey models: Ridgeline accelerations

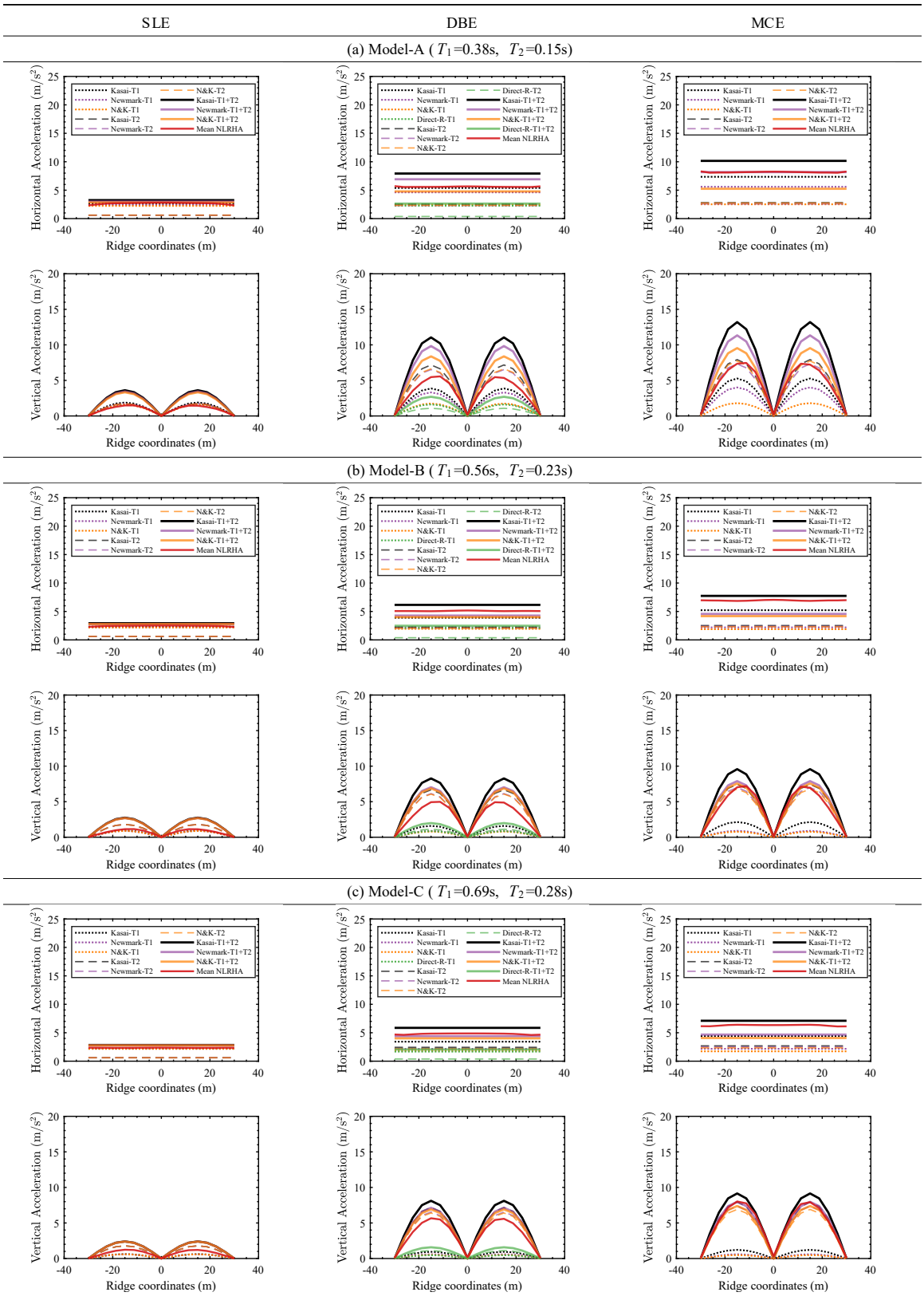

Figure 6-8: $p = 10\%$ 2-storey models: Ridgeline accelerations

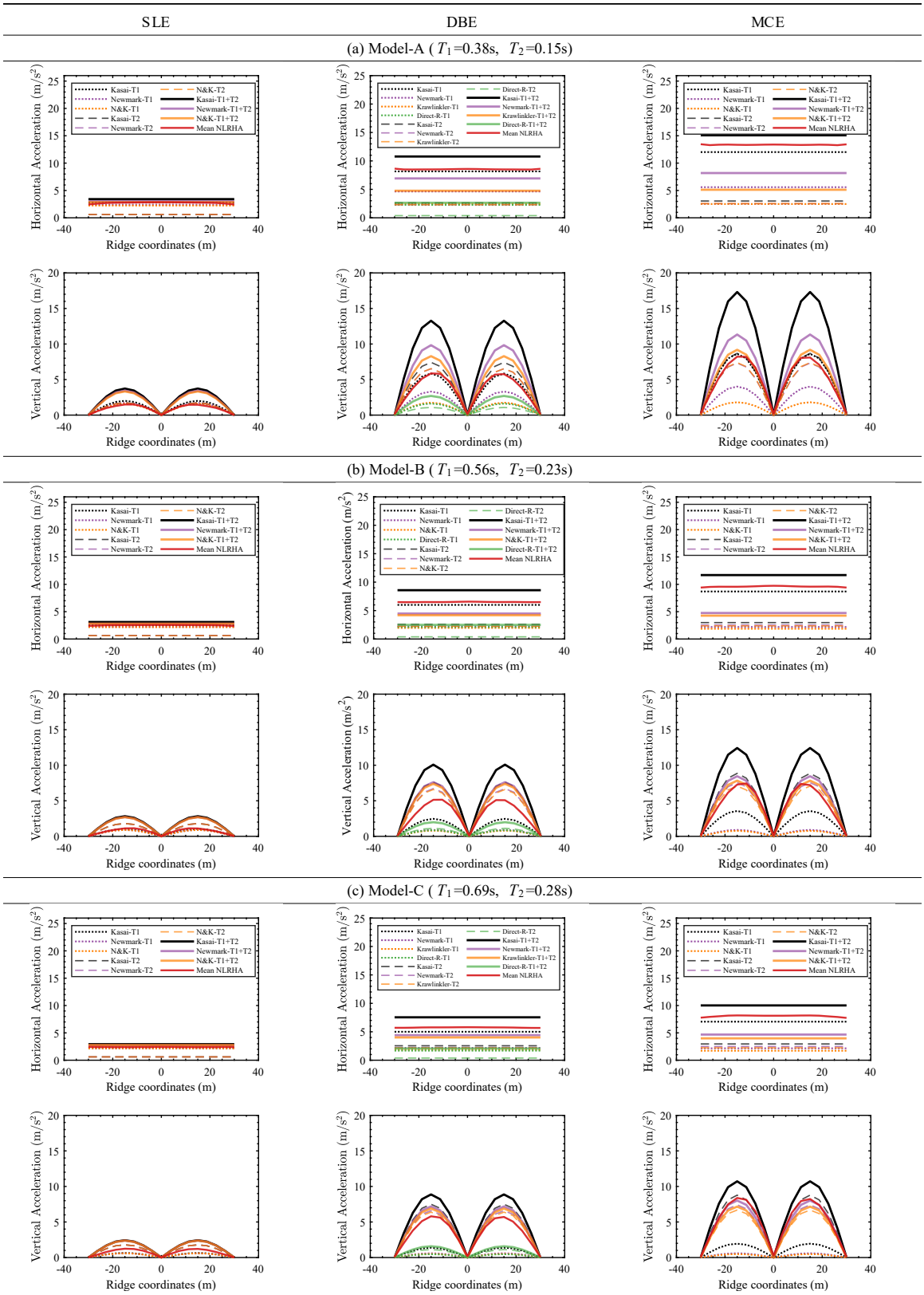

Figure 6-9: $p = 25\%$ 2-storey models: Ridgeline accelerations

6.2.4 Comparison of roof member forces

The proposed peak roof accelerations were then used to compute the corresponding equivalent static loads using Equations 4.11-4.12. Static analyses were performed by applying the obtained vertical and horizontal loads simultaneously to the roof nodes of the combined model in each of the patterns (corresponding to the roof's dominant anti-symmetric mode shape O1 expressed by Equations 4.7 and 4.8) as shown in Figure 4-25 [5].

The detailed results for the roof members of the two-storey models are compared with the mean NLRHA response in Figures 6-13-6-15. The proposed fit lines are also shown using dashed lines along the median response ratios shown separately in Figures 6-10-6-12. For each of the roof members, since each NLRHA load case was run after applying dead loads, the response from the dead loads (N_{DL} and M_{DL}) is deducted from the mean NLRHA response ($N_{NLRHA+DL}$ and $M_{NLRHA+DL}$) to obtain the response only from the earthquake motions (N_{NLRHA} and M_{NLRHA}) using Equations 5.32-5.33. Similarly, the seismic demand from only the equivalent static loads were obtained using Equations 5.34-5.35. The proposed fit lines are also shown using dashed lines. For all models analysed with $p = 2\%$, the axial forces and bending moments from the R-factor approaches are larger than the corresponding NLRHA response except for the direct-R method. Furthermore, the R-factor methods' and the Kasai method are nearly equal for models with $p = 2\%$. For $p < 10\%$, all the estimation methods present near identical responses for Model-B and Model-C (with T1 modes in the constant velocity region) accurately capturing the mean NLRHA response. For Model-A (with T1 mode in the constant acceleration region), the Newmark method followed by the Kasai method presents the most conservative response among the investigated estimation methods.

The percentage of members with underestimated responses are also listed in Tables 6.9-6.10. It was observed that the proposed Kasai method using the maximum acceleration envelope provides a conservative envelope of the member forces. The proposed forces and bending moments at the SLE level were found to be more conservative than the ridgeline accelerations. The underestimation of forces obtained from

the R-factor methods are more evident in the models with higher post-yield stiffness where the Kasai method (Figure 6-15 shown in black markers) exhibits much more conservative DBE and MCE level axial forces and bending moments when compared to the NLRHA method. As discussed in Sections 6.2.3 and 6.2.2, this is due to the underlying assumptions of R-factor approaches which were proposed considering idealised elastoplastic (or low post-yield stiffness) backbone behaviour and thus are recommended for models with relatively low post-yield stiffness. The SLE response for all models analysed are conservative as the corresponding accelerations proposed are conservative, as was observed in Figures 6-7-6-9.

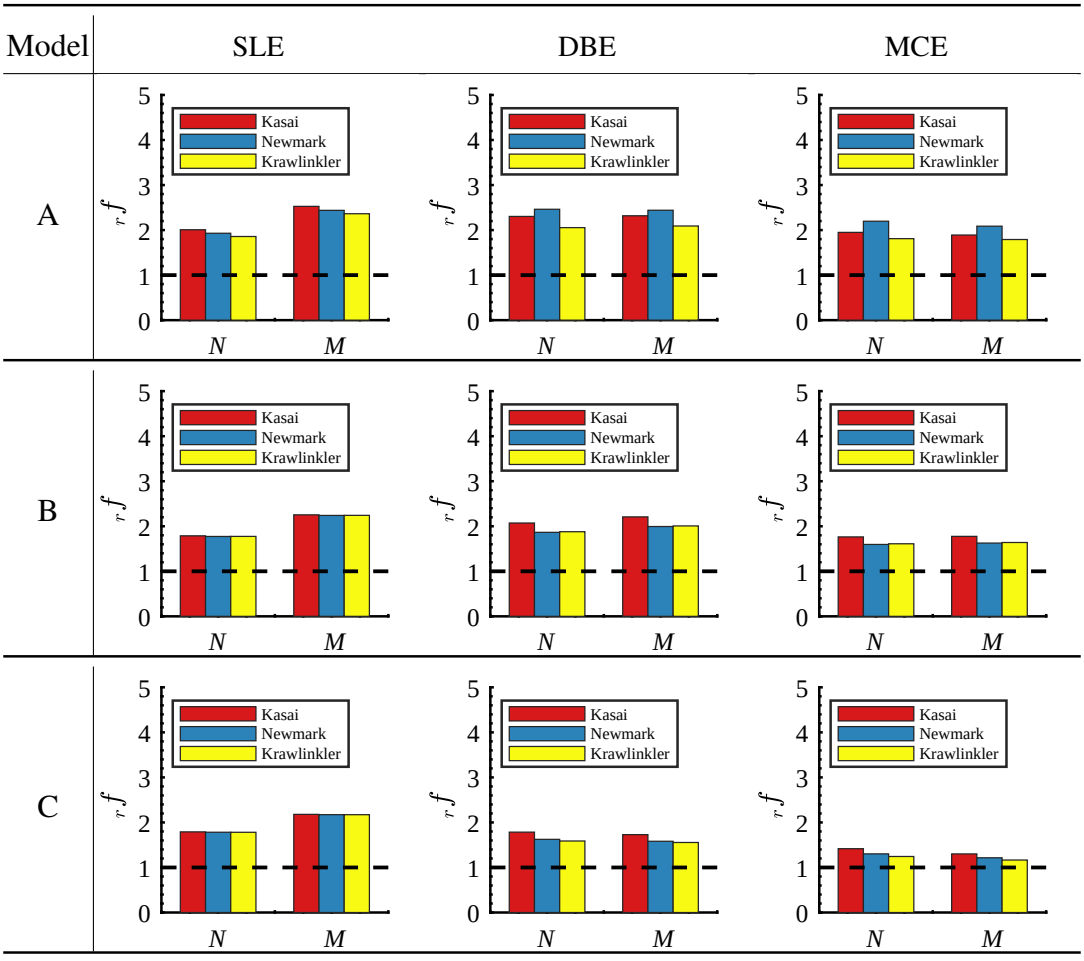

Figure 6-10: Two-storey $p = 2\%$ models: median response ratios

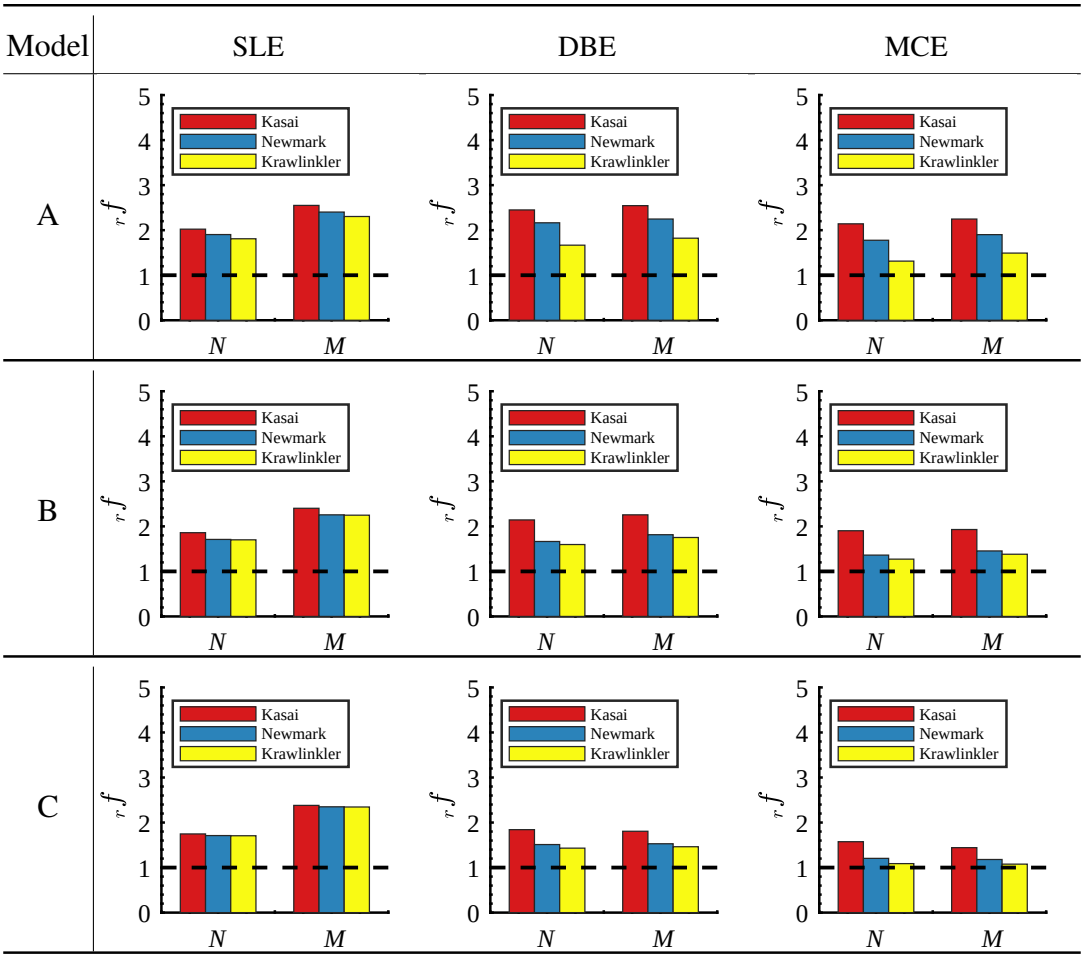

Figure 6-11: Two-storey $p = 10\%$ models: median response ratios

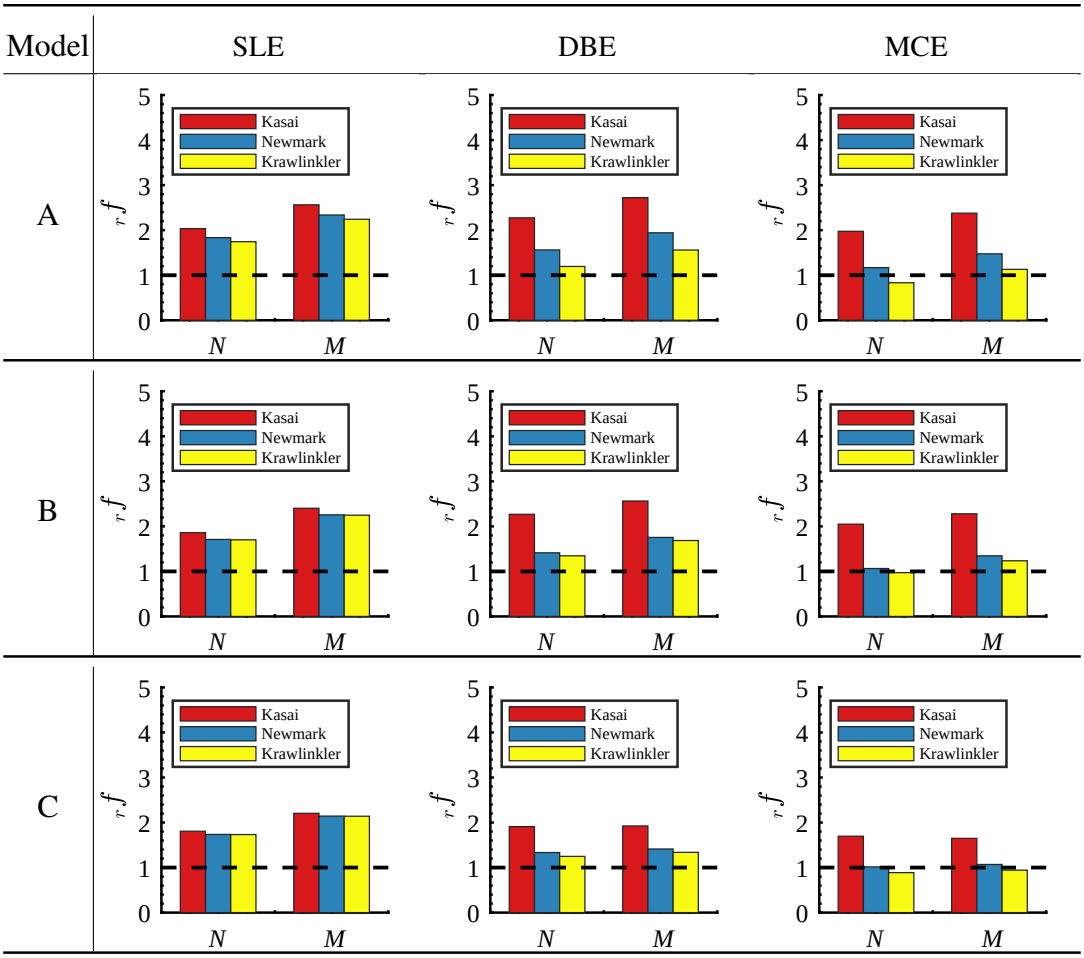

Figure 6-12: Two-storey $p = 25\%$ models: median response ratios

Table 6.9: % of roof members with underestimation of axial forces from seismic loads

Roof members with $N_{static} < N_{NLRHA}$ (%)						
Model	Level	p	Kasai	Newmark	N&K	Direct-R
Model-A	SLE	2	1.5	2.4	2.4	
Model-B	SLE	2	0.0	0.3	0.3	
Model-C	SLE	2	1.2	1.2	1.2	
Model-A	DBE	2	0.6	0.6	1.3	100.0
Model-B	DBE	2	0.3	0.7	0.6	100.0
Model-C	DBE	2	1.6	2.1	2.1	100.0
Model-A	MCE	2	1.3	0.9	1.3	
Model-B	MCE	2	0.4	8.1	6.5	
Model-C	MCE	2	2.9	7.1	9.9	
Model-A	SLE	10	1.5	1.8	2.1	
Model-B	SLE	10	0.3	0.3	0.3	
Model-C	SLE	10	2.4	2.9	2.9	
Model-A	DBE	10	0.6	0.6	5.8	100.0
Model-B	DBE	10	0.3	7.8	10.2	100.0
Model-C	DBE	10	1.2	2.9	8.0	100.0
Model-A	MCE	10	0.6	1.3	20.9	
Model-B	MCE	10	0.3	20.1	23.3	
Model-C	MCE	10	1.3	14.7	23.3	
Model-A	SLE	25	0.3	0.3	0.3	
Model-B	SLE	25	0.3	0.3	0.3	
Model-C	SLE	25	0.6	0.6	0.6	
Model-A	DBE	25	0.3	10.6	31.6	100.0
Model-B	DBE	25	0.3	19.9	22.3	100.0
Model-C	DBE	25	0.9	12.7	19.0	100.0
Model-A	MCE	25	0.6	31.1	74.6	
Model-B	MCE	25	0.3	43.5	53.1	
Model-C	MCE	25	1.2	44.4	84.5	

Table 6.10: % of roof members with underestimation of bending moment from seismic loads

Roof members with $M_{static} < M_{NLRHA}$ (%)						
Model	Level	p	Kasai	Newmark	N&K	Direct-R
Model-A	SLE	2	0.6	0.6	0.6	
Model-B	SLE	2	0.0	0.0	0.0	
Model-C	SLE	2	0.0	0.0	0.0	
Model-A	DBE	2	1.2	0.9	2.1	100.0
Model-B	DBE	2	1.2	1.8	1.8	100.0
Model-C	DBE	2	4.7	5.9	6.2	100.0
Model-A	MCE	2	3.8	2.1	5.0	
Model-B	MCE	2	2.1	2.4	2.1	
Model-C	MCE	2	8.0	10.6	13.0	
Model-A	SLE	10	5.6	5.9	5.9	
Model-B	SLE	10	5.0	5.0	5.0	
Model-C	SLE	10	6.5	6.5	6.5	
Model-A	DBE	10	0.6	1.2	4.1	100.0
Model-B	DBE	10	0.3	2.1	2.1	100.0
Model-C	DBE	10	3.8	5.6	6.2	100.0
Model-A	MCE	10	1.2	2.4	7.4	
Model-B	MCE	10	0.9	4.3	5.3	
Model-C	MCE	10	5.9	11.5	26.9	
Model-A	SLE	25	0.6	0.9	0.9	
Model-B	SLE	25	0.0	0.0	0.0	
Model-C	SLE	25	0.3	0.3	0.3	
Model-A	DBE	25	0.6	2.1	6.2	100.0
Model-B	DBE	25	0.0	2.1	2.7	100.0
Model-C	DBE	25	1.5	5.3	8.3	100.0
Model-A	MCE	25	0.6	5.3	16.2	
Model-B	MCE	25	0.0	5.9	7.7	
Model-C	MCE	25	2.7	17.3	71.8	

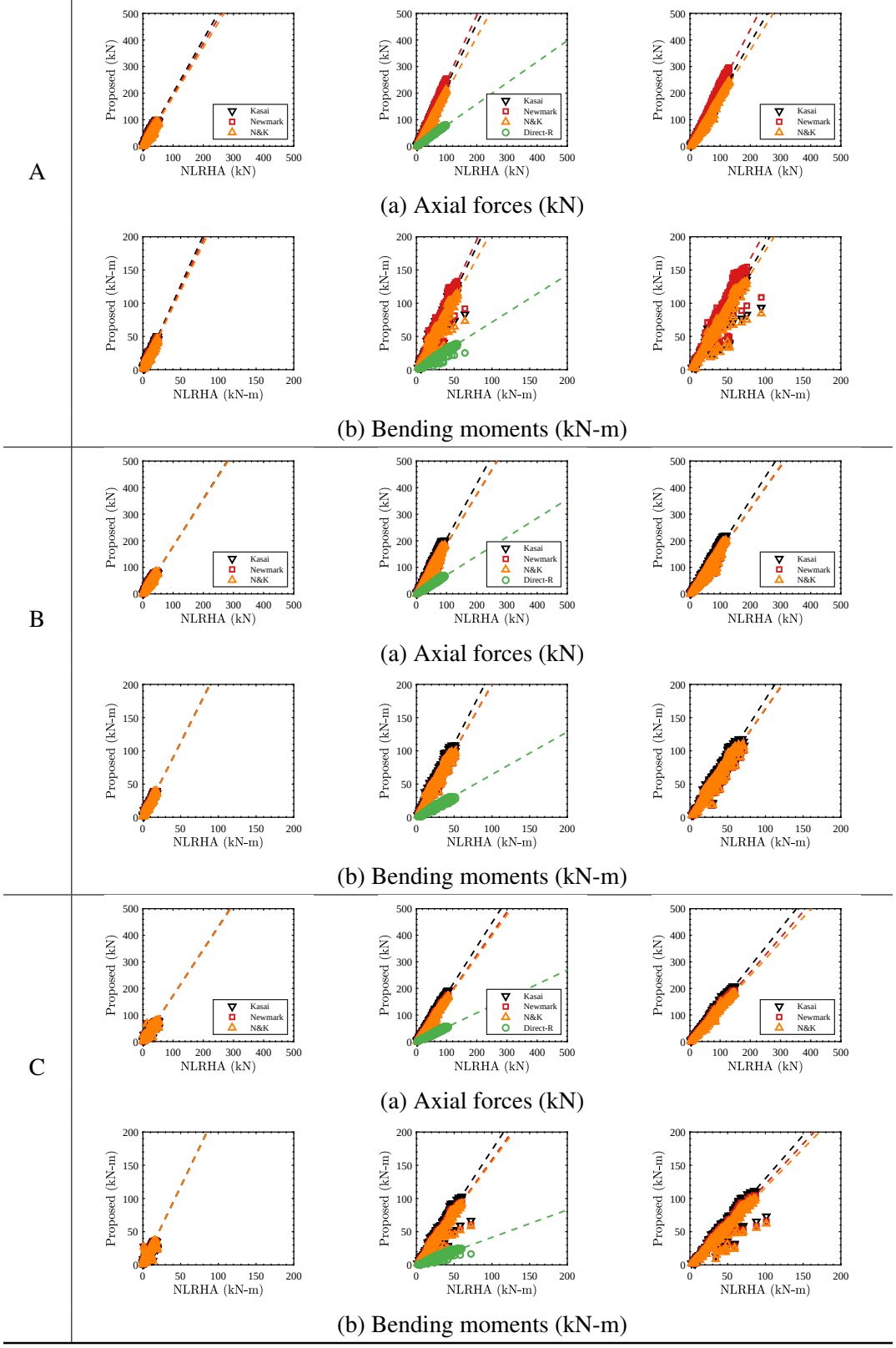

Figure 6-13: Two-storey $p = 2\%$ models: Comparison of member axial forces and bending moments

Model	SLE	DBE	MCE
A	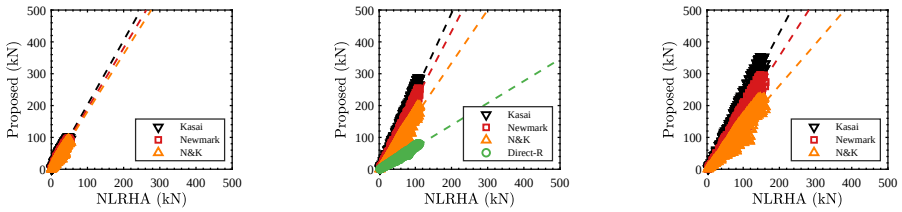		
	(a) Axial forces (kN)		
	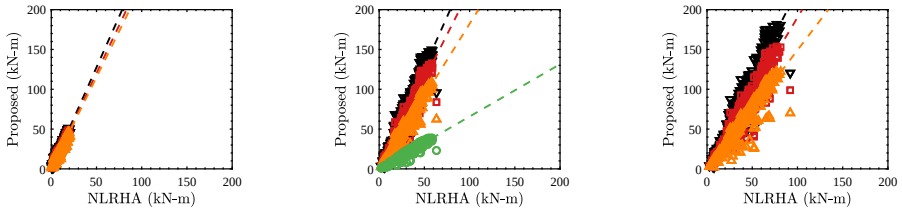		
	(b) Bending moments (kN-m)		
B	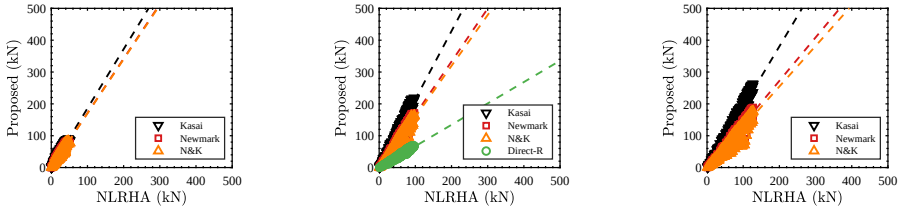		
	(a) Axial forces (kN)		
	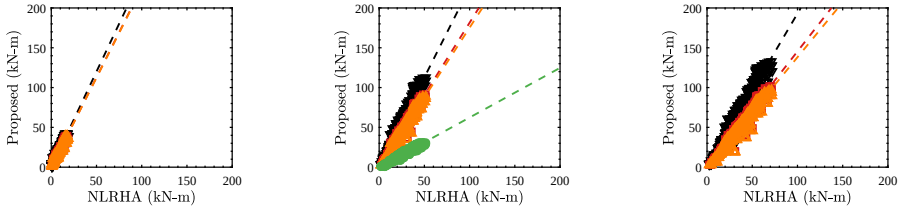		
	(b) Bending moments (kN-m)		
C	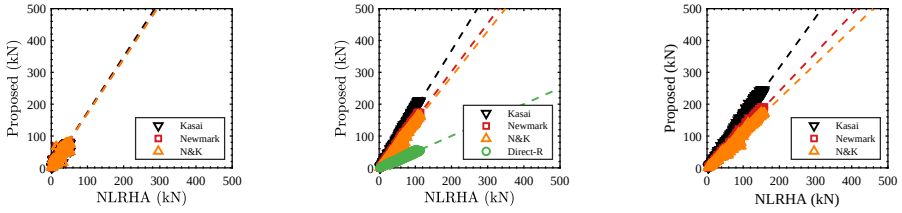		
	(a) Axial forces (kN)		
	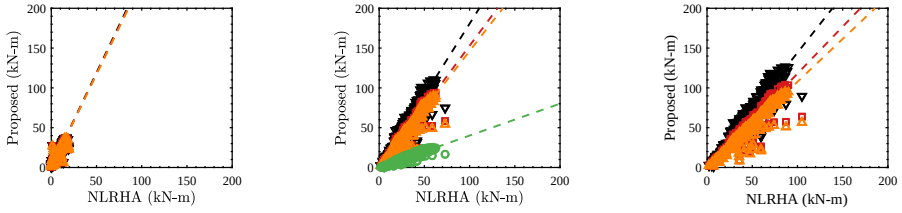		
	(b) Bending moments (kN-m)		

Figure 6-14: Two-storey $p = 10\%$ models: Comparison of member axial forces and bending moments

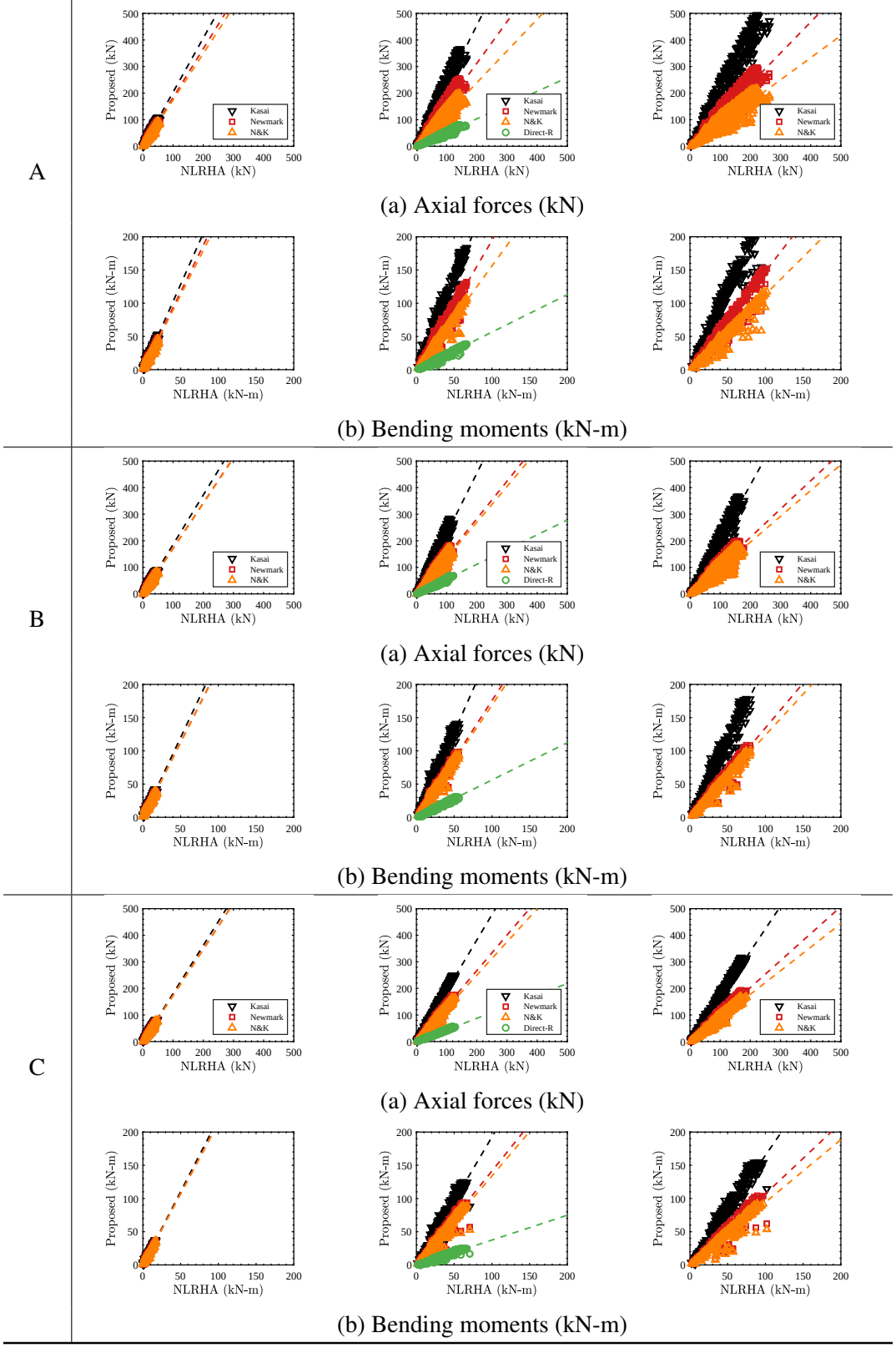

Figure 6-15: Two-storey $p = 25\%$ models: Comparison of member axial forces and bending moments

6.3 Inelastic response of 6-storey BRBF

To further investigate the effects of substructure higher-modes on the peak substructure acceleration and roof response, a 6-storey substructure with a height of 30m was also constructed as shown in the Figure 6-16. Commensurate with the geometry of the previous substructure models, the storey height for the 6-storey substructure is kept constant at 5m, each storey has a floor weight of 7kPa and the roof dead load is assumed to be 2kPa (Section 5.3). The gravity frame section sizes are also adopted from the 2-storey model given in Table 6.1. The BRBs were designed using the same design procedure and a standard post-yield stiffness ratio p=2% as outlined in Section 5.3.1 and the properties of the BRB links and design storey shears are given in Table 6.11. The benchmark combined analysis model (Model-B) was then constructed combining the roof model (Section 5.3.3) and the substructure model. To investigate the effect of post-yield stiffness, an additional substructure model with links modelled with a post-yield stiffness p=25% was also created keeping the BRB yield displacements the same as the p=2%.

Table 6.11: Equivalent Lateral Forces: Proportioning BRBs ($\sigma_y = 235$MPa)

Model-B ($T_1 = 0.93s, T_2 = 0.39s$)									
Storey	h (m)	kN W_x	kN V_x	kN BRB V_x	kN BRB V_{ix}	kN BRB P_i	mm δ_y	kN/m BRB K_{eqi}	mm^2 A_c
RFL	30	6064	1483	1483	43	75	4.12	18343	321
6FL	25	6032	2713	2713	77	138	4.12	33550	588
5FL	20	6032	3696	3696	106	188	4.12	45715	801
4FL	15	10968	5038	5038	144	256	4.12	62305	1091
3FL	10	10968	5932	5932	169	302	4.12	73364	1285
2FL	5	10968	6379	6379	182	325	4.12	78894	1382

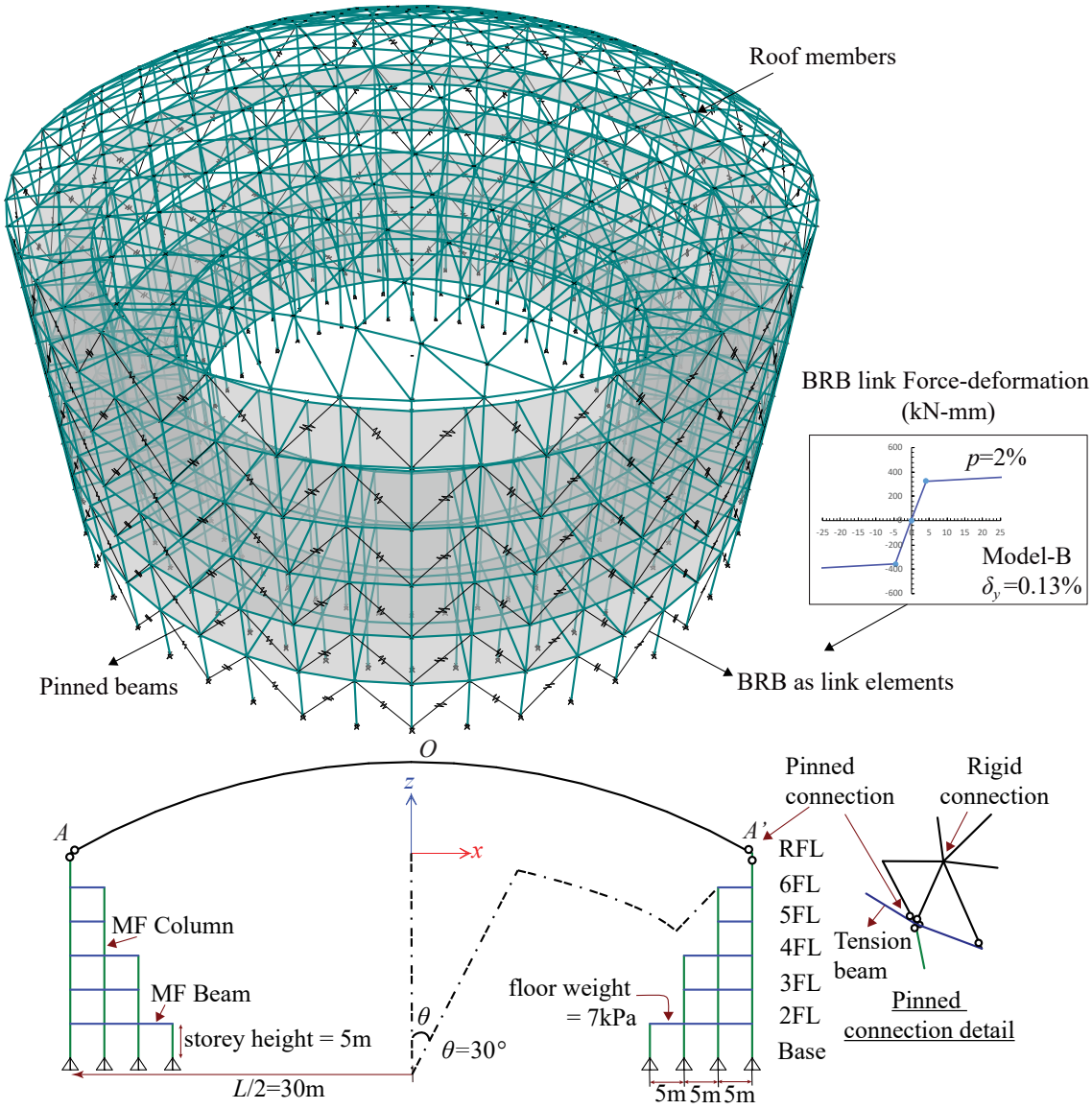

Figure 6-16: 6-storey Model-B (60m combined model): Perspective and elevation view

6.3.1 Inter-storey drifts

The mean peak inter-storey drifts and mean residual inter-storey drifts for the substructure of the combined models (Model-B) from NLRHA (using the spectrally matched input ground motions in Section 5.3.5) are given in Figure 6-17. ASCE-7 [3] prescribes an allowable storey drift of 2.0% for the DBE level. The obtained mean storey drifts are quite uniform along the substructure height and are within the permissible ASCE limits for all models with post-yield stiffness. Typical values of mean residual drift are approximately 0.3% for p=2% models under the DBE level. These values increase to 0.4% under the MCE level within the 0.5% limit for the immediate occupancy criteria for most storeys except the roof floor. While increasing the post-yield stiffness to p=25% reduces the peak inter-storey drifts, the improvement in residual drifts is much more significant with typical residual drifts for all three levels within 0.2%.

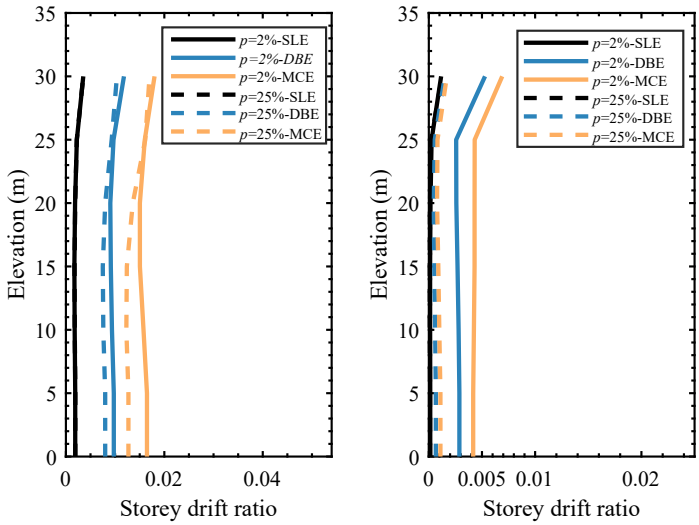

(a) Storey drift ratio (b) Residual drift ratio

Figure 6-17: Model-B: Mean of peak storey drift ratios of substructure

6.3.2 Peak Substructure acceleration

The first substructure mode T1 (fundamental translation mode) has a period of 0.93s and a mass participation (Γ_1) of 77% and the second translational mode T2 has a period of 0.39s and contributes to a mass participation (Γ_2) of 15%. The periods are longer than those of the 2-storey models resulting in longer period ratios. These longer period ratios imply that the roof-substructure interaction is weaker and corresponds to smaller vertical amplification factors, which have an inverse relationship with the period ratios in this range. The mass participation of the second mode is larger if compared to the 2-storey substructure models, leading to a higher contribution of the T2 mode to the peak substructure response.

For each of the models, modal pushover analyses was conducted to obtain the first and second modal pushover curves and the initial base shear to roof displacement stiffness (K_{1i}) was obtained as shown in Figure 6-18. For the $p = 2\%$ model, the first-mode pushover curve has a post-yield stiffness of 2% and the second-mode pushover curve was found to have a higher post-yield stiffness of 14% as the BRBs of all storeys do not yield at the same time and many of the braces remain elastic when the substructure is pushed using a force distribution based on the second mode shape. Similarly, for the $p = 25\%$ model, the first mode pushover curve has a post-yield stiffness of 25% and the second mode pushover curve was found to have a post-yield stiffness ratio of 36%.

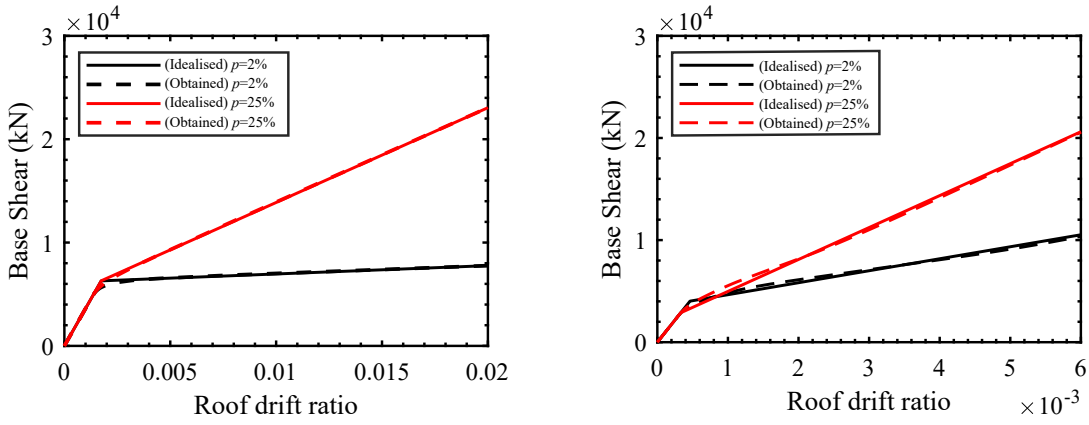

(a) First mode (T1)

(b) Second mode (T2)

Figure 6-18: Model-B: Modal pushover curves and idealisation of structural response

As for the 2-storey and single-storey models, the peak response of each model was computed for three levels of earthquake intensity-SLE, DBE and MCE. The reduction in acceleration (R_{ai}) and achieved damping parameters for each substructure mode from the Kasai method are given in Tables 6.12-6.15. For the DBE level, as both the seismic demand and reduction factors are large, the roof displacement ductility factors obtained from the first mode μ_1 were about 6. The second mode has a significant contribution to damping, as can be seen from the higher h_{eq2} values and the lower D_{h2} values in Tables 6.13 and 6.15 if compared to the 2-storey models in Tables 6.4 and 6.8. The shift in period and the reduction in acceleration was thus larger than those observed for the second mode in 2-storey models.

Table 6.12: $p = 2\%$ models: Peak substructure First-mode (T1) parameters

	h_{eq1}	K_{eq1}/K_1	D_h	R_d	R_a	μ_{t1}	T_1	T_{eq1}	T_R
Model-B-SLE	0.06	0.87	0.97	1.04	0.91	1.11	0.94	1.00	0.23
Model-B-DBE	0.37	0.18	0.47	1.10	0.20	5.53	0.94	2.19	0.23
Model-B-MCE	0.43	0.11	0.44	1.30	0.15	8.30	0.94	2.78	0.23

Table 6.13: $p = 2\%$ models: Peak substructure Second-mode (T2) parameters

	h_{eq2}	K_{eq2}/K_2	D_h	R_d	R_a	μ_{t2}	T_2	T_{eq2}	T_R
Model-B-SLE	0.05	1.00	1.00	1.00	1.00	1.00	0.39	0.39	0.23
Model-B-DBE	0.23	0.43	0.58	1.08	0.46	2.96	0.39	0.60	0.23
Model-B-MCE	0.31	0.33	0.51	1.10	0.36	4.44	0.39	0.69	0.23

Table 6.14: $p = 25\%$ models: Peak substructure First-mode (T1) parameters

	h_{eq1}	K_{eq1}/K_1	D_h	R_d	R_a	μ_{t1}	T_1	T_{eq1}	T_R
Model-B-SLE	0.05	0.91	0.98	1.03	0.94	1.11	0.94	0.98	0.23
Model-B-DBE	0.20	0.39	0.61	0.98	0.38	5.53	0.94	1.49	0.23
Model-B-MCE	0.20	0.34	0.61	1.04	0.35	8.29	0.94	1.60	0.23

Table 6.15: $p = 25\%$ models: Peak substructure Second-mode (T2) parameters

	h_{eq2}	K_{eq2}/K_2	D_h	R_d	R_a	μ_{t2}	T_2	T_{eq2}	T_R
Model-B-SLE	0.05	1.00	1.00	1.00	1.00	1.00	0.39	0.39	0.23
Model-B-DBE	0.19	0.51	0.63	1.05	0.54	4.13	0.39	0.55	0.23
Model-B-MCE	0.20	0.46	0.61	1.08	0.50	6.20	0.39	0.58	0.23

6.3.3 Comparison of peak roof accelerations

After obtaining the peak substructure response, the peak roof accelerations for the combined models were calculated for each of the modes from the inelastic response ${}_sA_{Heqi}$ and the corresponding first and second mode amplification factors using the proposed method as discussed in Chapter-4 and outlined in Section 4.1.4. Similar to the procedure for 2-storey models explained in Section 6.2.3, the peak roof accelerations for the combined models listed in Table 6.12-6.15 were calculated using the first and second mode amplification factors. The proposed envelope of ridgeline *A-O-A'* (Figure 6-16) roof accelerations are compared with the mean NLRHA results in Figures 6-19-6-20. The second mode achieves smaller ductility ratios (Tables 6.13 and 6.15) and the reduction in acceleration is lesser if compared to the T1 mode response. Therefore, in large ductility regimes for the DBE and MCE levels, ${}_sA_{Heq2}$ (T2 dashed lines) is higher than ${}_sA_{Heq1}$ (T1 dotted lines). Furthermore, the T2 mode exhibits relatively shorter period ratios ($R_{T2} < R_{T1}$) leading to larger vertical roof amplification factors ($F_{V2} > F_{V1}$) and therefore, the higher mode contribution towards the overall vertical roof response is much larger than the first mode, even though the mass participation of the higher mode is small. For $p = 2\%$ DBE level response results using direct-R factor method, the accuracy is relatively low as it assumes much larger force reduction factors than actually achieved in both the modes (severely underestimating the second mode response) and may not be realistic for multistorey structures with significant second mode contributions. However, the response from Newmark's method (T1+T2 response) is nearly equal to the Kasai method (T1+T2 response) in Figure 6-19, conservatively capturing the mean NLRHA response.

For the Newmark method, the ${}_sA_{Heq1}$ was computed following the equal displacement rule and ${}_sA_{Heq2}$ using the equal energy rule as the two substructure modes lie on different regions of the spectrum. This confirms the applicability of Newmark method for multistorey substructures with elastoplastic first mode response and considerable post-yield stiffness in the second mode. As observed in the previous 2-storey models (Figures 6-5-6-6), for structures with higher post-yield stiffness like the $p = 25\%$ models, the peak substructure response is underestimated by the R-factor methods leading to

unconservative overall peak roof responses (Figure 6-20). These errors increase as the level of the intensity increases from SLE to MCE with increasing ductility values. Nevertheless, the Newmark method provided a conservative estimate of the vertical response even for $p = 25\%$ models as the proposed vertical amplification factors are conservative enough to compensate for the underestimation of the substructure response. To summarise, the most conservative Kasai method is recommended for estimating responses of structures with higher post-yield stiffness ratios.

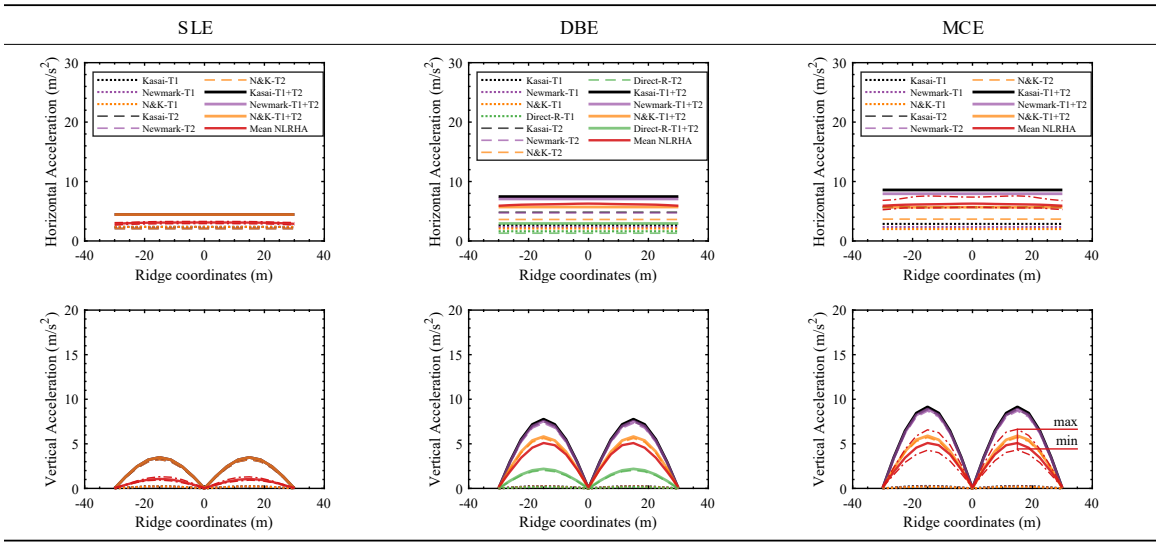

Figure 6-19: 6-storey (Model-B: T_1=0.94s, T_2=0.39s) $p = 2\%$: Ridgeline accelerations

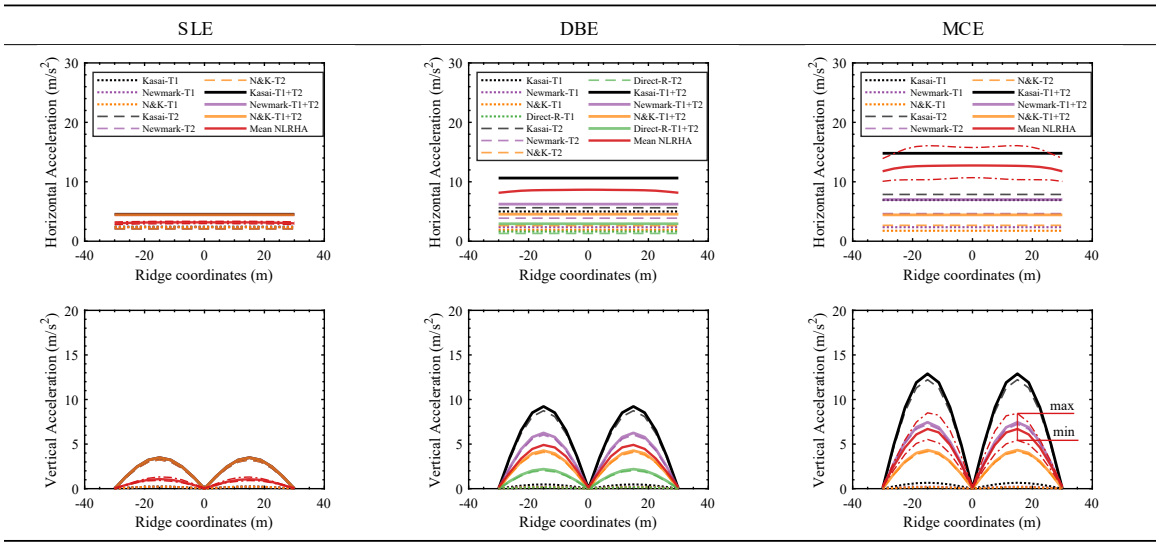

Figure 6-20: 6-storey (Model-B: T_1=0.94s, T_2=0.39s), $p = 25\%$: Ridgeline accelerations

6.3.4 Comparison of roof member forces

The proposed peak roof accelerations were then used to compute the corresponding equivalent static loads using Equations 4.11-4.12. Static analyses were performed by applying the obtained vertical and horizontal loads simultaneously to the roof nodes of the combined model in each of the patterns (corresponding to the roof's dominant anti-symmetric mode shape O1 expressed by Equations 4.7 and 4.8) as shown in Figure 4-25 [5].

The responses of the 6 storey models' roof members are also compared in detail in Figures 6-22-6-23. As the proposed accelerations were conservative, the proposed static member responses obtained using the Kasai method were also conservative for all models across all three levels of input ground motions. The axial forces and bending moments were found to be the most conservative for the SLE level. As observed for the peak ridge accelerations, the differences in the proposed member forces are more evident in the models with higher post-yield stiffness, where the Kasai method exhibits a much more conservative response with the errors in the R-factor method estimates larger in the higher ductility ranges (the DBE and MCE level). However, the Newmark method remained relatively conservative for the DBE level even as the post-yield stiffness increased to 25%.

The accuracy of the methods can be further evaluated by considering the percentage of roof members that are underestimated by each as listed in Tables 6.16-6.17 and the median response ratios are compared in Figure 6-21. Although the second mode has a higher post-yield stiffness in the 6-storey case, similar to the responses of the two-storey models, the accuracy of the Newmark method and the Kasai method remained nearly equal for models with $p = 2\%$. The Kasai method was observed to be highly conservative and underestimates the responses in less than 2% of the roof members. The Newmark method also presents a similar accuracy for $p = 2\%$ and this accuracy reduces to $p = 25\%$ models with up to 60% of the axial forces being underestimated at the MCE level. The Direct-R method is not recommended, as it severely underestimates all roof members' responses.

Therefore, it is recommended to use the proposed equivalent static load procedure in the preliminary design stages as a baseline method for initial sizing and approximate estimation

of the member forces. For the final design member check, it is recommended to use the more rigorous NLRHA method.

Table 6.16: % of roof members with underestimation in axial forces

Roof members with $N_{static} < N_{NLRHA}$ (%)						
Model	Level	p	Kasai	Newmark	N&K	Direct-R
Model-B	SLE	2	0.3	0.3	0.3	
Model-B	DBE	2	0.6	0.9	5.5	100.0
Model-B	MCE	2	0.9	1.0	27.6	
Model-B	SLE	25	0.3	0.3	0.3	
Model-B	DBE	25	0.3	23.6	90.0	100.0
Model-B	MCE	25	0.3	59.4	100.0	

Table 6.17: % of roof members with underestimation in bending moments

Roof members with $M_{static} < M_{NLRHA}$ (%)						
Model	Level	p	Kasai	Newmark	N&K	Direct-R
Model-B	SLE	2	0.3	0.3	0.3	
Model-B	DBE	2	0.6	0.6	0.9	99.7
Model-B	MCE	2	1.8	1.2	16.7	
Model-B	SLE	25	0.0	0.0	0.0	
Model-B	DBE	25	0.6	3.2	65.3	98.2
Model-B	MCE	25	0.0	7.7	100.0	

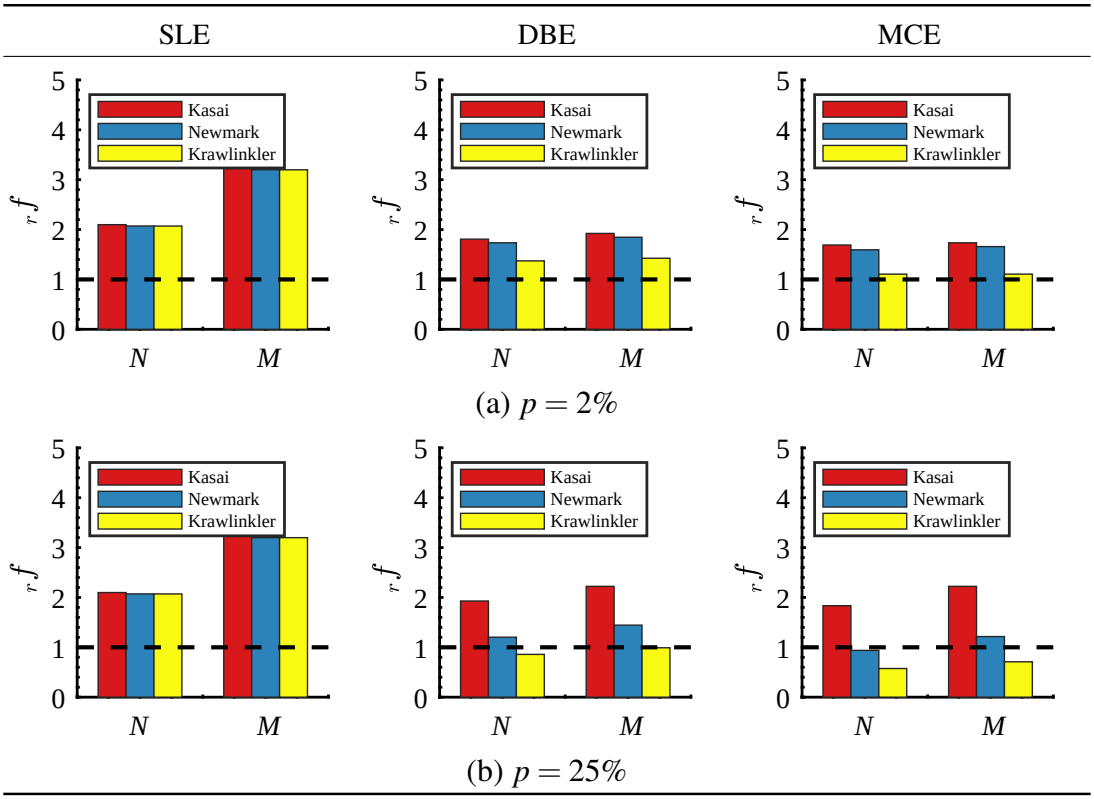

Figure 6-21: Six-storey models: median response ratios

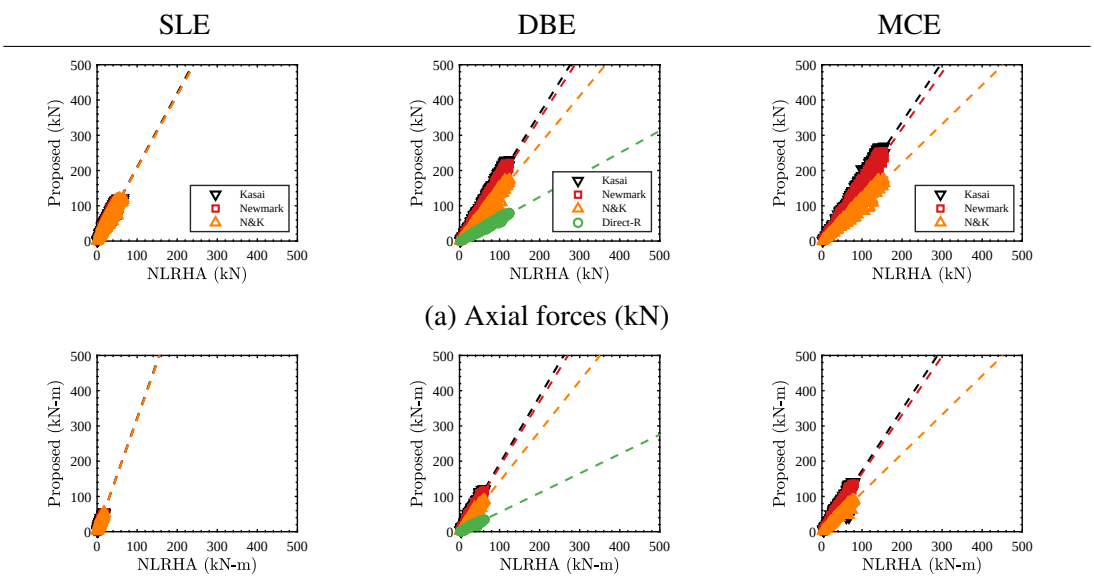

(a) Axial forces (kN)

(b) Bending moments (kN-m)

Figure 6-22: Six-storey $p = 2\%$ models: Comparison of roof member forces

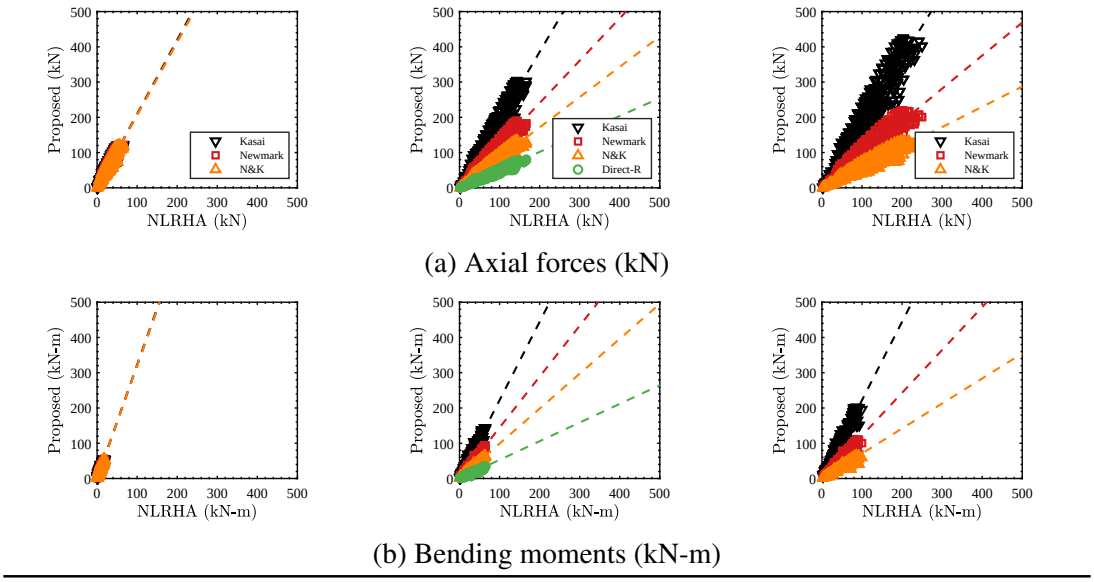

(a) Axial forces (kN)

(b) Bending moments (kN-m)

Figure 6-23: Six-storey $p = 25\%$ models: Comparison of roof member forces

6.4 Inelastic response of long-span 6-storey analysis models

This section discusses the applicability of the ductility based R-factor approach to estimate the peak substructure accelerations of longer 150m span multi-storey substructures in the constant velocity range. The peak roof accelerations and response from equivalent static loads are also discussed using the amplification factor approach.

The modelling assumptions are similar to the 60m span six-storey model in Section 6.3 and Section 3.2. The 150m spanned structure has six storeys and a roof level, each 5m high, and has a floor weight of 7 kPa. The dead load on the roof is assumed to be 3kPa (Section 3.2). Substructure geometry and frame section sizes are also adopted from the model $L150-DL3-\alpha1$ (Section 3.2) and are shown in Figure 6-24.

As for other nonlinear substructure models in the chapter, it was assumed that all lateral forces are resisted by the BRBs and so in the FE model, all the beams were assumed to be pinned and released at both ends. The columns were modelled to be continuous. The substructure model was designed with a BRB yield ratio of 1/750 following the procedure in Section 5.2 so that the fundamental period is in the region of constant velocity as given in Table 6.11. The BRBs have been modelled as links with bilinear hysteretic characteristics and a post-yield stiffness ratio (p) of 2%. The combined analysis models were then constructed combining the roof model and substructure model.

The geometry of the Roof-1 model was adopted from the $L150-DL3-\alpha1$ model (Section 3.2). As this designed substructure is more flexible and is designed to have significant energy dissipation capacity, an alternative more flexible dome is designed (labelled as 'Roof-2') for the reduced seismic demands on the roof. The roof frame sizes for both models are given in Table 6.18.

Table 6.18: 150m roof models: Member section sizes

Model	Dead Load (DL) (kPa)	Double-layer beam (mm)	offset d (cm)	Single-layer beam (mm)	m	Tension beam (mm)
Roof-1	3	2× ϕ511 t11	350	ϕ715.5 t15.5	51	ϕ2525 t25
Roof-2	3	2× ϕ500 t5.4	303	ϕ609 t9	51	ϕ2525 t25

* m = Out-of-plane stiffness modification factor

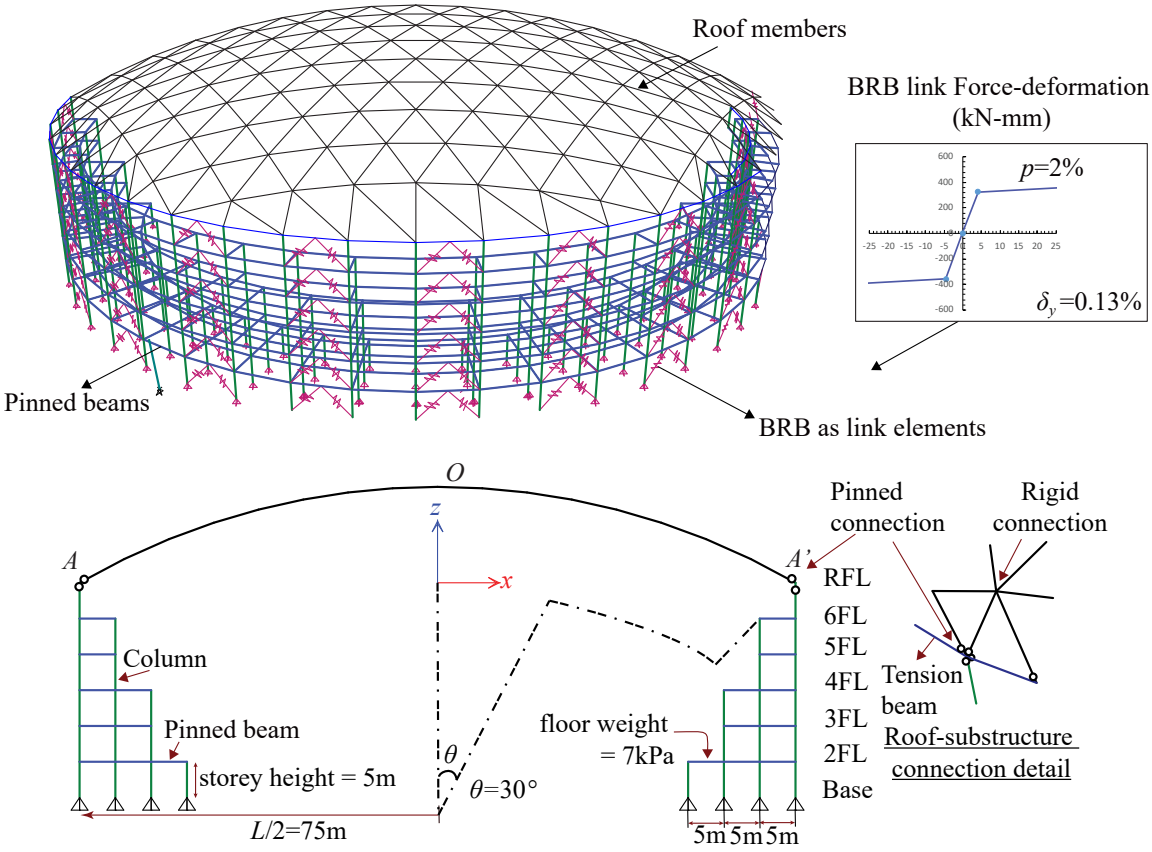

Figure 6-24: 6-storey 150m combined model: Perspective and elevation view

Table 6.19: Equivalent Lateral Forces: Proportioning BRBs ($\sigma_y = 235$MPa)

Model-A ($T_1 = 1.5s, T_2 = 0.48s$,)									
Storey	h (m)	kN W_x	kN V_x	kN BRB V_x	kN BRB V_{ix}	kN BRB P_i	mm δ_y	kN/m BRB K_{eqi}	mm^2 A_c
RFL	30	56840	7414	7414	177	252	4.67	53991	1073
6FL	25	15904	9143	9143	218	311	4.67	66580	1323
5FL	20	15904	10526	10526	251	358	4.67	76651	1523
4FL	15	30710	12529	12529	398	426	4.67	91236	1813
3FL	10	30710	13864	13864	330	471	4.67	100960	2006
2FL	5	44420	14830	14830	353	504	4.67	107992	2145

Dominant modes of combined models

The dominant modes of the roof models are given in Tables 6.20. Roof-2 is more flexible than the Roof-1 model, and all four modes lie in the constant-velocity region of the spectrum. The spectral values are therefore lower, but the modes are closer to the substructure modes, and hence the period ratios are smaller. The dominant modes of the combined models are shown in Figures 6-25-6-26. As the substructure is farther away from the roof periods, the sway mode dominates with 75% mass participation. The T2 mode interacts with O1 mode of the Roof-1 model and with the nearer O2 mode of the Roof-2 to form the next dominant mode in the combined models.

Table 6.20: $L150$ roof models: Periods (s) and mass participation (%)

Model	O1 ($_rT_R$)	O2	O2.5	I
Roof-1	0.56s, (18%)	0.29s, (5%)	0.17s, (53%)	0.11s, (6%)
Roof-2	0.82s, (17%)	0.46s, (5%)	0.25s, (60%)	0.16s, (6%)

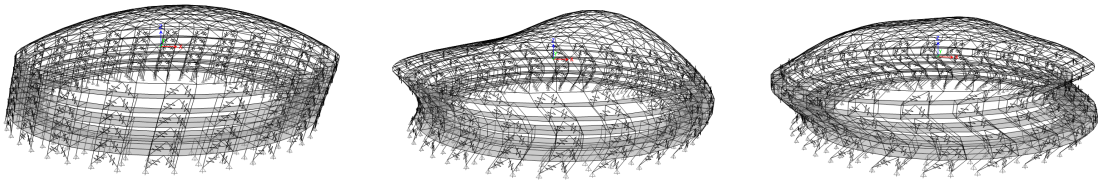

(a) O1+T1 (sway) 1.52s (75%) (b) O1+T2 0.49s (14%) (c) O2.5+T3 0.22s (4%)

Figure 6-25: 150m combined model (Roof-1) dominant modes

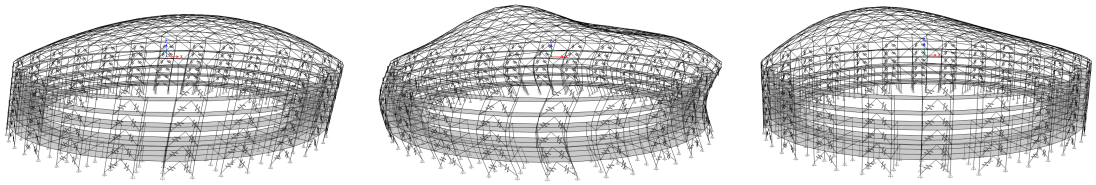

(a) O1+T1 (sway) 1.54s (73%) (b) O2+T2 0.51s (15%) (c) O1-T1 0.80s (2%)

Figure 6-26: 150m combined model (Roof-2) dominant modes

6.4.1 Input ground motions and target design spectrum

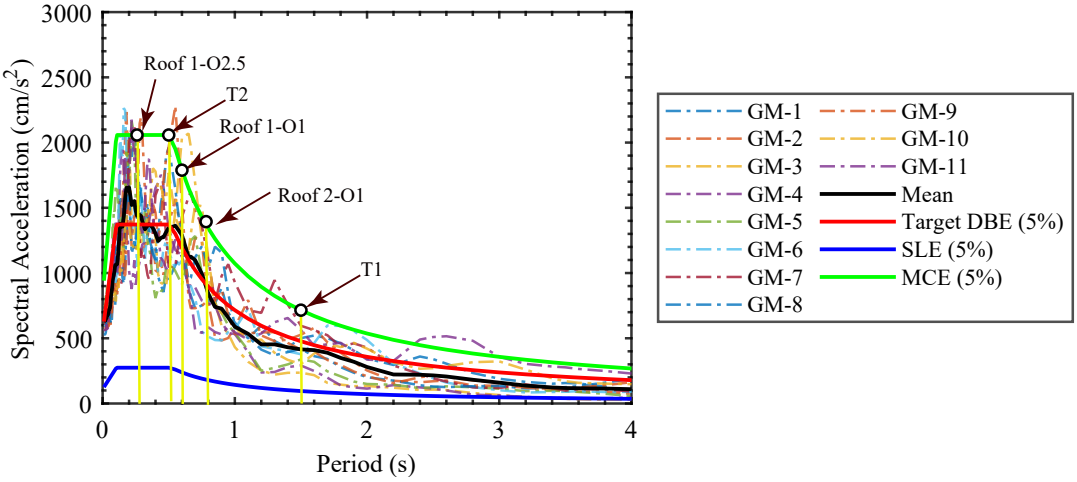

Figure 6-27: Target design spectrum and earthquake levels

As described in Section 5.3.5, 11 natural ground motions were selected from the strong motion database of the Pacific Earthquake Engineering Center [6]. An initial suite was obtained using a standard search criteria of minimum magnitude of 6.5, a maximum magnitude of 7.5, and maximum shear velocity of 400m/s. 11 of the selected ground motions (Horizontal-1 direction) listed in Table 6.21 were then scaled minimising the mean square error in accordance with Section 16.2 of ASCE 7-16 such that the average of the spectra is more than 90% of the target design spectrum (defined in Section 5.3) over the period range of 0.2T1-1.5T1 where T1 was considered as 0.9s (the approximate fundamental period). The response spectra of the 11 scaled ground motions and the average of their spectra (labelled as 'Mean') are shown in Figure 6-27.

For NLRHA performed on the combined models using these scaled waves, Rayleigh damping of 5% was assigned to the first and second mode and the analysis was performed using the integration approach using the Hilber-Hughes-Taylor (HHT) method [7], [8]. Two additional levels of ground motion intensity were considered to investigate the response at the maximum considered earthquake level (MCE) (1.5 $\times$ DBE level as prescribed by ASCE-7 [3]) and the serviceability level (SLE = 0.2 $\times$ the DBE level). As discussed in Section 5.3.5, for this study, the SLE spectrum spectrum was defined by retaining the shape of the DBE spectra, and then scaling it by 0.2.

Table 6.21: Input ground motions for 150m models from PEER database [6]

No.	Earthquake*	Year	Station name	M	R_{jb} (km)	PGA (g)	Scale factor
1	Northridge-01	1994	LA-Century City	6.7	16	0.26	2.36
2	Northridge-01	1994	LA- Hollywood	6.7	20	0.23	2.58
3	Northridge-01	1994	LA- N Faring Rd	6.7	12	0.28	2.73
4	Northridge-01	1994	LA- Saturn St	6.7	21	0.47	1.57
5	Northridge-01	1994	LA- UCLA Grounds	6.7	14	0.28	2.58
6	Kobe	1995	Kakogawa	6.9	23	0.25	2.47
7	Chuetsu-oki	2007	Sanjo Shinbori	6.8	16	0.32	1.93
8	El Mayor	2010	El Centro - Imperial	7.2	19	0.38	1.39
9	El Mayor	2010	El Centro Array	7.2	19	0.37	1.57
10	Darfield	2010	Kaiapoi North School	7.0	31	0.36	2.03
11	Darfield	2010	Pages Road	7.0	25	0.20	2.86

R_{jb} = closest horizontal distance between the vertical projection of the rupture plane and recording station, M = moment magnitude,
PGA = unscaled peak ground acceleration
*These records were obtained from the NGA-West2 online ground motion database tool

6.4.2 Inter-storey drifts

The mean of the 11 peak inter-storey drifts for the substructure of the Roof-1 combined model obtained from the NLRHA using the scaled input ground motions is given in Figure 6-28. For 4 storeys and above, Table 12.12-1 of ASCE-7 [3] prescribes an allowable storey drift of 2.0% for DBE level and 3.5% for MCE level. The obtained mean storey drifts were relatively uniform and well within the permissible ASCE limits for all models with post-yield stiffness.

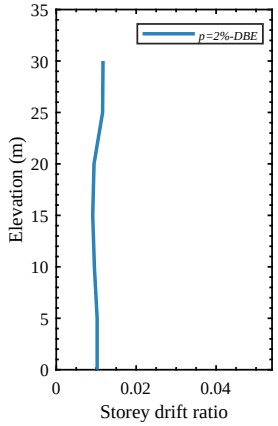

Figure 6-28: Mean of peak storey drift ratios of substructure

6.4.3 Peak substructure acceleration

For the substructure model, modal pushover analyses was conducted to obtain the first and second mode pushover curves and the initial stiffness (K_{1i}) was obtained as shown in Figure 6-29. The first substructure mode has a period of 1.5s and a mass participation of 77% and the second translational mode contributes to another 15%. Using the equivalent linearisation procedure, the reduction in acceleration (R_{ai}) was computed. For the R-factor approaches, the first mode has a post-yield stiffness of 2% and the second mode has a post-yield stiffness of 36%. The continuous columns were found to contribute less than 1% to the overall post-yield stiffness ratio and were neglected in this study.

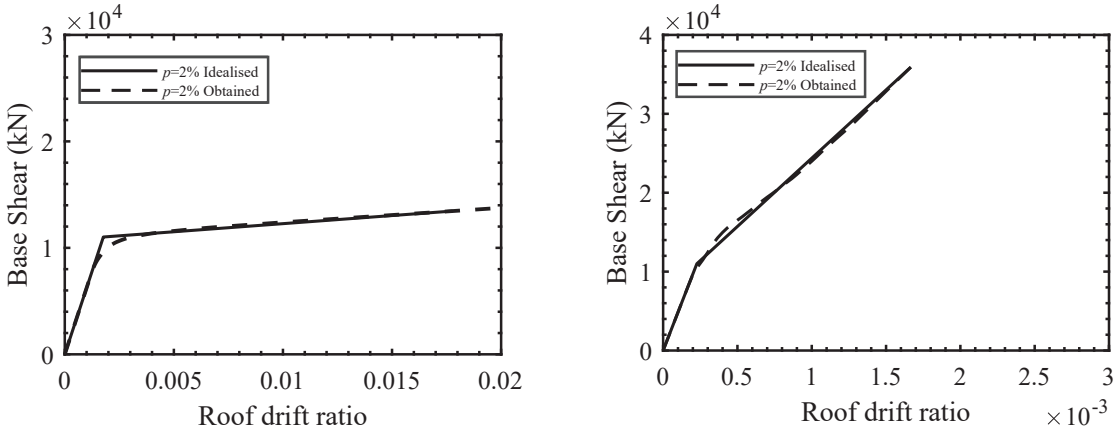

(a) First mode (b) Second mode

Figure 6-29: Modal pushover curves and idealisation of structural response

Both the combined models were subjected to three levels of earthquake -SLE, DBE and MCE resulting in different ductility ratios as given in Tables 6.22-6.23. The Roof-1 model is labelled as 'R1' and the Roof-2 model has been labelled as 'R2'. As both the seismic demand and reduction factors are large, the roof displacement ductility factors obtained from the first mode were about 6.6 for the DBE level. The second mode had a significant contribution to damping as well. The achieved damping, the shift in the substructure secant periods and reduction in acceleration was larger than that observed for the second mode in 6-storey 60m models. As a result, the ratio of secant periods of the substructures T_{eq1}/T_{eq2} has increased to around 6 for DBE level and 7 for the MCE levels.

Table 6.22: $p = 2\%$ models: Peak substructure First-mode (T1) parameters

	h_{eq1}	K_{eq1}/K_1	D_h	R_d	R_a	μ_1	T_1	T_{eq1}	R1-T_R	R2-T_R
Model-A-SLE	0.08	0.73	0.88	1.03	0.75	1.35	1.50	1.75	0.56	0.82
Model-A-DBE	0.40	0.15	0.45	1.18	0.17	6.75	1.50	3.91	0.56	0.82
Model-A-MCE	0.44	0.09	0.43	1.42	0.13	10.12	1.50	4.92	0.56	0.82

Table 6.23: $p = 2\%$ models: Peak substructure Second-mode (T2) parameters

	h_{eq2}	K_{eq2}/K_2	D_h	R_d	R_a	μ_2	T_2	T_{eq2}	R1-T_R	R2-T_R
Model-A-SLE	0.05	1.00	1.00	1.00	1.00	1.00	0.48	0.48	0.56	0.82
Model-A-DBE	0.31	0.51	0.51	0.77	0.39	4.32	0.48	0.68	0.56	0.82
Model-A-MCE	0.37	0.46	0.47	0.74	0.34	6.48	0.48	0.72	0.56	0.82

6.4.4 Comparison of peak roof accelerations

The peak roof accelerations for the combined models listed in Tables 6.22-6.23 were calculated using the first and second mode amplification factors [1]. The period ratios were calculated using the elastic periods of the substructures. The proposed accelerations are compared with the mean NLRHA results in Figure 6-30. For comparison, results accounting only for the substructure T1 mode (${}_sA_{Heq1}$) with the corresponding roof amplification factors (F_{H1} and F_{V1}) are also shown and labelled 'T1' and for the substructure T2 mode (${}_sA_{Heq2}$) response obtained with the corresponding roof amplification factors (F_{H2} and F_{V2}) are also shown and labelled 'T2'.

Both models when subjected to the SLE level earthquakes present a response with the T1 mode and T2 mode contributing equally to the horizontal response and the T2 mode governing the vertical response. When subjected to the DBE level earthquakes, the T1 mode's contribution decreases further due to the increased additional damping. Therefore, the T1 mode exhibits a negligible roof response in both horizontal and vertical directions. The T2 modes with smaller ductility ratios and shorter period ratios have larger roof response (and amplification), and so become significant, even though participations are small. This trend is further accentuated at the MCE level, where the T2 mode dominates both horizontal and vertical responses (Figure 6-30).

The overall peak roof accelerations of the 150m models are smaller than those of the shorter spanned 60m models in the same post-yield stiffness range (Figure 6-19). However, the overall amplification of the roof is greater since the elastic period ratios ($R_{T2} = 0.86, 0.59$) are shorter than those of the 60m models ($R_{T2} = 1.75$). Even though the second mode has a high post-yield stiffness ratio, among the proposed R-factor approaches, Newmark's approach presents the closest response to the Kasai method. For DBE level and MCE level response, the horizontal amplification of the second mode is underestimated by the proposed amplifications. This horizontal amplification is mainly due to the governing higher substructure modes interaction like T2-O2, T2-O1, and T3-O2.5. Horizontal amplification is greater in the Roof-2 model than in the Roof-1 models, since the higher mode T3 period in Roof-2 is closer to O2.5 than the proximity of

modes O1 and T2 in Roof-1 (Table 6.20 and Figures 6-25-6-26). Note that the horizontal response of the T1 mode was conservative for the 150m linear substructures (as seen in Figure 4-6 $\alpha = 1/6$) and covered any mild amplification arising from the higher T2 or T3 modes. The errors in the higher modes are now prominent as the T1 mode's contribution to the horizontal response in nonlinear substructures with sufficient damping is much lower than in the corresponding linear substructures leading to large ratios of substructure secant periods ($T_{eq1}/T_{eq2} = 6$ at DBE level). This suggests that the accuracy of the proposed method in estimating the higher mode's horizontal amplification may decrease for models with large additional damping, leading to large ratios of substructure secant periods (T_{eq1}/T_{eq2}). Nevertheless, the vertical proposed responses are conservative and may be sufficient to compensate for the underestimation in the horizontal amplification. To summarise, the proposed equivalent static loads procedure conservatively estimates the vertical acceleration of long-span models even under MCE level excitation but may underestimate the horizontal amplification in the large ductility regimes of long-span flexible models with long secant periods ($T_{eq1} > 3s$ corresponding to $T_1 >= 1.5s$ and ductility μ_t>6).

Model	SLE	DBE	MCE
Roof-1	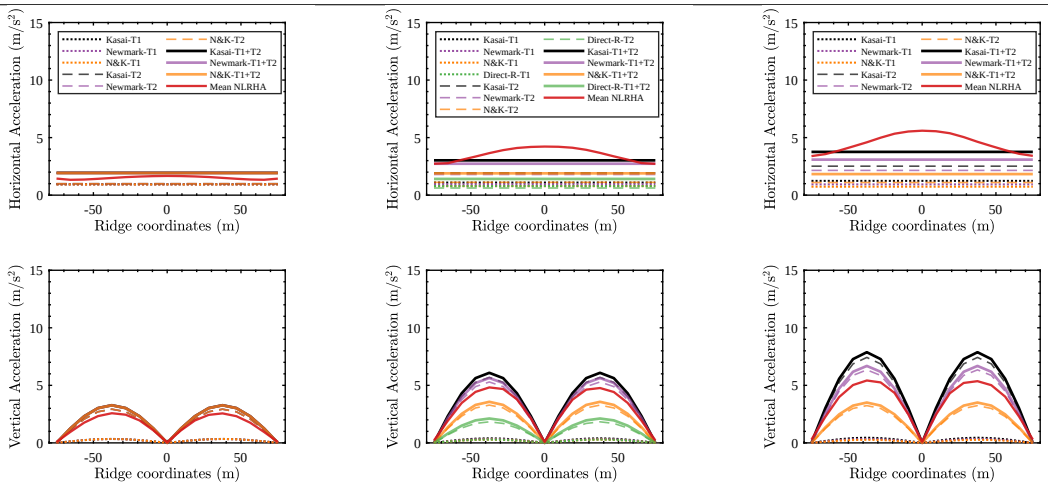		
Roof-2	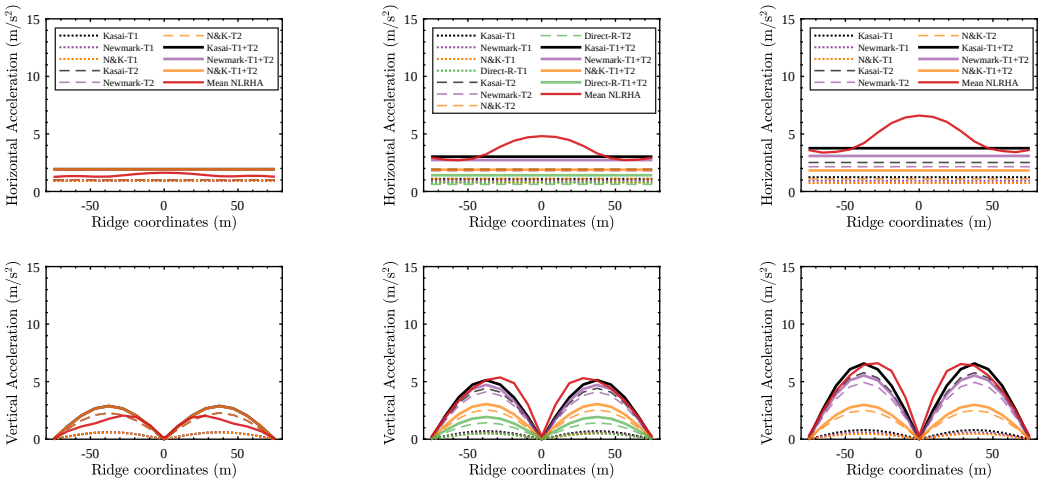		

Figure 6-30: Comparison of ridgeline accelerations of 150m models

6.4.5 Comparison of roof member forces

The proposed member forces obtained for the 150m models following the procedure outlined in Section 4.5.2 are compared in detail in Figures 6-32-6-33. The corresponding accuracies for each of the estimation methods have also been listed in Tables 6.24-6.25. Even though the horizontal amplification for the higher T2 mode was underestimated by the proposed equations, the vertical response was conservative, and as a result, the member responses for less than 20% of the roof members were underestimated by the Kasai method at the MCE level. The errors were slightly higher for the Newmark method as it underestimated 26% of the roof members' bending moments and about 20% of the members' axial forces. Krawlinkler's method was even more unconservative and is not recommended for estimation of response in the large ductility regimes or beyond the SLE level.

The overall accuracies of Kasai and Newmark method were found to be good and highly conservative for most members as the median response ratios at the MCE level were much more than 1 with ${}_{r}f = 1.75$ (defined in Section 4.5.2) for the Kasai method and ${}_{r}f = 1.5$ for the Newmark method as shown in Figure 6-31. The bending moments exhibited similar accuracies with response ratios ${}_{r}f = 1.76$ for the Kasai method and ${}_{r}f = 1.5$ for the Newmark method. This suggests that the simpler Newmark method that follows the R-factor approach is an efficient alternative to the iterative Kasai method for not only short-span as well as long-span roof structures with nonlinear substructures with post-yield stiffness of up to 2%.

Table 6.24: % of roof members with underestimation in axial forces

Roof members with $N_{static} < N_{NLRHA}$ (%)						
Model	Level	p	Kasai	Newmark	N&K	Direct-R
Roof-1	SLE	2	0.3	0.3	0.3	
Roof-1	DBE	2	5.8	9.6	70.5	100.0
Roof-1	MCE	2	7.2	14.3	100.0	
Roof-2	SLE	2	0.7	0.7	0.7	
Roof-2	DBE	2	8.7	13.9	47.9	99.3
Roof-2	MCE	2	9.9	20.4	89.5	

Table 6.25: % of roof members with underestimation in bending moment

Roof members with $M_{static} < M_{NLRHA}$ (%)						
Model	Level	p	Kasai	Newmark	N&K	Direct-R
Roof-1	SLE	2	0.3	0.3	0.3	
Roof-1	DBE	2	0.6	0.6	82.9	100.0
Roof-1	MCE	2	0.6	1.0	97.1	
Roof-2	SLE	2	3.8	3.8	4.0	
Roof-2	DBE	2	18.9	23.2	67.7	99.9
Roof-2	MCE	2	15.8	26.0	96.8	

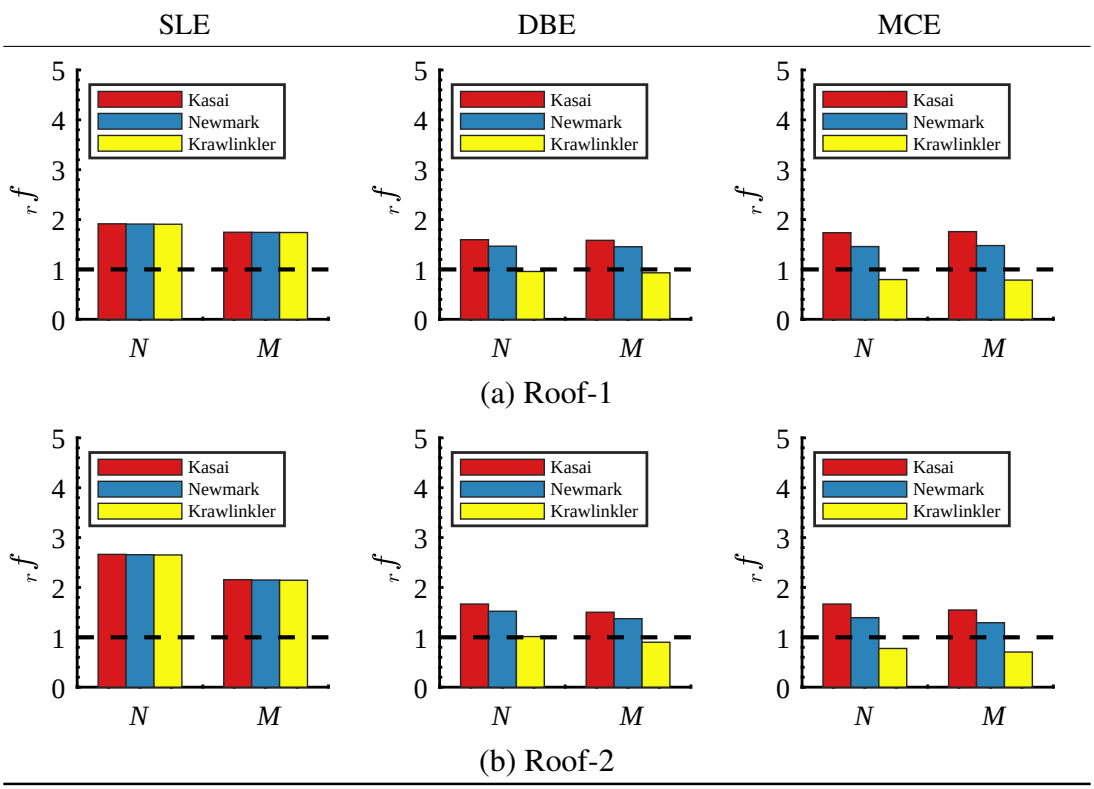

Figure 6-31: Six-storey 150m models: median response ratios

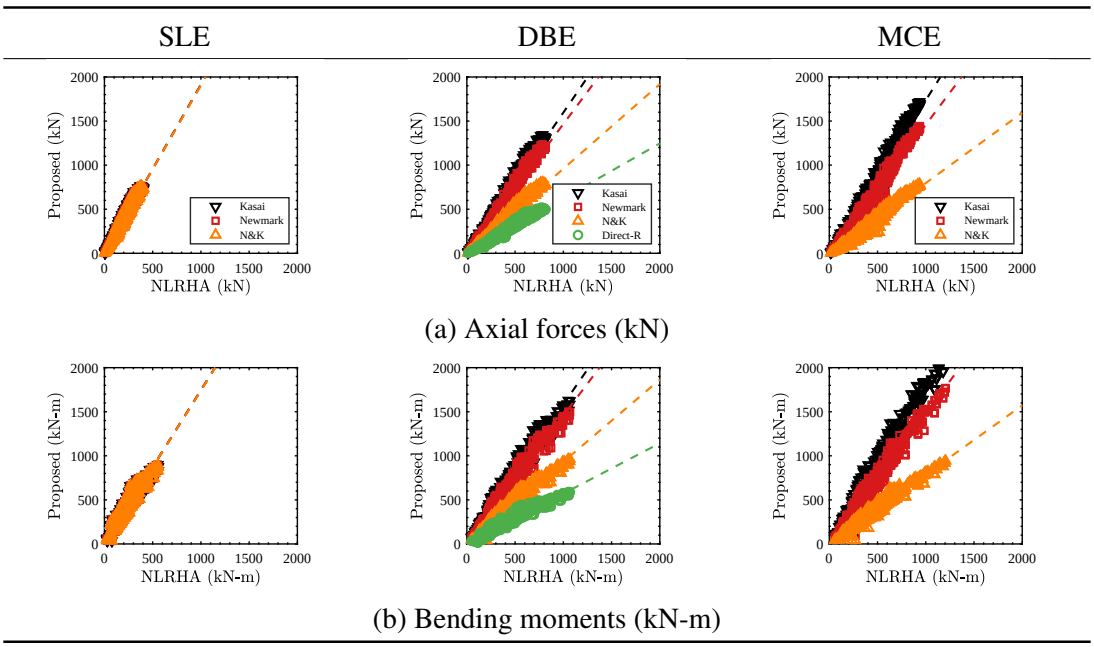

Figure 6-32: R1-150m model: Comparison of roof member forces

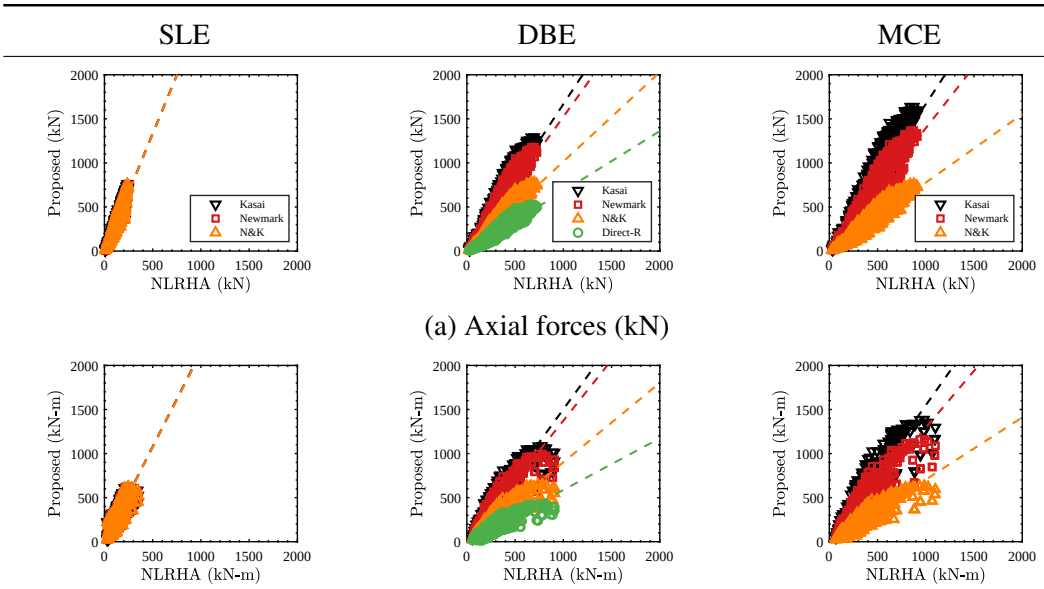

Figure 6-33: R2-150m model: Comparison of roof member forces

6.4.6 Estimation of double-layer member sizes from static results

After obtaining the seismic demand of the single-layer beams (N_S, M_S) of the roof using Equations 5.34 and 5.35, the demands of the top (N_{tc}) and bottom (N_{bc}) chords of the corresponding double-layer lattice may further be obtained approximately following the truss-beam analogy using Equations 6.3-6.4 and Figure 6-34, and adopt the same or reduced sections (around 1/5 [9]) for the diagonal/web members. As discussed in Sections 1.4.3 and 3.2.1, these formulas are meant to be used as a tool to estimate the approximate seismic demands for the initial sizing of the roof members only. For a final design check, it is recommended to use the double-layer model to confirm the strength against the force distribution throughout the roof plan.

The seismic demands obtained using Equations 6.3-6.4 are compared against the response of the top and bottom chords of the double layer 2d truss arch model (Figure 3-1) obtained from the results of static analysis using the equivalent static loads (computed for the L150-DL-3 (Roof-1) model in Section 6.4) in Figure 6-35. It may be observed that the estimates from Equations 6.3-6.4 are conservative and are more than the actual demands for both the top and bottom chords. Therefore, this method is a simple method to estimate the initial truss member sizes of the double-layer truss domed roof.

$$N_{tc} \approx N_S/2 - M_s/d \tag{6.3}$$

$$N_{bc} \approx N_S/2 + M_s/d \tag{6.4}$$

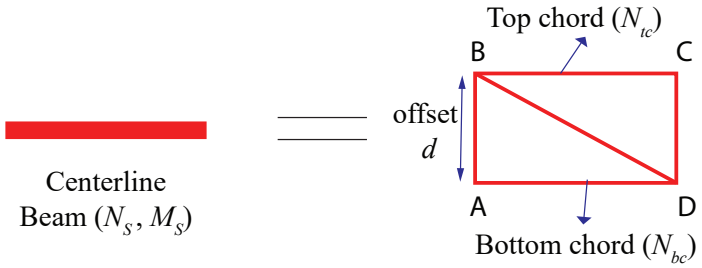

Figure 6-34: Estimating preliminary seismic demand of the double layer truss

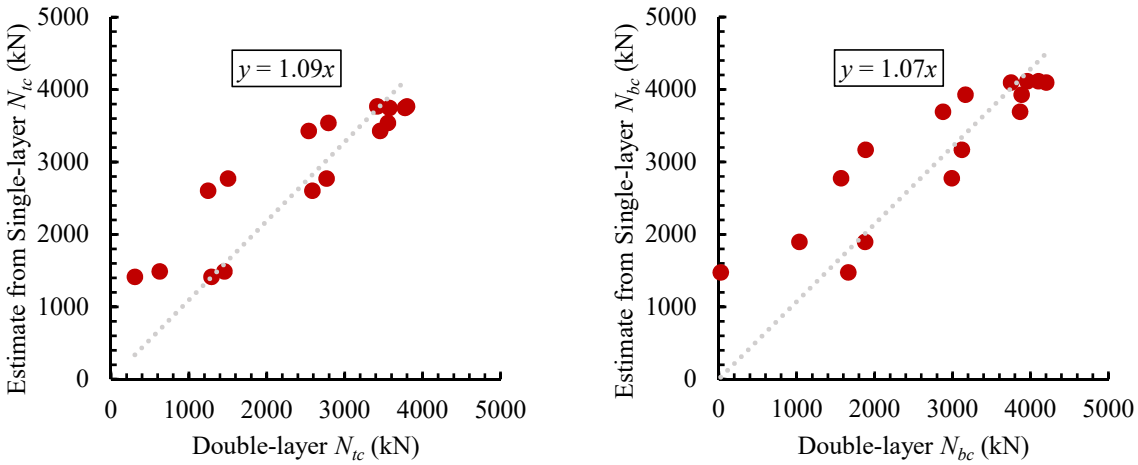

Figure 6-35: Comparison of top and bottom chords' estimate with the response

6.5 Validation of the proposed method for case-study models

Finally, this section confirms the applicability of the proposed methodology to the models investigated in detail for the case study in Chapter-2. The 150m analysis models (Figure 2-15) were designed to satisfy a design storey drift requirement of 1% under a Japanese level-2 earthquake, and the frame section and BRB sizes are described in Section 2.1. The roof response of four models- Spine-MF, Spine-P, BRB-MF and BRB-P models are estimated in this section using the R-factor approach and compared with the Kasai method. The member responses of the roofs are also validated using the mean responses obtained from the NLRHA of the models subjected to four spectrally matched waves (defined in Section 2.4 and Figure 2-8).

6.5.1 Nonlinear response of substructure

For each of the models, modal pushover analyses was conducted to obtain the first and second modal pushover curves and the initial base shear to roof displacement stiffness (K_{1i}) was obtained as shown in Figure 2-6 and the stiffnesses are listed in Table 2.5. For models with MRF, the first mode pushover curve has a high post-yield stiffness of 45% for the Spine-MF and 22% for the BRB-MF model (Figure 2-6). For models without MRF, the first mode pushover curves had low post-yield stiffness of 4% and 7%, respectively, for the Spine-P and BRB-P models (Figure 2-6). The Spine-MF and Spine-P exhibited elastic second mode behaviour as the top and bottom BRBs remain elastic when the substructure is pushed using a force distribution based on the second mode shape. The second mode pushover curves for the BRB-MF and BRB-P models were found to have a post-yield stiffness of around 20%. If compared to the Roof-1 combined models in Section 6.4 and Tables 6.22-6.23, the BRB-MF models are stiffer and exhibit higher post-yield stiffness.

The peak inelastic parameters for the substructure models obtained using the Kasai method are given in Tables 6.26-6.27. It was found that the ductility values obtained at the Japanese level-2 earthquake level for the models with MRF were lower, compared to the

models designed using a R-factor of 8 in Section 6.4 and Tables 6.22-6.23. Therefore, the ductility reduction factors were also smaller at $R_\mu \approx 3$. The Spine-P model exhibited the largest additional damping in the first mode at 24%. However, the second mode of the models with spine frames remained largely elastic leading to higher substructure responses. The models with BRBF exhibited yielding very similar to that in the first mode with additional damping reaching up to 16%.

Table 6.26: 150m case study models: Peak substructure First-mode (T1) parameters

	h_{eq1}	K_{eq1}/K_1	D_h	R_d	R_a	μ_1	T_1	T_{eq1}	T_R
Spine-MF	0.08	0.67	0.71	0.87	0.58	2.85	0.91	1.11	0.56
BRB-MF	0.08	0.64	0.72	0.90	0.57	2.07	0.91	1.14	0.56
Spine-P	0.24	0.30	0.46	0.85	0.25	4.44	1.18	2.17	0.56
BRB-P	0.14	0.47	0.58	0.85	0.40	2.70	1.14	1.67	0.56

Table 6.27: 150m case study models: Peak substructure Second-mode (T2) parameters

	h_{eq2}	K_{eq2}/K_2	D_h	R_d	R_a	μ_2	T_2	T_{eq2}	T_R
Spine-MF	0.02	1.00	1.00	1.00	1.00	1.00	0.31	0.31	0.56
BRB-MF	0.10	0.56	0.66	1.03	0.57	2.17	0.39	0.53	0.56
Spine-P	0.02	1.00	1.00	1.00	1.00	1.00	0.32	0.32	0.56
BRB-P	0.16	0.50	0.54	0.92	0.46	2.67	0.46	0.65	0.56

6.5.2 Comparison of peak roof accelerations

The peak roof accelerations for the combined models were calculated for each of the modes from the inelastic response ${}_sA_{Heqi}$ and the corresponding first and second mode amplification factors using the proposed method as discussed in Chapter-4 and outlined in Section 4.1.4. For the equivalent linearisation approach, the substructure's peak modal response ${}_sA_{Heqi}$ was computed considering the effect of both the period shift and the damping [5]. For the R-factor approach methods, the maximum inelastic accelerations of the substructure for each mode was obtained using Equation 5.10.

The proposed envelope of ridgeline *A-O-A'* (Figure 2-4(a)) roof accelerations are compared with the mean NLRHA results in Figure 6-36. The excitation of the O2 mode in the Spine-MF model is evident from the dual peaks appearing in the distribution of vertical acceleration. For models with damped spine frames, all proposed methods significantly overestimate the contributions of the T2 mode to the vertical response, as the vertical amplification factor F_{V2} is overestimated. The overestimation is less for the BRB models. Horizontal responses for all methods are captured accurately by all methods.

Although the post-yield stiffness is high in the first mode for the models with MRF, both the Newmark method and the Krawlinker method estimate the vertical peak responses with accuracies similar to the Kasai method, since the T2 modes' response largely governs the overall responses which are overestimated by the proposed methods. In the case of horizontal response, both T1 and T2 modes contribute to the response and therefore, the horizontal response for the Spine-MF and BRB-MF is slightly underestimated due to the underestimation in the T1 mode. As observed in the responses of the 2- and 6-storey BRBF models in Sections 6.2-6.4, the Kasai method conservatively estimates the response for all models.

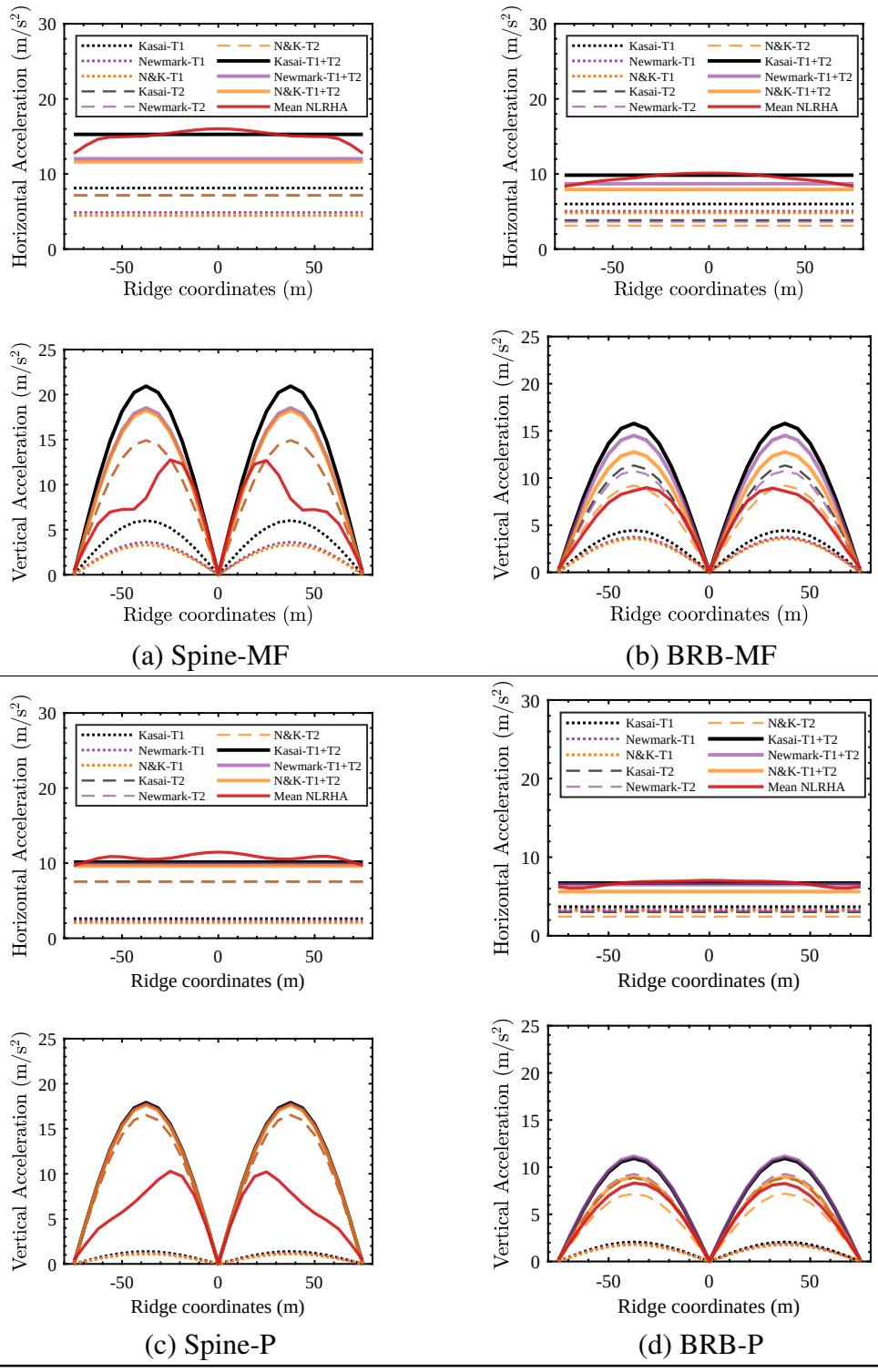

Figure 6-36: Level-2 response: Comparison of ridgeline accelerations of case-study models

6.5.3 Comparison of roof member forces

Table 6.28: % of roof members with underestimation in axial forces

Roof members with $N_{static} < N_{NLRHA}$ (%)				
Model	Level	Kasai	Newmark	N&K
Spine-MF	Level-2	1	9	10
BRB-MF	Level-2	3	6	10
Spine-P	Level-2	4	5	7
BRB-P	Level-2	8	8	23

Table 6.29: % of roof members with underestimation in bending moment

Roof members with $M_{static} < M_{NLRHA}$ (%)				
Model	Level	Kasai	Newmark	N&K
Spine-MF	Level-2	2	7	8
BRB-MF	Level-2	3	7	11
Spine-P	Level-2	2	2	2
BRB-P	Level-2	3	4	10

The proposed member forces obtained for the four models following the procedure outlined in Section 4.5.2 are compared in detail in Figure 6-38 and the median response ratios are compared in Figure 6-37. The corresponding accuracies for each of the estimation methods have also been listed in Tables 6.28-6.29. As the proposed vertical accelerations were much higher than those obtained from the NLRHA, the responses of the members were also generally conservative, with less than 10% of the roof members underestimated by the Kasai method and the Newmark method. The errors were slightly higher for the Krawlinkler method as it underestimated 11% of the bending moments of the roof members and about 20% of the axial forces of the members.

Despite the high post-yield stiffness in the Spine-MF and BRB-MF models, the general accuracy of the Kasai and Newmark methods was found to be very good and

highly conservative for most members, as the median response ratios for the Japanese Level-2 earthquakes were much higher than 1 with ${}_rf > 1.5$ (defined in Section 4.5.2) for the Kasai method and the Newmark method. The bending moments exhibited similar accuracies with response ratios ${}_rf = 1.9$ for the Kasai method and ${}_rf = 1.5$ for the Newmark method. This suggests that all the three methods from the R-factor approach are an efficient alternative to the iterative Kasai method for the long-span roof structures designed following the Japanese design practice with stiffer nonlinear substructures with higher first mode post yield stiffness in the medium ductility range of μ_{t1} up to 3.

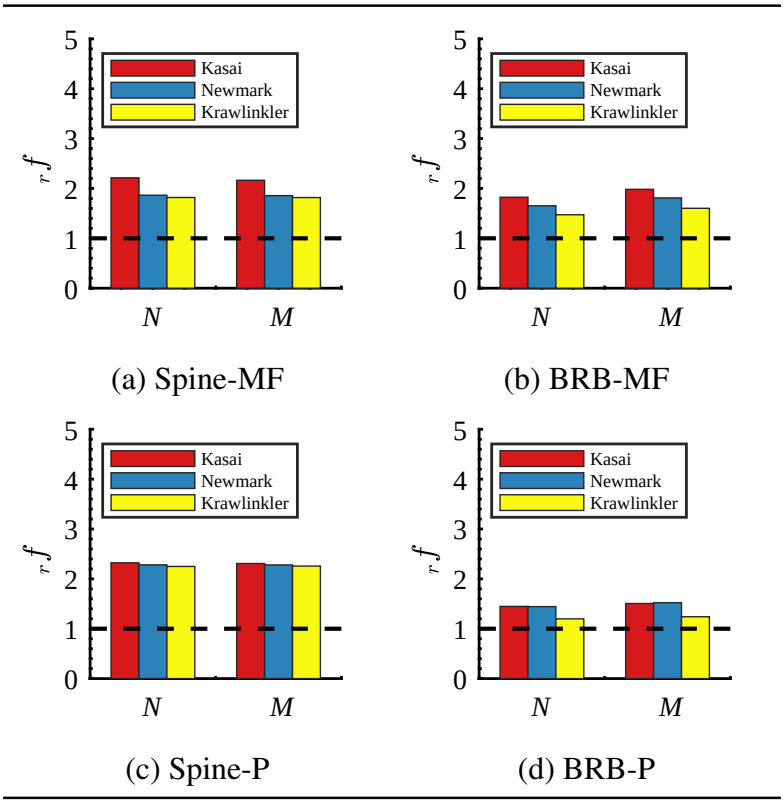

Figure 6-37: Case study models (Level-2): median response ratios

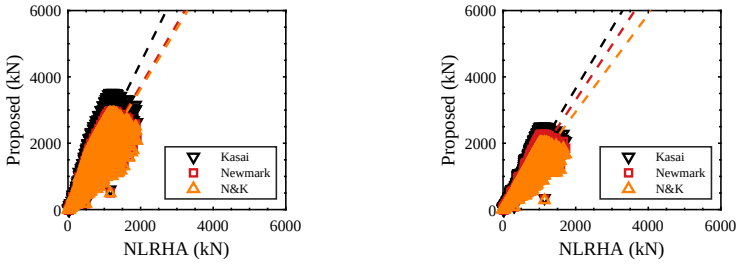

(a) Axial forces (kN)

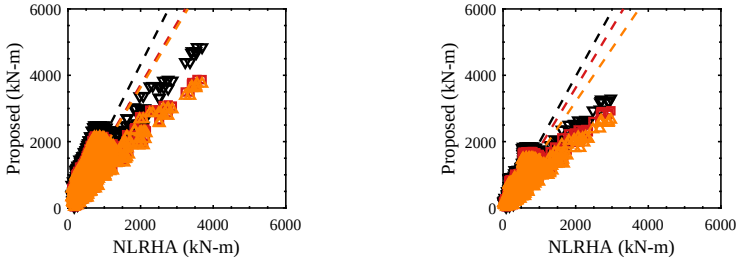

(b) Bending moment (kN-m)

(a) Spine-MF (b) BRB-MF

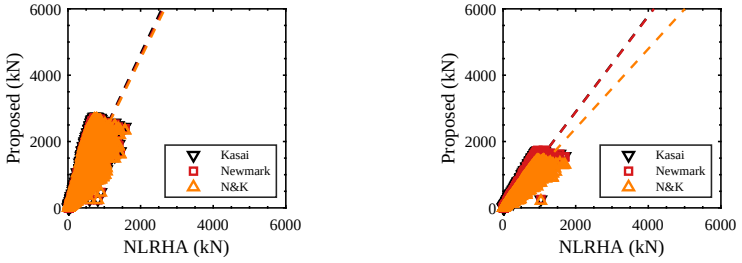

(a) Axial forces (kN)

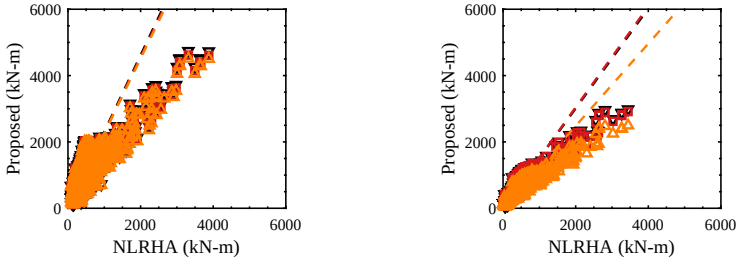

(b) Bending moment (kN-m)

(c) Spine-P (d) BRB-P

Figure 6-38: Level-2 response: Comparison of roof member forces

6.6 Extent of applicability of the proposed equivalent static loads

This section summarises the range of the models analysed and discusses the extent of applicability of the proposed equivalent static loads using the Kasai method following the equivalent linearisation approach.

6.6.1 Roof periods

The fundamental periods (T_R) of the roof models analysed lies in the range mathematically expressed as $0.2 \leq T_R \leq 0.8$ for roof spans ranging from 60m to 150m. It was observed that the proposed roof amplification factors were conservative in both the horizontal and vertical directions for all the models in the studied range with median response ratios well above 1. The magnitude of the roof excitation in long-span domes was also found to be significant despite the elongated natural periods (O1 mode). Throughout the studied range of spans, all asymmetric roof modes (O1, O2 and O2.5) were found to interact with the substructure depending on the proximity to the substructure modes.

6.6.2 Substructure secant period ratios

The summary of the secant periods of the substructure and their ratios for all models are shown in Figures 6-39-6-41. The secant periods (T_{eq1} (s)) of the substructures analysed lie in the range mathematically expressed as $0 \leq T_{eq1} \leq 6$ and their ratios lie in the range $2 \leq T_{eq1}/T_{eq2} \leq 7$.

In the case of nonlinear multistorey structures, in addition to the roof period ratios (R_{T1} and R_{T2}), the secant periods of the substructure (T_{eq1} and T_{eq2}) and their ratios (T_{eq1}/T_{eq2}) are important parameters that govern the peak substructure response. For example, a larger ratio of T_{eq1}/T_{eq2} indicates that the contribution of the substructure T1 mode may be much smaller than that of the T2 mode, compared to the response of the structure when no yielding has occurred. Consequently, the roof response from T1 mode decreases as the substructure period increases, and the contribution of the near-elastic T2

mode to the overall response increases in proportion.

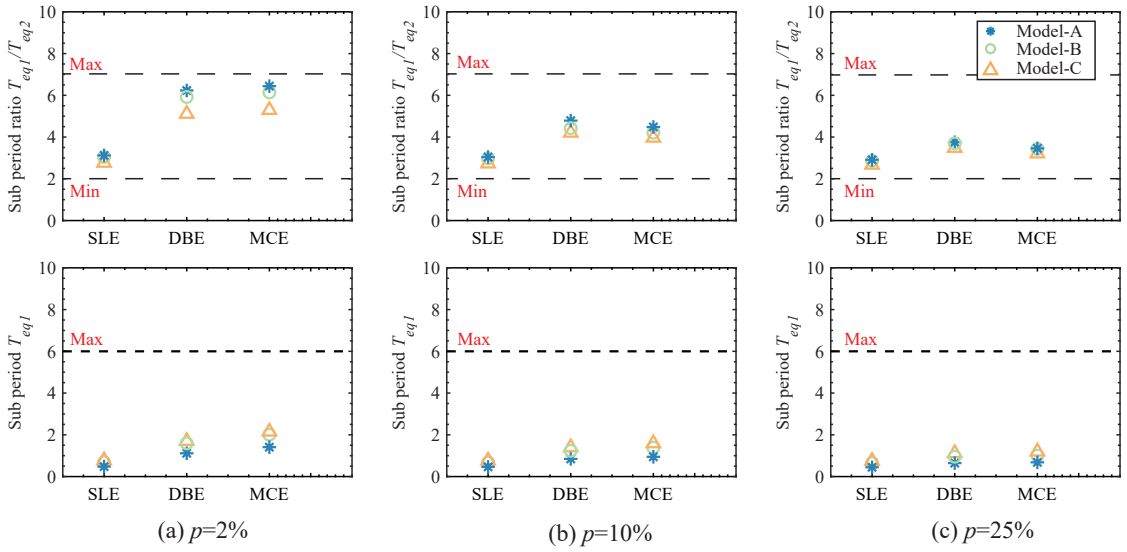

Figure 6-39: 2-storey 60m models: Range of substructure secant period and period ratios

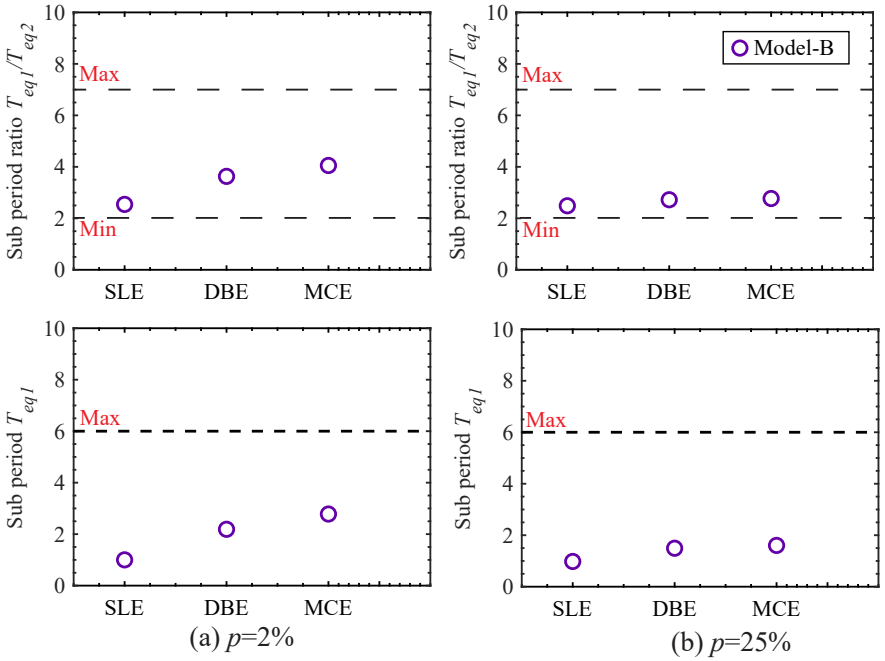

Figure 6-40: 6-storey 60m models: Range of substructure secant period and period ratios

For the models considered, the effect of *other higher* modes like the T3 or T4 modes were not prominent although some T3 effect was seen in the horizontal response of 150m models with high secant periods when $T_{eq1} \geq 3s$ corresponding to a $T_1 \geq 1.5s$). In such

cases, both T1 and T2 secant periods correspond to lowered spectral accelerations and even a mild horizontal amplification from the elastic higher substructure modes (like T3 and O2.5 interaction) may be underestimated by the proposed method. Nevertheless, the vertical responses were conservative throughout the range of models analysed and even in Roof-2 models with $T_{eq1} \geq 3s$, the median response ratios were found to be well over 1.

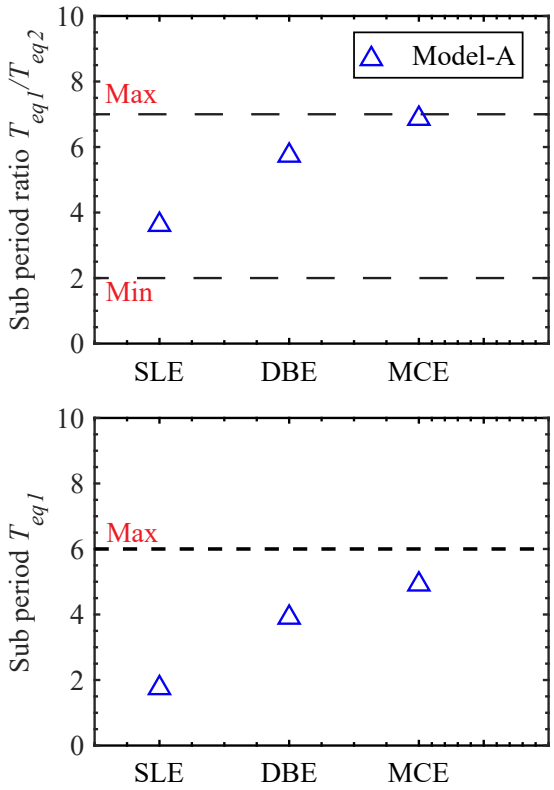

Figure 6-41: 150m models: Range of substructure secant period and period ratios

6.7 Conclusions

The following conclusions were drawn from this chapter.

1. The RSA based amplification factor approach proposed for elastic structures was extended for practical yielding BRBF multistorey substructures designed for a base shear using an *R*-factor of 8. It was observed that the peak inelastic roof response and the equivalent static loads were highly influenced by the post-yield stiffness (p) of the substructure, and so adopting the same *R*-factor (=8) for obtaining the inelastic force demands (as in the 'direct-R' method) severely underestimated the peak roof responses for models with $p > 2\%$.

2. For all (60m and 150m span) models analysed with multistorey substructures, the Newmark method was found to present the most conservative roof accelerations (and thereby the roof member forces) among the investigated methods based on the R-factor approach.

3. For all models with fundamental periods in the constant acceleration and post-yield stiffness of less than 10%, the Newmark method presented responses nearly equal to the Kasai method (based on the iterative equivalent linearisation approach) underestimating the member forces of less than 10% of the roof members at DBE (or Level-2) levels.

4. According to the results of the 2-storey models, the R-factor methods estimated the base shear and peak substructure accelerations with good accuracy for $p = 2\%$, with Newmark's method being the most conservative of all estimation methods in the short period range (or the constant acceleration range). As the post-yield stiffness ratio increased ($p = 25\%$), the Kasai method was found to be the most accurate if compared with the mean NLRHA response. For SLE level response (in low-ductility regimes), all the proposed methods were found to be equally accurate.

5. Kasai's equivalent linearisation method estimated the substructure response with accuracies very similar to the NLRHA for all the studied models. This method used

in combination with the proposed amplification factor approach is an efficient alternative to the NLRHA method to estimate a conservative envelope of the peak accelerations and the equivalent static loads for the preliminary design of the dome.

6. While multistorey structures exhibit significant higher mode response, for substructures with low (first-mode) post-yield stiffness ratios, Newmark's method in combination with the first and second mode amplification factors provides a conservative roof response with accuracies nearly equal to those of the iterative Kasai method. Therefore, for all structures with low post-yield stiffness ratios ($p <= 2\%$), it is recommended to adopt the simpler Newmark method in combination with the amplification factors to obtain the envelope of the peak roof response.

7. Equivalent static loads have been computed for domes with fundamental periods in the range expressed as $0.2s \leq T_R \leq 0.8s$ and BRBF multistorey substructures with fundamental periods in the range $0.4s \leq T_1 \leq 1.5s$ (with DBE level target global roof displacement ductility μ_{t1} reaching up to approximately 8) and post yield stiffness ratios of up to 25%. Although the amplification in the horizontal direction was underestimated by both Kasai and Newmark methods for long-span models with $T_1 = 1.5s$ in large ductility regions $\mu_{t1} > 6$, the median response ratios (using Kasai method) for all models in the studied range were well above 1, for all the three considered earthquake levels. The Newmark method also provided similar accuracy for models with lower post-yield stiffness. Therefore, the proposed equivalent static loads using amplification factors have been confirmed as an efficient alternative for the NLRHA for all models in the studied range.

References

[1] D. Nair, K. Ichihashi, Y. Terazawa, B. Sitler, and T. Takeuchi, "Higher mode effects of multistorey substructures on the seismic response of double-layered steel gridshell domes," *Engineering Structures*, vol. 243, p. 112 677, 2021.

[2] T. Takeuchi and A. Wada, *Buckling-restrained braces and applications*. Japan Society of Seismic Isolation, 2017.

[3] *Minimum Design Loads for Buildings and Other Structures*. ASCE Standard–ASCE/SEI 7–16: American Society of Civil Engineers (ASCE), 2016.

[4] J. Erochko, C. Christopoulos, R. Tremblay, and H. Choi, "Residual drift response of SMRFs and BRB frames in steel buildings designed according to ASCE 7-05," *Journal of Structural Engineering*, vol. 137, no. 5, pp. 589–599, 2011.

[5] D. Nair, Y. Terazawa, B. Sitler, and T. Takeuchi, "Seismic response of long-span domes supported by multi-storey substructures," *Journal of the IASS*, vol. 61, pp. 140–157, 2020.

[6] Pacific Earthquake Engineering Research Center, *PEER ground motion database*, 2020. [Online]. Available: https://ngawest2.berkeley.edu/.

[7] *Analysis reference manual for SAP2000, ETABS, SAFE and CSIBridge*. Computers and Structures, Inc., Berkeley, CA, USA, 2015.

[8] E. L. Wilson, *Three-dimensional static and dynamic analysis of structures*. Computers and Structures, 2002.

[9] T. Takeuchi, T. Ogawa, T. Kumagai, A. Nakama, and E. Sato, "Applicability of response evaluation method for lattice domes with substructures," *Journal of structural engineering. B*, no. 52, pp. 53–61, Mar. 2006, ISSN: 09108033.

Chapter 7

Conclusions

Contents

7.1 Summary and Conclusions

In this thesis, the complex seismic response interaction between multiple roof and substructure modes in domes with multistorey substructures was examined to develop equivalent static loads following the amplification factor approach, which may serve as a basis for integrating seismic demands in the preliminary design of gridshell roofs. Below are summaries and key findings from each chapter.

7.1.1 Chapter-1

In Chapter-1, the background and motivation behind this research was presented.

1. The literature review indicated that there are relatively few studies available for roofs with multistorey substructures. For linear gridshell structures, modal RSA using an appropriate combination rule accurately captured the complex dynamic characteristics. Equivalent static loads using amplification factors were found to be an efficient alternative for domes (verified for spans up to 60m) with linear single-storey substructures.

2. While there exist well-established response-reduction factors for design and estimation of the inelastic design spectra of conventional multistorey braced frames, their application to substructures of curved gridshell roofs had not yet been explored. Therefore, as neither reliable static load procedures nor realistic R-factors are available for such structural systems, the iterative time- and data-intensive NLRHA are often the only design route.

3. It was concluded that there was a need to develop effective yet simple formulations as equivalent static loads for incorporating seismic demands in the preliminary design of domed roofs with multistorey substructures, particularly in areas of high-seismic hazard, which formed the main objective of this research.

7.1.2 Chapter-2

In Chapter 2, the seismic response of a large-scale dome (150 m span) with multi-storey substructures was explored, which alternatively incorporated spine frames and buckling-restrained braces. The choice of the models were inspired from the preliminary substructure design of a recent project realised in Japan.

1. The magnitude of the roof excitation in long-span domes was significant despite the elongated natural periods. For substructures with higher modes lying on the constant acceleration region of the design spectrum, the higher modes may contribute significantly and may even govern the overall response of the roof. Therefore, it is important to consider the roof's higher modes as well that may combine with the substructure higher modes.

2. Adding spine and braced frames in the substructure proved to be effective in reducing the roof response. However, this was limited to the response derived from the substructure first mode. Incorporating a two segmented spine frame system in the substructure was found to be an effective response control strategy to reduce the response due to the substructure's higher mode.

3. Despite the reduced roof response associated with the fundamental substructure mode, the elastic higher substructure modes interacted with the roof's higher modes and notably amplified the response. This higher mode response was underestimated by the current AIJ (and IASS guidelines) equivalent static loads based on the substructure first mode and roof amplification factors. Based on this study, it was concluded that it is imperative to quantify the interaction between the higher mode of the substructure and the roof in order to improve the accuracy of the static loads.

7.1.3 Chapter-3

In Chapter-3, the roof-substructure interaction in single- and multistorey models was investigated by performing parametric studies on linear 60, 100 and 150m double-layered

domes featuring a range of substructure stiffness and roof-substructure mass ratios using response spectrum analysis.

1. The seismic response of domes with multistorey substructures may be interpreted as a combination of response from both T1-roof and T2-roof interactions. The relative contributions of the substructure T1 and T2 modes to the combined acceleration response were investigated using a dominance response ratio, which includes both the spectral acceleration and mass participation effects.

2. For roofs with multistorey substructures, the dominant modes were found to depend on the proximity of the dominant substructure and the roof mode, with the substructure modes T1 and T2 typically combining with the nearest roof mode. The vertical response of flexible multistorey substructures (α=1/6 and α=1/36) were governed by the O1 mode of the roof that interacts with the T1 and T2 modes, while the higher modes of the roof remained unexcited. Stiffer multistorey substructures (α=1 and α=6) with the T1 and T2 modes close to the O1 roof mode exhibit complex roof-substructure interaction, with significant excitation of the O1, O2, O2.5, and I roof modes.

3. The influence of the T2 mode on the vertical acceleration response was found to peak when the period ratio $R_{T2} \approx 1$ as T2 dominance ratio DR_2 peaked at almost 100% and became negligible for longer periods of substructure with $R_{T2} >> 2$. The contribution to the horizontal response was investigated using horizontal dominance ratios that were more evenly divided between the T1 and T2 modes for longer period substructures, while the T1-roof interaction dominated for stiff substructures with $R_{T1} < 2$, achieving a horizontal T1 dominance ratio of $DR_1 > 80\%$.

4. Single-storey substructures and first-mode dominated substructures (with mass participation from T1 mode of over 90%) may obtain the peak roof response solely from the first substructure mode (the current IASS/AIJ method), but neglecting higher substructure modes underestimated the peak horizontal and vertical accelerations for all the multistorey substructures with a significant T2 mode ($\alpha < 6$ or $R_{T1} > 1.5$).

7.1.4 Chapter-4

In Chapter-4, amplification factors were proposed to quantify the additional response from the higher substructure mode (the T2 mode) coupled with the roof modes, to develop a generalised equivalent static design procedure for domes with multistorey substructures.

1. The vertical response amplification was found to be sensitive to the period ratios of the T1 and T2 modes to the roof O1 mode (R_{T1} and R_{T2}) with peak amplification from the T2 mode F_{V2} reaching up to a value of 3 as R_{T2} approached 1. The horizontal response amplification (F_H) was primarily a result of the substructure T1 interacting with the roof's predominant modes (F_{H1}) while the peak amplification contribution from T2 mode towards the horizontal response (F_{H2}) was found to be around 1.

2. The greatest benefit from the proposed methodology was for substructures with dominant T2 modes ($1/6 <= \alpha <= 1$ in the period range $0.2 < R_{T2} < 2$)), with the percentage of roof members with underestimated forces up to around 100% when considering only the T1 mode reducing to just 1% when considering both T1+T2 modes. The method saw the least improvement for stiffer first mode dominated substructures (α=6), where the T1 mode's contribution alone produced a conservative response estimate leading to similar accuracy even after considering the T2 mode.

7.1.5 Chapter-5

In Chapter-5, the RSA-based amplification factor approach proposed for elastic structures was extended to single-storey buckling restrained braced frames with varying post-yield stiffness by investigating the applicability and effectiveness of two formulations of ductility-based reduction factors in estimating the peak inelastic accelerations of the substructure.

1. Kasai's equivalent linearisation method estimated the substructure response with accuracies very similar to the NLRHA for all the studied models. This method used in combination with the proposed amplification factor approach is an efficient alternative

to the NLRHA method to estimate a conservative envelope of the peak accelerations and the equivalent static loads for the preliminary design of the dome.

2. Both the R-factor methods- 'Newmark' and 'Nassar & Krawlinkler' present equivalent static loads with excellent accuracy for single-storey structures with $p <= 2\%$ and periods in the constant-velocity region as less than 5% of the roof members had underestimated member responses. For $p > 2\%$, these methods are unconservative due to the underlying assumptions, and so the Kasai method is recommended.

3. The Newmark method formulated based on the equal energy rule was found to have the best accuracy among the R-factor approaches for short-period structures with fundamental periods in the constant acceleration region and is recommended for models with post-yield stiffness of up to 10% ($p <= 10\%$).

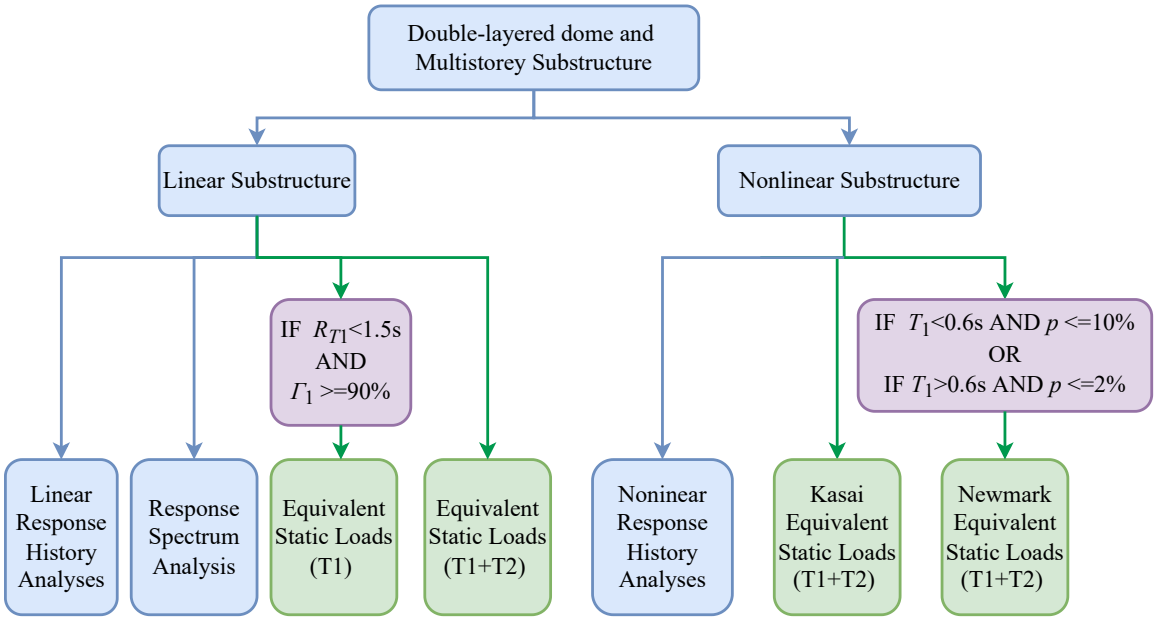

Figure 7-1: Seismic response estimation methods for domes with multistorey substructures (Proposed methods labelled in green boxes)

7.1.6 Chapter-6

In Chapter-6, the accuracies of the proposed R-factor approach were investigated for 60m and 150m multistorey BRBFs, and the scope of application of the proposed methodology

was discussed (summarised in Figure 7-1).

1. Although multi-story structures exhibit significantly higher mode response, for all (60m and 150m span) models analysed with multistorey substructures, the Newmark method was found to present the most conservative roof accelerations (and thereby the seismic force demand of roof members) among the investigated methods based on the R-factor approach.

2. Equivalent static loads have been computed for domes with fundamental periods in the range expressed as $0.2s \leq T_R \leq 0.8s$ and BRBF multistorey substructures with fundamental periods in the range $0.4s \leq T_1 \leq 1.5s$ (with DBE level target global roof displacement ductility μ_{t1} reaching up to approximately 8) and post-yield stiffness ratios of up to 25%. Although the amplification in the horizontal direction was underestimated by both Kasai and Newmark methods for long-span models with $T_1 = 1.5s$ in large ductility regions $\mu_{t1} > 6$, the median response ratios (using Kasai method) for all models in the studied range were well above 1, for all the three considered earthquake levels. The Newmark method also provided similar accuracy for models with lower post-yield stiffness. Therefore, the proposed equivalent static loads using amplification factors have been confirmed (Figure 7-1) as an efficient alternative to NLRHA for all models in the range studied.

List of Publications

1. Journal articles

The following journal articles were published in conjunction with this thesis. The organisation of this thesis follows the order of the publications, and the related chapters are listed alongside the articles.

Article Details	Related Chapter
1. **Nair D**, Terazawa Y, Sitler B, Takeuchi T, "Seismic Response of Long-Span Domes Supported by Multi-Storey Substructures", *Journal of the International Association for Shell and Spatial Structures*, 61.2 (2020): 140-157.	Chapter-2
2. **Nair D**, Ichihashi K, Terazawa Y, Sitler B, Takeuchi T, " Higher mode effects of multistorey substructures on the seismic response of double-layered steel gridshell domes", *Engineering Structures* 243 (2021): 112677.	Chapter-3 Chapter-4
3. Terazawa Y, **Nair D**, Ichihashi K, Terazawa Y, Takeuchi T, "Equivalent static seismic load for middle to large span latticed domes considering roof antisymmetric mode amplified by substructure second mode", *Journal of Structural and Construction Engineering (in Japanese)* 87.792 (2022): 194-204.	Chapter-3
4. **Nair D**, Terazawa Y, Takeuchi T, "Equivalent static loads for double-layered domes supported by multistorey buckling-restrained braced frames", *International Journal of Space Structures* (2022): 1097834.	Chapter-5 Chapter-6

2. International conference and symposia papers

The following articles were presented in international conferences and symposia.

[1] Nair, Deepshikha, et al. "Influence of roof-substructure interaction on the seismic response of double-layered long-span domes" *Proceedings of IASS Annual Symposia. Vol. 2020/21*, 2021.

[2] Nair, Deepshikha, et al. "Seismic Response Characteristics of long-span domes: Roof-substructure interaction." 2020 17WCEE Proceedings 2, 2020.

[3] Nair, Deepshikha, et al. "Seismic Response Evaluation of Long-span Domes Supported by Multi-storey Substructures Incorporating Spine Frames." *Proceedings of IASS Annual Symposia. Vol. 2019. No. 21,* 2019.

[4] Nair, Deepshikha, et al. "Equivalent static loads for design of long-span domes supported by multistorey substructures", *Proceedings of the PSSC 2019*, 2019.

[5] Nair, Deepshikha, et al. "Equivalent static loads for design of long-span domes incorporating higher mode effects", *Proceedings of the 6th Joint Workshop between Tokyo Tech & Tongji*, 2019.